MIXTURE FORMATION IN A PARTIALLY STRATIFIED CHARGE DIRECTLY INJECTED NATURAL GAS ENGINE

by

MALCOLM SHIELD

Master of Engineering (Hons.), Imperial College, University of London, 2003

A THESIS SUBMITTED IN PARTIAL FULFILLMENT OF
THE REQUIREMENTS FOR THE DEGREE OF

DOCTOR OF PHILOSOPHY

in

THE FACULTY OF GRADUATE STUDIES

(Mechanical Engineering)

THE UNIVERSITY OF BRITISH COLUMBIA

(Vancouver)

October 2011

ABSTRACT

A rapid compression machine was redesigned to allow the use of acetone UV laser diagnostics to investigate the mixture distribution that results from the injection of a methane partially stratified charge (PSC) and direct injection (DI) jet. A central composite test matrix was used to investigate the effect of relative injection timing and bulk charge air-fuel ratio upon the mixture distribution. Comparison was made between the distribution that resulted from a capillary injected PSC charge and a bespoke 'sparkplug insert' injected charge.

The capillary injected PSC jet was found to preserve a jet-like structure despite its interaction with the direct injection jet, while the effect of the DI jet upon the insert injected fuel was to encourage coalescence of the jets to form a largely homogeneous mixture at the point of injection and near the leading edge of the DI jet. The DI jet, with a weak bulk charge, served to reduce the fluctuations in relative air-fuel ratio compared to PSC injection into air; while the insert injected PSC charge exhibited increased fluctuation levels with advanced relative injection timing. The improved ignition of a partially stratified charge from the introduction of a weak bulk charge had been presumed to work through reductions in fuel concentration gradients, however the findings of the this work suggest that this works in unison with a decrease in fuel concentration fluctuations that increases ignition efficacy. The insert injected PSC fuel demonstrates scalar dissipation rates that are potentially too low to provide robust enough combustion for a viable partially stratified charge approach. The PSC insert engenders more mixing than a capillary injected PSC, but penetrates the DI jet less well. In all cases, and throughout the region of the interaction, there exists a finite probability of encountering pure fuel or the bulk fuel concentration that suggests mixing driven by engulfment rather than entrainment. The PSC 'sparkplug' insert offers better opportunity for mixing than the capillary injection and using a stochastic design approach should be pursued further to improve the performance of partially stratified charge combustion for natural gas engines.

TABLE OF CONTENTS

LIST OF TABLES

LIST OF FIGURES

LIST OF SYMBOLS & ABBREVAIATIONS

Nomenclature: Roman

B	Bayesian entropy	P	data 95% confidence interval
B_0	exit buoyancy	$P_a\,p_a$	ambient pressure
C	concentration	P_r	pressure ratio
c	concentration	Q	volume flux / normalising co-ordinate
$\bar{c}$	mean concentration		
$\bar{c}_0$	exit concentration	r_c	volume (compression) ratio
$\tilde{c}$	r.m.s. concentration	R	gas constant / Pearson product moment
$\tilde{c}_c$	centre-line r.m.s. concentration	r	radius
d	diameter	r_0	exit radius
$\mathscr{D}$	binary diffusion coefficient	s	solid angle
d	diameter	S_0	singlet ground state
d_e	equivalent diameter	S_f	fluorescent intensity
d_{ps}	pseudo-diameter	S_1	first excited singlet state
f	mixture fraction	sr	steridian
f_c	centre-line mixture fraction	T_1	first excited triplet state
g	gravity	u	(radial) velocity
g'	reduced gravity	u'	radial velocity fluctuation
h	Plank's constant	u_t	turbulent velocity
H	entropy	$\bar{u}$	mean radial velocity
k	kinetic energy	$\tilde{u}_c$	centre-line radial r.m.s. velocity
k_{jc}	jet constant for concentration	$\overline{u'^2}$	r.m.s. radial velocity fluctuation
k_{jw}	jet constant for velocity	w	axial velocity
K_s	mass flow rate constant	w'	axial velocity fluctuation
$\bar{k}^2$	mean kinetic energy squared	$\overline{w}_0$	mean exit velocity
$\mathscr{L}$	largest eddy lengthscale	$\overline{w}_c$	mean centre-line velocity
l_I	integral length-scale	$\overline{w'^2}$	r.m.s. axial velocity fluctuation
l_m	momentum buoyancy ratio length scale	x	design space variable
M_0	exit momentum	Y	mass fraction
$\dot{m}$	mass flow rate	z	axial co-ordinate
$\dot{M}_0$	exit mass flow rate	z^*	dimensionless axial co-ordinate
N_i	number of incident photons	Z_t	jet penetration

Nomenclature: Greek

α	diffusivity	μ	dynamic viscosity
α_e	entrainment velocity	μ	population mean
α_T	turbulent diffusivity	μ_{eff}	effective viscosity
Γ	jet penetration constant	v	kinematic viscosity
$\Delta\theta_c$	combustion duration	ξ	experimental variable
Δv	frequency shift (in wavenumber)	ρ_0	exit density
ε	turbulent kinetic energy dissipation rate	ρ_a	ambient density
η	dimensionless radial co-ordinate,	σ	population standard deviation
η	Kolomogorov lengthscale	τ	timescale
κ	Kleinstein decay constant	τ_I	integral time-scale
λ	relative air fuel ratio	τ_k	Kolomogorov time-scale
λ	profile width ratio	Φ	equivalence ratio
λ	wavelength	χ	scalar dissipation rate
λ	relative fuel-air-ratio		

Abbreviations

AC	alternating current	nmHC	non-methyl hydrocarbon
ATDC	after top dead centre	NG	natural gas
BMEP	break mean effective pressure	NO_x	oxides of nitrogen
bsfc	break specific fuel consumption	OHD-RIKES	optically heterodyned Raman induced Kerr effect spectroscopy
BTDC	before top dead centre	PAH	polyaromatic hydrocarbon
CAD	crank angle degrees	PAN	peroxyacetyl nitrate
CARB	California Air Resources Board	PARS	photoacoustic Raman spectroscopy
CARS	coherent anti-Raman scattering	PFC	perflurocarbon
CCD	charge coupled device	PIV	particle image velocimetry
CI	compression ignition	PM	particulate matter
$CI_{95\%}$	95% confidence interval	PMMA	polymethylmethacrylate (acrylic)
CNG	compressed natural gas	ppm	parts per million
CO	carbon monoxide	Pr	Prandtl number
CoV	coefficient of variation	PSC	partially stratified charge
CSRS	Stokes-shifted Raman scattering	PWM	pulse width modulation
DC	direct current	R&D	research & development
DI	direct injection	RC	resistor-capacitor
DISC	direct injection stratified charge	RCARS	rotational-CARS
EGR	exhaust gas recirculation	RCM	rapid compression machine
FAR	fuel-air-ratio	Re	Reynolds number
FWHM	full width half maximum	RELIEF	Raman excitation plus laser induced electronic fluorescence
GDI	gasoline direct injection	RFAR	relative fuel air ratio
HC	hydrocarbon	Ri	Richardson number
HCCI	homogeneous charge compression ignition	RIKES	Raman-induced Kerr effect spectroscopy
HFC	hydrofluorcarbon	RON	research octane number
HHV	higher heating value	RPV	reaction progress variable
HRR	heat release rate	Sc	Schmidt number
IMEP	indicated mean effective pressure	SI	spark ignition
IPCC	Intergovernmental Panel on Climate Change	SNR	signal-to-noise ratio
KrF	krypton-fluorine (laser)	SRGS	stimulated Raman gain spectroscopy
LDA	laser Doppler anemometry	SRLS	stimulated Raman loss spectroscopy
Le	Lewis number	SRS	spontaneous Raman spectroscopy
LIF	laser induced fluorescence	TTL	transistor transistor logic
M	third body (chemical reactions)	UHC	unburnt hydrocarbon
MBT	mean timing for best torque	UV	ultra violet
MW	molecular weight	VOC	volatile organic compound
Nd:YAG	neodymium-doped yttrium aluminium garnet	VVT	variable valve timing
		w.r.t.	with respect to

ACKNNOWLEDGEMENTS

It is a mistake to suppose that men succeed through success; they much more often succeed through failures. Precept, study, advice and example could never have taught them so well as failure has done.

Samuel Smiles, 1859

Chapter 1
INTRODUCTION

1•1 INTRODUCTION

This opening chapter serves only to put the rest of the manuscript in context. The greater need for research into improved energy efficiency is presented, with an emphasis on the need for more efficient and cleaner road transport. A technology to facilitate exactly these is outlined- that of partially stratified charge combustion. An enhanced understanding of this technology and its potential integration into a direct injection engine are sought through the current laser diagnostics study, the aims of which are made explicit with a clear and measureable set of objectives. The chapter concludes with an outline of the dissertation structure.

1▪2 THE NEED

Energy is at the very core of society, particularly those societies which form the countries of the OECD[1]. The primary sources of energy open to us, as a race, are few: solar, nuclear and fossil derived; any other 'sources', including all 'renewables', can be tied back to these primary sources. Currently fossil fuels account for 80% of world energy demand (which totals 130-140*GWh* annually), *cf. Figure 1-1*, resulting in anthropogenic CO_2 emissions of 29 *Gt/yr* [1].
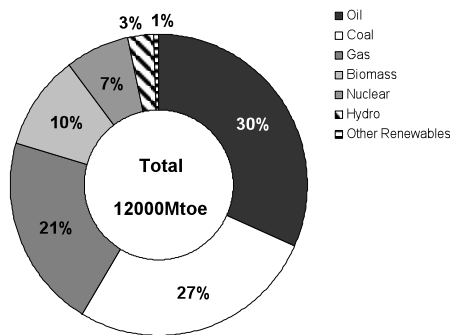
Figure 1-1 World Energy Consumption by Source, after [2].

Transport accounts for 23% of these emissions [1] and uses 61% of all produced oil, where gasoline avgas and diesel (including fuel bunker) account for 26%, 6% and 29% respectively [3]. Transport has been wedded to oil since the demise of coal; however, climate change and the scourge of urban pollution are forcing changes upon road transport. Rail, marine and air transport, although expected to improve, are not under the same pressures. World transport demand is set to grow by 45% by 2030 [2] and will account for three-quarters of total oil consumption increase [2]. Only a small fraction of this growth is expected to come from the OECD, *cf. Figure 1-2*.
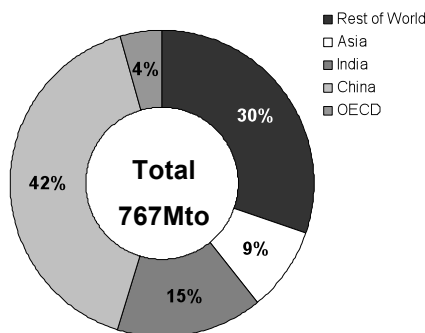
Figure 1-2 Energy Growth Due to Increased Transport Demand by Region 2006-2030, after [2].

---

[1] Organisation for Economic Co-operation and Development

Economic growth and improvement of the living standards are inexorably linked to increased energy demand, which until recently has been made with scant regard for the future, let alone regard for a sustainable future. Car consumers are their own fiduciaries and have forced the auto-industry to levels of efficiency and end-product performance which are the envy of most other manufacturers. Customer expectation will not support a move away from these standards in the name of pollution reduction, climate mitigation or sustainability. The International Energy Agency proposes in their *BLUE Map* scenario a cut in emissions of 50% (based on 2005 values) by 2050 to stabilise atmospheric CO_2 at 450-520*ppm*. These gains are to come from a range of the approaches, though it is the Second Generation transport solutions which must satisfy the most demanding consumers while addressing the emissions needs of years to come.

The technology to achieve these reductions is under development, some of which are nearing commercialization. Hybrid-electric cars are now widely available; and there is renewed vigour from Ford (Focus RV), Nissan (Leaf), Mitsubishi (MiEV), Subaru (G4e), Volvo (C30 electric) and Tesla (Roadster) in fully electric vehicles which Deutsche-Bank believe [3] to be the 'game changing technology' that will spell the end for oil and gas. Biofuels offer promise, although their exact benefit strongly depends on their nature: sugar-cane and corn-derived ethanol are not the same entity with respect to their carbon footprint. The touted hydrogen economy, the elixir of the sustainably growing economy, is still decades away from being realised and suffers a significant problem in that hydrogen is not an energy source but an energy carrier and arguably, some claim, an inefficient one at that. Accepting this, hydrogen still offers the potential to meet the toughest targets of *BLUE Map*. In moving towards these targets, natural gas (NG) offers significant potential. Oil has a current reserve to production ratio of around 40 years, while NG offers 60 [4] reaching 130 years [2] if flaring and venting are curtailed. Further, increased production capacity is likely to swell the capacity margin to about 27% (compared to ~12% presently) [2]. The larger technical and commercial problems of distribution and onboard storage need still to be overcome if the the potential benefits of a move to NG-powered transport ar to be realised. Natural gas technology currently offers CO_2 reductions of ~20% compared to gasoline and provides a technological stepping stone towards hydrogen combustion. Setting aside the climatic benefits, natural gas offers, in the short term, the most significant route to consistently meeting emissions regulations (which as of 2009 also regulate CO_2 on a manufacturer fleet-wide basis in the USA). The targets to be met by the auto-manufacturers are outlined in *Table 1-1*, which summarizes an expansive and complex set of regulation for light duty vehicles (those up to about 3500 *kg*). Optimized natural gas engines can exploit the inherent cleanliness of gas to meet these standards with an ease arguably not available from the incremental steps being made on conventionally fuelled spark ignition (SI) and compression ignition (CI) engines.

Regulatory Standard	Pertaining to Model Year	Vehicle Type	NOx (mg/km)		CO (mg/km)		PM (mg/km)		nmHC (mg/km)		CH$_2$O (g/km)		CO$_2$ (g/km)	
			SI	CI	SI	CI	SI	CI	SI	CI	SI	CI	SI	CI
CARB[2] Low Emission Vehicle II [5]	2009 onwards	<3864kg	31	---	2100	---	6.25[3]	---	47	---	9.4	---	202[4]	---
Euro 5 [6]	2009-2014	<3500kg	82	280	2270	740	5	5	108[5]	---	---	---	---	---
Euro 6 [6]	2014 onwards	<1760kg	82	125	2270	740	5	5	108[5]	---	---	---	---	---

Table 1-1 Core Current and Proposed Emissions Standards for 'Light Duty Vehicle' Road Transport

Engine development trends are trying to bring together, into a common platform, the benefits of SI engines (low NO$_x$ and PM) and those of SI engines (low HC and CO). To meet emissions demands across the full operating envelope, future engine architecture is likely to be a combination of enhanced SI and CI technology, with further additions from technology like HCCI and partial stratification.

1▪3 THE DIRECTLY INJECTED PARTIALLY STRATIFIED CHARGE NATURAL GAS ENGINE

Striving for emissions reductions and efficiency improvements, the research group of Prof. R L Evans has studied and developed a partially stratified charge, PSC, combustion system for natural gas SI-ICE's [7]. The approach uses a modified spark plug to inject a small amount of fuel (about 5% *w/w* of the total charge) adjacent to the plug electrodes, so generating a mixture that is locally rich. The bulk cylinder charge then comprises an ultra-lean mixture that would not ignite if an unmodified sparkplug were used.
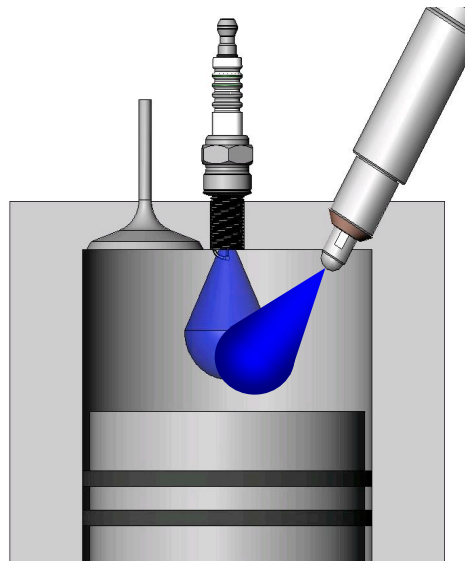
Figure 1-3 Partially Stratified Charge with Direct Injection.

---

[2] California Air Resources Board
[3] Beyond 80,000 *km* durability.
[4] Fleet-wide value, dropping to 133 *mg/km* by 2015.
[5] Total allowable tHC's 160 *mg/km*.

The modified sparkplug ignites the rich pilot charge which burns vigorously enough to inflame the remaining bulk charge. Load control may be achieved through varying the bulk charge air-to-fuel ratio, although the current work is concerned with an approach capable of providing still better control- direct injection. Direct injection, of any fuel, will provide volumetric efficiency gains and offers the potential of throttless operation and the elimination of pumping losses. The work herein is presented as a study of the fundamental mixture distribution that results from combining partial stratification with direct injection. It is intended as a step towards explaining the phenomenological effects reported by D. Gorby **[8]** in his study of DI-PSC in a single-cylinder research engine.

1▪4 AIMS

To Establish The Spatial Fuel Distribution Within The Cylinder of a Rapid Compression Machine Which Results From Both The Direct Injection & Partial Stratification of Natural Gas

The current study aims to understand the interaction of the partially stratified fuel jet with the jet generated by the direct injection of natural gas in a rapid compression machine. The study will achieve this through a detailed identification of the in-cylinder fuel distribution that results from the combined partial and direct-injection of fuel. The findings will be used to expand upon, and draw together, earlier work **[8]** on the utility of combined PSC-DI natural gas fuelling.

1▪5 OBJECTIVES

The objectives to support the stated aim of this study are:

- To quantitatively map the fuel air distribution which results from the partial- and direct-injection of natural gas into the cylinder of a rapid compression machine (RCM).
- To identify the level and extent of the fluctuations in fuel concentration at the location of the spark electrodes in the RCM.
- To understand the extent and role played by concentration gradients in the formation and ignition of the PSC fuel plume.
- To understand the differences in the fuel distribution generated by a bespoke partially stratified charge (PSC) spark-plug 'insert' and a capillary tube injected PSC jet.
- To understand the extent and implications of the inherent uncertainties associated with laser induced fluorescence imaging of acetone-doped natural gas jets in engine research.

1▪6 DISSERTATION STRUCTURE

Chapter 2 offers the reader background information on laminar and turbulent jets, pollutant formation in engines (with a discussion not limited to natural gas engines) and a basic understanding of natural gas engines. Laser diagnostics provide an expansive set of experimental techniques, each suited to providing slightly different information. *Chapter 3* provides an overview of these techniques and their application, while a more substantial justification and explanation of laser induced fluorescence is made in the second half. *Chapter 4* offers the reader the most salient details of the experimental apparatus used in the current study and outlines the experimental procedures used to obtain the results of *Chapters 6-8*. *Chapter 5* outlines the wide range of calibration experiments undertaken to ensure that the results of the LIF study are of the highest quality possible of the experimental apparatus. *Chapter 6* goes on to highlight some of the difficulties of establishing a quantitative LIF study for a highly underexpanded jet. Chapter 7 details the findings from a central composite test matrix that investigates the mixture distribution within the RCM cylinder for a range of relative direct injection injection timings and bulk charge air fuel ratios. The Chapter also establishes some basic behaviour of PSC injections made from a capillary tube and bespoke PSC 'insert'. *Chapter 8* repeats the same central composite test matrix to consider for a smaller region and in more detail the area where there is the interaction of the direct injection jet with that of the partially stratified charge produced from a capillary and contrasts it to that produced from the 'insert'. *Chapters 9 & 10* offer an assessment of the uncertainty in the experimental findings and some concluding remarks on the most important findings and recommended future work.

Appendices A-D present, respectively, the detailed redesign and design work undertaken to allow the RCM to be used for the current study, the timing and control hardware designed and implemented for the study, the relative air-fuel ratio probability density functions that resulted at a number of locations within the cylinder for the nine conditions of the test matrix and some fundamental information pertaining to the statistics used to assess the experimental results.

Chapter 2 GASEOUS JETS, GAS ENGINES & POLLUTANT EMISSIONS

2▪1 INTRODUCTION

Chapter 2 aims to bring the reader through what, at first sight, may appear to be three disparate themes, but which are in fact closely related. The first portion of the chapter establishes the fundamental principles of gaseous jets and interaction with their surroundings. It is this interaction and mixing which forms the ignitable mixture within a natural gas engine, and it is the various features and designs of natural gas engines which are considered in the central portion of this chapter. The chapter concludes with a discussion of the major pollutants to be expected from natural gas engines and the importance with respect to human health and climate change.

2▪2 TURBULENT GASEOUS JETS

The use of direct injection necessitates a fundamental understanding of turbulent free jets. The current discussion is limited to gaseous and submerged liquid jets. In general the flow from the nozzle of the injector used in the current work is fully turbulent ($Re \sim 5 \times 10^5$), choked and under-expanded [9].

2▪2▪1 INCOMPRESSIBLE JET STRUCTURE & DEVELOPMENT

Mass entrainment around the periphery of turbulent jets causes them to grow at, beyond the development region, a set half-angle. Early experimental work on this growth [10-13] confirmed the self-similarity first proposed for turbulent flows by Zel'Dovich [14], though there were still inconsistencies in the data. These centred on the failure of the turbulence intensities to attain self-similarity, and motivated the work of Wygnanski and Fiedler [15], whose hot-wire measurements provided the reference profiles for mean velocity, velocity fluctuation and turbulent stress for many years. Wygnanski & Fiedler's work, as in previous research, made use of a virtual origin (at a distance up- or downstream of the nozzle exit) to circumvent the problems of specifying an initial condition, and allowed the simple hyperbolic form for the axial velocity of *Eq. 2.1*

$$\frac{\overline{w}_0}{\overline{w}_c} = \frac{1}{k_{jw}}\left(\frac{z}{d_e}\right)$$

<div align="right">Eq. 2.1</div>

where d_e is the equivalent diameter first introduced by Thring & Newby [16] as $d(\rho_0/\rho_a)^{1/2}$ accounts for density differences between the jet and its surroundings. However, concerns about such treatment of the source were first raised by Baker [17] when he showed Wygnanski & Fiedler's formulation failed to preserve axial momentum. Using laser Doppler anemometry (LDA), Capp *et al.* [18] identified the source of the error as facility related, which motivated Schneider [19] to re-examine the theory of jets and show that the integrated momentum at any axial station is constant and equal to the rate at which it was added to the source. This extended understanding has led George [20] to revise the original implicit assumption of self-similarity, and assert that "the self-preserving state obtained [is] in fact … uniquely determined by the initial conditions.". That is, jets cannot 'forget' their origins and will always hold a unique, though small, dependence upon their initial (source) conditions, primarily Reynolds number and velocity profile. An extensive re-examination of the experimental literature by Carazzo *et al.* [21] supports George's work on local self-preservation, though it suggests that at large enough distances (where measurements have yet to be made) jets and plumes do indeed forget their initial condition and become fully self-similar with a non-Gaussian profile. Mi *et al.* [22] propose that before this state is achieved the source of local self-preservation is in the intermittent large-scale coherent structures of the flow. Close to the source such coherent structures have not formed, while at intermediate distances, large scale structures appear, but do

so only intermittently [23] and are still aware of their origin. Far enough away from the source these intermittent structures become permanent and self-similarity is obtained.

The evolution of velocity was shown by Wygnanski and Fiedler [15] to progress towards self-similarity in a stepwise fashion "since the energy is transferred from the mean motion directly to w' [axial] fluctuations, and only pressure-velocity-gradient correlations transfer the energy further to other components of the turbulent motion…", *i.e.* self-similarity can be obtained only after a balance is achieved in the mean flow velocity and its fluctuation. The turbulence of the jet is heavily anisotropic as far as 100 diameters downstream, and this longitudinal preference skews the energy towards the lower end of the turbulent energy spectrum and highlights the preferential transfer of energy from the mean motion to $\overline{w'^2}$ (mean axial velocity fluctuation) before $\overline{u'^2}$ (mean radial velocity fluctuation). The nature of the anisotropy may reasonably be expected to depend upon the initial conditions and so ultimately affect the form of the energy redistribution. This is contradicted somewhat by Papanicalaou & List [24] who find the mean and fluctuating velocities to converge to self-similarity at the same point about 50 diameters downstream. Consideration of the evolution of the Reynolds stresses, reduced gravity, and kinetic energy by George [20] support the assertion of a stepped, and unequal, progress amongst the flow variables. The nature of the energy transfer affects the rate at which self-similarity is asymptotically approached, with the nature of the energy transfer equations shown in [20] to be a function of the initial conditions, *i.e.* source Reynolds number. The evolution of the flow may vary with changes in the profile shape and/or with the relative width of the buoyancy and velocity profiles, *i.e.* the local turbulent Prandtl number (the ratio of viscous diffusion to thermal diffusion). The evolution is, in general, seen to progress from a situation which is momentum governed ($Pr_t \sim 1$) near the source to one in which vorticity transport dominates ($Pr_t \sim 0.5$) [21]. Across the jet, however, the energy and Reynolds stress balances are affected differently. Near the core, balances are convection driven, while towards the jet boundary the balance is primarily the result of the production, dissipation and pressure-strain rate interactions in the Navier-Stokes equations [25]. The entrainment rate of a jet, which is in essence the result of all the interactions discussed above, is the primary process governing the mixing of fuel and oxidizer in a directly injected engine cylinder.

Considering the macroscopic details of a jet and taking *a priori* that the appropriate scaling is based on nozzle exit momentum [19, 26] allows an analysis of the problem that includes density gradients, compressibility and under-expansion [9]. Indeed, this *a priori* assumption is shown in [9] to be fully adequate for fuel jets, given that the opening transient is short compared to the duration of injection. The starting nature of a plume is most often modelled using the approach of Turner [27] where a quasi-steady-state jet is headed by a 'vortex-ring', *cf. Figure 2-1*.
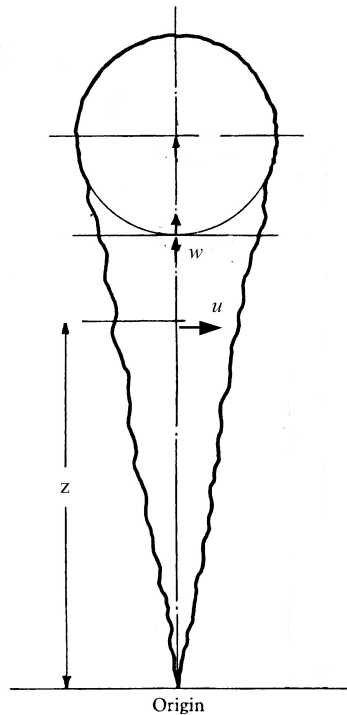
Figure 2-1 The Vortex Ball Model of a Transient Plume by Turner,
after [27]**.**

Turner's model is based upon buoyant atmospheric plumes, where an initial buoyant *thermal* rises and is subsequently 'fed' by the trailing quasi-steady-state plume that supplies about half of the mixed fluid in the 'cap' (the rest being entrained over the front of the cap). Assuming a spherical vortex and Gaussian velocity profile in the jet it can be shown that **[27]** the speed of advance for the cap is approximately 0.6 times that of the maximum velocity of the jet behind it, with a hyperbolic decrease in velocity with downstream location. It would be reasonable to assume that the dominant role of buoyancy in Turner's model limits its applicability to vertical plumes. However, as Turner notes **[27]** "since the cap merges gradually with the plume behind it, the exact form [of the velocity profile] to be taken for the cap is somewhat arbitrary", which also implies the role to be played by buoyancy in the formulation is somewhat arbitrary. This has led Abramovich & Solan **[28]** to successfully apply Turner's theory to non-buoyant transient laminar jets where the cap is assumed to gain mass solely through addition from the jet, though this may be questioned in that, Hill & Ouellette say of Rizk's photographs **[29]** "the head vortex…appears to have suffered little entrainment, and appears almost on the verge of pinching itself off from the preceding flow region.". Nonetheless, Witze **[30]** and Rubas *et al.* **[31]** have demonstrated the applicability of Turner's model to impulsively started incompressible turbulent jets. These works support the validity of the vortex-ball model far beyond the case presented originally and hence its suitability for engine relevant injections. Using Turner's model (with an entrainment constant specified by Ricou &

Spalding [32] as $\dfrac{\dot{m}}{\dot{m}_o} = K_S \dfrac{z}{d}$ where $K_S = 0.32$ and the ratio d/Z_t is 0.25±0.05 from [29]) to support their scaling arguments, Hill & Ouellette [9] are able to show that jet penetration is given by *Eq. 2.2*

$$Z_t = \Gamma \left(\frac{\dot{M}_0}{\rho_a} \right)^{\!1/4} t^{1/2}$$

<div align="right">**Eq. 2.2**</div>

where Γ is a pure constant- the *jet penetration constant*- with a value of 3.0±0.1. It is of note that *Eq. 2.2* is not directly dependent upon injection pressure. Using this expression with the experimental velocity data of Witze [30] to evaluate the arrival of the jet at a set location, Hill & Ouellette confirm the usefulness of Turner's simple model even though the Reynolds numbers for the experimental data used are three to seven times lower than the suggested lower limit [32] of 30,000 for a turbulent jet. Using flow visualisation and laser Doppler velocimetry (LDV) Cossali *et al.* [33] have investigated the early stages of injection prior to the formation of self-similarity. If the injection duration is short enough, or in the initial stages of a longer injection before self-similarity is obtained, the velocity field around the vortex cap is markedly different to that of the quasi-steady-state discussed previously. The jet head does indeed entrain air upon ejection from the nozzle, though it is posited that this is due to wrinkling of the jet boundary and not velocity differences. It is this which causes the initial jet volume to be larger than the final quasi-steady jet. This 'enhanced mixing' in the early stages curtails the applicability of the widespread assumption used in applying Turner's model, *viz.* that all the vortex-cap entrainment is from the jet. Cossali *et al.* do not, however, provide an alternative explanation. Of significance is that steady-state conditions are reached on the jet centre-line about twice as fast as for the edge "where the mixing mechanism requires longer times to reach equilibrium." [33]. This is attributed by the authors to the dominance of inertial effects on the jet axis in the near field; whereas the boundary is primarily influenced by turbulent diffusion of mass and momentum, with correspondingly longer characteristic times, and where the fluctuations may be of the order of the jet half-width [34]. The importance of r.m.s. fluctuations cannot be overlooked, with [35] showing that turbulent mass transport accounts for ~8% in jets.

The hyperbolic decay of mean (or centreline) velocity could reasonably be expected to apply to the scalar field of a jet, and early work by Hinze [11] and Field [36] confirmed this basic premise, with concentration decay from the source given by *Eq. 2.3*:

$$\frac{\bar{c}_0}{\bar{c}_c} = \frac{1}{k_{jc}} \left(\frac{z}{d_e} \right)$$

<div align="right">**Eq. 2.3**</div>

where the co-ordinate z is measured from the virtual origin, and the term in parentheses is termed z^*. The data of Birch *et al.* [37] suggest $k_{jc} = 4.0$ with the virtual origin 5.8d upstream of the nozzle exit. Birch *et al.* report k_{jc} to be in the range four to six, with more recent studies settling on values close to five, though without conclusive agreement (*e.g.* 5.4 [38], 5.37 [24] & 4.96 [39]). The location of the virtual origin suffers a wide range of reported values when based on velocity since the location at which self-

similarity is attained varies widely in the literature (*e.g.* $z^* \sim 10$ [40], 10-15 [29], 25 [37, 41], 30 [42], 50 [24, 43] and 70 [15, 44]). Birch *et al.* note that, as with velocity, there is an increase in the rate of spread for concentration in the near field before it settles to its (steady) far-field value at $z^* \sim 10\text{-}30$. The difference in the velocity and scalar fields is attributable to the fact that turbulence and buoyancy affect velocity and mixing very differently. Using Raman spectroscopy of a methane jet in air, Birch *et al.* [37] report that the unmixedness ($\tilde{c}/\bar{c}$) tends to 28.5% in the far field ($z^* > 70$). The initial development of unmixedness is rapid within the first $10d_e$ and is attributed to the r.m.s concentration reaching similarity before the mean concentration. The ratio of the concentration (or buoyancy) to velocity spread rates, λ (= $Pr^{-\frac{1}{2}}$ [21]) is important to the analysis of the jet, as is the Richardson number $\left(Ri = \dfrac{g l_m}{w^2} \right)$ where l_m is the characteristic lengthscale of buoyant jets (or plumes), $l_m = M_0^{\frac{3}{4}}/B_0^{\frac{1}{2}}$ [39]. It has been found consistently that the radial concentration profile is wider than the velocity profile at the same location with $\lambda \sim 1.19$ [24]. As noted by Carazzo *et al.* [21] "the route to self similarity is different for jets and plumes…[where] self-similarity occurs earlier in pure plumes than in jets [and] the effective turbulent Prandtl number is smaller in jets than plumes." Fundamental work by Wang & Law [41] using particle image velocimetry and laser induced fluorescence (LIF) suggest that a jet exists for $z/l_m < 0.6$ and a plume for $z/l_m > 6$ with a smooth transition between the two regimes ([24] find these values to be 1 and 5 respectively). Papanicolaou & List [24] suggest, that a lack of care in assessing the regime of the flow by various experimenters can explain the discrepancy in the constants reported in the literature.
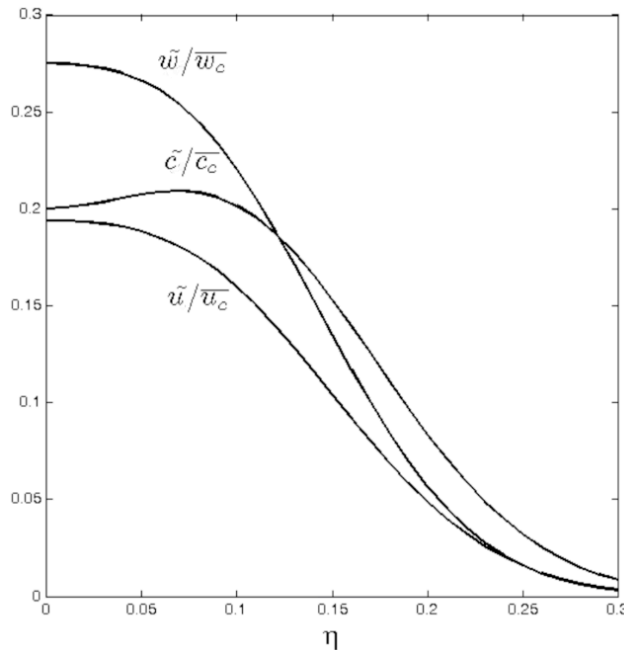
Figure 2-2 Normalised Radial r.m.s. Profiles of Axial Velocity (*w*), Radial Velocity (*u*) and Concentration (*c*), after curve fit coefficients presented in [41].

Typical r.m.s. velocity and concentration profiles are shown in *Figure 2-2*, though the extent of the intensities reported by different researchers are inconsistent (*cf. Table 2-1*). Common to almost all is that, in jets, the concentration fluctuations are smaller than the velocity fluctuations.

	$\widetilde{c}_c / \overline{c}_c$	$\widetilde{w}_c / \overline{w}_c$	$\widetilde{u}_c / \overline{u}_c$
Wang & Law [41]	0.224	0.27	0.19
Papanicolaou & List [24]	0.22	0.25	0.17
Birch *et al.* [37]	0.285	0.27	0.32

Table 2-1 Centre-line Root Mean Square Turbulent Fluctuation Values for Jet Concentration, Axial Velocity and Radial Velocity.

Despite their proximity, Papanicolaou & List and Wang & Law draw markedly different conclusions from their findings. Papanicolaou & List [24] assert from their LDA and LIF measurements that buoyancy produced turbulence accounted for twice the transport of turbulence than jet driven turbulence, with an increase in normalised momentum $(\dot{M}(z)/\dot{M}_0)$ of ~12% compared to the initial specific momentum flux (though the exact increase is related to the axial motion of the externally entrained fluid). Wang & Law, on the other hand, point to the fact that the normal and shear turbulent intensities in their jet and plume results are so similar that buoyancy has no effect on the turbulent velocity fluctuations, and acts mainly through the mean velocity. Shabbir and George's work [40] on the vertical plume suggests that the mean energy advection is primarily balanced by the radial turbulent transport, while the radial turbulent transport is responsible for balancing the mean advected momentum and buoyancy forces. This supports Wang & Law in that although the direct effect of buoyancy upon turbulence is substantial it is still small compared to the effect of shear. Buoyancy is the main driving force in the mean velocity field, which in turn produces the shear to enhance the turbulent flow properties [40]. Regardless, there is a high level of self-similarity in the mean and turbulent velocity fields. The same cannot be said of the respective concentration fields however. The peak r.m.s. concentrations in a jet may be 1.65 times that of the centreline mean. The importance of these fluctuations is further built on when concentration minima are considered [24]. Jets may see r.m.s. concentrations as low as 20% of centreline means, with this value dropping to zero beyond $\eta \sim 0.1$ ($\eta \equiv \frac{r}{z}$). Root mean square concentration (*cf. Table 2-2*) and velocity (*cf. Table 2-1*) values tend to decay like their mean counterparts [24] such that for a jet $\widetilde{c}_c \sim 1/z$ and $\widetilde{u}_c \sim 1/z$, while the contributions to scalar transport from the turbulent fluctuations are often overlooked, Wang & Law [41] have shown that they account for ~7-12%.

13

	$\hat{\tilde{c}}\big/\overline{c}_c$	at η
Wang & Law [41]	0.21	0.07
Papanicolaou & List [24]	0.25	0.1
Birch et al. [37]	0.22	0.07

Table 2-2 Maximum Root Mean Square Turbulent Fluctuation Values for Concentration (with Radial Position)

2▪2▪2 UNDER-EXPANDED COMPRESSIBLE JETS

The discussions presented above pertain to incompressible flows, yet at the pressures used in direct injection systems the resultant jet cannot be described as so. Early work by Kleinstein [45] showed that analytical solutions to the compressible laminar jet were tractable, and that the turbulent case could also be tackled [46]. Assuming: negligible axial pressure gradient, $Pr\sim1$, $Sc\sim1$, $Le\sim1$, and using adaptations of Prandtl's momentum transfer theory and Taylor's vorticity transport theory (both with an enhanced eddy viscosity that takes into account the thermodynamics of the problem), Kleinstein [46] showed that the axial decay of velocity and concentration (and entropy) follow the form of *Eq. 2.4*

$$\overline{u}_0;\overline{c}_0 = 1 - e^{-\left(2\kappa z^*\sqrt{\rho_a}-0.7\right)^{-1}}$$

<div align="right">**Eq. 2.4**</div>

where κ is the decay constant (0.074 for velocity and 0.104 for mass fraction [46]). Birch et al. [42] note of Kleinstein's solution that the agreement in the near field is only marginally better than the hyperbolic formulation (*Eqs.2.1 & 2.3*) and at large distances may be closely approximated by a hyperbola. However, Kleinstein's formulation is important in that it is shown to agree well with similar incompressible work by Schlichting [47] up to $Ma\sim2.5$, which may explain its persistent wide use [31]. The suggested similarity would imply that despite the well-known structural differences between compressible jets (as detailed by Shapiro [48]) and their incompressible counterparts, their inherent behaviour is the same. This is indeed shown to be the case, with the details of the early development region (where any shocks form) and the potential core ostensibly being 'forgotten' downstream. It would appear that the work of George [20] may bring this in to some doubt, but for engine related jets the more complex formulation of George provides no significant benefit. An under-expanded jet undergoes a rapid expansion upon leaving the nozzle to equilibrate in pressure with its surroundings. This expansion causes the subsequent jet to act as though its source were much larger than in reality. This discrepancy is easily overcome by specifying a *pseudo-diameter*- the diameter that would flow the same amount of mass were it subsonic, and is shown by Birch et al. [49] to be given by *Eq. 2.5*

$$\left(\frac{d_{ps}}{d}\right)^2 \approx \left(\frac{P_r}{P_a}\right)\left(\frac{2}{\gamma+1}\right)^{\gamma+1\big/2(\gamma-1)}$$

<div align="right">**Eq. 2.5**</div>

In later work [42] the pressure ratio was shown not only to affect the pseudo-diameter, but also the location of the jet's virtual origin. With this in mind Birch et al. [42] proposed the use of a *pseudo-source*

to fully describe the jet behaviour. This source would have a diameter given by *Eq. 2.5* with a (subsonic) *pseudo-velocity* at the source to maintain the mass flow rate for this larger diameter. Hill & Ouellette **[9]** are able to show that the work of Birch *et al.* is well defined, but that the more simple scaling of Thring & Newby **[16]** provides results which match equally as well. This has the implication that *Eq. 2.2* for jet penetration applies equally well across the sub-sonic and highly underexpanded jet regimes; with the preservation of the jet penetration constant at 3.0±0.1, and noting that although stagnation pressure losses are significant, the ¼ power dependence of penetration on momentum flux minimises the influence of the loss.

Gaseous jets have relatively simple analytical solutions if steady and laminar, and even a transition to turbulent gets allows a certain amount of analytical tractability. However, when considering jets in more detail and their transients it is apparent that entrainment is the mechanism driving their development and entrainment itself is non-trivial to predict.

2▪3 NATURAL GAS ENGINES

2▪3▪1 NATURAL GAS COMBUSTION ENGINES

McTaggart-Cowen *et al.* **[50]** offer an excellent review of on-road natural gas engines in terms of their market position and some of the larger technical and infrastructure concerns, yet here our attention is turned to the macroscopic combustion behaviour of natural gas engines.

Natural gas engines come in SI, CI and HCCI variants, where the gas may comprise the major or minor stake in the fuel mixture. Historic development has followed the order given, for ease of implementation, with the latest engines offering exceptionally low emissions, high thermal efficiencies and high power. In directly injected engines the fuel may be burnt as a premixed or non-premixed mixture, depending upon the time and duration of the injection event. Early injection affords the time for enhanced mixing, both diffusive and turbulent, to yield increased homogeneity. Late injection, with shorter times to ignition will yield a more poorly mixed, or stratified, charge which may auto-ignite or necessitate an ignition source. With the partially stratified charge approach used in the current system, combustion may be either pre-mixed or non-premixed depending upon the timing of the fuelling events. Non-premixed combustion is responsible for the burn in the partially stratified charge and direct injection plumes; while if there is a homogeneous bulk charge present, ignition by the PSC results in a premixed flame. The slow flame speed of premixed natural gas combustion results in slow heat release rates, HRR (that are proportional to propagation velocity), which in turn cause combustion instability and low combustion quality. The result is misfire and high UHC emissions, which are even more pronounced (as are cyclic variations), when leaning the mixture to reduce NO_x output. Leaning the charge mixture (for any fuel) yields lower NO_x

emissions through the provision of a heat sink from the excess air, which reduces combustion temperatures and hence thermal NO_x. Gupta *et al.* [51] report a low NO_x plateau of 1.12*g/kWh* (~220*ppm*) for Φ<0.7. Compared to gasoline, natural gas reduces the reactive hydrocarbons emitted when burnt close to stoichiometric, though, with natural gas, total HC emissions do tend to be higher when measured against the same baseline [52] since methane is considered a relatively unreactive compound, though has a significant global warming potential.

Higher charge pressures retard flame propagation and lower the auto-ignition temperature, which although better for HCCI designs increases the propensity for knocking in SI engines. Retarded timing tends to raise the mixture temperature in the end-zone above the knock temperature limit (which is independent of fuel composition [53]). Further, a drop in combustion duration, $\Delta\theta_c$ in Figure 2-3, reduces the thermal efficiency and, hence, power, since there is less heat release near TDC.
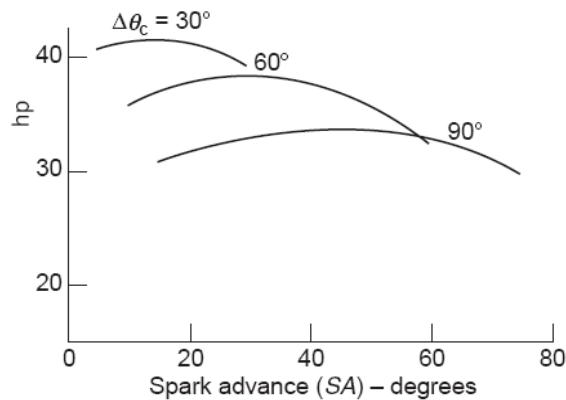
Figure 2-3 Power Reduction From Increased Burn Duration and Necessitated Spark Advance, reproduced from [54].

To circumvent the slow heat release rate, fuel additives are often used to increase the flame propagation velocity and get it close to the gas maximum of ~0.2*m/s* (for lean mixtures), which is independent of fuel composition (Payman in [53]). Diesel pilot ignition is often used to increase the strength of the initial combustion, which is dependent upon mixture temperature, jet mixing and jet penetration. This strong ignition encourages a faster second stage burn in the bulk charge with an overall HRR closely related to the percentage of the total charge which was pilot injected. Pre-chambers offer similar benefits, though their design is more complex with a wider range of variables affecting the second stage combustion of the bulk charge, particularly for multi-stage chamber designs [55]. Spark ignition of lean gas mixtures is inhibited by the high spark energies required, though early gas engine designs used a pre-chamber to ignite a rich mixture allowing lean spark-ignited gas engines to be some of the earliest used. Meyers [56] shows that pre-chamber designs with a volume of 2-3% of the cylinder can offer low emissions with high efficiency. However, Kubesh [57] notes that large pre-chambers (~20%) are required to offer full

throttless operation, though using a more traditional pre-chamber Goto *et al.* **[58]** achieve excess air ratios exceeding two. More contemporary designs use the diesel pilot to the same effect, though the pilot is the source of the majority of the overall emitted NO_x, where NO_x emissions are proportional to the percent pilot injection. Regardless, optimal gas engine performance (in terms of efficiency versus emissions) can only be achieved when the gas fuel has at least 80% methane; less than this and the overall fuel octane number is insufficiently low and can cause knocking. The increased reaction rates required for ignition can also be achieved through spark plug shrouding, whereby the electrodes are covered with a shroud, the enclosed volume of which is filled on the compression stroke. The enclosed, more quiescent mixture, is ignited producing strong flame jets, rich in radicals, which then ignite the bulk charge **[59]**. The enhancement of the radical pool through mini-chambers on the cylinder head has also been numerically investigated as a controlled source of auto-ignition, though is still awaiting experimental trial **[60]**.

The high knock resistance of methane/natural gas (RON ~125-135) allows for the use of higher compression ratios than gasoline SI engines and allows an efficiency increase of up to 6% as a direct result **[61]**. *Figure 2-8* shows schematically how CNG engines can achieve a 25% reduction in CO_2 emissions when compared to a gasoline baseline, and an overall emissions reduction of ~20% on a CO_2-equivalent basis.
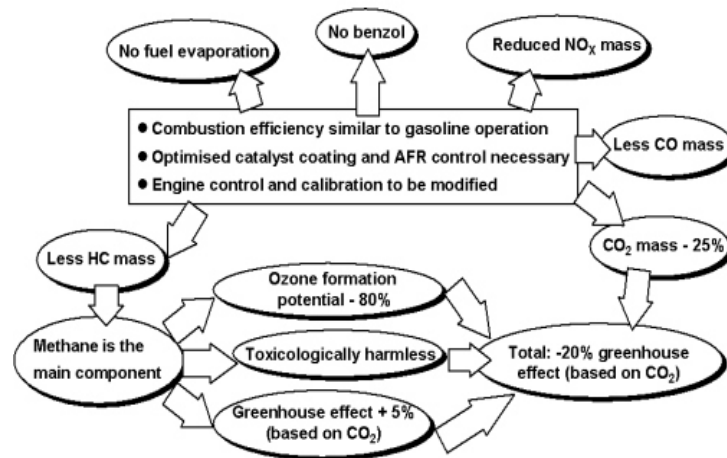
Figure 2-4 GHG Reduction Potential of CNG Engines Against Gasoline Equivalents, reproduced from [61].

Further, the high knock tolerance of NG yields a fuel that is well suited to turbocharging, which in itself lends the ability to downsize and meet the strictest emissions standards **[62]**. As a fuel, natural gas also offers a better ability to homogenate in the cylinder (if required) and an inherent reduction in nmHC's. Adaptation of existing engine configurations does not fully access all these thermodynamic advantages however, and there exists the need for bespoke NG engine designs. Bespoke engines could offer cylinder conditions aimed at optimising the burning velocity, not mixing, and hence reduce the required turbulence levels, minimizing wall heat loss.

Gaseous natural gas displaces about 10% of the cylinder air, reducing the volumetric efficiency that, when coupled with the stoichiometry of gas combustion, reduces the quantity of fuel available to produce power by about 15% and hence power by 10-15% [51]; while maximum torque levels are also seen to drop by ~10%. Volumetric efficiency is further reduced due to a lack of charge cooling with gaseous fuels, though this does mean that on cold start no enrichment is required and CO emissions are correspondingly reduced. It is further noted, that on a well-to-wheel basis, CNG shows the ability to offer 15% CO_2 savings over gasoline, beneficial but lower than the 25% when measured on a tank-to-wheel basis [63].

2▪3▪2   LEAN BURNING NATURAL GAS ENGINES

The stoichiometry of a reaction describes the extent to which there are enough reactants to complete the reaction, which in combustion are fuel and oxidizer. When there is enough oxidizer (or fuel) to complete the reaction with no excess or shortfall, the ratio of fuel to oxidizer, *i.e.* the fuel air mixture, is said be stoichiometric. Any excess fuel and the mixture is rich, any shortfall and the mixture is lean. The ratio of air to fuel (by mass), AFR, is used to quantify the stoichiometry of the mixture. Mixture composition is often expressed in terms of the relative air fuel ratio (RAFR), λ, which is the ratio of the AFR to that of the stoichiometric condition, the inverse of which is known as equivalence ratio, Φ.

Spark ignited engines must operate at an RAFR of around one, and so load control is obtained by throttling. There are significant pumping losses associated with this which are further exacerbated with natural gas. They range from 10% at full-load to over 25% at part-load, when compared to a diesel engine- a natural gas engine's obvious competitor [57]. Using a fuel that allows a move away from stoichiometric could potentially reduce, or eliminate, the need for throttling. Natural gas is well suited to such lean-burn applications because of its wide flammability limits and propensity to homogenate (even upon cold start). Modelling of a medium duty throttless naturally aspirated natural gas engine shows that at low load an unthrottled engine requires equivalence ratios as low as ~0.2 [64].

Late intake valve closure can achieve 15% thermal efficiency gains at up to 15% load, with throttling used at part- and full-load [65]. Engine load range can also be controlled by internal trapping and exhaust gas recirculation with supplemental charge heating [66]. It does however, result in higher NO_x at stoichiometric conditions compared to gasoline, since a lower residual gas fraction is employed because of significant differences in the required valve overlap. Honda appears to have overcome these problems with an electronically controlled VVT CNG engine with a variable length air intake [67]. Power is reported to increase by 15% over the non-VVT case, with a 5% reduction in fuel consumption.

Although methane has a similar ratio of specific heats to gasoline, advantage is to be had in thermal efficiency since as the charge is leaned the mixture ratio of specific heats increases monotonically to that of air. Further, volumetric efficiency gains can be realised over turbocharged and normally aspirated SI engines in that the need for more charge air necessitates a wider throttle with lower pumping losses. Karim *et al.* **[68]** and Klimstra & Jones **[69]** both report natural gas' ability to operate over a wide range of equivalence ratios with Gupta **[51]** reporting the same 10% COV$_{IMEP}$[6] at λ=1.6 compared to 1.4 for gasoline. Yet there are problems with gaseous fuelling and lean operation: high ignition energies and slow combustion durations. The first of these problems may be overcome with high energy ignition sources such as laser ignition **[70, 71]**, pilot charges or pre-chambers, where laser ignition is also shown to have emissions benefits over traditional spark ignition. The flame speed of a hydrocarbon mixture is strongly related to both the equivalence ratio and pressure of the charge, dropping rapidly with pressure and RAFR's above one. This is a serious problem for high pressure (large compression ratio) lean burn engines where extinction and misfire are to be avoided. Hassaneen *et al.* **[72]** report the initial flame kernel growth to be retarded by up to 60% at MBT, and the rapid burn duration by up to 33% when a gas mixture is leaned to Φ=0.6 against a stoichiometric baseline. However, the COV$_{IMEP}$ was typically less than 5%, showing good combustion stability. Increased levels of charge motion would elevate burn rates and permit the use of higher compression ratios or boosting, while avoiding knock through extreme leaning.
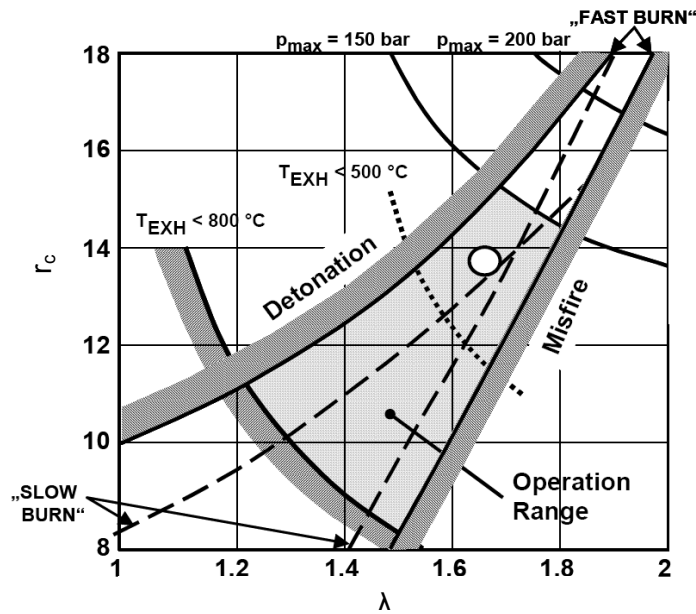
Figure 2-5 Operating Envelope for an SI Gas Engine,
reproduced from [61].

Figure 2-5 shows, schematically, that with an increase in turbulence, and hence burn rate, the engine operating envelope extends such that higher compression ratios and leaner mixtures can be supported.

---

[6] Coefficient of variation, CoV=σ/μ.

Using this approach Pischinger *et al.* **[61]** show the best full load fuel consumption compared to similarly specified SI and boosted CI engines and with 25% less CO_2. Combustion chamber and piston design are key to enhanced combustion through turbulence generation. The bowl-in-piston approach is most often used to generate squish and tumble **[73-75]**. A novel approach outlined by Evans *et al.* **[76-79]** uses a fence around the bowl, with gates designed to guide and funnel the squish motion into highly turbulent jets that converge at the ignition location.

Meyers & Kubesh **[80]** propose a markedly different approach to the use of lean burning engines. Their concept fuels a portion of a multi-cylinder engine with a very rich gas mixture, while the remaining cylinders are fuelled with a lean mixture of natural gas, air and the rich cylinder exhaust. Catalytic treatment of the high HC and CO concentrations in the rich cylinder exhaust is used to produce hydrogen that is then employed to enhance the combustion of the lean cylinders. This approach can offer NO_x as low as 8*ppm*, good combustion quality, combustion stability and thermal efficiencies from 24-28%.

Homogeneous charge compression ignition of lean gas mixtures is reported as pre-mixed charge compression ignition by Kawasaki *et al.* **[81]**. It shows that maximum specific power may be increased with engine speeds up to 2400*rpm* while maintaining an indicated thermal efficiency of 32% and NO_x emissions below 100*ppm*. However, "an increase in the engine speed extends the combustion duration, especially under a lean condition, and so the oxidation reaction is frozen at the last stage of combustion, and the indicated thermal efficiency decreases compared to the low speed condition."

2▪3▪3 STRATIFICATION AND THE PARTIALLY STRATIFIED CHARGE

The aim of stratification is to combine the benefits of a spark ignited engine and a compression ignition engine in a single platform. The inducted charge is globally beyond the lean limit, but through judicious charge motion the portion of the charge which is ignitable is brought to the sparkplug for ignition. Stratified charge engines can operate over a wide range of loads through controlled mixture strength, are knock resistant, and can accommodate a wide range of fuel compositions **[82]**. Abata **[83]** provides a detailed discussion of traditional stratified charge approaches and their application, with Toyota **[84]**, Honda **[85]** and Texaco **[86]** all releasing commercial stratified charge concepts. Zhao *et al.* **[87]** offer discussions on the more contemporary approach of direct injection stratified charge (DISC) based on the now widespread practice of gasoline direct injection (GDI). These approaches use a direct injection fuel jet that is wall or piston guided to the plug, during which time entrainment provides the mixing required to form an ignitable mixture. The complexities of the system (fluid-fluid interactions, fluid-surface interactions, injection pressures/timing, piston motion *etc.*) still remain problematic in that poor fuel utilisation results in high UHC emissions, especially at part load. Further, overmixing and poor delivery to the sparkplug result in significant misfire (with its own emissions penalty) **[57, 88, 89]**, though DISC

shows the potential for significant efficiency improvements **[90-92]**. The ignition problems associated with stratified charge may be overcome with local charge enhancement or partial stratification; whereby a small portion (typically <5% *w/w*) of the fuel is concentrated in the region of the ignition source. This easily ignitable source then provides the energy required to ignite the remaining fuel. This is particularly important in the ignition and stability of ultra-lean mixtures which require high ignition energies **[93, 94]**.

Partial stratification is known to enhance the combustibility of a mixture through increased turbulence generation; Acroumanis *et al.* **[95]** report an increase in peak cylinder pressure of 55% and similar flame speeds at equivalence ratios 0.2 lower. At the University of British Columbia a partially stratified charge (PSC) approach has been developed by Evans **[7]** whereby the pilot charge is injected next to the spark electrodes using a modified spark plug **[8, 96]**. The plug is then able to ignite the fuel rich pilot which can inflame the rest of the homogeneous charge. Extensive testing has been carried out on a fully instrumented Ricardo Hydra single cylinder engine, the details of which are described elsewhere **[8, 96, 97]**. No benefit in emissions or engine performance is found for $\lambda<1.4$, although when $\lambda>1.6$ at full load, there is a significant extension of the lean limit with an increase of 7% in BSFC. Of more significance are the part load improvements. As is clear from *Figure 2-6* there are gains to be made in BSFC and NO$_x$ emissions, which are coupled with (not shown) marked combustion stability improvements.
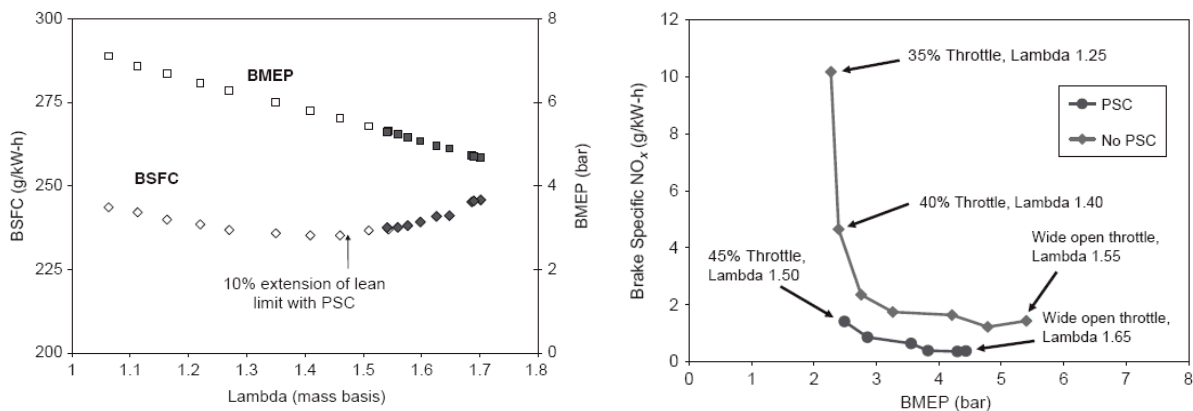
Figure 2-6 Lean Limit Extension & BSFC Reduction (left) and NO$_x$ Reduction Potential (right) of PSC reproduced from [98].

The work of Reynolds **[96]** and Brown **[97]** (who completed his studies on natural gas PSC with port injected gasoline) was built upon by Gorby whose "goal was [to] determine if mixture enrichment local to the spark plug would aid the combustion of a stratified DI fuel charge" **[8]**. The thinking behind the work was to improve fuel usage through a larger ignition zone for the DI plume, and to provide an ignition which was stronger and which could then progress in areas which would otherwise be overly lean. These benefits should engender a reduction in UHC's and "increase efficiency from improved combustion and reduced misfire.". The potential gains are shown schematically in *Figure 2-7* as given by Gorby **[8]**.
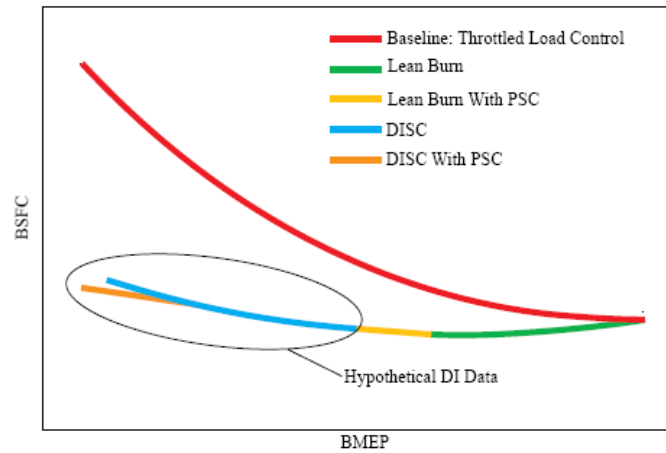
**Figure 2-7 Fuel Efficiency of Load Control Strategies,
reproduced from [8].**

These hypothesised gains were not observed, however. The optimal BSFC was found at early injection timings, the combustion performance degrading rapidly past a minimum threshold value. Further, the DI jet was most effective when directly aligned with the PSC injection; showing that only small gains were to be made from the increased volume of the ignition source. Finally, and most significantly, it was found that the PSC charge was not being reliably ignited and required a certain level of background fuelling to ignite, and a pure air charge impeded the ignition to the extent that it would fail to inflame the PSC injection. However, when the PSC charge was ignited reliably (COV_{IMEP}<5%) the late DI also ignited reliably and provided stable operation of the engine.

It is imperative that a strong combustion be caused through vigourous charge motion and charge ignition if natural gas is to be used as an alternative fuel for ICEs.

2▪3▪4   GAS COMPOSITION

Gas engines are known to have a sensitivity to gas composition that acts primarily through the observed ignition delay and the fuel/dilutant kinetics **[99]**. Ethane (the second most prevalent component in natural gas) decreases ignition delay and combustion duration **[99, 100]**, while the CO_2 in EGR gas has the reverse effect **[99]**. However, the type of ignition source has the dominant effect on ignition/composition interaction. In an unassisted (auto) ignition, non-reacting species such as nitrogen, are known to stabilise the ignition, while no benefit is observed when an ignition source such as a pilot charge is used **[101]**; highlighting the benefits of enhanced ignition sources to account for fuel composition variability. Further, Schiffgens *et al.* **[102]** and Pischinger *et al.* **[61]** both suggest that no matter, knock-controlled and lambda-controlled operation is required to account for the range of methane numbers (a measure of the composition of natural gas) encountered when fuelling gas engines. With engine combustion affected, delivered power is also affected. Kim *et al.* **[103]** suggest that such a clear relation exists between gas

22

composition and engine power that a simple relation based on the Wobbe Index[7] may be used as a practical method for power estimation based on fuel composition, although composition is not an integral part of the current.

2▪4 POLLUTANTS AND ENGINE EMISSIONS

Pollutants include, but are not limited to: oxides of nitrogen (NO_x), carbon monoxide (CO), hydrocarbons (HC's) and particulate matter (PM). Fuel bound sulphur is of concern since it will form SO_2 during combustion, which can then oxidize to SO_3, the source of acid rain. It is of note that the US EPA has recently recognised carbon dioxide as a pollutant (along with, methane (CH_4), nitrous oxide (NO), hydrofluorocarbons (HFC's), perfluorocarbons (PFC's) and sulphur hexafluoride (SF_6)) **[104]**.

The term NO_x covers both nitric oxide (NO) and nitrogen dioxide (NO_2), which in engine emissions total concentrations of 500-1000*ppm* **[82]**. Hydrocarbons from unburnt or partially oxidized fuel, blow-by, fuel evaporation or (in older engines) carburettor release may reach 3000*ppm*. Intrinsic to these releases there may also be HC's from oil films, quench products, crevice volumes and oil layer scavenging. Carbon monoxide resulting from ICE's can reach concentrations as high as 1-2%.

NO_x levels are similar for both SI and CI engines, while HC's may be up to five times higher for SI engines as a result of the exhaust process. There is little PM found in SI exhaust, though it may range from 0.2-0.5% (at $0.1\mu m$ diameter) of fuel mass for CI engines. The high pressures and ample quantities of oxygen found in the combustion process of non-premixed DI engines means that there is little CO present compared to that produced by an SI engine as the thermodynamics is driven towards complete combustion and the production of CO_2.

Detailed chemistry is needed to link pollutant formation due to combustion chemistry to that of the post combustion processes. This need arises since cylinder concentrations can differ significantly from equilibrium values in the exhaust stream. Fuel chemistry tends to drive CO, PM and organic pollutant formation, while post-combustion processes govern NO_x and SO_x emissions.

High combustion temperatures will form NO that is frozen during the expansion stroke. Rich combustion yields higher CO concentrations since there is not enough oxygen present to complete the fuel oxidation

---

[7] The Wobbe Index, I_W, is define as $HHV \big/ \sqrt{\rho_{specific}}$ and allows the direct comparison of different fuels on an energy basis.

and the CO is quenched on expansion. Lean combustion will have similar results though these are attributable to dissociation rather than partial oxidation.
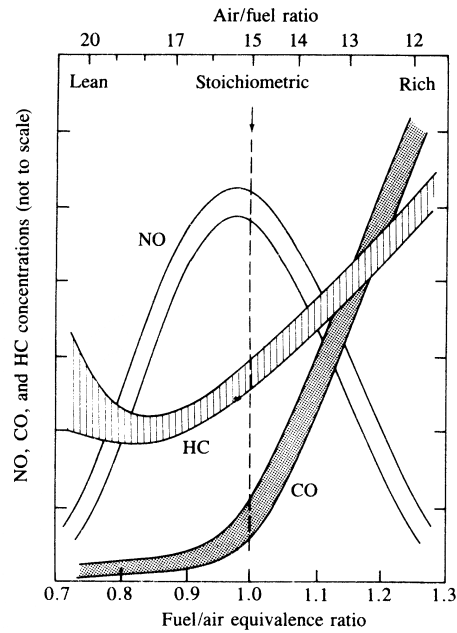
Figure 2-8 Engine Pollutant Concentrations Across the Range of Operating FAR's, reproduced from [82].

Emissions for SI engines are almost solely governed by equivalence ratio. With the exception of NO_x, pollutant concentrations rise with increased equivalence ratio as combustion quality starts to deteriorate, *cf. Figure 2-8*. On warm-up, HC and CO emissions increase because of the rich combustion, while under normal loads, exhaust gas recirculation (EGR) drops NO_x by lowering the combustion temperature, though at the expense of combustion quality. Emissions for CI engines are almost solely governed by fuel distribution.

2▪5 OXIDES OF NITROGEN

Oxides of nitrogen are integral to the formation of tropospheric (low level) ozone, as first noted by Haagen-Smit **[105]** and discussed extensively since (often with geographically specific chemistry, see for example **[106-112]**[8]). NO_x is also the cause of photochemical smog, which is discussed more extensively in *§2▪10*. The nitrogen required to form NO_x can be supplied from the air charge or may be fuel bound. Nitric oxide predominates in NO_x and is formed through several mechanisms **[113]**.

---

[8] The first seven hits for most recently published material on the NO_x-ozone relationship at the time of writing (July 2009).

2▪5▪1 NO FORMATION MECHANISMS

2▪5▪1▪1 ZEL'DOVICH (THERMAL) MECHANISM

First postulated in 1946 by Zel'Dovich and proven by Baulch *et al*. in 1994 **[114]** (with Lavoie *et al.* **[115]** establishing the significance of step *(c)* in *Eq. 2.6*) the thermal mechanism is the most commonly cited route to NO formation, *viz.*:

$$O + N_2 \leftrightarrow NO + N \qquad \textbf{(a)}$$
$$N + O_2 \leftrightarrow NO + O \qquad \textbf{(b)}$$
$$N + OH \leftrightarrow NO + H \qquad \textbf{(c)}$$

Eq. 2.6

Kuo **[116]** also suggests that the mechanism include the primary step:

$$O_2 + N_2 \leftrightarrow 2NO$$

Eq. 2.7

Steps *(b)* and *(c)* (of mechanism *Eq. 2.6*) are strongly temperature dependent and necessitate temperatures in excess of $\sim 1800K$ to exceed the high activation energy of nitrogen's triple bond. Reducing reactant concentrations or lowering the temperature will ultimately reduce final NO concentrations. The intrinsic timescales of the formation mean that the process is kinetically controlled and does not result in the equilibrium condition for the exhaust gas state **[117]**.

2▪5▪1▪2 FENIMORE (PROMPT) MECHANISM

The prompt mechanism first proposed by Fenimore **[118]** has the CH radical as a prerequisite, which limits its applicability to the flame front (*cf. Fig 17-4* of **[119]** for the complex oxidation mechanism of C_1 and C_2 hydrocarbons to produce the required CH radical). C_2H_2 is a precursor to CH and is primarily formed from CH_3 recombination in rich flames **[119]**, though the mechanism can be significant at temperatures as low as $\sim 1000K$.

2▪5▪1▪3 N_2O MECHANISM

A nitrous oxide route to the formation of NO was suggested by Wolfrum as an alternative to the two major mechanisms discussed above, and is more prevalent in situations where the relative air/fuel ratio is above 1.6 **[120]**. The mechanism is normally overlooked, but under lean conditions CH concentrations are suppressed (negating the prompt mechanism) and temperatures are low (eliminating the Zel'Dovich route). The nitrous oxide route is prompt at high pressure (as with all third body reactions).

2▪5▪2 NO FORMATION IN SI ENGINES

Early combustion contributes significantly to NO which is then frozen on expansion and may contribute many orders-of-magnitude more to the overall NO concentration **[82]** than late formation NO. The lack of significant bulk motion near the sparkplug also increases NO concentrations in this region. Given that the

thermal route to NO production predominates in SI engines, it would be expected, and has been shown **[121-123]**, that NO concentrations mirror the temperature gradients across the cylinder. Spark ignition engines achieve maximum combustion temperatures at an equivalence ratio of ~1.1, but the low oxygen concentration at this equivalence limits NO formation. As the charge is 'leaned out' the extra oxygen compensates for the drop in temperature such that NO concentrations peak at about Φ=0.9. Under lean conditions NO freezes early so there is little decomposition compared to rich mixtures, meaning that the gas composition at peak pressure is important.

2▪5▪3 *NO FORMATION IN CI ENGINES*

The kinetics of NO formation in CI engines are also primarily driven by the Zel'Dovich mechanism, though in a markedly heterogeneous fuel and temperature field. Some fuel is pre-mixed and burnt near a stoichiometric composition, while the remainder is non-premixed and burnt at stoichiometric. The critical stage for NO formation is, as with SI engines, at peak cylinder temperature, which is between the start of combustion and peak pressure. Early burning gives high NO concentrations that are frozen by subsequent expansion and the mixing of late burn (cooler) gases or air. It is this fact that limits NO decomposition in CI engines, with almost all NO formation taking place within 20CAD of start of combustion **[82]**.

Increases in overall fuel/air ratio increase both NO and NO_2 since it generates higher peak pressures and temperatures. Moving towards a rich mixture reduces NO, though the heterogeneity of the fuel distribution means the reduction is less marked than in SI engines. Most fuel is still burnt close to stoichiometric, with the result that NO formation is almost proportional to total fuel mass injected.

2▪6 CARBON MONOXIDE

Carbon monoxide (CO) is a known poison and is intrinsic to photochemical smog formation. CO production is primarily controlled by fuel-air-ratio. The higher the FAR for a fuel rich mixture the more CO is produced; while for lean mixtures CO concentration is independent of FAR, with mole fractions of ~10^{-3}. Since SI engines run at stoichiometric under part load and rich at full load CO emissions are significant. CO levels are observed to be lower than their maximum possible concentrations, but above equilibrium levels, which suggests the CO mechanism is kinetically controlled. Lean conditions promote CO concentrations well below those suggested by a kinetically controlled model, implying the partial oxidation of oil and crevice HC's during expansion and exhausting.

Reductions in CO levels have, to date, been achieved through more uniform mixture generation, charge leaning, reduced cylinder-to-cylinder variation, after treatment and better fuel metering during transients **[82]**. Mixture non-uniformity and transients are still the main sources of CO however **[124]**.

2▪7 HYDROCARBON EMISSIONS

Hydrocarbons (HC's), sometimes also referred to as tHC's (total hydrocarbons) or UHC's (unburnt hydrocarbons) are more strictly organic emissions. They result primarily from incomplete combustion. Total HC emissions are a good proxy for combustion efficiency, though not total pollution emissions [82].

Fuel composition is important to HC emissions in that rich combustion is known to increase aromatic and alkene concentrations, both of which are highly reactive. The combustion process, through pyrolysis and synthesis, changes the hydrocarbon structure significantly from those bound in the fuel. Oxygenates in the exhaust such as carbonyls and phenols (which are increased by the addition of alcohols to fuel) are important to the formation of photochemical smog (*cf. §2▪10*)

2▪7▪1 SPARK IGNITION DERIVED HYDROCARBONS

Typical levels range from 1000-3000 *ppm* C_1 for SI engine emissions. Hydrocarbon emissions rise significantly on the rich side of stoichiometric (*cf. Figure 2-8*). The four processes primarily at work are identified by Heywood [82] as: flame quenching, crevice volumes storage, absorption/desorption into/out of the oil layer and incomplete combustion (from high EGR, poor spark timing or mixture leaning). Maximum HC generation occurs on blowdown and at the end of the exhaust stroke with a 50/50 split on a mass basis (though the blowdown HC's tend to be significantly heavier) [82].

2▪7▪1▪1 OVERLEANING & OVERMIXING

Upon injection a fuel spray develops a mixture distribution similar to that shown schematically in *Figure 2-9*. The amount of fuel mixed beyond the lean limit ($\Phi=0.3$) rapidly increases with time [125]. The auto-ignition location is normally on the lean side of the stoichiometric contour, downstream of the leading edge of the jet. At this location there should be fuel which has spent the longest time in the combustible limit. The overmixed fuel will not support auto-ignition or a fast reaction, and is only capable of sustaining thermal oxidation, which is most likely to be incomplete. The results are unburnt fuel, decomposed or partial burnt products, most of which will be exhausted from the cylinder. The quantity exhausted will depend upon the amount of fuel injected during the ignition delay [126] and the cylinder conditions at ignition.
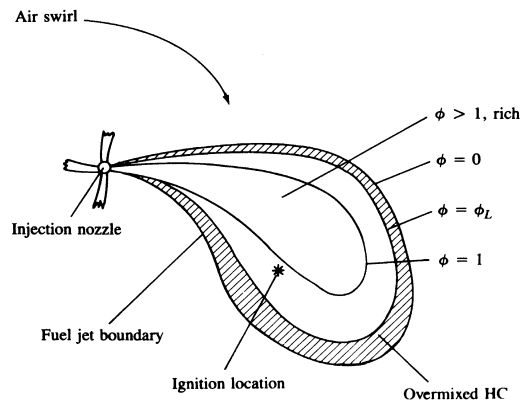
Figure 2-9 Fuel Jet Structure in a Compression Ignition Engine, reproduced from [82].

2▪7▪1▪2 UNDERMIXING

Undermixing is attributable to: low injection velocities, *i.e.* fuel injected late in the cycle, and that which escapes the sac volume; as well as excess fuel from overfuelling, *i.e.* poor load matching and metering. Fuel retained in the sac volume is vapourised as the cylinder temperature increases and enters the cylinder slowly, and may miss the primary combustion altogether. Heavier fuel fractions may stay in the sac and later be evacuated as UHC's or undergo post-combustion oxidation in the elevated temperature prior to blowdown. It has been shown **[127]** that the fuel retained, not in the sac, but in the holes of the injector, matter to overall HC emissions for CI engines. Direct injection compression ignition engines are limited to $\Phi \sim 0.7$ at full load to avoid smoking. They are lean overall, but locally rich during transients due to overfuelling in the power stroke. Hydrocarbon pollutant levels are ostensibly constant for increasing equivalence ratio (at constant speed and minimum ignition delay) until $\Phi = 0.9$, when there is a sharp jump in emissions, *cf. Figure 2-10*. This is critical to emissions under acceleration, although levels are still lower than those observed from overleaning **[125]**.
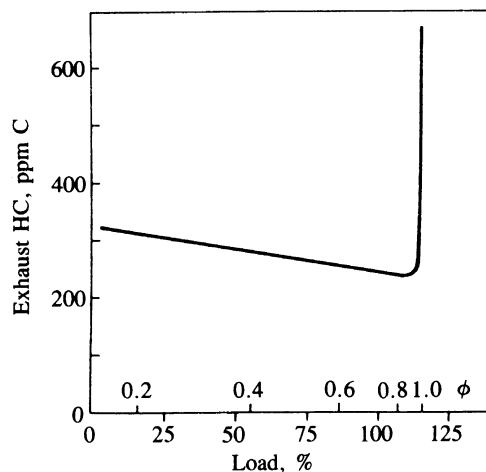
Figure 2-10 The Effect of Overfuelling on Exhaust HC Concentrations, reproduced from [82].

2▪8 PARTICULATE MATTER

Particulate matter (PM) is now considered the most important pollutant with respect to human health. The side effects of ingesting and breathing PM can be profound and long-lasting. In SI engines particulate matter can form from lead, sulphates and organic matter in the fuel, though the phasing out of leaded fuel has all but eliminated PM from lead compounds. Organic PM is mostly soot, while sulphates in unleaded fuel (at levels of 150-600*ppm*) are oxidized to SO_2 and then SO_3, which reacts with atmospheric water to produce sulphuric acid aerosols. Unleaded fuel generates PM emissions at ~20 *mg/km* comprised of mostly soluble and condensed organic matter. These emissions result from poorly adjusted engines and, under rich running, may contain significant amounts of black carbon (soot). Compression ignition engines emit mostly carbonaceous material with some adsorbed organic compounds, both of which originate mainly from incomplete combustion of fuel hydrocarbons.

Heywood **[82]** provides and excellent summary on the formation and nature of PM, where he points out that the composition of CI engine emitted PM is strongly affected not by the fuel make-up but by the exhaust system, and somewhat paradoxically by the analysis collection system. At temperatures above ~500^0C individual spherules with diameters of 15-30*nm* are observed whilst below this temperature the spherules are generally coated, despite their high porosity, in condensed material. The condensates may be any one or a combination of UHC's, oxygenated HC's (primarily ketones, esters and ethenes), PAH's or some inorganic species such as SO_2 or NO_2. Fuel oil has been shown to contribute between two and 25% of exhaust particulate matter and as much as 80% of the organic material. Traces of zinc, sulphur, calcium, iron, chromium and potassium in PM have also been found with the zinc, calcium and chromium linked to engine lubricating oil.

2▪8▪1   FORMATION PROCESSES

Soot originates primarily from fuel-bound carbon, that is to say chains of about 12-22 carbon atoms at a hydrogen to carbon ratio of about 2:1. This yields about 10^5 carbon atoms with an H:C ratio closer to 0.1:1 **[82]**. The processes at work to make this transformation are poorly and incompletely understood. The soot formation process, which has characteristic timescales in the order of milliseconds, is known to require high temperatures (1000-2500*K*) with pressures from 50-100*atm* and *overall* enough air to completely oxidize the charge.

Particulate formation requires the production of a condensed phase, most often from fuel species via oxidation or pyrolysis. Generally this phase consists of unsaturated hydrocarbons and PAH's, which undergo condensation reactions to form the soot nuclei (diameter less than ~2*nm*). Large numbers of these particles exist, though they form a negligible amount of the total sooting because of their small size.

Particle growth occurs according to: formation, surface growth, coagulation and agglomeration. Surface growth is primarily solid phase through gas-phase deposition, condensation and solidification, and is associated with dehydrogenation **[82]**.

Oxidation may occur at any of the growth stages to yield CO or CO_2, and soot formation is an inherent balance between formation and burn-out.

2▪8▪2 *FORMATION LOCATION*

In-cylinder particle distributions are almost solely related to fuel distribution and local heat release. Direct injection results in peak PM concentrations (mostly soot and hydrocarbons) along the jet centre-line. This locally rich core 'converts' up to 50% of the local fuel carbon to PM, with fuel pyrolysis in this core contributing the majority of the cylinder-formed soot. The concentration of particulate matter drops away from the jet centre-line, though near the outer edge of the jet, or in the vicinity of the piston bowl, PM concentrations again rise, albeit to levels an order-of-magnitude lower than the core. 90% of all soot is formed in the cylinder prior to exhaust **[82]**. Particulate formation increases significantly at about four or five degrees ATDC with peak number density occurring at $\sim20^0$ ATDC. There is then a rapid drop because of coagulation and (possible) oxidation. The volume fraction of PM is seen to rise smoothly much like the number density; however it peaks earlier at $\sim18^0$ ATDC and drops steadily until oxidation stops at $\sim40^0$ ATDC, when the PM concentration remains constant **[82]**.

2▪9 HYDROCARBON COMBUSTION & CARBON DIOXIDE PRODUCTION

Water and carbon dioxide are the lowest energy states of the hydrogen-oxygen and carbon-oxygen molecular pairs, and as a result it is inevitable that these will be the most prevalent products of hydrocarbon combustion. Aliphatic fuel combustion is essentially a series of fragmentations in which the chain is broken down into subsequently smaller and smaller intermediate species, each of which is oxidized according to the strict hierarchy of *Figure 2-11*.
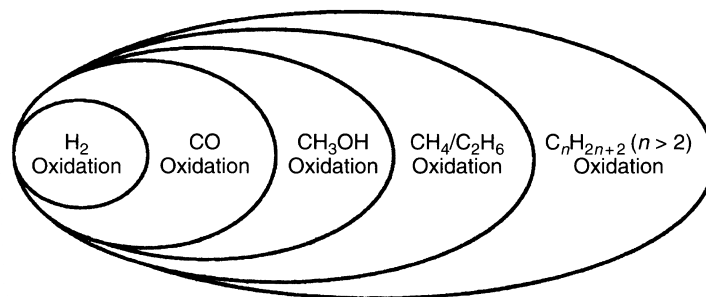
**Figure 2-11 Hierarchical Nature of HC Combustion,
Reproduced from Westbrook [128].**

The intermediate species CO and H_2 are common to all parent fuels as are the radicals H, O, OH, HO_2 and HCO [116]. The CO is slowly oxidized to CO_2 while the other species are key to the oxidation of hydrogen. The detailed kinetics of HC combustion are elucidated most comprehensively by Westbrook and Dryer [128, 129].

2▪10 PHOTOCHEMICAL SMOG & TROPOSPHERIC OZONE

As has been alluded to, engine emissions, primarily NO_x and UHC's, but also CO, provide the precursors to photochemical smog. Photochemical smog has been shown to consist of generic hydrocarbons, peroxyacetyl nitrate (PAN, $C_2H_3NO_5$), NO_x, ozone and nitric acid (NHO_3) [130]. Tropospheric ozone (with desirable levels below $0.1ppm$ [131]) is highly stable and its measurement thus acts as a proxy for general air quality. 'Difficulty regulating O_3 occurs because in regions of high NO_x (primarily urban centres and power plant plumes), O_3 formation is limited by the availability of hydrocarbons.'[132], while in rural regions it is the availability of NO_x which is the limiting factor in O_3 production [133].

The addition of VOC's (most commonly biogenic isoprene [132]) and CO to the atmospheric chemistry alters the reaction mechanism significantly, since the VOC's initiate different precursor reactions [134]. The complex interactions of the O_3-NO_x-VOC system ensure that smog chemistry is strongly non-linear and the concerned reader is referred to Sillman's seminal paper *The Relation Between Ozone, NO_x, and Hydrocarbons in Urban and Polluted Rural Environments* [134].

2▪11 HEALTH IMPLICATIONS OF ENGINE EMISSIONS

The pollutants discussed previously are significant in that their role on atmospheric chemistry and conditions may be contended, but the negative effects of engine emissions on respiratory health are beyond doubt. Hydrocarbon volatiles and aldehydes irritate the eyes and respiratory tract, while phenols have a similar effect and are an odorant. Hydrocarbons, as has been noted, are critical in photochemical smog formation, which is itself an eye and respiratory tract irritant. Aromatic compounds resealed from CI engines are known carcinogens, while contemporary thinking puts PM at the fore of health concerns related to air quality. Tropospheric ozone is know to cause significant respiratory morbidity and has been related to mortality [135, 136]. The problem of urban air quality management is difficult in that the chemistry is non-linear and temperature dependent [137].

The PM problem is complex. There is 'emerging evidence of PM-related cardiovascular health effects and growing knowledge regarding interconnected general pathological pathways that link PM exposure with cardiopulmonary morbidity and mortality' [138]. Despite toxicological studies of the effects of PM upon

respiratory health **[139-143]** establishing a direct casuality between PM and mortality/ill-health is not without significant problems, 'however, recent research has increased confidence that the PM-cardiopulmonary health effects observed in the epidemiology are "biologically plausible".' **[138]**. The concentration-response function for PM is almost conclusively linear and as such 'further improvements in air quality are likely to result in corresponding improvements in public health' **[138]**. There is still a significant lack of knowledge, however, in our understanding of which pollutants, or combinations thereof, cause which symptoms and the role of coarse and ultra-fine PM in the pathological systems.

2▪12   CLIMATIC IMPLICATIONS OF ENGINE EMISSIONS

The realm of climate change is vast and nebulous. The discussion about it in the scientific and popular communities has been vitriolic and heated. The Earth's atmosphere contains a large number of chemical species, some natural, and many anthropogenic. The role of these chemicals is wide and varied, but even small concentrations play a significant part in regulating tellurian climate.

The complexity of the climate system makes it almost impossible to model. Progress has been steady as atmospheric models have started to include more detailed chemistry and the role of water vapour, though the role of the complete hydrological and carbon cycles are not fully understood and are not at the stage of being accurately modelled. Many of the climate sceptics' main arguments for non-anthropogenic forcing (solar activity, poor data and temperature lagging CO_2 increases) have been recently debunked. As the UN IPCC makes clear in its latest report **[144]** much of the data pertaining to climate change is incomplete but the science is still sound and must act as a foundation for future action. Current atmospheric CO_2 levels are around 380*ppm*, and the IPCC reckons that stabilising these at ~540*ppm* is economically viable and 'safe'. Any increase beyond this will significantly endanger human activity on the planet. The IPCC report **[144]** predicts temperature rises anywhere from 1.1-6.4^{0}C in the next 100 years. A clear 'bottom line' has been drawn under anthropogenic radiative forcing. Regardless of the benefits to human health, reductions in the level of pollutants emitted from ICE's is imperative if the climate change problem is to be mitigated.

2▪13   CONCLUSIONS

Arguments have been presented that describe the behaviour of incompressible and compressible gaseous jets. The suitability of natural gas fuelling for transport engines has been argued and a description of the main technological approaches used was made, with particular attention paid to partial stratification- the technology at the core of the current work. The nature of the pollutant formation in engines has been discussed. The general nature of hydrocarbon combustion has been offered before considerations were made to pollutant effects upon human health and the climatic environment.

Chapter 3   LASER IMAGING TECHNIQUES & PLIF FUNDAMENTALS

3∎1 INTRODUCTION

Chapter 3 provides an overview of several techniques used in laser-based species concentration measurement. The Chapter provides the most relevant details of each approach, and briefly outlines their suitability for combustion diagnostics. The reader is taken through the approaches offered by: Rayleigh and Mie scattering; Raman spectroscopy; advanced Raman techniques; and laser induced fluorescence. The majority of the Chapter is concerned with the basic principles of planar laser induced fluorescence (PLIF), its background and applicability to experimental flows. Building upon this, a qualitative explanation is made with regard to how PLIF can be used in elucidating mixing processes and, in particular, mixture formation in internal combustion engines. A case is made for the use of acetone over the many other possible options as a gaseous fuel tracer, and a detailed explanation of the photophysical process behind acetone LIF provided.

3▪2 BACKGROUND

Laser diagnosis provides the ability to investigate harsh environments, such as those in the combustion chamber of internal combustion engines, whilst being non-intrusive and can yield high spatial and temporal resolution. Fluid and chemical parameters can be simultaneously or individually resolved at any point or across a plane, with contemporary techniques providing full three dimensional information. State specific, species specific and non-equilibrium chemical compositions may all be scrutinized and, if desired, related to the temperature field.

Modern lasers have advanced the field of combustion diagnostics through their high powers, coherent light production, spectral purity, short pulse durations (down to ~10ns) and small probe volumes [145]. High laser powers allow the exploration of weak events, including some that were previously unattainable with arc and flash lamps. Further, the coherence of laser light opens up the opportunity to use spectroscopic techniques only available with coherent stimulation. Species and state resolution have been enhanced with the improved spectral purity of lasers and allow specific electronic states to be targeted. The ability to sweep a range of spectra or multiplex multiple light sources presents the opportunity to simultaneously investigate a range of species. The latter point is complimented by the ability to focus laser light sources into probe volumes as small as 50μm^2, which, coupled with short pulse durations, allows both chemistry and flow to be frozen on the smallest of scales.

Laser diagnostics can be split into four main areas: velocity determination (both point and plane); the use of Rayleigh scattering for density determination; Raman techniques for major species (~1% concentration [146]); and laser induced fluorescence for minor species (in the order of *ppm*).

3▪3 COHERENT AND INCOHERENT PROCESSES

An incoherent process will result in the emission of light which is non-directional, that is to say it will be emitted over the full *4πrs* steridian solid angle of the molecule/particle. A scattered signal will result from each point along the path of the laser beam and as such allows for easy extension of these techniques to 2D measurement. Coherent phenomena emit light in a specific direction much like a laser beam. The probe volume is now governed by the intersection volume of the incident laser beams, where all the light emitted from the molecule is collected by the collection optics. This gives a stronger signal than incoherent approaches, but makes the experimental set-up more complex since the exact direction of emission must be established *a priori*. Eckbreth [145] lists the advantages and disadvantages of each as:

	Incoherent	**Coherent**
Advantages	Linear Intensity independent Single ported Spectral simplicity Simple calibration	Strong signals Laser-like signal beams Interference tolerant
Disadvantages	Large solid angles Prone to interferences	Non-linear Intensity independent Multi-ported Complicated Spectra Difficult to normalize Refraction sensitive

Table 3-1 Advantages and Disadvantages to Coherent and Incoherent Laser Diagnostics Techniques, after [145]

3▪4 VELOCITY TECHNIQUES

The importance of the flowfield within a combusting environment cannot be understated and as a result a brief outline of laser based and optical velocity tracking techniques is presented herein. For a full discussion the reader is referred to the excellent books of Durst *et al.* **[147]** and Taylor **[148]** and the review of Adrian **[149]**.

Non-intrusive velocity measurement is now possible, with high resolution, at a single point or across a plane. Particle image velocimetry, PIV, uses a CCD camera to cross-correlate, across a number of sub-regions, laser light which has been elastically scattered by particles seeded into the flow. High laser powers provide a strong signal that can also be enhanced with high seed densities (which are tolerable since particles are not tracked individually but throughout the sub-region of the image). Laser Doppler velocimitry, LDV, uses the Doppler shift in the light elastically scattered from seed particles to ascertain the flow velocity at a point.

3▪5 RAYLEIGH AND MIE SCATTERING

Both Rayleigh and Mie scattering involve the elastic scattering of light incident upon a particle or molecule. There is no energy transfer between the incident photons and the target molecule, which means that the scattered light is not frequency shifted. The process is incoherent and for $d/\lambda<<1$ is termed Rayleigh scattering while for $\pi d/\lambda \geq 1$ it is Mie scattering. The lack of photonic interactions means that both processes are species independent and as a result can only provide generic density information and only under some circumstances species concentration **[145]**. The processes do provide high signal intensity, yet may be prone to spurious light interference. Combination with LDV provides a powerful diagnostic tool **[150]**. A comprehensive summary of Rayleigh scattering's use in combustion diagnostics has been presented by Zhao and Hiroyasu **[151]**. The Mie scattering effect generates a weak signal in

unseeded flows and is most commonly used in naturally seeded flows, *i.e.* soot studies where the technique is now in competition with laser induced incandescence (LII).

3▪6 RAMAN SCATTERING

Raman processes are characterised by inelastic scattering, and may be based on changes in one, two or all of the rotational, vibrational or electronic states of the molecule. The process is almost instantaneous ($\sim 10^{-12}s$), hence linear Raman spectroscopy is referred to as spontaneous Raman spectroscopy, SRS. The photons generated from Raman scattering are shifted from the incident frequency by a quantity $\Delta \upsilon$, where υ is wavenumber. For $\Delta \upsilon < 0$ the spectral lines produced are termed Stokes lines while for $\Delta \upsilon > 0$ they are anti-Stokes (*cf. Figure 3-1*). The latter requires energy addition *from* the target molecule and as such the molecule must first be in an excited state or at elevated temperature.

Given the wide range of transitions that can take place to produce a Raman shift the hyperfine structure is grouped according to changes in rotational quantum number, *J. Q*-branch transitions are those for $\Delta J=0$ and $\Delta v=\pm 1$ (*i.e.* the principall quantum number changes by one). When $\Delta J=\pm 1$ the branches are termed *P* and *R*-branches respectively, while for $\Delta J=\pm 2$ the *O* and *S*-branches are obtained.
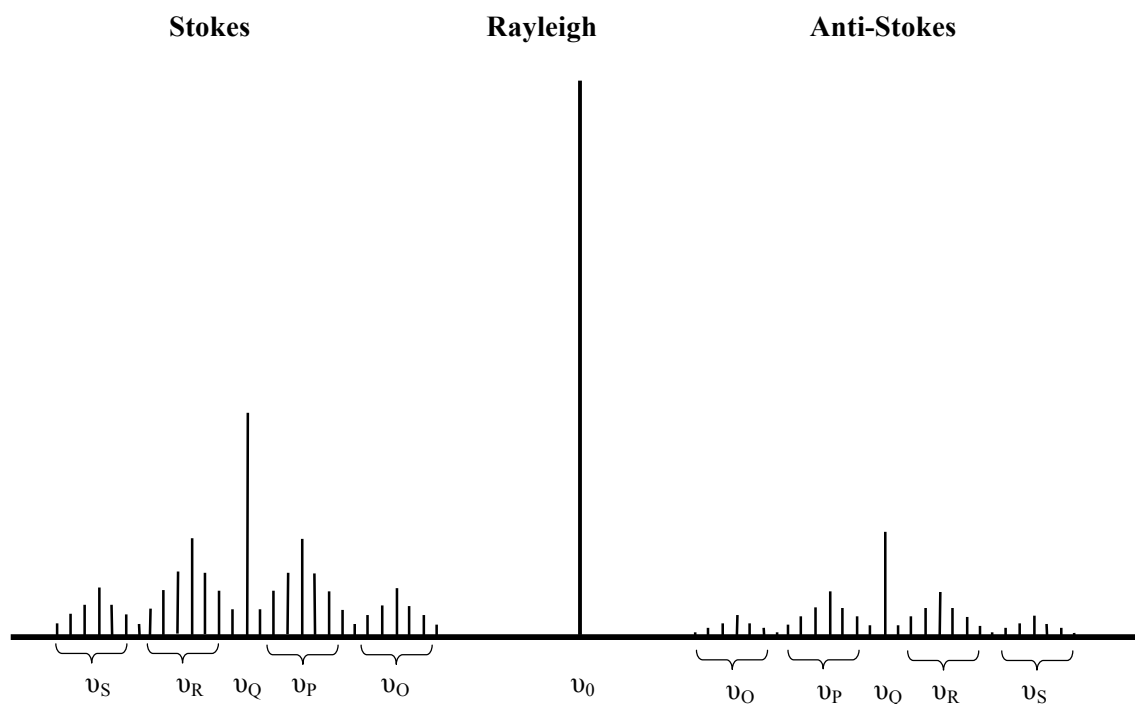
Figure 3-1 Ro-vibronic Structure of the Raman Spectrum, adapted from [152].

Scattering intensity scales with the fourth power of frequency **[145]**, which means that UV diagnostics are preferable. Further, as a result of energy quantization the Raman shift observed is unique to each chemical

species and proportional to molecular number density. This all means that Raman is well suited to species identification and concentration measurement; however with a scattering cross section of $\sim 10^{-31} cm/sr$ signals are weak.

Near-resonant Raman uses laser excitation to excite target molecules near an electronic resonance, thereby increasing the scattering cross section by as much as six orders-of-magnitude [145], similar to those of laser induced fluorescence (*cf. §3▪8*). The difference is that the incident photon is not absorbed by the target molecule; with the result that the scattering is much shorter in duration, and not subject to quenching effects. However, for combustion diagnostics there are few species which can be excited at near resonant frequencies.

3▪6▪1   HYPER-RAMAN TECHNIQUES

Hyper-Raman is the term given to any generic Raman emission that results from multi-photon excitation. The resultant emission is coherent though the excitation is weak, leading to a taxing experimental setup. This is often prohibitive, though coherent anti-Raman scattering (CARS, *cf. §3▪7*) provides the exception to the rule.

Stimulated Raman gain spectroscopy (SRGS) and stimulated Raman loss spectroscopy (SRLS) are induced emissions techniques at the Stokes and anti-Stokes frequencies respectively. The target molecules are excited with both a pump and probe laser. SRGS and SRLS have the advantage that experimentally they are very similar to spontaneous Raman scattering as they are based on a resonant phenomenon to produce the emission and do so without the lineshape complications of other hyper-Raman techniques, while still providing a signal proportional to number density [145]. Nonetheless, beam multiplexing is required to reduce the interrogation time whilst still ensuring a strong signal. This is difficult to achieve and coherent anti-Raman scattering (*cf. §3▪7*) is favourable under these conditions. Beam steering that results from turbulent fluid motion impedes diagnostic significance and cannot be corrected for. This, and the experimental complexity, mean that SRGS and SRLS are of primary use in the fundamental research of molecular photophysics.

Raman induced Kerr-effect spectroscopy, RIKES [153] is a Raman based effect whereby the target molecule is pumped (by a two colour phase matched system) such that the molecule takes on a polarized rotation at the Raman frequency. This induces an emission at the corresponding Raman shifted frequency and with the corresponding polarization. A polarizer is used to block the pump light, while the resultant emission still has components from the resonant and non-resonant parts of the excitation, the latter of which requires filtering. The difficulties of RIKES arises from poor signal strength due to extensive filtering and polarization of signal beams both of which contribute to a poor signal-to-noise ratio.

Turbulence in the region of interest also introduces significant anisotropy, for which the induced polarization is likely to be weak. This practically limits the technique to high density media, *i.e.* liquids, and curtails its diagnostic utility **[145]**.

The problems of poor *susceptibility* (in essence, the ability to excite a molecule) and incomplete probe laser rejection in RIKES are circumvented with optically heterdyned-RIKES (OHD-RIKES). The details of this technique are somewhat nuanced and not of current concern, though the interested reader is referred to works of Eckbreth **[145]** and Eesley **[154]**.

Photoacoustic Raman spectroscopy, or PARS, is very much like SGRS except that the collection 'optics' are now acoustically based and collect the pressure wave that results from the photomolecular de-excitation. This means that the signal collection is free of all electromagnetic contamination. It is possible to detect signals down to 1*ppm*, though the noise requirements for this, or anything useful, are prohibitive for diagnostic application.

3▪7 COHERENT ANTI-RAMAN SCATTERING

Coherent anti-Raman scattering, CARS, is a three or four colour non-linear technique whereby the pump laser, ω_1, and the probe laser, ω_2 (which is Stokes shifted from the pump), combine to stimulate the emission of a wave at $\omega_3 = 2\omega_1 - \omega_2$ (*cf. Figure 3-2*). Based upon this approach Eckbreth **[145]** also reports the technique of coherent Stokes-shifted Raman scattering (CSRS) whereby ω_2 is now shifted to the anti-Stokes lines instead of the Stokes lines, though this application is much less widely used and is, as yet, unreported for diagnostic purposes.

CARS can exhibit significant constructive and destructive interference because of the non-linear ro-vibronic interactions of the target molecule, though their interpretation is still analytically tractable **[145]**. The non-resonant part of the Raman signal can be removed through simple polarization techniques, though this significantly affects the quality of the signal such that the experimental set-up quickly becomes shot-noise-limited. Phase matching is not guaranteed automatically, though since gasses (which are the main target for CARS) are dispersionless, ensures that simple overlapping of the pump and probe beams generate phase matching. This does in turn limit the spatial resolution of the apparatus in collinear systems. Higher resolution necessitates the use of crossed-beam approaches and their inherent phase matching complexities. CARS is most commonly employed to excite the vibrational branches of the target molecule (particularly the *Q*-branch). However, similar techniques to those outlined here can be used to hit the rotational branches of the Raman spectrum **[155]**. Rotational CARS (RCARS) allows for simultaneous investigation of multiple species **[146]** and is less prone to carbon poisoning. Further

advances in CARS ease of use and applicability have been made by Eckbreth *et al.* **[156]** and Alden *et al.* **[155]**.
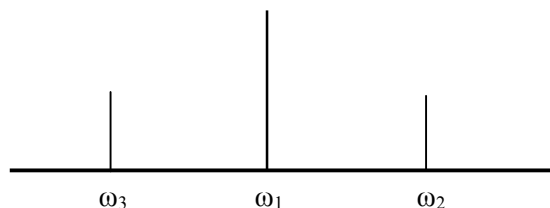
Figure 3-2 CARS adapted from [146]

The advantages of CARS are that it provides a signal many orders-of-magnitude larger than SRS; its coherent signal allows for complete collection; there is no fluorescent inference since emission is on the anti-Stokes side of the Rayleigh line and is more robust than SRS in harsh environments **[145]**. CARS is impeded by its limited sensitivity to species concentration and the requirement for concentrations greater than ~0.1%, though this is similar to that required by Raman, and much higher than that tolerable in many LIF techniques. LIF's inability to cope with high concentrations (due to saturation) means that LIF and CARS may be seen as complimentary, as has been demonstrated by Mokhov & Levinsky **[157]**. Miles *et al.* **[158]** have also extended the idea to their RELIEF (Raman excitation plus laser induced electronic fluorescence) technique which can provide velocity information. Rotational CARS has also been shown to provide significant thermometric data **[159]**.

3▪8 LASER INDUCED FLUORESCENCE

Laser induced fluorescence uses the energy bound in the incident beam to promote the target molecule to a higher energy state. This 'optical absorption' is followed by an almost instantaneous relaxation which may, or may not, be radiative. The entire process has a timescale of 10^{-10}-$10^{-4}s$ **[145]**. Fluorescence is the radiative emission that maintains the spin multiplicity of the ground state, while phosphorescence is that which results from a state of different spin multiplicity. Phosphorescence is characterised by much longer timescales, typically 10^{-4}-$10^{-2}s$. The radiative emission may result from a number of states whether excited, predissociated or photoionized; while the yield may be linear or saturated depending upon the exact treatment of the subject molecule. Fluorescent emission can be at the incident wavelength (resonance fluorescence) or, more commonly, hypsochromically shifted from the incident frequency. Fluorescence gives signal strengths many orders of magnitude higher than Raman based techniques and as a result can be used to image very low concentrations (down to trace or *ppm*) and is readily expandable to planar analyses. Of most concern to the experimentalist is the strong tendency for excited molecules to be quenched. Quenching refers to any process which deactivates a molecule without directly leading to radiative emission.

3▪9 APPLICATIONS OF PLANAR LASER INDUCED FLUORESCENCE

Laser diagnostics have a wide range of uses applicable across a range of transient [160] and steady flows which may be sub-, or even, super-sonic [161-165] (although the latter has its limitations [161, 166]). Flow properties such as: velocity (using metal atom tracing [167], iodine [168-170] and nitric oxide [171] fluorescence), periodic instability [172]; or the extent of entrainment [173]
 are obtained easily. With added experimental and computational complexity more fundamental flow properties may be obtained. These include: levels of vorticity and strain [174]; the dissipation length scales of energy and mixture fraction [175]; small scale turbulent structure identification [176, 177]; conserved scalar behaviour [178]; and heat transfer characteristics [179, 180]. LIF is primarily used to study mixing [181, 182] and the resulting concentration field [160, 183-194], with the works of [173, 180, 193, 195-199] on concentration fields in jets of particular note. The technique of LIF may even be extended to visualise concentrations in three dimensions [199]. Advances in molecular photophysics and the role of temperature within it (*cf. §3▪11▪6*) have extended LIF application to the temperature imaging for, amongst other things, gaseous flows [169, 184, 186, 200-205] and liquid droplets [206].

Laser induced fluorescence has provided much experimental data on combustion and flames. The fuels studied range from coal [207] and acetylene [208, 209] to the more pertinent: LPG (liquid petroleum gas) [210]; hydrogen [160, 184, 211-213]; natural gas [214] and methane [187, 188, 194, 215-226]. Using LIF, it is now possible to gain insight into sooting [227-231], flame surfaces structure [232] and blowout [233]. Existing engine related laser diagnostics cover: flame kernel growth [234, 235]; swirl [236]; heat release rates [237, 238], pyrolysis [239]; flame position [240] and mixture formation (*cf. §3▪9▪1*); and are applicable to homogeneous (including homogeneous charge compression ignition [241-243]) and stratified mixtures [244-246] alike.

3▪9▪1 LIF FOR MIXTURE FORMATION AND DISTRIBUTION

Early work centred on mixture distribution imaging from Rayleigh scattering [247] or with fibre optic imaging of CH and C_2 [248]. The C_2 signal provided flame position while the ratio of the CH to C_2 signals provided equivalence ratio. Established laser techniques such as Raman scattering have been used to investigate major flame species (CH_4, O_2, N_2, H_2O and CO_2) as well as minor components (H_2) [215], the concentrations of which, when combined with Rayleigh scattered light, can provide temperature information [249]. However, for most minor species (NO, CO and OH) LIF is the experimenter's only recourse. Frank *et al.* [215] use three Nd:YAG lasers to probe methane/air flames with equivalence ratios of 0.6, 0.7 and 0.8. The species concentration results compare favourably with laminar flame calculations. Acetone emission displays only a small temperature dependence at 266*nm* excitation. However, Fujikawa *et al.* [250] in their study of gasoline direct injection stratified mixture formation perform a number of cell

experiments to identify the variation in LIF behaviour at different temperatures and pressures. An analytical approach is used to calculate the DI jet temperature due to evaporative charge cooling and fuel superheating, with the effects upon the LIF signal then taken into account to produce an accurate temperature corrected fuel-air-ratio (FAR) field. Fujikawa *et al.* use acetone as the fuel dopate, which is substantially different in nature to the *iso*-octane fuel, wiyj the inaccuracies are compounded by low laser energies (60*mJ/pulse*) necessitating high seed concentrations (10% *w/w*). The concerns of differential evaporation are cursorily addressed by noting the highly elevated cylinder temperatures, though the consequences of differential diffusion, fractional distillation, and the effects of the high seed concentration upon combustion are not discussed. It is subtleties like these that must be addressed since, as is noted by Kraemer *et al.* **[251]**, two seemingly identical initial mixtures may yield significantly different combustion characteristics. Kraemer *et al*. use a benzene/TEA[9] trace for *iso*-octane mixture formation in a DI SI ICE. Since the tracer is consumed during the combustion event, flame tracking is also performed. Mixture formation and flame front propagation are further studied by Wolff **[252]** who also investigates relative fuel density and residual gas distribution using an acetone doped (non-specified) fuel for an in-line four cylinder SI engine with equivalence ratios from 0.3-1. Of more use to gasoline, *iso*-octane and two phase fuel systems is the work of Ipp *et al*. **[253]** who use laser induced exciplex fluorescence of benzene/TEA to track both fuel phases. Their technique (which is validated in the liquid phase by Mie scattering and Raman scattering in the gas phase) allows the specification of probability density functions for the FAR at a series of locations. The same tracer combination was used by the same authors **[254]** to investigate (with Raman validation) mixture formation in lean ($\Phi = 0.8$) GDI engines where substantial fuel concentration gradients are found. The Raman investigation yielded sharper gradients due to its smaller probe volume, while the utility of completing Beer-Lambert attenuation calculations for incident laser intensity was brought into doubt. TEA also has application to gaseous fuel tracking **[255]** where it yields qualitative injection development information and can be temperature corrected to provide quantitative FAR values that correspond well to simultaneous Raman. TEA was also shown to track *iso*-octane and helium well (which was used as a safer proxy for hydrogen in motored studies), with only a ±3% error reported at a relative air fuel ratio of three. However, problems with TEA pyrolysis and retained gas fraction were noted to skew the LIF results under motored conditions. No such problems were encountered by Medaerts *et al.* **[214]** when they used toluene to track natural gas and gasoline. Using excitation at 248*nm*, mixture heterogeneity (for Φ=0.9-1.0) was elucidated. Pre-combustion diagnostics of lean hydrogen mixtures (Φ=0.55) is achieved with an acetone trace in the work of White **[256]**, who simultaneously uses OH* chemiluminescence to investigate the flame structure. A lack of detailed knowledge about the quenching behaviour and kinetics of OH* limits the investigation to the qualitative, which is further complicated by line of sight signal integration and the symmetry of the

---

[9] triethanolamine

OH* intensity about $\Phi = 1$. Similar imitations are placed upon the LIF signal due to the low seed densities which result from the limited vapour pressure at the high injection pressures. Despite these shortcomings the importance of injector geometry, injection timing and injection pressure are established for gaseous fuelling. Oh & Bae [257] have similar problems with a weak signal in their LPG LIF study, which uses acetone in a lean stratified mixture, though they do obtain meaningful mixture distributions in the richer zones and good flame front tracking. The work of Kaminski *et al.* [221] compares well with DNS predictions. The LIF signal, which is calibrated against 1D laminar flame calculations, provides good mixture fraction values (±30%) which are ostensibly temperature independent at the excitation wavelength of 282*nm*. The effect of highly controlled turbulence (the extent of which is verified by laser Doppler anemometry) is also evident, as are the quenching and surface reaction effects of the electrodes upon ignition. By applying a 2*μs* delay to one of the CCD flames and capturing OH* chemiluminescence, flame kernel structure was also investigated, while the calculation of the Reynolds and Karlowitz numbers allowed the establishment of flame rate and surface to volume ratio. A judicious use of tracer and excitation sources allowed a temperature map to be established simultaneously with a mixture distribution map. The pioneer of this technique, Marc Thurber, details this approach in [258] whereby he (and his colleagues) employs a method that uses a simple acetone dopate (at either 3% or 9%*v/v* for a co-flowing jet) excited at 248 and 308*nm* concurrently. This yields both the temperature and mole fraction fields. The short (30*ns*) lifetime of the fluorescence freezes the flow while careful concentration adjustment and laser sheet alignment ensure good agreement with the existing literature. A similar excitation scheme was used by Einecke *et al.* [186] to excite acetone's linear cousin 3-pentenone and make use of its 10*nm* hypsochromic shift per 100*K* increase in temperature (for any change in absorption behaviour is reflected in the emitted light intensity). However application was limited to small loads in a two-stroke engine since lean conditions (Φ=0.62) were required to avoid excessive self quenching.

3▪10 TRACER CHOICES

The current work is solely related to stratified natural gas combustion, and as such the discussion herein limits the innumerable set of tracer and fluorescing species to those suitable for gas phase diagnostics. Methane, the major component of natural gas, does not fluoresce under the influence of any known radiation sources. The consequence is that it must be doped with a fluorescent compound which acts as a proxy for the methane. The most important parameters for a tracer are those listed below (which have been paraphrased and adapted from [259] & [260]

- Possess a high fluorescent yield at easily available high-power laser wavelengths.

- Absorption and excitation of the tracer should still leave the fuel/tracer/air mixture 'optically thin'[10].

- A good spectral separation between the absorption and emission wavelengths is required so as to ease the implementation of the excitation and collection optics, but more importantly to avoid fluorescent trapping whereby the emitted light may be absorbed before reaching the detection source.

- It is desirable to have the fluorescent intensity independent of bath composition, temperature and pressure, yet strong enough to allow 2D visualisation. The lifetime must also be short enough to freeze the flow.

- The tracer must be structurally stable at the temperatures and pressures found in ICE's (for the duration of the cycle at least).

- The tracer should be consumed during the combustion process so as to avoid tracer build up.

- It should be inert with respect to the combustion process while tracking the fuel well.

- The dopate should have a high vapour pressure to facilitate low seed concentrations (which will also help the preceding point).

- Finally, the tracer must be non-toxic.

3▪10▪1 METAL ATOMS

Metal atoms are known to have large absorption cross sections with strong emission spectra, yet their production generally requires high temperatures [261]. Seeding levels may be kept low because of their strong emission, hence metal atoms allow the use of low power lasers. Consequently, saturation of the signal is easily achieved, which results in low signal strengths, despite the positive spectral properties.

3▪10▪2 INORGANIC MOLECULES

Many non-organic compounds are known to fluoresce when excited by a wide range of photon energies. Some, most notably water [262] and oxygen, display a weak signal that requires low pressures (almost vacuum) or high temperatures to fluoresce. Oxygen, even at moderate pressures ($\sim 10bar$) is rapidly collisionally quenched [263]. Despite this, the work of Lee and Hanson [264] paved the way for excitation in the deep UV (193nm), which provided meaningful O_2 concentration and temperature results ([265, 266] respectively).

Nitric oxide (NO) has been used extensively to study mixing, diesel sprays [267] and pollutant formation in flames [268] and combustors [269]. The spectral properties of nitric oxide have been exhaustively

---

[10] The incident radiation should exhibit no appreciable change in properties after passing through the medium/object.

reported in two seminal papers by Bessler *et al.* [270, 271], and build upon the earlier understanding provided by Di Rosa *et al.* [272]. With an absorption peak at 225.83nm [272] nitric oxide is easily excited with: the fourth harmonic of an Nd:YAG laser (214.34nm) [273]; a tuneable UV laser [271]; or a pumped dye laser [274, 275]. The collection requirements for the broadband UV emission are not excessively onerous. For accurate results the NO LIF signal must be extensively corrected for: temperature dependencies; differential diffusion; self quenching; the quenching effects of other bath gases; and signal interference from O_2 fluorescence [276]. The problems of seeding a fuel with NO can be circumvented by mixing the nitric oxide into the oxidiser stream, potentially allowing the mixture formation to be imaged 'inversely' [261], though this technique, to the author's knowledge, has not been applied quantitatively as yet. Further, substantial problems are also encountered due to the markedly different evaporative and diffusive characteristics of NO when compared to most fuels. This is most easily overcome by causing photodissociation of seeded NO_2 [171, 176] or the O_2 content of air [277], which provide the precursors to NO. This approach does not, however, allow for substantive 2D mapping and is limited by its short lifetime [261]. All these factors mean that NO LIF is suited to combustion events, rather than the mixing processes involved in engine mixture preparation.

Rather than photodissociate NO_2, the compound itself may be used directly as a fluorescent tracer. Nitrogen dioxide has many rovibronic excitation levels, and as such has correspondingly wide absorption and emission spectra. Typically, a frequency doubled Nd:YAG (532nm) laser is used for the excitation [273, 278, 279] although the spectra is broadband from ~250-666nm with a peak at ~357nm [280]. The fluorescent emission is seen to fluctuate significantly between 450 and 760nm, albeit with an increase in intensity towards longer wavelengths. Despite the insight into cyclic variations from Zhao *et al.* [279] on the applicability of NO_2 LIF to engine diagnostics, nitrogen dioxide is of more use in examining reaction kinetics; as has been demonstrated by Cattolica *et al.* [273]. Yet, it must be noted that, in general, NO_2 suffers the same problems as NO for tracking mixture formation in ICEs, and is less spectrally favourable for the same applications.

Sulphur is exclusively utilised for LIF studies as sulphur dioxide (SO_2). SO_2 displays a clear rovibronic structure with absorption throughout the UV, which strengthens at shorter wavelengths (Greenbough *et al.* [281] use a mercury lamp to excite over the range 180-390nm). A clear peak is observed in the absorption spectra at ~200nm, which produces "a broad structureless emission with a maximum at around 360nm" [282], though Greenbough *et al.* later pin-point the maximum to 374nm [281]. With a bathochromic shift in excitation Strickler & Howell note a marked increase in the phosphorescent to fluorescent emission ratio (×4, in the range 289-313nm) [282]. This observation is further corroborated by Mettee [283] who studied fluorescent lifetime from excitation at several wavelengths (313, 302, 296, 285 & 265nm), and attributed the shift to vibrational relaxation having a more marked effect than quenching, which would in

turn, explain the reduced fluorescent emission at longer wavelengths. Sulphur dioxide emission is heavily self quenched, the quenching being some twenty times stronger than that for CO_2 **[281]**, while it is also noted that oxygen only quenches the singlet emission **[281, 282]**. Nitrogen is also shown by Rao **[284, 285]** and Mettee **[283]** to heavily quench the emission, which correspondingly limits the applicability of SO_2 to combustion environments. More pertinently, the general observation that there are significant numbers of quench partners means that emission intensity is severely limited by increases in pressure. Through the use of sulphur doped fuels SO_2 LIF is deemed to be of more use in studying exhaust gases **[260]** or residual gas fraction and its influence on mixture preparation than the mixing process itself.

The body of work to support the OH radical as a fluorescent tracer is vast, though its application to the current study is limited. Generation and subsequent seeding of OH into a flow is impractical due to the short lifetime of the OH radical. Photodissociative production of OH from vibrationally hot water has been reported by Pitz *et al.* **[286]** to circumvent the seeding problem, though the approach is spectrally limited. The interested reader is referred to **[287]** for the details of OH LIF (and CH & C_2, which are similar in nature).

Iodine is highly corrosive and toxic, but has nevertheless been used as a fluorescent medium because of its favourable spectral properties. Hiller **[288]**, and references therein, review extensively the use of iodine to track pressure, temperature, density and velocity. Of particular note in the application of these approaches are Kido *et al.* **[173]** who use iodine to study gas entrainment in intermittent low speed jets; Lefebvre *et al.* **[169]** whose experimental apparatus provides simultaneous pressure, velocity and temperature fields and Lemoine *et al.* **[170, 289]** who use iodine LIF in compressible flows. Absorption is broadband in the green (usually with a 514.5nm argon ion laser excitation), though has a weak transition probability due to its spin forbidden nature. The forbidden transition generates a long emission lifetime (0.3-7μs, **[290]**) which allows for velocity specification. Excitation in the green provides a highly resolved ro-vibronic structure that results from nuclear-molecular spin interactions and yields some 45000 lines between 500 and 650nm **[288]**. Below 499nm the incident energy is enough to predissociate the iodine **[288]**. Molecular nitrogen and oxygen are known to be good quench partners though good fluorescent efficiency offsets this somewhat. This efficiency is due, in part, to the large absorption cross-section of iodine, yet this 'advantage' may limit the suitability of the gas since the fluorescent signal is easily saturated. The low diffusivity (0.07cm/s) of gaseous iodine explains its utility for flow tracking, but the difficulties of seeding at a constant rate (with levels typically at ~400ppm **[288]**) can hinder its experimental applicability **[261]**.

3▪10▪3 ORGANIC MOLECULES

The field of organic molecular photophysics is itself almost boundless. This is reflected in the vast body of work presented by Birks in his two volume *Organic Molecular Photophysics* **[291, 292]**, and his reliance on the contributions of two dozen contributing authors and innumerable cited works. Polyatomic molecules exhibit wide broadband absorption since the large number of quantum interactions permits many 'allowed' states and transitions. The large number of excited states provides a correspondingly wide emission spectra. Matching the tracer to the fuel, primarily in terms of boiling point and mass diffusivity, should ensure (as much as is possible) that the mixing processes are similar in the two substances.

3▪10▪3▪1   AROMATIC COMPOUNDS

Aromatic compounds are far less widely used than aliphatic ones (*cf. §3▪10▪3▪2*). The most widely used aromatic compound is toluene ($C_6H_5CH_3$). Toluene absorbs broadband UV from ~220-280nm, peaking at 262nm; with emission over the range 265-350nm and a maximum intensity at 284nm **[293]**. Initial work by Reboux *et al.* **[294]** at 248nm excitation found a linear dependence of fluorescent intensity upon incident laser energy (up to 5mJ/mm^2). The same study also found 5%v/v toluene in *iso*-octane to be optically thin, and not self-quenching. The effects of nitrogen, water vapour and CO_2 upon fluorescent intensity were found by the same authors to be negligible. Oxygen was hypothesised to be toluene's main quench partner (which was later studied in detail by Koban *et al.* **[295]**) and the direct relationship observed between intensity and oxygen concentration suggested a linear FAR-LIF relationship. However, Reboux *et al.* noted a temperature dependence of ~20%/100^0C which was later used by the same researchers **[294]** to investigate charge inhomogeneity in SI-ICE's. The purported results are quoted as being accurate to within 2%, yet the work of Koban *et al.* **[296, 297]**, in the author's opinion, casts doubt upon this assertion, in that the toluene signal does not scale linearly with oxygen partial pressure. Koban *et al.* **[295]** propose a detailed two step fluorescent model which accurately predicts the behaviour of toluene emission in the presence of oxygen at bath compositions relevant to ICE's. Indeed, in 2002 Frieden *et al.* **[298]** used toluene's oxygen dependent behaviour to predict oxygen concentrations in a directly injected spark ignited engine. For the current study however, toluene is of limited use since its physical properties lend it to tracking *iso*-octane (rather than methane), though the work of Fujikawa *et al.* **[250]** compares the use of toluene to acetone at 1bar and 20^0C and notes that at 248nm toluene is 90 times more fluorescent than acetone.

Polycyclic aromatic hydrocarbons (PAHs) may be seeded into a flow or, as is more often the case, be part of the (commercial) fuel[11] to be studied. Their absorption in the blue-UV range is complex, though well documented and noted to shift hypsochromically with increased pressure **[292]**, *Ch.3*. Similarly, the emission, which occurs over a similar wavelength to the absorption (the details of which are heavily dependent upon the exact structure of the compound), is broadband and highly structured **[292]**, *Ch2*. The large absorption cross section of PAHs and their high quantum yields ($\Phi_f = 0.17 - 0.82$ **[261]**) makes them ideal tracers from a spectroscopic point of view (**[299]**, **[292]** *Ch. 2-3*). The fluorescent lifetime of the emission may even be used to map the composition of the PAH ensemble, given that each is unique **[300]** and may be coupled with detailed knowledge of the hypsochromic shifts observed for increased compound size **[261]**. The large number of PAHs available allows tailoring of tracers for a bespoke fit to complex fuels; though ensuring a matched boiling point does not ensure fuel following behaviour **[301, 302]**. Further, any PAHs larger than toluene or benzene need to be seeded at above room temperature because of their low vapour pressure **[261]**. Thijissen *et al.* **[192]** have conducted *in situ* LIF PAH concentration measurements in an industrial scale fuel rich natural gas flame. Excitation using an argon ion laser at 488*nm* established a correlation between the LIF signal intensity and the PAH concentration. It was found that LIF emission is strongest from high molecular weight PAH's (*e.g.* coronene), and that their fluorescence emission spectra are similar to those from flames. The difficulty of seeding PAHs directly and matching their mass diffusion properties to gaseous fuels has not been overcome, while the health concerns of these compounds also often precludes their use.

3▪10▪3▪2   ALIPHATIC COMPOUNDS

Aliphatic compounds are easily excited in the UV though tend to photo-dissociate. Longer unsaturated or conjugated systems are generally unstable and are prone to polymerization **[261]**. The need for an easily accessible chromophore leads to structures like ketones (R_2CO), aldehydes (R-CHO) or amines (R_3N)[12], while conjugation is also know to produce marked hypsochromic shifts in the fluorescence spectra **[261]**.

Ketones have been studied extensively for their spectral and photochemical properties. Their pressure and temperature dependencies are relatively easily modelled (**[303, 304]** and **[305]** respectively), and the fluorescent lifetime of ketones is well established **[306]** for a range of temperatures and pressures **[307]**. Knowledge of the role of oxygen in ketonic systems is also well established **[308]**. The combined effect of this extended understanding has allowed several authors to present detailed ketone photophysics **[303, 309]**. The range of accessible vapour pressures allows ketones to track gas phase fuels well (*e.g.* the use of acetone to track natural gas: **[310, 311]**); as well as liquid phase fuels where 3-pentenone (or a mixture

---

[11] Gasoline contains high concentrations of single ring aromatics (toluene and xylene) while diesel has plenty of two-ring compounds (naphthalene and its derivatives)
[12] Where R is a saturated hydrocarbon

of 3-pentanone and 3-hexanone [312]) has been used widely to track gasoline [307, 313, 314], or more commonly iso-octane. Biacetyl ($CH_3(CO)_2CH_3$) is widely used in fluorescent and phosphorescent studies since its boiling point of 88^0C matches well that of liquid fuels and in some cases can be deemed suitable for gaseous flows and it exhibits a high phosphorescent yield (~15% [261]) in oxygen-free flows. However, biacetyl has a low vapour pressure, which makes it difficult to seed.

Formaldehyde (CH_2O) is difficult to dope since it polymerizes easily [261], though its temperature dependent fluorescent behaviour also allows the identification of temperature variations in the immediate pre-combustion field [190, 315-317]. Formaldehyde LIF is often used simultaneously with CH LIF for flame front imaging [318, 319]. Further, coupling of the CH_2O and OH LIF signals has been shown by Paul *et al.* [237] to correlate well with the local heat release rate. The applications of CH_2O LIF are widespread and accurate [190, 200, 243, 316, 317, 320, 321], but are tied to the combustion process as the method of CH_2O production, and as such leave CH_2O of no use in mixture formation diagnostics.

The next homologous molecule to formaldehyde is acetaldehyde (CH_3CHO), which has been successfully used as a tracer by Arnold *et al.* [322]; however, acetone is commonly used in preference since it is less harmful. Aldehydes exhibit small quantum yields compared to aromatic compounds in the absence of oxygen, yet are comparable in the presence of air. Hexafluoracetone is suggested as an alternative to acetone since its quantum yield is an order-of-magnitude greater [323], though there are problems with its toxicity. Hansen and Lee [324] have investigated the radiative and nonradiative lifetimes of linear aldehydes. Radiative emissions share much the same lifetime as large aldehydes and follow well the Stickler-Berg equation, expect for acetlylealdehyde which has a much longer radiative lifetime than expected.

CH LIF provides similar information and is applied in much the same was as CH_2O LIF. It is particularly useful in methane and natural gas combustion studies. It is, however, applicable across a wide range of hydrocarbon fuels due to its prevalence in hydrocarbon combustion pathways. Yet, without a flame the practicalities of generating and seeding CH prohibit its use in mixture studies when easier and more effective tracers are available.

Carbon dioxide LIF can be spectrally resolved in the 215-255nm range using an Nd:YAG pumped dye laser and has been successfully used by Lee *et al.* [325] to study $CH_4/O_2/Ar$ and CH_4/air flat-flames at fuel/air ratios from 0.8-1.9 in the pressure range 5-40bar. Emission is broadband in the range 200-450nm and has a weak structure. Further, the signal was found to scale linearly with laser fluence and pressure (within the range stated). However, in general, the signal from CO_2 is weak and strongly temperature dependent, precluding its use as a direct measure of concentration [261].

Amines, as is common to most aliphatic compounds, fluoresce under UV excitation. They are however, effectively quenched by oxygen and often deemed prohibitively toxic for widespread use. Amines used in their own right include ethylamine **[326]** and N,N-dimethylaniline (DMA) **[327]**, though they are more commonly used in exciplex systems particularly as aniline groups (*i.e.* NH_2 on a benzene ring) **[261]**.

3▪11   ACETONE AS A FLUORESCENT MEDIUM

Acetone (also called propanone, dimethyl ketone, 2-propanone, propan-2-one and *β*-ketopropane) is an aliphatic ketone with formula $(CH_3)_2CO$, *cf. Figure 3-3*, and molecular weight 58.08. Its high vapour pressure (24 kPa at 20^0C) facilitates high seeding densities, while its vapour pressure behaviour fits the Antonie equation well **[196]**. The photochemical properties of acetone have been studied extensively, starting with the work of Heicklen **[328, 329]** and Groh **[330]**. Typical of ketones, acetone exhibits strong absorption from 225-320nm, with a peak at 277nm **[331]**, though the absorption spectrum is ostensibly flat between 270-280nm **[196]**. The emission spectrum of acetone is broadband blue between 350-550nm with peaks at 445 and 480nm **[196]**; the spectra is, however, affected markedly by vibrational relaxation prior to emission (*cf. §3.11.4*). Acetone has flammability limits which are easily accommodated and it is not carcinogenic or excessively toxic, though prolonged exposure is advised against.
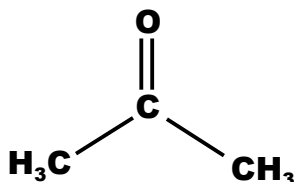
Figure 3-3 Molecular Acetone, $(CH_3)_2CO$

Upon excitation, various process are competing to deactivate acetone, *cf. Figure 3-4*. From the first excited singlet state, S_1, there may be: fluorescence, the spontaneous emission of radiation resulting from a transition which maintains spin multiplicity, $S_0 \leftarrow S_1(n,\pi^*)$; intersystem crossing, the conversion from one state to another of different multiplicity $T_1(n,\pi^*) \leftarrow S_1(n,\pi^*)$ **[309]**; internal conversion, the non-radiative conversion from one state to another of equal spin, $S_0 \leftarrow S_1(n,\pi^*)$; or photodissociation of the acetone to several possible photo-products.
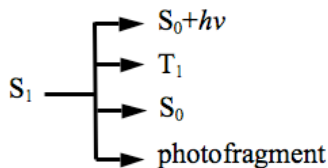
Figure 3-4 Deactivation Pathways for the First Excited Singlet, S_1, of Acetone,
adapted from [332]

Acetone's status as the *de facto* tracer for methane comes from its similarity to methane in the most salient of physical properties, *cf. Table 3-2*.

	Methane	Acetone
Molecular Weight (*g/mol*)	16.043	58.080
Density @ 25^0C (*g/cm³*)	--	0.786
Boiling Pt. (*^0C*)	-161.48	56.1
Lower Heating Value (*MJ/kg*)	50	28.6
Heat of Vapourisation @ 25^0C (*kJ/mol*)	--	30.99
Heat of Combustion (*MJ/mol*)	0.8908	1.8207
Max. Burning Velocity @ 25^0C with *Φ* Specified (*cms⁻¹*)	44.8 @ 1.08	44.4 @ 0.93
Flash point (*^0C*)	-188	-18
Autoignition Temp. in Air (*^0C*)	537-632	465-727
Flammability Limits in 1 *bar* Air (*% vol*)	5.0-15	2.6-13
Gas Phase Viscosity at 100^0C (*μPa s*)	13.4	9.5
Gas-Phase Diffusion Coefficient in 1 *bar* air @ 100^0C (*cm²s⁻¹*)	0.344	0.166
Gas-Phase Diffusion Coefficient in 8 *bar* air @ 130^0C (*cm²s⁻¹*)	0.0493	0.0239

Table 3-2 Physical & Thermodynamic Properties of Methane and Acetone Gas, excerpts from [259, 261] and references therein.

3▪11▪1 EXCITATION SOURCE CHOICE

The broad absorption spectrum of acetone facilitates the use of many excitation sources. It is important to note that as the absorption cross-section increases for shorter wavelengths, the fluorescent efficiency decreases slightly due to higher dissociation (*cf. §3▪11▪3*) The 'figure of merit' (sic, [196]), *Eσ*, in the final column of *Table 3-3* is the product of pulse energy and absorption cross-section at the laser wavelength, and provides a metric against which to measure the efficiency of each excitation source. With the exception of the difficult to use flashlamp pumped rhodamine 590 dye laser the krypton fluorine (KrF) laser shows the best applicability, and as such is used in the current work.

Laser	λ (*nm*)	Energy/pulse (*mJ*)	*Eσ* (x10⁻²⁰ *Jcm²*)
XeCl excimer	308	300	0.48
KrF excimer	**248**	**300**	**0.7**
Quadrupled Nd:YAG	266	120	0.52
Flashlamp Pumped Rhodamine 590	280	400	1.9
Raman Shifted ArF Excimer	254	2	0.006
	284	1	0.0045

Table 3-3 Acetone Excitation Sources, after [196]

3▪11▪2 ABSORPTION

Upon excitation the singlet ground state of acetone is excited to the first electronic state of similar spin multiplicity **[333]**, which is 30435 *cm^{-1}* above the ground state **[334]** (although Thurber *et al.* **[305]** use 30440*cm^{-1}* in their modelling work). The chromophoric C=O bond undergoes a transition to elevate an electron from its non-bonding, *n*, oxygen orbital to that of an anti-bonding *π** orbital*,* leaving the electron unpaired and the oxygen with a partially filled p-type orbital (*cf. Figure 3-6*). The *n→π** transition is orbital-forbidden though spin-allowed **[307]**, and is thus weak. In its excited state the weakened C=O bond leads to carboxyl out-of-plane wagging and stretch **[333, 335]**, while also causing molecular lengthening and pyramindization at the carbonyl carbon atom through increased C-C torsion **[309, 333, 335]**. The low energy of all these behaviours means that their frequencies are much lower than that of the molecular vibration, obscuring any rotational structure in the absorption band for acetone **[336, 337]**, *cf. Figure 3-5*. A hypsochromic shift, of about 2*nm*/100*K*, in the absorption spectra for 3-pentanone (which, as $(C_2H_5)_2CO$ is a corollary of acetone) is noted by Grossman *et al.* **[307]**. These findings were later extended and confirmed to apply to acetone by Thurber *et al.* **[305, 306]** and Ossler & Aldén **[306]**, the former also noting that the absorption cross-section increase significantly with temperature. The increased absorption cross-section roughly compensates for the loss in cross-section caused by the hypsochromic shift for excitation wavelengths shorter than the peak at 277*nm* (at ambient temperatures).
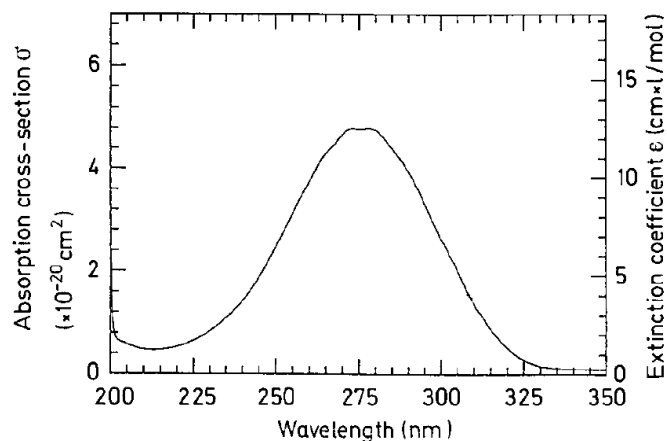
**Figure 3-5 Absorption Spectrum of Acetone at Room Temperature and 1 *atm*,
reproduced from [196]**

3▪11▪3 PHOTODISSOCIATION OF MOLECULAR ACETONE

The cleaving of the α-CC bond occurs since the bond overlaps the vacant non-bonding oxygen orbital in the excited *π** state (*Figure 3-6*) **[338]**. The latest *ab initio* studies by Liu *et al.* **[339]** suggest that the dissociation barrier for the lower energy methyl acetyl split, *Fig.3-6a*, lies at 556 *kJ/mol* above the ground sate.

(a)

(b)
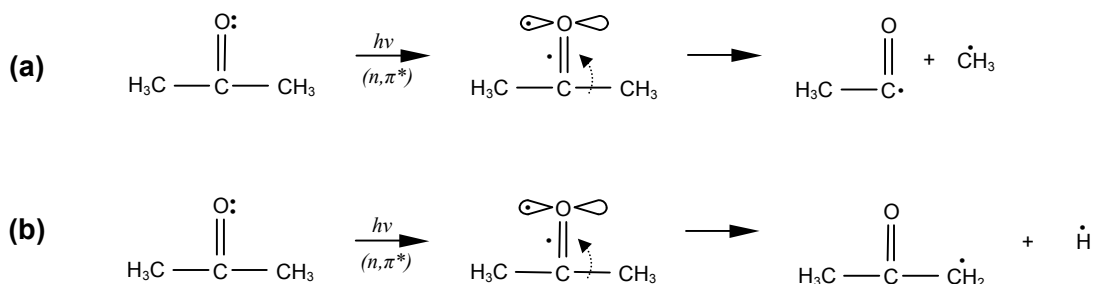
Figure 3-6 Acetone Dissociation through α-Cleavage,
adapted from [338]

This cleavage reaction allows for multiple products, though the methyl acetyl split is more thermodynamically preferable **[338]**, and explains the predominance of *Eq.3.1* in the photodissociation of acetone **[340, 341]**.

$$(CH_3)_2 CO + hv \rightarrow CH_3\dot{C}O + \dot{C}H_3 \qquad \textbf{Eq. 3.1}$$

For excitation at less than 312*nm* **[196]**, and particularly under 300*nm* **[342]**, the alternative *Eq. 3.2* is more likely.

$$(CH_3)_2 CO + hv \rightarrow 2\dot{C}H_3 + CO \qquad \textbf{Eq. 3.2}$$

It is noted by Liu *et al*. **[339]** that the energies required to form the products of *Eq.3.2* are unattainable by direct 248*nm* excitation, and a step wise decomposition of the $(CH_3)_2CO$ molecule is more likely **[343]**. Consequently, at wavelengths below 250*nm* the reaction outlined by Calvert & Pitts **[344]** and generalised by Gilbert **[338]** may also occur (*Figure 3-6(b)*), *viz.*:

$$(CH_3)_2 CO + hv \rightarrow CH_3C(O)CH_2 + H \qquad \textbf{Eq. 3.3}$$

Haas **[309]** proposes a detailed 11 step mechanism for the photodissociation of acetone, which outlines exact product formations, including that of biacetyl (*cf. §3▪11▪3▪1*). Observed reductions in phosphorescent intensity with decreased wavelength indicate that photodissociation increases with excitation energy **[345]**. Excitation of acetone at 248*nm* through the global step of *Eq. 3.1* leaves many (~30%) **[343]** of the photofragments with enough excess energy that the acetyl radical may spontaneously decompose to form, with the original methyl radical, the products of *Eq.3.2*. The linear Stern-Volmer plot obtained from the data of Blitz *et al.* **[342]** for λ<300*nm* suggests deactivation from only one excited state- the singlet state S_1- according to the scheme (that may include any third body, *M*):

$$
\begin{aligned}
S_0 + hv &\rightarrow S_1, S_1{}^* \\
S_1 \quad &\rightarrow CH_3\dot{C}O + \dot{C}H_3 \\
S_1{}^* \quad &\rightarrow 2\dot{C}H_3 + CO \\
S_1 + M &\rightarrow S_0 + M
\end{aligned}
\qquad \textbf{Eq. 3.4}
$$

3▪11▪3▪1   BIACETYL POISONING

The main products of acetone photochemical pyrolysis are: ethane, methane and carbon monoxide [309]; however, the acetyl radical resulting from *Eq. 3.1* is important since it may recombine to form biacetyl, $(CH_3CO)_2$, which produces a strong phosphorescent signal [346]. This competes with the fluorescence of the acetone S_1 state, and may complicate the collection of a high fidelity fluorescence signal. Biacetyl formation from triplet acetone is only of concern for excitation above 300*nm* [342] or at temperatures below 100^0C [347]. However, when present biacetyl effectively quenches the T_1 state of acetone, reducing the tendency for acetone to phosphoresce, but in the process exciting itself to phosphoresce (at wavelengths similar to acetone) [328]. Although biacetyl triplets are known to phosphoresce with high efficiency (~15%) they are also effectively quenched by oxygen; while biacetyl fluorescence has a very low efficiency below 320*nm* [196]. For excitation at 248*nm* it is observed that there is a move away from *Eq.3.1* towards that of *Eqs. 3.2 & 3.3* reducing the biacetyl concentration to a level which is not of concern [309]. While, under thermal conditions the low concentration of acetyl radicals negates the need to worry about biacetyl formation [309]. All of these features mean that for the oxygenated environment of the RCM, biacetyl poisoning may be disregarded.

3▪11▪3▪2   THERMAL DISSOCIATION

Thermal pyrolysis of acetone, through the Rice-Herzfield mechanism [348], primarily yields carbon monoxide, methane and ketene ([349] in [309]), with small amounts of butanone, ethane and 2,5-hexanedione [309]. However, the process is not significant for temperatures below ~800*K*, which the compression stroke of the RCM fails to generate.

3▪11▪4 NON-RADIATIVE DEACTIVATION

Throughout the following discussions reference to *Figure 3-7* may be of help to the reader. Hansen and Lee [332] assert that "…the non-radiative processes predominate over the radiative processes at least by two orders-of-magnitude in simple ketones.", the low zero-pressure fluorescence quantum yield of ~0.002 reported by Heicklen [328] and Shortridge *et al.* [350] supporting such a view. Inter-system crossing from the singlet state is known to peak at intermediate energies [345], which suggests competing pathways for the deactivation of the S_1 state based upon its vibrational state [303]. Rapid inter-system crossing (ISC) (k_{ISC} between 4 x 10^8 s^{-1} [350] and 3 x 10^8 s^{-1} [303], and $\tau_{ISC} \leq 10ns$ [345]), depopulates the first excited singlet state to that of the first triplet manifold at 28000cm^{-1} above the ground state [334]. Although the process is spin-forbidden the first singlet and triplet states of acetone are closely coupled such that ISC efficiencies approach 100% [351-353]. The small energy difference between S_1 and T_1 means that collisions also effectively populate T_1 from S_1 [354]. The resultant mix of excited acetone in its singlet and triplet states has a predominant triplet character because of the efficient ISC [354]. The triplet

component may come from increased excess energy above the S_1 state, which increases molecular vibration and rotation to promote ISC to the T_1 state, or by direct optical preparation [354]. The $n \rightarrow \pi^*$ transition is known to produce a movement of electron density away from the oxygen molecule, with the methyl moieties able to inductively donate electron desnity, stabilising the excited state [338]. This allows ISC to take place (potentially following vibrational relaxation, VR, in the excited singlet state) before rapid, fluorescent deactivation that is independent of the bath phase [303].

The vibrationally hot triplet state, T_1^{**}(which predominates in the high pressure and liquid phases of acetone [354]) may phosphoresce ($\tau_{T1**} \sim 30\mu s$ [345]), dissociate or relax to a thermally equilibrated state, T_1 [355], where it cannot be fully quenched due to its high reactivity [309], though may still dissociate through the Rice-Hertzfeld mechanism [348] (*cf. §3▪11▪3▪2*), or phosphoresce. Bitto [356] asserts that it is the vibrational coupling of the torsional modes in the symmetrically favourable triplet manifold which increases the lifetime of the triplet state. This thermal triplet, T_1, does not however correlate directly with the triplet ground state [309] and so no fluorescence is observed from a possible $T_0 \leftarrow T_1$ transition.
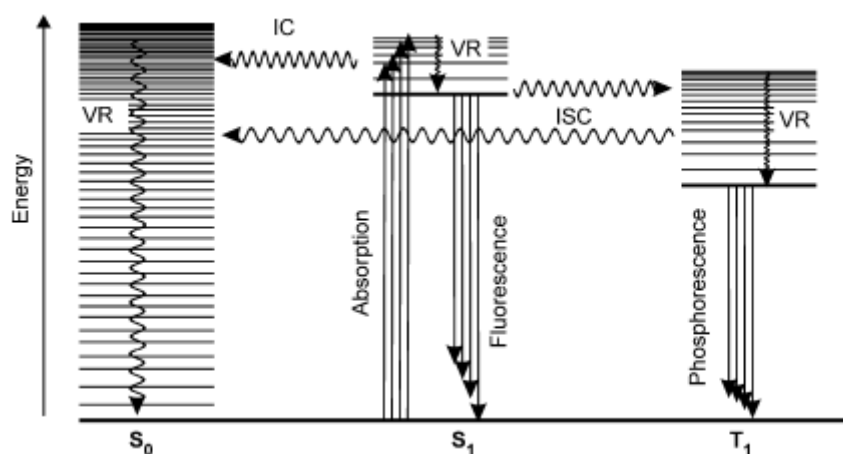
Figure 3-7 Jablonski Diagram for a Electronically Excited Organic Molecule, reproduced from [261].

3▪11▪5 RADIATIVE DECAY

The mixed singlet-triplet state leads to a quasi-biexponential decay of the excited state [337] whereby the nature of the emission is governed by the rovibronic interactions of the molecule [354]. When excited to near the S_1 origin, decay to the S_0 ground state is most likely through fluorescent emission [354]. Yet for stronger stimulation the small number of molecules left in the S_1 excited state after ISC may relax to a vibrationally excited ground state, S_0^*, through internal conversion (IC). Those molecules left in the metastable T_1 state (populated directly from ISC or thermally relaxed T_1^{**} molecules) have a lifetime which is purported by Bitto [356] to be extended due to symmetrically favoured vibrational coupling. This accounts for the long lifetime observed for the phosphorescent relaxation to the ground state S_0 ($\tau_{T1} \sim$

$200\mu s$ **[345] & 196**). The emissions spectra of acetone are shown in *Figure 3-8* where the lower energy of the triplet emission shows a clear hypsochromic shift.
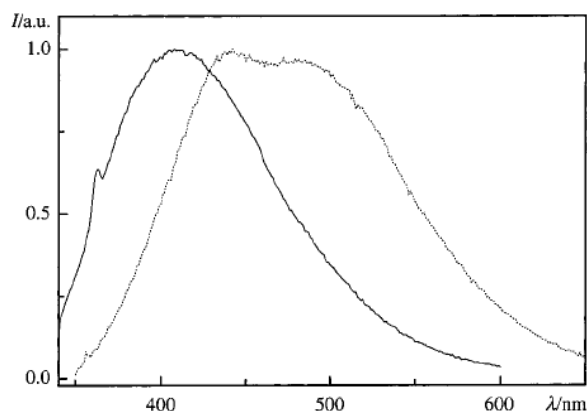
Figure 3-8 Fluorescent (solid line) and Phosphorescent (broken line) Emission Spectra for Pure Acetone, reproduced from [331]

3▪11▪6 FLUORESCENT SIGNAL LINEARITY, QUENCHING & THERMODYNAMIC STATE EFFECTS

For weak excitation of acetone, the fluorescent intensity is known to be proportional to incident laser intensity (up to ~1 *J/cm²*) **[196, 357]**. To remain linear however Lozano *et al*. **[196]** assert that the inequality *Eq.3.5* must hold true.

$$N_i << (\sigma\tau)^{-1}$$

<div align="right">**Eq. 3.5**</div>

For 248*nm* excitation the absorption cross-section and lifetime yield N_i to be $\sim 4\times10^{28}$ *photons/cm²s*. For a 20*ns* pulse at this wavelength, incident laser intensities must reach ~630 *J/cm²* to saturate the signal, yet the KrF excimer used in the current work can only supply a maximum of 166 *J/cm²*, implying that all fluorescent intensity values may be deemed proportional to laser beam energy. Copeland and Crosley **[336]** assert that the lowest photodissociation barrier for acetone is at 360*kJ/mol* above the ground state. For a constant 1*mm* thick laser sheet in the RCM cylinder, with an acetone concentration of 1%, the maximum laser power (of 400*mJ*) would excite the acetone to ~42*kJ/mol* above its ground state. This suggests that 248*nm* excitation avoids the need to consider dissociative effects- an assertion supported by the work of Liu *et al*. **[339]**. Finally, the fluorescent intensity observed is also known to be proportional to the partial pressure of acetone vapour **[196, 357]**.

The failure to generate a Boltzman population of the probe volume in the S_1 state upon excitation (because of the fast ISC from the singlet to triplet states) yields the prompt fluorescent emission observed, which in turn limits the susceptibility of singlet acetone to quenching **[258, 358]**. Oxygen, which has a triplet ground state, is the notable exception to this. The small but distinct quenching effects of oxygen upon acetone fluorescence are reported by several authors **[304-307]**, and are well understood for excited molecules in general **[330, 359, 360]**. The triplet state of oxygen is a more effective quencher than its singlet equivalent **[308]**, which may result from its energetic similarities to the $^1(n,\pi^*)$ state of acetone.

The consequence is that oxygen quench rates are close to, or exceed, the gas kinetic rate constant for acetone **[354]**. For ketone oxygen interactions Grossman *et al.* suggest the mechanism of oxygen quenching to be based upon "…the formation of a charge transfer complex with the ketone, involving the electronegative oxygen atom of the excited carbonyl bond and the electrons of the [oxygen] double bond." **[307]**. The work of Nau *et al.* in the liquid phase suggests a similar mechanism to that of Grossmann *et al.* with the formation, upon ketone-oxygen collision, of an encounter complex which if stable will give an overall quench rate proportional to collision frequency (**[361]** in **[357]**). Breuer *et al.* **[303]** suggest the findings of Nau *et al.* to be due to oxygen enhanced ISC that serves to depopulate the S_1 state. They correspondingly adjust the work of Thurber *et al.* **[305]** to correct for fluorescence yield at shorter (248*nm*) wavelengths, though no significant new trends were observed. Excitation of acetone at shorter wavelengths is noted to increase the likelihood of quenching since further excitation above the S_1 origin allows for more vibrational relaxation before ISC or radiative deactivation **[307]**. The vibrational level of the excited state is also known to have a small effect on the encounter probability of oxygen assisted ISC **[357]**.

In the gas or vapour phase the effects of quenching manifest themselves through differences in fluorescent intensity at different temperatures and pressures. The work of Thurber & Hanson **[357]** indicates that in a nitrogen bath gas fluorescent intensity increases asymptotically towards a high pressure limit (at ~16.5*atm* for 248*nm* excitation)- attributable to full vibrational relaxation of the S_1 state prior to ISC. This limit will be reached sooner at longer excitation wavelengths since there is less vibrational relaxation to take place before radiative decay. Similar trends are observed in a pure oxygen bath gas, with the high pressure limit being reached sooner (at ~4*atm*) because of more effective oxygen quenching (though the fluorescent intensity is also observed to decrease for increases in pressure past the upper limit). The data of Grossmann *et al.* **[307]** which pertains to a synthetic air bath gas, unsurprisingly, shows a tendency to reach a high pressure limit (at ~8-10 *bar*) which sits between the two cases of Thurber & Hanson. The behaviour is not paralleled exactly however. For 248*nm* excitation an increase in fluorescent intensity is observed up to eight bar, where the high pressure limit is apparently reached, yet past ~25 *bar* a steady drop of ~1% per *bar* is then observed without explanation (up to an experimental maximum of 50 *bar*). These findings are at odds with those of Yuen *et al.* **[304]** who, for their air bath studies, report the drop in fluorescence to start at ~5 *bar* and continue until the experimental maximum of 8 *bar*.

Temperature affects emission by varying the product of absorption cross-section and fluorescent yield for a given molecule. Koch and Hanson report no significant change in intensity for 3-pentanone fluorescence in air over a range of bath temperatures **[358]**. This is consistent with the observation, in another study by Koch & Hanson **[362]**, that acetone has an almost constant absorption cross-section at

248*nm* excitation (the absorption cross section was observed to rise by only ~5% over a 600*K* temperature increase). However, other significant works **[305, 307, 363, 364]** show small though clear dependencies of acetone and 3-pentanone emission on temperature. Grossman *et al.* **[307]** report (for 248*nm* excitation in synthetic air) a steady drop in fluorescent intensity of ~*35%* per 100*K* while Ghandi & Felton **[363]** report similar, though slightly less dramatic, findings for acetone in a heated jet and a motored engine (at 266*nm*). All the studies are able to discount thermal dissociation for the decrease. The findings of Thurber *et al.* **[305]** are in agreement with those of Tait & Greenhalgh **[364]** (who use 308*nm* excitation of acetyhldehyde) and Grossman *et al.* **[307]**, and extend the results from a 600*K* experimental maximum to 975*K*. Beyond ~800*K* the drop in fluorescence is seen to reduce by ~*8%* per 100*K*, with a smooth transition between the two regimes. Although there is a significant increase in absorption cross-section with temperature it does not correct for the decrease in fluorescence and so a marked drop in fluorescent yield is observed for increased temperatures **[305]**, and as such is a useful temperature diagnostic.

According to the model of Thurber & Hanson **[357]**, when the above tendencies for pressure and temperature are combined for acetone, at 248*nm* excitation, a rise in fluorescent yield is still observed. Indeed, it is noted that pressure effects are stronger for the shorter wavelengths and the reduction in fluorescent yield due to temperature rise mitigate only slightly the rise due to pressure. For increased pressure and temperature Ossler & Aldén **[306]** report similar effects on fluorescence decay time to those of fluorescence intensity. From a 'zero-pressure' minimum up to ~10*bar* the fluorescent lifetime increases linearly from ~0.9*ns* (with a slope of ~0.15*ns/bar* at 323*K* decreasing to ~0.02*ns/bar* at 723*K*) as in *Figure 3-9*.
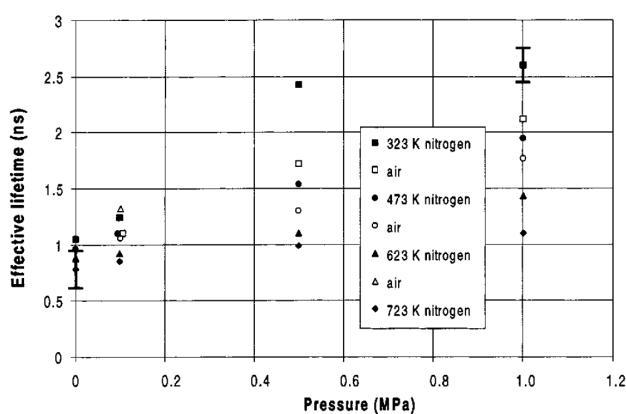
Figure 3-9 Fluorescent Lifetime Variation of Acetone with Pressure, reporoduced from [306]

3▪12   CONCLUSIONS

The most salient details of the main techniques that could be used to study species concentration have been outlined. The suitability of each to combustion diagnostics has been discussed, and from this the utility of laser induced fluorescence made patent. The versatility and diversity of LIF applications has

been outlined and a comprehensive discussion of possible gaseous tracer compounds made. A strong case for the use of acetone as a proxy for methane/natural gas has been made, primarily on the basis of their well matched physical properties. Further discussion has been offered as to the utility of acetone, its spectral properties, and how these properties vary with engine relevant conditions. Acetone LIF has been studied extensively and its behaviour is well understood, so allowing the contemporary experimentalist to draw meaningful and accurate inferences from its use.

Chapter 4
EXPERIMENTAL SETUP & PROCEDURES

4•1 INTRODUCTION

Chapter 4 offers the most important details of the rapid compression machine used in the current study. Important changes are highlighted, primarily with respect to the improvements that allow combustion studies to be supported and the control systems required to operate the fuelling and laser diagnostics systems. The experimental test matrix is outlined, with all pertinent parameters and operational details provided to the reader, along with the rational behind the choices made.

4▪2 THE RAPID COMPRESSION MACHINE

The rapid compression machine, RCM, was designed and built by Döhring **[365]** and can simulate any two consecutive strokes of an internal combustion engine. The RCM is shown schematically in *Figure 4-1*. The most important features are considered in detail below.

Driver Section

Cylinder

Braking Section
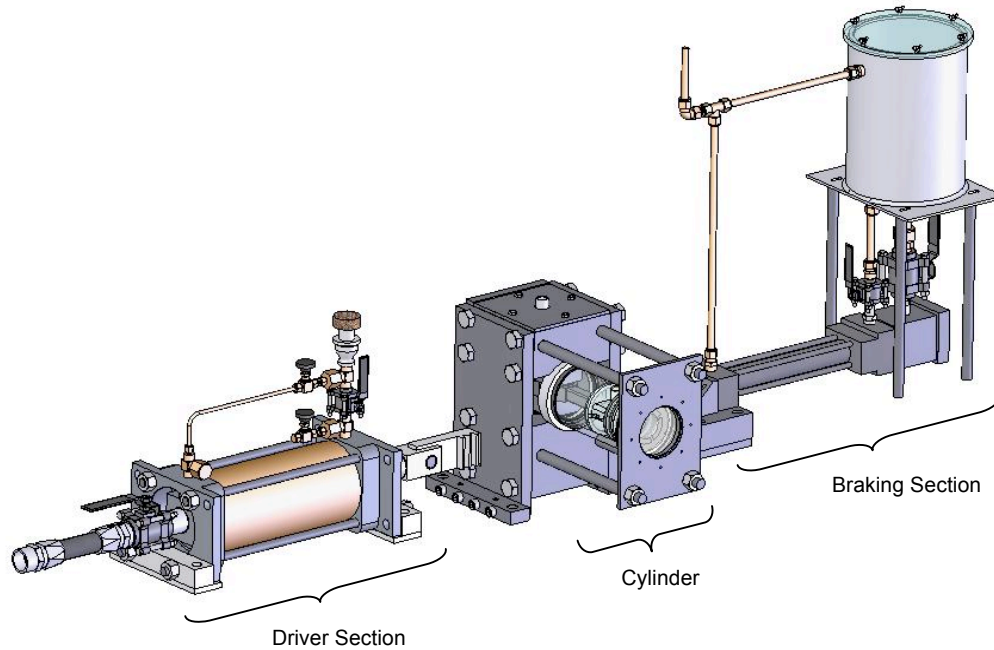
Figure 4-1 Schematic of Rapid Compression Machine (RCM)

The principle of operation is as follows. The RCM piston and con-rod are driven by a vertical crank shaft, which is itself driven by a rack, where the rack is actuated by a pneumatic cylinder. The braking force is provided by a hydraulic piston on the opposite side of the rack. The pneumatic cylinder is supplied by an 80*gal* accumulator, which is charged from the regulated laboratory compressed air supply. The braking side is a closed loop system filled with 20W30 oil. When air pressure is supplied to the driver cylinder, the rack is prevented from moving by the solenoid valve on the braking side. This valve prevents flow in the oil loop. To actuate the RCM the solenoid valve is triggered so that the oil in the braking cylinder is allowed to flow up into the reservoir. When the rack is returned to the start position, a small secondary loop is opened on the braking side such that the braking piston is allowed to fill from the reservoir. The details of RCM operation have been covered previously **[365, 366]**, and only those operational changes pertinent to this study shall be reported herein.

The single shot nature of the RCM, its lack of intake and exhaust manifolds, and the omission of the valve train mean that cyclic variability is almost eradicated, whilst also ensuring strict control of the in-cylinder

charge motion. Any motion may be fully eliminated to give a quiescent starting state from which all subsequent fluid movement is imparted by the piston.

4▪3 NEW RCM CYLINDER

As part of the current work the rapid compression machine was altered significantly from its previous incarnations. Prior studies using the RCM **[365, 366]** have been based on cold flow. The PMMA cylinder arrangement of the RCM was redesigned and retrofitted with a UV grade HPFS (high purity fused silica) cylinder and fire deck, and a new 316 stainless steel cylinder and cylinder head installed to allow combustion (*cf. Figure 4-2*).
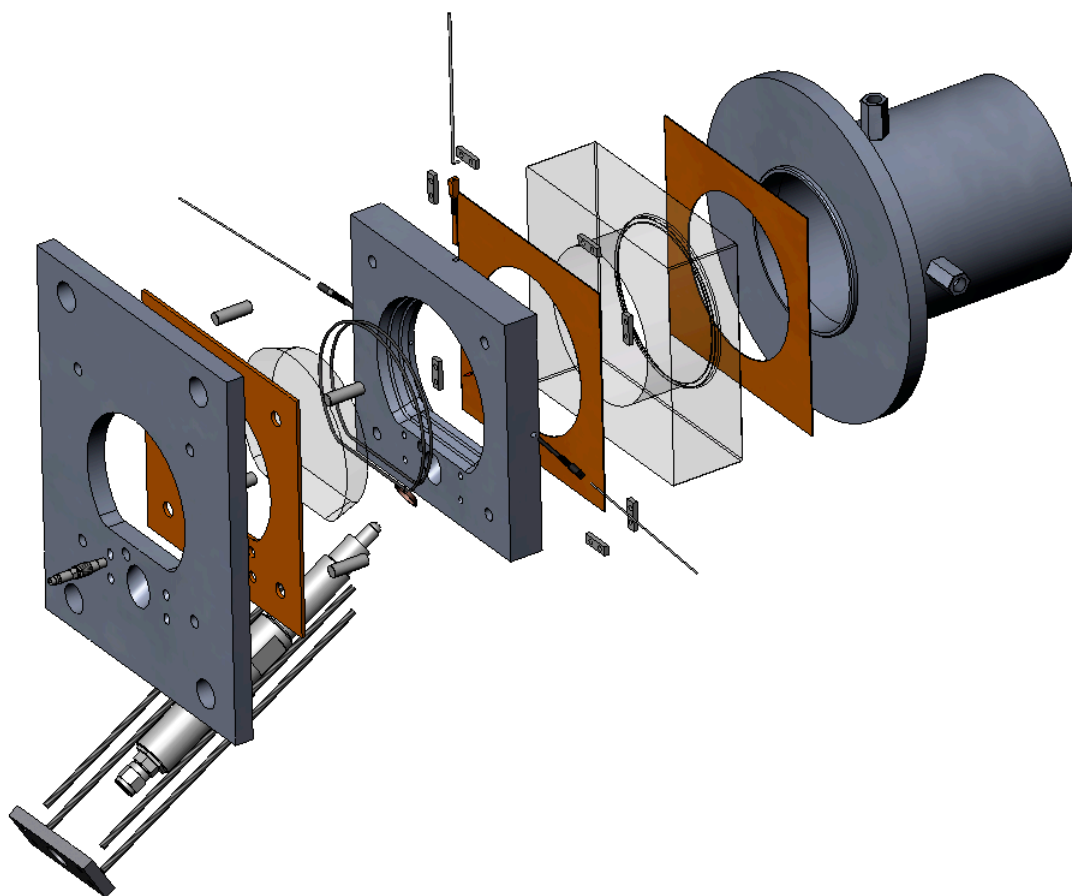
Figure 4-2 Exploded View of New RCM Cylinder

4▪4 RCM FUELLING SYSTEM

The RCM is set up to have its mixture prepared from three different sources. A premixer is used to prepare homogenous NG/air mixtures based upon partial pressures. The premixer is instrumented for NG line pressure, total pressure and mixture temperature. This premixed charge can be supplied directly to the RCM cylinder for homogenous fuelling, or may also be supplied to the PSC capillary for premixed PSC

studies. The PSC capillary tube, which has its injection controlled by an *Omega* SV-121 high-pressure solenoid valve, can also inject pure methane. The final source of fuel for the RCM cylinder is the J43M direct injector, which can only inject methane into the RCM cylinder.

The laser induced fluorescence technique used in this study requires that acetone be mixed with NG fuel. The high-pressure seeder used to achieve this is covered in *§4▪5* The seeded NG may be sent to the PSC the direct injector or to the premixer. This allows LIF studies to be carried out on any combination, of the fuel sources.

The piping diagram to achieve the abilities outlined above is shown in *Figure 4-3*, while its details are presented in *Appendix A*.
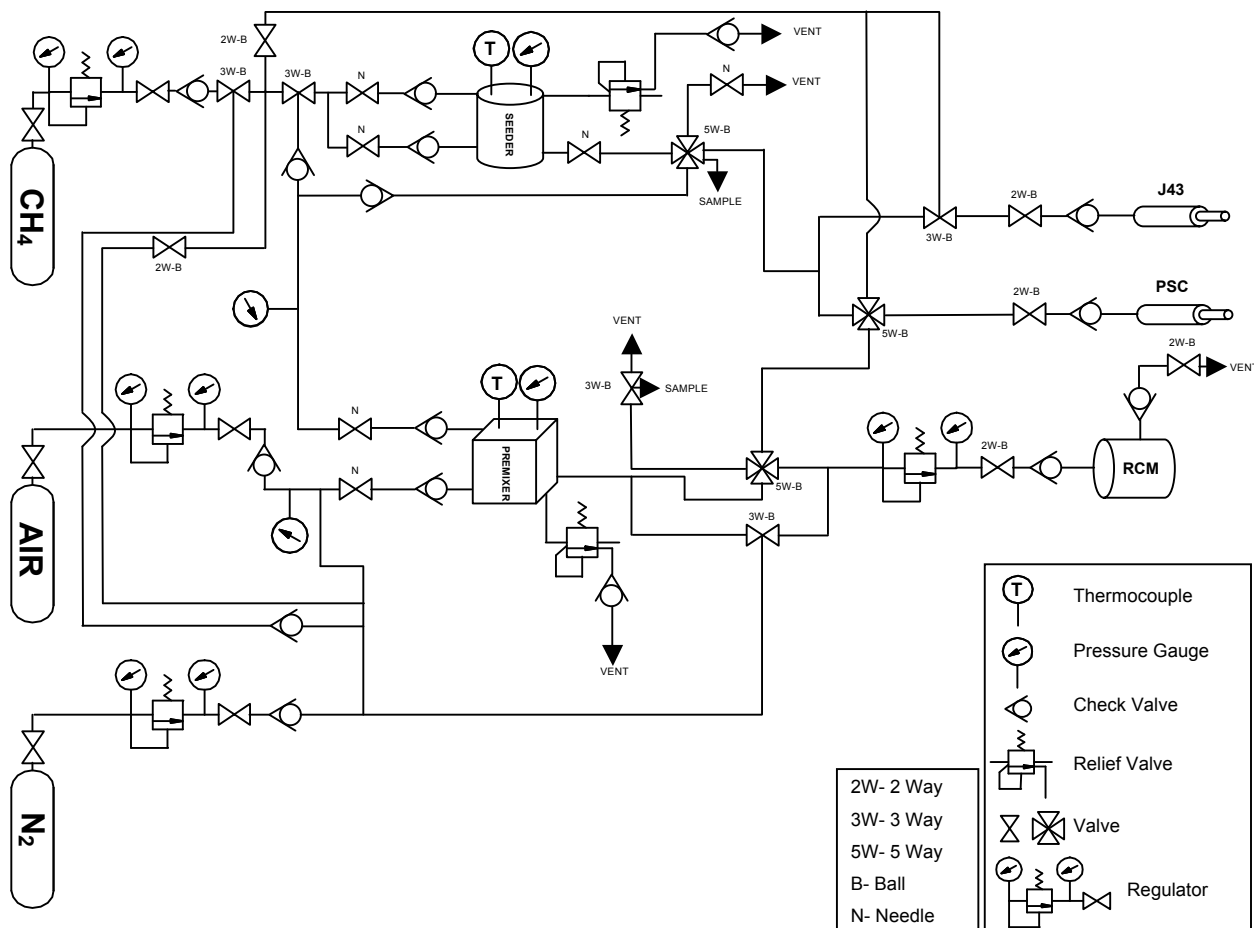
Figure 4-3 Schematic of RCM Fuelling System

The mixture within the RCM cylinder can be ignited with a spark between tungsten electrodes. The electrodes have a 4^0 angle *w.r.t.* the fire deck to clear the PSC capillary tube. The electrode position also has a small amount of adjustability so that the location of the spark within the PSC plume or homogenous charge can be adjusted.

4▪4▪1   THE WESTPORT® *J43M INJECTOR*

Much of the information pertaining to the J43M natural gas injector is proprietary and confidential. The injector was developed by Westport Innovations Inc. as part of its own R&D program and was not a commercial product. The actuation of the injector needle is achieved through the energizing of a magnetorestricitive material. Upon imposition of a magnetic field to the *Terfenol-D*™, the magnetic regions within this ferrous material realign which causes the volumetric expansion which actuates the needle. The movement of the needle allows the gas supply (at up to 3600*psi*) to flow through the injector. The injector is PWM controlled, however the injector requires a 5*V* logic signal for the entire injection duration. Further, rate shaping is possible by varying the logic level of the needle lift signal. In the current work no rate shaping was required and maximum needle lift was always specified.

Two J43M injectors were originally specified for the current study: one to supply the direct injection fuel plume and one the partially-stratified-charge injection. The characterisation information for both injectors is listed in *Chapter 5*. However, persistent technical problems with the PSC injector necessitated its replacement with a high-pressure (1000*psi*) solenoid valve (Omega SV-121). The solenoid was connected directly to the capillary tube supplying the RCM cylinder. The implications of this change for the current study are minimal in that it is only the initial stages of the injection that are relevant to PSC DI interaction. However, the overall reliability and repeatability of the response of this model of solenoid have posed significant problems to other researchers **[7, 367]**.

Provision of the PSC charge can also be made through the use of an 'insert' that replaces the PSC capillary tube. The RCM cylinder quartz window in the cylinder head may be replaced with an aluminium equivalent which is threaded with a ¾" parallel thread. This thread accepts the insert, which hold a 14mm sparkplug. The insert, pictured in *Figure 4-4*, has natural gas supplied by the same solenoid as for the capillary tube; however, the insert now provides a flow path to direct the fuel in front of the plug electrodes.
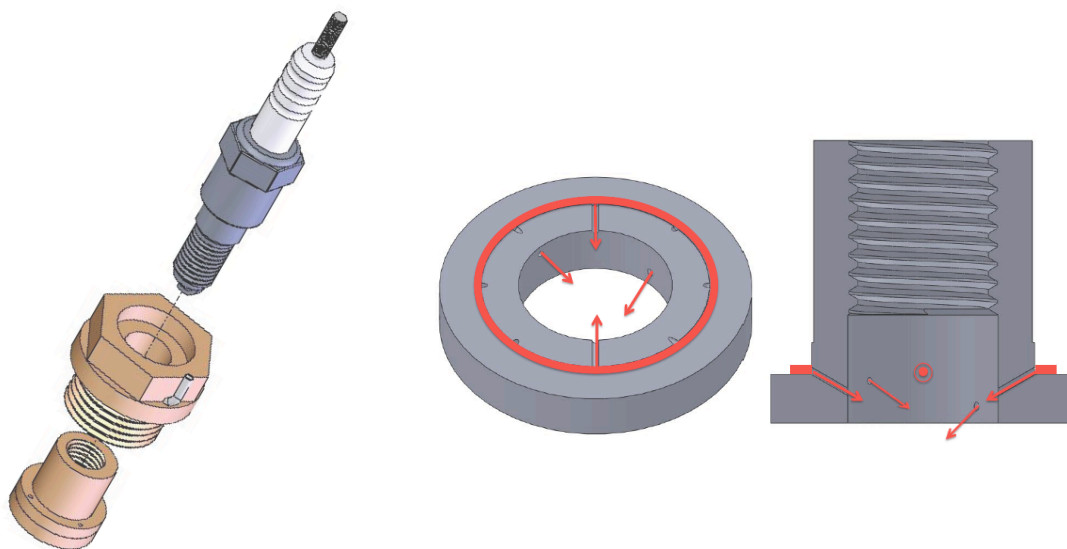
Figure 4-4 PSC Insert

4▪5 FLOW SEEDING

As was alluded to previously, the LIF studies of the current work require the fuel to be doped since natural gas does not naturally fluoresce. This is achieved with the high-pressure bubbler shown in *Figure 4-5*, which is based on the design presented by Neij **[259]**, and adapted for higher pressures. The detailed design information for the seeder is presented in *Appendix A*, though the basic principles of operation are outlined here. The vessel is a thick-walled 316 stainless steel chamber with flanged ends. There are a number of tapings to the vessel: two gas inlets, one gas outlet, a refill inlet, a pressure relief valve, pressure gauge and a thermocouple tapping (shielded type-K). The last two provide state information for the seeder, while the former allows methane to be fed into the seeder in batches (based on supply pressure) or continuously. The two inlets vary the flow path. One inlet bubbles gas through the liquid acetone, while the second inlet (not shown in *Figure 4-5*) bypasses the liquid acetone. The two flow paths then mix as they pass through a bed of glass beads before effluxing. The flowpath of the feed gas is shown in blue in *Figure 4-5*. This arrangement allows the acetone concentration in the effluent to be varied according to the fraction of the flow which was bubbled through the acetone.
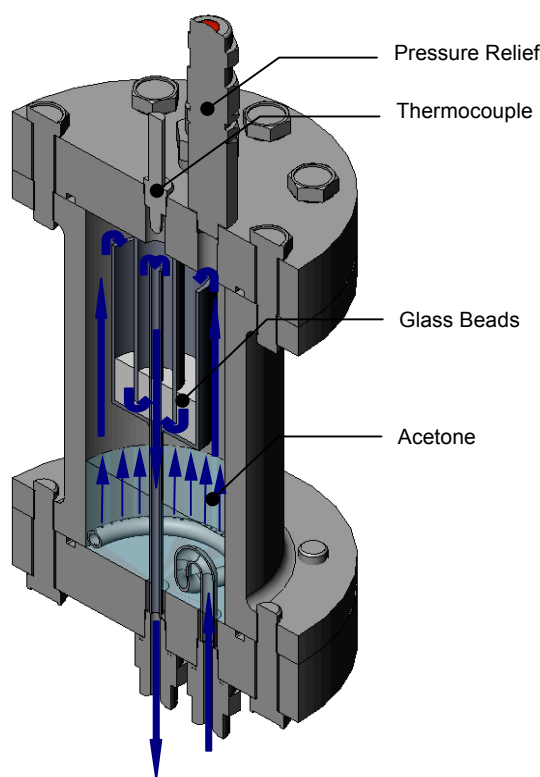
Figure 4-5 Section View of RCM Seeder

4▪6 LASER & OPTICAL SYSTEM

A UV laser system is used to excite the acetone doped gas. 248*nm* UV light, with a spectral width of 3*nm* at full-width half maximum is supplied by a *CompexPro 102* krypton-fluorine (KrF) excimer laser manufactured by Lambda Physik (now Coherent Inc.). The beam dimensions are 12*mm* x 24*mm* at the exit aperture, with a divergence half-angel of 3*mrad*. The beam path to the RCM and its formation into a light sheet are shown in *Figure 4-6*. The beam is immediately sampled with a Melles-Griot 248*nm* beam sampler. About 16% of the beam energy is directed to the power meter (*cf. §4▪7▪1*, below), the remainder going to a broadband metallic mirror in a kinematic gimbal that turns the beam though 90^0 horizontally to a beam steerer. The beam steerer steps the beam up by approximately 300*mm*, with the beam exiting in line with the RCM cylinder axis. Two 50.8*mm* x 50.8*mm* UV grade cylindrical lenses (*fl$_1$*=200*mm* & *fl$_2$*=300*mm*) are then used to form a Galilean telescope. The light from the telescope is directed onto a high-power dielectric mirror (that is both wavelength and direction specific in its reflectivity) mounted on a kinematic gimbal. This mirror turns the light through ~98.5^0 so that the beam enters the cylinder at an angel of ~8.5^0. This angle allows the majority of the optical section of the cylinder to be illuminated, while also minimizing the area obscured by the beam impinging upon the PSC capillary. Adjustment of the final cylindrical lens and the high-power mirror allow the beam to set-up so that it is on the cylinder axis and vertical. By changing the length of the telescope it is possible to have the beam waist (the optically invariant minimum thickness) of ~0.8*mm* on the central axis of the cylinder. However, a lack of

collimation after the 300*mm* lens means the beam is ~1.45*mm* thick at the cylinder bore. The beam is finally collected, to prevent the scattering of potentially dangerous UV light, by a beam dump under the RCM cylinder (not shown). LIF luminosity is collected with a *Cooke Corporation DiCam Pro* intensified CCD camera, fitted with a *Nikkor AF Micro*105*mm*, *1:2.8D*, lens and *B+W F-Pro* UV filter.
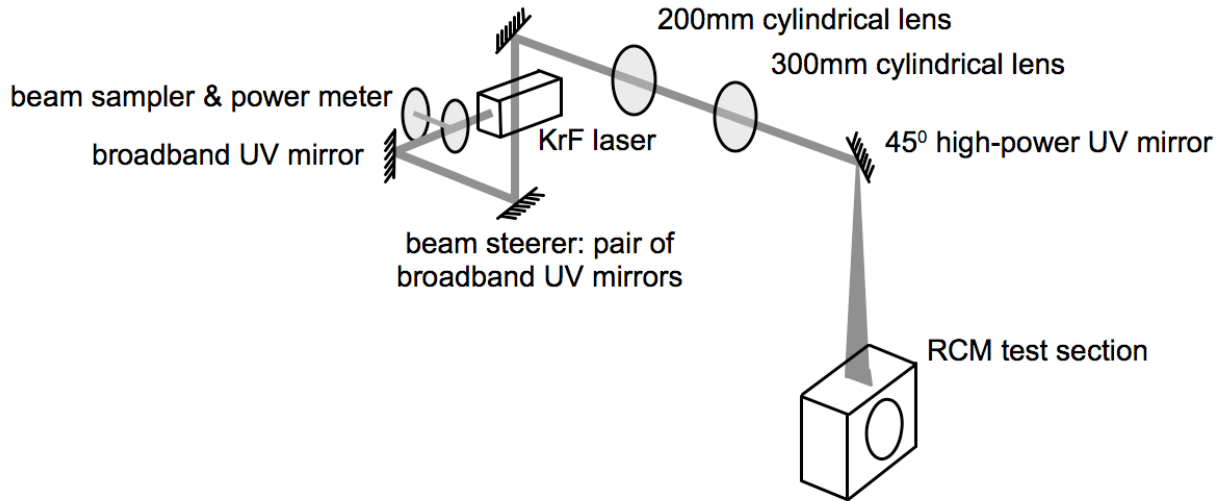
Figure 4-6 Laser Sheet Formation

4▪7 EVENT & TIMING CONTROL

The details of the RCM event and timing control system are offered in *Appendix B*. Here a brief overview is presented to provide some context for subsequent discussions. *Figure 4-8* shows the timing diagram for the pertinent RCM events. Those events are:

Event	Pulse or Step
PSC injection	Step
Direct injection	Step
Camera trigger	Pulse
Laser trigger	Pulse

Table 4-1 RCM Timed Events

All the events listed in *Table 4-1* are timed from the crank angle encoder, which gives a single pulse every 0.036CAD. The RCM is triggered by actuating a solenoid valve on the braking side that allows the rack to move and which causes the crank angle encoder to rotate. The 5*V* TTL pulse train from the encoder is gated so that no pulses pass the gate until an index pulse is reached. For rotation after this index, pulses are allowed to propagate. This system is used to circumvent the variability in the rack start position. The pulse train is supplied to the RCM control box which counts the number of pulses in the train and compares it against the set start value for each event. When the value is reached, a positive TTL trigger pulse is

released by the control box for that event. This signal is a pulse, the duration of which is set internally by an RC constant (at ~10*ns*), or a top-hat with a set duration (in encoder counts).
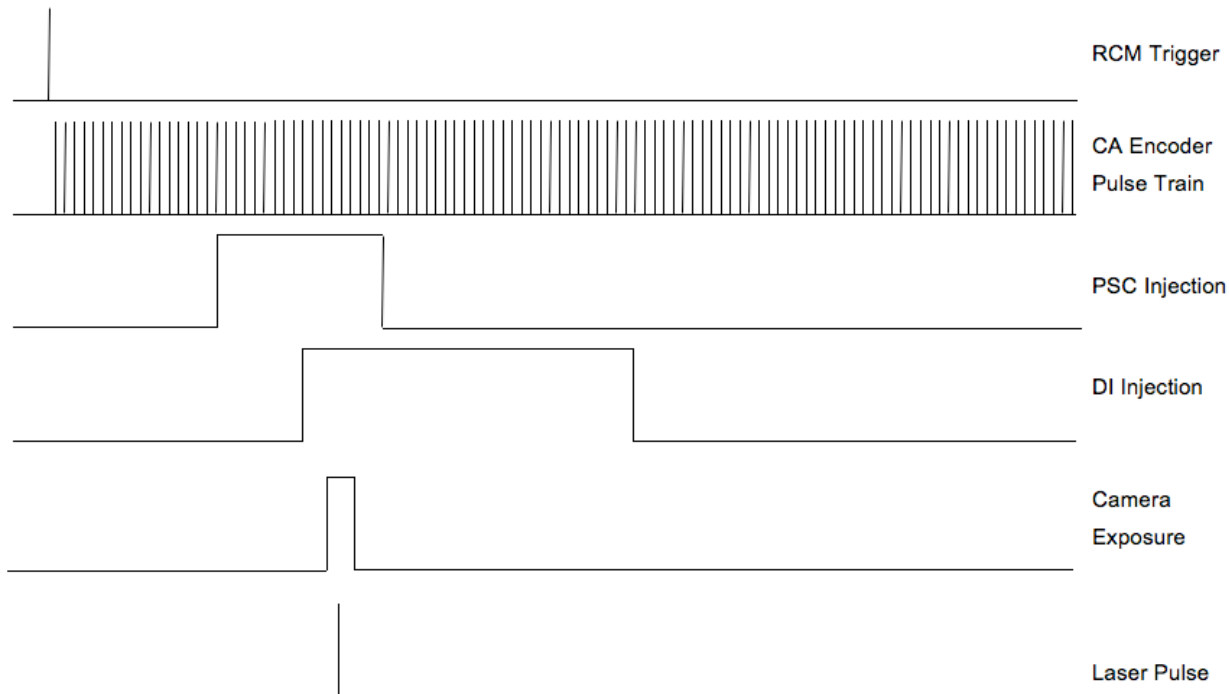
Figure 4-7 RCM Event Timing Diagram

4▪7▪1   INSTRUMENTATION

Further to the control system, the RCM is instrumented with a high dynamic response piezoelectric pressure gauge (*PCB Electronics 0112A*), which is connected to a charge amplifier (*Kistler 5010*) that has its output voltage displayed on an oscilloscope (*Tektronix 2014B*). The oscilloscope is connected to a PC with *OpenChoice Desktop* installed that allows the trace to be electronically recorded. The PC is also equipped with the camera control software (*CamWare* and *CineControl*). In the case of the LIF studies an iCCD (*Cooke Corporation DiCam Pro*) was used, while for the flame propagation investigation a high frame-rate CCD was used (Phantom). The final use for the PC in the RCM control system is to record and display the reading from the laser power meter (*Coherent FieldMax Pro II*) using proprietary *FieldMax II PC* software.
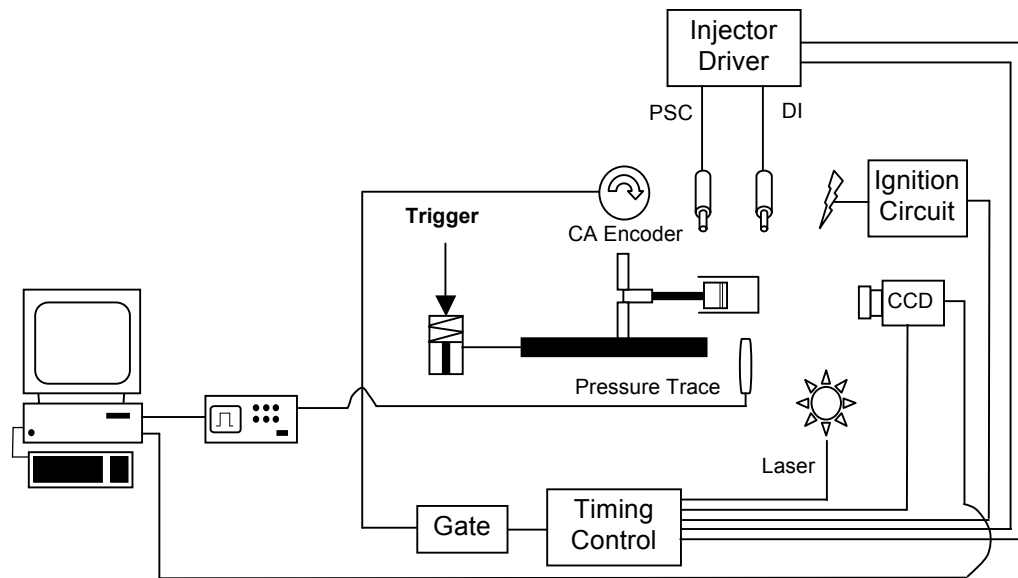
Figure 4-8 RCM Instrumentation Schematic

4▪8 TEST MATRIX

4▪8▪1 FUELLING RATIONAL

The work of Gorby **[7]** on the use of PSC with late DI was marked by difficulty in getting the PSC plume to ignite reliably. The problem of poor inflammation was resolved if a weak background mixture was induced through a traditional port-fuelled approach. The minimum RAFR found to produce reliable PSC ignition was 1.79, thus the value forms the basis for the current study. Centering the central-composite designed text matrix (*cf. §4▪8▪3*) on this value, or close to it, allowed the investigation of the effect of the bulk charge fuel concentration. The current work used bulk RAFR's close to the threshold value reported in **[7]**, and to the rich and lean sides of it.

The fuelling levels for each of the three fuel sources in the RCM cylinder (*i.e.* the background bulk charge, the PSC injection and the direct injection) were chosen to provide an overall RAFR of one. The PSC injection was held constant at 3%*w/w* of the total charge. The DI injection duration was altered to maintain the $\lambda=1$ condition after accounting for the fuel in bulk charge.

4▪8▪2 TIMING RATIONAL

The test matrix was designed to meet the objectives listed *Chapter 1*. The overarching aim of the study was to understand the interaction of the PSC fuel plume with that of DI fuel jet. As discussed in *Chapter 2*, the structure of gaseous jets is well-established and Turner's vortex ball model predicts two distinct regions to any given starting jet. The head of the jet is comprised of a ball, or vortex, which grows in size through leading-edge entrainment and mass supply from the trailing steady-state jet. It is thus apparent

that the PSC fuel jet (which itself must have the same structure, although on a smaller scale) can interact with the DI jet in three distinctly different regions. The PSC jet may intersect the DI fuel jet: *i)* along its leading edge, *ii)* at the centre of the vortex-ball *iii)* following the vortex-ball in the steady-state jet. Case *ii* is shown schematically in *Figure 4-9* with the expected rich regions shown in red, the stoichiometric ocntour in yellow and the lean areas in blue.
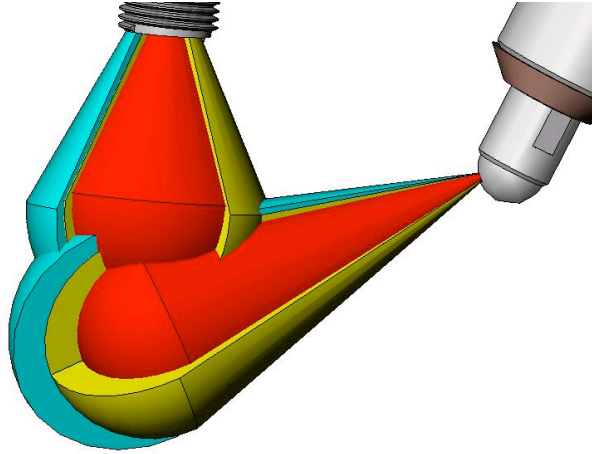
Figure 4-9 Partially Stratified Charge Jet and Direct Injection Jet Interaction

To achieve this the PSC injection timing was held constant at 120*CAD* BTDC (duration 6CAD) so that the nature of the PSC plume would remain constant regardless of its subsequent interaction with the DI jet. Further, all images were taken at the same time of 90CAD BTDC. This ensured the cylinder conditions were, within experimental error, the same for each image case. It must be made clear that these timings were not optimised for potential combustion quality, but were made on the grounds of obtaining the most information to meet the objectives of the study. The image timing of 90CAD BTDC is advanced when compared to the late injection regime of a typical DISI engine. An understanding was sought for the full extent of the DI and PSC plumes, and use of a timing later than 90CAD BTDC would have had the piston impinge upon the image region.

4▪8▪3   CENTRAL COMPOSITE DESIGN

Appendix E contains the mathematical background to the use of central composite designs and how they offer a statistically rigorous way of avoiding a full factorial test matrix. The two experimental variables (background charge AFR and DI injection timing), are mapped to the design variables x_1 and x_2, where -1<x<1. Given that the design variables are at the limit of the experimental equipment range, the CCD must be *inscribed*. The inscribed CCD yields the data point locations of *Figure 4-10*, which correspond to the values given in *Table 4-2*. At each data location 51 repeats were taken, which, by the central limit theorem **[368]**, allows a normal distribution in the responses to be assumed. Further, at the central run

location ((x_1,x_2) = [0,0]) three repeats were made (of 51 runs each) to minimise the response variance across the entire design space.

Data Point Location	x_1	x_2	ξ_λ	ξ_{time}
1	-1	0	1.5	0
2	-1/√2	1/√2	1.57	3.52
3	0	1	1.75	5
4	1/√2	1/√2	1.92	-3.52
5	1	0	2	0
6	1/√2	-1/√2	1.92	3.52
7	0	-1	1.75	-5
8	-1/√2	-1/√2	1.57	-3.52
9	0	0	1.75	0

Table 4-2 Data Point Locations in Design (x) and Experimental Space (ξ)
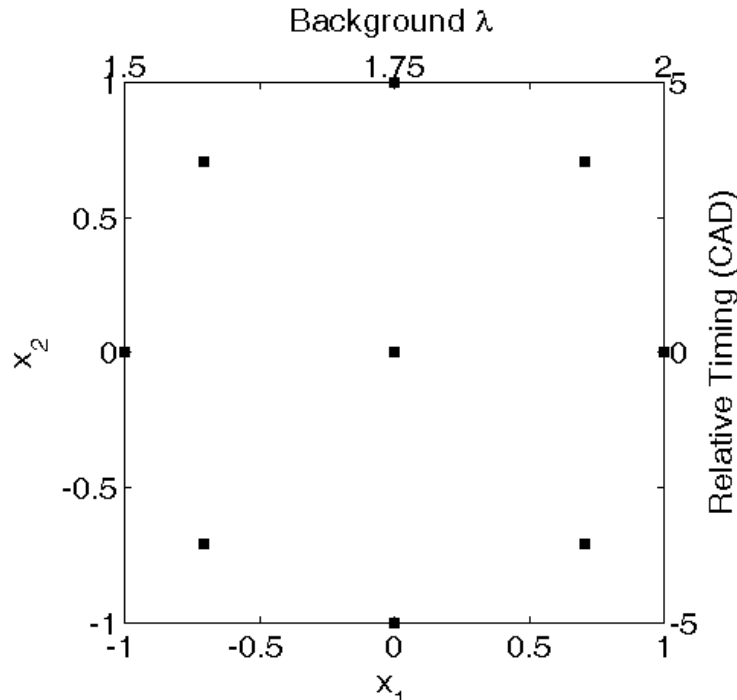
Figure 4-10 Central Composite Design for Test Matrix

4▪8▪4   OPTICAL SET-UP PROCEDURE

A set-up jig was manufactured that allowed a $0.5mm^2$ grid to be held on any longitudinal plane of the RCM cylinder. When horizontal it was used to provide a reference plane upon which to focus the laser sheet forming optics. The separation between the two lenses of the Galilean telescope was varied until the sheet -waste was on the RCM centre-line. Aligning the grid vertically allowed the camera focus to be set coincident with the laser sheet (any slight difference was accommodated by the $4mm$ depth of field), and the spatial calibration of the camera sensor.

4▪8▪5   EVENT TIMING PROCEDURE

Initially, a *Berkley Nucleonics 565* pulse generator was used to establish rough estimates for the time behaviours of the PSC and SI injection events. Under atmospheric conditions (without firing the RCM) LIF images were captured to asses the delay between commanded injection and the emergence of a fuel jet from the PSC capillary, and the extent of DI jet penetration at different image times.

Using the time estimates from the pulse generator study, a series of initial set-up runs were performed to match the jet interactions according to the design matrix, ultimately establishing the *(x₁,x₂),=[0,0]* case and the *(x₁,x₂) =[0,1]* case; the other points following from the constraints of a rotatable CCD or experimental bounds. The results of the timing set-up procedure, shown in *Table 4-3* to *Table 4-5*, form the data points of the CCD as previously described, with injection durations varied to maintain an overall $\lambda=1$ (*Table 4-5*)

Event	Start		Duration	
	CAD BTDC	Encoder Counts	CAD BTDC	Encoder Counts
PSC injection	138	1411	6	167
Direct injection	variable	variable	variable	variable
Camera trigger	90	2744	---	---
Laser trigger	89.8	2850	---	---

Table 4-3 Control Box Capillary Injected PSC Event Timings

Event	Start		Duration	
	CAD BTDC	Encoder Counts	CAD BTDC	Encoder Counts
PSC injection	90	78	6	167
Direct injection	variable	variable	variable	variable
Camera trigger	90	2744	---	---
Laser trigger	89.8	2850	---	---

Table 4-4 Control Box Insert Injected PSC Event Timings

Data Point Location	ξ_λ	DI Injection Start Time ξ_{time}		DI Injection Duration	
		CAD (BTDC)	Encoder Counts	CAD	Encoder Counts
1	1.5	117.36	1984	4.152	115
2	1.57	113.83	2082	4.642	129
3	1.75	112.36	2123	5.640	157
4	1.93	113.83	2082	6.437	179
5	2	117.36	1984	6.629	184
6	1.93	120.89	1886	6.437	179
7	1.75	122.5	1842	5.640	157
8	1.57	120.89	1886	4.642	129
9	1.75	117.36	1984	5.640	157

Table 4-5 Data Point Experimental Setup Values

Background charge compositions were mixed according to the partial (gauge) pressures of *Table 4-6*

NG Partial Pressure (*psi*)	Total Pressure (*psig*)				
	λ =1.5	λ =1.57	λ =1.75	λ =1.92	λ =2
30	445	465	515	565	585
35	520	545	605	660	685
40	595	625	690	755	785
45	670	705	780	855	885
50	750	785	865	950	985
55	825	865	955	1045	1085
60	900	945	1045	1140	1185
65	975	1020	1130	1240	1285
70	1055	1100	1220	1335	1385
75	1130	1180	1310	1430	1485
80	1205	1260	1395	---	---
85	1285	1340	1485	---	---
90	1360	1420	---	---	---
95	1435	---	---	---	---

Table 4-6 Homogeneous Charge Partial Pressure (Gauge) Values Assuming Prior Air Flush.

4▪8▪6   *MISCELLANEOUS EQUIPMENT SETTINGS*

Equipment	
KrF Laser	
Mode:	Constant Energy, 300*mJ*
Trigger:	External
Gas Supply:	Partial Gas Replacement
DiCam Pro	
MCP Decay:	2*ms*
MCP Gain:	99.5%
Analogue Gain:	Normal
Trigger:	External
ROI:	17:29 × 5:29
Exposure:	1200*ns*
f$_\#$	2.8
Focal Distance	0.7*m*
DI Fuel Injector	
Needle Lift:	5*V*
Hold Duration:	*cf. Table 4-5*
***Kistler* Charge Amplifier**	
Response:	1*pC/psi*
	20*psi/V*
Time Constant:	short, 0.1*s*

Table 4-7 Miscellaneous Equipment Settings

4▪8▪7   TEST RUN RANDOMIZATION

Each of the eleven test condition that form the CCD test matrix (nine point and three central repeats) was entered in Excel and repeated 51 times. Each row (corresponding to a test condition) was assigned a random number between 0 and 1 and the tests were then completed in ascending random number order. *Table 4-8* shows the test order for the capillary injected PSC tests and *Table 4-9* those of the insert injected tests.

Run ID	Bulk Charge	Timing Condition	Run ID	Bulk Charge	Timing Condition	Run ID	Bulk Charge	Timing Condition	Run ID	Bulk Charge	Timing Condition	Run ID	Bulk Charge	Timing Condition
CAP001	2	0	CAP113	1.75	0	CAP225	1.57	3.53	CAP337	1.75	0	CAP449	1.93	3.53
CAP002	1.57	3.53	CAP114	1.93	3.53	CAP226	1.75	0	CAP338	1.93	-3.53	CAP450	1.93	3.53
CAP003	1.75	0	CAP115	1.57	-3.53	CAP227	1.57	-3.53	CAP339	1.93	-3.53	CAP451	1.5	0
CAP004	1.75	0	CAP116	1.93	3.53	CAP228	1.57	3.53	CAP340	1.57	3.53	CAP452	1.93	3.53
CAP005	1.93	3.53	CAP117	1.57	3.53	CAP229	1.75	0	CAP341	1.75	-5	CAP453	1.75	0
CAP006	1.5	0	CAP118	1.75	0	CAP230	1.5	0	CAP342	1.93	3.53	CAP454	1.75	5
CAP007	1.75	0	CAP119	1.75	5	CAP231	1.75	0	CAP343	1.75	0	CAP455	1.75	5
CAP008	1.5	0	CAP120	1.75	0	CAP232	1.93	3.53	CAP344	1.5	0	CAP456	1.75	0
CAP009	1.75	-5	CAP121	1.93	3.53	CAP233	2	0	CAP345	1.75	-5	CAP457	1.75	5
CAP010	1.75	5	CAP122	1.57	-3.53	CAP234	1.75	5	CAP346	1.75	-5	CAP458	1.75	-5
CAP011	1.75	0	CAP123	2	0	CAP235	1.57	-3.53	CAP347	1.57	3.53	CAP459	1.75	0
CAP012	1.57	3.53	CAP124	1.75	0	CAP236	1.93	-3.53	CAP348	1.57	3.53	CAP460	1.57	-3.53
CAP013	1.75	0	CAP125	1.75	0	CAP237	1.75	-5	CAP349	1.57	3.53	CAP461	1.93	-3.53
CAP014	1.93	-3.53	CAP126	1.5	0	CAP238	1.75	0	CAP350	1.57	3.53	CAP462	2	0
CAP015	1.75	-5	CAP127	1.57	3.53	CAP239	2	0	CAP351	1.75	5	CAP463	1.93	3.53
CAP016	1.93	3.53	CAP128	1.57	-3.53	CAP240	2	0	CAP352	1.75	0	CAP464	1.75	-5
CAP017	1.57	-3.53	CAP129	1.93	-3.53	CAP241	1.5	0	CAP353	1.93	-3.53	CAP465	1.5	0
CAP018	1.57	3.53	CAP130	1.75	0	CAP242	1.75	0	CAP354	2	0	CAP466	1.57	3.53
CAP019	2	0	CAP131	1.5	0	CAP243	1.75	5	CAP355	1.93	-3.53	CAP467	1.57	3.53
CAP020	1.57	-3.53	CAP132	1.5	0	CAP244	1.5	0	CAP356	1.75	0	CAP468	1.5	0
CAP021	1.57	-3.53	CAP133	1.75	0	CAP245	1.75	0	CAP357	2	0	CAP469	1.75	0
CAP022	1.75	0	CAP134	1.93	-3.53	CAP246	1.57	-3.53	CAP358	1.93	3.53	CAP470	1.93	-3.53
CAP023	1.75	-5	CAP135	2	0	CAP247	1.75	5	CAP359	1.93	3.53	CAP471	1.75	-5
CAP024	1.57	-3.53	CAP136	1.57	-3.53	CAP248	1.57	3.53	CAP360	1.57	3.53	CAP472	1.93	3.53
CAP025	1.75	0	CAP137	1.75	5	CAP249	1.75	-5	CAP361	1.75	0	CAP473	1.75	0
CAP026	1.93	-3.53	CAP138	2	0	CAP250	1.5	0	CAP362	1.75	-5	CAP474	1.75	0
CAP027	1.57	-3.53	CAP139	1.75	0	CAP251	2	0	CAP363	1.75	-5	CAP475	1.75	0
CAP028	2	0	CAP140	1.75	-5	CAP252	1.75	0	CAP364	1.75	0	CAP476	1.5	0
CAP029	1.57	-3.53	CAP141	1.75	5	CAP253	1.57	3.53	CAP365	1.75	5	CAP477	1.75	0
CAP030	1.93	3.53	CAP142	1.93	-3.53	CAP254	1.75	5	CAP366	1.93	3.53	CAP478	1.75	0
CAP031	1.75	0	CAP143	1.75	-5	CAP255	1.5	0	CAP367	1.57	3.53	CAP479	1.57	-3.53
CAP032	1.5	0	CAP144	1.75	0	CAP256	1.93	3.53	CAP368	2	0	CAP480	1.75	5
CAP033	1.5	0	CAP145	1.93	3.53	CAP257	1.93	3.53	CAP369	1.93	3.53	CAP481	1.75	0
CAP034	1.75	0	CAP146	2	0	CAP258	2	0	CAP370	2	0	CAP482	1.93	-3.53
CAP035	1.5	0	CAP147	1.75	0	CAP259	1.75	0	CAP371	1.75	0	CAP483	1.75	0
CAP036	1.75	0	CAP148	1.75	0	CAP260	1.93	3.53	CAP372	1.57	3.53	CAP484	2	0
CAP037	1.75	0	CAP149	1.75	0	CAP261	1.93	-3.53	CAP373	1.75	0	CAP485	1.57	3.53

Run ID	Bulk Charge	Timing Condition	Run ID	Bulk Charge	Timing Condition	Run ID	Bulk Charge	Timing Condition	Run ID	Bulk Charge	Timing Condition	Run ID	Bulk Charge	Timing Condition	Run ID	Bulk Charge	Timing Condition
CAP038	1.5	0	CAP150	2	0	CAP262	1.75	5	CAP374	1.75	0	CAP486	1.57	3.53
CAP039	1.75	0	CAP151	1.57	-3.53	CAP263	1.75	0	CAP375	2	0	CAP487	1.93	-3.53
CAP040	1.75	0	CAP152	1.75	5	CAP264	1.75	0	CAP376	1.75	5	CAP488	1.75	5
CAP041	1.75	0	CAP153	1.75	5	CAP265	1.75	0	CAP377	1.93	-3.53	CAP489	1.75	0
CAP042	1.93	3.53	CAP154	1.75	-5	CAP266	2	0	CAP378	1.75	-5	CAP490	1.57	-3.53
CAP043	1.57	-3.53	CAP155	1.57	-3.53	CAP267	1.75	0	CAP379	1.75	0	CAP491	1.57	3.53
CAP044	1.75	0	CAP156	1.75	0	CAP268	1.75	0	CAP380	1.93	-3.53	CAP492	1.93	-3.53
CAP045	1.75	0	CAP157	1.57	-3.53	CAP269	1.93	-3.53	CAP381	1.75	0	CAP493	1.75	0
CAP046	1.75	0	CAP158	2	0	CAP270	1.5	0	CAP382	1.57	-3.53	CAP494	1.57	3.53
CAP047	1.75	0	CAP159	1.75	0	CAP271	1.75	-5	CAP383	1.93	3.53	CAP495	2	0
CAP048	1.75	0	CAP160	1.75	5	CAP272	1.93	3.53	CAP384	1.75	5	CAP496	1.93	3.53
CAP049	1.93	-3.53	CAP161	1.57	-3.53	CAP273	1.75	0	CAP385	1.75	0	CAP497	1.5	0
CAP050	1.75	0	CAP162	1.75	5	CAP274	1.75	-5	CAP386	1.57	-3.53	CAP498	1.75	-5
CAP051	1.93	3.53	CAP163	1.57	-3.53	CAP275	1.75	5	CAP387	1.93	-3.53	CAP499	1.75	0
CAP052	1.93	-3.53	CAP164	1.57	-3.53	CAP276	1.75	5	CAP388	1.57	3.53	CAP500	1.75	5
CAP053	1.93	-3.53	CAP165	1.75	-5	CAP277	1.57	-3.53	CAP389	1.5	0	CAP501	1.93	3.53
CAP054	1.57	3.53	CAP166	1.75	0	CAP278	1.75	-5	CAP390	1.75	0	CAP502	1.75	0
CAP055	1.57	3.53	CAP167	1.57	-3.53	CAP279	1.75	5	CAP391	1.93	-3.53	CAP503	1.5	0
CAP056	1.75	0	CAP168	1.5	0	CAP280	1.75	-5	CAP392	1.57	-3.53	CAP504	1.5	0
CAP057	2	0	CAP169	1.75	0	CAP281	1.75	0	CAP393	1.75	5	CAP505	1.57	3.53
CAP058	1.57	3.53	CAP170	1.93	3.53	CAP282	1.75	-5	CAP394	1.93	3.53	CAP506	1.75	-5
CAP059	2	0	CAP171	2	0	CAP283	1.75	0	CAP395	1.5	0	CAP507	1.57	3.53
CAP060	1.57	3.53	CAP172	1.75	0	CAP284	1.5	0	CAP396	1.57	3.53	CAP508	1.57	3.53
CAP061	1.75	-5	CAP173	1.75	0	CAP285	2	0	CAP397	2	0	CAP509	1.57	-3.53
CAP062	1.93	-3.53	CAP174	2	0	CAP286	1.75	-5	CAP398	1.75	0	CAP510	1.75	0
CAP063	1.75	0	CAP175	1.75	0	CAP287	1.75	5	CAP399	1.75	0	CAP511	1.57	3.53
CAP064	1.57	-3.53	CAP176	1.93	-3.53	CAP288	1.75	0	CAP400	1.75	-5	CAP512	2	0
CAP065	1.75	-5	CAP177	2	0	CAP289	1.93	3.53	CAP401	1.75	0	CAP513	1.57	-3.53
CAP066	1.75	5	CAP178	1.93	-3.53	CAP290	1.5	0	CAP402	1.75	5	CAP514	1.75	0
CAP067	1.93	-3.53	CAP179	1.75	5	CAP291	1.57	-3.53	CAP403	1.75	0	CAP515	1.93	3.53
CAP068	1.75	0	CAP180	1.75	0	CAP292	1.93	-3.53	CAP404	1.75	-5	CAP516	1.75	-5
CAP069	1.75	-5	CAP181	1.75	-5	CAP293	1.75	-5	CAP405	1.5	0	CAP517	1.93	-3.53
CAP070	1.75	5	CAP182	1.93	3.53	CAP294	1.57	3.53	CAP406	1.75	0	CAP518	1.5	0
CAP071	1.75	0	CAP183	1.75	-5	CAP295	1.75	0	CAP407	1.75	0	CAP519	1.93	3.53
CAP072	1.93	-3.53	CAP184	1.57	3.53	CAP296	1.57	3.53	CAP408	1.93	3.53	CAP520	1.75	-5
CAP073	1.5	0	CAP185	1.75	0	CAP297	1.57	3.53	CAP409	1.57	-3.53	CAP521	1.75	0
CAP074	1.75	-5	CAP186	1.57	3.53	CAP298	1.75	0	CAP410	1.93	-3.53	CAP522	1.93	-3.53
CAP075	1.57	3.53	CAP187	1.75	-5	CAP299	2	0	CAP411	1.93	-3.53	CAP523	1.75	0
CAP076	1.75	0	CAP188	1.57	3.53	CAP300	1.5	0	CAP412	1.75	0	CAP524	1.75	0
CAP077	1.5	0	CAP189	1.57	-3.53	CAP301	1.75	0	CAP413	1.57	3.53	CAP525	1.75	0
CAP078	1.93	3.53	CAP190	1.75	5	CAP302	1.93	-3.53	CAP414	2	0	CAP526	2	0
CAP079	1.75	5	CAP191	1.75	0	CAP303	1.75	0	CAP415	1.75	0	CAP527	1.57	-3.53
CAP080	2	0	CAP192	1.75	5	CAP304	1.93	-3.53	CAP416	1.93	-3.53	CAP528	1.5	0
CAP081	1.75	-5	CAP193	2	0	CAP305	2	0	CAP417	1.57	3.53	CAP529	1.93	3.53
CAP082	1.75	0	CAP194	2	0	CAP306	1.93	3.53	CAP418	1.75	0	CAP530	2	0
CAP083	1.75	0	CAP195	1.5	0	CAP307	1.75	0	CAP419	1.57	-3.53	CAP531	1.5	0
CAP084	1.75	0	CAP196	1.93	3.53	CAP308	1.75	5	CAP420	1.75	5	CAP532	1.75	0

Run ID	Bulk Charge	Timing Condition	Run ID	Bulk Charge	Timing Condition	Run ID	Bulk Charge	Timing Condition	Run ID	Bulk Charge	Timing Condition	Run ID	Bulk Charge	Timing Condition
CAP085	1.57	-3.53	CAP197	1.75	0	CAP309	1.57	-3.53	CAP421	1.75	-5	CAP533	1.75	0
CAP086	1.75	5	CAP198	1.93	-3.53	CAP310	1.75	0	CAP422	1.75	0	CAP534	1.75	5
CAP087	1.75	0	CAP199	1.75	0	CAP311	1.75	0	CAP423	1.93	3.53	CAP535	1.75	0
CAP088	1.5	0	CAP200	1.93	3.53	CAP312	1.5	0	CAP424	1.93	-3.53	CAP536	1.93	3.53
CAP089	1.93	3.53	CAP201	2	0	CAP313	1.75	5	CAP425	2	0	CAP537	1.5	0
CAP090	1.75	-5	CAP202	1.93	-3.53	CAP314	1.75	0	CAP426	1.75	0	CAP538	1.93	3.53
CAP091	1.75	-5	CAP203	1.5	0	CAP315	1.75	5	CAP427	1.75	0	CAP539	1.75	-5
CAP092	1.75	-5	CAP204	2	0	CAP316	1.5	0	CAP428	1.57	-3.53	CAP540	1.75	0
CAP093	1.75	0	CAP205	2	0	CAP317	1.75	-5	CAP429	1.57	3.53	CAP541	1.75	5
CAP094	2	0	CAP206	1.75	0	CAP318	1.5	0	CAP430	2	0	CAP542	1.75	0
CAP095	1.75	0	CAP207	1.75	5	CAP319	1.75	0	CAP431	1.93	-3.53	CAP543	1.57	3.53
CAP096	1.75	5	CAP208	1.57	-3.53	CAP320	1.75	5	CAP432	1.93	-3.53	CAP544	1.93	3.53
CAP097	1.93	-3.53	CAP209	1.57	3.53	CAP321	1.75	0	CAP433	1.5	0	CAP545	2	0
CAP098	1.75	-5	CAP210	1.57	-3.53	CAP322	1.75	5	CAP434	1.57	-3.53	CAP546	1.93	-3.53
CAP099	1.75	0	CAP211	1.75	0	CAP323	1.75	0	CAP435	1.57	-3.53	CAP547	1.75	0
CAP100	1.75	0	CAP212	1.57	-3.53	CAP324	1.5	0	CAP436	1.57	3.53	CAP548	1.75	0
CAP101	1.57	-3.53	CAP213	1.93	-3.53	CAP325	1.93	3.53	CAP437	1.75	0	CAP549	1.75	0
CAP102	2	0	CAP214	1.75	5	CAP326	1.75	-5	CAP438	1.93	3.53	CAP550	1.93	3.53
CAP103	1.57	-3.53	CAP215	1.75	0	CAP327	1.57	-3.53	CAP439	1.57	-3.53	CAP551	1.75	0
CAP104	1.5	0	CAP216	1.93	3.53	CAP328	1.5	0	CAP440	1.75	5	CAP552	1.75	0
CAP105	1.5	0	CAP217	1.75	0	CAP329	1.75	0	CAP441	2	0	CAP553	1.93	-3.53
CAP106	1.93	-3.53	CAP218	1.75	-5	CAP330	1.57	3.53	CAP442	1.93	-3.53	CAP554	1.75	0
CAP107	1.75	5	CAP219	1.93	3.53	CAP331	2	0	CAP443	1.5	0	CAP555	1.57	3.53
CAP108	1.75	5	CAP220	1.75	0	CAP332	1.57	-3.53	CAP444	1.75	0	CAP556	1.5	0
CAP109	1.75	0	CAP221	1.93	3.53	CAP333	1.57	3.53	CAP445	1.5	0	CAP557	1.75	-5
CAP110	1.93	-3.53	CAP222	2	0	CAP334	1.75	0	CAP446	1.5	0	CAP558	1.93	3.53
CAP111	1.75	-5	CAP223	2	0	CAP335	1.93	-3.53	CAP447	1.75	5	CAP559	1.93	-3.53
CAP112	1.57	-3.53	CAP224	1.57	3.53	CAP336	1.75	0	CAP448	1.57	3.53	CAP560	1.75	-5
												CAP561	1.57	-3.53

Table 4-8 Capillary Injected PSC with DI Experimental Test Order

Run ID	Bulk Charge	Timing Condition	Run ID	Bulk Charge	Timing Condition	Run ID	Bulk Charge	Timing Condition	Run ID	Bulk Charge	Timing Condition	Run ID	Bulk Charge	Timing Condition
INS001	1.75	0	INS113	1.57	3.53	INS225	1.75	0	INS337	1.75	0	INS449	1.57	-3.53
INS002	1.57	-3.53	INS114	1.57	-3.53	INS226	1.93	3.53	INS338	1.93	3.53	INS450	1.75	-5
INS003	1.75	-5	INS115	1.75	0	INS227	2	0	INS339	1.5	0	INS451	1.75	5
INS004	1.57	3.53	INS116	1.93	3.53	INS228	1.75	0	INS340	1.75	0	INS452	1.57	3.53
INS005	1.75	0	INS117	1.5	0	INS229	1.93	3.53	INS341	1.75	0	INS453	2	0
INS006	1.57	3.53	INS118	1.75	0	INS230	1.75	0	INS342	1.57	-3.53	INS454	2	0
INS007	1.75	0	INS119	1.93	3.53	INS231	1.75	5	INS343	1.93	-3.53	INS455	1.75	-5
INS008	1.93	3.53	INS120	1.57	-3.53	INS232	1.93	3.53	INS344	1.75	0	INS456	1.75	0
INS009	1.93	-3.53	INS121	1.93	-3.53	INS233	1.5	0	INS345	2	0	INS457	1.75	0
INS010	2	0	INS122	1.57	3.53	INS234	1.75	-5	INS346	1.75	0	INS458	1.75	0
INS011	2	0	INS123	2	0	INS235	1.93	-3.53	INS347	1.75	0	INS459	1.75	5
INS012	1.5	0	INS124	1.75	0	INS236	1.57	-3.53	INS348	1.75	-5	INS460	1.57	-3.53
INS013	1.75	0	INS125	1.75	-5	INS237	2	0	INS349	1.75	5	INS461	1.93	3.53
INS014	1.75	-5	INS126	1.75	5	INS238	1.57	3.53	INS350	1.75	-5	INS462	1.57	-3.53
INS015	1.57	-3.53	INS127	1.75	0	INS239	1.57	-3.53	INS351	1.75	0	INS463	1.75	0

Run ID	Bulk Charge	Timing Condition	Run ID	Bulk Charge	Timing Condition	Run ID	Bulk Charge	Timing Condition	Run ID	Bulk Charge	Timing Condition	Run ID	Bulk Charge	Timing Condition
INS016	1.75	0	INS128	1.93	3.53	INS240	1.75	0	INS352	1.5	0	INS464	1.93	-3.53
INS017	1.93	3.53	INS129	1.75	0	INS241	1.75	0	INS353	1.75	0	INS465	1.75	0
INS018	1.75	0	INS130	2	0	INS242	1.75	0	INS354	1.75	0	INS466	1.75	0
INS019	1.75	0	INS131	1.5	0	INS243	1.75	0	INS355	1.57	3.53	INS467	1.57	3.53
INS020	1.93	3.53	INS132	1.75	5	INS244	1.75	5	INS356	1.93	3.53	INS468	2	0
INS021	1.57	3.53	INS133	1.75	0	INS245	1.57	-3.53	INS357	1.75	0	INS469	1.75	-5
INS022	1.93	-3.53	INS134	2	0	INS246	1.93	3.53	INS358	1.57	3.53	INS470	1.75	-5
INS023	1.57	-3.53	INS135	1.93	-3.53	INS247	1.75	0	INS359	1.75	0	INS471	1.93	3.53
INS024	1.75	0	INS136	1.75	0	INS248	1.75	0	INS360	1.57	3.53	INS472	2	0
INS025	1.5	0	INS137	1.75	0	INS249	1.57	3.53	INS361	1.75	0	INS473	1.75	0
INS026	1.75	0	INS138	2	0	INS250	1.75	5	INS362	1.93	3.53	INS474	1.57	3.53
INS027	1.75	0	INS139	1.57	3.53	INS251	2	0	INS363	1.75	5	INS475	1.75	0
INS028	1.93	-3.53	INS140	1.5	0	INS252	1.93	-3.53	INS364	1.57	3.53	INS476	1.93	-3.53
INS029	1.57	3.53	INS141	1.75	0	INS253	1.5	0	INS365	1.75	-5	INS477	1.75	0
INS030	1.75	5	INS142	1.75	0	INS254	1.75	-5	INS366	2	0	INS478	1.75	5
INS031	1.75	0	INS143	1.93	3.53	INS255	1.93	-3.53	INS367	1.57	-3.53	INS479	1.75	0
INS032	1.93	-3.53	INS144	1.57	3.53	INS256	1.5	0	INS368	1.93	3.53	INS480	1.57	-3.53
INS033	1.57	-3.53	INS145	1.57	-3.53	INS257	2	0	INS369	1.75	0	INS481	1.57	3.53
INS034	1.75	5	INS146	2	0	INS258	1.93	-3.53	INS370	1.57	3.53	INS482	1.57	3.53
INS035	1.75	0	INS147	1.75	-5	INS259	1.75	0	INS371	1.75	-5	INS483	1.75	0
INS036	1.57	-3.53	INS148	1.75	0	INS260	2	0	INS372	1.75	-5	INS484	1.93	-3.53
INS037	1.75	0	INS149	2	0	INS261	1.75	-5	INS373	2	0	INS485	1.75	5
INS038	1.5	0	INS150	1.5	0	INS262	1.75	5	INS374	1.5	0	INS486	1.93	-3.53
INS039	1.75	0	INS151	1.5	0	INS263	1.93	3.53	INS375	1.75	5	INS487	1.75	0
INS040	1.75	0	INS152	1.75	0	INS264	1.75	0	INS376	1.93	3.53	INS488	1.75	-5
INS041	1.75	5	INS153	1.93	3.53	INS265	1.75	0	INS377	1.57	3.53	INS489	1.75	0
INS042	1.75	0	INS154	1.93	3.53	INS266	1.57	-3.53	INS378	1.5	0	INS490	2	0
INS043	1.5	0	INS155	1.75	0	INS267	1.75	5	INS379	1.75	-5	INS491	1.75	0
INS044	1.75	5	INS156	1.75	5	INS268	1.75	0	INS380	1.57	3.53	INS492	1.93	-3.53
INS045	1.75	0	INS157	1.75	5	INS269	1.75	0	INS381	1.57	-3.53	INS493	1.57	-3.53
INS046	1.57	3.53	INS158	1.57	-3.53	INS270	1.75	-5	INS382	1.75	5	INS494	1.93	3.53
INS047	1.57	-3.53	INS159	1.75	5	INS271	1.93	-3.53	INS383	1.5	0	INS495	1.57	3.53
INS048	1.75	-5	INS160	1.57	-3.53	INS272	1.57	-3.53	INS384	1.75	0	INS496	1.75	0
INS049	1.75	0	INS161	1.93	-3.53	INS273	1.75	0	INS385	1.75	5	INS497	1.93	3.53
INS050	1.57	-3.53	INS162	1.93	3.53	INS274	1.93	-3.53	INS386	1.57	3.53	INS498	1.75	0
INS051	1.75	0	INS163	1.93	-3.53	INS275	1.57	3.53	INS387	1.57	-3.53	INS499	1.75	5
INS052	1.93	3.53	INS164	1.93	3.53	INS276	1.93	-3.53	INS388	1.75	0	INS500	1.75	5
INS053	1.75	5	INS165	1.75	0	INS277	1.75	0	INS389	1.5	0	INS501	1.75	-5
INS054	1.75	5	INS166	1.75	0	INS278	1.75	5	INS390	1.75	0	INS502	1.57	-3.53
INS055	1.75	5	INS167	1.75	0	INS279	1.75	5	INS391	1.75	0	INS503	1.75	0
INS056	1.75	0	INS168	1.75	0	INS280	1.93	3.53	INS392	1.5	0	INS504	1.57	-3.53
INS057	1.57	-3.53	INS169	1.93	3.53	INS281	1.5	0	INS393	1.93	-3.53	INS505	1.93	-3.53
INS058	1.93	-3.53	INS170	2	0	INS282	1.75	0	INS394	1.75	0	INS506	1.57	3.53
INS059	1.5	0	INS171	2	0	INS283	1.57	-3.53	INS395	1.75	-5	INS507	1.93	3.53
INS060	1.93	-3.53	INS172	1.75	-5	INS284	1.75	-5	INS396	1.5	0	INS508	1.75	-5
INS061	1.57	-3.53	INS173	1.57	3.53	INS285	1.75	0	INS397	1.75	0	INS509	1.57	3.53
INS062	2	0	INS174	1.75	0	INS286	1.75	0	INS398	2	0	INS510	1.75	0

Run ID	Bulk Charge	Timing Condition	Run ID	Bulk Charge	Timing Condition	Run ID	Bulk Charge	Timing Condition	Run ID	Bulk Charge	Timing Condition	Run ID	Bulk Charge	Timing Condition
INS063	1.75	0	INS175	1.75	5	INS287	1.75	5	INS399	1.75	-5	INS511	2	0
INS064	1.75	0	INS176	1.75	5	INS288	1.5	0	INS400	1.75	0	INS512	1.75	-5
INS065	1.57	-3.53	INS177	1.75	0	INS289	1.57	3.53	INS401	1.75	5	INS513	1.75	-5
INS066	1.93	-3.53	INS178	1.75	0	INS290	2	0	INS402	1.93	3.53	INS514	1.75	0
INS067	1.5	0	INS179	2	0	INS291	2	0	INS403	1.5	0	INS515	1.75	0
INS068	1.57	3.53	INS180	2	0	INS292	1.57	3.53	INS404	1.5	0	INS516	1.75	-5
INS069	1.75	-5	INS181	1.5	0	INS293	1.93	3.53	INS405	1.75	-5	INS517	1.75	-5
INS070	1.75	0	INS182	2	0	INS294	2	0	INS406	1.5	0	INS518	1.93	3.53
INS071	2	0	INS183	2	0	INS295	2	0	INS407	1.57	-3.53	INS519	1.75	-5
INS072	1.75	0	INS184	1.75	5	INS296	1.75	5	INS408	1.75	-5	INS520	1.93	3.53
INS073	1.75	5	INS185	1.93	-3.53	INS297	1.75	5	INS409	1.5	0	INS521	1.93	-3.53
INS074	1.57	-3.53	INS186	1.75	0	INS298	1.75	5	INS410	1.93	-3.53	INS522	1.93	3.53
INS075	1.93	3.53	INS187	1.75	-5	INS299	2	0	INS411	1.93	-3.53	INS523	2	0
INS076	1.75	5	INS188	1.75	-5	INS300	1.93	-3.53	INS412	1.93	3.53	INS524	1.75	0
INS077	1.93	-3.53	INS189	1.57	3.53	INS301	1.5	0	INS413	1.75	0	INS525	1.75	-5
INS078	1.75	0	INS190	1.5	0	INS302	1.75	0	INS414	1.5	0	INS526	1.75	0
INS079	1.57	3.53	INS191	1.93	3.53	INS303	1.75	0	INS415	1.57	-3.53	INS527	1.93	3.53
INS080	1.75	0	INS192	1.75	-5	INS304	1.75	5	INS416	1.93	-3.53	INS528	1.93	-3.53
INS081	1.93	-3.53	INS193	1.75	0	INS305	1.57	-3.53	INS417	1.75	0	INS529	1.75	-5
INS082	1.57	3.53	INS194	1.75	5	INS306	1.57	3.53	INS418	1.75	0	INS530	1.75	0
INS083	1.57	3.53	INS195	1.75	5	INS307	1.75	5	INS419	1.93	3.53	INS531	1.93	-3.53
INS084	1.93	-3.53	INS196	1.75	0	INS308	1.5	0	INS420	1.75	-5	INS532	1.93	-3.53
INS085	1.75	5	INS197	1.75	0	INS309	1.93	-3.53	INS421	1.75	0	INS533	1.75	0
INS086	1.57	3.53	INS198	2	0	INS310	1.93	-3.53	INS422	1.93	-3.53	INS534	1.57	3.53
INS087	1.5	0	INS199	1.5	0	INS311	1.93	3.53	INS423	1.75	0	INS535	1.57	3.53
INS088	1.75	0	INS200	1.75	-5	INS312	1.75	0	INS424	1.93	3.53	INS536	1.75	0
INS089	2	0	INS201	1.57	3.53	INS313	1.93	-3.53	INS425	2	0	INS537	1.93	3.53
INS090	1.57	3.53	INS202	1.75	0	INS314	1.75	0	INS426	1.93	-3.53	INS538	1.75	0
INS091	1.93	3.53	INS203	1.93	-3.53	INS315	1.57	-3.53	INS427	1.57	-3.53	INS539	1.75	0
INS092	1.93	-3.53	INS204	2	0	INS316	1.75	5	INS428	1.75	0	INS540	1.93	3.53
INS093	2	0	INS205	1.75	-5	INS317	1.75	-5	INS429	1.57	-3.53	INS541	2	0
INS094	1.75	0	INS206	1.57	-3.53	INS318	1.75	0	INS430	1.75	-5	INS542	1.57	3.53
INS095	1.75	-5	INS207	1.75	0	INS319	1.75	0	INS431	1.75	0	INS543	1.75	0
INS096	1.75	5	INS208	1.93	-3.53	INS320	1.5	0	INS432	1.75	5	INS544	1.57	-3.53
INS097	1.93	-3.53	INS209	1.93	3.53	INS321	1.5	0	INS433	1.75	0	INS545	1.57	-3.53
INS098	1.57	-3.53	INS210	1.57	3.53	INS322	1.75	0	INS434	1.75	5	INS546	1.5	0
INS099	1.57	-3.53	INS211	1.75	0	INS323	2	0	INS435	1.57	3.53	INS547	1.5	0
INS100	2	0	INS212	1.75	0	INS324	2	0	INS436	1.57	-3.53	INS548	2	0
INS101	1.75	0	INS213	1.75	-5	INS325	1.75	-5	INS437	1.57	-3.53	INS549	1.5	0
INS102	1.75	0	INS214	1.75	0	INS326	1.5	0	INS438	1.93	-3.53	INS550	1.57	-3.53
INS103	1.75	0	INS215	1.57	3.53	INS327	1.57	3.53	INS439	1.75	5	INS551	1.75	0
INS104	1.93	3.53	INS216	1.57	3.53	INS328	1.5	0	INS440	1.5	0	INS552	1.5	0
INS105	1.75	0	INS217	1.5	0	INS329	1.93	-3.53	INS441	1.75	0	INS553	1.93	3.53
INS106	1.5	0	INS218	2	0	INS330	1.75	-5	INS442	1.75	-5	INS554	1.5	0
INS107	1.75	0	INS219	2	0	INS331	1.75	0	INS443	1.75	0	INS555	1.93	3.53
INS108	1.57	-3.53	INS220	1.75	5	INS332	1.57	3.53	INS444	1.5	0	INS556	1.93	-3.53
INS109	1.57	-3.53	INS221	1.75	0	INS333	1.5	0	INS445	1.57	3.53	INS557	1.5	0

Run ID	Bulk Charge	Timing Condition	Run ID	Bulk Charge	Timing Condition	Run ID	Bulk Charge	Timing Condition	Run ID	Bulk Charge	Timing Condition	Run ID	Bulk Charge	Timing Condition
INS110	1.93	3.53	INS222	1.75	-5	INS334	2	0	INS446	1.57	-3.53	INS558	1.75	0
INS111	1.93	3.53	INS223	1.75	-5	INS335	2	0	INS447	1.57	-3.53	INS559	1.93	-3.53
INS112	1.5	0	INS224	1.75	0	INS336	1.93	3.53	INS448	1.75	0	INS560	1.75	0
												INS561	1.57	3.53

Table 4-9 Insert Injected PSC with DI Experimental Test Order

Chapter 5
REPEATABILITY & CALIBRATION TESTS

5▪1 INTRODUCTION

To ensure the quality of the data collected form the LIF system there are a number of supporting assessments that must be made of the experimental system. *Chapter 5* details the procedures followed and the findings of a series of experiments that were undertaken to assess a range of factors: the repeatability of the camera timing, the spatial and temporal variation in the camera CCD response and the laser beam profile. Theoretical presentations are made that demonstrate the fluorescent response to be linear with laser power, while experimental findings are used to show that any fluorescence from natural gas may be discounted when compared to the signal produced from acetone. An assessment of the polytropic exponent for the RCM compression stroke is made and high speed camera footage of the combustion in the RCM cylinder demonstrates the lack of in cylinder turbulence. Finally, the experimental calibration curves for the fuel injectors, acetone seeder and acetone fluorescent response are presented.

5▪2 CAMERA TRIGGER REPEATABILITY

The triggering of the iCCD camera was checked for its repeatability with respect to piston position. The RCM supply pressure was regulated to 80*psi* while the camera timing was randomly selected to be 4300, 4800 or 5800 shaft encoder counts. Each image was binarised and the piston edge identified by thresholding; piston position could then be inferred from to total black pixel count. For each set of 101 images a running mean position was calculated and the standard deviation evaluated accordingly. Finally, through imaging a calibration grid, the pixel counts were converted into a 'true' position in *mm*. The results for three different timings show that the camera trigger may be deemed repeatable to within 0.9*CAD*.
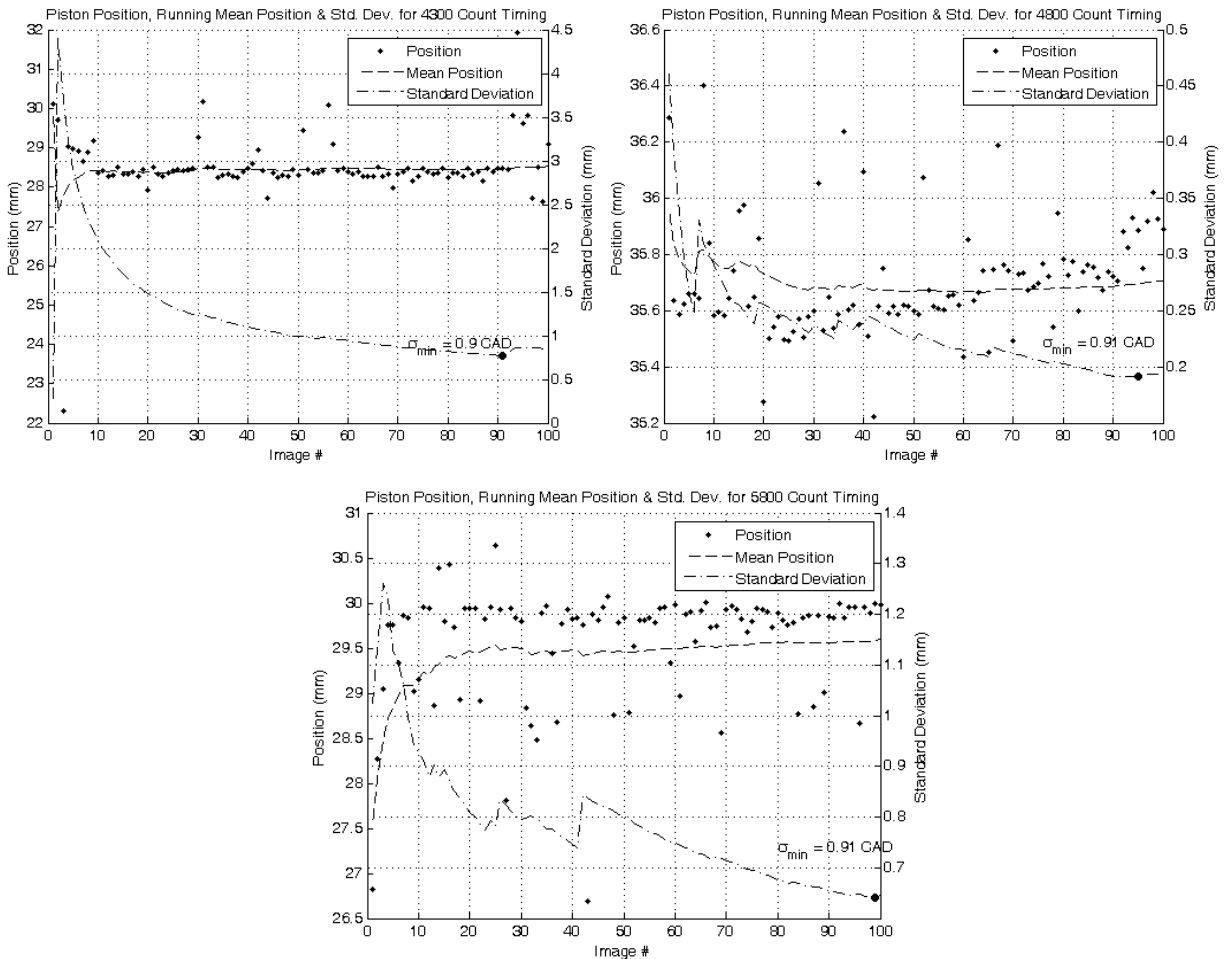
Figure 5-1 Mean Piston Position and Standard Deviation of Position for 4300, 4800 and 5800 Camera Trigger Count Timing

5▪3 ICCD CALIBRATION

The ICCD camera is known to add noise and spatial discrepancy (spatial noise) to images; each was evaluated according to the procedures detailed below. All images were taken with a *Cooke Corporation DiCam Pro* ICCD camera with a *Nikor AF Micro* lens, 105*mm*, 1:2.8*D*, set to $f_\#$2.8 and camera intensifier gain of 99.5% (lowest noise setting for the MCP).

5▪3▪1 SPATIAL VARIATION OF ICCD INTENSITY COUNT

A 15 by 12 array of diffuse blue LED's (λ_{peak} = 428*nm* and $\lambda_{dominant}$ = 466*nm,* 50% intensity at ±30^0) uniformly spaced at 0.3" was used to form a flat field light source. The light emitted was imaged at right angles to a set of theatrical screening which had the LED array behind it. An exposure of 350μs was chosen to match the peak of the image intensity histogram to the middle of the camera's dynamic range. Each exposure was repeated 256 times and then arithmetically averaged (using the camera's *CamWare* imaging software) to provide the final image. *Figure 5-2* shows two representations of the same control image. The left shows the basic image across the full intensity range, while that on the right shows the same image with a range crop applied to the intensity levels.
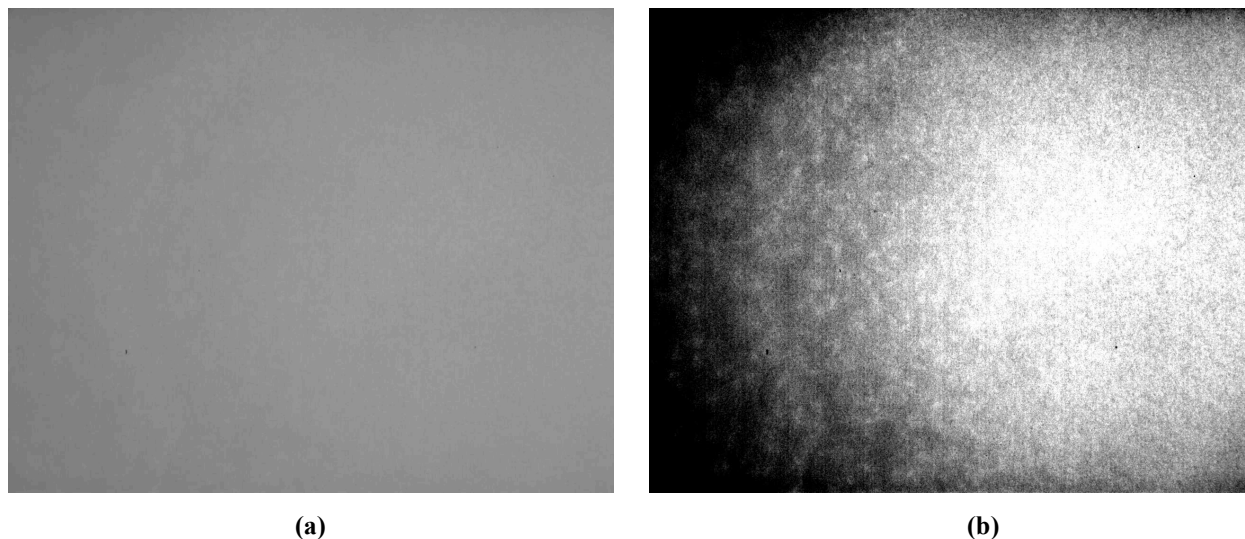
(a)   (b)
Figure 5-2 iCCD Flat Field Image with Mean Intensity at 2^6 Bits, With (right) and Without (left) Range Cropping

A clear variation in the intensity of the image is visible in the right hand image of *Figure 5-2(b)*. The peak intensity is about 11.8±2.4% (95% confidence) above the field mean, with the minimum intensity correspondingly low by about 11.6±1.9% (95% confidence). Following discussions with the camera manufacturer the variation is believed to come from manufacturing variance in the MCP of the camera intensifier. There is no on-board correction procedure and the variation must be corrected for in post-processing.

5▪3▪2   NOISE FLOOR FOR ICCD

The noise found in any image produced from a CCD, intensified or not, can be attributed to a number of sources. Spatial inconsistency (*i.e.* noise) is directly related to the wavelength of the incident radiation **[369]**, but in the visible spectrum the wavelength of the system noise is substantially shorter than that of the incident light, allowing the spatial noise attributable to incident radiation frequency to be overlooked. However, there are three primary noise sources on the camera/CCD which cannot be overlooked. Readout noise occurs directly from transferring charge from one well to the next when reading the charge off the chip to the serial register(s), and scales linearly with readout rate. Secondly, the Johnson-Nyquist noise (also called dark or thermal noise) is attributable to the thermal excitation of the electrons on the CCD, and is directly proportional to both the chip temperature and readout time. The intensifier further adds to the system noise because of the amplification it is designed to provide and its non-ideal quantum efficiency. The individual effects of each of these factors cannot be separated and together form the noise floor for the camera.

A series of 51 dark images were taken, each of which was the arithmetic average of 256 exposures (made using the camera's *CamWare* image control software). These images were made in a completely darkened laboratory at an exposure of $350\mu s$. The imaging surface was that used in the spatial variation study (*cf. §5▪3▪1*). The dark field image for the camera used in this study was found to have a full range of 8 pixel counts, with a mean of 87. *Figure 5-3* shows the mean pixel count against the standard deviation for the series of 51 dark images. The broken lines indicate the mean image count and mean standard deviation for the complete image set. The figure indicates that the higher the average dark field count the higher the noise level (standard deviation) in the image. The random nature of the noise floor cannot be corrected for, and will be taken to have a value of 87±0.06 (95% confidence) counts for the purpose of all image processing.
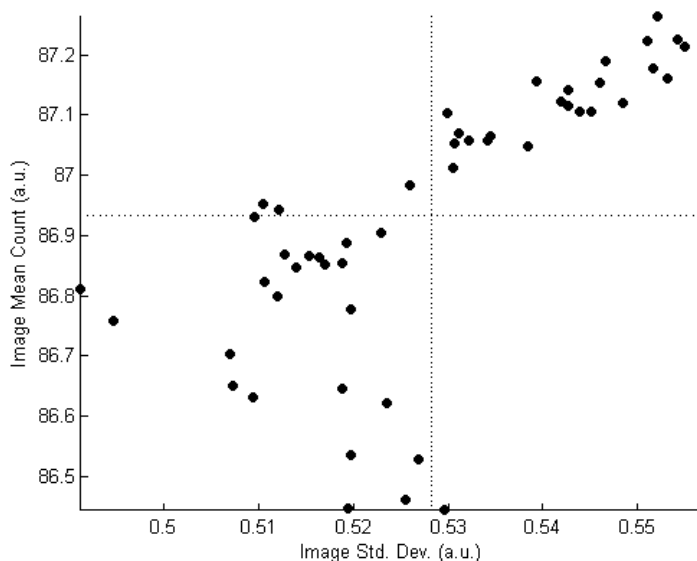
Figure 5-3 Mean and Standard Deviation for the iCCD Dark Field

5▪3▪3 TEMPORAL VARIATION

In order to assess properly the noise floor of the iCCD, any temporal variation in the imaging procedure must be quantified. Using the approach outline by Rothamer & Gandhi **[369]** the temporal variation of the camera flat field was studied. A series of 51 flat field images was taken over an eight hour period. As discussed in *§5▪3▪1* the flat field image taken by the camera is not flat. To account for this a subregion was identified around the image maximum. The subregion was defined to be 200×200 pixels, giving a total area of 40000 pixels^2. *Figure 5-4* shows plots for the central row of pixels in the *x* (left) and *y* (right) directions for the subregion.
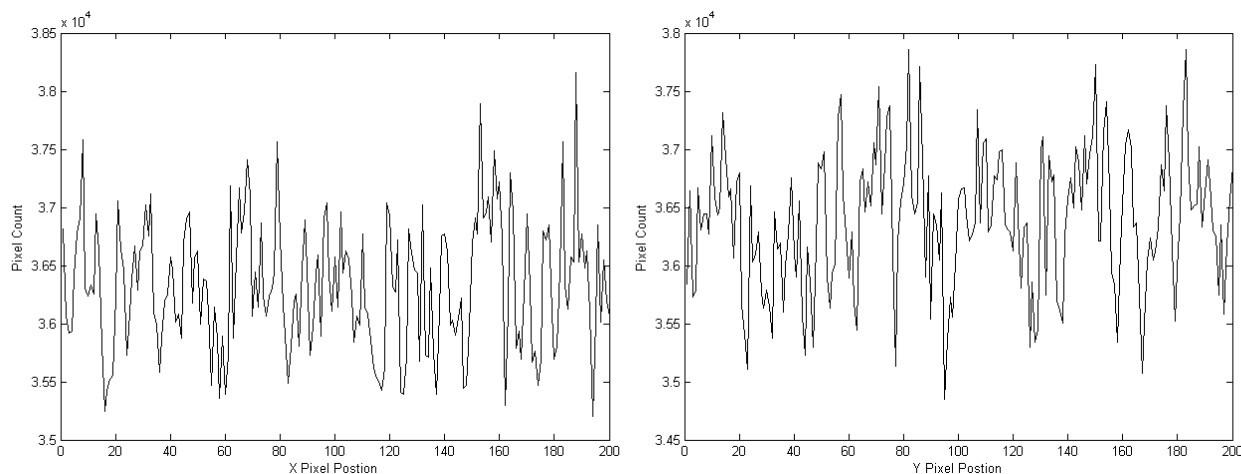
Figure 5-4 Central Row (left) and Column (right) for iCCD Flat Field Subregion

Both plots show good uniformity, however, in processing the images for any time variation, the uniformity of the image is no longer assured. The subregion in each image was normalised against the mean for the entire image set. This provided a time normalised result for each image. Each subregion, was

83

subsequently divided into four further regions, for which each sub-subregion mean was normalised against the mean for the other three. This provided a spatially normalised result for each image. The time and spatially normalised mean values were plotted against each other to form *Figure 5-5*.

The four rows of data points make it apparent that the flat field is not perfectly spatially uniform. Error bars are not shown since the $CI_{95\%}$ values were 5.15×10^{-5} and 3.85×10^{-5} for the abscissa and ordinate values respectively. Without making the subregion insignificantly small this variation cannot be suppressed. This does not, however, preclude the use of *Figure 5-5* in evaluating the temporal variation in the flat field.
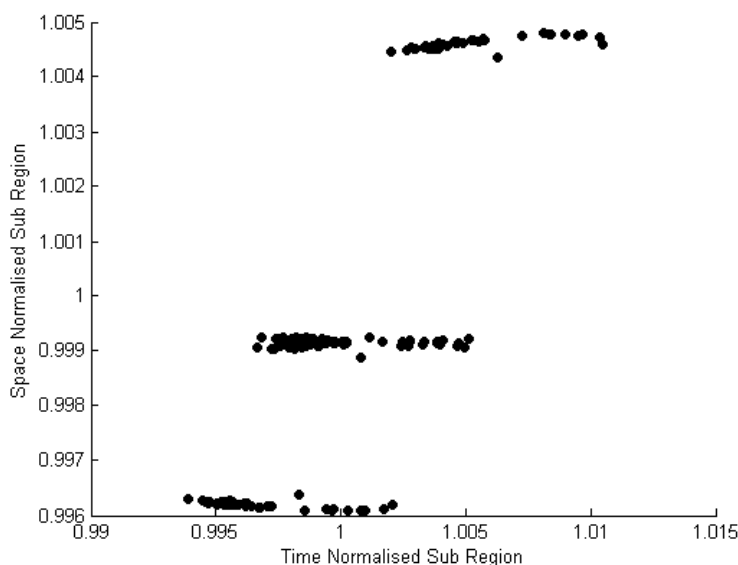
Figure 5-5 Mean Temporal-Spatial Correlation Plots for iCCD Flat Field

The confidence interval (for any individual sub-subregion) is of the order $CI_{95\%}$ ±0.15%, which corresponds to an SNR of ~1350. This value is far beyond that achievable in the shot-noise-limited case (which corresponds to about ~100 **[369]**). The order of magnitude difference between the temporal and shot-noise SNR allows any temporal variation in camera behaviour to be disregarded.

5▪4 FLUORESCENT SIGNAL CHECKS

5▪4▪1 SIGNAL LINEARITY & DISSOCIATION CHECKS

When trying to ascribe natural gas concentrations to the intensity count recorded by the iCCD, it is assumed that the signal from the acetone is proportional to both laser power and acetone concentration. For this to hold, population inversion of the excited acetone must be avoided to preclude saturation of the signal. This is achieved when **[196]**

$$N_i << (\sigma\tau)^{-1}$$ **Eq. 5.1**

Assuming a fluorescent lifetime of $\tau_{flu} \sim 1.1 \times 10^{-9} s$ **[306]** and an absorption cross-section of $\sigma_{abs} \sim 2.3 \times 10^{-20}$ cm^2 at $248nm$ **[196, 305]**; $N_i \approx 3.95 \times 10^{28}$ *photons/cm²s*. Each photon has an energy given by

$$E_{pho} = \frac{\hbar c}{\lambda}$$

Eq. 5.2

which, for a 20*ns* pulse, results in a required intensity of ~633 *J/cm²* for signal saturation. However, the laser used in this study provides 166 *J/cm²* at maximum power, avoiding signal saturation. Further, dissociation of the acetone must be avoided. The lower dissociation limit for acetone is 86 *kcal/mol* **[336]**, or ~360*kJ/mol*. Yet the current laser provides 400*mJ* maximum energy, which equates to 42*kJ/mol* at 1% acetone *v/v* at TDC- well below the dissociation limit.

5▪4▪2   *THE FLUORESCENCE OF NATURAL GAS*

The odour markers included in commercial natural gas are most commonly based on a series of compounds called mercaptans (sulphurous equivalents to alcohols). THT (tetrahydrothiophene, $(CH_2)_4S$) is also commonly used and is known to fluoresce significantly in the UV, and has consequently been used as a fuel tracer **[370]**, though this is eschewed in the current study. The composition of natural gas varies geographically and with the time of year. Vancouver natural gas has an approximate composition as shown in *Table 5-1*. Depending upon the exact sulphur content of the gas blend, 8-24 *mg/m³* of marker are added of which 65% is *t*-butyl mercaptan, $(CH_3)_3CSH$, and the reminder methyl-ethyl sulphide, $(CH_3)_4S$; both of which are UV transparent[13].

Compound	Chemical Formula	Mole Fraction %	Molecular Mass (g/mol)	Gas Constant (J/kg.K)	Ratio of Specific Heats
Methane	CH_4	94.6643%	16.04	518.33	1.304
Ethane	C_2H_6	1.8016%	30.07	276.49	1.187
Propane	C_3H_8	0.4236%	44.10	188.53	1.27
Butane	C_4H_{10}	0.1589%	58.12	143.05	1.094
Pentane	C_5H_{12}	0.0461%	72.15	115.23	1.07
Hexane	C_6H_{14}	0.0076%	86.17	96.48	1.06
Heptane	C_7H_{16}	0.0000%	---	---	---
Octane	C_8H_{18}	0.0000%	---	---	---
Nitrogen	N_2	0.5975%	28.01	296.82	1.40
Carbon Dioxide	CO_2	0.1698%	44.01	188.91	1.289

Table 5-1 MicroGC Natural Gas Composition Results[14]

To ensure this UV transparency a series of tests where conducted to compare the fluorescent signal obtained from a natural gas and acetone-doped natural gas. Using the RCM, 31 images were taken of homogeneous natural gas charges and 31 natural gas charges seeded with 1% *v/v* acetone. Arithmetic mean images were created and normalized against a similar mean image for air. *Figure 5-6(a)* shows the

---

[13] Thanks must go to Jim Cox of *Terasen Inc.* for the information on odour markers in BC gas.
[14] Results from Westport Innovations average of January to July 2009

natural gas image normalized against an air charge, while *Figure 5-6(b)* shows the air normalised gas/acetone mixture.

(a)   (b)
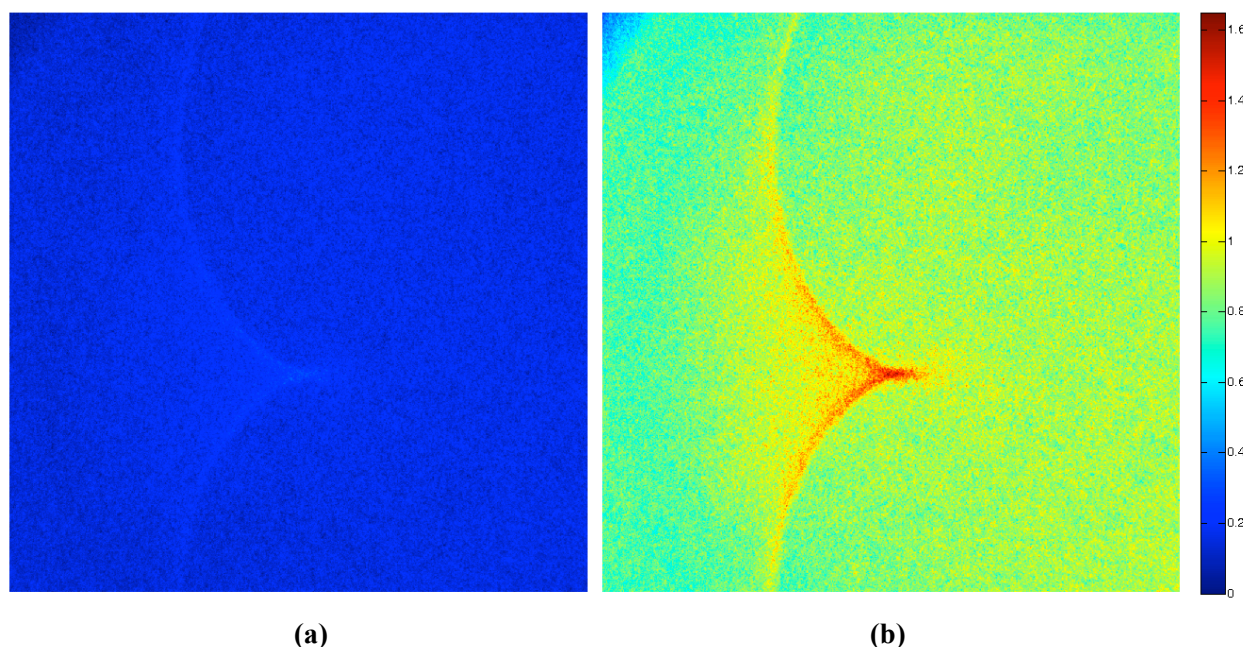
Figure 5-6 Air Normalised Images of Fluorescent Intensity from Natural Gas (left) and Natural Gas with 1% Acetone *v/v* (right).

The natural gas images produce a signal ~20% stronger than air, which may be attributed to poorly excited LIF of various compounds, or inelastically scattered light. The gas/acetone mixture has a signal ~90% stronger than air, significantly higher than that of the unseeded natural gas. The strong signal from the inelastic scattering of the laser light, which causes significant spatial noise, is evident. From the data presented it is not possible to fully discount the signal produced by the natural gas, but given that it is ~4.5 times lower than that produced by the acetone doped charge, and of an intensity which is within the system noise it is possible to attribute the LIF signal in all future images to the acetone/methane mixture present which is dominated by that of the acetone.

5▪4▪3   DISCOUNTING RAYLEIGH SCATTERING

In any laser diagnostics system the Rayleigh signal dwarfs those of Raman and LIF. However, the Stokes shift of the latter two allows easy filtering of the Rayleigh signal. Acetone fluoresces in the blue at ~350-550*nm*, which is 100-300*nm* away from the excitation wavelength. Correspondingly, rejection of elastically scattered laser light of the Rayleigh signal can be achieved with a commercial high grade optical UV filter. To ensure that this is the case a series of 31 images were taken of a homogenous air charge and 31 more of the same charge with a natural gas injection event. There should be no discernable difference in the recorded images. Following a similar procedure to that outlined for the natural gas fluorescence checks the two image sets were compared, *Figure 5-7*. The injection event occurred in the

bottom left of the image and extended to the top right; given that no discernable structure is apparent Rayleigh scattering may be discounted.
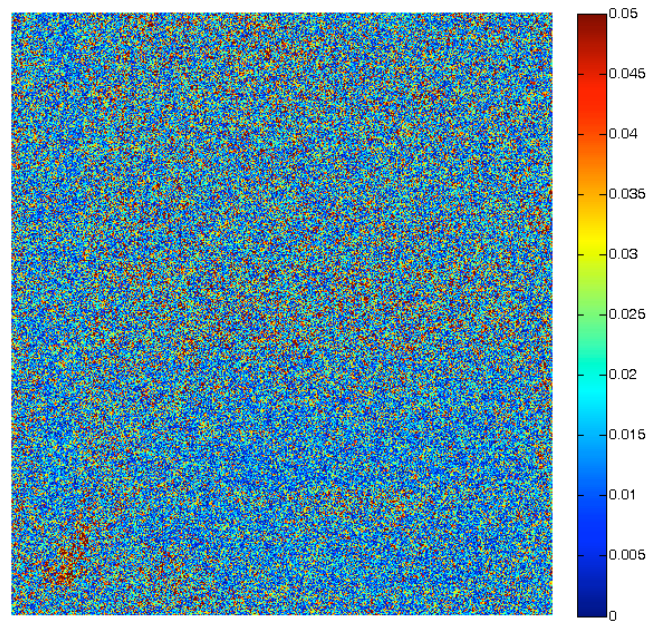
Figure 5-7 Unseeded Direct Injection Event Normalised Against Quiescent Air Charge

5▪5 PRESSURE TRANSDUCER CALIBRATION

A piezoelectric dynamic pressure transducer is used to capture the pressure in the RCM cylinder. The *PCB Electronics* 112A dynamic pressure transducer was installed in a small volume which has a hand operated ball valve on the inlet and outlet. The transducer output was amplified with a Kistler 5051B charge amplifier set at 1*pC/psi* and a scale of 300 *psi/V*. A regulated 2000*psi* nitrogen supply was connected to the inlet, which provided the required pressure step when the inlet valve was opened. The output from the charge amplifier was recorded on a Tektronix 2024B digital oscilloscope. The oscilloscope was also used to analyse the signal for peak-to-peak voltage change. Fifty-one pressurisations and depressurisations were performed and the transducer/amplifier response recorded. The results showed a mean voltage change of 7.4*V* which corresponds to 3.7*mV/psi*. It must be noted however that the following effects cannot be accounted for (in order of significance):

- The precision of the supply pressure;
- The effects of the dead volume, pressure wave formations and shape on valve opening;
- Thermal considerations such as charge cooling upon valve actuation;
- Case over/under torquing;
- Transducer linearity.

5▪6 POLYTROPIC EXPONENT CALCULATION

When considering the compression stroke of an ICE the process is assumed to be isentropic, an assumption which is well established in its validity. However, the process is far from reversible or adiabatic. These factors can be taken into account by evaluating the polytropic exponent of the working fluid, the value of which will be different to the theoretical one. The evaluated polytropic exponent can then be used for subsequent calculations.

The rapid compression machine was filled with an atmospheric air charge at ambient pressure. The machine was then fired and the cylinder pressure trace recorder with the calibrated pressure transducer. The charge signal from the transducer was amplified and converted to a voltage signal which along with, crank position and index pulse, was recorded on a Tektronix 1024B oscilloscope. This voltage data was subsequently converted to a pressure reading (in *psi*), while the index pulse and crank position were used to calculate the cylinder volume (in *cu. in.*) for each data point. Following the method outlined by McCullough [371] the slope of a log-log plot of pressure *vs.* volume provided the polytropic exponent with heat and pressure losses accounted for. The data presented below are an average of 31 separate runs. The procedure outlined was also repeated identically for a stoichiometric CH_4/atmospheric air mixture.
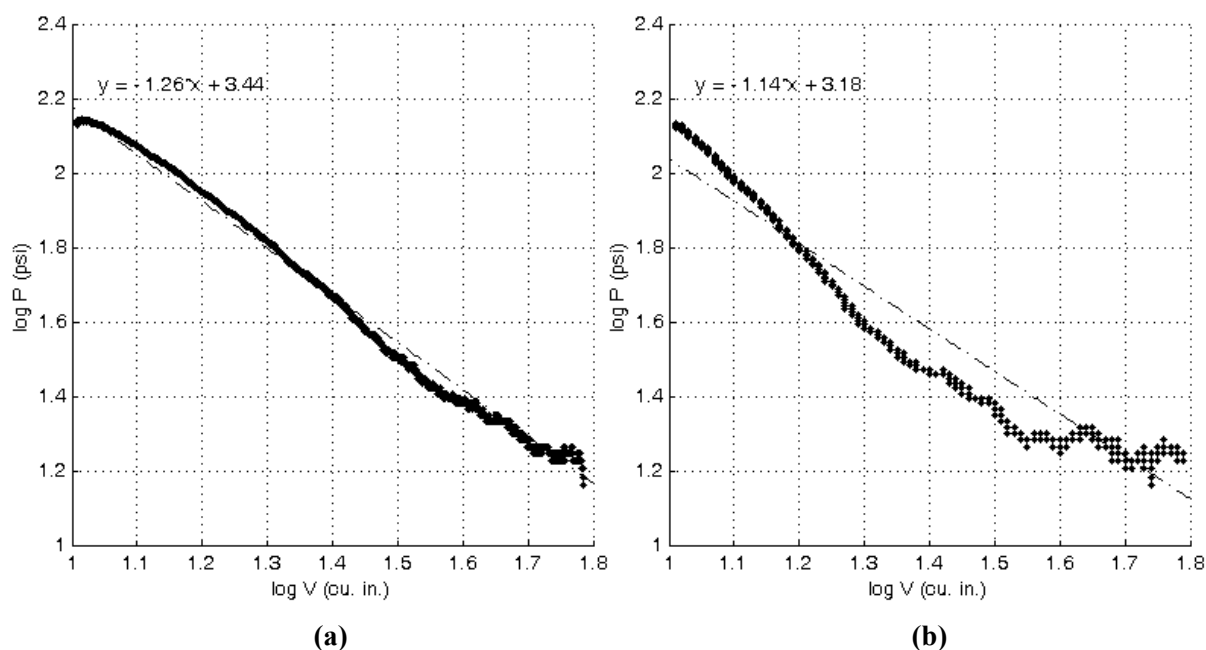
Figure 5-8 Polytropic Exponent Plots for Air (left) and Stoichiometric CH₄ Mixture (right)

Figure 5-8(a) clearly shows a strong linear relationship between the natural-logarithms of pressure and volume. As would be expected [371] the peak pressure is seen to be advanced of TDC due to heat loss and leakage. A least squares fit ($R^2 = 0.9936$) of the data suggest a polytropic exponent of 1.26 (10% lower than the true value) which is reasonable when compared to the only other known published value of 1.24

[372]. Based on a least squares fit ($R^2 = 0.9064$) to the stoichiometric data, *Figure 5-8(b)*, the polytropic exponent was calculated to be 1.14, or 13.6% below the theoretical value for the mixture. Although not as good as that of acetone the effect upon the experimental results is expected to be small since the exponent value is use to establish the state within the cylinder, and is not used directly in the fuel concentration specification.

5▪7 LASER SHEET PROFILE CORRECTION

The beam profile of an excimer laser is known to be approximately Gaussian longitudinally and top-hat transversely **[152]**. The transverse uniformity of the beam and small width of the light sheet ensure a well defined interrogation volume in one dimensions, however the Gaussian profile of the beam must be corrected for in the second dimension. The RCM cylinder was filled with a pure air charge and, without any cylinder motion, injected with 250 3*ms* injections from the DI injector (at 62*mg/injection*). The resultant homogeneous charge of natural gas with 1% *v/v* acetone vapour was imaged with 31 consecutive shots of the laser. Each image was corrected for background light intensity and had a central region across the image *x*-direction 10 pixels wide investigated. Each subregion had pixel values averaged for each column and this was repeated for each image. The values for each image were then averaged themselves to form a representative profile of the laser sheet intensity. The result of this process is shown in *Figure 5-9*.
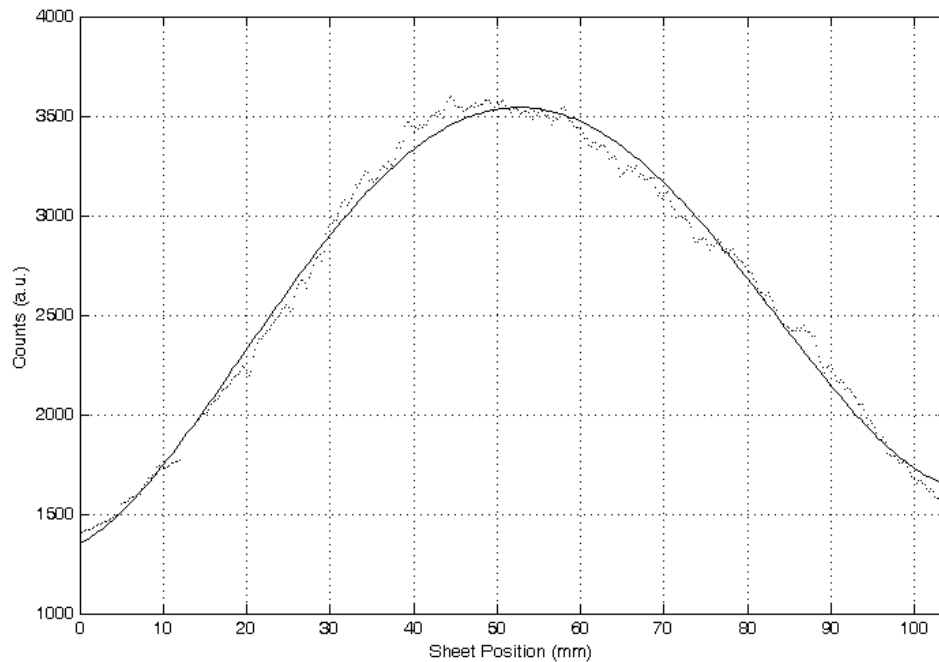
Figure 5-9 Laser Sheet Profile; Recorded (•) and with a 4th Order Fit (-)

The recorded data had a fourth order fit applied (since it offered better conditioning than a double Gaussian fit) with the coefficients listed in *Table 5-2*.

Fit	x^4	x^3	x^2	x^1	x^0
Based on Pixel Value	8.4×10^{-7}	-6.9×10^{-4}	0.1326	5.5419	1342.9
Based on Sheet Position (*mm*)	2.2×10^{-4}	-0.044	2.0883	23.220	1348.5

Table 5-2 Least Squares Fit Coefficients for Laser Sheet Profile

5▪8 OPTICAL DISTORTION CORRECTION

The optical distortion caused by the emitted light passing through the curved surface of the RCM bore mustbe be corrected for. A calibration grid comprising alternate black and white squares measuring 2×2*mm* was placed in the RCM cylinder and imaged. On the cylinder centreline, where no distortion is expected, the number of pixels per *mm* can be calibrated. The number of pixels that comprise each alternate black and white square on a calibration grid can be counted and compared to the value on the centreline. The distortion factor, *δ*, can then be defined by, *Eq. 5.3*

$$\delta = \frac{grid\ pixel\ count}{true\ pixel\ count}$$

Eq. 5.3

Figure 5-10 shows the distortion factor for each set of 2×2*mm* grids starting at the cylinder centreline and progressing towards to the cylinder bore. The 'steps' occur because the 2×2*mm* grids can only correspond to integer pixel dimensions. The curve in *Figure 5-10* corresponds to a *sine* curve over the interval 2.25 – π *radians*. The first value in this range matches the distortion factor to the experimental value at the cylinder bore, while the second value specifies zero distortion at the centreline. The agreement between the calculated distortion factor and the experimental value is seen to be good.
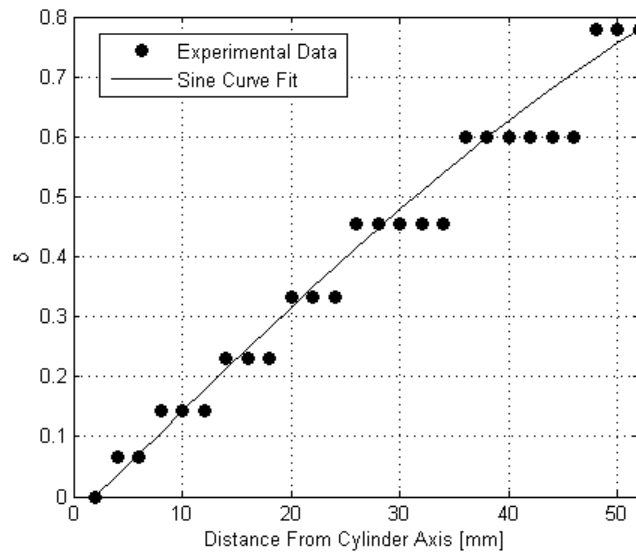
Figure 5-10 Cylinder Optical Distortion

Images are then corrected by binning the image into 2×2*mm* blocks and stretching them in a piece-wise fashion to the corrected size (according to *Eq. 5.4*), with inserted pixel values interpolated from those on either side of it.

$$new\ dimension = old\ dimension \times (1+\delta)$$

<div align="right">

Eq. 5.4

</div>

The correction is made in the radial direction only and pixel dimensions rounded to the nearest integer value. This approach leads to images that are 832 pixels tall (when no on-chip camera binning is used). The calibrated pixel size (at the cylinder centreline) is 0.125*mm,* yielding a corrected image size of 104*mm*, which is the cylinder bore.

5▪9 PIXEL INTENSITY AIR-FUEL-RATIO CALIBRATION

The RCM seeder and premixer were used to generate acetone doped mixtures of natural-gas and air. Mixtures were prepared according to fuel partial-pressures, which were calculated according to the composition given in *Table 5-1*. Homogeneous charges were prepared at relative air-fuel ratios of: 0 (pure fuel), 0.3, 0.5, 1, 1.5, 2 and ∞ (pure air). The RCM was then filled with the appropriate mixture and a homogeneous charge image collected. Mixtures were prepared to allow batches of fives runs; a total of 51 images were taken for each mixture concentration. All collected images were corrected for background noise, CCD chip-spatial variation, laser power variation, and sheet intensity variation. The corrected images were then averaged and a sub-region, away from reflections, spatially averaged to obtain an intensity count for the given mixture RAFR. From the signal linearity checks of *§5▪4▪1* it is axiomatic that that signal intensity should be linear with respect to acetone number count. Assuming fully homogenised seeding the fuel number count can be used as a proxy for acetone number count. The fuel normalised acetone number count $\left(\dfrac{N_{fuel}}{N_{total}}\right)$ was plotted against the fluorescent intensity. The result is *Figure 5-11*, which is reassuringly linear ($R^2 = 0.995$).
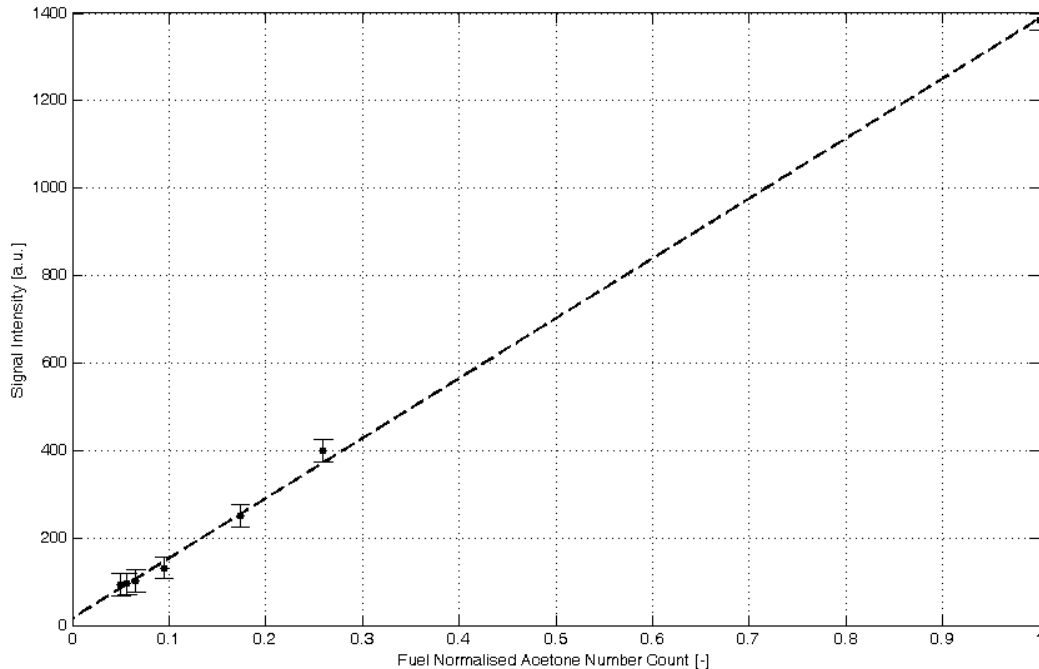
Figure 5-11 Normalised Fuel Number Count *vs* Signal Intensity

This normalised calibration curve based on number count is equated with relative air fuel ratio as follows. By taking the quotient of the perfect gas equation of state for the air and fuel in the RCM cylinder, the total pressure of air within the mixture can be expressed *Eq5.5*

$$P_{air} = \left(\frac{m_{air}}{m_{fuel}} \right) \left(\frac{MW_{fuel}}{MW_{air}} \right) P_{fuel} \qquad \text{Eq. 5.5}$$

Noting that the mass quotient of *Eq5.5* is the AFR and given that the relative air-fuel ratio (RAFR) is (*Eq5.6*):

$$RAFR = \frac{AFR}{AFR_{stoic}} \qquad \text{Eq. 5.6}$$

it is possible through substitution and simple manipulation to yield the calibration equation of *Eq5.7,*which can be evaluated fully since the ratio P_{total}/P_{fuel} (equal to N_{fuel}/N_{total}) is given by the expression for the calibration line of *Figure 5-11* and all other quantities are known (*cf. Table 5-3*)

$$RAFR = \frac{P_{total}/P_{fuel} - 1}{AFR_{stoic} \left(\dfrac{MW_{fuel}}{MW_{air}} \right)} \qquad \text{Eq. 5.7}$$

Property	Value
AFR$_{stoic}$	16.911
Molar AFR	9.5098
Molecular Weight	16.2878 *g/mol*
Specific Gas Constant	501.7 *J/kgK*
Ratio of Specific Heats	1.2644
H:C ratio	3.927
CoV Methane	0.761%
CoV AFR	0.234%

Table 5-3 Mixture Properties Based on Data in *Table 5-1* and Original GC Data

5▪10   IMAGE BINNING

A comparison of image SNR was made between an un-binned, a 2×2, and 4×4 binned image to assess whether the loss in spatial resolution associated with binning is outweighed by the increased signal-to-noise ratio. Homogeneous doped natural gas/air charges were prepared as they were for the air-fuel ratio calibration tests of *§5▪9*. On-chip binning of the CCD wells allows for increased pixel intensity (larger optical collection area) without increased camera-noise, while the probabilistic nature of photon detection by CCD's is well described by Poisson statistics. For an intensified image the signal-to-noise ratio is given

by *Eq5.8* **[373]** where *I* and I_0 are the signal intensity and camera noise floor respectively and the other parameters are as listed in *Table 5-4*.

$$SNR = \frac{\eta G I}{\sqrt{\eta G^2 \kappa I + I_0^2}}$$

Eq. 5.8

Parameter	Value
Photocathode Efficiency, η	0.4
Intensifier Noise Factor, κ	1.03
Intensifier Gain	99.5

Table 5-4 DiCam Pro iCCD Noise Parameters

The unbinned pixel corresponded to physical dimensions 0.125×0.125 *mm*, and provided prohibitively poor signal levels above the camera-noise floor, such that only the a 2×2, and 4×4 binned images were assess for their SNR. The SNRs for the eight tested concentrations are as shown in *Figure 5-12* (low signal strength detail in inset).
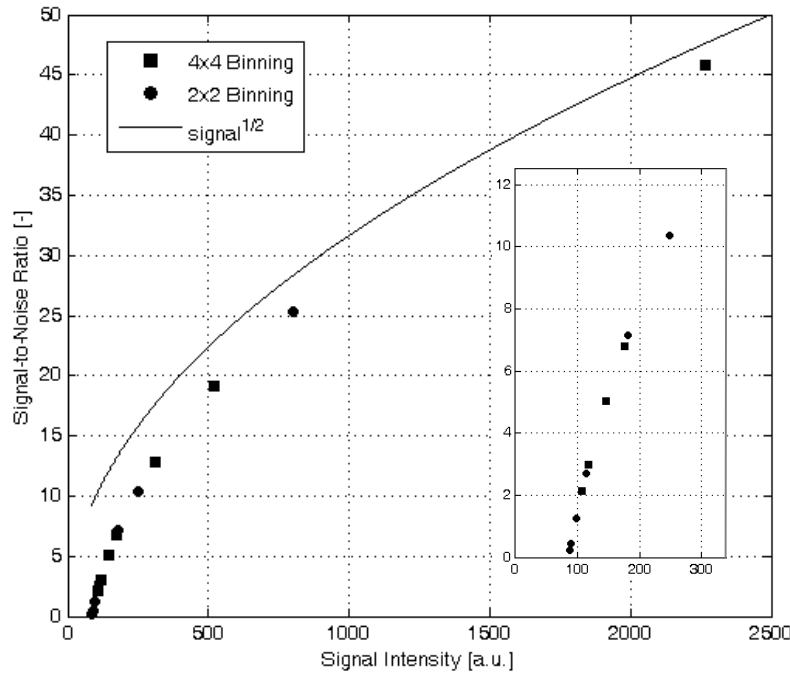
Figure 5-12 Signal-to-Noise Ratio for 2×2 and 4×4 On-Chip Binning at Different Signal Intensities & Maximum SNR Curve

In Poisson statistics the mean and variance are equal and as such, in the shot-noise limit the SNR tends to $\sqrt{I}$ (curve shown in *Figure 5-12*), but it is apparent from *Eq5.8* that the shot-noise limited case for an intensified system $\left(\eta G^2 \kappa I \gg I_0^2\right)$ will have an SNR reduced from its maximum by $\sqrt{\kappa}$, approximately the difference observed at the highest signal intensity. The range of intensities from the fuel concentrations shows that all LIF images will be in transition from system to shot-noise limited, depending upon the fuel

concentration. This informed the decision to take all images with a 4×4 on-chip bin to maximise the image SNR without compromising spatial resolution or causing image saturation (the result of 8×8 binning).

5▪11   SEEDER CHARACTERISATION

The seeder used to dope acetone into the methane fuel supply is described in *§4▪5* and in detail in *Appendix A*. The two supplies to the seeder were set so that the flow through the acetone accounted for 0, 25, 50, 75 or 100% of the total seeder gas flow. Three repeats were carried out for each flow condition, with the setting chosen at random. The seeder was allowed to settle to a steady state, with 15 minutes (1.5 residence times) elapsing between samples. The samples were collected in 1 litre Tedlar® bags with two venting samples taken prior to each data sample. The 15 samples were sent for gas chromatograph and mass spectrometry analysis at PowerTech Laboratories Inc., Surrey, BC, Canada. Calibration samples were prepared by *PowerTech Labs Inc.*

The GC/MS results of *PowerTech Labs Inc.* report, project#: 15808-43, are presented *Figure 5-13*. A linear fit provides a regression co-efficient, R^2, of 0.9553. A lack of knowledge about the experimental procedures and errors precludes the specification of error bars [15].

---
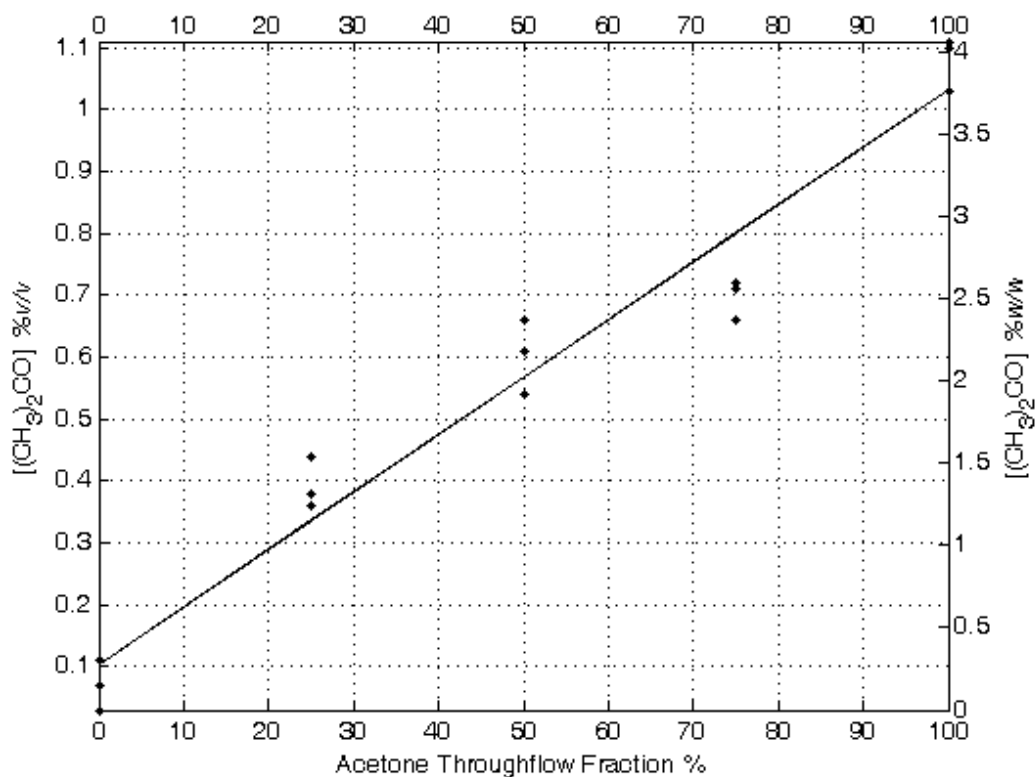
[15] Thanks must go to Ed Hall of *PowerTech Labs* for his help in completing the analysis.

Figure 5-13 Acetone Seed Concentrations

5▪12   FLOW ENVIRONMENT IN RCM CYLINDER

The premise of the RCM is that it provides engine-like cylinder conditions with a simplified flow field. The lack of valve system ensures that any turbulence generation is from, in the absence of direct fuel injection, piston motion alone. High speed camera footage (2000 *fps*) of a stoichiometric homogeneous charge ignition and propagation, with piston motion, was taken using a *Vision Research Phantom* camera. The flame kernel and subsequent propagation are shown in the four panels of *Figure 5-14*. Some slight distortion of the flame front is present due to heat transfer along the (horizontal) electrodes, and due to the disruptive effect of the (vertical) PSC capillary tube. However, the flame remains predominantly circular demonstrating a lack of turbulence which would wrinkle the flame front significantly.
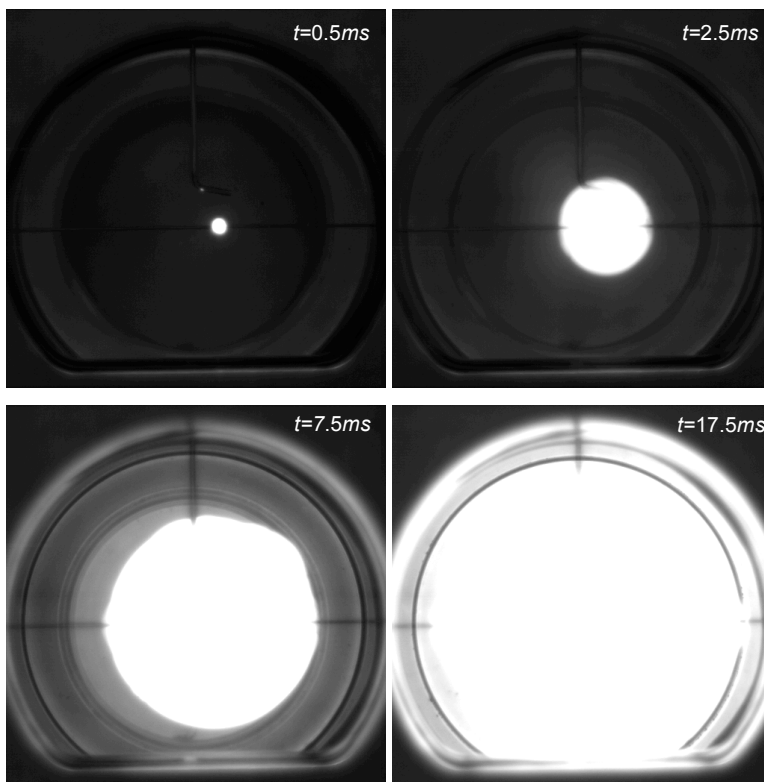
Figure 5-14 Flame Propagation for a Stoichiometric Mixture in RCM Cylinder (time listed after spark)

5▪13   J43M INJECTOR CALIBRATION

The Westport J43M injectors were used to supply the fuel for the direct injection and partially stratified injection events. The hole size for each injector was designed using the assumption of an isentropic expansion of a prefect gas through the injector orifice. Iaconis **[374]** first proposed this for the Westport J41 injectors (the precursor to the J43M's) and obtained good agreement with experimental data. Further, an assumed loss of 10% in stagnation pressure through the injector (as recommended by Hill & Oulette

[8]) was made to identify the state at the injector sack prior to ejection. The hole for the DI injector was sized to be Ø0.75*mm*, while that for the PSC injector was sized at Ø0.26*mm*.
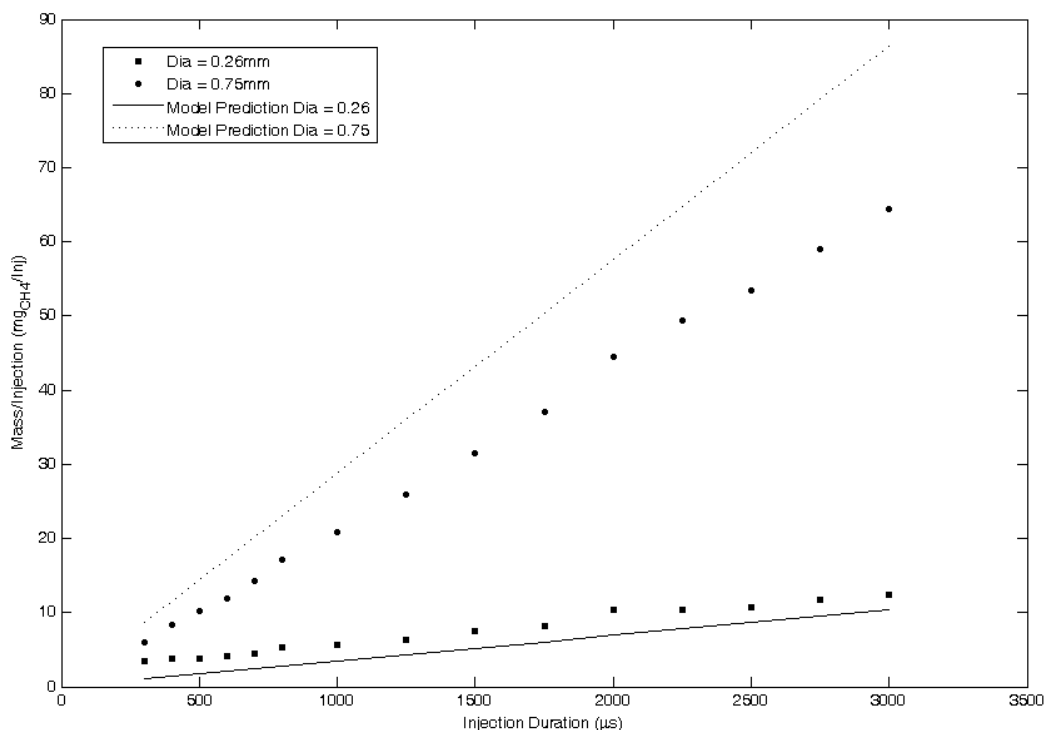
Figure 5-15 J43M Injector Characterisation Data and Model Prediction

The discrepancies in the recorded data and the model predictions may be attributed primarily to the two key assumptions in the model, namely: isentropic expansion and 10% stagnation losses in the injector. It can be seen that the model under predicts injection fluxes for the smaller hole injector and over predicts for the larger hole. This would suggest that the losses in the injector are related to the mass flow rate directly and so by assuming 'across the board' losses of 10% in stagnation properties and isentropic behaviour the discrepancy increases with increased mass flow, as can be seen in *Figure 5-15*. The general trends are in good agreement however, and support the use of the model as a design tool to establish the required hole size for the injectors.

5▪14   CONCLUSION

Chapter 5 has detailed the experimental results that allow the correction and calibration of the LIF intensity images. Camera CCD and laser beam profile corrections have been presented, as has an appraisal of the experimental signal-to-noise ratio. An evaluation of the compression stroke polytropic exponent allows the specification of the RCM cylinder state, while turbulence in the early stages of the compression can be neglected based upon inspection of the luminescent flame front. The calibration curves for the acetone seeder, the fuel injectors and fluorescent response of the acetone mixture have also been introduced.

Chapter 6 IMAGE CALIBRATION

6▪1 INTRODUCTION

Chapter 6 uses the LIF results from a single point in the test matrix to highlight some of the correction procedures used to ensure that the collected data is corrected for known error sources. The chapter goes on to outline the difficulties in setting-up and calibrating LIF images for high speed, highly turbulent flows. The discussions highlight the need for temperature field data if LIF images are to be accurately calibrated. Further to this, arguments are presented that rule out condensation of the acetone seed as the source of the observed calibration errors. Finally, the practical implications for the current work are presented, while quantifying the effect of the uncertainties is left until *Chapter 9*.

6▪2 IMAGE PROCESSING PROCEDURES AND PRESENTATION

6▪2▪1   GLOBAL PROCEDURE

All image processing and post-processing was carried out in *Matlab* (R2009a), using a combination of library functions and bespoke code. The images from the iCCD camera were stored and imported to the processing code as 12*bit* TIF images. The images were subsequently converted to 16*bit* (double precision) TIF images for processing. *Figure 6-1* presents the route followed in the post-processing and correction of the LIF images.
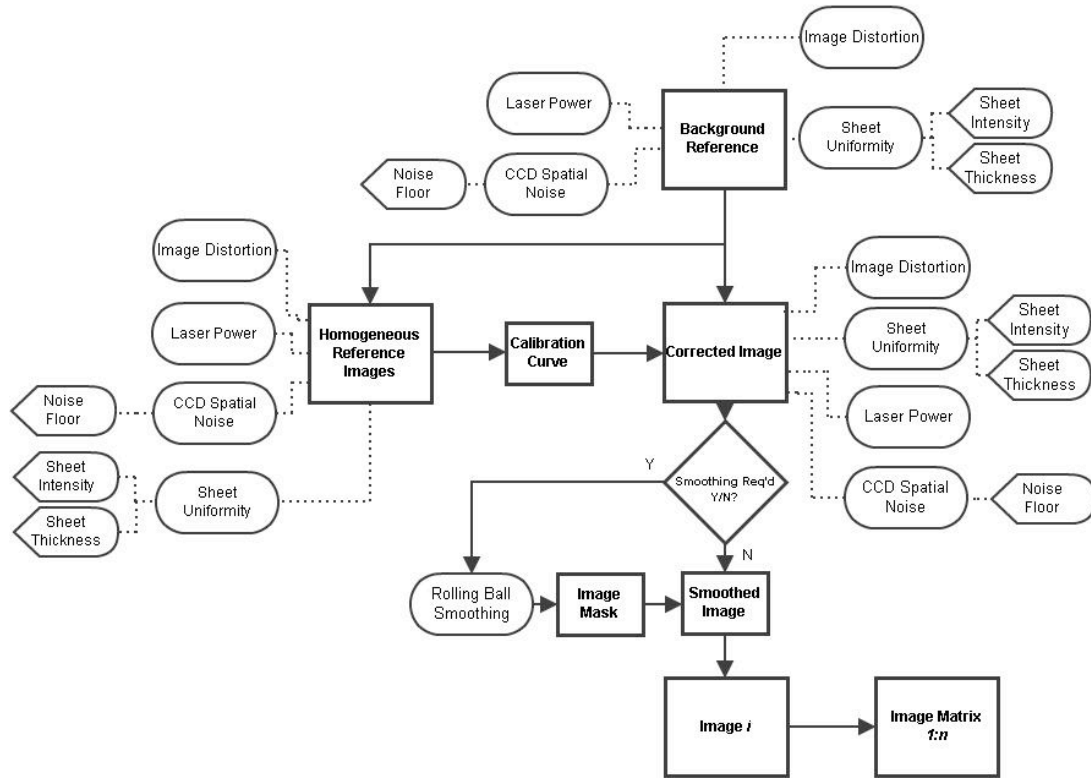
Figure 6-1 Image Post-Processing Road Map

A background reference image is taken of a homogeneous unseeded NG charge. This image is corrected for optical distortion, laser and camera CCD effects, namely: laser sheet thickness, laser sheet profile, laser power and CCD spatial variation. The series of 51 calibration images is treated similarly, with the additional step of background light removal. This is repeated for a range of seeded NG homogeneous charges at different AFR's. These images provide the calibration reference for image intensity. Any given experimental image is corrected for laser effects, camera CCD distortion, background light collection, and if required the distortion from passing through a curved cylinder bore. Each image is stored to form an array $x \times y \times n$ where the image is $x \times y$ pixels and there are a total of n images.

6▪3 CORRECTION PROCEDURES

6▪3▪1   EXCITATION (LASER) ASSOCIATED CORRECTIONS

The collected LIF intensity, S_f, is given by **[375]**, *Eq. 6.1*:

$$S_f = \frac{\eta\Omega}{4\pi}VC_a\sigma_a\eta_f I_0 e^{-\sigma_a\int C_a dy}$$

<div align="right">**Eq. 6.1**</div>

where the quotient represents the optical yield and the remaining terms the emitted fluorescent intensity. The exponential term in *Eq. 6.1* pertains to the extent that the laser excitation energy is attenuated by the gas mixture, and is expanded upon in *§6▪3▪1▪1*. For a fixed excitation wavelength and optical collection system, it is apparent that the signal intensity is proportional to interrogation volume, seed concentration and laser intensity.

$$S_f \propto V \cdot C_a \cdot I_0$$

<div align="right">**Eq. 6.2**</div>

To remove the volume and laser intensity dependency of the signal, the original LIF images were corrected for laser power variation, laser-sheet thickness variation and laser intensity profile. Power correction was made by recording the laser power at which the image was collected. A small (invariant) subregion of the image was used to calculate a representative intensity for the image. Given that image intensity scales linearly with power, a linear regression was performed to yield the proportionality between intensity and laser power. All images were then scaled to be at the equivalent of 300*mJ* (the energy level requested of the laser). The laser sheet optics are known to produce a sheet which is thinnest, at ~0.8*mm*, on the cylinder centre-line (also the image centreline) and varies almost linearly to a thickness of ~1.45*mm* at the bore. With this knowledge all intensity values were scaled to be as though they were from a constant interrogation volume 0.8*mm* thick. The laser sheet passes through the test section of the RCM at an angle of ~8.5^0; correspondingly each row of the captured image was scaled according to the laser profile of *Figure 5-9* (*p.*89), to bring the counts in line with the profile mean.

6▪3▪1▪1 BEER-LAMBERT ATTENUATION

The attenuation term in *Eq. 6.1* has been dropped from *Eq. 6.2*. As a laser passes through an absorbing medium it must lose energy to the medium. Considering now the lightsheet passing through the RCM cylinder, the laser energy is distributed across the air (primarily nitrogen and oxygen), natural gas (with its many components) and acetone. At 248*nm* excitation the only chemical present with an appreciable absorption cross-section is acetone. The Beer-Lambert absorption law describes the level of attenuation due to absorption according to *Eq. 6.3*

$$I = I_0 e^{-\sigma_a Cl}$$

<div align="right">**Eq. 6.3**</div>

where σ_a is the molecular absorption cross-section, 2.2×10^{-20} *cm^2* **[376]** and the pathe length *l*. At the image time the thermodynamic state in the RCM cylinder yields an acetone concentration (based on a

maximum seed concentration of 1%*v/v*, (*cf.* §5▪11) of ~2.5×10^{17} *molcules/cm³*. From this and *Eq. 6.3* the intensity ratio I/I_0 is ~0.99 *cm⁻¹*, or 1% loss in laser intensity per centimetre at maximum acetone concentration. Given the low seed concentration in the bulk charge and the short path length for the laser at higher concentrations (*i.e.* the jet dimension) it was deemed that correction for laser attenuation was not required.

6▪4 RESULTS

Application of the image correction procedures outlined previously yields the intensity image of *Figure 6-2* for the central condition of the CCD test matrix. Under these conditions there is a background charge of RAFR = 1.75 and the timing of the DI jet should cause the PSC injection to catch the central portion of the vortex ball at the head of the DI jet.
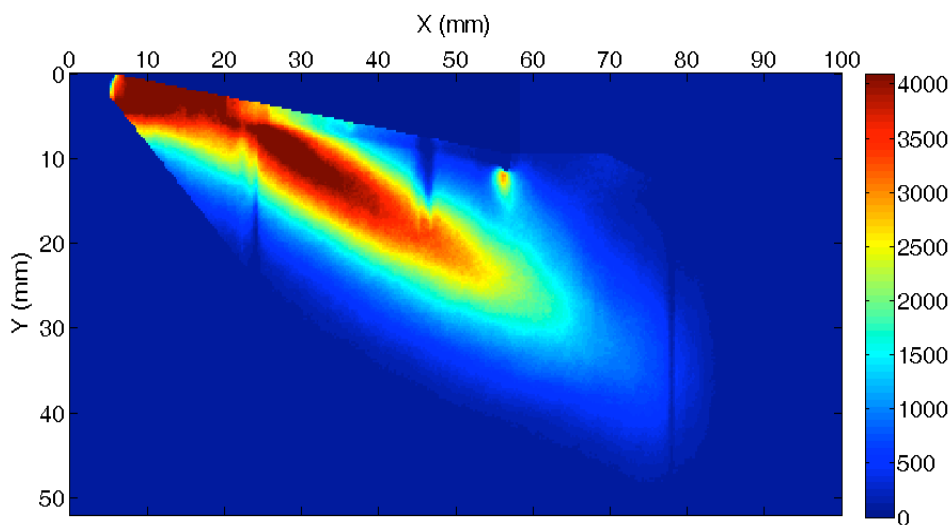
Figure 6-2 Intensity Image for Test Matrix Central Location

6▪5 DISCUSSION

6▪5▪1 IMAGE CALIBRATION DIFFICULTIES

It is clear from *Figure 5-11* (*p.*92) that pure fuel should yield a count of ~1385, while *Figure 6-2* shows counts extending to the full 12bit range of the camera. By returning to the fundamental equations that govern fluorescent intensity it is possible to assess the possible causes of the discrepancy. Assuming linear excitation, the fluorescent signal intensity is given by **[258]** (a recast form of *Eq. 6.4)*:

$$S_f = \frac{E}{\hbar c/\lambda} \eta_{opt} V_c \left[\frac{X_{acetone} P}{kT} \right] \sigma(\lambda, T) \phi\left(\lambda, T, P, \sum X_i\right)$$

Eq. 6.4

assuming that bath-gas composition does not affect the fluorescence. In considering *Eq. 6.6* laser power and wavelength may be disregarded since they are constant for any given image and laser source and

presupposing a single-phase flow; the observed intensity is proportional to temperature, pressure and mole fraction, *Eq. 6.5*:

$$S_f \propto \left[\frac{X_{acetone}P}{kT} \right] \sigma(T)\phi(T,P)$$

<div align="right">Eq. 6.5</div>

It is possible to assess the temperature change in an isenthalpic process through consideration of the Joule-Thomson coefficient, *μ*, defined by *Eq. 6.6*:

$$\mu = \frac{\partial T}{\partial P}\bigg|_{h=const}$$

<div align="right">Eq. 6.6</div>

which is negative for an observed temperature rise, identically zero for constant temperature and positive for a decrease in temperature. To make an assessment of the jet temperature at the final Mach disk, which may extend as far as ~15-20 orifice diameters downstream [377, 378], the Joule-Thomson relationship may be used. Assuming that no mixing takes place over the expansion fan boundary, assuming the expansion to be isenthalpic, using the Joule-Thomson coefficients reported by Budenholzer *et al.* [379] for methane and applying a cubic fit to data (R^2=0.9995) over the range 1800-35*psi*, the temperature was evaluated to be ~247*K*. The pressures chosen for the range over which the Joule-Thomson coefficient was applied were the stagnation pressure at the injector nozzle (equal to the reservoir pressure less 10% [374] due to friction within the injector) and the cylinder pressure at the time of injection. At the calculated temperature, the jet density is ~44% higher than the calibration charge. The cylinder charge is known to have a temperature of ~350*K* at the image time, and Grossman *et al.* [307] have shown that fluorescent yield decreases by about 35% for every 100*K* temperature rise. Further, the increased gas density can reasonably be expected to increase the fluorescent intensity due to effects similar to those of higher pressure. The gas density present in the jet corresponds to a pressure of ~3.5*bar* at cylinder temperatures that, according to the data of Braeuer *et al.* [380], would increase the fluorescent intensity by about 40%. The density increase, which acts through increased absorption efficiency and increased acetone number density, along with higher fluorescent yields at reduced temperatures would generate a signal strength for pure fuel of ~6600*counts* (assuming all three effects combine linearly). It is evident that as the jet mixes downstream of the Mach disk and before the jet recovers the cylinder conditions there would still be counts exceeding the calibration range.

Despite being able to specify this 'initial' condition there is no appropriate analytical approach which may be applied with certainty to downstream locations that would circumvent the need to identify the thermodynamic state for any given pixel; specification of the fuel concentration requires knowledge of the temperature field.

6▪5▪2   TEMPERATURE FIELD SPECIFICATION

The need to specify a temperature field is evident by considering, once more, *Eq. 6.4* and reintroducing the wavelength dependency of the absorption cross-section and fluorescent yield. Exciting any given region of a flow with two different wavelengths will produce two different fluorescent signals. Taking the ratio of these two signals eliminates the number density from expression *Eq. 6.5* to yield *Eq. 6.7*

$$\frac{S_{f,\lambda_2}}{S_{f,\lambda_1}} = \frac{\sigma(T,\lambda_2)\phi(T,P,\lambda_2)}{\sigma(T,\lambda_1)\phi(T,P,\lambda_1)}$$

Eq. 6.7

of which it is stated in **[258]** that "if the right-hand-side of *Eq. 6.7* is a known function of temperature for the given excitation wavelength and a pressure sufficiently close to that encountered in the flow, the fluorescence ratio measurement, with a single calibration point, yields temperature data. Temperature measurement with [a simultaneous] dual-wavelength technique enables quantitative measurement of concentration in cases where temperature variation previously precluded the possibility".

Upon first inspection it may appear that an experimental technique exists to circumvent the calibration problems in the current work. However, the technique is highly dependent upon having accurate calibration data for the fluorescent response of acetone at different temperatures and different wavelengths. The early work on the temperature response of acetone was limited in scope (excitation wavelength, bath gas, pressure *etc.*) and only in qualitative agreement. Similar reductions in fluorescent intensity were reported by **[307, 363, 364]** at increased temperatures. The only notable exception was Wolff *et al.* **[252]**, who report no discernable structure to the temperature response and report figures which have a ±15% fluctuation about their mean. Thurber *et al.* **[258, 305, 381]** made significant steps in characterising the temperature response of acetone, with later enhancements made by Braeuer *et al.* **[380]** and Kearney & Reyes **[203]**. All the results were in generally good agreement though Kearney & Reyes suggest a slightly lower fluorescent response than Thurber *et al.*. *Figure 6-3* shows the data of Thurber *et al*, Braeuer *et al.* and Kearney and Reyes for 248*nm* excitation of acetone in the bath gas noted in the legend. The data of Grossmann *et al.* **[307]** is also replicated despite being for 3-pentanone since. as the next homologous molecule to acetone and with the same C=O chromophore it can be expected to behave similarly. The results show a good level of agreement.

The data presented covers the temperature range from ambient to ~1000*K*, while for the current study temperatures in the DI jet can be expected to in the order of 200-350*K*. Response data in this range is limited to the single, low pressure, study of Bryant *et al.* **[311]**, which reverses the trend seen in the data presented above. Bryant *et al.* report a 6% *increase* in signal intensity with increased temperature from 240 – 300*K*. This set of observations needs further work to be reconciled with the previous findings.
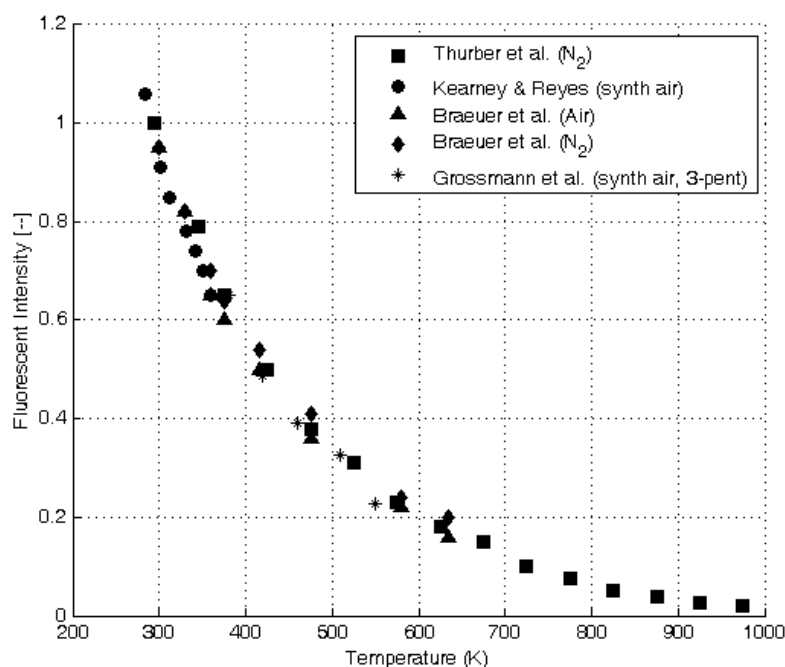
Figure 6-3 Acetone Fluorescent Yield Variation with Temperature at 248*nm* Excitation, reproduced from data [203, 258, 307, 380]

As described previously, temperature measurement can be made by utilising the difference in the fluorescent intensity of acetone when excited at different wavelengths. This was first proposed by Grossmann *et al.* **[307]** using a 308/248*nm* combination since the signal intensities from each wavelength diverge at increased temperature. This was built upon by Thurber *et al.* **[258]**, to produce *Figure 6-4*. The most significant implication of *Figure 6-4* for the current work is that as temperatures approach room temperature the fluorescent signal ratio (the result of *Eq. 6.7*) monotonically approaches unity, negating the ability to gain meaningful temperature information.
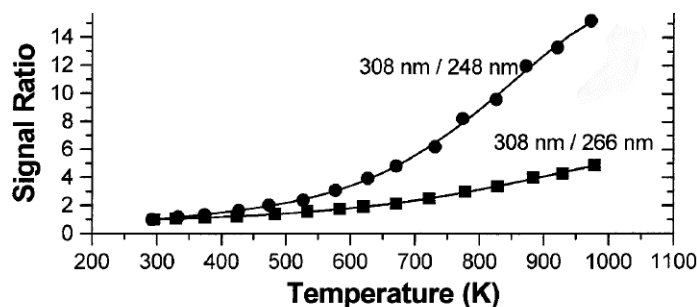
Figure 6-4 Fluorescent Signal Ratio Temperature Variation for 308/248*nm* and 308/266*nm* Pairs. Reproduced from [258]

The problem of calibrating the signal intensity from the DI jet is compounded further in that although the jet has recovered the cylinder pressure, it is not homopynic. Given that pressure dependent reactions act through interaction probabilities and third bodies, pressure can be taken as a proxy for density. Accepting that the excited, singlet, state of acetone is rapidly deactivated to the triplet manifold with almost unity

efficiency by inter-system crossing (ISC, *cf.* §3▪11▪4 and **[303, 324, 382]**), fluorescent intensity has been found to be independent of pressure **[328]** (supported by Wolff **[252]** in the range 1-18*atm*), suggesting that collisional effects upon fluorescence for the singlet state are unimportant (be they due to bath density or composition). However, more recent works by Grossmann *et al.* **[307]**, Yuen *et al.* **[304]**, Thurber *et al.* **[357]** and Braeuer *et al.* **[380]** all suggest significant changes in fluorescent intensity with increased pressure above ambient due to changes in the rate of ISC. The reported pressure responses are, generally, in qualitative agreement particularly for the latter works of Braeuer *et al.*, Thurber *et al.* and Yuen *et al.* who all report a gradual increase in fluorescent intensity with increased pressure up to ~5*bar,* from where there is a transition to a high pressure plateau at about 15*bar*. However, the inconsistencies in the data make it hard to draw any significant conclusions with respect to the effects of gas density upon the current work.

6▪5▪3   *POTENTIAL ACETONE CONDENSATION*

The arguments presented presume a single phase flow. Consideration must be given to the potential for the acetone seed to condense. Assuming the jet to be a binary, single-phase mixture of methane and acetone, the jet total pressure is, by Dalton's Law, the sum of the partial pressures. Assuming the system to be in equilibrium, the acetone partial pressure must equal its vapour pressure. Using the ideal gas equation of state the acetone partial pressure may be expressed according to *Eq. 6.8*:

$$\frac{P_{acetone}}{P_{mixture}} = \frac{m_{acetone}}{m_{mixture}} \frac{R_{acetone}}{R_{mixture}}$$

Eq. 6.8

The mass quotient is known to be 0.0375 (from calibration of the seeder, *cf §5▪11*), while the ratio of specific gas constants is known to be 485.7 (from calculations based upon the composition data in *Table 5-1* and seeder calibration concentration data). The acetone vapour pressure is thus ~1.14% of the total pressure, or ~2815*Pa*. Acetone is known to follow well the Antoine equation **[196]**, *Eq. 6.9*, which describes the vapour pressure of pure substances, *viz.*

$$\log_{10} P = A - \frac{B}{C + T}$$

Eq. 6.9

where *A, B & C* are constants (with values according to *Table 6-1*) and *T* temperature (in *K*).

Constant	kPa
A	6.25478
B	1216.689
C	-42.875

**Table 6-1 Antoine Equation Coefficients for Acetone,
reproduced from [383]**

The values in *Table 6-1* yield, at the jet temperature of ~247K, a vapour pressure of ~1963*Pa*, which is below the partial pressure of acetone in the jet. Consequently, it is possible though unlikely that, provided

nucleation sites were available, condensed acetone may result in increased fluorescent intensity due to a second liquid phase. To investigate if droplet formation was taking place the DI jet was imaged with a ×12 high magnification *Nivitar* lens and *LaVision Compact Imager* CCD camera. Shadowgraph images were taken under identical cylinder conditions to those of the LIF study and illuminated using a *Photonics Analysis PalFlash 500* capacitive discharge flash. A calibration grid showed each camera pixel to be ~1.5μm square, practically limiting the diameter of detectable droplets to ~5μm.

No droplets can be seen in the images from the acetone seeded injections (*Figure 6-5 (b) & (d)*) or the unseeded injections (*Figure 6-5 (a) & (c)*). Condensation is a complex process and it is possible that droplets less than ~1μm could have formed in the jet and their presence give rise to the strong signal observed. The timescales for the condensation, the role played by potential nucleation sites, the expansion fan shock structure and the thermodynamic state make it very hard to categorically rule out condensation as the source of the strong fluorescent intensity. The droplets, if present, are unlikely to be ballistic and carried into the jet far field, the region of most interest, and are also likely to have had time to evaporate as the jet increases in temperature. In the author's opinion the thermodynamic arguments presented previously provide stronger grounds upon which to base the calibration difficulties.

(a)

(b)

(c)

(d)
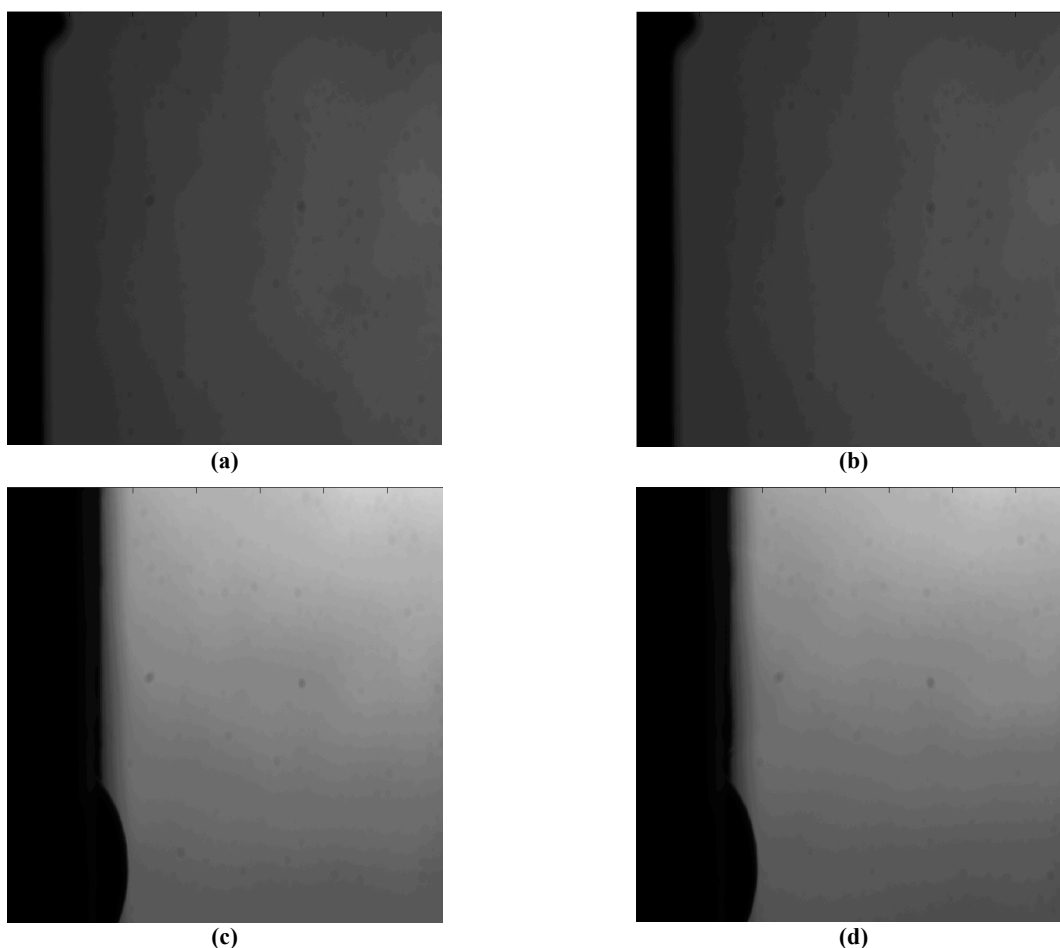
Figure 6-5 High Magnification Shadowgraph Images of Jet: (a) natural-gas jet, far-field (b) acetone seeded NG jet, far-field; (c) NG jet, near-field; (d) acetone seeded NG jet, near-field

6▪5▪4   THERMODYNAMIC STATE & FLOW FIELD INSIGHT FROM CFD

The fluorescent intensity measured by an iCCD camera is the combination of pressure and temperature affecting the absorption cross-section and fluorescent yield as well as the thermodynamic state of the acetone (natural gas). Given the shortcomings of experimental techniques to establish the temperature field, insight was sought through computational fluid dynamics. Mr. Ehsan Faghani, a fellow student and researcher at the UBC Clean Energy Research Centre, is conducting extensive numerical research into the injection of natural gas for natural gas engines. A previous model developed by Faghani had geometries identical to those used in the current work for the DI injection, and gave the results shown in *Figure 6-6*.

The model uses an irregular uniform 18,000 cell axisymmetric mesh generated in Gambit® with mesh density decreasing away from the jet origin and jet centreline. A velocity inlet specified the jet inlet boundary condition, a pressure outlet downstream specified the flow exit, while symmetric boundaries along the jet centreline and faces and walls on the remaining faces closed the computational domain. The transient governing equations were solved in Flunet® with an implicitly time stepped k-ε Reynold's stress closure of the upwind differenced Reynold's averaged Navier-Stokes equations. Walls were treated using a 'law of the wall', while convergence was deemed to have been achieved when the residuals on all parameters was <10^{-4}.

The injection pressure and chamber conditions matched those of the experimental study. Downstream of the expansion fan the jet can be expected to behave as if it were correctly expanded. As outlined by Ouellette & Hill **[384]** the isentropic Mach relations of *Eq. 6.02* can be used with Ma=1 to specify the thermodynamic state of the jet at the Mach disk (with gas composition data according to that of *Table 5-1 & Table 5-3*).

$$\frac{P_0}{P} = \left\{ + \frac{1}{2}(1-\gamma)Ma^2 \right\}^{\gamma/\gamma-1} = \left\{ \frac{T_0}{T} \right\}^{\gamma/\gamma-1}$$

$$u = \sqrt{\gamma R T}$$

Eq. 6.10

which yield critical values at the Mach disk of: pressure 995*psi* (6.85*MPa*); temperature 262*K*; and velocity 407*m/s*. Further, Ouellette & Hill are able to show that the equivalent jet diameter, d_e,- that which maintains the mass flow rate and injected momentum is given by

$$\frac{d_e}{d_0} = \left\{ \frac{P_0}{P_a} \right\}^{1/2}$$

Eq. 6.11

and it is this diameter of 4*mm* with the critical values listed that are specified for the jet inlet in the CFD model.

It is apparent from *Figure 6-6(a)* that although the cylinder pressure can be assumed recovered, the thermodynamic state within the jet is highly nonuniform, which in turn yields itself in large density gradients. Temperatures at the jet origin are similar to those predicted from the Joule-Thomson calculations through ~10-15*K* warmer. This is significant in that the value of 260K at the jet origin when substituted into the Antoine equation, *Eq. 6.9*, gives an acetone vapour pressure of ~4480*Pa*. This is well above the partial pressure of acetone in the jet (2815*Pa*), and supports the experimental indications of no acetone condensate. Of more significance is the insight provided by the density plot. The high flow velocity means that since the pressure is uniform throughout the domain, the fluid density must adjust to match the changes in velocity. This interplay shows the fallibility of equating lower temperatures with higher density and its effects upon acetone number density and fluorescent intensity.
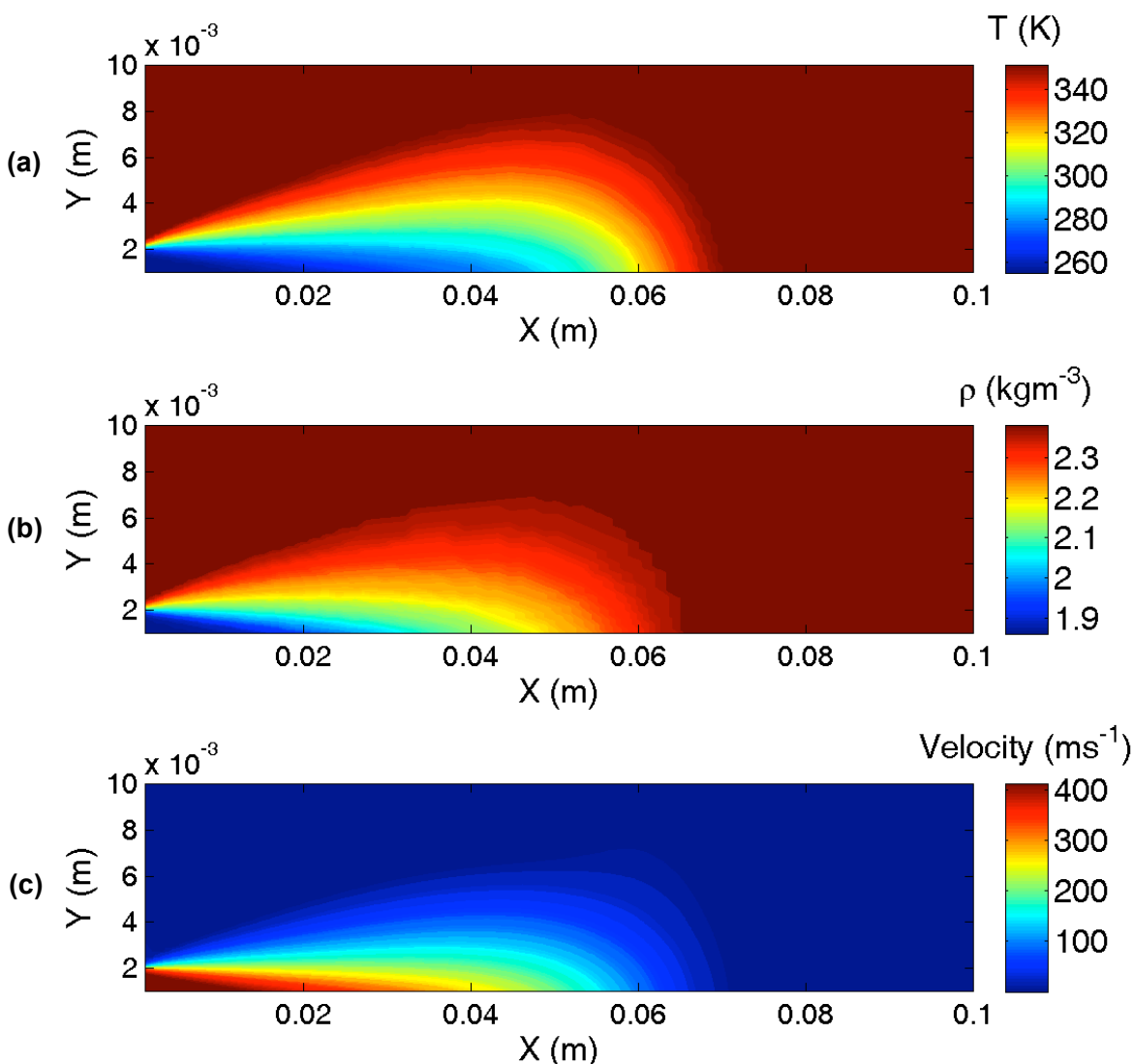
Figure 6-6 CFD Gas Injection Predictions of (a) Temperature, (b) Density and (c) Velocity

6▪5▪5   THE ROLE OF VELOCITY IN HIGH SPEED LIF IMAGES.

The jet velocity ranges from ~400*m/s* at the jet inlet to ~200*m/s* at the RCM cylinder centreline (*z*~0.05*m*), where the PSC would be anticipated to be, and where any LIF image would be of most interest. The image of *Figure 6-2* is comprised of pixels which correspond to 0.25*mm* × 0.25*mm*, and which were exposed for 1000*ns*. It is accepted practice to circumvent the delay and jitter in triggering the laser source by exposing the camera and triggering the laser pulse to fall within the exposure duration (*cf.* experimental timing diagram, *Figure 4-7 p.*67). With an exposure of 1000*ns*, phosphorescence should be effectively shuttered since it has a significantly longer lifetime than fluorescence at 30*μs*-200*μs* for emission from the hot triplet and normal triplet states respectively (*cf. §3▪11▪4*). The laser pulse duration is ~20*ns*, and with rapid activation of the acetone it can be expected that any given molecule within the interrogation volume, defined by the pixel dimensions and the laser sheet thickness, will undergo only a single fluorescent event. Given the almost unity probability with which ISC takes place (fluorescent yield Φ_{fl}~0.0017) it is unlikely that any given molecule will fluoresce return to its ground state, be re-activated and fluoresce again, it will in all likelihood undergo ISC to the triplet manifold and relax from this state.

In the case of the DI jet (and also the PSC jet) the discussion must be framed in terms of the number of molecules which are open to excitation over the course of the laser pulse. The interrogation volume, although stationary in space, does not contain the same gas throughout the laser pulse and camera exposure because of mass transport into and out of the volume. With fluid flow there is the opportunity for more acetone molecules to be transported into the interrogation volume and excited prior to the laser pulse ending. The acetone molecules that were in the volume originally are excited to the singlet state and through ISC go on to populate the triplet manifold. Those left in the single state may fluoresce and be reactivated, however given that the majority (99.83%) of the acetone is still residing in the triplet state any acetone transported into the pixel volume will also undergo excitation, while those that exited the volume are likely to be in the non-fluorescent triplet state and represent no loss in molecules which would contribute to the fluorescent signal. The mass transport is in effect increasing the ground state population from which activation and subsequent fluorescence may take place. There now exists a larger number of excited molecules than were the excited complex to be populated from a ground state population solely comprised of original molecules. These can subsequently fluoresce and have their emissions captured during the (long) 1000*ns* exposure. It is these extra advected acetone molecules which may be ascribed to the stronger signal observed in the DI jet when compared to the calibration case.

6▪5▪5▪1 PIXEL VOLUME MASS EXCHANGE

Mass exchange through entrainment is only part of the consideration. The regions within the jet that demonstrate excessive intensity are towards the core of the jet, away from the shear layer where

entrainment would be most prevalent. The entrainment coefficient varies from 0.024 to 0.118 depending upon the original jet velocity profile, though is often accepted to be 0.057 **[385]**. At this level, over the course of the 20ns pulse, the mass exchange in the pixel volume is negligible and the can certainly be assumed frozen on the basis of entrainment velocity. Making an assessment based on entrainment further misses the role of mixing in image calibrations, since it need not be ambient gas that is brought into the pixel-volume to increase the signal it need merely be *any* ground-state acetone doped gas that was not originally present.

In this way it is important to now consider the role played by the large coherent structures in the jet and the associated energy cascade. The energy held by the jet has a distribution similar to that shown in *Figure 6-7*, with eddy lengthscales ranging in size from the jet width ($\mathscr{L}$) to the Kolomogorov lengthscale, η. Of most concern are the eddies associated with inertial subrange.
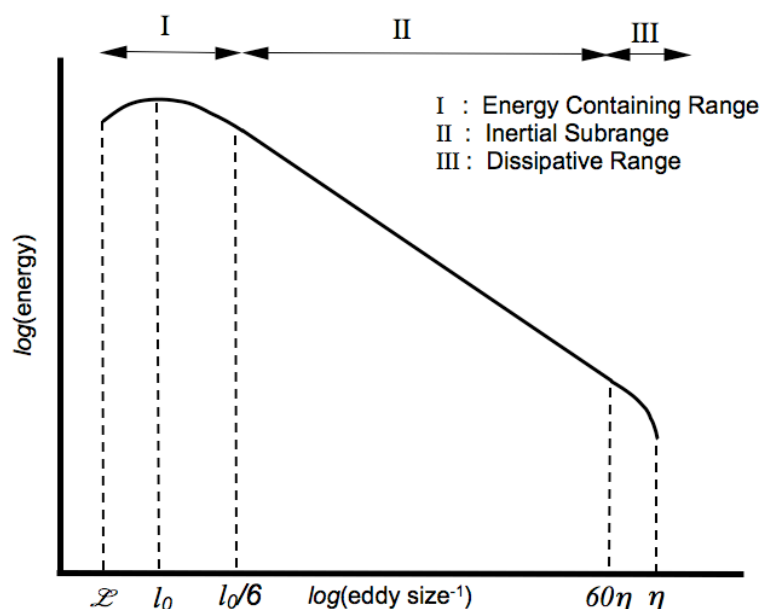
Figure 6-7 The Turbulent Energy Cascade

The increase in signal intensity over the calibration case can be attributed not to mixing *per se*, but the transport of fuel (acetone) into the pixel-volume, necessitating consideration of the local flow. The eddies associated with the dissipative range, and the Kolomogorov lengthscale, are wholly within the pixel volume and cannot be responsible for transport into the pixel; yet the lower lengthscale of the inertial subrange is defined with respect to the Kolomogorov lengthscale. Given that the jet Reynold's number is independent of downstream location it is appropriate to scale the flow against this and in doing so Pope **[386]** is able to show that:

$$\frac{\eta}{l_0} = \text{Re}^{-3/4}$$

$$\frac{u_\eta}{u_0} = \text{Re}^{-1/4}$$

<div align="right">**Eq. 6.15**</div>

$$\frac{\tau_\eta}{\tau_0} = \text{Re}^{-1/2}$$

where $\tau_0 = \dfrac{l_0}{u_0}$ and l_0 is of the order $\mathscr{L}$. For the DI jet the characteristic large eddy timescale is ~$20\mu s$, and

with the exposure of *Figure 6-2* set to 1000*ns* the eddy rotation is deemed too slow to significantly affect transport into the pixel. With the majority of the turbulent kinetic energy held in the large structures and with energy destruction only on the Kolomogorov scale and below, the inertial subrange, which is responsible for the transfer of energy through vortex straining and the conservation of angular momentum **[387]**, is responsible for the mass transport into the pixel-volume. The inertial subrange extends from ~$l_0/6$ at the energy/inertial subrange interface (l_{EI}) to ~60η at the inertial/dissipative interface (l_{DI}) **[386]**. At these limits the characteristic lengthscales are approximately l_{DI}~0.024*mm* and l_{EI}~2*mm*, precisely the range over which transport into the pixel-volume is of concern. Using a scaling based on length [*m*] and dissipation rate [m^2/s^3] Pope deduces that

$$u(l) \sim u_0 \left(l/l_0 \right)^{1/3}$$

<div align="right">**Eq. 6.16**</div>

$$\tau(l) \sim \tau_0 \left(l/l_0 \right)^{2/3}$$

which, with substitution of l_{DI} and l_{EI} for *l*, yields velocities from 55-220*m/s* and timescales of 395-9000*ns* in the inertial subrange. With interrogation volume dimensions of *0.25 × 0.25 × 0.8 mm* the eddy sizes of concern are those with about twice the face dimension (0.25*mm*) or of the laser sheet thickness (1*mm*). These dimensions represent flow velocities in the range ~150-200*m/s* with timescales of ~3000-5000*ns*. As with the entrainment velocity, over the 20*ns* pulse of the laser, the velocities and timescales alone are not able to account for the increase in LIF intensity alone.

The out of calibration problem may be circumvented to a large extent by reducing the iCCD exposure duration, and this was used subsequently for all data collection in this study. The laser trigger delay was established by finding the threshold at which a LIF signal was captured. With this established (to be 980*ns*), and accepting that the jitter in the laser pulse is 10*ns* the minimum camera exposure was set to 40*ns*. This allowed the full laser pulse to be captured even at the maximum extents of the laser jitter. By reducing the camera exposure the extent to which 'fresh' acetone was entrained into the interrogation volume was not reduced, but the likelihood of capturing its fluorescent light was.

<div align="center">110</div>

6▪6 CONCLUSIONS

Having made corrections for experimental errors, and having discounted seed condensation as the source of the observed calibration errors, there are two distinct aspects at work in attempting to make quantitative concentration measurements by comparison to a calibration image. The first is that the thermodynamic state cannot be equated in the jet and calibration cases, and secondly that there is significant motion in the jet case that is not present in the calibration image. When the camera shutter speed is reduced to its experimental minimum, the jet images fall within the range of the calibration curve. This would suggest that although the thermodynamic uncertainty is still present it is within the experimental error, and that although the mass exchange and mixing arguments presented do not offer a complete explanation of gas motion is the predominant cause of the calibration difficulties. All existing work on high speed flows **[158, 161, 163]** use laser systems that allow much smaller interrogation volumes to be formed (typically about $50 \times 50 \times 200 \mu m$), so limiting the extent to which mixing needs to be considered. Furthermore, the studies do not seek concentration measurements, they are designed for the most part to offer qualitative structural information **[158, 161, 163]**, the remainder providing temperature field **[165]** or velocity insights **[388]**.

Chapter 7 PARTIALLY STRATIFIED CHARGE, DIRECT INJECTION & INSERT FUEL JETS

7▪1 INTRODUCTION

Chapter 7 is concerned with the initial findings of the central composite test matrix. Using the example of the fuel concentration fluctuations, the shortcomings of the RCM optical set-up in imaging the full RCM bore are presented. The inability to completely correct for background noise and scattered light interference is discussed but, despite the shortcomings, some basic observations about the interaction of the PSC and DI jets are made. With the limitations identified the chapter goes on to discuss the results of the LIF images obtained for a capillary injected PSC jet into air and an insert generated jet into background charges of RAFR 1.5-2. The behaviour of these injections, without the presence of a DI fuel jet are used to form the baseline from which comparisons in behaviour will be made in the *Chapter 8*.

7▪2 DATA PRESENTATION

As is often the case with visualisation studies, there is a significant challenge in presenting the data from across the full range of the CCD test matrix. The LIF images are presented according to the schematic shown in *Figure 7-1*, with laser illumination from the right-hand edge of the image.
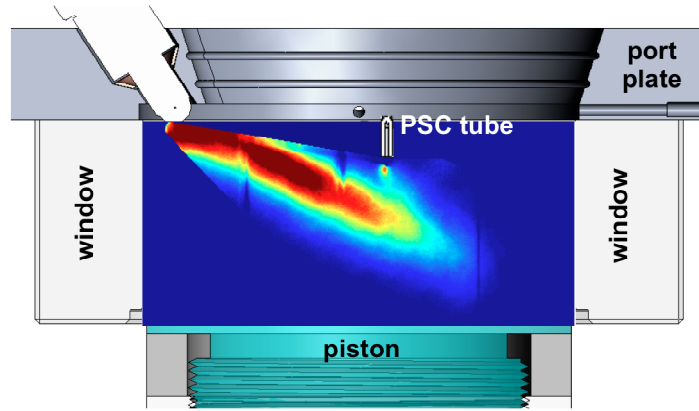
Figure 7-1 Data Visualisation Schematic

Unless otherwise noted the data displayed is from the central composite test matrix described in *§4▪8* where each data point corresponds to 51 realisations, except for the central condition that had three repeats totalling 153 realisations. In some circumstances data will be presented from the central region of the image only. In the images from the insert study the insert sits flush with the firedeck and is not evident in the images. In the case of the capillary injections an image mask has been applied to mask the images where the laser sheet was obscured by the capillary or where the capillary was located. The cylinder centreline is located at 50*mm* in the full bore images and at 0*mm* in the central detail images.

7▪3 INEFFECTUAL BACKGROUND CORRECTION

Background light correction adjusts an image for light that originates from inelastically scattered laser light. The correction is made by collecting 51 images of the RCM cylinder filled only with air. Following correction for optical distortion and camera CCD variation the images are arithmetically averaged to yield a mean image such as the one shown in *Figure 7-2*.
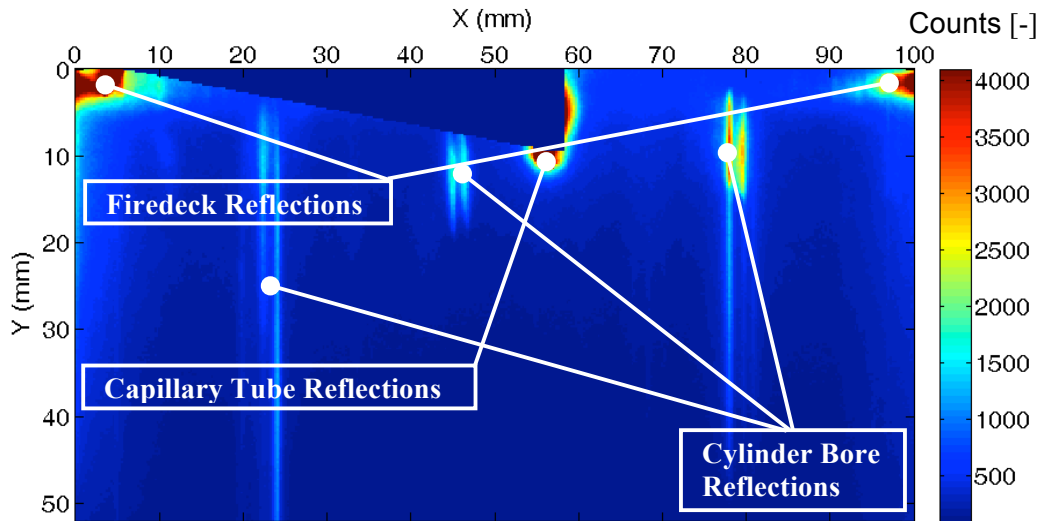
Figure 7-2 Background Correction Image

The high count along the top edge of the image is the reflection from the RCM fire-deck, while those near the centre are from the laser-sheet impinging on the PSC capillary tube. The vertical streaks are reflections from the internal bore of the quartz window. The common mindset within the laser diagnostics community is that subtraction of this image from subsequent images will provide an image that is devoid of scatted light and background interference. Application of this procedure to *Figure 7-3* yields *Figure 7-4*, from which it is evident that the background correction is failing to completely remove background interference. This happens because the DI jet produces fluorescent light that enhances the reflections of *Figure 7-2*. In this way, the elastically scattered light will always have more spatial variability and higher levels than the background image can correct for.
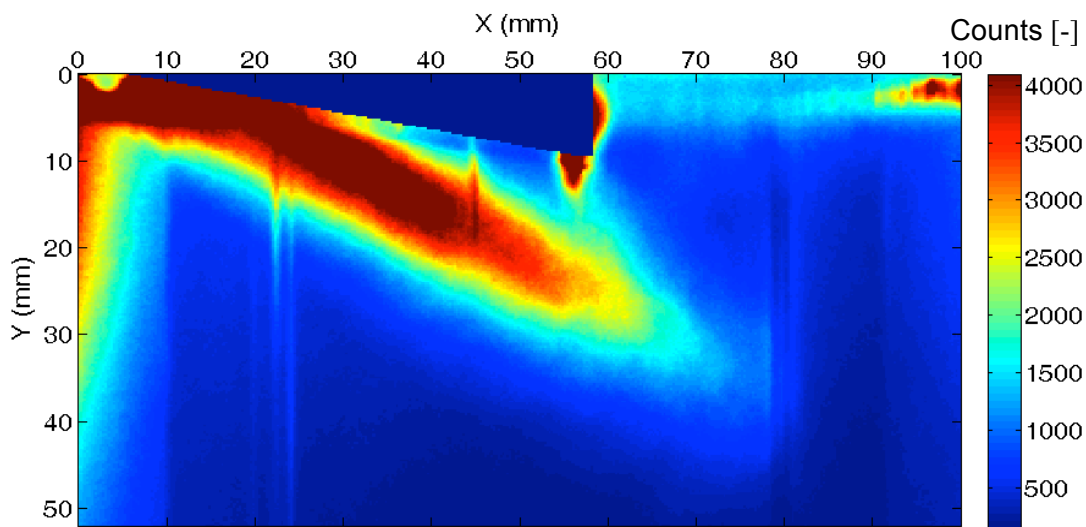
Figure 7-3 Raw LIF Image
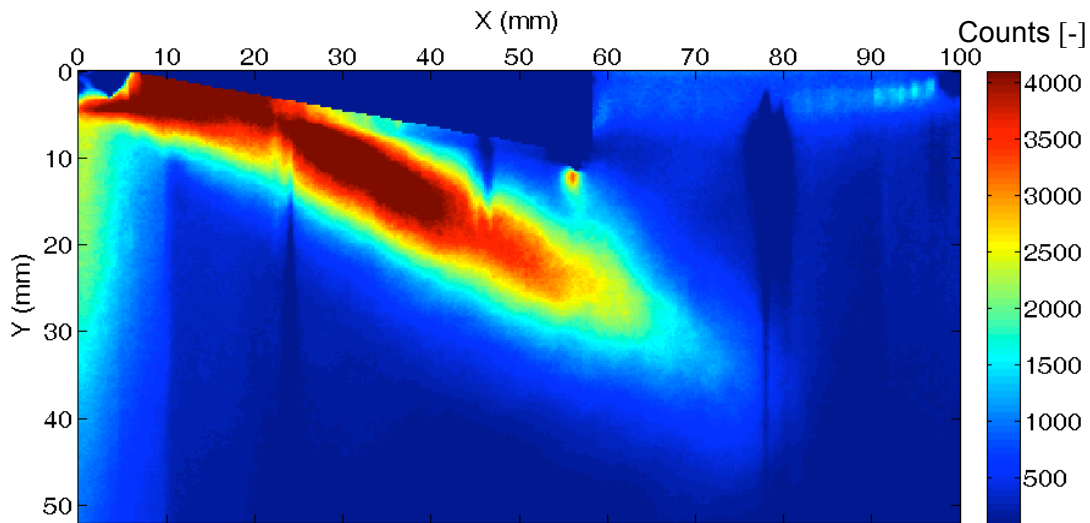
Figure 7-4 Ineffectual Background Corrected Image

7▪3▪1   ROLLING BALL SMOOTHING

In optical investigations of liquid fuel sprays, it is common practice to use a rolling ball smoothing technique to smooth the image backgrounds, a technique itself borrowed from biomedical research and diagnosis. The technique involves the application of an image 'erosion' (removal of high count pixels) followed by a dilation (smoothing) to remove the background interference. The erosion is applied by specifying a 'structuring element' which is a local mask describing how the image pixels are to be altered within the mask. The processing attempted in the current study used a ball element, an element which is circular in the *xy* plane and which maps the pixel values within its radius to the surface of the ball. The element is traversed across the image (hence the term rolling ball) in both the *x* and *y* directions and any pixel counts which fall outside the 'radius' of the ball are brought down to the value of the ball radius. This is more readily seen in *Figure 7-5* where the ball structuring element will accurately follow the larger features of the image but 'erode' the sharp peak. The dilation process involves ascribing the same value to all the pixels within the structuring element, based on a number of possible rules. In doing this the pixel counts are spatially smoothed to reduce image gradients.
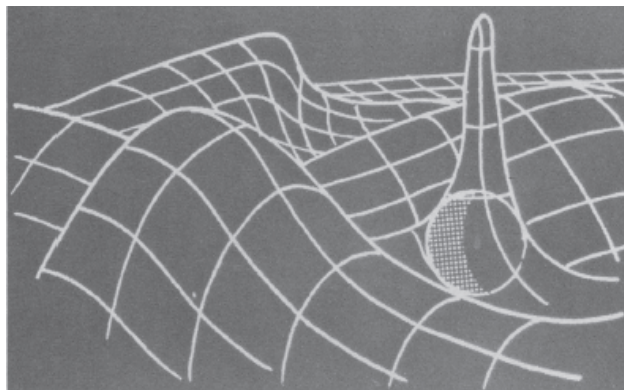
**Figure 7-5 Rolling Ball Erosion,
reproduced from [389]**

115

These techniques, although very powerful, could not provide any significant improvement in the image quality for the current work. This may be attributed to the fact that the noise often changes gradually, limiting the effectiveness of the erosion. Of greater concern is the effect of the rolling ball upon the structure and gradients at the jet boundary- the very aspects of the jet structure that this study is concerned with. Application of the rolling ball to the jet would destroy the structures under investigation and as such an image mask would need to be applied so that different processing procedures could be applied to different parts of the image. The difficulty in doing this is identifying the pixel threshold value at which the edge of the jet is found and the background begins. This is further complicated by the occurrence of the threshold values in the background noise facets. No acceptable method was found to circumvent these interference concerns. As a result, the region of interest was reduced so that, for the most part, LIF images were collected from the portion of the cylinder not affected by background interference. This also afforded a higher spatial resolution that provided better structural clarity and helped to reduce the adverse affects of pixel mass exchange addressed in *Chapter 6*.

7▪4 PARTIAL STRATIFICATION WITH DIRECT INJECTION- FULL BORE IMAGING

7▪4▪1 CALIBRATION

The investigations into the SNR effects of different on-chip binning approaches (*§5▪10*) gave the two calibration lines of *Figure 7-6* and were constructed using an approach identical to that outlined in *§5▪9*. It is apparent that a 4×4 bin provides a stronger signal and offers a more favourable SNR. To increase image signal strength a 4×4 bin was used in all studies despite the loss in spatial resolution.
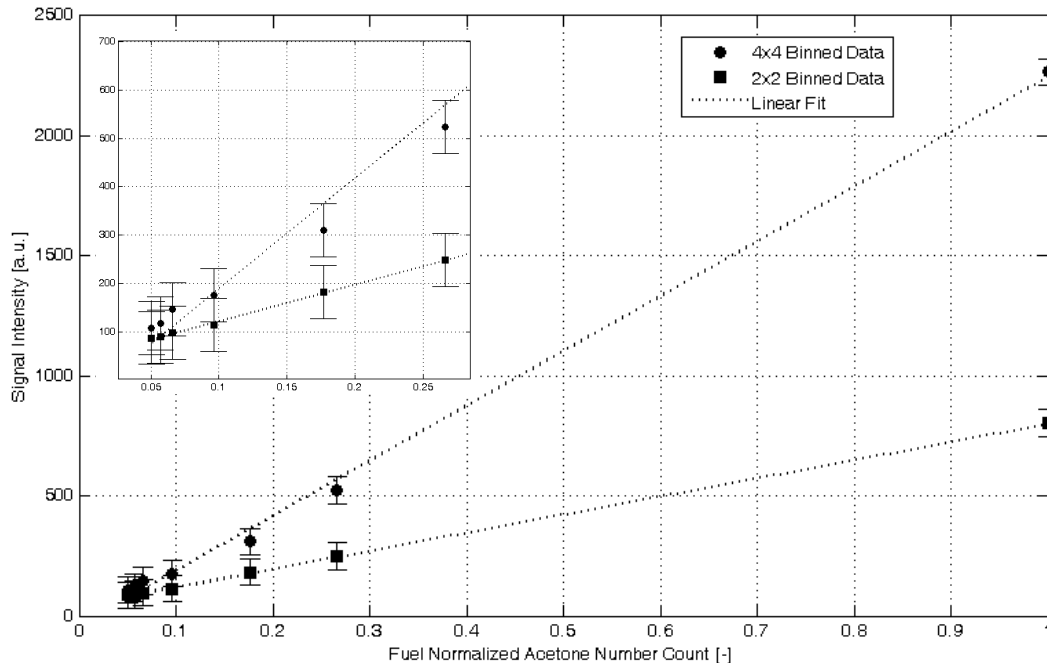
Figure 7-6 4×4 and 2×2 On-Chip Binning Calibration Lines, Inset Detail for Low Signal Intensity

The 4×4 calibration line takes the form of *Eq7.1*

$$S_f = 2217\left(\frac{N_{fuel}}{N_{total}}\right) + 56$$

<div align="right">**Eq. 7.1**</div>

where N_{fuel}/N_{total} is the normalised fuel number count and S_f the signal intensity. The inset in *Figure 7-6* shows that the calibration may be less accurate at lower concentrations, though is still within the experimental error and appears as a '*y*-intercept' of ~56, not the camera noise floor of 87.

7▪4▪2   CONCENTRATION FLUCTUATIONS

The ability to conduct detailed analysis in the region of the DI-PSC interaction is limited because of the poor spatial resolution that results form a 4×4 on-chip bin (pixel dimension 0.5×0.5mm), while inference of the overall structure of the jet and its effects upon the cylinder charge are limited by background interference. The most informative images to consider are those of the normalized root mean square fluctuations in RAFR. Detailed methane fuel jet structures are reported by Bruneaux **[390]**, as are the r.m.s fluctuations. The images of *Figure 7-7* show, for the most part, the PSC jet interacting with the bulk of the head vortex or its trailing edge. The late DI injection (*Figure 7-7 t = -5CAD*) shows that the PSC jet is not catching the head vortex along its leading edge but about 8*mm* after it.
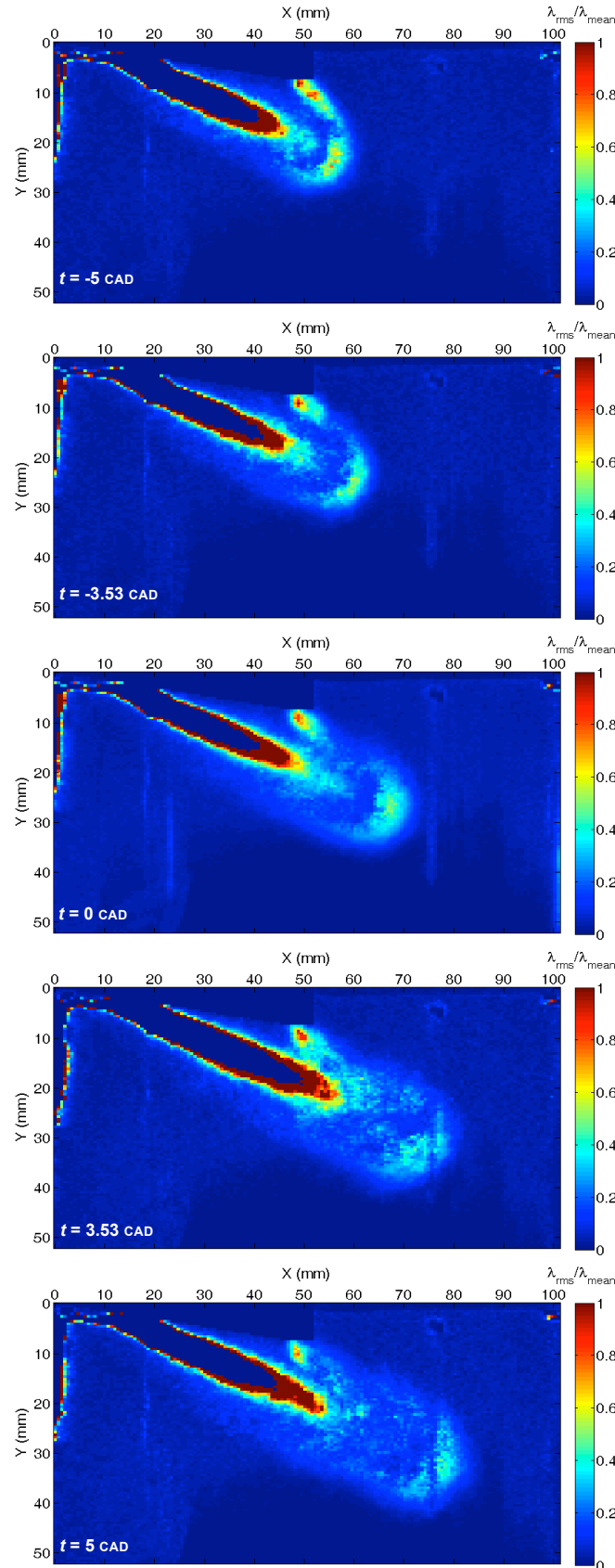
Figure 7-7 Normalized r.m.s Fluctuations in RAFR for Direct Injection with PSC at Relative Time Indicated

The jet shows fluctuations in RAFR that are very similar in position and magnitude to those reported by Bruneaux **[390]**. The leading edge of the vortex ball shows fluctuations on the same scale as the concentration value. The fluctuations around the core of the DI jet are larger than reported by Bruneaux but less significant to the current work, since the DI-PSC interaction is primarily driven by the shear layer at the boundary of the jets. The inner core of the DI jet shows fluctuation levels of almost zero. This contradicts previous works (*cf. §2▪2▪1*) which report normalised concentration r.m.s. levels on the jet centreline of about 20%. The current zero levels point to the calibration difficulties discussed in *Chapter 6*. The thermodynamic state of the jet and potential mixing can produce LIF intensities higher than that allowed by the calibration line of *Figure 7-6*. In these cases the calibration procedure artificially brings the count down to the maximum allowable, that corresponding to pure fuel. This process removes the ability to assess the fluctuations in the jet core and may contribute to the high fluctuation levels seen around the invariant core.

The interdiction of the PSC jet along the top edge of the DI jet perturbs the DI jet along this edge. The PSC injection itself is seen to have normalised r.m.s fluctuations in RAFR in the range 0.8-1.0 in all cases but there are differences in how the fluctuations are manifested in the DI jet shear layer. At the latest timing (t = -5 *CAD*) the PSC injection is seen to increase the fluctuations along the top edge of the DI jet, almost extending to the location on the leading edge where there are significant r.m.s. fluctuations. These fluctuations may be attributed to the increased velocity at the edge of the vortex ball as fluid circulates back (*cf.* schematic of jet structure *Figure 2-1, p.*10), entraining the capillary delivered fuel. Earlier injections, at t = -3.52 & 0 *CAD* shows the capillary delivered fuel causing little perceptible difference in RAFR fluctuations from those which may be expected in the DI jet alone. These timings coincide with the trailing edge of the vortex ball, at which point the flow velocities are more closely aligned with the PSC injection axis and as a result cause less shear and lower observed fluctuations, although some shearing would still be expected. As the DI injection timing is advanced still further (t = 3.52 *CAD*) and the PSC delivered fuel intersects the DI jet at the interface of the head vortex and the trailing jet, the flow once more starts to shear the PSC jet, increasing the observed normalized RAFR fluctuations to ~0.6-0.7. At this location the PSC injected fuel is serving to increase the local entrainment into the jet and then into the vortex ball since it is known that the vortex ball is fed from the trailing jet, although to what extent is still unclear because of the entrainment implied by the fluctuations on the leading edge. It is apparent that, as the DI jet develops, the level of normalized RAFR fluctuation decreases, though without reference to the absolute levels, it is not apparent to what extent leading edge entrainment is diminishing. This is not the focus of the current work and comparison becomes difficult because of the background noise facet that cuts through the leading edge of the jet for the earliest two timings. In the earliest timing, where the PSC jet intersects the 'steady state' portion of the DI jet (according to Turner's model, *§2▪2▪1*), the fluctuations

in normalised RAFR are shown to drop once more as shearing of the PSC jet is now derived from the jet velocity alone with no role played by the vortex ball. The nature of the perturbations generated by the PSC jet is likely governed by the local flow pattern at the location of the PSC-DI interaction, the details of which would have to be sought from laser velocimetry techniques such as PIV of LDV.

7▪5 PARTIAL STRATIFICATION WITH CAPILLARY TUBE INJECTION

7▪5▪1 AIR FUEL RATIO

The images of *Figure 7-8* show the PSC jet generated by fuel injection from a capillary into the RCM chamber when filled with air. The timings are comparable to those used in the central composite test matrix. The RAFR images are generated from the calibration line of *Figure 7-6* with 4×4 on-chip binning and have pixel dimensions that correspond to $0.0625 \times 0.0625mm$. The capillary exit is located at ~$0.5mm$ from the image (cylinder) centreline and ~$2.5mm$ off the firedeck (image top edge). The high count levels to the right of the image mask and the 'spike' on the bottom right corner of the mask are attributable to light scattered from the PSC capillary and cylinder bore. These facets cannot be fully corrected for.

The most notable feature from the set of images in *Figure 7-8* is that the jet appears to have parallel edges and shows little sign of increasing width with downstream position. This would imply little entrainment and mixing. For the latter three timings, the thickness of the layer containing a fuel concentration gradient is almost constant and on the order of $0.25mm$ thick. In all cases it is apparent that the fuel undergoes most mixing along the leading edge of the jet and is starting to generate a stoichiometric mixture at about $7mm$ from the firedeck. The fuel-rich core of the impulsively started jet persists for longer than may be expected and may point to plug flow which could also explain the slow growth in jet width. The colour-scale appended to the image is also likely to be masking some of the jet structure. The background air charge should be displayed with an infinite RAFR but for image presentation an upper limit of 2.5 was imposed so that the jet structure could be presented, though this is likely to be obscuring the leaner portions of the jet. This difficulty can, to a certain extent, be circumvented by representing mixture concentration by mixture fraction which, by definition, covers the range zero to one. However, with this approach, a lot of the detail pertinent to combustible mixtures is compressed into a small range of values and when interpreting data relevant to engines, air-fuel ratio or equivalence ratio are more widely understood and interpreted. Data presentation will be made using the measure that best supports the argument being made.
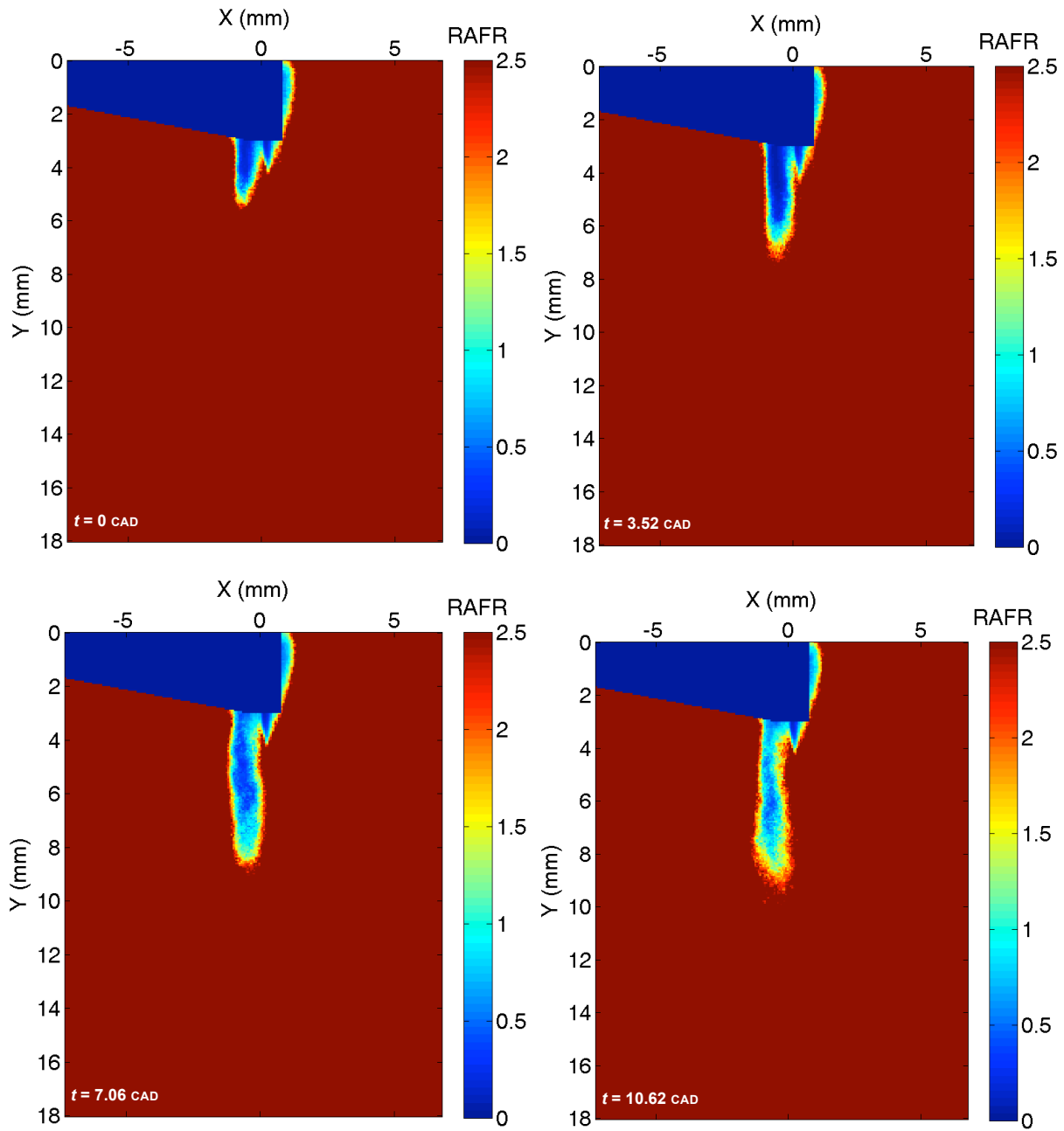
Figure 7-8 RAFR for PSC Jet from Capillary Tube at Times Indicated

It has been demonstrated that signal strength is proportional to fuel concentration and, in considering the signal intensity insight to the PSC jet concentration structure is obtained. *Figure 7-9* shows, for the four times indicated, the fluorescent signal intensity from the centreline of the PSC jet against the axial position from the fire deck. The profiles are not those which may be expected for an impulsively started jet or the initial transient stages of an injection.
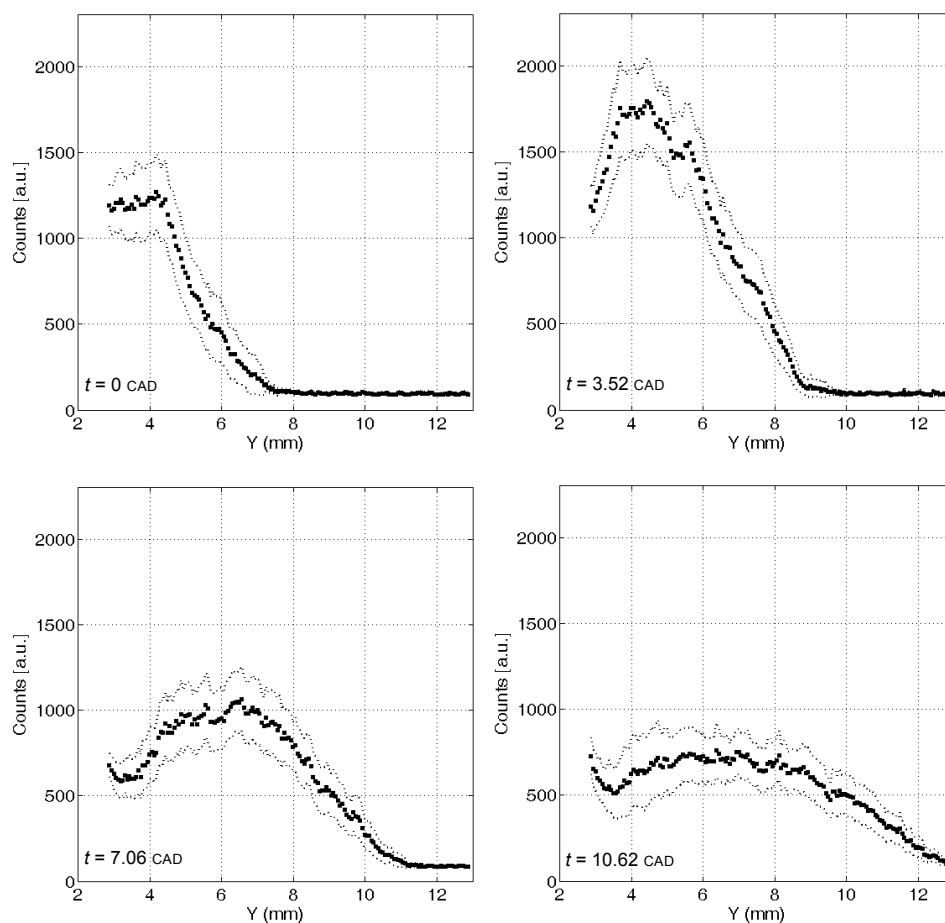
Figure 7-9 PSC Capillary Injected Jet Centreline Count Levels (Broken Lines Indicate 95% Confidence)

The intensity (concentration) decay with axial position is not as described by previous authors (*cf.* *§2▪2▪1*). The profile at *t*=0 *CAD* shows a decay which is similar to that expected form *Eq. 2.3* or *Eq. 2.4* from ~3.5*mm* onwards, yet upstream of this location there is an almost constant count level. The count is not that which corresponds to pure fuel and may be lower due to the bulk air charge being forced into the PSC capillary as the piston compresses the cylinder charge prior to injection. At *t*=3.52 *CAD* the count is seen to increase dramatically downstream of the PSC capillary exit before starting to decay, a decay that appears to be almost linear and not the expected hyperbola. The feature could also result from inaccurate background light correction. This structure persist as the flow penetrates further, although the maximum count level decreases and the profile broadens. These observations may be attributed to two different causes. The first is that the flow from the PSC capillary may be that of a plug. Ahead of the plug is gas that was forced into the capillary prior to injection and has undergone some mixing with the fuel already in the capillary to produce the mixture of the concentration observed in the first timing. As the plug, which was upstream of the mixed gas and which has a higher fuel concentration, emerges from the capillary exit it starts to mix with the cylinder air charge. As the plug continues to travel into the cylinder it mixes further such that its concentration reduces, since it is not 'fed' from behind with fuel to maintain high concentrations. The observed intensity variation may also be explained by the variability of the injection

events. The solenoid used to control the PSC injection is known to be variable in its response time and its opening profile. These two factors will deliver jets of different structures and at different times. This is especially true of the early stages of the transient before differences in jet structure have been lessened by mixing.

The penetration behaviour of transient jets has been described by Hill & Ouellette **[8]**, and comparison with their results can provide further insight. Hill & Ouellette provide scaling arguments which show the jet penetration, Z_t, to be proportional to the momentum injected and time elapsed, with the constant of proportionality, Γ, termed the penetration constant and equal to the pure constant 3.0±0.1 **[8]**, *viz.*:

$$Z_t = \Gamma \left(\frac{\dot{M}_0}{\rho_a} \right)^{1/4} t^{1/2}$$

Eq. 7.2

It is apparent from *Eq. 7.2* that a plot of $Z_t \Big/ \left(\frac{\dot{M}_0}{\rho_a} \right)^{1/4}$ *vs.* $t^{1/2}$ will yield the jet penetration constant. Based upon the penetration values from *Figure 7-9* (*i.e.* the location at which the intensity drops to background) and the approach of Ouellette & Hill **[384]** to calculate the momentum injection rate, the jet penetration constant was evaluated to be 3.87. Although the linear fit has a regression coefficient of 0.9212, the data may still not be linear. The evaluated penetration constant is close to Hill & Ouellette's value and may suggest jet-like behaviour. However, a lack of literature on emergent plugs does not allow comparison of characteristic features like spread rate, concentration profile and penetration.
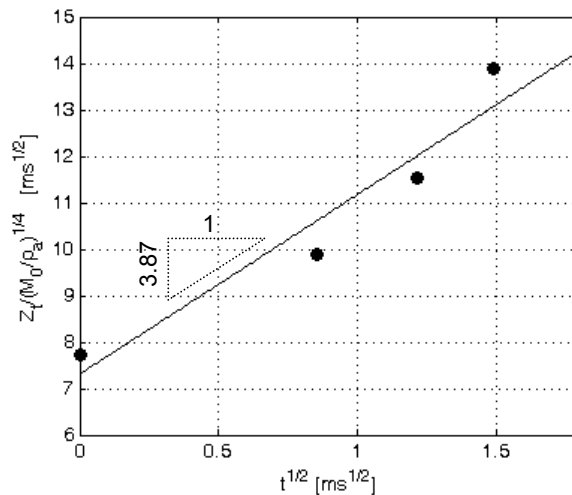
Figure 7-10 Capillary Injected PSC Jet Penetration; (•) PSC Data (-) Least Squares Fit

There is insufficient data in the current study to truly establish which of the two effects suggested is causing the discrepancy from accepted jet structure or if it is a combination of the two. The arguments

supporting the repeatability influences are built upon further through consideration of the jet concentration fluctuations.

7▪5▪2   CONCENTRATION FLUCTUATIONS

When considering the interaction of the PSC with the DI jet the levels of concentration fluctuation will be important and, as such, a baseline is presented here for the capillary injected PSC jet. The concentration fluctuations extend to about 7*mm* from the firedeck at *t=0 CAD*. This is about 2*mm* further into the chamber than the concentration image of *Figure 7-8* at *t=0 CAD* would suggest and points to the variability not in the jet itself but in the ability of the solenoid to trigger the jet repeatabley. The jet displays fluctuations which are not wholly consistent with those seen for the DI jet in *§7▪4* or those reported elsewhere **[390]**. At time *t=3.52 CAD* a fluctuating 'core' and large fluctuations on the leading edge of the jet can be seen, as would be expected from the work of **[390]**. However, in the two earliest cases, the area over which the fluctuations extend is not confined to the jet leading edge because of the variability in jet penetration for a set injection time. At the later timings (*t=7.06 CAD* & 10.62 *CAD*), the fluctuations appear to have a spatial distribution much more akin to those of the concentration field.

This is, again, likely due to the inability of the PSC solenoid to deliver a repeatable jet and the subsequent spatial variations for each realisation over-riding any jet structures. There is in both latter cases a slight suggestion of an invariant core with normalised RAFR r.m.s levels of about 0.25 lower than the region surrounding it, though to assess this in detail would require further investigation.

The observed fluctuation structure would not support the plug flow argument presented earlier, since it would not be expected that the plug show concentration fluctuations increases towards its centre; the fluctuations should be confined to the shear layer around the boundary of the plug **[391]**. These concerns, and those raised in *§7▪5▪1*, cannot be fully explained, though for the current study provide limited impediment since it is the interaction of the PSC jet, whatever form it may take, with the DI jet that is of concern, not the jet structure itself.
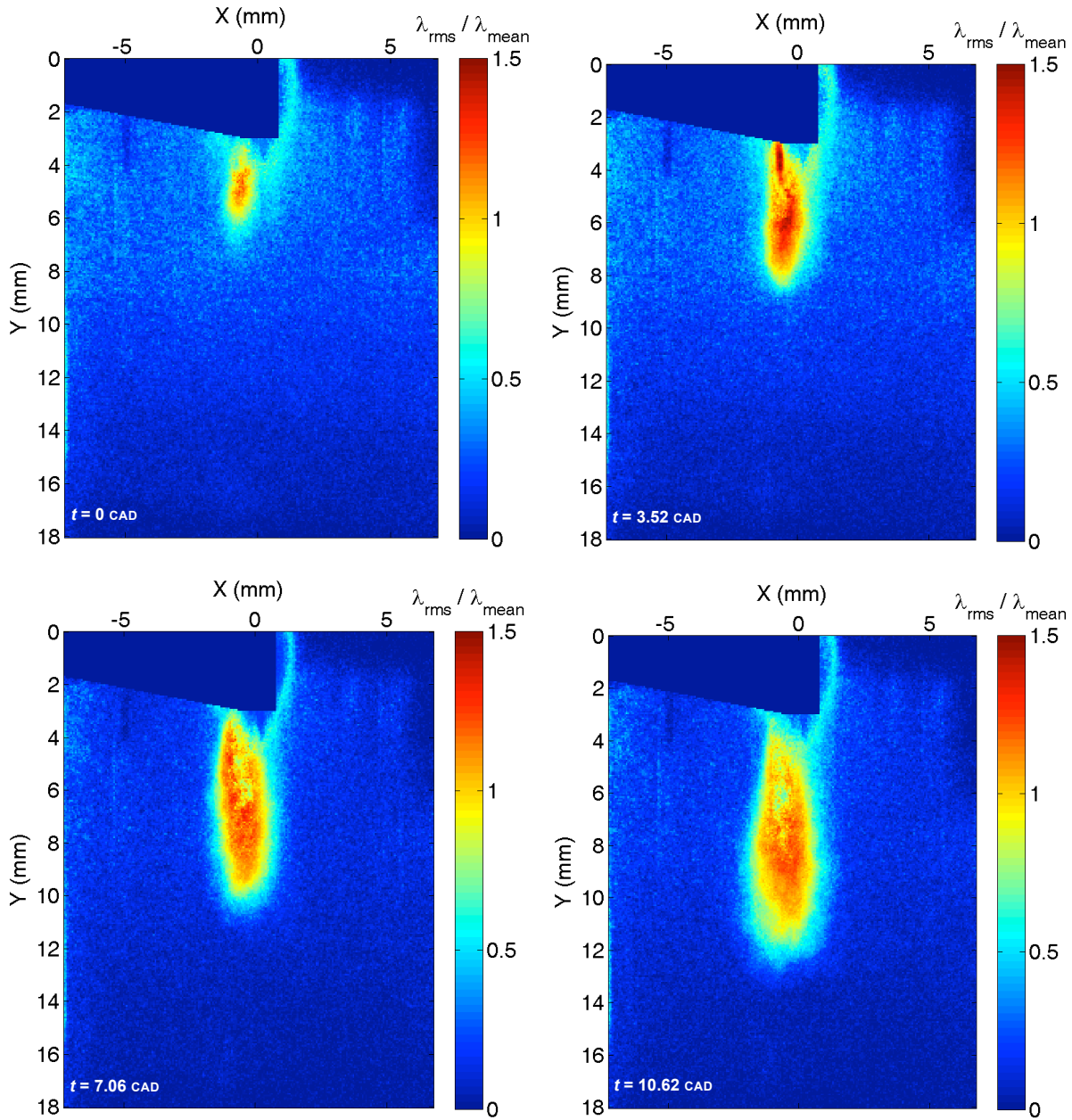
Figure 7-11 Normalized r.m.s Fluctuations in RAFR for Capillary Injected PSC at Times Indicated

7▪5▪3   CONCENTRATION GRADIENTS

It has been posited in previous work on the combination of PSC with DI that excessive fuel gradients limit the ability of the PSC charge to ignite **[7]**. The PSC fuel concentration gradients (as *RAFR/mm*) generated from a capillary injection are displayed in *Figure 7-12*. The images show that with increased time the concentration gradients reduce by ~50% (from *t*=3.52 *CAD* to *t*=10.62 *CAD*) since there is increased time for mixing to dilute the injected fuel; however, the reduction in the observed gradients from *t*=3.52 *CAD* to *t*=10.62 *CAD* appears excessive. The electrodes to ignite the PSC charge can be expected to be on the cylinder centreline, about *4mm* from the firedeck and at this location the concentration gradients are in the range 1-3 *λ/mm* depending upon the spark timing. This indicates the necessity to accurately control the

location of the spark within the PSC jet if the mixture is to be within the fuel flammability limits but also the need to ensure that jet delivery is repeatable.

To circumvent the extent to which these spatial constraints must be imposed, a PSC 'insert' has been designed to increase the mixing between the PSC jet and the cylinder charge. The jet produced by the insert is the focus of *§7▪6*.
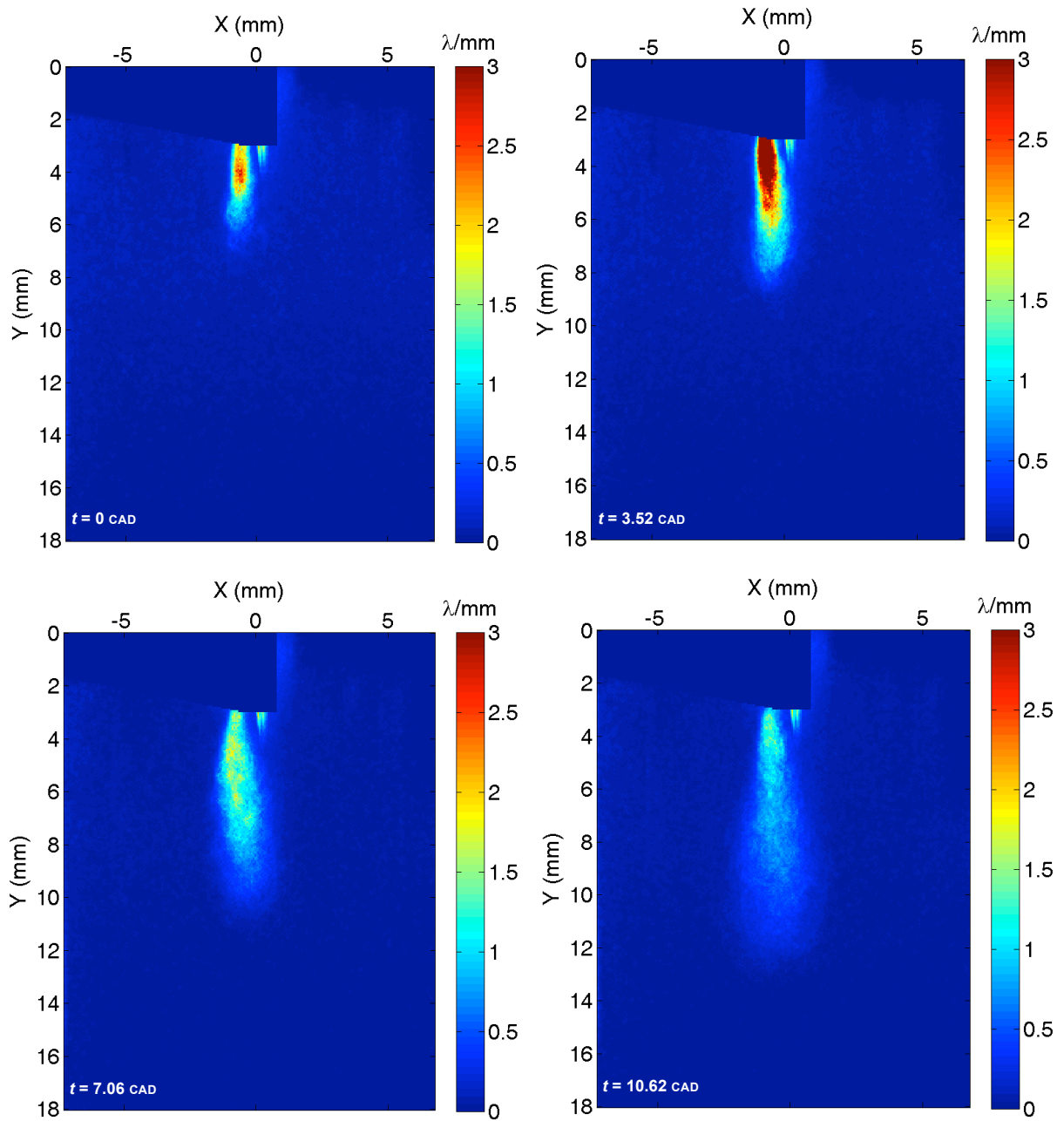
Figure 7-12 Spatial Fuel Gradients for Capillary Injected PSC at Times Indicated

7▪6 PARTIAL STRATIFICATION WITH SPARK PLUG INSERT INJECTION

7▪6▪1   JET DEVELOPMENT
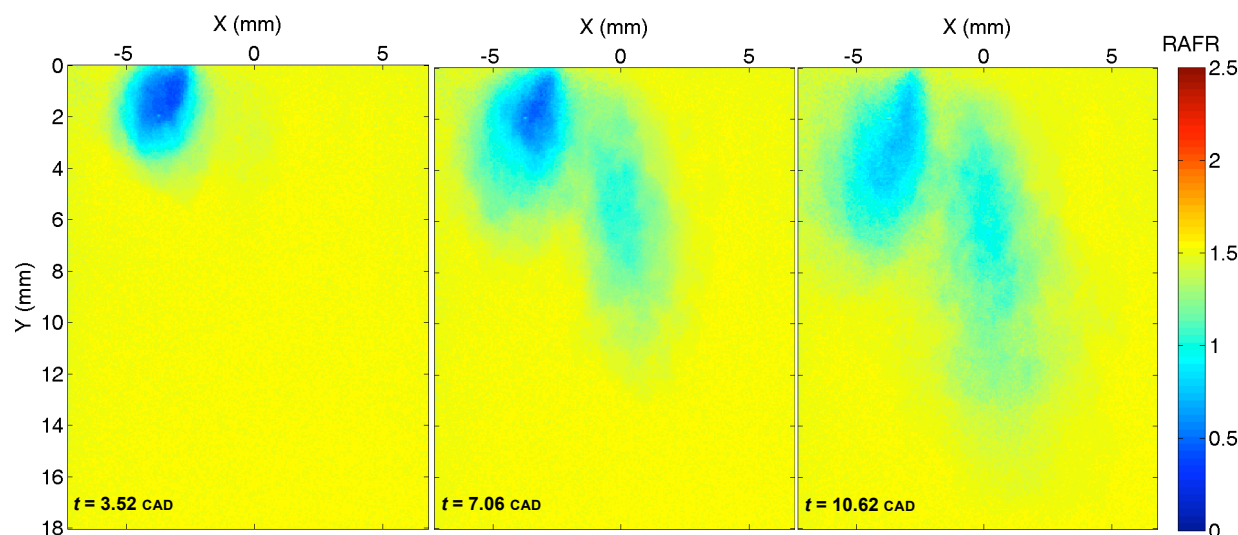
Figure 7-13 Jet Development for Insert Injected PSC at Times Indicated

The images of *Figure 7-13* point to some design limitations of the PSC insert. The insert is located by a thread and as such the angular orientation of the insert is not controlled. The insert is tightened to ensure a gas-tight seal and to align the face of the insert with the RCM firedeck. With these two constraints there is no way to ensure that one of the eight gas flow paths aligns with the cylinder centre-line and laser sheet. The images of *Figure 7-13* show one gas jet to enter the laser sheet at about -3*mm* and a second on the cylinder centreline (not apparent at *t*=3.52 CAD).

It is immediately apparent that the concentration field is not that of a single jet or the multiple jets that the insert would be expected to produce; the fuel concentration profile is much wider than for a jet. For any given axial location the jet width is larger than would be expected from the spread rates reported in the literature (*cf §.2▪2▪1*). To a certain extent this is to be expected since the individual jets formed by the insert mix prior to entering the cylinder and, as such, there exists the potential for any of the jets to undergo entrainment from other jets or the small volume that forms the 'chamber' of the insert. Considering only the jet with origin at -3*mm*, it can be seen that as time increases the fuel concentration reduces and the width takes on a form which is closer to that expected of a jet. These observations point to the likelihood of the jet transecting the laser sheet at an angle rather than passing along the sheet (as is the case with the capillary injected PSC). At *t*=3.52 CAD the structure may correspond to that of the vortex ball at the head of the jet and as the ball passes a structure more like that of a steady jet is observed. This hypothesis is not without contradiction from the images however. The drop in fuel concentration would not be explained were it solely the passing vortex ball and the subsequent jet that were being visualised.

127

For similar reasons to those presented for the capillary injected PSC it is possible that some type of plug flow is present or, given the mixing generated by the insert, some combination of plug and jet flow. Furthermore, the injection for the insert is controlled by the same solenoid as the capillary injections and the same concerns about the injection repeatability persist.

The images of *Figure 7-13* also demonstrate a number of other features that are of concern to the insert design and its efficacy. The second jet, which is apparent on the centreline, at no stage shows an origin on the cylinder firedeck (image top edge), nor does it appear in the earliest timing (t=3.52 CAD) and yet it shows greater penetration than the jet at -3*mm* for the latter two timings. The lack of contact with the firedeck and larger penetration suggest that the jet is coming from further out of plane than the jet at -3*mm* and as a result has undergone more mixing to bring its fuel concentrations down from the higher levels observed in the jet at -3*mm*. However, the jet clearly demonstrates the large spatial extent to which a stoichiometric (or close to) mixture has been developed when compared to the spatially limited jet from the capillary injection. There is a clear spatial distinction between the two jets and this is preserved downstream. This suggests that the desired mixing and coalescence of the individual jets from the PSC insert is not taking place and the orientation of the holes in the insert needs further design consideration.

Of further import is the lack of evidence of a jet to mirror that at -3*mm*. There is no jet seen at any location on the right-hand side of the image, even as far downstream as 18*mm*. Investigation of the insert's alignment with the laser sheet and firedeck showed the capillary that delivers fuel to the toroidal annulus which supplies the individual injection points (*cf. Figure 4-4*, *p.*64), was closest to the jet at -3*mm*. Given the high mixture strength of this jet, the relative weakness of the jet on the centreline and the lack of a jet at ~3*mm*, it can be surmised that the flow within the insert is significantly affecting each jet produced by the insert. It could also be possible that the orifices furthest from the delivery capillary are receiving such little fuel that they are not effectively forming jets.

7▪6▪2   SPATIAL FUEL GRADIENTS

Gorby [6] was able to ignite the PSC charge more repeatable with a weak background charge of RAFR = 1.79. The images of *Figure 7-14* present the PSC injection from the insert at a constant timing of t=7.06 CAD into bulk charges with the fuel concentrations noted. Comparison with *Figure 7-12* shows the concentration gradients to be about an order of magnitude lower with the insert, although their overall structure is comparable to that of the capillary injected PSC jet (notwithstanding the previous assertions on insert jet structure). The jet at -3*mm* appears to show very similar concentration gradients no matter what the background charge and may point to the fact that the shear layer, where the background charge would be expected to have an effect on fuel gradients, is particularly small for the insert jets at this location. The jet on the centreline is seen to have a decrease in fuel gradients for λ_{bulk}=1.75 & 2 when compared to the

case with λ_{bulk}=1.5. This may, at first, seem contradictory since it would be expected that a larger difference between the jet and bulk fuel concentrations exists. However, the observed result may point to the effect of entraining into the jet a mixture that is significantly different in fuel concentration and, as such, serves to reduce the jet concentration, bringing it closer to that of the bulk charge, thereby reducing the observed gradients. This may be expanded upon further by considering the relative-fuel-air distribution of the jets in different background charge concentrations.
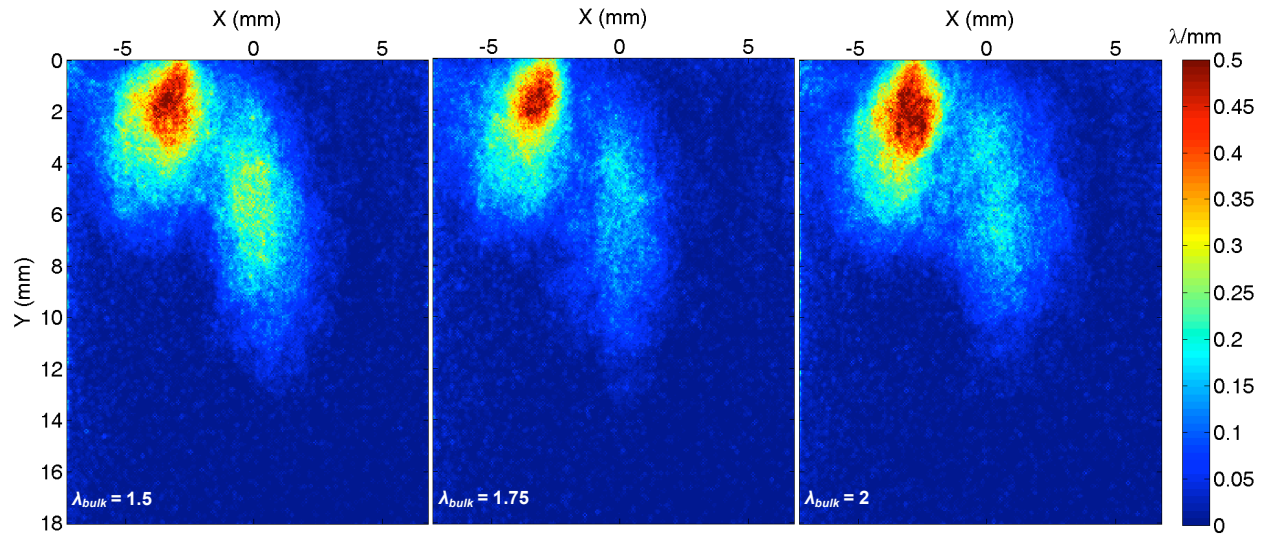
Figure 7-14 Fuel Concentration Gradients for Insert Injected PSC With Bulk Charge RAFRs Indicated

7▪6▪3   BACKGROUND CHARGE EFFECTS
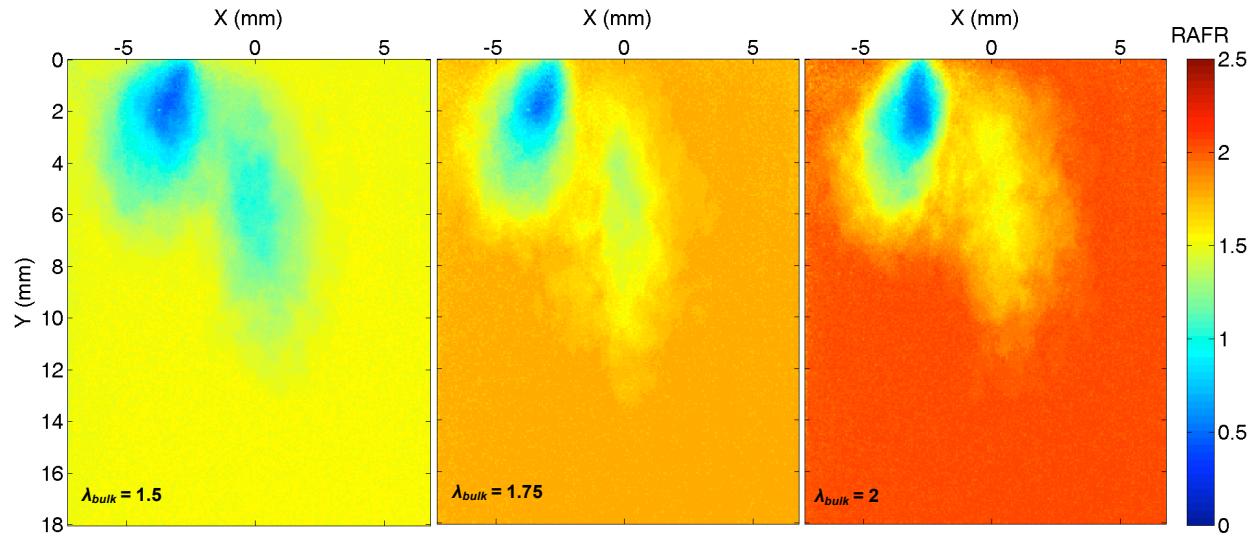
Figure 7-15 Background Charge Effect upon Insert Jet Mixture Distribution

The assertion that entrainment of a weak mixture serves not to enhance gradients but encourage the 'mixing out' of an otherwise rich mixture to that of a stoichiometric mixture would appear to be borne out by *Figure 7-15*. The images of *Figure 7-15* depict the same injection conditions as those of *Figure 7-14* but now present the relative air-fuel ratio. As the background charge concentration is increased from λ_{bulk}=2 to λ_{bulk}=1.5 the spatial extent of the stoichiometric contour is seen to increase. This implies that the background charge concentration needs to be matched to the PSC fuel concentration profile to ensure that the jet is sufficiently diluted, but not overmixed. With no explicit control over the range of background charges tested by Gorby the improvement in ignitability of the PSC with a weak background charge may be attributed to the formation, through mixing, of a larger region of roughly stoichiometric conditions, particularly when the stochastic nature of jet structures is considered.

7▪7 CONCLUSION

Despite the stochastic nature of jets, a high level discussion of the DI jet behaviour was made with respect to its normalised concentration fluctuations, providing a basic understanding of the DI-PSC interactions and, in particular, the extent to which fluctuations vary depending on where the PSC jet intersects the DI jet. The findings in this Chapter serve as a basis upon which the interaction between the DI jet and PSC may be assessed. The limited ability of the RCM optical set-up to provide data pertaining to the full cylinder bore has been demonstrated, as has the difficulty in correcting the background light interference. It has been shown that the PSC insert is not generating the mixture structure that would be expected from its design and the lack of coalescence of the jets necessitates further consideration; particularly with regard to how the mixture is ignited and how the kernel propagates into the homogeneous mixture or from one PSC jet to another.

Chapter 8 THE INTERACTION OF PARTIALLY STRATIFIED & DIRECT INJECTION FUEL JETS

8∙1 INTRODUCTION

Chapter 8 considers, with greater spatial resolution than *Chapter 7*, the interaction of the PSC and DI fuel jets. The mixture distribution generated by a capillary injected PSC jet and a specifically designed PSC 'insert' are discussed and their differences highlighted. For both PSC injection approaches assessments are made as to the effects of relative DI injection timing and bulk charge fuel concentration upon the mixture formation, fuel concentration gradients, r.m.s fluctuations in RAFR and fuel concentration by volume. At a number of locations within the interaction region the minimum, mean and maximum fuel concentrations are considered and the probability density functions for the location presented. The local scalar dissipation rate is also calculated for all nine test conditions. The implications for the potential to ignite the PSC injected fuel are considered, and comparison made between the two injection approaches to assess if the PSC insert is having the desired effect of improved mixing and ignition potential.

8▪2 BACKGROUND

The findings of the previous chapters highlighted the need to focus on the region of the PSC-DI interaction. The same central composite test matrix as outlined in *Chapter 5* was repeated for injections from a capillary and PSC insert. *Figure 8-1* is provided as a reminder of the nine conditions tested, where the background charges were chosen to span those of the work by Gorby and the timings, such that the PSC injection would catch the leading edge of the DI jet, the body of the vortex ball and the steady-state jet behind the vortex ball.
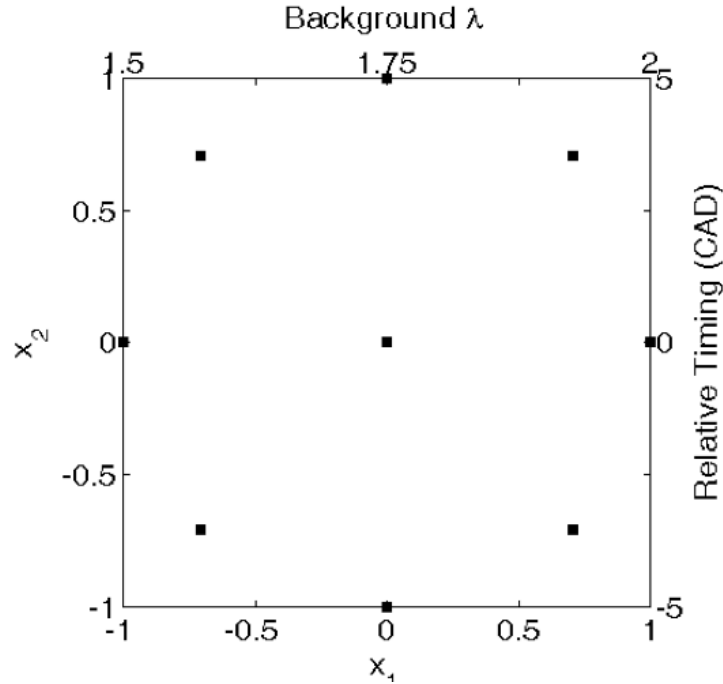
Figure 8-1 Central Composite Test Matrix

The data from the test matrix is presented in 3×3 arrays of visualisations, where each visualisation corresponds to its position within the test matrix, although for compactness of presentation the two data-points at t=3.52CAD are presented in line with that of t=5CAD and similarly, the points at t=-3.52 are presented in-line with t=-5CAD. For the same reason, these four data-points are presented in line with the maximum or minimum bulk mixture fraction as appropriate. For clarity these conditions are noted in each image for the RAFR visualisations presented and is implied for all other visualisation arrays unless otherwise noted.

8▪3 MIXTURE DISTRIBUTION

8▪3▪1   CAPILLARY INJECTED PARTIALLY STRATIFIED CHARGE

The most obvious feature of the PSC DI interaction in *Figure 8-2* is that the PSC jet structure is preserved and penetrates that of the DI jet. The fluid motion of the DI jet is not enough to significantly alter the air-fuel ratio of the PSC jet. In all nine cases it is the interaction of the fuel rich core from each jet that dominates the mixture distribution in the vicinity of a potential spark location. *Figure 8-3* shows the image intensity levels from the centreline of the PSC capillary injection with a DI injection. The plots are similar to those of the PSC injection alone (*Figure 7-9*, *p.*122), in that there is an observed rise to an intensity (concentration) maximum before a concentration decay occurs. In all cases a stoichiometric mixture is not reached until the far side of the DI jet, at about 9*mm* from the firedeck, regardless of background charge or injection timing. However, the structure of the counts differs from the PSC only case in that the concentration 'plateau' of *Figure 7-9* (*p.*122) is not seen and the decay in concentration is closer to that which may be expected of a jet. In the three cases with richer bulk mixtures in the range λ=1.5-1.57 (right-hand column of *Figure 8-2*) the decay appears to be closer to the expected hyperbola, than in the other cases, which appear more linear. This is most likely attributable to the fact that the locus along which the points were taken is neither axially along the di jet nor transverse to it, so it could easily be expected that the profile demonstrate a shape which is the superposition of a hyperbolic axial decay and the more Gaussian radial profile.

There is no significant increase in area of the RAFR=1 contour in any of the nine cases, either due to relative timing or bulk charge concentration. The indication that timing has had no strong effect suggests that in order to maximize the area of the stoichiometric contour the leading edge of the PSC and DI jets must interact. In the case of the capillary injected PSC this is difficult because of the limited spatial extent of the stoichiometric mixture contour (*cf Figure 7-8, p.*121.) and that the region with an approximate stoichiometric composition is dominated by the DI jet. Considering the cases with the weakest bulk mixtures, *i.e.* those from λ=1.75-2 (two right most columns of *Figure 8-2*), there is little difference in structure along the edges of the DI jet; for example the thickness of the λ=1.5 contour (yellow) is constant at about 2*mm* in all cases. This suggests that, on average, mixing is confined to shear layers of similar dimensions in all cases and that the background charge strength does not largely change the spatial extent of the mixing in the DI jet. The head of the DI jet in these same cases shows some difference however, suggesting that mixing over the leading edge of the jet is more variable. In the cases with a stronger background charge (central column) the head of the DI jet appears to mix towards a stoichiometric composition over a larger area than in the case of the weaker mixtures (right column), which appear to preserve the DI head structure. This indicates that it is important to match the background charge

composition with the amount of mixing anticipated, so that the mixture composition can be optimized for engine relevant conditions.
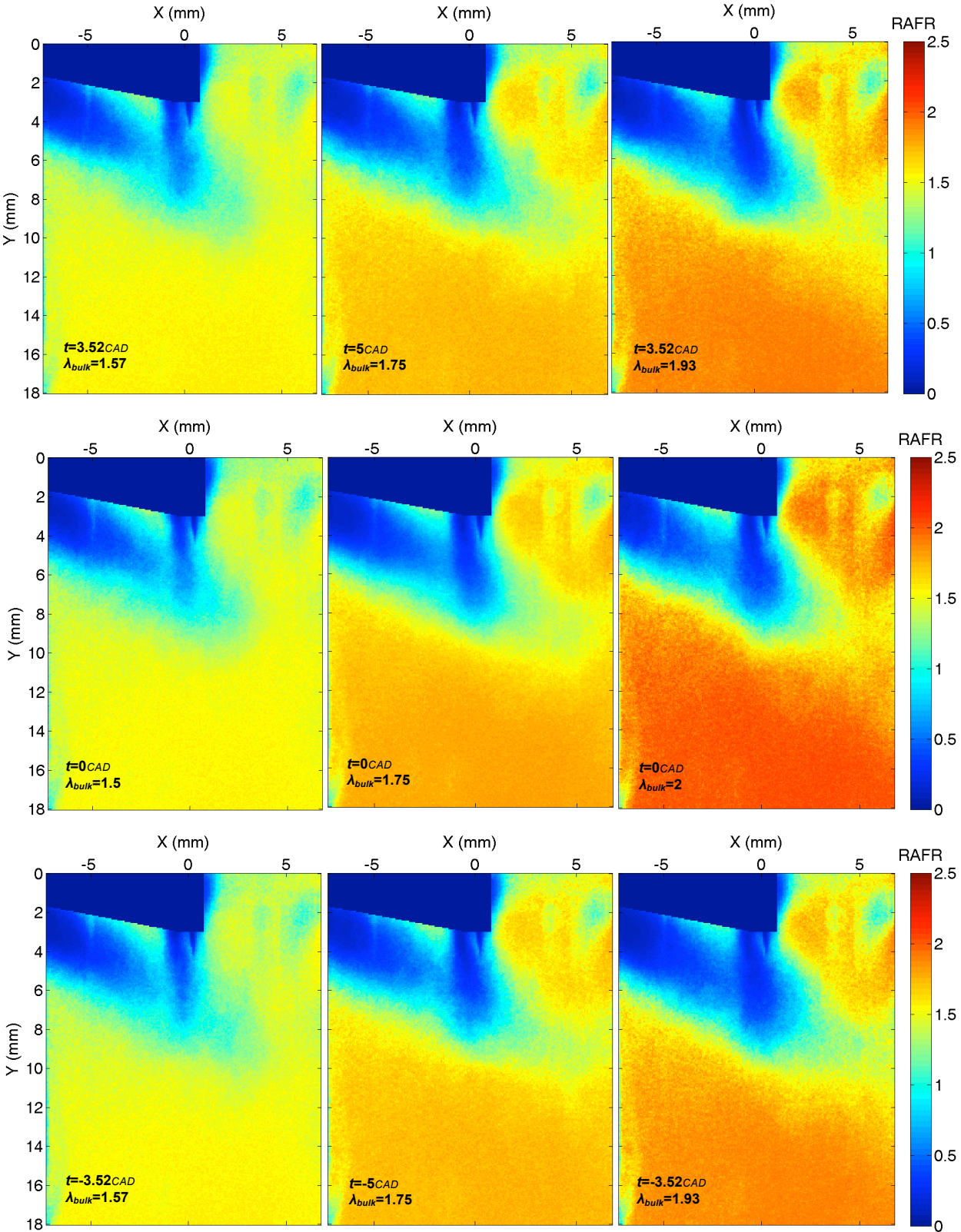
Figure 8-2 RAFR Distribution with Capillary Injected PSC with Direction Injection
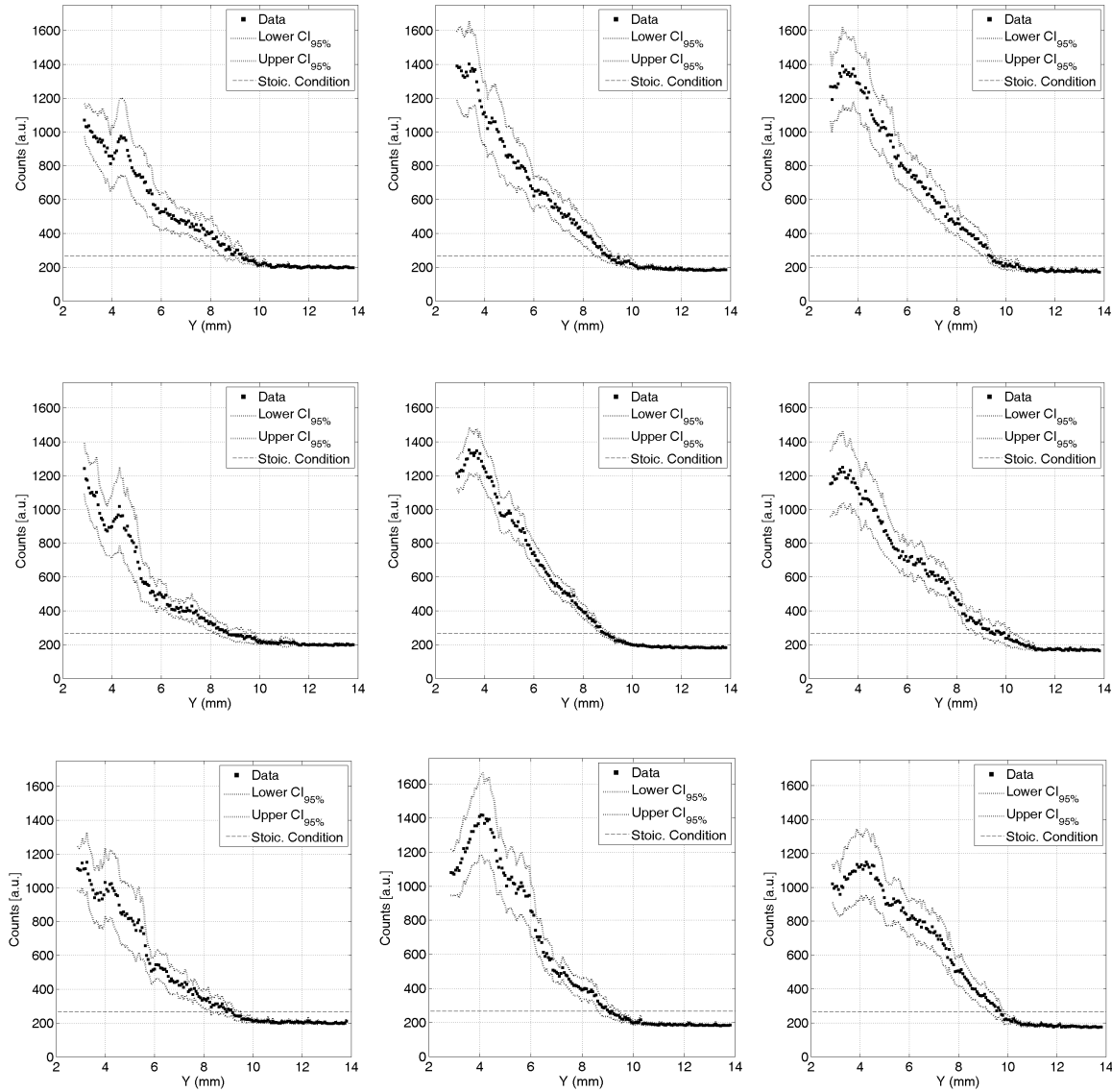
Figure 8-3 Capillary Injected PSC Jet Centreline Image Intensity

8▪3▪2   INSERT INJECTED PARTIALLY STRATIFIED CHARGE

It is apparent from comparison of *Figure 8-4* to *Figure 8-2* that the PSC insert significantly alters the form of the interaction between the two jets. The lower momentum of the insert injected fuel, compared to the capillary injected jet, means the jet structure is more readily perturbed by the momentum of the DI jet. The distinct jet structures of the insert have now been replaced with a single region of similar stoichiometry, the form of which is affected by DI jet timing and bulk charge. For bulk charges with RAFR 1.5-1.57 (left column of *Figure 8-4*) a rich core persists for the injected PSC fuel. At the most retarded timing for these three conditions (*t*=-3.5*CAD*), the fuel mixture is more homogenous and has a higher RAFR, which may be attributable to the higher DI jet turbulence at this timing causing more mixing of the background charge.

135
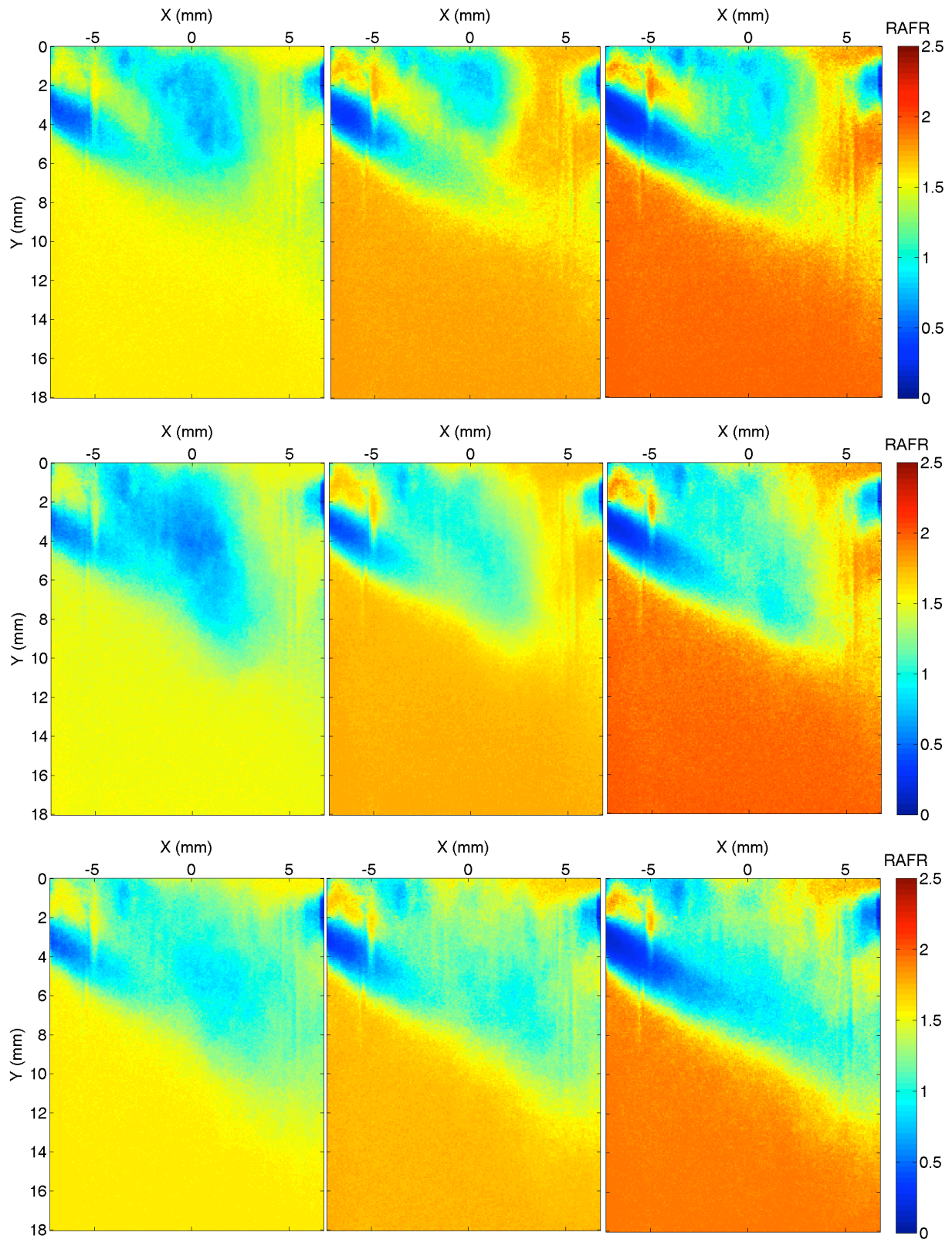
Figure 8-4 RAFR Distribution with Insert Injected PSC with Direction Injection

At the most retarded DI injection timing (*Figure 8-4* top row, centre) the PSC injected fuel still maintains some of its original structure when compared to all other timings; this shows the PSC injected fuel to have

been entrained into the jet, eliminating the DI jet head/vortex ball structure. In as much as the area covered by a stoichiometric mixture is larger with the PSC insert, the mixture is less rich than the capillary injected mixture and as such its combustion may be less robust. The essential role of the PSC fuel is to provide a strong initial combustion to inflame the bulk charge or, in the current case, the DI injected fuel. A less vigorous burn of the PSC fuel may leave it more susceptible to extinction from bulk charge motion or the motion imparted by the DI jet. In some individual realisations the DI jet is shown to deflect the capillary injected PSC jet, *Figure 8-5*. Under these circumstances the DI jet is not causing mixing within the PSC jet since it is straining the jet in a direction primarily normal to the PSC jet flow, and as such there is limited shear to induce mixing. No such deflections were observed for the insert injected PSC, since the flow is already likely to be chaotic enough that either the phenomenon would not be observed or is absent altogether.
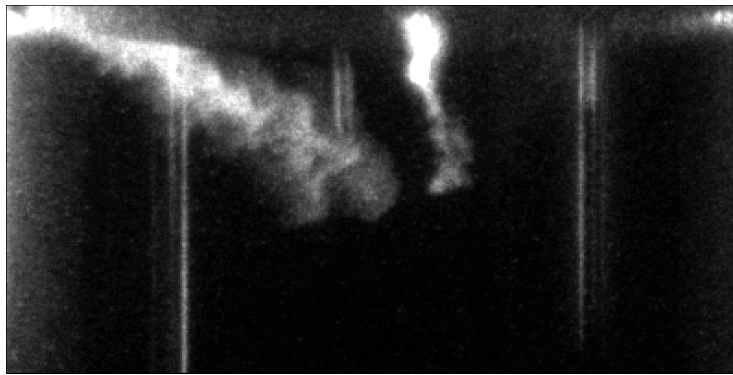
Figure 8-5 Deflection of Capillary Inject PSC Jet

8▪4 CAPILLARY INJECTED PSC IGNITION & INFLAMMATION POTENTIAL

Gorby reported difficulty in igniting the PSC jet **[7]** unless a weak background charge was present. It was postulated in his work that this was because the fuel concentration gradients were too large but, as was suggested in the previous chapter it may, in fact, be a matter of the background charge altering the area over which an ignitable mixture exists, particularly when stochastic variations in the mixture distribution are taken into account. *Figure 8-6* shows the spatial gradients in RAFR (as mm^{-1}). Interpretation of the images is hampered somewhat by the background reflections in the top right corner and left-hand edge of each image. Despite this, some clear trends exist. The core of the DI and capillary injected PSC jets show fuel gradients that are similar and of the order $1mm^{-1}$. The shear layer that forms the boundaries of the PSC & DI jets have gradients which are about twice this level. The shear layer of the DI jet (shown as yellow to red tones) is an order of magnitude thicker than that of the PSC jet, and increases with weakening background charge concentration. The fuel RAFR gradients in the range $2\text{-}5mm^{-1}$ occur in a region of approximately the same thickness for the leading edge and shear layers of the DI jet ($\sim 2mm$), yet show no clear structure in the range $\sim 3.5\text{-}5.5 \ mm^{-1}$ where they form an ensemble of levels over the area that they

cover. Furthermore, the gradients do not appear to be changed by the relative timing of the PSC event to that of the DI injection (differences along columns of *Figure 8-7*). In the work of Gorby the spark would have been at the core of the PSC jet, although delivered from a modified sparkplug, not a capillary. This precludes direct comparison although it would not seem, from the findings of the current work, that fuel gradients were the sole cause of difficult ignition; ignition potential is also likely to be affected local mixture variability.

Figure 8-7 shows the RAFR fluctuations normalised against the local mean RAFR. The central condition of the test matrix shows substantially higher levels of normalised fluctuation suggesting that the other conditions have not reached an experimentally converged condition; however, since it is a comparison and not an absolute value which is sought, some conclusions may still be drawn. The structure of the fluctuations show a maximum at the core of the jets decreasing towards their boundaries over which distance there is almost an order of magnitude difference. With a decrease in bulk fuel concentration the normalised fluctuations are seen to increase in magnitude (*eg.* top row of *Figure 8-7* which has values λ_{bulk}=1.57, 1.75 & 1.93 from left to right), supporting the assertion that it is fuel concentration variability which is reduced by the background charge, in combination with the fuel concentration gradients.

The interaction of the DI and PSC jets has normalised fluctuation levels which are two to three times lower than the capillary injected PSC alone (*cf. Figure 7-11*, *p.*125), and comparable to the leading edge of the DI jet (*cf. Figure 7-7*, *p.*118). The literature on jets largely reports time averaged profiles, to which the current work shows some level of agreement. However, the work of Schefer *et al.* **[22]** shows the difference between time averaged and instantaneous profiles to be marked. Instantaneous radial velocity and concentration profiles may essentially be 'top hat' **[392]** and, as such, the average profiles misrepresent large scale coherent 'engulfment' rather than entrainment. Two models for the engulfment have been proposed: the axisymmetric mode **[393]**, and the helical mode **[394]**. In both modes the structures are large scale, quasiperiodic, organized and exists equally **[22]**. The instantaneous radial concentration profile is gradually eroded by engulfment such that the 'top hat' profile becomes more triangular downstream of the jet origin. The concentration decay for the instantaneous profiles can be expected to show clear step-wise decreases, with the formation of 'ramps' and 'plateaus', associated with the engulfed vortices, on the scale of the local jet diameter **[22]**.
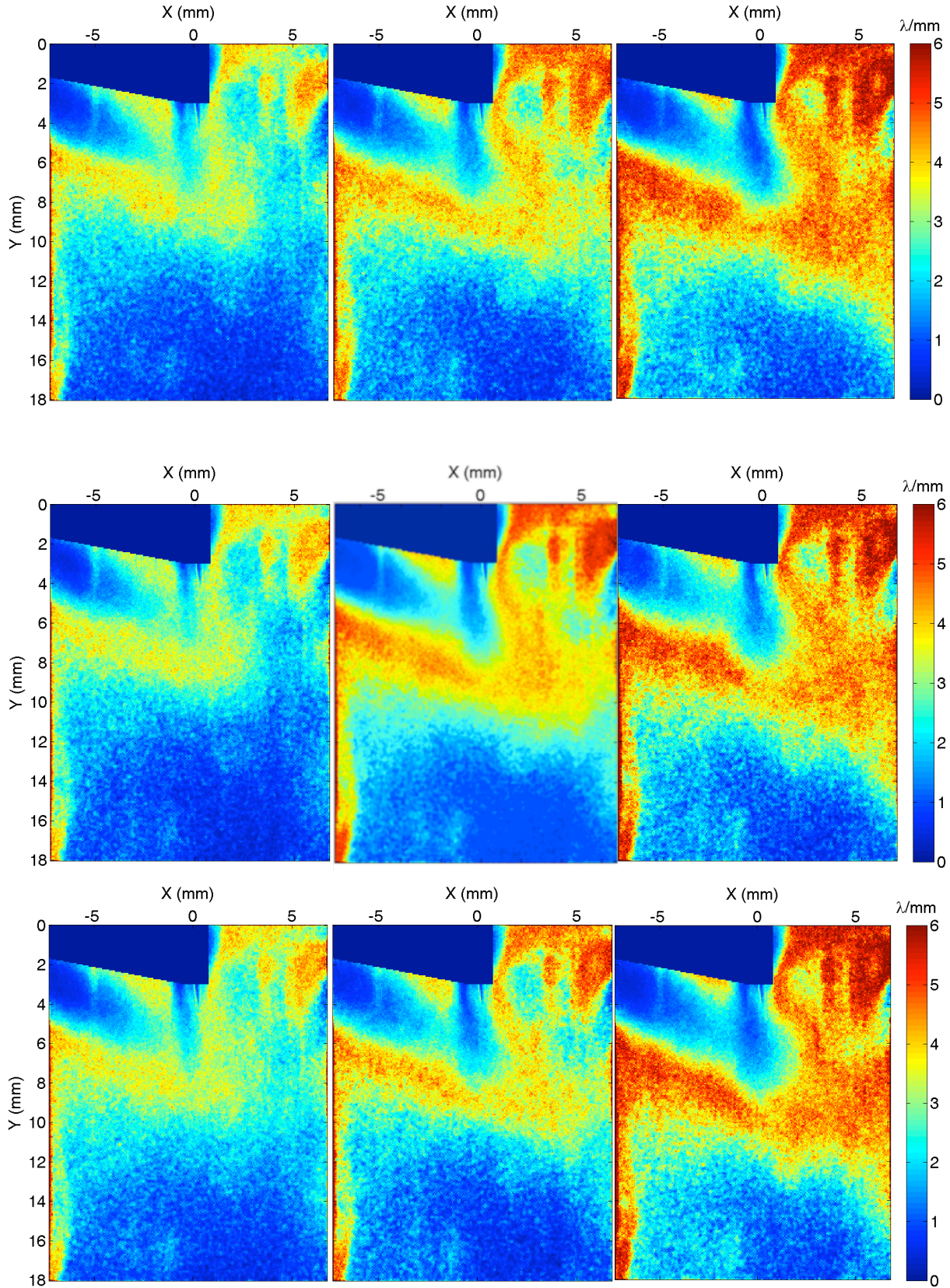
Figure 8-6 Capillary Inject PSC & DI Jet RAFR Gradients
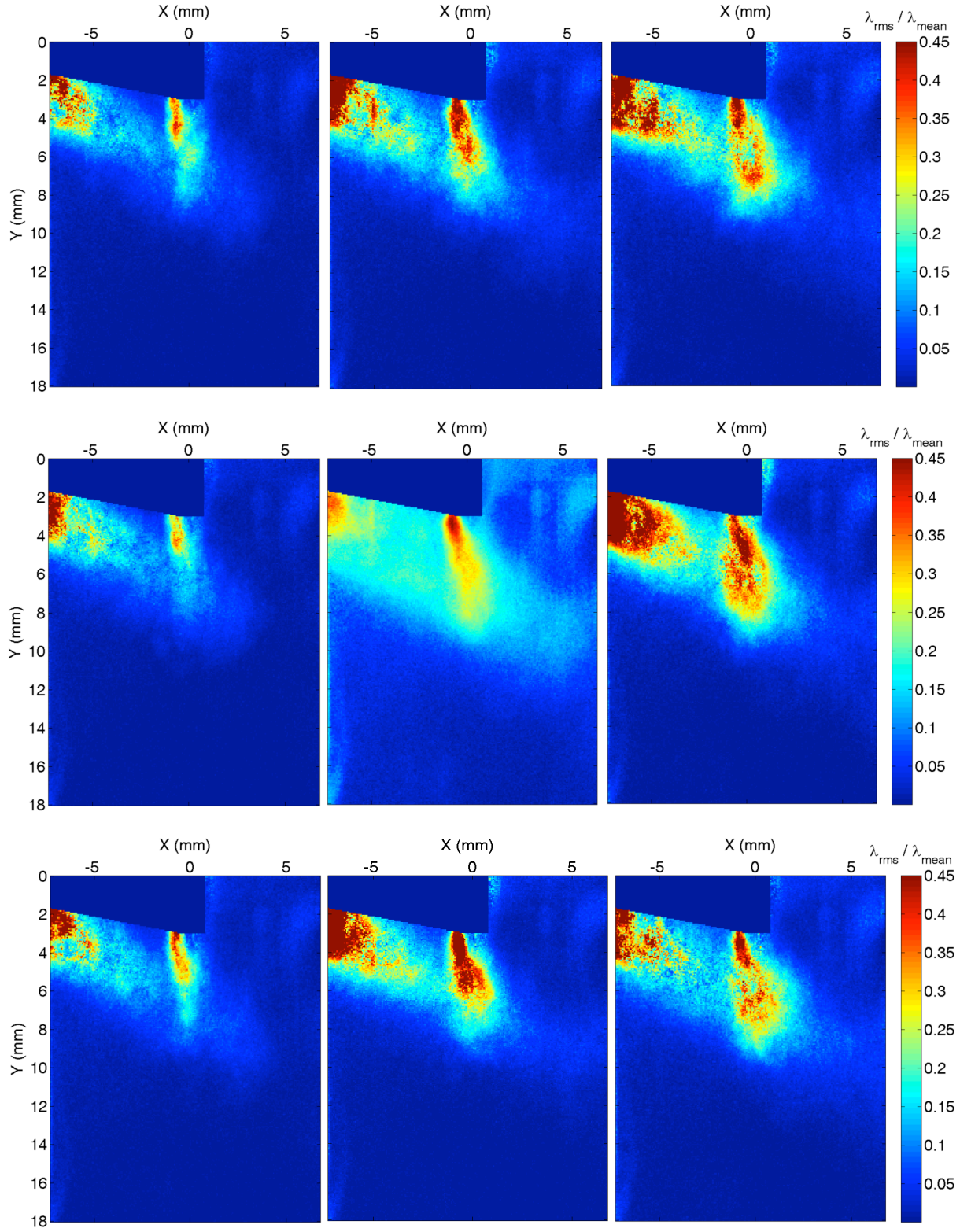
Figure 8-7 Capillary Injected PSC and DI Jet Normalised RAFR Fluctuations

The work of Schefer *et al.* **[22]** shows a demonstrable monotonic tendency towards the widely accepted mean and r.m.s. axial and radial concentration profiles, and shows the need to ensure a fully converged experimental average, as well as the stochastic nature of each experimental realisation. To elucidate this stochastic nature at a given location it is pertinent to consider the probability density function (*pdf*) of the relative air-fuel ratio. This was done for four different stations within the RCM cylinder as shown in *Figure 8-8* and detailed in *Table 8-1*. Each station corresponded to an area of $1mm^2$.
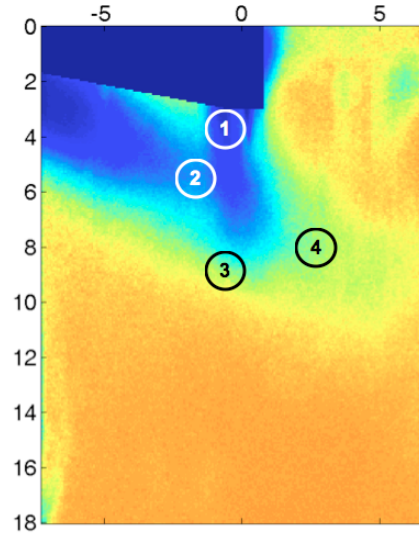
Figure 8-8 Sample Station Locations for Capillary Injected PSC & DI Jets

	Image Position (*mm*)	
Station #	*x*	*y*
1	-0.5	4
2	-1	5
3	-0.5	9
4	2	8

Table 8-1 Capillary injected PSC Sample Station Locations

At each station the probability density function was calculated using all 13,000 or 39,000 pixels that correspond to the $1mm^2$ area for the 51 or 153 images that form the data point. The full set of *pdf*s for all four stations over all nine test conditions is presented in *Appendix C*. The stations were chosen to match locations of particular interest: 1) where a spark might reasonably be designed to be, 2) the upstream side of the PSC-DI interaction, 3) the head-vortex of the DI jet having passed through the PSC jet and 4) the shear layer in the DI jet ahead of the PSC jet. These locations were chosen to help guide future decisions about the structure of the jets PSC injection should be generating. With the exceptions noted below, the form of the *pdf*s for any given station were independent of injection timing and background charge. Those

presented in *Figure 8-9* are taken from the central condition (λ_{bulk}=1.75, t=0 *CAD*) of the test matrix. For

stations one and two (*Figure 8-9 (a) & (b)*) it is apparent that there is a much more significant probability

of having a rich mixture than a stoichiometric or lean one, and even within the core of the PSC jet, at

station one, there is a small but finite chance of the bulk charge being present. For the PSC jet core the

probability of encountering the bulk charge composition is comparable to that of encountering a

stoichiometric mixture, while the probability of having a rich mixture increases rapidly for RAFR values

less than 0.8. At the interface of the DI core and the PSC jet boundary, station two, there is still a high

probability of encountering a mixture with the bulk charge, a probability that at ~2.5-3% is three times

higher than that of encountering a stoichiometric mixture. The highest probabilities cover the range of

RAFRs from 0.3-0.8, demonstrating that the interface of the DI and PSC jets is still predominantly rich, and

if ignitable, capable of producing the robust burn required by partially stratified combustion. As may be

expected, the *pdf*s of RAFR for the DI shear layer (station three, *Figure 8-9(c)*) and the central portion of

the vortex ball of the DI jet (station four, *Figure 8-9(d)*) are similar, however the similarity is closer than

may be expected. Station three shows a slight plateau in probability around the stoichiometric

composition.

(a)   (b)

(c)   (d)
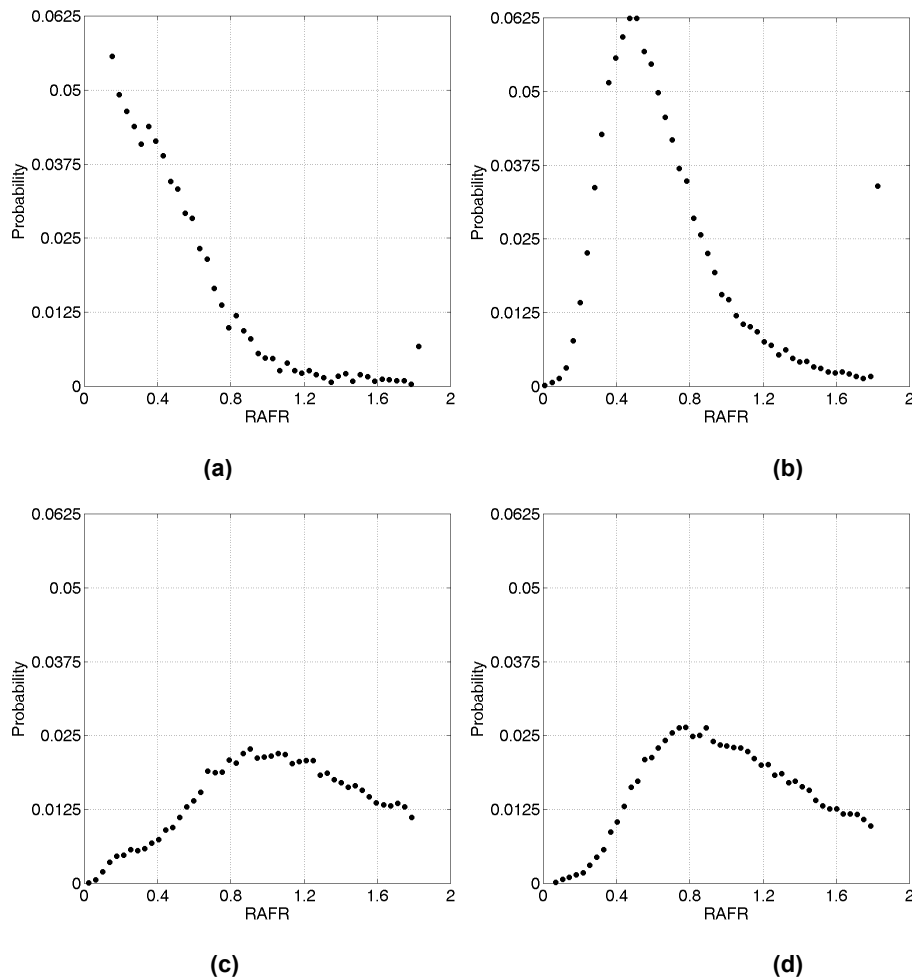
**Figure 8-9 Probability Density Functions for Central Condition of the Test Matrix at (a) Station One, (b)
Station Two, (c) Station Three and (d) Station Four.**

The only data points that displayed RAFR *pdf*s that varied from the central condition of the test matrix were those of station one for conditions which corresponded to a) λ_{bulk}=1.57 t=-3.53*CAD* (Figure 8-10*(a)*) and b) λ_{bulk}=1.5 t=0*CAD* (*Figure 8-10(b)*). There is a clear reduction in the probability of generating mixtures in the range of RAFR from 0 to 0.4. There is no ready explanation for this observation since the observed drop cannot be isolated from either the background charge or timing variables, nor is the drop seen in the corresponding bulk charge or timing data-points of the test matrix.

(a)   (b)
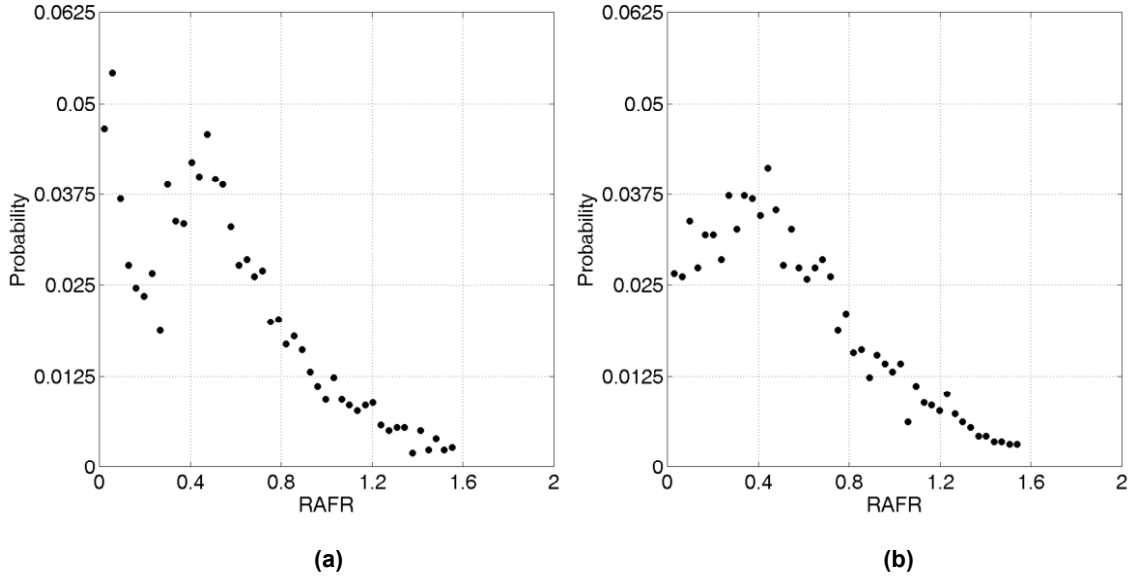
Figure 8-10 Probability Density Functions for Capillary Injected PSC Jet with DI at Station One for (a) RAFR=1.573 *t*=-3.53CAD and (b) RAFR=1.5 and *t*=0CAD.

The propensity for a mixture to ignite is governed by, amongst other things, its composition. In trying to establish the likelihood of ignition for the PSC jet the same four stations examined for their RAFR *pdf*s were evaluated for their RAFR minima, maxima and means. *Figure 8-11* shows the calculated values for stations one through four (*(a)-(d)* respectively), for each of the nine test conditions. Station one, the core of the PSC jet, would be expected to yield only pure fuel compositions, yet it is clear from *Figure 8-11(a)* and the *pdf* of *Figure 8-10(a)* that other mixture compositions are also encountered, and that the minima is equal to the background charge strength. The same is true of the other stations, as is the propensity for the fuel maximum concentration to be that of pure fuel, or very close to it. These findings support the work of Schefer *et al.* **[22]** who suggest mass engulfment is responsible for gas entrainment. Ahmed & Mastorakos **[395]** report ignition probability to decrease rapidly downstream of the stoichiometric contour, and with increased dilution. This raises some concerns about igniting the PSC mixture on its shear boundary or at its head vortex, since if its structure is similar to that of the DI jet, these locations have mean mixture RAFRs lean of stoichiometric (*Figure 8-11 (c) & (d)*).

(a)

(b)

(c)

(d)
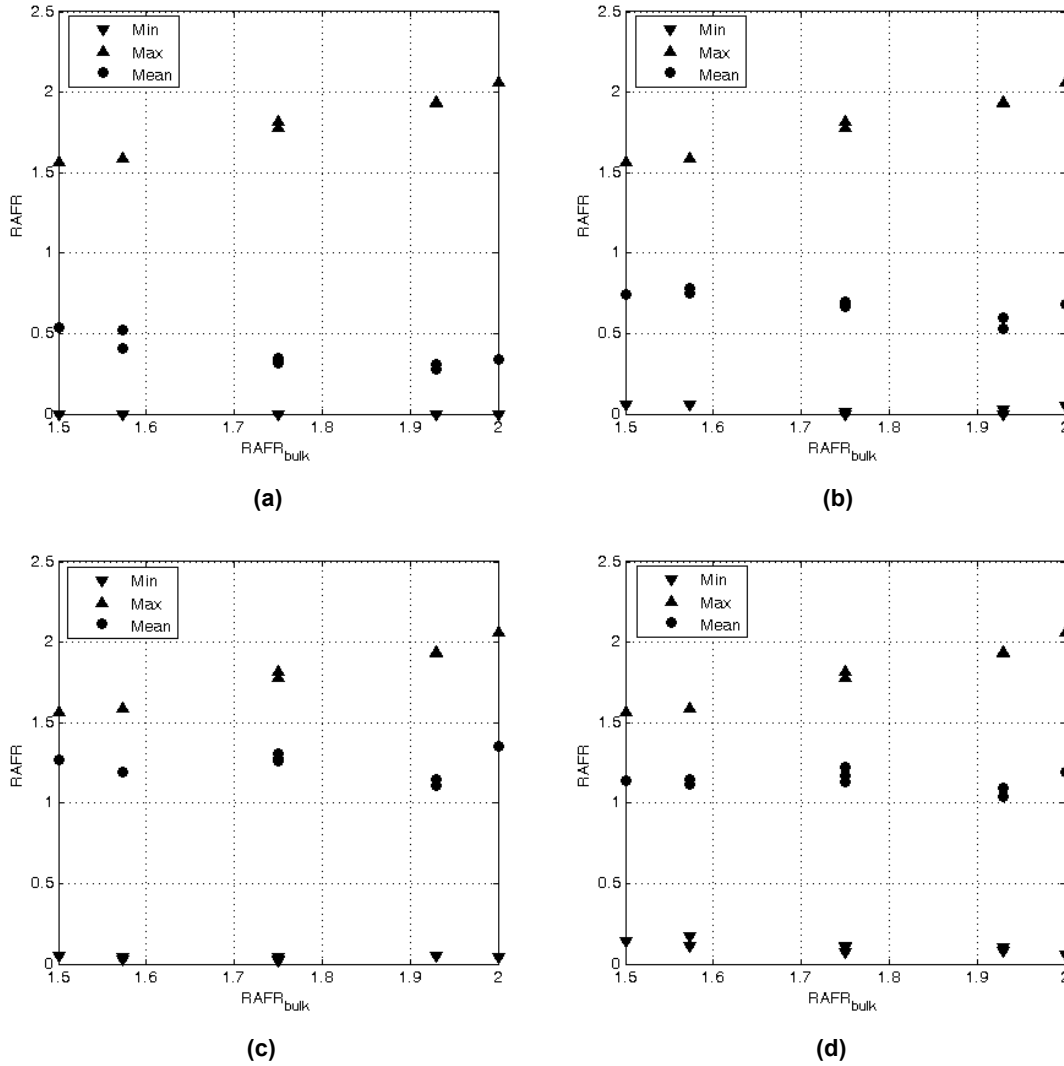
Figure 8-11 Maxima, Minima and Mean RAFR for all Capillary Injected PSC Test Conditions at (a) Station One, (b) Station Two, (c) Station Three and (d) Station Four.

The probability density functions, and extrema plots of *Figure 8-11* only indentify part of the mixtures' propensity for ignition. *Table 8-2* shows the nine test conditions and the corresponding probability that any given pixel within the $1mm^2$ is within the flammability limits of methane as specified by **[396, 397]**. The limits applied from **[396, 397]** are for a mixture at 1 *atm* and 25^0C; however, it is noted by Jessen **[397]** that, with "the existence of cool flames at elevated temperatures, upper limits often increase drastically and unpredictably with a slight increase in temperature", which certainly may be the case for the environment within the RCM cylinder, although it is noted by Burgess & Hertzberg **[396]** that the increase in pressure is unlikely to affect the flammability limits. These observations notwithstanding, it is apparent that at all stations the probability of encountering a mixture within the flammability limits is typically less than 50%, and substantially less at station one for all conditions, although slightly over at station four. Neither the injection timing nor the bulk charge RAFR were found to have a correlation with the probability of the mixture falling within the flammability limits for any of the stations, suggesting that the interaction of the two jets did not significantly alter the entrainment or engulfment behaviour of either

144

at these locations. It is desirable to ignite the PSC jet where the composition is rich, since there is a higher probability of successful ignition and a higher ignition kernel growth rate **[395]**, both of which are desirable for successful ignition of the DI jet or homogeneous charge.

λ_{bulk}	Relative Timing (CAD)	Probability Within Flammability Limits			
		Stn. 1	Stn. 2	Stn. 3	Stn. 4
1.5	0	0.32	0.49	0.48	0.50
1.573	3.53	0.30	0.50	0.48	0.54
1.75	5	0.15	0.40	0.57	0.58
1.937	3.53	0.09	0.28	0.52	0.60
1.75	0	0.13	0.36	0.49	0.51
1.937	-3.53	0.11	0.24	0.57	0.55
2.0	-5	0.13	0.37	0.53	0.55
1.573	-3.53	0.22	0.47	0.50	0.51
1.75	0	0.15	0.41	0.55	0.60

Table 8-2 Probability of Mixture Falling Within Flammability Limits for Capillary Injected PSC Jet with DI at Stations One to Four

Despite the limited probability of a flammable mixture at these locations, the mean area over which a rich flammable mixture exists is itself significant, as is evident from *Figure 8-12*(regions outside the flammability limits of methane are shown in black). The stronger the background charge, the smaller the region within the PSC jet that falls outside the flammability limits (rows viewed from right to left), presumably due to the introduction of the bulk charge which is itself closer to the median flammable concentration. However, Ahmed & Mastorakos **[395]** note that there is a finite probability of ignition over an area that is larger than the locus of the lean and rich flammability limits, most likely due to the convection of hot gas generated by the spark into a region within the flammability limits. This would suggest an even larger area over which the PSC jet may be ignited. The argument is even extended to show a finite ignition probability in areas where there are no r.m.s concentration fluctuations and the streams may be considered to be of pure fuel or air **[398]**.
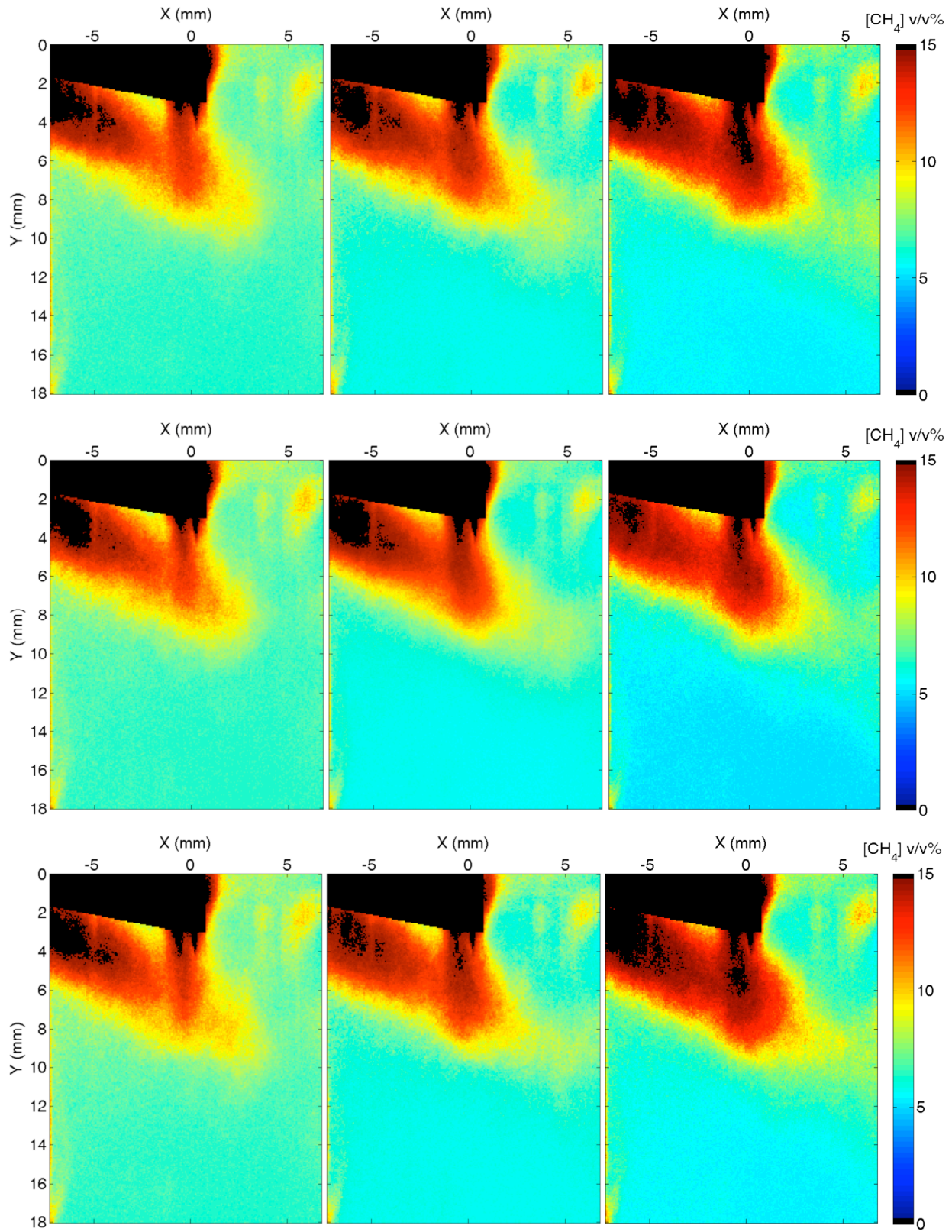
Figure 8-12 Capillary Injected PSC with DI Jet Fuel Concentrations by Volume.
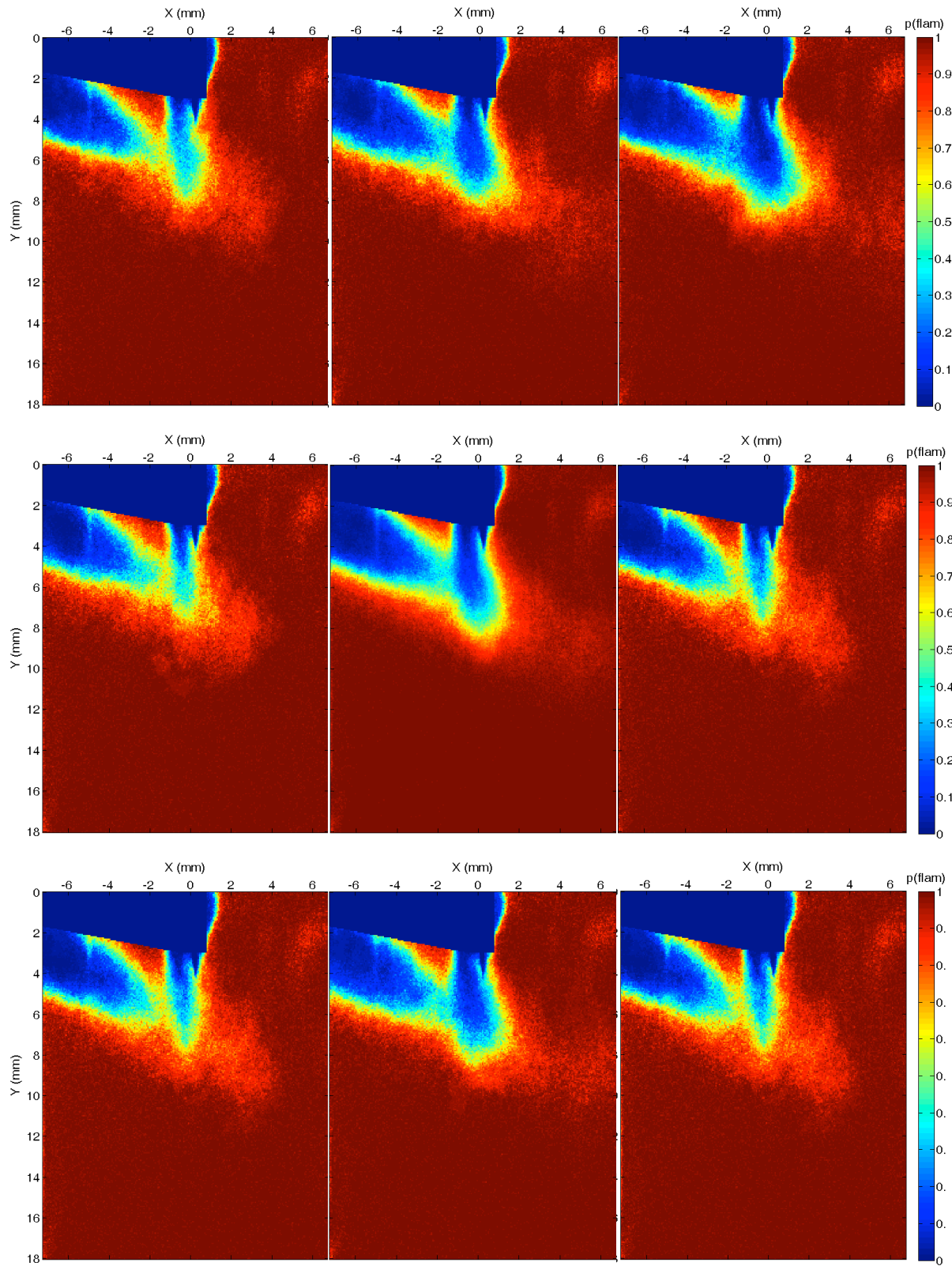
Figure 8-13 Probability of Encountering a Mixture Within the Flammability Limits of Methane for Insert Injected PSC

Figure 8-13 shows the probability of encountering a mixture within the flammability limits of methane based upon the 51 or 153 realisations of each test condition. The most notable observation is that there is a remarkable similarity between the conditions with neither bulk charge concentration nor injection timing having a significant effect upon the probability. There are some small differences in the PSC jet and at the head of the DI jet where it interacts with the PSC jet. The core of both jets exhibit low, but not zero, probability of having a mixture within the flammability limits, while in the head of the PSC jet and within the shear layers of both jets the probability of encountering a flammable mixture is far from guaranteed with probabilities in the range 0.4-0.7. The only regions where there is almost certainty of encountering a flammable mixture are those which would be deemed over mixed, i.e. those at the head of the DI jet.

Fluid motion and chemical kinetics must act together if a flame is to persist or if ignition is to be attained. If the DI jet is to be inflamed and stay so it must not be excessively strained. Turbulent motion ensures that throughout the jets there is an ensemble of strains and strain rates which vary in space and time. Turbulence serves to mix the fuel and oxidizer to attain a combustible mixture, yet the same mixing also serves to dilute the radical pool generated by increased temperatures and transport heat away. The initial chain branching reactions associated with increased temperature are critical to ignition. Methane ignition typically follows the path

$$CH_3 \rightarrow CH_3O \rightarrow CH_2O \rightarrow HCO \rightarrow CO$$

with the kinetically controlled quasi-steady-state species, like HCO, showing a narrow localised concentration profile and the 'sink' species, like CH_2O, showing a much larger profile [399]. During the ignition delay the chain branching reactions yield a radical pool that grows exponentially with time [119] but for which the slower more spatially distributed species are susceptible to mass transport. Fotache *et al.* [399] note that "methane/air ignition involves the effects of convective and diffusive losses, as well as chemical heat release". The interaction of all these variables is complex, as is noted by Grout *et al.* [400] who observe that at high temperatures (high radical pool concentration), turbulence hinders ignition while at low temperatures (lower radical concentration), turbulence encourages ignition. In the methane/air (H-C-O) system pressure does not change the ignition mechanism [399] since the initial branching reactions do not necessitate a third body. No simple conclusion as to the effect of strain can be made since strain affects inflammation differently at different times. Ahmed *et al.* [398] note that local straining is detrimental to ignition because the strain and dilation act to reduce temperatures curtailing the radical pool; yet, following the primary stages of the ignition the slower species are affected directly by strain induced mass transport and help propagate the flame. The current LIF set-up cannot ascertain the strain rate, and as such this critical parameter should be sought through computational fluid dynamics (as scalar variance [401]) or through laser velocity techniques.

"Scalar dissipation describes the rate at which concentration nonuniformities relax towards zero due to molecular diffusion. As such, it provides an important measure of the local rate of mixing at the molecular scale. Knowledge of this mixing rate is particularly important…where chemical reaction rates may be limited by the rate at which reactants are mixed locally" [22]. Scalar dissipation, χ, is calculated according to *Eq. 8.1* where Z is the mixture fraction and the binary diffusion coefficient, $\mathscr{D}$, of methane into nitrogen $22mm^2/s$ [22] (a reasonable proxy for the multi-component system of natural gas into air).

$$\chi = 2\mathscr{D}\left(\frac{\partial Z}{\partial x_i}\right)^2$$

Eq. 8.1.

As expected there are high dissipation rates near the PSC origin (*Figure 8-14*), however, the location of the higher dissipative region later in the jet is not as may be expected. It would be expected, and has been reported [402], that the dissipation is coincident with the AFR r.m.s fluctuations, and the regions of highest scalar dissipation are not dissimilar to those found in the work of Markides & Mastorakos [178] who looked at the dissipation and mixing of an acetone jet into co-flowing air. It is clear, however, that the dissipation is increased in the vicinity of the PSC, and to such an extent that combustion may not be supported. Numerical work by Rogg *et al.* [403] on a counter-flowing methane-air flame suggests a critical scalar dissipation rate of $20.6s^{-1}$, above which combustion will not occur since convective-diffusive heat removal is increasing while heat generation drops from the reduced reaction rate.

The PSC insert (*cf. §4▪4▪1*) was designed by Logan [404] to generate better mixing of the PSC injected fuel with the bulk charge and as such reduce the fuel concentration gradients. The current work assesses to what extent this has been achieved, and allows an assessment of how this has been achieved with the aim of informing future insert designs. As was seen previously (*cf. Figure 8-4*), the insert alters significantly the fuel distribution within the RCM cylinder, and the spatial extent to which the PSC injected fuel interacts with that of the DI jet.
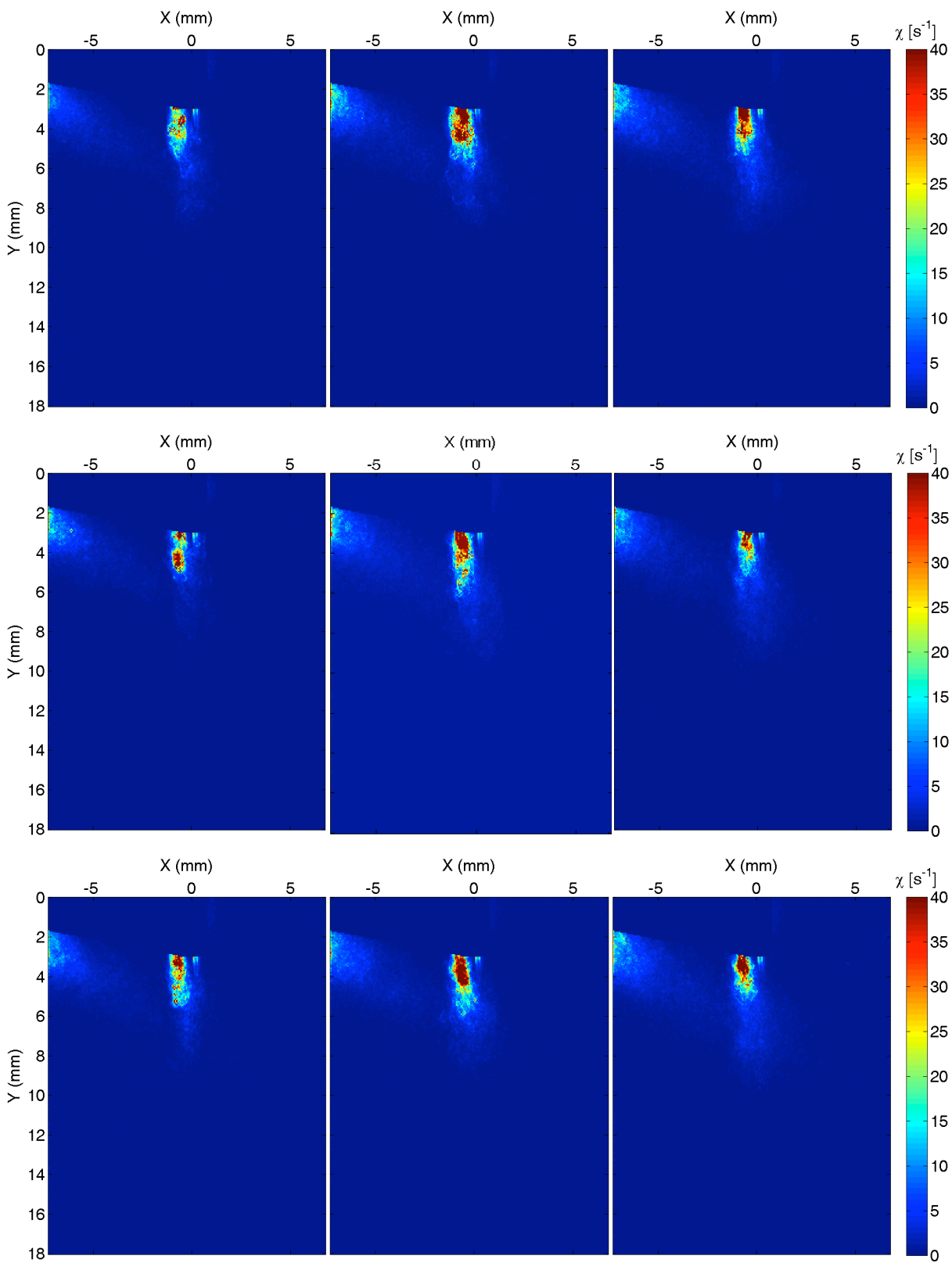
Figure 8-14 Scalar Dissipation Rate for Capillary Injected PSC with DI Jet

8▪5 PSC INSERT INJECTION IGNITION & INFLAMMATION POTENTIAL
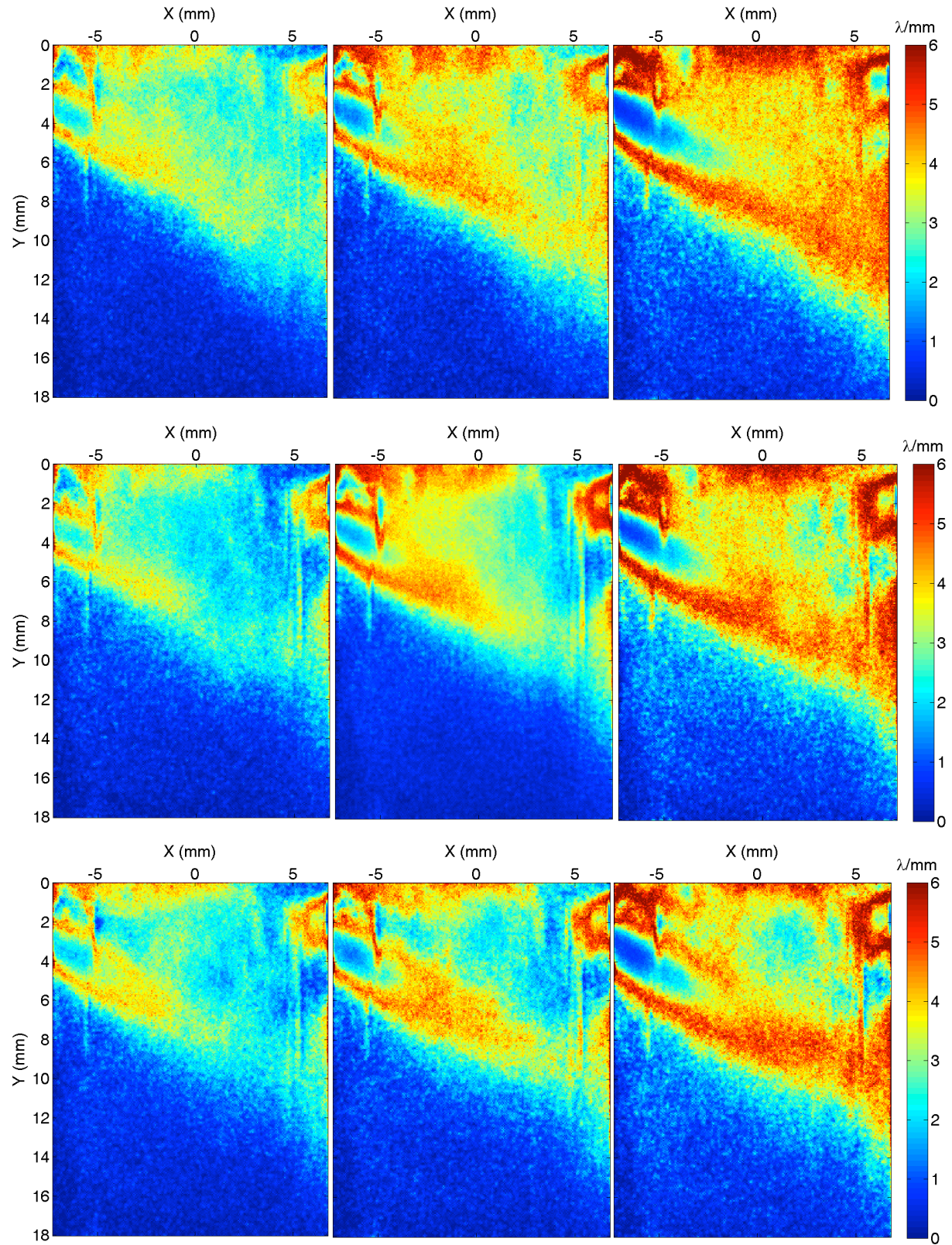
Figure 8-15 Insert Inject PSC & DI Jet RAFR Gradients
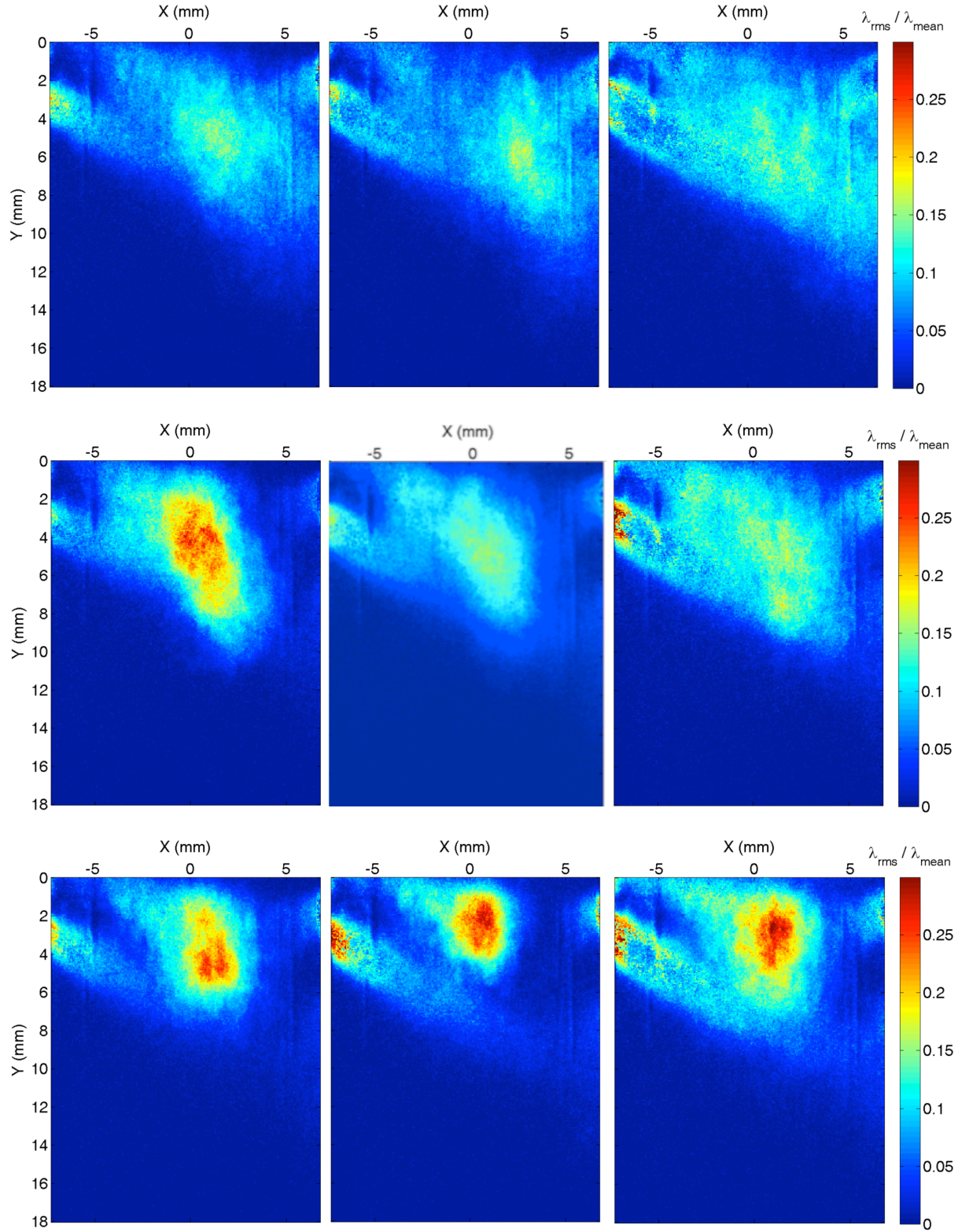
Figure 8-16 Insert Injected PSC and DI Jet Normalised RAFR Fluctuations

The bulk charge is seen to have two contrasting effects upon the insert injected PSC-DI interaction. The first, and most apparent, is that as with the capillary injected PSC, the more rich the bulk charge the greater the observed reduction in RAFR gradients for the regions, of the DI jet in shear and, in this case, the injected PSC fuel (reduction in observed gradients across rows of *Figure 8-15* from right to left). The magnitude of the RAFR gradients in these regions is comparable to those for the capillary injected PSC-DI case. The second observation contrasts that of the shear regions in that the core of the DI jet demonstrates an increase in RAFR gradient with increased bulk charge fuel concentration; this also contrasts the capillary injected PSC case that shows no discernable difference in the RAFR gradients for the DI jet core with varying RAFR (*cf. Figure 8-6*). These observations are most likely attributable to the fact that the mixing of the DI jet core is unaffected by the PSC capillary injection, and the mixing confined to the jet shear layer, notwithstanding the discussions of mass engulfment. In the case of the insert injected PSC fuel, the injection and subsequent interaction act over a much larger area and, as seen from the mixture distribution images of *Figure 8-4,* to extend into the core of the DI jet. Furthermore, the lower velocities that the insert generates means that the structure of the insert injection is more susceptible to perturbation and subsequent mixing from the DI jet than the capillary injected jet. Injection timing shows no effect upon the observed gradients (images viewed along colums of *Figure 8-15*).

In contrast to the capillary injected PSC normalised r.m.s. RAFR flutuations of *Figure 8-7*, the images of *Figure 8-16* show both timing and background charge to have an effect, while in general the r.m.s. levels are lower with maximum fluctuations about 33% lower. The images for the top row of *Figure 8-16* are simlar, as are those for the bottom row. The timings for these rows of images are similar but not identical, with the central images being ±1.47*CAD* offset from those at the end of the rows (*cf.* central composite test matrix, *Figure 8-1*). What is apparent from these images, that is not so apparent from the RAFR images of *Figure 8-4*, is that the two distinct jets produced by the insert within the interrogation volume (*Figure 7-13*, *p.*127) have been mixed into a single larger region. At retarded relative DI injection timings a homogeneous normalised r.m.s. RAFR structure exists with a centre at about x=2-3*mm*, while for advanced DI injection timings a distinct fluctuating core with a centre at about x=0.5-1*mm* is seen; there is also seen to be roughly a two-and-a-half fold increase in the flutuation level between the the two timings. This shows that the relative timing of the jets, through momentum exchange and mixing, is able to change the location at which RAFR fluctuations occur- something that was not seen with the capillary injected PSC jet because of the dominance of the PSC momentm over that of the DI jet by the time it reaches the cylinder centreline. As with the capillary injected PSC event, the fluctuations are most prominent in the PSC injected fuel, with the DI jet showing levels about two-thirds lower. This would suggest that when sustaining a flame after spark and its propagation to the DI jet, it is the flutuations and implied strain within the PSC injection not the DI jet that are of concern. The images of Figure *8-16* imply that it is not bulk charge or timing that act to control the fluctuation levels but the combination of the two; the data

points for retarded DI timings and weaker bulk charge (top right of the test matrix CCD) show lower RAFR fluctuation levels than those for advanced relative DI timing and stronger bulk charge mixtures.

As with the capillary injected PSC-DI interaction, the stochastic nature of the mixture distibution was considered at five locations (*Figure 8-17* & *Table 2-2*), one more than for the capillary inject case. These locations were chosen to assess variation with distance from the firedeck (stations one to three), the point at which the DI jet centreline is interacting with the insert inject fuel (station four) and the location on the downstream side of the DI jet after it has passed through the insert injected fuel (station five).
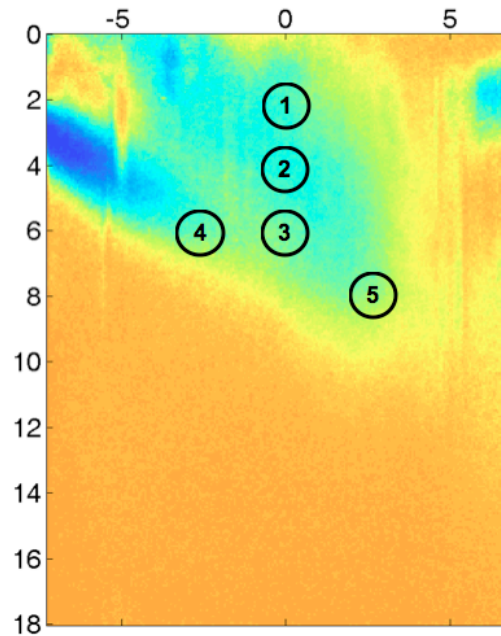
Figure 8-17 Sample Station Locations for Insert Injected PSC DI Events

Station #	Image Position (mm)	
	x	y
1	0	2
2	0	4
3	0	6
4	-2.5	6
5	2.5	8

Table 8-3 Insert Injected PSC Sample Station Locations

The probability density function was produced for each set of 13,000 or 39,000 points that corresponded to the 1mm^2 area at each location for the 51 or 153 realisations of that test condition, and are presented with a point at the centre of each RAFR interval (set to be 1/48 of the total RAFR range). The results for

stations one to three are shown in *Figure 8-18* for the central row of the test matrix, *i.e.* a relative injection timing of 0*CAD*. No data is presented for test conditions at different timings since inspection of the full set of *pdf*s (shown in *Appendix C*) displayed little or no dependence up timing. At station one (closest to the firedeck) the three *pdf*s of *Figure 8-18(a)* show much the same form, suggesting that the bulk charge has had no chance to mix with the insert injected fuel, and that the RAFR probability distribution is governed by the mixing within the insert prior to the fuel entering the cylinder. At station two (*Figure 8-18(b)*), 4*mm* off the firedeck, the bulk charge with the strongest fuel concentration (λ_{bulk}=1.5, left-hand image) shows a marked increase in the chance of encountering a mixture with RAFR~0.2, while the case with λ_{bulk}=1.75 shows little difference to the case for station one, and at the leanest case only a slight increase in the maximum probability, which occurs at the same RAFR (0.5) as the λ_{bulk}=1.75 case. These observations suggest that the mixing mechanisms at work exhibit threshold or stepped behaviour in their propensity to mix the background charge with the injected fuel. Schefer *et al.* **[22]** found distinct 'plateaus' and 'ramps' in the instantaneous concentration distributions for their methane jet, whose effect upon the background charge entrainment may be directly related to the lengthscale of the coherent structures and their associated entrainment. This is supported further by consideration of *Figure 8-18(c)*, the *pdf*s for station three, which show for the richest background charge a similar distribution to the same condition for station two, although with a reduced peak probability; while the distribution for the weakest bulk charge condition (λ_{bulk}=2, *Figure 8-18(c)* right-hand image) at station three shows little discernable difference from the equivalent condition at station one, 2*mm* from the firedeck. This 'matching' of mixing lengthscales to background charge may also explain the slight increase in the peak probability at RAFR~0.4 for station one and bulk charge RAFR=1.5, although the scatter in the data and the sudden drop in probabilities at RAFR~0.5 make this assertion difficult to fully support. The RAFR distribution at λ_{bulk}=1.75 of station three is the only case (of all those for stations one to three) that shows a decrease in peak probability and a plateau in RAFR probability for bulk RAFR values in the range ~0.4-1.2. Of final note is that the probability distributions for stations two to three (*Figure 8-18(a) & (b)*) show significantly less local variability in RAFR. The differences in probability from one RAFR value to another change gradually, while those at the low and high bulk RAFR values for station one show more scatter. This may be a result of the mixing process which takes place within the insert having started, but not completed, prior to mixing with the bulk charge. In the cases of the stations further from the firedeck the mixing process is more advanced and less time/location dependant. It should, however, be noted that the case for λ_{bulk}=1.75 at station one (*Figure 8-18(a)*, centre) does not show the same scatter as the two other cases (*Figure 8-18(a)*, left and right). There is no immediately clear reason for this difference, although it is worth noting that the work of Gorby used a bulk charge RAFR of 1.79 (very close to the 1.75 condition) and a spark plug which would produce a PSC jet more akin to that of the insert than the capillary and found more reliable ignition at this condition. The lack of scatter in the RAFR *pdf* may further point to the bulk charge smoothing RAFR fluctuations rather than smoothing concentration

gradients, particularly if the lengthscales of the mixing process match that required by the bulk charge to produce a 'desirable' ignition condition (with the details of what constitutes a 'desirable' condition still in need of exact definition).
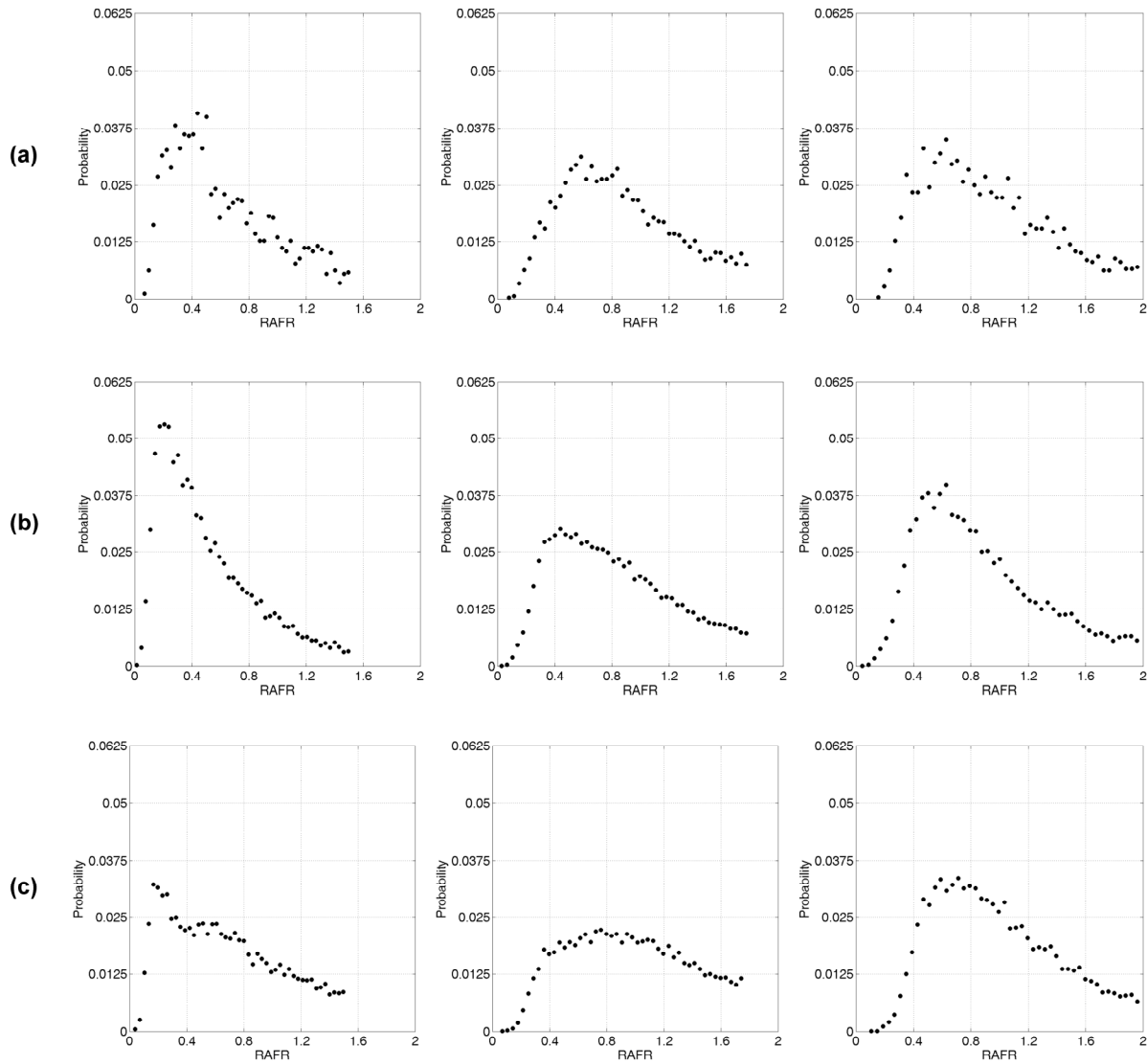
Figure 8-18 RAFR Probability Density Functions for *t*=0*CAD* at λ_{bulk}=1.5 (left), λ_{bulk}=1.75 (centre) and λ_{bulk}=2 (right) for (a) Station One, (b) Station Two and (c) Station Three.

Stations four and five exhibit *pdf*s that are markedly different to those of stations one to three and are markedly different to each other despite what would appear from the RAFR images of *Figure 8-18* to be similar regions. Station four (*Figure 8-19(a)*) shows a reduction in bulk RAFR to move the peak probability in local RAFR from ~0.7 to ~1, for a change in bulk RAFR of 1.5 to 2. Furthermore, the magnitude of the peak probability is seen to increase from ~3% to ~5.75%, increasing the kurtosis ('peakyness') of the distribution correspondingly. The distribution for station four with λ_{bulk}=2 demonstrates a significant probability that the bulk charge concentration will still be present, a probability that, at 3.75%, is comparable to encountering RAFR values of ~0.5 or ~0.9. This suggests that the

engulfment mechanisms proposed by Schefer *et al.* **[22]** are still present and that their extent, and the mixing they cause, is dependent upon bulk charge fuel concentration. Station five (*Figure 8-19(b)*), at the front of the DI jet after it has passed through the insert injected fuel, shows less marked variations with bulk RAFR changes. The two leanest bulk charges (λ_{bulk}=1.75 & 2) show similar forms to their *pdf*s, although at λ_{bulk}=1.75 the distribution rises rapidly to a peak probability of ~1.5% at a bulk RAFR of ~0.5, dropping by only ~0.5% over the range λ_{bulk}=0.5-1.75. With a bulk RAFR of two, the peak probability of ~2.5% extents over the range λ_{bulk}=0.4-0.8, before dropping steadily to a probability of ~1% at bulk RAFR, where no sudden increase in probability is observed as for station four. The most rich bulk RAFR (1.5) is observed to cause a peak probability of ~2.5% in the local RAFR at 0.3, but which is not sustained and falls to a plateau at ~1% over the range of ~0.5-1.5.
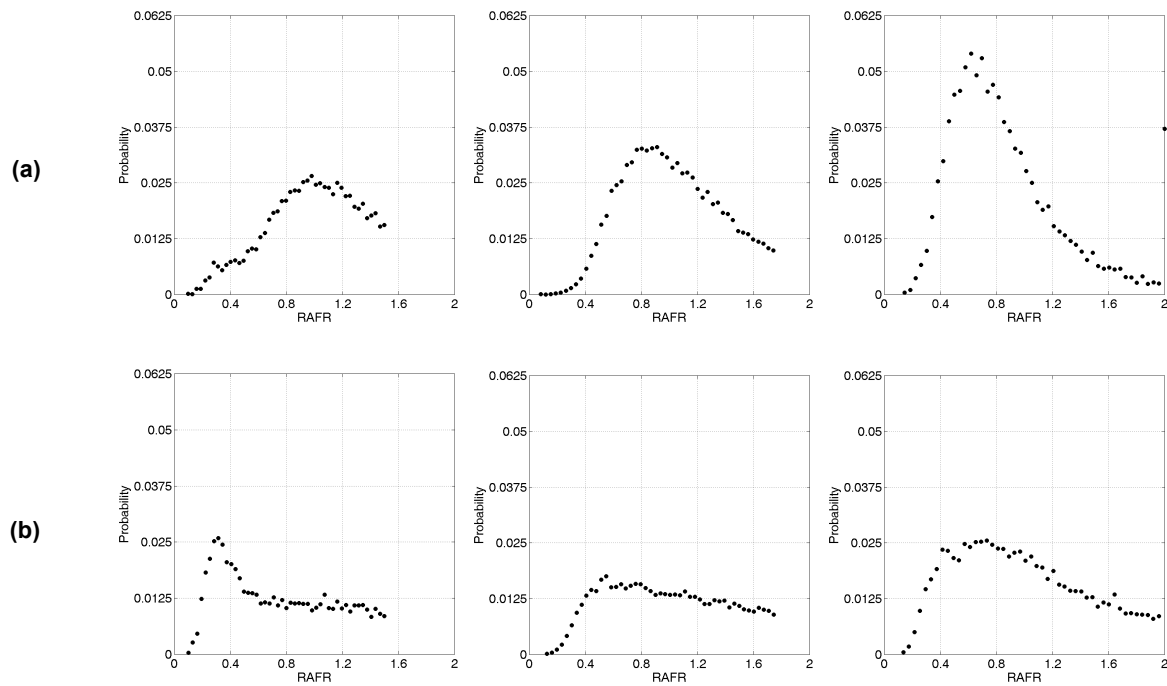
Figure 8-19 RAFR Probability Density Functions for *t*=0*CAD* at λ_{bulk}=1.5 (left), λ_{bulk}=1.75 (centre) and λ_{bulk}=2 (right) for (a) Station Four and (b) Station Five.
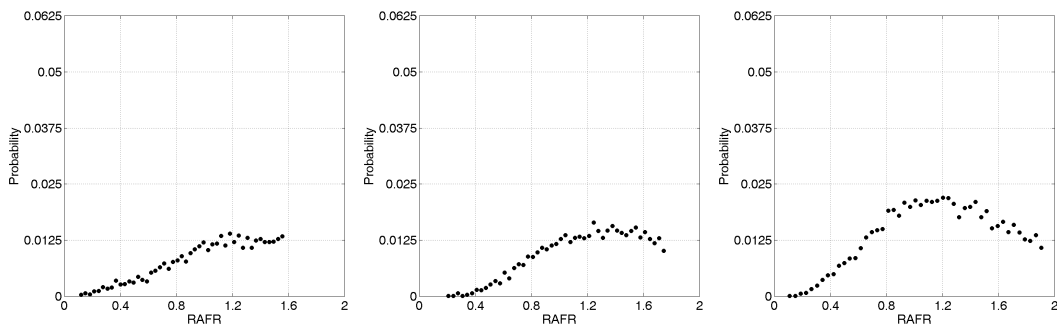
Figure 8-20 RAFR Probability Density Functions for *t*=-5*CAD* (centre) and *t*=-3.53*CAD* (left & right) at λ_{bulk}=1.57 (left), λ_{bulk}=1.75 (centre) and λ_{bulk}=1.93 (right) for Station Five.

For station five, at the two most advanced injection timings (t=-3.53 & -5CAD) (*Figure 8-20*), the RAFR probability distributions are a lot less variable than those at more retarded timings, showing a gradual increase in local RAFR from 0.1 to the bulk RAFR. The bulk RAFR is seen to be the maximum RAFR for λ_{bulk}=1.5, while for the leaner bulk RAFR cases the bulk charge serves to increase the probability of richer local mixtures, although lean of stoichiometric. The trends in the pdfs of *Figure 8-20(b)* demonstrate once more the need to match bulk RAFR with timing and the level of mixing that any given timing engenders.

Figure 8-21 shows some similar features to that of the capillary injected insert with respect to the minimum, mean and maximum RAFR that are encountered at stations one to three (*Figure 8-21(a)-(c)* respectively). In all cases the maximum RAFR is that of the bulk charge, while the mixing that takes place within the PSC insert raises the mean RAFR slightly to ~0.5-1. The exception is station one where, in the cases for λ_{bulk}=1.5 & 2, mixing has failed to fully eliminate packets of pure fuel. The need to match the bulk charge RAFR to the level of mixing at the desired spark location is once again clear, with station one showing, on average, rich mixtures for bulk charges of λ_{bulk}=1.5 & 1.57, while for λ_{bulk}=1.75, 1.93 & 2, the mean condition is close to stoichiometric. The opposite is true of station two where, from bulk RAFR=1.5-1.75, the mean RAFR is approximately stoichiometric while, for bulk RAFRs higher than 1.75, the mean condition is rich. Investigation of the station's RAFR dependence on injection timing showed no correlation, although it is apparent from *Figure 8-18(c)*, which corresponds to station three, that there is still a large range, spanning 0.8 to 1.25 at λ_{bulk}=1.75, in the expected value of RAFR for the $1mm^2$ of the station. This may be attributable to the fluctuations still present in the insert injected fuel RAFR being increased by those associated with the DI jet fluctuation maximum, which occurs slightly off-axis (*cf.§2▪2▪1*).

(a) (b) (c)
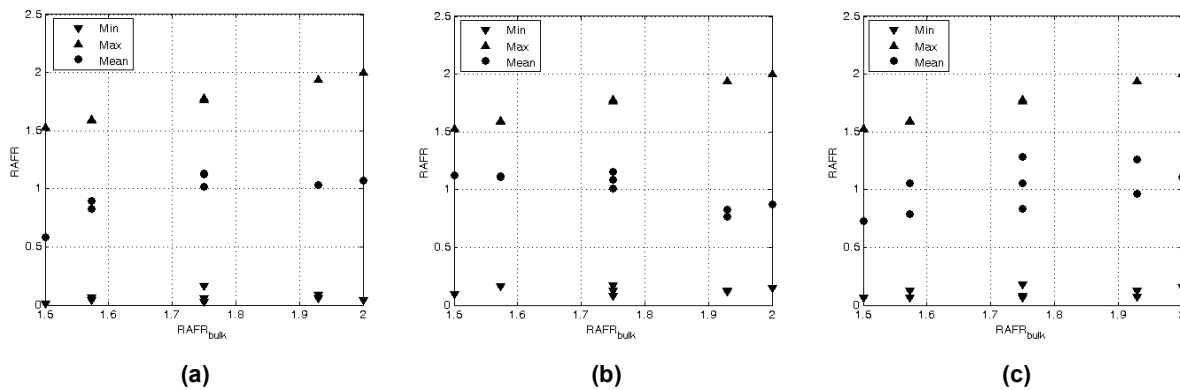
Figure 8-21 Maxima, Minima and Mean RAFR for all Insert Injected PSC Test Conditions at (a) Station One, (b) Station Two and (c) Station Three

Stations four and five (*Figure 8-22 (a) & (b)* respectively) show maxima and minima in line with those of station one to three. Station four demonstrates mean RAFR variations similar to station one, although no direct link between the two is thought to exist. The range of mean RAFRs for station four ranges from ~0.8

to ~1.2, with the leanest cases all at bulk RAFR of 1.75. At station five the mean RAFR is consistently on the lean side of, or close to, stoichiometric, covering the range ~1 to ~1.5. The data does not support an effect from the bulk RAFR, with the station RAFR appearing almost independent of bulk RAFR, and more likely to be driven by the mixing which takes place upstream as the fuel from the DI jet interacts with that of the PSC insert.

(a)   (b)
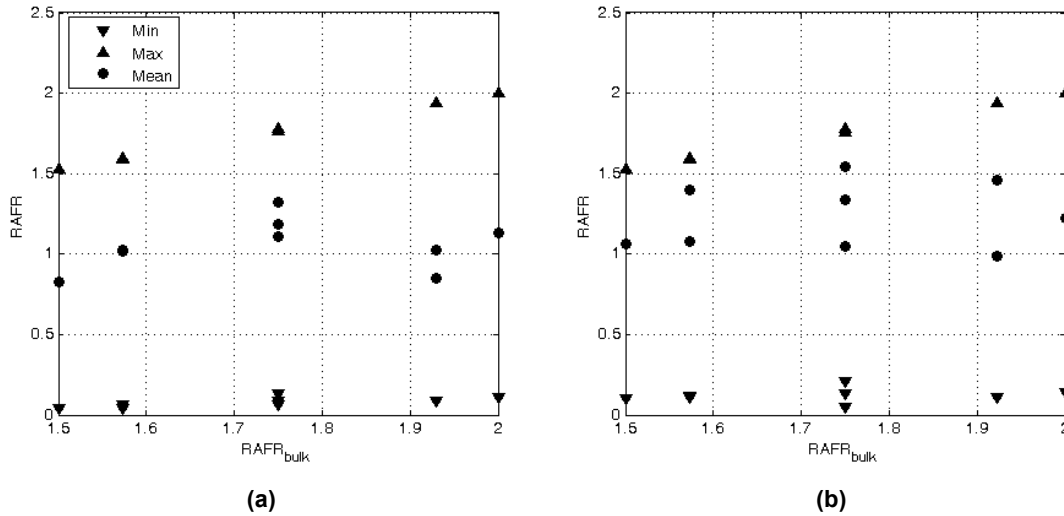
Figure 8-22 Maxima, Minima and Mean RAFR for all Insert Injected PSC Test Conditions at (a) Station Four and (b) Station Five

Figure 8-23 shows the mean RAFR against the relative injection timing for stations one and five (no other stations showed a dependency upon injection timing, nor did any on bulk charge RAFR). An increase from a mean RAFR of ~0.8 to ~1.3 with a 10*CAD* advance in relative DI injection timing (regression coefficient 0.575) was observed at station five, while the same timing change caused a decrease in mean RAFR from ~1.55 to ~1 for station five (R^2=0.831). It can be seen from this that the mixing generated by the interaction of the PSC and DI jets has distinctly different effects upon different locations within the cylinder and, as such, mixing must be considered in conjunction with the specific location of the spark. The timing must be assessed in combination with an assessment of the desired local RAFR, and the extent to which a rich mixture is desirable for its increased combustion strength.

For the insert injected PSC jet, the probability that any given pixel within the test station area (for all realisations) will fall within the flammability limits of methane for the nine test conditions is shown in *Table 8-4*. Stations one to three show similar trends with the highest probabilities of a flammable mixture being found at about λ_{bulk}=1.75, with a 6-10% increase in the probability from station one to three. The data on bulk charge effect did not support more firm conclusions beyond this, with the most apparent second order polynomial returning regression coefficients less than 0.5 for all three stations. Injection timing offered no demonstrable effects upon forming a mixture that falls within the flammability limits.
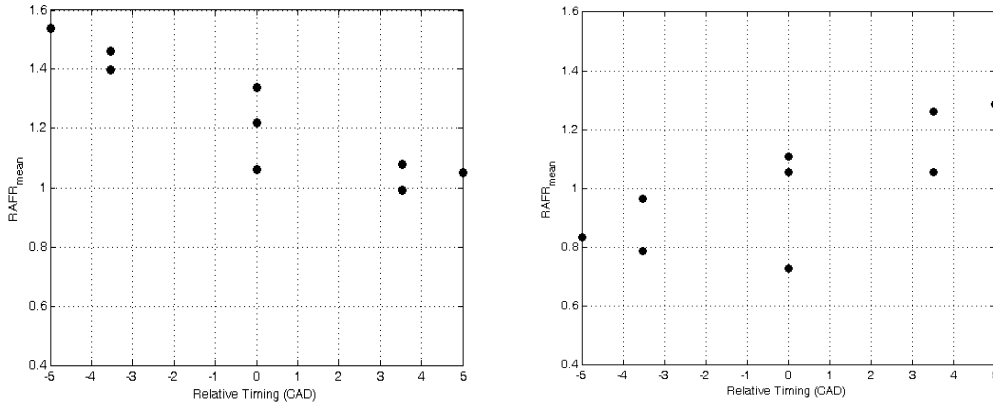
Figure 8-23 Effect of Relative injection Timing on Mean RAFR for Station One (left) and Station Five (right)

The increase in the probability of the mixture falling within the flammability limits of methane was calculated for stations one and five, since they are at locations comparable to those of the capillary injected PSC-DI event. It is clear from *Table 8-5* that the increase is far from uniform for the different bulk charge RAFRs and injection timings, and showed no correlation to either timing or bulk charge. The two locations do show different general responses however, with station one (immediately after the point of PSC injection) seen to exhibit two-and-a-half to six-fold increases in the probability of encountering a flammable mixture for the cases, in which λ_{bulk}=1.75-2, while at low background RAFR the increases are small (13%-95%). At station five, the point after the DI jet has passed through the PSC jet, the insert is seen to offer only very small increases in the probability of encountering a flammable mixture (3-8%) for bulk RAFR of 1.75 to 1.93, while in all other cases there is a reduction in the probability of 9-37%.

λ_{bulk}	Relative Timing (CAD)	Probability Within Flammability Limits				
		Stn. 1	Stn. 2	Stn. 3	Stn. 4	Stn. 5
1.5	0	0.36	0.27	0.38	0.61	0.31
1.573	3.53	0.43	0.47	0.50	0.67	0.49
1.75	5	0.54	0.61	0.64	0.69	0.50
1.937	3.53	0.63	0.61	0.58	0.56	0.62
1.75	0	0.57	0.52	0.63	0.65	0.55
1.937	-3.53	0.44	0.39	0.53	0.59	0.57
2.0	-5	0.34	0.31	0.57	0.73	0.40
1.573	-3.53	0.43	0.37	0.38	0.68	0.32
1.75	0	0.51	0.48	0.52	0.71	0.40

Table 8-4 Probability of Mixture Falling Within Flammability Limits for Insert Injected PSC Jet with DI at Stations One to Five

λ_{bulk}	Relative Timing (CAD)	Increase in Probability Station Mixture is Within Flammability Limits			
		Stn. 1		Stn. 5	
		---	% Increase	---	% Increase
1.5	0	0.04	13%	-0.19	-38%
1.573	3.53	0.13	43%	-0.05	-9%
1.75	5	0.39	260%	-0.08	-14%
1.937	3.53	0.54	600%	0.02	3%
1.75	0	0.44	338%	0.04	8%
1.937	-3.53	0.33	300%	0.02	4%
2.0	-5	0.21	162%	-0.15	-27%
1.573	-3.53	0.21	95%	-0.19	-37%
1.75	0	0.36	240%	-0.2	-33%

Table 8-5 Increase in Probability of Mixture Falling Within Flammability Limits for Insert Injected PSC Jet Over Capillary Injected Jet at Stations One and Five

It can be seen from *Figure 8-24* that the injected mean fuel concentration lies almost wholly within the flammability limits of methane, and is in the upper half of the range. The regions of lower volume fraction are confined to the weak bulk charge; even the shear layer of the DI jet shows fuel volume fractions of ~ 10%, while the spatial extent of those regions is constant at ~1*mm* regardless of injection timing or bulk charge RAFR. In all cases the PSC injected fuel appears to have similar volume fraction distributions, namely an inner core with fuel concentrations in the range 10-13%, reducing at the edges to ~8%. Of most note is the effect of the bulk charge RAFR upon the core of the DI jet. In the cases with RAFR from 1.5 to 1.57 (left-hand column of *Figure 8-24*) the DI core is fully within the flammability limits while, as the bulk charge is leaned, the extent of the core that falls outside the flammability limits increases (more black in right-hand column than centre). This seems at first counter-intuitive, the mixing in of a more dilute mixture should dilute the DI core more than a richer bulk charge, as was seen with the capillary injected PSC & DI combination. In the capillary injected PSC case, it was noted that the PSC injection maintained its structure and had little effect upon the DI jet upstream of the injection point. In the case of the insert injected PSC jets the mixing is over a larger area and affects the mixing and entrainment that the DI jet undergoes. It is, therefore, necessary to consider the mechanisms driving the mixing. The larger concentration gradient between the jet core and the bulk charge at high bulk RAFRs would drive greater diffusion; yet, since air has both a higher viscosity and molecular weight than methane, it is reasonable to expect that at higher RAFRs there is less viscous mixing taking place. The data from the current study are not able to support a comprehensive assertion as to whether this is the case, and assessment of the local Prandtl number would need to be made, which could be done through either

computational fluid dynamics or a combination of laser based experiments to assess local fluid motion and temperature (which would then need to be related to the diffusivity of methane into air). Consideration of the flow field would also then allow an assessment of the local strain rate, an important factor in both ignition and flame propagation, and its relation to the local scalar diffusion rate.

Figure 8-25 shows the probability of encountering a mixture within the flammability limits of methane, and it shows some clear differences to that of the capillary injected case (*cf. Figure 8-13*). The less strong the bulk charge to lower the probability of encountering a flammable mixture in the core of the DI jet, the probabilistic data confirming the observations of the mean case (*Figure 8-24*). The mixed region of the PSC and DI jets shows probabilities which relate closely to the mean mixture concentration. The higher the concentration the higher the probability of having a flammable mixture, although there is no clear direct correlation. In all cases the mixed region has probabilities of being with the flammability limits in the range 0.5-0.8, although where there is still a richer core present (the three cases of λ_{bulk}=1.5, and t=-3.53 with λ_{bulk}=1.57 & λ_{bulk}=1.93) within the mixed region this probability drops to 0.4-0.5. In general the insert has been seen to raise the chance of encountering a flammable mixture from ~0.5 to ~0.8, though more significantly the are of which a flammable mixture can be expected is an order of magnitude larger.
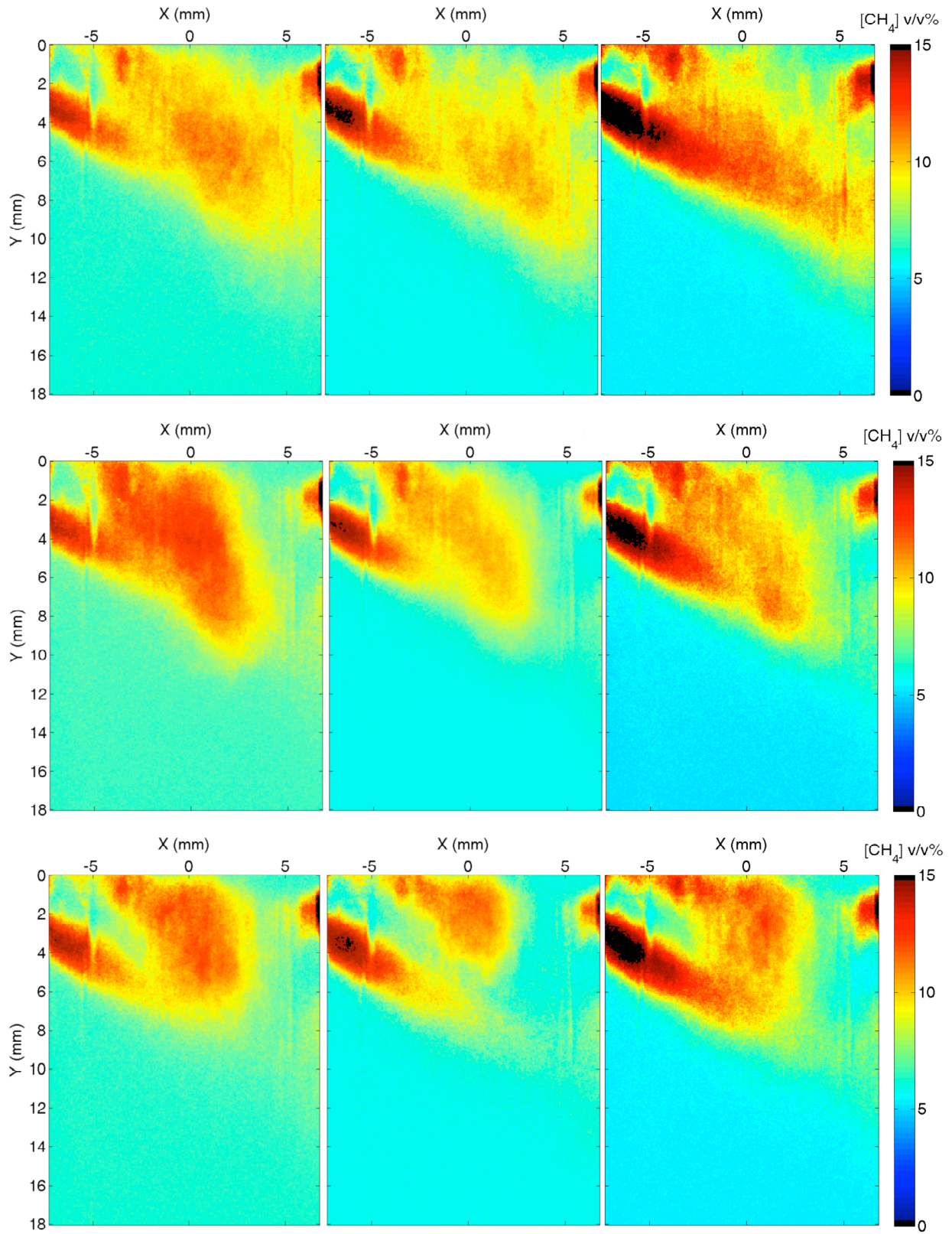
Figure 8-24 Insert Injected PSC with DI Jet Fuel Concentrations by Volume.
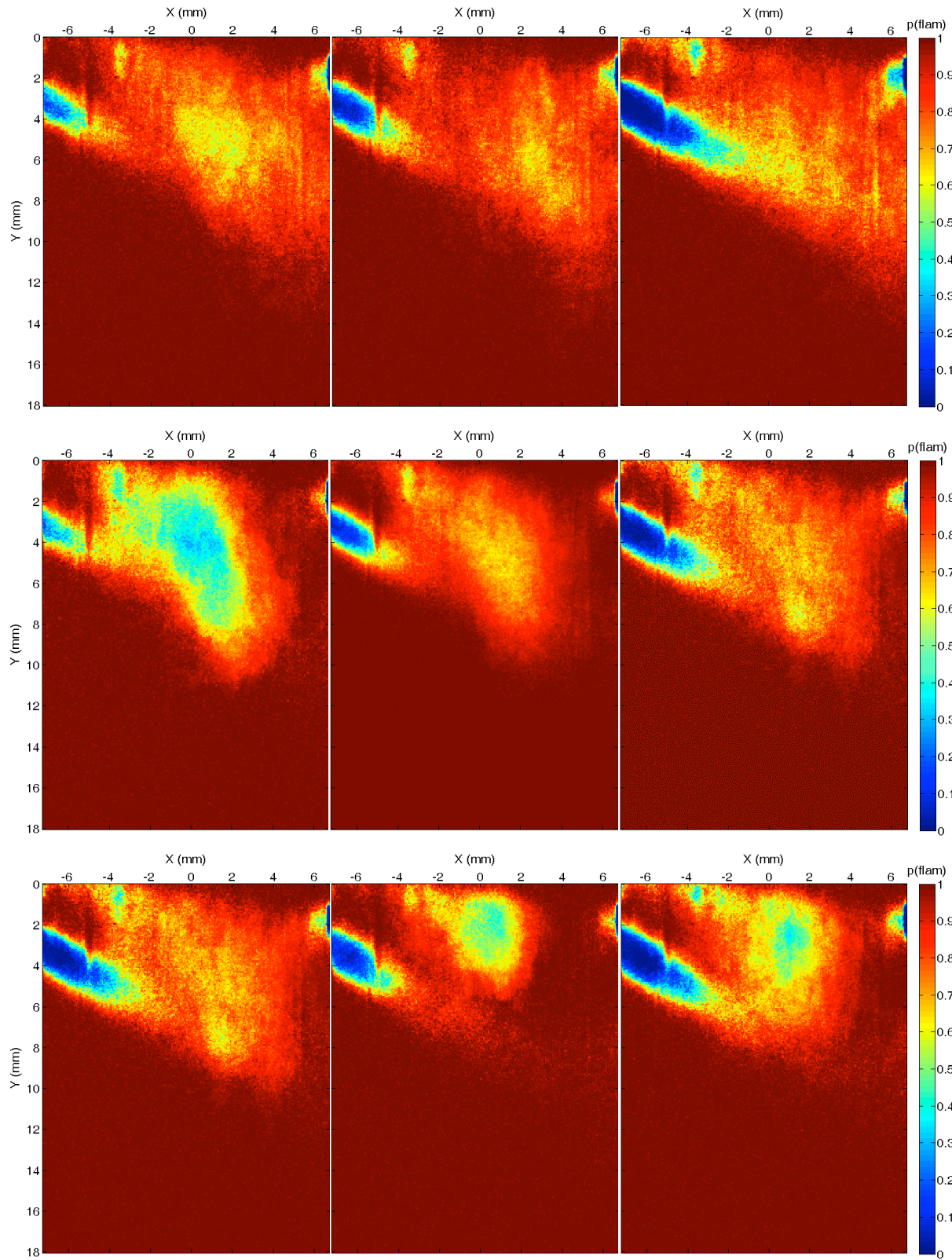
Figure 8-25 Probability of Encountering a Mixture Within the Flammability Limits of Methane for Insert Injected PSC

As was seen from the scalar dissipation data for the capillary injected PSC, ignition was unlikely since the dissipation rate was above that which can support combustion. However, the insert is shown in *Figure 8-26* to lower the scalar dissipation rate to values well below the critical extinction value of $20.6s^{-1}$ **[403]**, and values which are an order of magnitude lower than the capillary injected PSC jet. The difference is large enough that the dissipation rate may be too low to support a robust combustion, and is in need of more investigation. The dissipation, as may be expected, has a spatial distribution almost identical to that of the r.m.s. fluctuations **[402]**; however, it must be cautioned that the out-of-plane component of the scalar dissipation rate cannot be assessed. This was of little concern in the capillary injected jet since, if desired, it could be assessed to be similar to that in *x*-direction, yet for the insert injected fuel there is no way to ascribe a value to the out of plane component. To circumvent this problem, a series of images across the section of the injected fuel would need to be made, and on two planes.
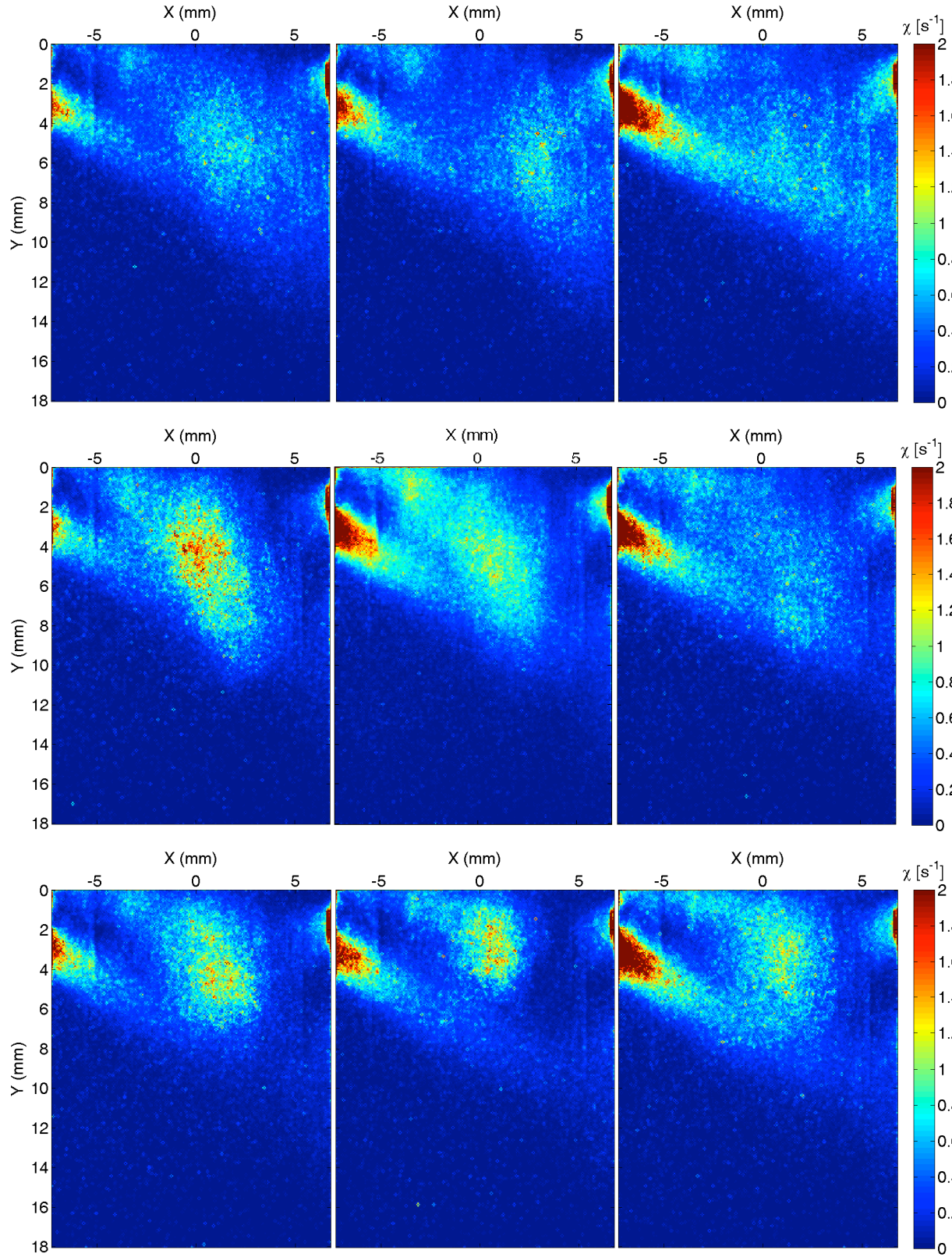
Figure 8-26 Scalar Dissipation Rate for Capillary Injected PSC with DI Jet

8▪6 CONCLUSIONS

Chapter 8 has presented the findings of repeating the test matrix presented in *Chapter 7* with a smaller image area that contains more detail of the PSC-DI interaction, and with higher fidelity LIF signals. Comparison has been made between a PSC injection delivered from a capillary tube and one from a PSC sparkplug 'insert'.

The interaction of the DI jet with that of the capillary injected PSC jet is seen to maintain the structure of the PSC injection and perturb the DI jet only locally to the PSC jet. The mixing is still confined to shear layers of the DI jet and is unaffected by the bulk charge RAFR, yet the bulk RAFR is seen to alter the mixture distribution in the head structure of the DI jet, increasing the area covered by an approximately stoichiometric composition. In contrast to the capillary injected PSC jet, that of the insert jet was readily altered by the DI jet, since the momentum of the insert injection was lower than that of the capillary injection, resulting in the individual insert jets being amalgamated into a single almost homogeneous region. The head vortex structure of the DI jet was almost fully supplanted with the amalgamated distribution. The quasi-homogeneous mixture had a composition close to stoichiometric and may burn vigorously enough to inflame a lean bulk mixture or the DI jet, although this depends on a wide range of local and global in-cylinder conditions, including strain. The insert showed, on average, no discernable differences in structure as a result of the approaching DI jet, yet for some individual realisations the capillary injected PSC jet showed clear deflections.

The potential for the capillary injected PSC to be ignited was considered with respect to the fuel concentration gradients. The shear layer in the DI jet was an order of magnitude thicker than that of the PSC jet, although it was proposed that the effects of the background charge was not solely to alter the concentration gradients but to also reduce the fluctuations in RAFR, increasing the likelihood of encountering a flammable mixture. This is of particular importance, since the work of Schefer *et al.* **[22]** has been drawn on to provide insight into the entrainment mechanisms at work. The entrainment of the bulk charge was not likely to be uniform or steady; mass 'engulfment' being more likely with the coherent structures giving rise to large local variations in mixture AFR that may vary significantly from the experimental average condition. The probability density functions for a range of stations within the mixture were presented, all of which displayed the full range of RAFR values from pure fuel to bulk mixture concentration, even for locations where the experimental average suggested these concentrations were not possible. In many cases the overall probability of encountering a flammable mixture throughout the area of the station was less than 50%. There was found to be a marked similarity in the RAFR *pdf*s for the locations at which the DI centreline interacts with the PSC jet and the DI head vortex after it had passed through the PSC jet. Both relative injection timing and bulk RAFR were found to have little effect upon the

mixture distribution. The discussions presented on the likelihood of ignition were based upon fuel concentration and scalar dissipation rate, which was deemed excessive for the central portion of the PSC jet. However, the absence of strain rate data precludes any firm assessments of the ignition probability, and must be a priority for future works.

The insert injected mixture distribution was compared to that of the PSC to offer some assertions as to whether it was more likely to be ignited, and the potential for it to inflame a lean mixture or the DI jet. As with the capillary injected PSC, the more rich the bulk RAFR the greater the reduction in observed RAFR gradients. The spatial extent of the insert fuel mixing was larger and altered the DI core to yield lower gradients than would otherwise have been expected. The relative timing of the injections altered the structure of the resultant mixture with more advanced timings moving the location of the RAFR fluctuations off the centreline and reducing their level. The relative timing and bulk charge RAFR combined to control the mixing level and subsequent mixture distribution and fluctuation levels. The *pdfs* of RAFR for the stations considered suggest that close to the firedeck the mixture is governed by the mixing that takes place within the insert, not the cylinder, and that mixing further into the cylinder is stepped in nature and exhibits thresholds in the extent to which it takes place. It appeared that the engulfment mechanism was still present, and that its extent was dependent upon bulk charge fuel concentration, potentially due to changes in the physical properties of the bulk gas, although an assessment of the local Prandtl number would be needed to offer greater understanding. The insert acted to increase the probability of encountering a mixture within the flammability limits of methane but at all stations the probability was still considerably below 100%. The scalar dissipation rate was an order of magnitude lower with the insert injected PSC, and was low enough to deem further research necessary to understand if the burn of the PSC charge is robust enough to inflame a lean homogeneous charge or DI jet, although the lower strain rates were considered beneficial to ignition.

Chapter 9 ERROR AND UNCERTAINTY ANALYSIS

9▪1 INTRODUCTION

Chapter 9 addresses some of the most significant uncertainties associated with the experimental technique used. The chapter begins by demonstrating that the lack of consideration of buoyancy and its effects in *Chapters 7 & 8* is well-founded since examination of the jet Richardson number show the injection to be momentum dominated. The chapter moves on to assess shot invariance for the experimental data, and using quintile-quintile plots and data entropy techniques assess the extent of experimental convergence. Finally, an uncertainty analysis is conducted, something that has not been reported in LIF fuel concentration studies to date.

9▪2 DISCOUNTING BUOYANCY

The discussions presented in *Chapters 8 & 9* make no reference to the role of buoyancy. This is because the jets, both DI and PSC, are deemed to be momentum dominated. The Reynolds number for the DI injection is $\sim44\times10^3$, which although clearly turbulent does not in itself negate the need to consider buoyancy. Following the shock and associated pressure recovery the DI jet has a specific buoyancy, B_0, and specific momentum, M_0, of $0.0425m^4/s^3$ and $5.23m^4/s^2$ respectively. These yield a Richardson number of 6.97×10^{-4} and a mixing length, l_m, of $16.79m$ (§2▪2▪1, p.19). Wang and Law [40] suggest that for a jet $z/l_m <0.6$, and with a cylinder bore of 4" on the RCM it is possible to conclude that buoyancy at no stage need be considered in the analysis. A similar analysis of the insert injected PSC jets is more difficult since the state of the jets as they enter the cylinder is not known. Assuming the PSC jets to also be choked at the point of injection, they must share the same momentum flow rate as the DI injector, and are injecting into the same environment so must share the same buoyancy value. Based on this, for the insert to generate a z/l_m value less than 0.6 requires velocities on the order of 1.64m/s, which it can safely be assumed are not encountered within the field view at the timings used in the current research.

9▪3 CYCLIC INVARIANCE

To ensure that one image realisation was not related to the previous, image-to-image variation was assessed. The procedure followed the *de-facto* industry standard of return maps [405-408], which determine the correlation, if any, between an observation, x, and one off-set by the return lag l (*i.e.* $x+l$). The correlation is assessed using the Pearson Product-Moment of *Eq9.1*

$$R = \frac{E\left[(x - \mu_x)\left((x+l) - \mu_{x+l}\right)\right]}{\sigma_x \sigma_{x+l}}$$

Eq. 9.1

where the numerator is the covariance between the distributions for the images and their off-set counterparts. The Pearson Product-Moment lies in the range $-1<R<1$, where $R\sim0$ suggests no correlation and $R\pm1$ a strong correlation (the value of R represents the extent of the correlation and the sign the direction but not slope of that correlation). The Pearson Product-Moment for the central condition of the test matrix was evaluated at locations one, three and five for the image intensity averaged over the $1mm^2$ area of each location., with a return lag of one.

Background Charge RAFR	Stn. 1	Stn. 3	Stn. 5
1.5	0.1747	0.0559	0.1161
1.75	-0.1007	0.0149	-0.0312
2.0	0.1688	0.0446	-0.0439

Table 9-1 Pearson Product-Moment For Capillary Injected PSC DI Images

It is accepted that absolute values in the range 0-0.09 indicate no correlation and that those in the range 0.1-0.3 represent only a low correlation. It is evident from *Table 9-1* that there is little, if any, correlation between one data point and the previous one. The RCM results are thus deemed cyclically invariant.

9▪4 EXPERIMENTAL CONVERGENCE

The stochastic nature of the turbulence injection events means that a statistical approach must be taken to assess the significance of the experimental findings. The central limit theorem has two significant implications in this respect: first that a sample of more than 30-50 realisations should have a mean and standard deviation that represent the population mean and standard deviation; and secondly that beyond this value the distributions of any given set of realisations used to calculate the final distribution become less important and the distribution product will itself be normally distributed. With this in mind, it can be expected that pixel values at any location within the jet will tend towards a normal distribution for the 51 experimental realisations. Once a normally distributed intensity is reached for all pixels, a converged experimental image can be assumed in which the average image intensity well represent the population for all cases.

Figure 9-1 shows quintile-quintile plots for the mean pixel count of station one and station three for the capillary injected PSC-DI event, with background charges of λ=1.5, 1.75 and 2 (*Figure 9-1(a)*, *(b) & (c)* respectively). The data shows marked curvature away from the line both within the interquartile range (solid line in *Figure 9-1*) and for the upper and lower quartiles (broken lines), thus indicating a significant deviation from normality. The case of station one (*Figure 9-1(b),* left) with a background charge of $\lambda=1.75$ is the notable exception. The conformity of this location to normal distribution is composed of two facets. The first is that this data is plotted from the central condition of the test matrix and as such comprises 153 repeats not the 51 repeats of *Figure 9-1 (a)* and *(c)*; and furthermore, of the two locations presented for this case the fluorescent intensity (pixel count) is higher and would be expected to be more normally distributed than the lower count intensity of the downstream location of station three.
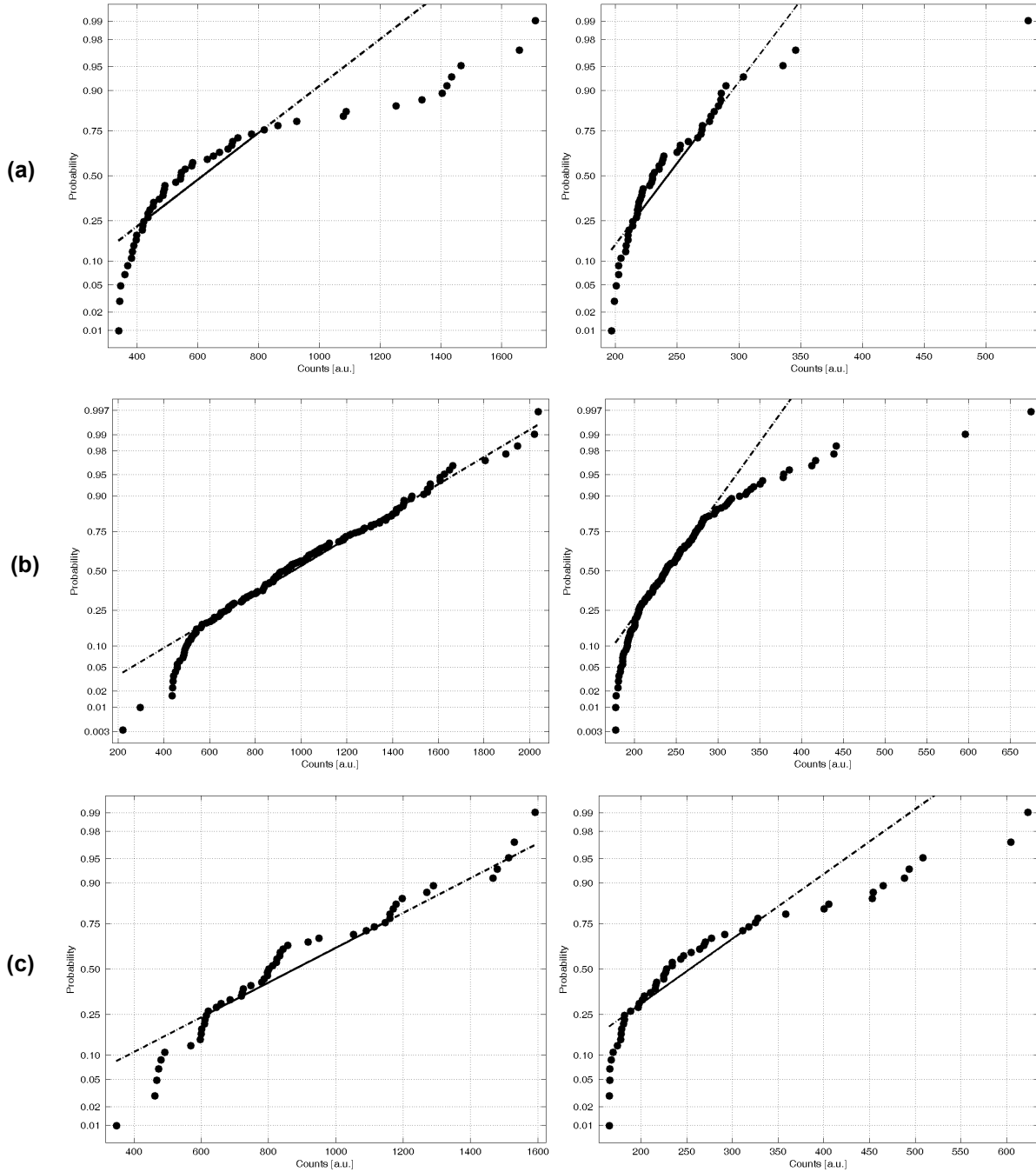
Figure 9-1 Quintile-Quintile Plots for Mean Pixel Intensity at Stations 1 (left) & 3 (right) for Capillary Injected PSC-DI Event with Bulk Charge RAFR of 1.5 (a), 1.75 (b) and 2.0 (c)

The insert PSC-DI data shows better agreement to normality (*Figure 9-2*), with the largest deviations from linearity in the upper and lower quartiles, suggesting that it is the tails of the data distribution that do not conform to the normal distribution. In an attempt to quantify the significance of the deviation from normality upon the experimental results some insight was sought from information theory.
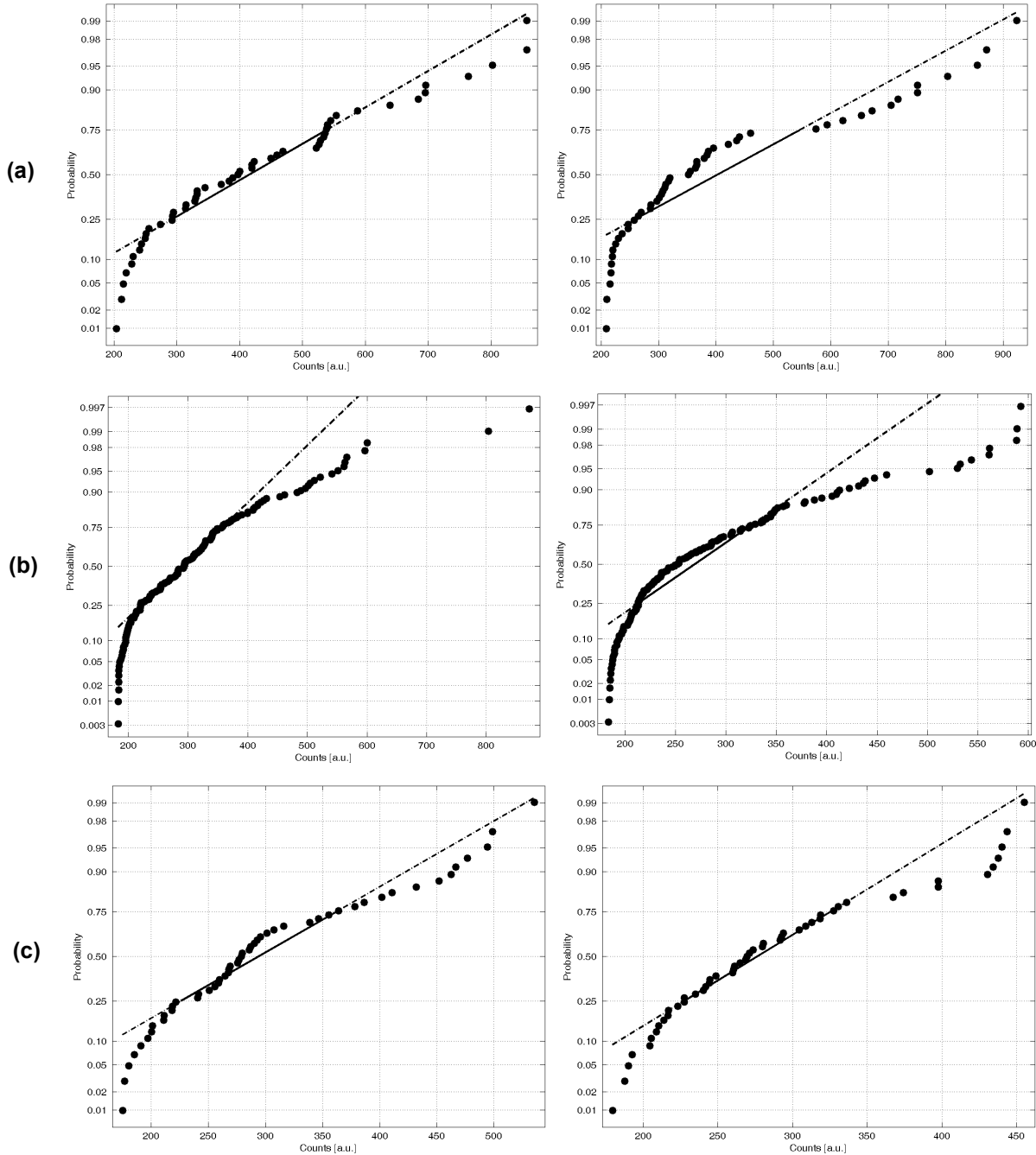
Figure 9-2 Quintile-Quintile Plots for Mean Pixel Intensity at Stations 1 (left) & 3 (right) for Insert Injected PSC-DI Event with Bulk Charge RAFR of 1.5 (a), 1.75 (b) and 2.0 (c)

9▪4▪1   INFORMATION THEORY

Any probability distribution or set of experimental data has, inherent to it, an amount of uncertainty. The use of 'entropy' and information theory are an attempt to quantify and account for this uncertainty. The concept of entropy is used, through its maximization, to asses information accuracy. When entropy is

maximized (within certain constraints) the bias is reduced to a minimum. Any increase in certainty (a reduction in bias) would require the application of further information.

Based only on partial information (often *E(x)* or a distribution of event probabilities) one seeks the least biased distribution or, as Jaynes describes it, the distribution that is *maximally non-committal* [409]. Shannon [410] suggests a measure of entropy of any distribution according to *Eq9.2*

$$H_n(p_1, p_2, ..., p_n) = -\sum_{i=1}^{n} p_i \ln p_i \qquad \text{Eq. 9.2}$$

which was subsequently shown to be a specific case of any entropy measure which must be of the general form $-k\sum_{i=1}^{n} p_i \ln p_i$ [411] in which *k* is a positive constant. It is the function *H* which must then be maximized to yield expressions for p_i. In the absence of any constraints the maximization is degenerate, yet it is always possible to apply the known constraint that for *n* trials *Eq9.3* must be true.

$$\sum_{i=1}^{n} p_i = 1 \qquad \text{Eq. 9.3}$$

When maximised *Eq9.2* becomes:

$$\hat{H}_n = \sum_{i=1}^{n} \frac{1}{n} \ln \frac{1}{n} = \ln n \qquad \text{Eq. 9.4}$$

with

$$p_1 = p_2 = ... = p_n = \frac{1}{n} \qquad \text{Eq. 9.5}$$

the *uniform distribution*. The implication of this result is that *H* can be taken as a numerical measure of uncertainty ranging from a minimum of 0 (maximum information, minimum bias) to a maximum of *ln(n)* (minimum information, maximum bias).

In many cases there is extra information available beyond that of *Eq9.3*. A prior distribution may be assumed whereby

$$p_1 = \alpha_1; \ p_2 = \alpha_2; \ ...; \ p_n = \alpha_n$$

in which case Shannon's entropy measure is replaced with the Bayesian entropy, *B*,

$$B(p) = -\sum_{i=1}^{n} p_i \ln \frac{p_i}{\alpha_i / \alpha_i^{\min}} \qquad \text{Eq. 9.6}$$

where $\alpha_i^{\min}$ is the minimum of the values in the set $\alpha_i \in \Re > 0$. Kapur [411] outlines the method by which the entropy of any given distribution may be calculated. For the current work the maximum entropy probability distributions (MEPD) of most concern are those of the normal and Poisson distributions; *Table 9-2* shows equations for the MEPD of each.

Distribution	Entropy (*nats*)	
Gaussian (non-zero mean)	$\ln(\sigma\sqrt{2\pi e})$	**Eq. 9.7**
Poisson	$\lambda(1 - \ln \lambda) + e^{-\lambda} \sum_{z=1}^{\infty} \dfrac{\lambda^z \ln z!}{z!}$	**Eq. 9.8**

Table 9-2 Maximum Entropy for Non-zero Mean Normal Distribution, after [411]

Assuming a normal prior distribution the Bayesian entropy for the signal intensity images was calculated for two representative cases from the text matrix- those at zero CAD relative injection timing and bulk charge RAFRs of 1.5 and 1.75. The entropy levels where normalised against the MEPD value for the normal distribution as given by *Eq9.7*, yielding *Figure 9-3* (the insert injected corollaries to these cases were very similar in nature). It is immediately apparent that there is a large range in the normalised entropy level from about 0.1 to about unity (no pixel is identically one), representing locations where there is, respectively, little information and almost full information- *given the assumption of normally distributed data.* The regions with highest information are those with the highest intensity and *vice versa*, yet the information is not a direct result of the pixel intensity. The transition in entropy level is attributable to the image signal-to-noise-ratio at the intensity level. At low intensities, as was seen in *§5▪10*, the image is camera noise limited while at higher intensities the SNR is almost shot-noise limited. Camera noise is governed by Poisson statistics while shot-noise can be expected to be normally distributed, and it is the transition from one distribution to another that is displayed by the entropy range. This is confirmed by *Figure 9-4,* which shows the result of repeating the entropy calculation and normalisation process above with a Poisson prior distribution. The uniform background, which is ostensibly shot-invariant, is almost *maximally non-committal*; while in areas where a normal distribution predominates (the jets) there are very low information levels. It is interesting to note that in both cases the right hand image, which is composed of 153 individual images compared to the 51 of the left-hand images, shows little improvement in entropy level (information). This would suggest that increasing the number of experimental realisations beyond 51, assuming a normal or Poisson prior distribution does not substantially reduce the uncertainty. However, it is the assumption of any prior distribution that precludes the assertion. The very reasons used to specify central repeats in response surface modelling and central composite test matrices implies that there is more information gained by having more realisations, yet this information can only be realised with the correct assumption about the prior distribution. The form that the 'correct' prior distribution should take when in transition from a camera to shot noise limited case is in need of further research, to allow a full assessment of the extent to which the non-normality shown in the quintile-quintile plots is of concern.
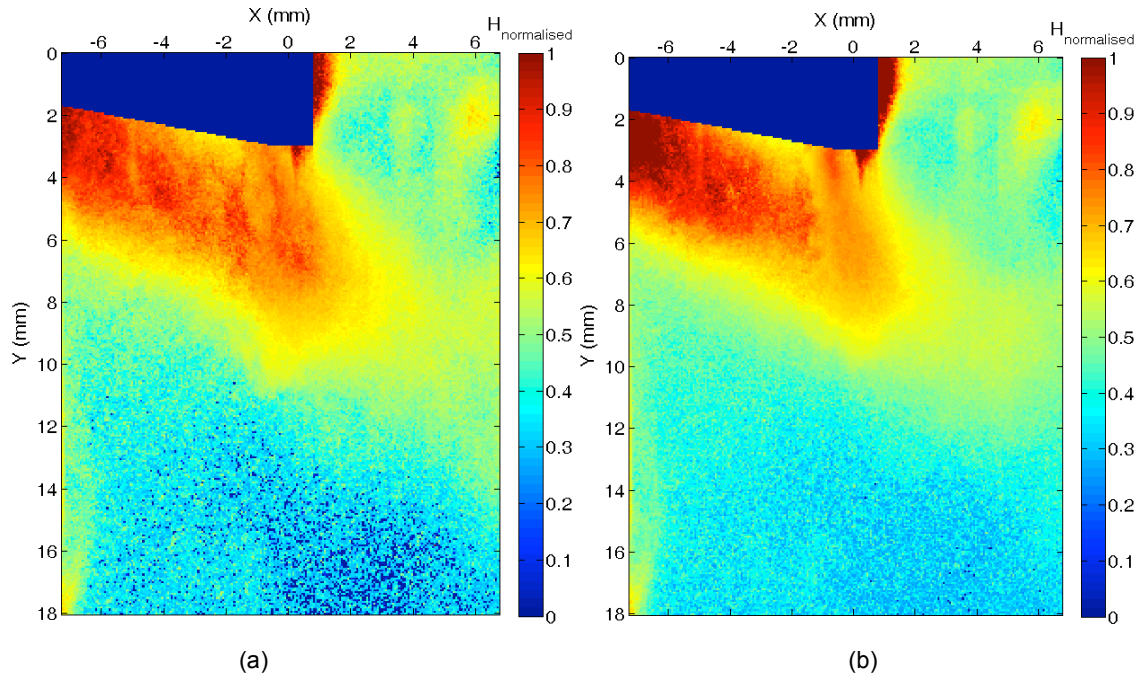
Figure 9-3 Normalised Entropy Images of LIF Intensity for Capillary Injected PSC with DI at *t*=0*CAD* and (a) RAFR = 1.5 and 51 Repeats, and (b) RAFR = 1.75 and 153 Repeats Based on a Normal Distribution.
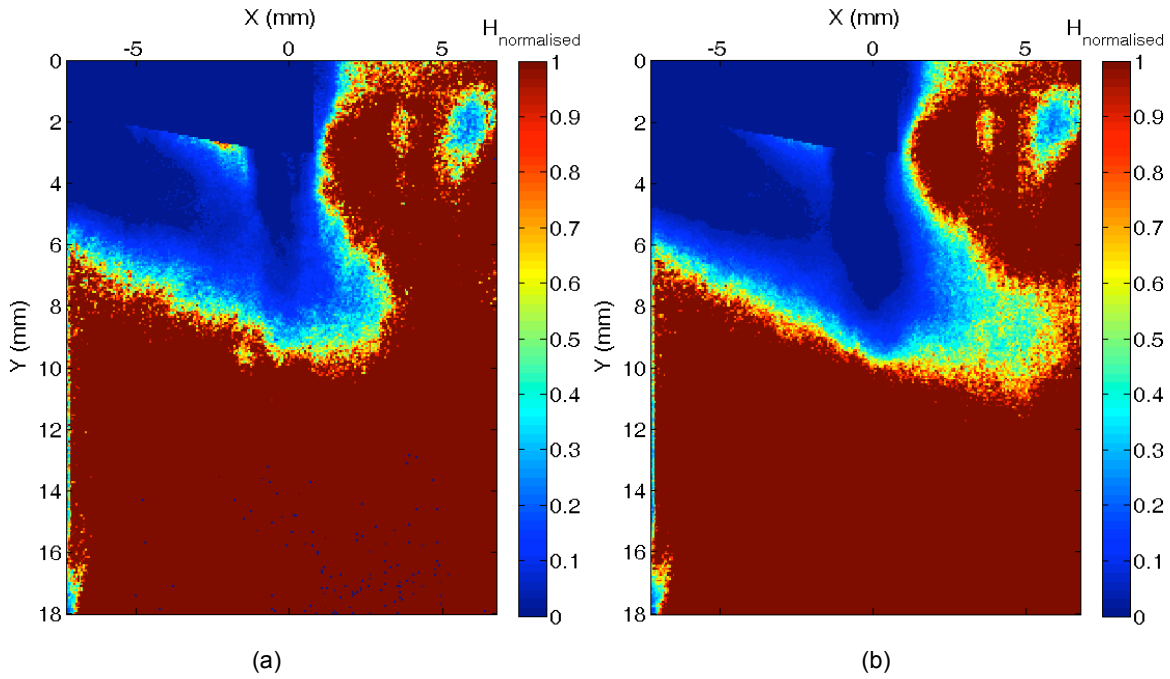
Figure 9-4 Normalised Entropy Images of LIF Intensity for Capillary Injected PSC with DI at *t*=0*CAD* and (a) RAFR = 1.5 and 51 Repeats, and (b) RAFR = 1.75 and 153 Repeats both Based on Poisson Statistics

9▪5 UNCERTAINTY ANALYSIS

In reviewing the literature the author was unable to find a LIF fuel concentration study that detailed the uncertainty in the concentration measurements. Following the approach recommended by the Journal of

Fluids Engineering **[412]** the total uncertainty, w, in a parameter is given by the sum in quadrature of the instrument error, B, and the 95% confidence interval of the parameter reading, P, *viz.*:

$$w = \sqrt{B^2 + P^2}$$

Eq. 9.9

Should a parameter, Y, be made up of several measured variables $(x_1, x_2, ..., x_n)$ the errors in each are propagated according to **[413]**, *Eq9.10*:

$$w_H = \sqrt{\left(\frac{\partial Y}{\partial x_1} w_1\right)^2 + \left(\frac{\partial Y}{\partial x_2} w_2\right)^2 + ... + \left(\frac{\partial Y}{\partial x_n} w_n\right)^2}$$

Eq. 9.10

An assessment of the uncertainty in RAFR value was made according to these principles. Given the calibration line of *Eq7.1*, an assessment of the uncertainty in the regression coefficients was made by finding the equation of the lines with the lowest and highest slopes that still fell within the 95% confidence interval of the calibration data. The instrument error of *Eq9.9* was deemed negligible. This method provided the uncertainty for the regression coefficients shown in *Eq9.11*.

$$S_f = 2217 \pm 47 \left(\frac{N_{fuel}}{N_{total}}\right) + 56 \pm 2.6$$

Eq. 9.11

Given that the RAFR is calculated from signal intensity by *Eq5.7*, repeated here for convenience as *Eq9.12*, application of *Eq9.10* yields an error in RAFR, w_{RAFR}, given by *Eq9.13*.

$$RAFR = \frac{P_{total}/P_{fuel} - 1}{AFR_{stoic}\left(\dfrac{MW_{fuel}}{MW_{air}}\right)}$$

Eq. 9.12

$$w_{RAFR} = \left\{\left(\frac{\partial(RAFR)}{\partial\left(P_{total}/P_{fuel}\right)} w_{P_{total}/P_{fuel}}\right)^2 + \left(\frac{\partial(RAFR)}{\partial(AFR_{stoic})} w_{AFR_{stoic}}\right)^2\right\}^{1/2}$$

Eq. 9.13

For each pixel within the intensity image the uncertainty, $w_{Ptotal/Pfuel}$, in the pressure quotient (equivalent to the inverse of fuel number density) was calculated by evaluating *Eq9.11* for the pixel and then evaluating the difference between it and the 'standard' value with no regression uncertainty. The 95% confidence interval for the AFR$_{st}$ value of *Table 5-3* was not available, although its coefficient of variation (CoV) was. Assuming a normal distribution to the AFR values in the sample and taking 3σ as a proxy for the $CI_{95\%}$ the error is the AFR$_{st}$ value was evaluated by *Eq9.14*. The results of evaluating *Eq9.13* for the three cases of the insert injected PSC test matrix with zero relative injection timing are shown in *Figure 9-5*. Variability in the molecular weight of the fuel was neglected.

$$w_{AFR_{st}} = 3 AFR_{stoic} \times CoV$$

Eq. 9.14
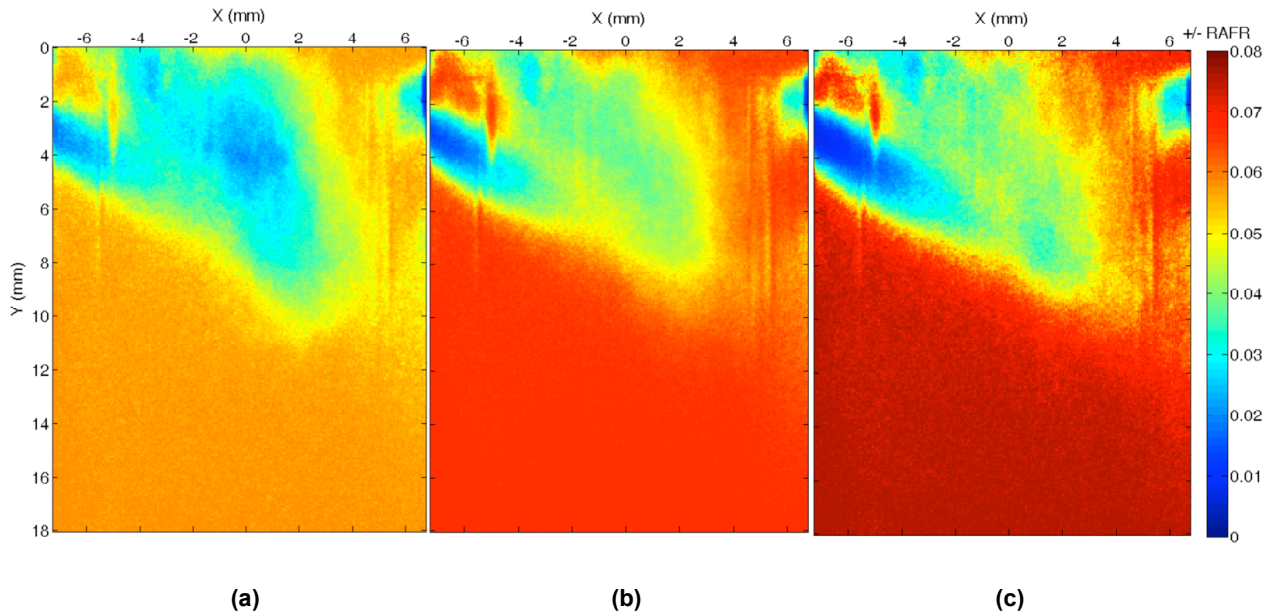
Figure 9-5 Uncertainty in Relative Air-fuel ratio for Insert Injected PSC with DI at *t*=0*CAD* and (a) λ_{bulk}=1.5 (b) λ_{bulk}=1.75 and (c) λ_{bulk}=2.0

As may be expected there is least error in the locations with highest signal strength (lowest RAFR), *i.e.* the jet core, where the RAFR value error is about ±0.01. The background charge, with significantly lower signal intensities still displays low RAFR errors of at most about ±0.08. Furthermore, as would be expected the uncertainty increases with increased RAFR, since the pixel intensities that yield these RAFRs are moving progressively further away from the calibration line's 'centre of gravity'- the location at which the uncertainty is at its minimum (for the calibration data of *Figure 7-6* this is at RAFR~1).

This uncertainty analysis simplifies the analysis and overlooks a number of key points. There is no assessment made of the variation of fuel composition and this cannot be overcome without gas chromatograph analysis of every fuel batch. Neither is there any assessment made of the effect upon the uncertainty in the data with respect to the error undergoing transition from camera to shot noise limited. As was noted in *Chapter 6*, the local thermodynamic state has a large effect upon the LIF signal and calculated RAFR, and this is not captured by the calibration line of *Figure 7-6*. The line of *Figure 7-6* would need to be replaced with a calibration surface with number density (fuel concentration) and temperature as the independent variables. Furthermore, if the mixture distribution was sought over a wide range of timings, and hence cylinder pressures, the surface would need to be replaced with a three-dimensional manifold. However, to complete the specification of the local RAFR a local temperature from within the cylinder at the image timing would be required and as was discussed in Sec xx there is currently no 2D experimental technique that can provide this and recourse must be made to CFD.

9▪6 CONCLUSIONS

The arguments presented have legitimised the oversight of buoyancy effects within the mixing process and shown the data of the RCM to be cyclically invariant. The findings with respect to the experimental convergence and uncertainty are less conclusive however. Examination of the quintile-quintile plots for the capillary injected and insert injected PSC events showed the capillary injected PSC data to be non-normally distributed, while it is primarily the tails of the data distribution for the insert injected PSC which are of concern. In an attempt to quantify the extent of the non-normality, information theory techniques were successfully used to identify the entropy of the data, yet the noise properties of the experimental optical set-up cause the data to be in transition from camera noise to shot-noise limited, each of which has a different statistical distribution. Until further understanding of this transition and its effects upon the entropy of the data are ascertained no further insight can be gained from information theory. The uncertainty analysis conducted on the RAFR data showed a high level of accuracy from the variables that were experimentally controlled, however uncertainties introduced by thermodynamics and collection optic noise were not accounted for.

Chapter 10
CONCLUSIONS & RECOMMENDATIONS

10▪1 INTRODUCTION

A brief summary of the equipment designed and implemented to conduct the experimental work is presented as are the most salient findings. The implications for future work are outlined and a series of recommendations made on furthering the understanding of partial stratification, its ignition and propagation.

10▪2   CONCLUSIONS

A rapid compression machine has been utilised, in conjunction with laser diagnostics, to provide a greater understanding of the mixture distribution within the cylinder of a partially stratified direct injection natural gas engine. An existing rapid compression machine (RCM) used for cold flow studies has had its cylinder and cylinder head redesigned so that it can accommodate the increased temperatures and pressures generated by combustion. The RCM has a new fuelling system designed and installed to allow the injection of gaseous fuels through a direct injector and a secondary partially stratified source, while also allowing a homogenous mixture to be introduced into the cylinder. A bubbler was designed and installed to allow acetone to be seeded into the fuel for use with laser induced fluorescence. New control and timing systems were also installed. The redesign allowed the use of 2D UV acetone laser induced fluorescence to image natural gas fuel concentration.

10▪2▪1 CONTRIBUTIONS TO THE FIELD

To date only a single laser induced fluorescence concentration study on the injection of highly underexpanded gaseous jets has been made, this work presents a progression in understanding the use of LIF for highly underexpanded gaseous jets. Bruneaux **[390]** uses a biacetal seed to track methane, which is less accurate than the acetone used in the current work, while CFD calculation is used to support the neglect of temperature effects in the concentration calculations. This last oversight is of particular concern to the current work since the injection is into a cylinder temperature and pressure environment which mimics that of an engine, unlike the work of Bruneaux that mimics only the pressure. The difficulties in establishing an accurate calibration highlight the shortcomings of failing to consider in detail the thermodynamics and fluids mechanics of the injection and undermine te numerical calibration used by Bruneaux. The current work also considers in more detail than the works of Reboux {{449 Reboux, Puechberty J. 1994}} and Kaminski *et al.* {{340 Kaminski, C.,F. 2000}} the errors associated with LIF concentration measurements and the difficulty in being more prescriptive. Experimental error specification for LIF results is not widely reported in the literature. Finally, the study provides insight into the hypothesised fuel distributions and phenomenological assertions of Gorby {{514 Gorby, D. 2007}} and Logan {{961 Logan, J-M. 2011}}.

10▪2▪2 EXPERIMENTAL FINDINGS

Meaningful insight was gained from the central region of the images away from the bore reflections. The fluctuations in relative air fuel ratio in the vicinity of the PSC injection are on the same order as those of the leading edge of the DI jet at ~40% and are attributed to the flow associated with the DI head vortex.

181

The jet centreline intensity counts suggested that the injection may be that of a plug flow, however information in the literature was limited as to how plugs behave upon injection, while the variability of the injection timing precluded firm conclusions as to the behaviour observed of the capillary injected PSC jet. The image results from the full bore test matrix demonstrate the inability to fully correct for background noise and scattered light since the intensity of the reflections are dependent upon the amount of fluorescent light emitted. Over the duration of the injection from $3.52CAD$ to $10.62CAD$ the RAFR gradients were shown to drop by ~50%. Investigation of the 'insert' injected PSC mixture distribution, without a DI jet present, showed the separate jets were not coalescing as the insert design might have intended and there exists the potential for little fuel flow through the injection points of the insert furthest from where the fuel is supplied to the insert. There are indications that the increase in ignitability that was reported by Gorby [7] when PSC was used with a weak bulk charge are not solely attributable to reduced fuel gradients as hypothesised by Gorby, but also to reductions in the level of the RAFR r.m.s. fluctuations. The implication is that the extent to which mixing is engendered by the insert and the strength of the bulk charge need to be considered in unison.

More detailed insight was gained from consideration of the region specific to the interaction of the capillary injected and insert injected PSC fuel with that of the DI jet. No matter the relative injection timing of the DI jet, or the bulk RAFR, the experimentally averaged capillary injected PSC jet preserved a jet-like structure, most likely because of the higher momentum in the PSC jet than the DI jet near the cylinder centreline. This caused stoichiometric concentrations not to occur until about $9mm$ from the firedeck, suggesting that there is a need for enhanced mixing if a spark is to ignite the PSC jet close to the firedeck. The experimental average images showed mixing to be confined to the jet shear layers, although the DI jet showed an increase in the area of the stoichiometric contour with a reduction in bulk charge RAFR, further supporting the need to match the bulk RAFR with the level of mixing generated by the PSC and DI injections. Yet, the complexity of doing so is highlighted in some individual images where there is clearly a propensity for the DI jet to deflect the PSC jet. The interaction of the DI jet with the jets of the PSC insert resulted in a mixture distribution that was substantially different to that without the DI injection. The lower PSC fuel momentum allowed the insert jets to coalesce with the DI jet. There is a large, almost homogeneous, region at the PSC injection point that extends into the DI head vortex, although the inhomogeneity that does remain increases with retarded DI injection timings.

The capillary injected PSC jet was seen to exhibit gradients in relative fuel-air-ratio within the shear layer that were twice the level of those within the core, while those in the DI jet (which ranged from $2\text{-}5mm^{-1}$) covered the same spatial extent in the shear layer and head vortex. The RAFR gradients increase towards the centre of the shear layer and vortex ball although no clear structure exists in the central region that has values in the range $3.5\text{-}5mm^{-1}$. It was again seen in the RAFR fluctuation images that the normalised

fluctuations decreased with decreased bulk RAFR, supporting once more the argument that the increase in ignitability reported in Gorby's work has roles from both local mixture variability and as well as fuel concentration gradients. It is also of note that throughout the capillary injected PSC tests the RAFR fluctuations were 2-3 times lower than for the capillary injected PSC jet into air. These findings support the work of Schefer *et al.* **[22]** and the assertion that mixing of the ambient gas into the jets, both PSC and DI, occurs through mass engulfment rather than steady entrainment. Examination of the RAFR probability distributions shows that although rich compositions dominate adjacent to the PSC injection location, there is still a finite probability that the bulk charge RAFR will be encountered, a probability that is comparable to encountering a stoichiometric mixture. Further from the injection point the probability increases to 2-3 times that for a stoichiometric composition. At the interface of the DI jet centreline and the PSC jet boundary there is peak in the RAFR *pdf* over the range 0.3-0.8, which suggests a robust combustion could be generated, as required by the PSC to propagate the inflammation to the DI jet or a homogenous charge. At the location where the DI jet has passed through the capillary injected PSC jet the *pdf* is smoother, with a sharp rise to a peak probability at RAFR~0.8, from where there is a steady decline in probability towards the bulk RAFR. Despite these global trends, the data showed that at any given location the bulk charge RAFR may be encountered as may that of pure fuel. Near the injection origin there exists, on average, only a 15-30% chance of encountering a mixture that falls within flammability limits of methane. Just 2*mm* downstream of this location those percentages increase to 30-50%; however, even at the most well mixed locations at the DI-PSC interface and the DI head downstream of the PSC jet, the likelihood of having a flammable mixture is still only about 50%. Examination of the scalar dissipation rate showed the core of the capillary injected PSC jet to exceed the extinction limit of $20.6s^{-1}$ **[403]**, although, within about 3*mm* of the injection origin the dissipation rate is at levels that will support combustion. To have a more complete picture of the mixture's propensity to ignite at any given location the local strain rate must be sought, potentially through PIV or LDV (or numerically).

With the insert injected PSC, changes in bulk RAFR were seen to have two distinct effects. The first was that the higher the bulk charge fuel concentration the larger the reduction in RAFR r.m.s. fluctuations within the PSC injected fuel. Secondly, it was observed that for the DI core the more rich the bulk mixture the higher the RAFR r.m.s. fluctuations. These observations result from the fact that mixing is no longer confined to the shear layers of the jets, as for the capillary insert, and the two fuel sources interact over a larger area, where the PSC injected fuel no longer maintains its structure. Retarding the relative injection timing lowers the r.m.s. fluctuations in RAFR, while at the most advanced timing, a fluctuating core was seen to persist with fluctuation levels about 2.5 times higher than those of the most retarded timing. As with the capillary injected PSC charge, the fluctuation levels within the insert injected PSC are higher than those of the DI jet in the vicinity of the cylinder centreline and, as such, should be considered in preference to those of the DI jet for ignition and flame propagation of partially stratified charges. The *pdf*s

of RAFR show that near the firedeck the insert injected fuel has had little time to mix with the bulk charge, while downstream of the injection point there is a stepped behaviour in the effect of the bulk charge RAFR upon the RAFR *pdf*; this supports the engulfment over entrainment argument. The core of the DI jet, when mixed with the insert injected PSC fuel, displayed increasing fuel concentrations for reductions in bulk fuel concentration and at the same time an increase in the probability of higher concentrations. This reinforces further the assertion that engulfment is the primary mechanism at work in the mixing, and that the mixing is governed to some extent by the bulk RAFR. These arguments are advanced further still by consideration of the flammability limits for the mixture that results from the insert injected PSC and DI interaction. The portion of the core of the DI jet that exceeds the flammability limits of methane increases with lower bulk charge fuel concentration, which at first seems contradictory since the introduction of a lower concentration bulk charge should reduce the core concentration by a greater amount. However, the higher the bulk RAFR the more viscous the bulk gas and the higher its molecular weight, both of which serve to reduce the extent to which mixing penetrates the jet. Downstream of the PSC injected fuel, at the head of the DI jet, the most uniform distribution in RAFR probability was found, with a peak at RAFR~0.5 and a consistent decrease towards the bulk RAFR. The lowest bulk RAFR produced a spike in the probability of rich compositions at this location and demonstrates once more the need to match bulk RAFR with the level of momentum driven mixing. At all locations there was a finite probability of encountering the bulk charge fuel composition or pure fuel, although the average case is substantially different to that of the capillary injected PSC. There is no clear relation between in-cylinder location and the increase in probability that the mixture will fall within the flammability limits of methane compared to the capillary injected case. In fact, at the DI head there is a slight decrease in the probability of falling within the flammability limits for most cases, yet at the centreline of the DI jet ,where it interacts with the insert injected PSC fuel, there is an increase of approximately two to three times in the probability of encountering a flammable mixture. However, examination of the local scalar dissipation rate, which is on the order of $0.8\text{-}1.2s^{-1}$, suggests that flame propagation may be difficult because of the low rate at which reactants can be supplied.

10▪2▪3 EXPERIMENTAL UNCERTAINTY

The LIF technique used has been shown to be independent of buoyancy effects and demonstrates no cyclic variability, yet is dependent upon the local thermodynamic state of the gas within the interrogation volume. However, there is no experimental technique suitable that could yield the temperature field. For the current work, the data has been presented for a region that is deemed to have recovered the cylinder temperature, circumventing these concerns; though if a wider field of view is sought, the specification of the temperature field within the cylinder must be made through computational fluid dynamics. The effect of camera and shot noise have also been presented, and use made of statistical entropy to indicate the difficulty introduced by the transition from one to the other based upon LIF signal intensity. The

uncertainty of LIF concentration data has not been presented in the literature to date, and the interaction of the thermodynamic state, system noise, and experimental uncertainty should be tackled as a research priority if concentration results are to be presented with representative errors.

10▪3   RECOMMENDATIONS & FUTURE WORK

10▪3▪1 RECOMMENDATIONS

The findings of this study have some clear implications for the design of the PSC system. The first, and most critical, is an improved PSC injection system that delivers more reliability and greater repeatability. With this in place, more consideration must be given to the stochastic nature of fuel injections and all subsequent testing conducted in a statistically rigorous way. The findings of future work cannot be based on the mean or time average field but must actively consider coherent structures and the engulfment of gas rather than its entrainment. It is not solely the mixing of the PSC charge that must be elucidated, there is a need to consider the local scalar dissipation and strain rates. The difficulties encountered with partial stratification and DI are unlikely to be associated with the ignition of the DI jet but with the ignition and propagation of the flame in the PSC injected fuel [7]. As such, the author recommends focusing future work on the PSC injection from the insert (and future insert designs) and mapping, in full, the transient concentration and flow fields that are generated on both time averaged and individual bases.

10▪3▪2 FUTURE WORK

Using the existing experimental set-up, with some minor modifications, a series of LIF concentration images should be made on planes parallel to the firedeck and at $1mm$ spaces, and validated with 1D Raman spectroscopy [253, 254]. This will allow a full three-dimensional transient image of the insert injected fuel concentration and scalar dissipation field to be constructed. To support this a similar study should be completed to assess the local strain rates. Given that laser Doppler velocimetry can only elucidate point velocities and that there is a large variation in space and time of the expected strain rate for the injected fuel, particle image velocimetry provides a more viable experimental option. The combination of fuel concentration, scalar dissipation and strain rates should then allow a better understanding of ignition potential. This potential should be explored with an ignition study that examines the probability of successful ignition in a fashion similar to that of Ahmed *et al.* [414] where the data can subsequently be used to construct ignition probability maps for the PSC injected fuel. Following a successful ignition it is important to understand how the mixture distribution translates into flame progress. There are a number of options with the current optical set-up, the easiest of which would be high-speed camera footage of the luminescent flame front. There also exists the potential to track the consumption of the acetone behind the flame to demarcate unburnt and burnt gas, which also has the advantage of providing the mixture distribution ahead of the flame at the image time. Changing from the

current 248nm UV laser source to two sources, one at ~281nm to track the OH radical and one at ~390nm to track the CH radical, would allow detailed flame front tracking since each occurs, respectively, ahead of and behind the flame [240]. Formaldehyde plays an important role in natural gas combustion and can be tracked in its own right using excitation near 353nm, though Paul & Najm [237] outline a method that uses the product of the formaldehyde concentration with the OH concentration to yield the local heat release rate; something that would provide valuable insight into the ability of the ignited PSC fuel to propagate a flame. Given that it appears to be the combination of bulk charge fuel concentration and momentum driven mixing that drives the local mixture concentration the two, in unison, should be investigated further with a more simple geometry. The assertion that changes in the bulk RAFR act to change the levels of mixing through altered physical properties should be investigated further and can be done so with the current RCM LIF experimental apparatus. Varying the injection momentum will significantly alter the mixing process [8], and the new injection system recommended for the RCM should have the capability to do this through the use of gases with varying molecular weights. Given the large number of parameters involved in the mixture generation at any given location within the cylinder it is recommended that a location for the spark be fixed. Based upon the findings of the work recommended above a fuel delivery system should be designed to deliver the desired composition and distribution at the chosen location. To understand the role of the vortex more, a PIV or LDV study should be conducted to ensure that the RAFR r.m.s. fluctuations do indeed map to the flow field. The LIF study of the capillary injected PSC jet showed the shear layer to be of almost constant thickness, with no difference observed in the jet head vortex. The images also display a fuel rich core that penetrates the cylinder for longer than may be expected.

REFERENCES

[1] *CO₂ Emissions from Fuel Combustion: Highlights 2009 Edition.* International Energy Agency; 2009

[2] *World Energy Outlook.* International Energy Agency; 2009

[3] Sankey P., Micheloto S., Clark D. T. *The Peak Oil Market: Price Dynamics at the End of the Oil Age.* Deutsche Bank; 2009 4th October 2009

[4] *BP Statistical Review of World Energy 2009.* 2009

[5] California Low Emissions Vehicle Regulations, www.arb.ca.gov, 2009

[6] *Euro 5 & 6 Emissions Standards for Cars and Vans: Position Paper.* European Federation for Transport & Environment; 2006

[7] Gorby D. *An Evaluation of Partially Stratified Charge Ignition in a Direct Injection Natural Gas Engine [dissertation].* Vancouver: University of British Columbia; 2007

[8] Hill P. G., Ouellette P. *Transient Turbulent Gaseous Fuel Jets for Diesel Engines.* Journal of Fluids Engineering 1999, 121 , pp.93-101

[9] Corrsin S. *Investigation of the Flow in an Axially Symmetrical Heated Jet of Air.* Washington: National Advisory Committee for Aeronautics; 1943. Report No.: Wartime Report W-94

[10] Hinze J. O., van der Hegge Zijnen, B.G. *Transfer of Heat and Matter in the Turbulent Mixing Zone of an Axially Symmetrical Jet.* Applied Science Results, Part A 1949, 1 , pp.435-461

[11] Corrsin S., Uberoi M. S. *Further Experiments of the Flow and Heat Transfer in a Heated Jet.* Washington: National Advisory Committee for Aeronautics; 1950. Report No.: Report 998

[12] Corrsin S., Uberoi M. S. *Spectra and Diffusion in a Round Turbulent Jet.* Washington: National Advisory Committee for Aeronautics; 1951. Report No.: Report 1940

[13] Zel'Dovich Y. B. *Limiting Laws for Turbulent Flows in Free Convection.* Journal of Experimental anf Theoretical Physics 1937, 7 (12), pp.1463

[14] Wygnanski I., Fiedler H. *Some Measurements in the Self-Preserving Jet.* Journal of Fluid Mechanics 1969, 38 (3), pp.577-612

[15] Thring M. W., Newby M. P. *Combustion Length of Enclosed Turbulent Jet Flames.* Fourth Symposium on Combustion 1953, , pp.789

[16] Baker C. B., 1980. *In Hussein, J.H., Capp, S.T. & George, W.K. Velocity Measurements in a High Reynolds Number Momentum Conserving Axisymmetric Turbulent Jet.* Journal of Fluid Mechanics 1994, 258 , pp.31-75

[17] Capp S. P., 1983. *In Hussein, J.H., Capp, S.T. & George, W.K. Velocity Measurements in a High Reynolds Number Momentum Conserving Axisymmetric Turbulent Jet.* Journal of Fluid Mechanics 1994, 258 , pp.31-75

[18] Schneider W. *Decay of Momentum Flux in Submerged Jets.* Journal of Fluid Mechanics 1985, 154 , pp.91-110

[19] George WK. The self-preservation of turbulent flows and its relation to the initial conditions and coherent structures. In: George WK, Arndt REA, editors. Advances in Turbulence. Hemisphere; 1989. p. 39-72

[20] Carazzo G., Kaminski E., Tait S. *The Route to Self-Similarity in Turbulent Jets and Plumes.* Journal of Fluid Mechanics 2006, 547 , pp.137-148

[21] Mi J., Nobes D. S., Nathan G. J. *Influence of Jet Exit Conditions on the Passive Scalar Field of an Axisymmetric Free Jet.* Journal of Fluid Mechanics 2001, 432 , pp.91-125

[22] Schefer R. W., Kerstein A. R., Namazian M., Kelly J. *Role of Large Scale Structure in a Non-Reacting Turbulent CH_4 Jet.* Physics of Fluids 1994, 6 , pp.652-661

[23] Papanicolaou P. N., List J. E. *Investigations of Round Vertical Turbulent Buoyant Jets.* Journal of Fluid Mechanics 1988, 195 , pp.341-391

[24] Hussein H. J., Capp S. P., George W. K. *Velocity Measurements in a High Reynolds Number Momentum Conserving Axisymmetric Turbulent Jet.* Journal of Fluid Mechanics 1994, 258 , pp.31-75

[25] Schetz J. A. *Injection and Mixing in Turbulent Flow*; 1980 New York: American Institute for Astronauntics and Aeronautics; ISBN: 0-915928-35-3.

[26] Turner S. *The 'Starting Plume' in Neutral Surroundings.* Journal of Fluid Mechanics 1962, 13 , pp.356-368

[27] Abramovich S., Solan A. *The Initial Development of a Submerged Laminar Round Jet.* Journal of Fluid Mechanics 1973, 59 (4), pp.791-801

[28] Rizk W. *Experimental Studies of the Mixing Process and Flow Configurations in Two-Cylinder Engine Scavenging.* Proceedings of the Institution of Mechanical Engineers: Part E 1958, 172 , pp.417-424

[29] Witze P. O. *The Impulsively Started Incompressible Turbulent Jet.* 1980. Report No.: SAND80-8617

[30] Rubas P. J., Paul M. A., Martin G. C., Coverdill R. E., Lucht R. P., Peters J. E., et al. *Methane Jet Propagation in a Direct Injection Natural Gas Engine.* SAE Technical Paper Series 1998,

[31] Ricou F. P., Spalding D. B. *Measurements of Entrainment by Axisymmetric Turbulent Jets.* Journal of Fluid Mechanics 1973, 59 (4), pp.21-32

[32] Cossali G. E., Goghe A., Araneo L. *Near-Field Entrainment in an Impulsively Started Turbulent Gas Jet.* AIAA Journal 2001, 39 (6), pp.1113-1122

[33] Lahbabi F. Z., Borée J., Nuglisch H. J., Charnay G. *Analysis of Starting and Steady Turbulent Jets by Image Processing Techniques.* ASME Fluids Engineering Division- Experimental and Numerical Flow Visualization 1993, 172 , pp.315-321

[34] Wang D., Mao X. J., Wang J. X., Zhuo B. *Experimental Study on the Operating Range Restrictions of a Lean-Burn Turbocharged SI Natural Gas Engine.* Energy & Fuels 2009, 23 , pp.3054-3062

[35] Field M. A., Gill D. W., Morgan B., Hawksley P. G. W. *Combustion of Pulverised Coals.* 1967,

[36] Birch A. D., Brown D. R., Dodson M. G., Thomas J. R. *The Turbulent Concentration Field of a Methane Jet.* Journal of Fluid Mechanics 1978, 8 (3), pp.431-449

[37] Dahm W. J. A., Dimotakis P. E. *Mixing at Large Schmidt Number in the Self Similar Far-Field of Turbulent Jets.* Journal of Fluid Mechanics 1990, 217 , pp.299-330

[38] Fischer H. B., List E. J., Imberger J., Brooks N. H. *Mixing in Inland and Coastal Waters*; 1979 New York: Academic Press; ISBN: 0122581504.

[39] Shabbir A., George W. K. *Experiments on a Round Turbulent Buoyant Plume.* Journal of Fluid Mechanics 1994, 275 , pp.1-32

[40] Wang H., Law A. W. *Second Order Integral Model for a Round Turbulent Buoyant Jet.* Journal of Fluid Mechanics 2002, 459 (397), pp.428

[41] Birch A. D., Brown D. R., Dodson M. G., Swaffield F. *Velocity Decay of High Pressure Jets.* Combustion Science and Technology 1987, 52 , pp.161-171

[42] Townsend A. A. *The Structure of Turbulent Shear Flow*; 1956 Cambridge: Cambridge University Press; ISBN: 0 521 20710 X.

[43] Panchapakesan N. R., Lumley J. L. *Turbulent Measurements in Axisymmetric Jets of Air and Helium: Part 1- Air Jet.* Journal of Fluid Mechanics 1993, 246 , pp.197-223

[44] Kleinstein G. *An Approximation Solution for the Axisymmetric Jet of a Laminar Compressible Fluid.* Quarterly Applied Mathematics 1962, 20 (1), pp.49-54

[45] Kleinstein G. *Mixing in Turbulent Axially Symmetric Free Jets.* Journal of Spacecraft and Rockets 1964, 1 (4), pp.403-408

[46] Schlichting H. *Boundary Layer Theory*; 1979 7th ed. McGraw-Hill

[47] Shapiro A. H. *The Dynamics and Thermodynamics of Compressible Fluid Flow*; 1953 John Wiley & Sons Inc.; ISBN: 978-0-471-06691-0.

[48] Birch A. D., Brown D. R., Dodson M. G., Swaffield F. *The Structure and Concentration Decay of High Pressure Jets of Natural Gas.* Combustion Science and Technology 1984, 36 , pp.249-261

[49] McTaggart-Cowan G. P., Reynolds C.,C., Bushe W. K. *Natural-Gas Fuelling for Heavy-Duty on-Road use: Current Trends and Future Direction.* International Journal of Environmental Studies 2006, 63 (4), pp.421-440

[50] Gupta M., Bell S. R., Tillman S. T. *An Investigation of Lean Combustion in a Natural Gas-Fueled Spark-Ignited Engines.* journal of Energy and Resources Technology 1996, 118 , pp.145-151

[51] Fritz S. G., Egluonon R. I. *Emissions from Heavy Duty Trucks Converted to CNG.* ASME Paper 1992, 92-ICE-10

[52] Chen S. K., Beck N. J. *Gas Engine Combustion Principles and Applications.* SAE Technical Papers 2001, 2001-01-2489

[53] Campbell A. S. *Thermodynamic Analysis of Combustion Engines*; 1979 New York: John Wiley & Sons Inc.; ISBN: 0898747740.

[54] Crane M. E., King S. R. *Emission Reductions through Precombustion Chamber Design in a Natural-Gas, Lean Burn Engine.* Journal of Engineering for Gas Turbines and Power-Transactions of the Asme 1992, 114 (3), pp.466-474

[55] Meyers D. P., Bourn G. d., Hendrick J. C., Kubesh J. T. *Evaluation of Six Natural Gas Combustion Systems for LNG Locomotive Applications.* SAE Technical Papers 1997, 972967

[56] Kubesh J. T. *Development of a Throttleless Natural Gas Engine.* 2002. Report No.: Final Report: NREL/SR-540-31141

[57] Goto S., Itoh Y., Higuchi Y., Nagai T. *Niigata Ultra Lean Burn SI Gas engines~Achieving High Efficiency and Low NO_x Emission.* SAE Technical Papers 1990, 901608

[58] Kettner M., Fischer J., Nauwerck A., Tribulowski J., Spicher U., Velji A., et al. *The BPI Flame Jet Concept to Improve the Inflammation of Lean Burn Mixtures in Spark Ignition Engines.* SAE Technical Paper Series 2004,

[59] Blank D. A. *CNG/Methane-Combustion in a Homogeneous-Combustion, Radical-Ignition D.I. Diesel Engine.* SAE Technical Papers 2007, 2007-01-0047

[60] Pischinger S., Umierski M., Hüchtebrock B. *New CNG Concepts for Passenger Cars: High Torque Engines with Superior Fuel Consumption.* SAE Technical Papers 2003, 2003-01-2264

[61] Tilagone R., Venturi S. M., G. *Natural Gas- An Environmentally Friendly Fuel for Urban Vehicles: The SMART Demonstrator Approach.* SAE Technical Papers 2005, 2005-01-2186

[62] Prieur A., Tilagone R. *A Detailed Well to Wheel Analysis of CNG Compared to Diesel Oil and Gasoline for the French and the European Markets.* SAE Technical Papers 2007, 2007-01-0037

[63] Podnar D. J., Kubesh J. T. *Development of the Next Generation Medium-Duty Natural Gas Engine, Final Report.* National Renewable Energy Laboratory; 2000. Report No.: NREL/SR-540-27503

[64] Zhang H., Chiu J., Bartel J. *Late Intake Valve Closing with Throttle Control at Light Loads for a Lean-Burn Natural Gas Engine.* SAE Technical Papers 1999, 1999-01-3485

[65] Yap D., Magaratis A., Wyszynski M. L., Hongming X. *Residual Gas Trapping for Natural Gas HCCI.* SAE Technical Papers 2004, 2004-01-1973

[66] Watanabe O., Nakajima S., Goto H., Matsunaga T. *Development of CNG Engine with Variable Valve Timing Electronic Control.* SAE Technical Papers 2007, 2007-01-3615

[67] Karim G. A., Wierzba I. *Experimental and Analytical Studies of the Lean Operational Limits in Methane Fuelled Spark Ignition and Compression Ignition Engines.* SAE Technical Paper 1989, 891637

[68] Klimstra J. *Performance of Lean Burn Natural Gas Fueled Engines on Specific Fuel Consumption, Power Capacity and Emissions.* SAE Technical Paper 1990, 901495

[69] Richardson S., McMillan M. H., Woodruff S. D., McIntyre D. *Misfire, Knock and NO_x Mapping of a Laser-Spark-Ignited, Single-Cylinder, Lean-Burn Natural Gas Engine.* SAE Technical Papers 2004, 2004-01-1853

[70] Gupta S. B., Bihari B., Sekar R., Klett G. M., Ghaffapour M. *Ignition Characteristics of Methane-Air Mixtures at Elevated Temperatures and Pressures.* SAE Technical Papers 2005, 2005-01-2189

[71] Hassaneen A. E., Vardy K., Bawady A. H., Morgan A. *A Study of the Flame Development and Rapid Burn Durations in a Lean-Burn, Fuel-Injected Natural Gas S.I. Engine.* SAE Technical Papers 1998, 981384

[72] Dordaei H., Hazhir A., K. Eisazadeh Far K. *Pollutant Emissions Study of Gas-Fueled SI Engines.* SAE Technical Papers 2005, 2005-01-3790

[73] Iyer R. C., Vaggar M., Seetharam T. R., Channiwala S. A. *Investigations on the Influence of Ignition Voltage, Higher Compression Ratio and Piston Crown Geometry on the Performance of Compressed Natural Gas Engines.* SAE Technical Papers 2008, 2008-01-1762

[74] Middleton A., Neuman B., Khatri D. S. *Development of Dedicated CNG Engine with Multipoint Gas Injection System.* SAE Technical Papers 2008, 2008-28-0014

[75] Lappas P., Evans R. L. *Fluid Flow in the Squish-Jet Combustion Chamber.* Proceedings of the Institution of Mechanical Engineers, Part A: Journal of Power and Energy 2006, 220 (4), pp.355-378

[76] Lappas P., Evans R. L. *Experimental Validation of an Improved Squish Velocity Model for Bowl-in-Piston Combustion Chambers.* Journal of Engineering for Gas Turbines and Power 2006, 128 (2), pp.403-413

[77] Lappas P., Evans R. L. *A Numerical and Experimental Study of the Squish-Jet Combustion Chamber.* International Journal of Engine Research 2006, 7 (6), pp.471-487

[78] Evans R. L., Blaszczyk J. *Fast-Burn Combustion Chamber Design for Natural Gas Engines.* Transactions of the ASME 1998, 120 , pp.232-236

[79] Meyers D. P., Kubesh J. T. *The Hybrid Rich-burn/lean-Burn Engine.* Journal of engineering for gas turbines and power-transactions of the ASME; JAN; ; 1997 pp.243-9

[80] Kawasaki K., Takegoshi A., Yamane K., Ohtsubo H., Nakazono T., Yamauchi K. *An Experimental Study on the Improvement of Engine Performance and Exhaust Emissions from Small-Scale PCCI Engines.* SAE Technical Papers 2005, 2005-01-2124

[81] Heywood J. B. *Internal Combustion Engine Fundamentals*; 1988 Singapore: McGraw-Hill; ISBN: 0-07-100499-8.

[82] Abata D. *A Review of the Stratified Engine Concept.* Automotive engine alternatives, international symposium on alternative and advanced automotive engines; ; 1986

[83] Bishop I. N., Simko A. *A New Concept of Stratified Charge Combustion – the Ford Combustion Process (FCP).* SAE Technical Papers 1968, 680041

[84] Yagi S. *NOx Emission and Fuel Economy of the Honda CVCC Engine.* SAE Technical Papers 1974, 741158

[85] Alperstein M. *Texaco's Stratified Charge Engine – Multifuel, Efficient, Clean, and Practical.* SAE Technical Papers 1974, 740563

[86] Zhao F., Harrington D. L., Lai M. -. *Automotive Gasoline Direct-Injection Engines*; 2002 SAE; ISBN: 0-7680-0882-4.

[87] Turner J. W. G., Pearson R. J., Kenchington S. A. *Concepts for Im[Roved Fuel Economy from Gasoline Engines.* International Journal of Engine Research 2005, 6 (2), pp.137-157

[88] Huang Z., Shiga S., Ueda T., Nakamura H., Ishima T., Obokata T., et al. *Combustion Characteristics of Natural Gas Direct Injection Timings.* Proceedings of the Insitution of Mechanical Engineers: Part D 2002, 217 , pp.393-401

[89] Brehob D., Flemming J. E., Haghgooie M., Stein R. A. *Stratified-Charge Engine Fuel Economy and Emission Characteristics.* SAE Technical Papers 1998, 982704

[90] Dinc C., Arslan H., Mehdiyev R. *CO2 Emission Reduction using Stratified Charge in Spark-Ignition Engines.* ENERGY & FUELS 2009, 23 (Sp. Iss.), pp.1781-1785

[91] Taniguchi S., Tsukasaki Y., Yasuda A. *Study of Compressed Natural Gas Direct Injection Engine.* SAE Technical Papers 2006, 2006-05-0214

[92] Green R. K., Zavier C. C. *Charge Stratification in a Spark Ignition Engine.* Proceedings of the Insitution of Mechanical Engineers: Part A 1992, 206 , pp.59-64

[93] Acroumanis C., Hull D. R., Whitelaw J. H. *An Approach to Charge Stratification in Lean-Burn Spark-Ignition Engines.* SAE Technical Papers 1994, 941878

[94] Acroumanis C., Hull D. R., Whitelaw J. H. *Optimizing Local Charge Stratification in a Lean-Burn Spark Ignition Engine.* Proceedings of the Institution of Mechanical Engineers: Part D 1997, 211 , pp.145-156

[95] Evans R,L., inventor; Control method for spark ignition engines. United States 2000 October 2, 1998

[96] Reynolds C.,C. *Performance of a Partially Stratified Charge Natural Gas Fuelled Engine [dissertation].* Vancouver: University of British Columbia Editor; 2001

[97] Brown G. *Performance of a Partially Stratified-Charge Gasoline Engine [dissertation].* Vancouver: University of British Columbia Editor; 2003

[98] Dunn-Rankin D. *Lean Combustion: Technology & Control*; 2007 Academic Press; ISBN: 978-0123706195.

[99] Yossefi D., Belmont M. R., Ashcroft S. J., Maskell S. J. *A Comparison of the Relative Effects of Fuel Composition and Ignition Energy on the Early Stages of Combustion in a Natural Gas Spark Ignition Engine using Simulation.* Proceedings of the Institution of Mechanical Engineers Part D-Journal of Automobile Engineering 2000, 214 (D4), pp.383-393

[100] McTaggart-Cowan G. P., Wu N., Jin B., Rogak S. N., Davy M. H., Bushe W. K. *Effects of Fuel Composition on High-Pressure Non-Premixed Natural Gas Combustion.* Combustion Science and Technology 2009, 181 (3), pp.397-416

[101] McTaggart-Cowan G. P., Rogak S. N., Hill P. G., Munshi S. R., Bushe W. K. *Fuel Dilution Effects in a Direct Injection of Natural Gas Engine.* Proceedings of the Insitution of Mechanical Engineers: Part D 2008, 222 (3), pp.441-453

[102] Schiffgens H. J., Endres H., Wackertapp H., Schrey E. *Concepts for the Adaptation of Si Gas-Engines to Changing Methane Number.* Journal of engineering for gas turbines and power-transactions of the asme; OCT; ; 1994 pp.733-9

[103] Kim K., Kim H., Kim B., Lee K., Lee K. *Effect of Natural Gas Composition on the Performance of a CNG Engine.* Oil & Gas Science and Technology-Revue De L Institut Francais Du Petrole 2009, 64 (2), pp.199-206

[104] Environmental Protection Agency. *Mandatory Reporting of Greenhouse Gases: Proposed Rules.* Federal Register 2009, 74 (68), pp.16448-16731

[105] Haagen-Smit A. J. *Chemistry and Physiology of Los Angeles Smog.* Industrial and Engineering Chemistry 1952, 44 (6), pp.1342-1346

[106] Eastoe E. F. *A Hierarchical Model for Non-Stationary Multivariate Extremes: A Case Study of Surface-Level Ozone and NOx Data in the UK.* Envirometrics 2009, 20 (4), pp.428-444

[107] Neuman J. A., Nowak J. B., Zheng W., Flocke F., Ryerson T. B., Trainer M., et al. *Relationship between Photochemical Ozone Production and NOx Oxidation in Houston, Texas.* Journal of Geophysical Research- Atmospheres 2009, 114

[108] Shrestha K. L., Kondo A., Kaga A., Inoue Y. Brebbia C. A., Longhurst J. W. S., editors. *High-Resolution Air Quality Modelling and Time Scale Analysis of Ozone and NOx in Osaka, Japan.* Air pollution XVI; WIT Transactions on Acology and the Environment; ; 2008 pp.429-38

[109] Vivanco M. G. *Relation between Ozone Levels and NOx and VOC Emissions in the Sao Paulo Metropolitan Area for an Episode of August, 1998.* International Journal of Pollution and Environment 2008, 35 (1), pp.90-98

[110] Shao M., Zhang Y., Zeng L., Tang X., Zhang J., Zhong L., et al. *Ground-Level Ozone in the Pearl River Delta and the Roles of VOC and NOx in its Production.* Journal of Environmental Management 2009, 90 (1), pp.512-518

[111] Derwent R. G., Stevenson D. S., Doherty R. M., Collins W. J., Sanderson M. G. *How is Surface Ozone in Europe Linked to Asian and North American NOx Emissions?* Atmospheric Environment 2008, 42 (32), pp.7412-7422

193

[112] Kaynak B., Hu Y., Martin R. V., Russell A. G., Choi Y., Wang Y. *The Effect of Lightning NOx Production on Surface Ozone in the Continental United States.* Atmospheric Chemistry and Physics 2008, 8 (17), pp.5151-5159

[113] Bowman C. T. *Control of Combustion-Generated Nitrogen Oxide Emissions: Technology Drive by Regulation.* Proceedings of the Combustion Institute 1993, 24 , pp.859

[114] Baulch D. L., Cobos C. J., Cox, A. M., Frank, P., Hayman G., Just T., Kerr J. A., et al. *Compilation of Rate Data Fro Combustion Modelling Supplement.* International Journal of Physical Chemistry Reference Data 1994, 23 , pp.847

[115] Lavoie G. A., Heywood J. B., Keck J. C. *Experimental and Theoretical Study of Nitric Oxide Formation in Thermal Combustion Engines.* Combustion Science and Technology 1970, 1 , pp.313-326

[116] Kuo K.,K. *Principles of Combustion*; 2005 John Wiley & Sons; ISBN: 0-471-04689-2.

[117] Newhall H. K., Shahed S. M. *Kinetics of Nitric Oxide Formation in High-Pressure Flames.* Proceedings of the Thirteenth International Symposium on Combustion 1971, , pp.381-390

[118] Fenimore C. P. *Studies of Fuel-Nitrogen in Rich Flame Gases.* Proceedings of the Combustion Institute 1979, 17 , pp.661

[119] Warnatz J., Maas U., Dibble R. W. *Combustion: Physical &Chemical Fundamentals, Modeling and Simulation, Experiments, Pollutant Formation*; 2001 3rd ed. Springer; ISBN: 3-540-67751-8.

[120] Correa S. M. *A Review of NO_x Formation Under Gas-Turbine Conditions.* Combustion Science and Technology 1992, 87 , pp.329-362

[121] Alperstein M., Bradow R. L. *Exhaust Emissions Related to Engine Combustion Reactions.* SAE Technical Papers 1966, 75 (660781)

[122] Starkman E. S., Stewart H. E., Zvonow V. A. *Investigation into the Formation and Modification of Exhaust System Precursors.* SAE Technical Papers 1669, 690020

[123] Lavoie G. A. *Spectroscopic Measurement of Nitric Oxide in Spark Ignition Engines.* Combustion and Flame 1970, 15 , pp.97-108

[124] Stone R. *Introduction to Internal Combustion Engines*; 1999 Third ed. Society of Automotive Engineers; ISBN: 0-7680-0495-0.

[125] Yu R. C., Shahed S. M. *Effects of Injection Timing and Exhaust Gas Recirculation on Emissions from a DI Diesel Engine.* SAE Transactions 1981, 90 (811234)

[126] Weiss P., Keck J. C. *Fast Sampling Valve Measurements of Hydrocarbons in the Cylinder of a CFR Engine.* SAE Transactions 1981, 90 (810149)

[127] Greeves G., Khan I. M., Wang C. H. T., Fenne I. *Origins of Hydrocarbon Emissions from Diesel Engines.* SAE Transactions 1977, 86 (770259)

[128] Westbrook C. K., Dryer F. L. *Chemical Kinetic and Modelling of Combustion Processes.* Proceedings of the Eighteenth International Symposium on Combustion 1981, , pp.749

[129] Westbrook C. K., Dryer F. L. *Chemical Kinetic Modelling of Hydrocarbon Combustion.* Progress in Energy and Combustion Science 1984, 10 , pp.1-57

[130] Watkins L. H. *Air Pollution from Road Vehicles*; 1991 London: HMSO; ISBN: 978-0115510007.

[131] Sher E, editor. Handbook of air pollution from internal combustion engines. 1st ed. Boston, MA: Academic Press; 1998

[132] Mauzerall D. L., Sultan B., Kim N., Bradford D. *NO_x Emissions from Large Point Sources: Variability in Ozone Production, Resulting Health Damages and Economic Costs.* Atmospheric Environment 2005, 39 , pp.2851-2866

[133] Sillman S., Logan J. A., Wofsy S. C. *The Sensitivity of Ozone to Nitrogen Oxides and Hydrocarbons in Regional Ozone Episodes.* Journal of Geophysical Research 1990, 95 , pp.1837-1851

[134] Sillman S. *The Relation Between Ozone, NO_x, and Hydrocarbons in Urban and Polluted Rural Environments.* Atmospheric Environment 1999, 33 , pp.1821-1845

[135] Dockery D. W., Pope A. C. *Acute Respiratory Effects of Particulate Air Pollution.* Annual Review of Public Health 1994, 15 , pp.107-132

[136] Lippmann M. *Health Effects of Tropospheric Ozone: Review of Recent Research Findings and their Implications for Ambient Air Quality Standards.* Journal of Exposure Analysis and Environment Epidemiology 1993, 3 , pp.103-129

[137] Bell M. L., McDermott A., Zeger S. L., Samet J. M., Dominici F. *Ozone and Short-Term Mortality in 95 US Urban Communities, 1987-2000.* Journal of the American Medical Association 2004, 292 (19), pp.2372-2378

[138] Pope A. C., Dockery D. W. *Health Effects of Fine Particulate Air Pollution: Lines that Connect.* Journal of the Air & Waste Management Association 2006, 56 , pp.709-742

[139] Greim H., Borm P., Schins R., Donaldson K., Driscoll K., Hartwig A., et al. *Toxicity of Fibres and Particles and Particles: Report of the Workshop Held in Munich.* 26-27 October 2000; Munich, Germany. ; 2001 pp.737-54

[140] Mauderly J. L. *Diesel Emissions: Is More Health Research Still Needed?* Toxilogical Science 2001, 62 , pp.6-9

[141] Ghio A. J., Huang Y. C. *Exposure to Concentrated Ambient Particles (CAP's): A Review.* Inhalation Toxicology 2004, 16 , pp.53-59

[142] Schlesinger R. B., Künzli N., Hindy G. M., Gotschi T., Jerrett M. *The Health Relevance of Ambient Particulate Matter Characteristics: Coherence of Toxicological and Epidemiological Inferences.* Inhalation Toxicology 2006, 18 , pp.95-125

[143] Schlesinger R. B., Cassee F. *Atmospheric Secondary Inorganic Particulate Matter: The Toxicological Perspective as a Basis for Health Risk Assessment.* Inhalation Toxicology 2003, 15 , pp.197-235

[144] Solomon S., Qin D., Manning M. *Climate Change 2007: The Physical Science Basis. Contribution of Working Group I to the Fourth Assessment Report of the Intergovernmental Panel on Climate Change.* 2007, , pp.1-74

[145] Eckbreth A.,C. *Laser Diagnostics for Combustion Temperature and Species*; 1988 Tunbridge Wells: Abacus Press; ISBN: 0-85626-344-3.

[146] Alden M., Bengtsson P. -., Georgiev N., Loefstroem C., Martinsson L., Neij H. *Application of Laser-Induced Fluorescence and CARS for Combustion Diagnostics.* Berichte der Bunsengesellschaft fuer Physikalische Chemie 1993, 97 (12), pp.1643-1649

[147] Durst F., Melling A., Whitelaw J., H. *Principles and Practice of Laser-Doppler Anemometry*; 1981 London: Academic Press; ISBN: 0122252608.

[148] Taylor, A. M. K. P. *Instrumentation for Flows with Combustion*; 1993 London: Academic Press; ISBN: 0126839204.

[149] Adrian R. J. *Multi-Point Optical Measurement of Simultaneous Vectors in Unsteady Flow- A Review.* Int.J.Heat & Fluid Flow 1986, 7 (2), pp.127-143

[150] Driscoll J. F., Schafer R. W., Dibble R. W. *Mass Fluxes of ρ´u´ and ρ´v´ Measured in a Turbulent Nonpremixed Flame.* Nineteenth Symposium on Combustion 1983, , pp.477-485

[151] Zhao F., Hiroyasu H. *The Applications of Laser Rayleigh Scattering to Combustion.* Progress in Energy and Combustion Science 1993, 19 , pp.447-485

[152] Zhao H., Ladommatos N. *Engine Combustion Instrumentation and Diagnostics*; 2001 Danvers, MA: Society of Automotive Engineers; ISBN: 0-7680-0665-1.

[153] heiman D., Hellwarth R. W., Levenson M. D., Martin G. *Raman Induced Kerr Effect.* Physical Review Letters 1976, 36 , pp.189-192

[154] Eesley G. L. *Coherent Raman Spectroscopy*; 1981 Oxford: Pergamon; ISBN: 0080250580.

[155] Aldén M., Bengtsson P. E., Edner H. *Rotational CARS Generation through a Multiple Four-Color Interaction.* Applied Optics 1986, 25 (23), pp.4493-4500

[156] Eckbreth A.,C., Anderson T. J. *Simultaneous Rotational Anti-Stokes Raman Spectroscopy and Coherent Raman Spectroscopy with Arbitrary Pump-Stokes Spectral Separation.* Optics Letters 1986, 11 (8), pp.496-498

[157] Mokhov A. V., Levinsky H. B. *A LIF and CARS Investigation of Upstream Heat Loss and Fluegas Recirculation as NOx Control Strategies for Laminar, Premixed Natural-gas/air Flames.* 28th international symposium on combustion; Jul 30-Aug 4 2000; Edinburgh, United Kingdom: Combustion Institute; 2000 pp.2467-74

[158] Miles R. B., Connors J. J., Markovitz, E. C., Howard, P. J., Roth G. J. *Instantaneous Profiles and Turbulence Statistics of Supersonic Free Shear Layers by Raman Excitation Plus Laser Induced Electronic Fluorescence (RELIEF) Velocity Tagging of Oxygen.* Experiments in Fluids 1989, 8 , pp.17-24

[159] Aldén M., Bengtsson P. E., Edner H., Kröll S., Nilsson D. *Rotational CARS: A Comparison of Different Techniques with Emphasis on Accuracy in Temperature Determination.* Applied Optics 1989, 28 (15), pp.3206-3219

[160] Tomita E., Yoshisuke H., Yoshiyama S., Toda H. *Measurement of Fuel Concentration Distribution of Transient Hydrogen Jet and its Flame using Planar Laser Induced Fluorescence Method.* JSAE Review 1998, 19 (4), pp.329-335

[161] Bryant R. A., Driscoll J. F. *Structure of Supersonic Flames Imaged using OH/acetone Planar Laser-Induced Fluorescence.* AIAA Journal 2001, 39 (9), pp.1735-1741

[162] Yang S., Zhao J., Yu G., Zhang X. *Planar Laser Induced Fluorescence Imaging of OH Radical in Supersonic Combustor.* Optical technology and image processing for fluids and solids diagnostics 2002; Sep 3-6 2002; Beijing, China: The International Society for Optical Engineering; 2003 pp.470-5

[163] Lee M. P., McMillin B. K., Palmer J. L., Hanson R. K. *Planar Fluorescence Imaging of a Transverse Jet in a Supersonic Crossflow.* Journal of Propulsion and Power 1992, 8 (4), pp.729-735

[164] Hoshina K., Kohguchi H., Ohshima Y., Endo Y. *Laser-Induced Fluorescence Spectroscopy of the C4H and C4D Radicals in a Supersonic Jet.* Journal of Chemical Physics 1998, 108 (9), pp.3465-3478

[165] McMillin B. K., Palmer J. L., Hanson R. K. *Temporally Resolved, Two-Line Fluorescence Imaging of NO Temperature in a Transverse Jet in a Supersonic Cross Flow.* Applied Optics 1993, 32 (36), pp.7532-7545

[166] Havermann M., Beylich A. E. *Performance and Limitations of the Laser-Induced Fluorescence Measurement Technique and the Established Experimental Methods for the Study of Supersonic Mixing.* Heat and Technology 1997, 15 (2), pp.3-10

[167] Bo Y., Bao C., Zhu Y., Wang D., Yu Y. *Measurement of Crosswise Velocity Distribution of Metal Atomic Vapor by LIF.* Qinghua Daxue Xuebao/Journal of Tsinghua University 2000, 40 (10), pp.16-19

[168] Hirai E., Teshima K., Kurita K., Takahara S. *Velocity Measurement of Free Jets using Nuclear Hyperfine Structure of I2.* JSME International Journal, Series B 1997, 40 (3), pp.501-508

[169] Lefebvre X., Leporcq B. *Simultaneous Measurements of Pressure, Temperature and Velocity using Laser-Induced Iodine Fluorescence.* Part 4 (of 4); Jul 7-11 1996; San Diego, CA, USA: ASME, New York, NY, USA; 1996 pp.189-94

[170] Lemoine F., Lefebvre X., Leporcq B. *Pressure and Velocity Measurements in Compressible Flows using Iodine Fluorescence Induced by a Single-Mode Laser.* Proceedings of the 1995 ASME/JSME fluids engineering and laser anemometry conference; Aug 13-18 1995; Hilton Head, SC, USA: ASME, New York, NY, USA; 1995 pp.81-7

[171] Nakaya S., Kasahara M., Tsue M., Kono M. *Velocity Measurements of Reactive and Non-Reactive Flows by NO-LIF Method using NO2 Photodissociation.* Heat Transfer - Asian Research 2005, 34 (1), pp.40-52

[172] Giezendanner R., Keck O., Weigand P., Meier W., Meier U., Stricker W., et al. *Periodic Combustion Instabilities in a Swirl Burner Studied by Phase-Locked Planar Laser-Induced Fluorescence.* Combustion Science and Technology 2003, 175 (4), pp.721-741

[173] Kido A., Ogawa H., Mayamoto N., Sano T. *Quantitative Analysis of the Gas Entrainment Process of Intermittent Gas Jets with Laser-Induced Fluorescence of Ambient Gas (LIFA).* Nippon Kikai Gakkai Ronbunshu, B Hen/Transactions of the Japan Society of Mechanical Engineers, Part B 1993, 59 (559), pp.865-871

[174] Rehm J. E., Clemens N. T. *Relationship between vorticity/strain and Reaction Zone Structure in Turbulent Non-Premixed Jet Flames.* Symposium (International) on Combustion 1998, 1 , pp.1113-1120

[175] Wang G., Karpetis A. N., Barlow R. S. *Dissipation Length Scales in Turbulent Nonpremixed Jet Flames.* Combustion and Flame 2007, 148 (1-2), pp.62-75

[176] Orlemann C., Schulz, C., Wolfrum, C. *NO-Flow Tagging by Photodissociation of NO_2. A New Approach Fro Measuring Small-Scale Flow Structures.* Chemical Physics Letters 1999, 307 , pp.15-20

[177] Gulati A., Warren R. E.,Jr. *NO2-Based Laser-Induced Fluorescence Technique to Measure Cold-Flow Mixing.* Journal of Propulsion and Power 1994, 10 (1), pp.54-61

[178] Markides C. N., Mastorakos E. *Measurements of Scalar Dissipation in a Turbulent Plume with Planar Laser-Induced Fluorescence of Acetone.* Chemical Engineering Science 2006, 61 (9), pp.2835-2842

[179] Sakakibara J., Hishida K., Maeda M. *Vortex Structure and Heat Transfer in the Stagnation Region of a Two-Dimensional Impinging Jet (Simultaneous Measurements of Velocity and Temperature Fields by DPIV and LIF).* Nippon Kikai Gakkai Ronbunshu, B Hen/Transactions of the Japan Society of Mechanical Engineers, Part B 1994, 60 (573), pp.18-25

[180] Sakakibara J., Hishida K., Maeda M. *Quantitative Visualization of Convective Heat Transfer Near the Stagnation Region of an Impinging Jet.* Proceedings of the 1993 ASME winter annual meeting; Nov 28-Dec 3 1993; New Orleans, LA, USA: Publ by ASME, New York, NY, USA; 1993 pp.93-9

[181] Van Vliet E., Van Bergen S. M., Derksen J. J., Portela L. M., Van Den Akker H. E. A. *Time-Resolved, 3D, Laser-Induced Fluorescence Measurements of Fine-Structure Passive Scalar Mixing in a Tubular Reactor.* Experiments in Fluids 2004, 37 (1), pp.1-21

[182] Guillard F., Fritzon R., Revstedt J., Tragardh C., Fuchs M. A. L. *Mixing in a Confined Turbulent Impinging Jet using Planar Laser-Induced Fluorescence.* Experiments in Fluids 1998, 25 (2), pp.143-150

[183] Arnold A., Bombach R., Kappeli B., Schlegel A. *Quantitative Measurements of OH Concentration Fields by Two-Dimensional Laser-Induced Fluorescence.* Applied Physics B: Lasers and Optics 1997, 64 (5), pp.579-583

[184] Boyarshinov B. F., Fedorov S. Y. *Measurement of Temperature and Concentration of OH Radicals in Combustion of Hydrogen and Ethanol by the Laser-Induced Fluorescence Technique.* Fizika Goreniya i Vzryva 2004, 40 (5), pp.16-20

[185] Choudhuri A. R., Gollahalli S. R. *Measurement of OH Concentrations in Turbulent Diffusion Flames using Combined LIF and Raman Spectroscopy.* 35th intesociety energy conversion engineering conference; Jul 24-Jul 28 2000; Las Vegas, NA, USA: Institute of Electrical and Electronics Engineers Inc., Piscataway, NJ, USA; 2000 pp.1137-46

[186] Einecke S., Schulz C., Sick V. *Measurement of Temperature, Fuel Concentration and Equivalence Ratio Fields using Tracer LIF in IC Engine Combustion.* Applied Physics B: Lasers and Optics 2000, 71 , pp.717-723

[187] Guan X., Liu J., Huang M., Hu Z., Zhang Z., Ye X., et al. *Detection of CO Concentration in a Methane-Air Flame by TP-LIF.* Qiangjiguang Yu Lizishu/High Power Laser and Particle Beams 2005, 17 (1), pp.17-21

[188] Juchmann W., Latzel H., Shin D. I., Peiter G., Dreier T., Volpp H. -., et al. *Absolute Radical Concentration Measurements and Modeling of Low-Pressure CH4/O2/NO Flames.* Symposium (International) on Combustion 1998, 1 , pp.469-476

[189] Myhr F. H., Driscoll J. F. *Oxygen-Atom Concentrations Measured in Flames: A Method to Improve the Accuracy of Laser-Induced Fluorescence Diagnostics.* Applied Optics 2001, 40 (30), pp.5388-5394

[190] Schiessl R., Pixner P., Dreizler A., Maas U. *Formaldehyde Formation in the Endgas of Otto Engines: Numerical Simulations and Quantitative Concentration Measurements.* Combustion Science and Technology 1999, 149 (1), pp.339-360

[191] Su L. K., Han D., Mungal M. G. *Measurements of Velocity and Fuel Concentration in the Stabilization Region of Lifted Jet Diffusion Flames.* 28th international symposium on combustion; Jul 30-Aug 4 2000; Edinburgh, United Kingdom: Combustion Institute; 2000 pp.327-33

[192] Thijssen J. H., Toqan M. A., Beer J. M., Sarofim A. F. *Monitoring of PAC Concentrations in Semi-Industrial Scale Turbulent Diffusion Flames by Laser Induced Fluorescence.* Combustion Science and Technology 1993, 90 (1-4), pp.101-110

[193] Tsujimura T., Ohta A., Tokunaga Y., Senda J., Fujimoto H. *Distribution of Gaseous Fuel Concentration in Unsteady Jet Measured by Planar Laser-Induced Rayleigh Scattering (Quantitative Measurement for Mixture Concentration in a High-Pressure Ambient).* Nihon Kikai Gakkai Ronbunshu, B Hen/Transactions of the Japan Society of Mechanical Engineers, Part B 2006, 72 (8), pp.2041-2047

[194] Vyrodov A. O., Heinze J., Dillmann M., Meier U. E., Stricker W. *Laser-Induced Fluorescence Thermometry and Concentration Measurements on NO A-X (0-0) Transitions in the Exhaust Gas of High Pressure CH4/air Flames.* Applied Physics B: Lasers and Optics 1995, 61 (5), pp.409-414

[195] Chu C. R., Li K. S., Wu R. S. *Concentration Measurements of Buoyant Jets using Planar Laser-Induced Fluorescence.* Part B-1; Aug 10-15 1997; San Francisco, CA, USA: ASCE, New York, NY, USA; 1997 pp.197-202

[196] Lozano A., Yip B., Hanson R. K. *Acetone: A Tracer for Concentration Measurements in Gaseous Flows by Planar Laser-Induced Fluorescence.* Experiments in Fluids 1992, 13 , pp.369-376

[197] Lozano A., Smith S. H., Mungal M. G., Hanson R. K. *Concentration Measurements in a Transverse Jet by Planar Laser-Induced Fluorescence of Acetone.* AIAA Journal 1994, 32 (1), pp.218-221

[198] Qubbaj A. R., Gollahalli S. R. *Laser-Induced Fluorescence Measurements in Venturi-Cascaded Propane Gas Jet Flames.* Heat transfer division - 1999 ((the ASME international mechanical engineering congress and exposition); Nov 14-Nov 19 1999; Nashville, TN, USA: ASME, Fairfield, NJ, USA; 1999 pp.155-66

[199] Tian X., Roberts P. J. W. *A 3D LIF System for Turbulent Buoyant Jet Flows.* Experiments in Fluids 2003, 35 (6), pp.636-647

[200] Bockle S., Kazenwadel J., Kunzelmann T., Shin D., Schulz C., Wolfrum J. *Simultaneous Single-Shot Laser-Based Imaging of Formaldehyde, OH, and Temperature in Turbulent Flames.* 28th international symposium on combustion; Jul 30-Aug 4 2000; Edinburgh, United Kingdom: Combustion Institute; 2000 pp.279-85

[201] Del Vecchio A., Palumbo G., Koch U., Guelhan A. *Temperature Measurements by Laser-Induced Fluorescence Spectroscopy in Nonequilibrium High-Enthalpy Flow.* Journal of Thermophysics and Heat Transfer 2000, 14 (2), pp.216-224

[202] Funatani S., Fujisawa N., Ikeda H. *Simultaneous Measurement of Temperature and Velocity using Two-Colour LIF Combined with PIV with a Colour CCD Camera and its Application to the Turbulent Buoyant Plume.* Measurement Science and Technology 2004, 15 (5), pp.983-990

[203] Kearney S. P., Reyes F. V. *Quantitative Temperature Imaging in Gas-Phase Turbulent Thermal Convection by Laser-Induced Fluorescence of Acetone.* Experiments in Fluids 2003, 34 (1), pp.87-97

[204] Sakakibara J., Adrian R. J. *Measurement of Temperature Field of a Rayleigh-Benard Convection using Two-Color Laser-Induced Fluorescence.* Experiments in Fluids 2004, 37 (3), pp.331-340

[205] Williams B. A., Fleming J. W. *Rapid Determination of Flame Temperature Profiles using OH LIF on a Limited Number of Rotational Lines.* Laser applications in combustion and combustion diagnostics II; Jan 25-26 1994; Los Angeles, CA, USA: Publ by Society of Photo-Optical Instrumentation Engineers, Bellingham, WA, USA; 1994 pp.74-8

[206] Castanet G., Lavieille P., Lebouche M., Lemoine F. *Measurement of the Temperature Distribution within Monodisperse Combusting Droplets in Linear Streams using Two-Color Laser-Induced Fluorescence.* Experiments in Fluids 2003, 35 (6), pp.563-571

[207] Hwang S. M., Kurose R., Akamatsu F., Tsuji H., Makino H., Katsuki M. *Application of Optical Diagnostics Techniques to a Laboratory-Scale Turbulent Pulverized Coal Flame.* Energy and Fuels 2005, 19 (2), pp.382-392

[208] Tichy F. E., Bjorge T., Magnussen B. F., Bengtsson P. E., Mauss F. *Two-Dimensional Imaging of Glyoxal (C2H2O2) in Acetylene Flames using Laser-Induced Fluorescence.* Applied Physics B: Lasers and Optics 1998, 66 (1), pp.115-119

[209] Joklik R. G., Daily J. W. *LIF Study of CH $A^2\Delta$ Collision Dynamics in a Low Pressure Oxy-Acetylene Flames.* Combustion and Flame 1987, 69 (2), pp.211-219

[210] Lee S., Tananka D., Kusaka J., Daisho Y. *Two-Dimensional Laser Induced Fluorescence Measurement of Spray and OH Radicals of LPG in Constant Volume Chamber.* JSAE Review 2002, 23 (2), pp.195-203

[211] Zhang Y., Yoon Y., Kelly P. B., Kennedy I. M. *LIF Measurements of Atomic Arsenic in Hydrogen and Methane Diffusion Flames.* Symposium (International) on Combustion 1998, 2 , pp.1777-1783

[212] Yamada E., Shinoda M., Yamashita H., Kitagawa K., Arai N. *Magnetic Effect on OH Radical Distributions in a Hydrogen-Oxygen Diffusion Flame.* 2001 international joint power generation

conference; Jun 4-7 2001; New Orleans, LA, United States: American Society of Mechanical Engineers, New York, NY 10016-5990, United States; 2001 pp.139-44

[213] Barlow R. S., Carter C. D. *Raman/Rayleigh/LIF Measurements of Nitric Oxide Formation in Turbulent Hydrogen Jet Flames.* Combustion and Flame 1994, 97 (3-4), pp.261-280

[214] Medaerts F., Puechberty D. *In-Cylinder Fuel/Air Mixture and Flame Front Visualization in a Transparent Engine using PLIF: A Comparison between Natural Gas and Gasoline used as a Fuel.* SAE Technical Paper Series 1998,

[215] Frank J. H., Barlow R. S. *Simultaneous Rayleigh, Raman, and LIF Measurements in Turbulent Premixed Methane-Air Flames.* Symposium (International) on Combustion 1998, 1 , pp.759-766

[216] Charlston-Goch D., Chadwick B. L., Morrison R. J. S., Campisi A., Thomsen D. D., Laurendeau N. M. *Laser-Induced Fluorescence Measurements and Modeling of Nitric Oxide in Premixed Flames of CO+H2+CH4 and Air at High Pressures. I. Nitrogen Fixation.* Combustion and Flame 2001, 125 (1-2), pp.729-743

[217] Bergmann V., Meier W., Wolff D., Stricker W. *Application of Spontaneous Raman and Rayleigh Scattering and 2D LIF for the Characterization of a Turbulent CH4/H2/N2 Jet Diffusion Flame.* Applied Physics B: Lasers and Optics 1998, 66 (4), pp.489-502

[218] Etzkorn T., Muris S., Wolfrum J., Dembny C., Bockhorn H., Nelson P. F., et al. *Destruction and Formation of NO in Low Pressure Stoichiometric CH4/O2 Flames.* Proceedings of the 24th international symposium on combustion; Jul 5-10 1992; Sydney, Engl: Publ by Combustion Inst, Pittsburgh, PA, USA; 1992 pp.925-32

[219] Gibaud C., Snyder J. A., Sick V., Lindstedt R. P., Schofield K., Dunn-Rankin D., et al. *Laser-Induced Fluorescence Measurements and Modeling of Absolute CH Concentrations in Strained Laminar methane/air Diffusion Flames.* Proceedings of the Combustion Institute 2005, 30 (1), pp.455-463

[220] Heard D. E., Jeffries J. B., Smith G. P., Crosley D. R. *LIF Measurements in methane/air Flames of Radicals Important in Prompt-NO Formation.* Combustion and Flame 1992, 88 (2), pp.137-148

[221] Kaminski C.,F., Hult J., Aldén M., Lindenmaier S., Dreizler A., Maas U., et al. *Spark Ignition of Turbulent Methane/Air Mixture Revealed by Time-Resolved Planar Laser Induced Fluorescence and Direct Numerical Simulations.* Proceedings of the Combustion Institute 2000, 28 , pp.399-405

[222] Malmsten Y., Axner O. *Detection of OH by-Laser-Induced Fluorescence in a CH4/N2 - O2/N2 Counter-Flow Atmospheric Pressure Diffusion Flame.* Chalmers Tekniska Hogskola, Goteborg, Sweden; 1997

[223] Meier W., Barlow R. S., Chen Y. -., Chen J. -. *Raman/Rayleigh/LIF Measurements in a Turbulent CH4/H2/N2 Jet Diffusion Flame: Experimental Techniques and Turbulence-Chemistry Interaction.* Combustion and Flame 2000, 123 (3), pp.326-343

[224] Sepman A., Mokhov A. V., Levinsky H. B. *A Laser-Induced Fluorescence and Coherent Anti-Stokes Raman Scattering Study of no Formation in Preheated, Laminar, Rich Premixed, methane/air Flames.* Twenty-ninth international symposium on combustion hokkaido university sapporo japan; Jul 21-25 2002; Sapporo, Japan: Combustion Institute; 2002 pp.2187-93

[225] Sick V., Hildenbrand F., Lindstedt P. *Quantitative Laser-Based Measurements and Detailed Chemical Kinetic Modeling of Nitric Oxide Concentrations in Methane-Air Counterflow Diffusion Flames.* Symposium (International) on Combustion 1998, 1 , pp.1401-1409

[226] Watson K. A., Lyons K. M., Donbar J. M., Carter C. D. *Simultaneous Rayleigh Imaging and CH-PLIF Measurements in a Lifted Jet Diffusion Flame.* Combustion and Flame 2000, 123 (1), pp.252-265

[227] Aizawa T., Kosaka H. *Spectroscopic Analysis of Early Soot Formation Region in a Transient Spray Flame Via Pyrene-LIF Technique.* Nihon Kikai Gakkai Ronbunshu, B Hen/Transactions of the Japan Society of Mechanical Engineers, Part B 2006, 72 (7), pp.1850-1856

[228] Brockhinke A., Hartlieb A. T., Kohse-Hoeinghaus K., Crosley D. R. *Tunable KrF Laser-Induced Fluorescence of C2 in a Sooting Flame.* Applied Physics B: Lasers and Optics 1998, 67 (5), pp.659-665

[229] Crua C., Kennaird D.,A., Heikal M.,R. *Laser-Induced Incandescence Study of Diesel Soot Formation in a Rapid Compression Machine at Elevated Pressures.* Combustion and Flame 2003, 135 , pp.475-488

[230] Goh S. F., Gollahalli S. R. *Fuel Jet Dilution Effects on the Sooting Characteristics of Propylene Diffusion Flames Near the Smoke Point.* 42nd AIAA aerospace sciences meeting and exhibit; Jan 5-8 2004; Reno, NV, United States: American Institute of Aeronautics and Astronautics Inc., Reston, United States; 2004 pp.6267-75

[231] Smyth K. C., Harrington J. E., Johnsson E. L., Pitts W. M. *Greatly Enhanced Soot Scattering in Flickering CH4/air Diffusion Flames.* Combustion and Flame 1993, 95 (1-2), pp.229-239

[232] Hult J., Gashi S., Chakraborty N., Klein M., Jenkins K. W., Cant S., et al. *Measurement of Flame Surface Density for Turbulent Premixed Flames using PLIF and DNS.* 31st international symposium on combustion; Aug 5-11 2006; Heidelberg, Germany: Elsevier Ltd, Oxford, OX5 1GB, United Kingdom; 2007 pp.1319-26

[233] Tacke M. M., Linow S., Geiss S., Hassel E. P., Janicka J., Chen J. Y. *Experimental and Numerical Study of a Highly Diluted Turbulent Diffusion Flame Close to Blowout.* Symposium (International) on Combustion 1998, 1 , pp.1139-1148

[234] Ungut A., Gorgeon A., Gokalp I. *Planar Laser Induced Fluorescence Study of Turbulent Flame Kernel Growth and Fractal Characteristics.* Combustion Science and Technology 1993, 92 (4-6), pp.265-290

[235] Xu J., Warnatz J. *Two-Dimensional Imaging of OH Radicals in Spark Ignition Kernels by Laser Induced Fluorescence.* Berichte der Bunsengesellschaft fuer Physikalische Chemie 1993, 97 (12), pp.1741-1744

[236] Frieden D., Sick V. *Investigation of the Fuel Injection, Mixing and Combustion Processes in an SIDI Engine using Quasi-3D LIF Imaging.* SAE Technical Paper Series 2003, 2003-01-0068

[237] Paul P.,H., Najm H.,N. *Planar Laser Induced Fluorescence Imaging of Flame Heat Release Rate.* Twenty seventh symposium (international) on combustion; The Combustion Institute; 1998 pp.43-50

[238] Choi G. -., Yang J. -., Kim D. -., Tanahashi M., Miyauchi T. *Estimations of Local Heat Release Rate in the Methane-Air Premixed Flames.* Thermochimica Acta 2007, 455 (1-2), pp.34-39

[239] Ragucci R., De Joannon M., Cavaliere A. *Analysis of Pyrolysis Process in Diesel-Like Combustion by Means of Laser-Induced Fluorescence.* Part 2 (of 2); Jul 28-Aug 2 1996; Napoli, Italy: Combustion Inst, Pittsburg, PA, USA; 1996 pp.2525-31

[240] Watson K. A., Lyons K. M., Donbar J.,M., Carter C.,D. *Scalar and Velocity Field Measurement in a Lifted CH4-Air Diffusion Flame.* Combustion and Flame 1999, 117 , pp.257-271

[241] Fayoux A., Dupré S., Scouflaire P., Houille S., Pajot O., Rolon J. C. *OH and HCHO LIF Measurements in HCCI Engine.* 12th International symposium on applications of laser techniques to fluid mechanics; Lisbon, Portugal: ; 2004

[242] Kashdan J., Bruneaux G. *Mixture Preparation and Combustion in an Optically-Accessible HCCI, Diesel Engine.* Oil and Gas Science and Technology 2006, 61 (1), pp.25-42

[243] Schrewe M. R., Ghandhi J. B. *Near-Wall Formaldehyde Planar Laser-Induced Fluorescence Measurements during HCCI Combustion.* 31st international symposium on combustion; Aug 5-11 2006; Heidelberg, Germany: Elsevier Ltd, Oxford, OX5 1GB, United Kingdom; 2007 pp.2871-8

[244] Akihama K., Fujikawa T., Hattori Y. *Laser-Induced Fluorescence Imaging of NO in a Port-Fuel-Injected Stratified-Charge SI Engine - Correlations between NO Formation Region and Stratified Fuel Distribution.* Proceedings of the 1998 SAE international spring fuels & lubricants meeting & exposition; May 4-6 1998; Dearborn, MI, USA: SAE, Warrendale, PA, USA; 1998 pp.91-101

[245] McGee J., Alger T., Blobaum E., Wooldridge S. *Evaluation of a Direct Injection Stratified Charge Combustion System using Tracer PLIF.* SAE Technical Paper Series 2004,

[246] Strand T. E., Rathamer D. A., Ghandhi J. B. *Flame Structure Visualization of Stratified Combustion in a DISI Engine Via PLIF.* SAE Technical Paper Series 2001,

[247] Acroumanis C., Enotiadis A. C. *In-Cylinder Fuel Distribution in a Port-Injected Model Engine using Rayleigh Scattering.* Experiments in Fluids 1991, 11 , pp.375-387

[248] Chou C. C. -., Tsai C., Shiu C., Liu S. C., Zhu T. *Measurement of NOy during Campaign of Air Quality Research in Beijing 2006 (CAREBeijing-2006): Implications for the Ozone Production Efficiency of NOx.* JOURNAL OF GEOPHYSICAL RESEARCH-ATMOSPHERES} 2009}, 114}

[249] Frank J. H., Kaiser S. A., Long M. B. *Reaction-Rate, Mixture-Fraction, and Temperature Imaging in Turhulent methane/air Jet Flames.* Twenty-ninth international symposium on combustion Hokkaido university sapporo japan; Jul 21-25 2002; Sapporo, Japan: Combustion Institute; 2002 pp.2687-94

[250] Fujikawa T., Hattori Y., Koike M., Akihama K., Kobayashi T., Matsushita S. *Quantitative 2-D Fuel Distribution Measurements in a Direct-Injection Gasoline Engine using Laser-Induced Fluorescence Technique.* JSME International Journal, Series B 1999, 42 (4), pp.760-767

[251] Kraemer H., Muench K., Leipertz A. *Comparison of Two Injectors by LIF with Respect to Mixture Formation and Combustion Inside the Cylinder of a Transparent SI Engine.* Proceedings of the 1997 international fall fuels & lubricants meeting & exposition; Oct 13-16 1997; Tulsa, OK, USA: SAE, Warrendale, PA, USA; 1997 pp.63-71

[252] Wolff D., Schlüter H., Beushausen V., Andresen P. *Quantitative Determination of Fuel Air Mixture Distributions in an Internal Combustion Engine using PLIF of Acetone.* Berichte der Bunsengesellschaft fuer Physikalische Chemie 1993, 97 (12), pp.1738-1741

[253] Ipp W., Egermann J., Wagner V., Leipertz A. *Visualization of the Qualitative Fuel Distribution and Mixture Formation Inside a Transparent GDI Engine with 2D Mie and LIEF Techniques and Comparison to Quantitative Measurementsof the Air/Fuel Ratio with 1D Raman Spectroscopy.* SAE Technical Paper 2000, 200-01-1793

[254] Ipp W., Egermann J., Schmitz I., Wagner V., Leipertz A., Hartmann M., et al. *2D Mapping and Quantification of the in-Cylinder Air Fuel-Ratio in a GDI Engine by Means of LIF and Comparison to Simultaneous Results from 1D Raman Measurements.* SAE Technical Paper Series 2001,

[255] Blotevogel T., Egermann J., Goldlücke J., Leipertz A., Hartmann M., Schenk M., et al. *Developing Planar Laser-Induced Fluorescence for the Investigation of the Mixture Formation Process in Hydrogen Engines.* SAE Technical Paper Series 2004,

[256] White C. *A Qualitative Evaluation of Mixture Formation in a Direct-Injection Hydrogen-Fuelled Engine.* SAE Technical Papers 2007, 2007-01-1467

[257] Oh S., Bae C. *Mixture Distribution and Flame Propagation in a Heavy-Duty Liquid Petroleum Gas Engine with Liquid Phase Injection.* International Journal of Engine Research 2004, 5 (6), pp.513-524

[258] Thurber M. C., Hanson R. K. *Simultaneous Imaging of Temperature and Mole Fraction using Acetone Planar Laser-Induced Fluorescence.* Experiments in Fluids 2001, 30 (1), pp.93-101

[259] Neij H. *Development of Laser-Induced Fluorescence for Precombustion Diagnostics in Spark-Ignition Engines [dissertation].* Lund: Lund University Editor; 1998

[260] Sick V. *Exhaust-Gas Imaging Via Planar Laser-Induced Fluorescence of Sulfur Dioxide.* Applied Physics B: Lasers and Optics 2002, 74 , pp.461-463

[261] Schulz C., Sick V. *Tracer-LIF Diagnostics: Quantitative Measurement of Fuel Concentration, Temperature and Fuel/Air Ratio in Practical Combustion Systems.* Progress in Energy and Combustion Science 2005, 31 , pp.75-121

[262] Neij H., Aldén M. *Application of Two-Photon Laser-Induced Fluorescence for Visualization of Water Vapor in Combustion Environments.* Applied Optics 1994, 33 (27), pp.6514-6523

[263] Decker M., Sick V., Heinze J., Stricker W. *2-D Temperature Measurements in High Pressure Flames using LIF of Molecular Oxygen.* Pacific Rim Conference on Lasers and Electro-Optics, CLEO - Technical Digest 1996, , pp.50-51

[264] Lee M. P., Hanson R. K. *Calculations of O_2 Absorption and Fluorescence at Elevated Temperatures for a Broadband Argon-Fluoride Laser Source at 193nm.* Journal of Quantitative Spectroscopy and Radiative Transfer 1986, 36 , pp.425-440

[265] Komiyama M., Tanaka T., Takagi T. *Measurements of O2 Concentration and Temperature in Diffusion Flame by Excimer-Laser-Induced Fluorescence and Rayleigh Scattering.* JSME International Journal, Series B: Fluids and Thermal Engineering 1993, 36 (2), pp.378-382

[266] Roller A., Arnold A., Decker M., Sick V., Wolfrum J., Hentschel W. *Non-Intrusive Temperature Measurements during the Compression Phase of a DI Diesel Engine.* SAE Technical Paper Series 1995, 952461

[267] Nakagawa H., Endo H., Deguchi Y., Noda M., Oikawa H., Shimada T. *NO Measurement in Diesel Spray Flame using Laser Induced Fluorescence.* Proceedings of the 1997 international congress and exposition; Feb 24-27 1997; Detroit, MI, USA: SAE, Warrendale, PA, USA; 1997 pp.187-96

[268] Cooper C. S., Laurendeau N. M. *Parametric Study of NO Production Via Quantitative Laser-Induced Fluorescence in High-Pressure, Swirl-Stabilized Spray Flames.* 28th international symposium on combustion; Jul 30-Aug 4 2000; Edinburgh, United Kingdom: Combustion Institute; 2000 pp.287-93

[269] Deguchi Y., Noda M., Murata M., Inada M., Nishida H. *OH and NO Visualization Inside a Gas Turbine Combustor using Laser-Induced Fluorescence.* Nippon Kikai Gakkai Ronbunshu, B Hen/Transactions of the Japan Society of Mechanical Engineers, Part B 1996, 62 (594), pp.787-792

[270] Bessler W. G., Schultz C., Lee T., Jeffries J. B., Hanson R. K. *Carbon Dioxide UV Laser Induced Fluorescence in High Pressure Flames.* Chemical Physics Letters 2003, 375 , pp.344-349

[271] Bessler W. G., Schulz C., Lee T., Jeffries J. B., Hanson R. K. *Strategies for Laser Induced Fluorescence Detection of Nitric Oxide in High-Pressure Flames. I. A-X(0,0) Excitation.* Applied Optics 2003, 41 (18), pp.3547-3557

[272] Di Rosa M. D., Klavuhn K. G., Hanson R. K. *PLIF Imaging of NO and O2 in High-Pressure Flames.* Optical techniques in fluid, thermal, and combustion flow; Jul 10-13 95; San Diego, CA, USA: Society of Photo-Optical Instrumentation Engineers, Bellingham, WA, USA; 1995 pp.509-18

[273] Cattolica R. J. *Combustion-Torch Ignition: Fluorescence Imaging of NO2.* Symposium (International) on Combustion 1988, 21 (1), pp.1551-1552, IN1-IN4, 1553-1559

[274] Ravikrishna R. V., Laurendeau N. M. *Laser-Induced Fluorescence Measurements and Modeling of Nitric Oxide in Methane-Air and Ethane-Air Counterflow Diffusion Flames.* Combustion and Flame 2000, 120 (3), pp.372-382

[275] Ravikrishna R. V., Cooper C. S., Laurendeau N. M. *Comparison of Saturated and Linear Laser-Induced Fluorescence Measurements of Nitric Oxide in Counterflow Diffusion Flames.* Combustion and Flame 1999, 117 (4), pp.810-820

[276] Meyer T. R., King G. F., Martin G. C., Lucht R. P., Schauer F. R., Dutton J. C. *Accuracy and Resolution Issues in NO/acetone PLIF Measurements of Gas-Phase Molecular Mixing.* Experiments in Fluids 2002, 32 (6), pp.603-611

[277] Dam N., Klein-Douwel R. J. H., Sijstema N., ter Meulen J. *Nitric Oxide Flow Tagging in Unseeded Air.* Optics Letters 2001, 26 , pp.36-38

[278] Donnelly K. M., Kaufman F. J. *Mechanism of NO_2 Fluorescence Quenching.* Journal of Chemical Physics 1977, 67 (10), pp.4768-4769

[279] Zhao F., Taketomi M., Nishida K., Hiroyasu H. *PLIF Measurements of the Cyclic Variability of Mixture Concentration in an SI Engine.* SAE Technical Paper Series 1994, 940988

[280] Lievin J., Delon A., Jost R. *Absorption Cross Section of NO2 by the Reflection Method from Ab Initio Calculations Involving the Three Low Lying Electronic States.* Journal of Chemical Physics 1998, 108 (21), pp.8931

[281] Greenough K. F., Duncan A. B. F. *The Fluorescence of Sulfur Dioxide.* Journal of the American Chemical Society 1960, 83 , pp.555-560

[282] Strickler S. J., Howell D. B. *Luminescence and Radiations Transitions in Sulphur Dioxide Gas.* The Journal of chemical physics 1968, 49 (1), pp.1947-1951

[283] Mettee H. D. *Fluorescence and Phosphorescence of SO$_2$ Vapor.* Journal of Chemical Physics 1968, 49 , pp.1784-1793

[284] Rao T. N., Collier S. S., Calvert J. G. *Primary Photophysical Processes in the Photochemistry of Sulfur Dioxide at 2875 Å.* Journal of the American Chemical Society 1968, 91 (7), pp.1609-1615

[285] Rao T. N., Collier S. S., Calvert J. G. *The Quenching Reactions of the First Excited Singlet and Triplet States of Sulphur Dioxide with Oxygen and Corbon Dioxide.* Journal of the American Chemical Society 1968, 91 (7), pp.1616-1621

[286] Pitz R. W., Wehrmeyer J. A., Ribarov L. A., Oguss D. A., Batliwala F., DeBarber P. A., et al. *Unseeded Molecular Flow Tagging in Cold and Hot Flows using Ozone and Hydroxyl Tagging Velocimitry.* Measurement Science and Technology 2000, 11 (9), pp.1259-1271

[287] Wolfrum J. *Lasers in Combustion: From Basic Theory to Practical Devices.* Twenty-seventh symposium (international) on combustion; The Combustion Institute; 1998 pp.1-14

[288] Hiller B., Hanson R. *Properties of the Iodine Molecule Relevant to Laser Induced Fluorescence Experiments in Gaseous Flows.* Experiments in Fluids 1990, 10 , pp.1-11

[289] Lemoine F., Antoine Y., Wolff M., Lebouche M. *Simultaneous Temperature and 2D Velocity Measurements in a Turbulent Heated Jet using Combined Laser-Induced Fluorescence and LDA.* Experiments in Fluids 1999, 26 (4), pp.315-323

[290] Capelle G. A., Broida H. P. *Lifetimes and Quenching Cross Sections of I$_2$ (B$_3\Pi_{Ou}^+$).* Journal of Chemical Physics 58 (10), pp.4212-4222

[291] Birks JB, editor. Organic molecular photophysics. John Wiley & Sons; 1975

[292] Birks JB, editor. Organic molecular photophysics. John Wiley & Sons; 1973

[293] Berlman I. B. *Handbook of Fluorescence Spectra of Aromatic Molecules*; 1971 New York, Academic Press; ISBN: 0120926563.

[294] Reboux P. J., Dionnet F. *A New Approach of Planar Laser Induced Fluorescence Applied to Fuel/Air Ratio Measurement in the Compression Stroke of an Optical S.I. Engine.* SAE Technical Paper Series 1994, 941988

[295] Koban W., Koch J. D., Hanson R. K., Schulz C. *Oxygen Quenching of Toluene Fluorescence at Elevated Temperatures.* Applied Physics B 2005, 80 (6), pp.777-784

[296] Koban W., Koch J. D., Hanson R. K., Schultz C. *Toluene LIF at Elevated Temperatures: Implications for Air-Fuel Ratio Measurements.* Applied Physics B 2005, 80 (2), pp.147-150

[297] Koban W., Koch J. D., Sick V., Wermuth N., Hanson R. K., Schulz C. *Predicting LIF Signal Strength for Toluene and 3-Pentanone Under Engine-Related Temperature and Pressure Conditions.* Proceedings of the Combustion Institute 2005, 30 (1), pp.1545-1553

[298] Frieden D., Sick v., Gronki J., Schultz C. *Quatitative Oxygen Imaging in an Engine.* Applied Physics B 2002, 75 , pp.137-141

[299] Karcher W, Fordham RJ, Dubois JJ, Glaude, P. G. J. M., Ligthart JAM, editors. Spectral atlas of polycyclic aromatic compounds. Springer; 1991

[300] Allain L. R., Stratis D. N., Cullum B. M., Mobley J., Hajaligol M. R., Vo-Dinh T. *Real-Time Detection of PAH Mixtures in the Vapor Phase at High Temperatures.* Journal of Analytical and Applied Pyrolysis 2003, 66 (1), pp.145-154

[301] Davy M.,H., Williams P., Han D., Steeper R. *Evaporation Characteristics of 3-Pentanone-Iso-Octane Binary System.* Experiments in Fluids 2003, 35 , pp.92-99

[302] Lin M., Sick V. *Mixture Evaporation Characteristics Prediction for LIF Measurements using PSRK (Predictive Soave-Redlich-Kwong) Equation of State.* SAE Technical Paper Series 2002, 2002-01-2750

[303] Breuer G. M., Lee E. K. C. *Fluorescence Decay Times of Cyclic Ketones, Acetone, and Butanal in the Gas Phase.* The Journal of Physical Chemistry 1971, 75 (7), pp.989-990

[304] Yuen S. L., Peters J. E., Lucht R. P. *Pressure Dependence of Laser Induced Fluorescence Form Acetone.* Applied Optics 1997, 36 (15), pp.3271-3277

[305] Thurber M. C., Grisch F., Kirby B. J., Votsmeier M., Hanson R. K. *Measurements and the Modelling of Acetone Laser-Induced Fluorescence with Implications for Temperature-Imaging Diagnostics.* Applied Optics 1998, 37 (21), pp.49634978

[306] Ossler F., Aldén M. *Measurement of Picosecond Laser Induced Fluorescence from Gas Phase 3-Pentanone and Acetone: Implications to Combustion Diagnostics.* Applied Physics B: Lasers and Optics 1997, 64 , pp.493-502

[307] Grossmann F., Monkhouse P. B., Ridder M., Sick V., Wolfrum J. *Temperature and Pressure Dependences of the Laser-Induced Fluorescence of Gas-Phase Acetone and 3-Pentanone.* Applied Physics B: Lasers and Optics 1996, 62 , pp.249-253

[308] Nau W. M., Scaiano J. C. *Oxygen Quenching of Excited Aliphatic Ketones and Diketones.* Journal of Physical Chemistry 1996, 100 , pp.11360-11367

[309] Haas Y. *Photochemical α-Cleavage of Ketones: Revisiting Acetone.* Photochemical & Photobiological Science 2004, 3 , pp.6-16

[310] Green R. M., Cloutman L. D. *Planar LIF Observations of Unburned Fuel Escaping the Upper Ring-Land Crevice in an SI Engine.* Proceedings of the 1997 international congress and exposition; Feb 24-27 1997; Detroit, MI, USA: SAE, Warrendale, PA, USA; 1997 pp.1-18

[311] Bryant R. A., Driscoll J.,F. *Acetone Laser Induced Fluorescence for Low Pressure Low Temperature Flow Visualisation.* Experiments in Fluids 2000, 28 , pp.471-476

[312] Han D., Steeper R. R. *An LIF Equivalence Ratio Imaging Technique for Multicomponent Fuels in an IC Engine.* Proceedings of the Combustion Institute 2002, 29 , pp.727-734

[313] Neij H., Johansson B., Aldén M. *Development and Demonstration of 2D-LIF for Studies of Mixture Preparation in SI Engines.* Combustion and Flame 1994, 99 , pp.449-457

[314] Arnold A., Buschmann A., Cousyn B., Decker M., Vannobel F., Sick V., et al. *Simultaneous Imaging of Fuel and Hydroxyl Radicals in an in-Line Four Cylinder SI Engine.* SAE Technical Papers 1993, 932696

[315] Schießl R., Maas U. *Analysis of Endgas Temperature Fluctuations in an Si Engine by Laser-Induced Fluorescence.* Combustion and Flame 2003, 133 (1-2), pp.19-27

[316] Burkert A., Grebner D., Muller D., Triebel W., Konig J. *Single-Shot Imaging of Formaldehyde in Hydrocarbon Flames by XeF Excimer Laser-Induced Fluorescence.* 28th international symposium on combustion; Jul 30-Aug 4 2000; Edinburgh, United Kingdom: Combustion Institute; 2000 pp.1655-61

[317] Burkert A., Triebel W., Stafast H., Konig J. *Single-Shot Imaging of Gas Temperatures in Low-Temperature Combustion Based on Laser-Induced Fluorescence of Formaldehyde.* Twenty-ninth international symposium on combustion hokkaido university sapporo japan; Jul 21-25 2002; Sapporo, Japan: Combustion Institute; 2002 pp.2645-51

[318] Klein-Douwel R. J. H., Jeffries J. B., Luque J., Smith G. P., Crosley D. R. *CH and Formaldehyde Structures in Partially-Premixed methane/air Coflow Flames.* Combustion Science and Technology 2001, 167 (1), pp.291-310

[319] Luque J., Jeffries J. B., Smith G. P., Crosley D. R. *Quasi-Simultaneous Detection of CH2O and CH by Cavity Ring-Down Absorption and Laser-Induced Fluorescence in a methane/air Low-Pressure Flame.* Applied Physics B: Lasers and Optics 2001, 73 (7), pp.731-738

[320] Bäuerle B., Warnatz J., Behrendt F. *Time Resolved Investigation of Hot Spots in the Gas of an S. I. Engine by Means of 2D Doubled Pulse LIF of Formaldehyde.* Twenty-sixth symposium (international) on combustion; The Combustion Institute; 1996 pp.2619-26

[321] Brackmann C., Nygren J., Bai X., Li Z., Bladh H., Axelsson B., et al. *Laser-Induced Fluorescence of Formaldehyde in Combustion using Third Harmonic Nd:YAG Laser Excitation.* Spectrochimica Acta - Part A: Molecular and Biomolecular Spectroscopy 2003, 59 (14), pp.3347-3356

[322] Arnold A., Becker H., Suntz R., Monkhouse P., Wolfrum J., Maly R., et al. *Flame Front Imaging in an Internal Combustion Engine Simulator by Laser Induced Fluorescence of Acetaldehyde.* Optics Letters 1990, 15 , pp.831-833

[323] Gandini A., Whytock D. A., Kutschke K. O. *The Effect of Mercury on the Triplet State of Hexafluoroacetone.* Berichte der Bunsengesellschaft fuer Physikalische Chemie 1968, 72 (2), pp.296-301

[324] Hansen A.,D., Lee E.,K.C. *Radiative and Nonradiative Transitions in the First Excited Singlet State of Simple Linear Aldehydes.* Journal of Chemical Physics 1975, 62 , pp.3272-3277

[325] Lee T., Jeffries J. B., Hanson R. K., Bessler W. G., Schulz C. *Carbon Dioxide UV Laser-Induced Fluorescence Imaging in High-Pressure Flames.* 42nd AIAA aerospace sciences meeting and exhibit; Jan 5-8 2004; Reno, NV, United States: American Institute of Aeronautics and Astronautics Inc., Reston, United States; 2004 pp.177-82

[326] Pringsheim P. *Fluorescence*; 1948 Interscinece Publishers Inc, New York

[327] Itoh T., Kakuho A., Hishinuma H., Urushihara T., Takagi Y., Horie K., et al. *Development of a New Compound Fuel and Fluorescent Tracer Combination for use with Laser Induced Fluoescence.* SAE Technical Papers 1995, 952465

[328] Heicklen J. *The Fluorescence and Phosphorescence of Biacetyl Vapour and Acetone Vapour.* Journal of the American Chemical Society 1959, 81 , pp.3863-3866

[329] Heicklen J., Noyes W. A. *The Photolysis and Fluorescence of Acetone and Acetone-Biacetyl Mixtures.* Journal of the American Chemical Society 1959, 81 , pp.3858-3863

[330] Groh H., Lewkey G. W., Noyes W. A. *The Mechanism of Acetone Vapor Fluorescence.* The Journal of Chemical Physics 1953, 21 (1), pp.115-119

[331] Pischel U., Nau W. M. *Switch-Over in Photochemical Reaction Mechanism from Hydrogen Abstraction to Exciplex-Induced Quenching: Interaction of Triplet-Excited Versus Singlet-Excited Acetone Versus Cumyloxyl Radicals with Amines.* Journal of the American Chemical Society 2001, 123 (40), pp.9727-9737

[332] Hansen A.,D., Lee E.,K.C. *Radiative and Nonradiative Transitions in the First Excited Singlet State of Symmetrical Methyl-Substituted Acetones.* Journal of Chemical Physics 1974, 62 (1), pp.183-189

[333] Liao D. W., Mebel A. M., Hayashi M., Shiu Y. J., Chen Y. T., Lin S. H. *Ab Initio Study of the n-π* Electronic Transition in Acetone: Symmetry-Forbidden Vibronic Spectra.* Journal of Chemical Physics 1999, 111 (1), pp.205

[334] Borge M. J. G., Figuera J. M., Luque J. *Study of the Emission of the Excited Acetone Vapour at Intermediate Pressures.* Spectrochimica Acta - Part A: Molecular and Biomolecular Spectroscopy 1990, 46 (4), pp.617-621

[335] Muñoz-Caro C., Niño A., Moule D. C. *Theoretical Determination of the Torsion-Wagging Structure of the $S_1 \leftarrow S_0$ Electronic Spectrum of Acetyladehyde.* Chemical Physics 1994, 186 , pp.221-231

[336] Copeland R. A., Crosley D. R. *Radiative, Collisional and Dissociative Processes in Triplet Acetone.* Chemical Physics Letters 1985, 115 (4), pp.362-368

[337] Greenblat G. D., Ruhman S., Haas Y. *Fluorescent Decay Kinetics of Acetone Vapour at Low Pressures.* Chemical Physics Letters 1984, 112 (3), pp.200-206

[338] Gilbert A., Baggott J. *Essentials of Molecular Photochemistry*; 1991 Blackwell Scientific Publications; ISBN: 0-8493-7727-7.

[339] Liu D., Fang W., Fu X. *An Ab Initio Study of Photodissociation of Acetone.* Chemical Physics Letters 2000, 325 , pp.86-92

[340] Norrish R. G. W., Crone G. H., Saltmarsh O. D. *Primary Photochemical Reactions. Part V. the Spectroscopy and Photochemical Decomposition of Acetone.* Journal of the Chemical Society 1934, , pp.1456-1464

[341] Lee E. K. C., Lewis R. S. *Photochemistry of Simple Aldehydes and Ketones in the Gas Phase.* Advances in Photochemistry 1980, 12 , pp.1-95

[342] Blitz M. A., Heard D. E., Pilling M. J. *Study of Acetone Photodissociation Over the Wavelength Range 248-330nm: Evidende of a Mechanism Involving both the Singlet and Triplet States.* Journal of Physical Chemistry A 2006, 110 , pp.6742-6756

[343] North S. W., Blank D. A., Danial Gezelter J., Longfellow C. A., Lee Y. T. *Evidence for Stepwise Dissociation Dynamics in Acetone at 248nm and 193nm.* Journal of Chemical Physics 1995, 102 (11), pp.4447-4460

[344] Calvert JG, Pitts JN. Photochemistry of the polyatomic molecules. In: Photochemistry. New York: John Wiley & Sons, Inc.; 1966. p. 366-556

[345] Emrich M., Warneck P. *Photodissociation of Acetone in Air: Dependence on Pressure and Wavelength. Behavior of Excited Singlet State.* Journal of Physical Chemistry A 2000, 104 , pp.9436-9442

[346] Almy G. M., Anderson S. *Lifetime of Fluorescence in Diacetyl and Acetone.* Journal of Chemical Physics 1940, 8 , pp.805-814

[347] Hunt R. E., Noyes W. A. *Photochemical Studies. XXXIX. A further Study of the Fluorescence of Acetone.* Journal of the American Chemical Society 1948, 70 , pp.467-476

[348] Rice F. O., Herzfeld K. F. *The Thermal Decomposition of Organic Compounds from the Standpoint of Free Radicals. VI. the Mechanism of some Chain Reactions.* Journal of the American Chemical Society 1934, 56 , pp.284-289

[349] Kerr J. A., Parsonage M. J. *Evaluated Kinetic Data on Gas Phase Hydrogen Transfer Reactions of Methyl Radicals*; 1976 London: Butterworth; ISBN: 0408707798.

[350] Shortridge R. G., Rusbult C. F., Lee E. K. C. *Fluorescence Excitation Study of Cyclobutanone, Cyclopentanone and Cyclohexanone in the Gas Phase.* Journal of the American Chemical Society 1971, 93 (8), pp.1863-1867

[351] Zuckermann H., Schmitz B., Haas Y. *Acetone Photophysics in Seeded Supersonic Molecular Beams.* Journal of Physical Chemistry 1989, 93 , pp.4083-4091

[352] Cundall R. B., Davies A. S. *Primary Processes in the Gas Phase Photochemistry of Carbonyl Compounds.* Progress in Reaction Kinetics 1967, 4 , pp.149-213

[353] Borkman R. F., Kearns D. R. *Electronic-Relaxation Process in Acetone.* The Journal of Chemical Physics 1966, 44 (3), pp.945-949

[354] Haas Y., Ruhman S., Greenblatt G. D., Anner O. *Infrared Photochemistry of Tetramethyldioxetane. 2. the Nature of Electronically Excited Products.* Journal of the American Chemical Society 1985, 107 , pp.5068-5074

[355] O'Neal E. H., Larson C. W. *Primary Processes and the Acetone Photochemical System.* Journal of Physical Chemistry 1969, 73 (4), pp.1011-1022

[356] Bitto H. *Dynamics of the S_1 Acetone Studied with the Single Rotorvibronic Level Resolution.* Chemical Physics 1994, 186 , pp.105-118

[357] Thurber M. C., Hanson R. K. *Pressure and Composition Dependencies of Acetone Laser-Induced Fluorescence with Excitation at 248, 266, and 308nm.* Applied Physics B: Lasers and Optics 1999, 69 , pp.229-240

[358] Koch J. D., Hanson R. K. *Temperature and Excitation Wavelength Dependencies of 3-Pentanone Absorption and Fluorescence for PLIF Applications.* Applied Physics B: Lasers and Optics 2003, 76 , pp.319-324

[359] Fleming G. R., Gijeman O. L. J., Lin S. H. z. *Theory of Intramolecular Vibrational Relaxation in Large Systems.* The Faraday Transactions II 1974, 70 , pp.37-44

[360] Merkel P. B., Kearns D. R. *Oxygen Quenching and Radiationless Decay of Excited Singlet and Triplet Carbonyl Compounds.* The Journal of Chemical Physics 1973, 58 (1), pp.398-400

[361] Brown R. G., Philips D. *Quenching of the First Excited Singlet State of Substituted Benzenes by Molecular Oxygen.* Transactions of the Faraday Society II 1974, 70 , pp.630-636

[362] Koch J. D., Hanson R. K. *Ketone Photophysics for Quantitative PLIF Imaging.* 39th aerospace sciences meeting and exhibition; Jan 8-11; Reno, NV. ; 2001

[363] Ghandhi J. B., Felton P. G. *On the Fluorescent Behaviour of Ketones at High Temperatures.* Experiments in Fluids 1996, 21 , pp.143-144

[364] Tait N. P., Greenhalgh D. A. *2D Laser Induced Fluorescence Imaging of Parent Fuel Fraction in Nonpremixed Combustion.* Proceedings of the 24th international symposium on combustion; Jul 5-10 1992; Sydney, Publ by Combustion Inst, Pittsburgh, PA, USA; 1992 pp.1621-8

[365] Döhring K. *The Relative Effects of Intake and Compression Generated Turbulence on I.C. Engine Combustion Duration [dissertation].* Vancouver: University of British ColumbiaEditor; 1986

[366] Lappas P. *An Experimental and Computational Study of the Flow in a Squish Jet Combustion Chamber [dissertation].* Vancouver: University of British ColumbiaEditor; 2003

[367] Mezo A. *An Image Based Analysis of Stratified Natural Gas Combustion in A Constant Volume Bomb [dissertation].* Vancouver: University of British Columbia; 2008

[368] Bowker A. H., Lieberman G. J. *Engineering Statistics*; 1972 2nd ed. New Jersey: Prentice-Hall; ISBN: 0-13-279455-1.

[369] Rothamer D. A., Ghandhi J. B. *On the Calibration of Single-Shot Planar Laser Image Techniques in Engines.* SAE Technical Papers 2002, 2002-01-0748

[370] Kazenwadel J., Koban W., Kunzelmann T., Schultz C. *Fluorescence Imaging of Natural Gas/Air Mixing without Tracers Added.* Chemical Physics Letters 2001, 345 , pp.259-264

[371] McCullough J. D. *Engine Cylinder Pressure Measurement.* SAE Transactions 1953, 61 , pp.557573

[372] Davy M. H. *Two-Phase Fuel Visualization in a Gasoline Direct Injection Engine [dissertation].* London: University College London, Univeristy of London; 2000

[373] Paul P. H., Vancruyningen I., Hanson R. K., Kychakoff G. *High Resolution Digital Flowfield Imaging of Jets.* Experiments in Fluids 1990, 9 , pp.241-251

[374] Iaconis J. -. *An Investigation of Methane Autoignition Behaviour Under Diesel Engine-Relevant Conditions [dissertation]*. Vancouver: University of British Columbia Editor; 2001

[375] Ben L., Charnay G., Bazile R., Ferret B. *Quantitative Imaging of Equivalence Ratios in a Natural Gas SI Engine Flow Bench using Acetone Fluorescence*. Experiments in Fluids 2007, 43 (1), pp.77-88

[376] Thurber M. C. *Acetone Laser-Induced Fluorescence for Temperature and Multiparameter Imaging in Gaseous Flows [dissertation]*. Stanford: Stanford UniversityEditor; 1999

[377] Birkby P., Page G. J. *Numeical Predictions of Turbulent Underexapnded Sonic Jets using Pressure-Based Methodology*. Proceeding of the Institute of Mechanical Engineers, Part G 2001, 215 , pp.165-173

[378] Chuech S. G., Lai M. C., Faeth G. M. *Structure of Turbulent Sonic Underexpanded Free Jets*. AIAA Journal 1989, 27 , pp.549-559

[379] Budenholzer R. A., Sage B. H., Lacey W. N. *Phase Equilibria in Hydrocarbon Systems*. Industrial and Engineering Chemistry 1939, 31 (3), pp.369-374

[380] Braeuer A., Beyrau F., Leipertz A. *Laser-Induced Fluorescence of Ketones at Elevated Temperatures for Pressures Up to 20 Bars by using a 248nm Excitation Laser Wavelength: Experiments and Model Improvements*. Applied Optics 2006, 45 (20), pp.4982-4989

[381] Thurber M. C., Grisch F., Hanson R. K. *Temperature Imaging with Single- and Dual-Wavelength Acetone Planar Laser Induced Fluorescence*. Optics Letters 1997, 22 (4), pp.251-253

[382] Halpern A. M., Ware W. R. *Excited Singlet State Radiative and Non-Radiative Transition Probabilities for Acetone, Acetone-d_6 and Hexafluoroacetone in the Gas Phase, in Solution and in the Neat Liquid*. Journal of Chemical Physics 1971, 54 (3), pp.1271-1276

[383] Ambrose D., Sprake C. H. S., Townsend R. *Thermodynamic Properties of Organic Oxygen Compounds XXXIII. the Vapour Pressure of Acetone*. The Journal of Chemical Thermodynamics 1974, 6 (7), pp.693-700

[384] Ouelette P., Hill P. G. *Turbulent Transient Gas Jets*. ASME Journal of Fluids Engineering 2000, 122 , pp.743-753

[385] Falcone A. M., Cataldo J. C. *Entrainment Velocity in an Axisymmetric Turbulent Jet*. Journal of Fluids Engineering, Transactions of the ASME 2003, 125 (4), pp.620-627

[386] Pope S. B. *Turbulent Fflows*; 2000 Cambridge University Press; ISBN: 0521598869.

[387] Tennekes H., Lumley J. L. *A First Course in Turbulence*; 1972 Cambridge, MA: MIT Press; ISBN: 9780262200196.

[388] Barker P., Bishop A., Rubinsztein-Dunlop H. *Supersonic Velocimetry in a Shock Tube using Laser Enhanced Ionisation and Planar Laser Induced Fluorescence*. Applied Physics B: Lasers and Optics 1997, 64 (3), pp.369-376

[389] Sternberg S. R. *BIOMEDICAL IMAGE PROCESSING*. Computer 1983, 16 (1), pp.22-34

[390] Bruneaux G. *A Study of Mixture Formation in a Direct Injection Diesel Like Conditions using Quantitative Fuel Concentration Visualizations in a Gaseous Fuel Jet.* SAE Technical Papers 2002, 2002-01-1632

[391] Papanicolaou P. N. *Piston Driven Jet for the Study of the Zone of Flow Establishment.* Experiments in Fluids 1994, 17 (4), pp.287-289

[392] van Cruyningen I., Lozano A., Hanson R. K. *Quantitative Imaging of Concentration by Planer Laser-Induced Fluorescence.* Experiments in Fluids 1990, 10 , pp.41-49

[393] Dahm W. J. A., Dimotakis P. E. *MEASUREMENTS OF ENTRAINMENT AND MIXING IN TURBULENT JETS.* AIAA Journal 1987, 25 (9), pp.1216-1223

[394] Mungal M. G., O'Neil J. M. *Visual Observations of Turbulent Diffusion Flames.* Combustion and Flame 1989, 78 (3-4), pp.377-389

[395] Ahmed S. F., Mastorakos E. *Spark Ignition of Lifted Turbulent Jet Flames.* Combustion and Flame 2006, 146 (1-2), pp.215-231

[396] Burgess D., Hertzberg M. *The Flammability Limits of Lean Fuel Air Mixtures: Thermochemical and Kinetic Criteria for Explosion Hazards.* ISA transactions 1975, 14 (2), pp.129-136

[397] Jessen PF. Technical data on fuel. In: Rose JW, Cooper JR, editors. 7th ed. New York: John Wiley & Sons; 1977. p. 246-72

[398] Ahmed S. F., Balachandran R., He Y. -., Mastorakos E. *Spark Ignition of Turbulent Premixed and Non-Premixed Opposed Jet Flames.* AIAA/ASME/SAE/ASEE 42nd joint propulsion conference, july 9, 2006 - july 12; 2006; Sacramento, CA, United states: American Institute of Aeronautics and Astronautics Inc; 2006 pp.7470-8

[399] Fotache C. G., Kreutz T. G., Law C. K. *Ignition of Counterflowing Methane Versus Heated Air Under Reduced and Elevated Pressures.* Combustion and Flame 1997, 108CH4 as an alternative ref 12 good paper on methane combustion in general , pp.442-470

[400] Grout R. W., Bushe W. K., Blair C. *Predicting the Ignition of Turbulent Methane Jets using Conditional Source Term Closure.* Combustion Theory and Modelling 2007, 11 (6), pp.1009-1028

[401] Marchione T., Ahmed S. F., Mastorakos E. *Ignition of Turbulent Swirling n-Heptane Spray Flames using Single and Multiple Sparks.* Combustion and Flame 2009, 156 (1), pp.166-180

[402] Namazian M., Kelly J., Schefer R. W., Johnston S. C., Long M. B. *Nonpremixed Bluff Body Burner Flow and Flame Imaging Study.* Journal of Experimental Fluids 1989, 8 (3-4), pp.216-228

[403] Rogg B., Behrendt F., Warnatz J. *Turbulent Non-Premixed Combustion in Partially Stratified Pre-Mixed Diffusion Flamelets with Detailed Chemistry.* Proceedings of The Combustion Institute 1986, 21 , pp.1533-1541

[404] Logan J. *Evaluation of Partially Stratified Charge Insert in a Natural Gas Engine [dissertation].* Vancouver: University of British Columbia; 2011

[405] Wagner R., Drallmeier J. *Prior-Cycle Effects in Lean Spark Ignition Combustion– Fuel/Air Charge Considerations.* SAE Technical Papers 1998, 981047

[406] Chiriac R., Apostolescu N. *Cyclic Variability Patterns in a Spark Ignition Engine Fueled with LPG.* SAE Technical Papers 2004, 2004-01-1920

[407] Litak G., Kaminski T., Czarnigowski J., Zukowski D., Wendeker M. *Cycle-to-Cycle Oscillations of Heat Release in a Spark Ignition Engine.* Meccanica 2007, 42 , pp.423-433

[408] Daw C., Kennel M., Finney C., Connolly F. *Observing and Modeling Nonlinear Dynamics in an Internal Combustion Engine.* Physical Review E: Statistical Physics, Plasmas, Fluids, and Related Interdisciplinary Topics 1998, 57 , pp.2811-2819

[409] Jaynes E. T. *Probability Theory: The Logic of Science*; 2003 Cambridge: Univeristy Press; ISBN: 0 521 59271 2.

[410] Shannon C. E. *A Mathematical Theory of Communication.* The Bell System Technical Journal 1948, 27 (3), pp.379-414

[411] Kapur J. N. *Maximum Entropy Models in Science and Engineering*; 1989 New York: John Wiley & Sons Inc.; ISBN: 0-470-21459-7.

[412] Rood E. P., Demetri P. T. *Editorial: Journal of Fluids Engineering Policy on Reporting Uncertainties in Experimental Measurements & Results.* Journal of Fluids Engineering 1991, 113 (3), pp.313-314

[413] Holman J. P. *Experimental Methods for Engineers*; 2000 McGraw-Hill,Inc.; ISBN: 0073660558.

[414] Ahmed S. F., Balachandran R., Mastorakos E. *Measurements of Ignition Probability in Turbulent Non-Premixed Counterflow Flames.* 31st international symposium on combustion, august 5, 2006 - august 11; 2006; Heidelberg, Germany: Elsevier Ltd; 2007 pp.1507-13

[415] Reynolds C.,C., Evans R.,L. *Improving Emissions and Performance Characteristics of Lean Burn Natural Gas Engines through Partial Stratification.* Int.J.Engine Res. 2004, 5 (1), pp.1-10

[416] Reynolds C.,C., Evans R.,L. *The Low NOx Potential of Partially Stratified-Charge Combustion in a Natural Gas Engine.* CICS; May 9-12th 2004; Ontario, Canada: ; 2004

[417] Myers R. H., Montgomery D. C. *Response Surface Methodology: Process and Product Optimization using Designed Experiments*; 2002 2nd ed. John Wiley & Sons Inc.; ISBN: 0 471 41255 4.

Appendix A RCM Apparatus & Re-Design

### A▪1 Introduction

The RCM has previously been used in cold flow studies only. This appendix details the changes made to the design of the RCM so that it is capable of generating and supporting combustion. The reasoning behind the design choices is outlined and the contract drawings for manufacture shown (where appropriate). The appendix covers the details of: the new RCM cylinder, including the quartz windows used to provide optical access; the new RCM piston; the details of the fuelling system, including the fuel injectors; and the circuit used to generate the ignition spark.

A▪2 BACKGROUND

The 'old' RCM, as used in the work of Lappas **[366]** is shown in *Figure A-1* with the pneumatic driver, crank & cylinder, and hydraulic braking sections labelled for reference.
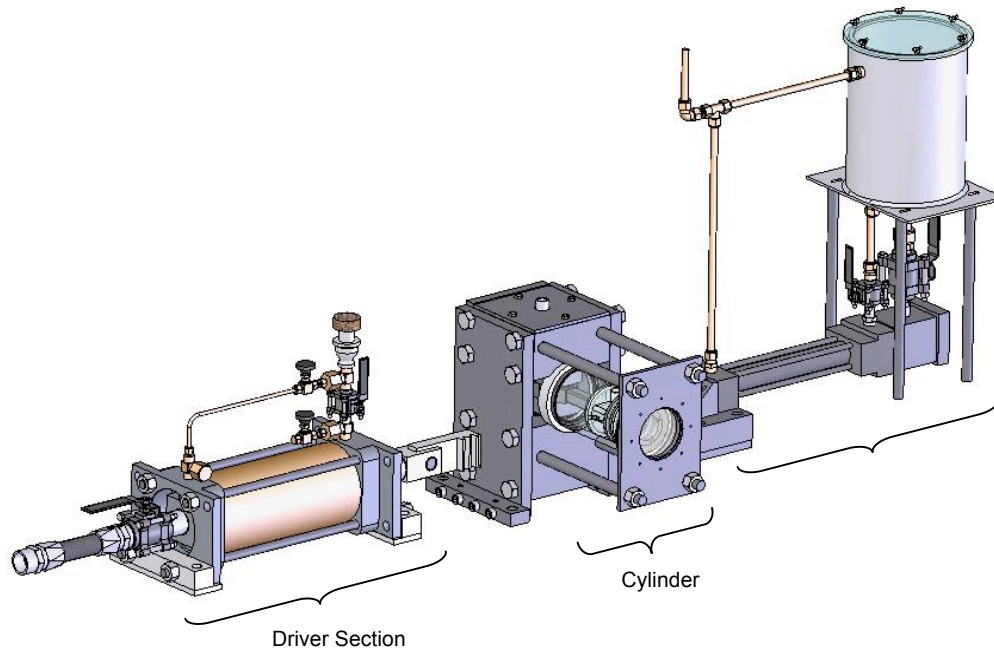

Figure A-1 RCM Schematic

The changes made to support combustion all pertain to the cylinder and piston of the RCM. The driver, crank and braking systems of previous studies **[365, 366]** have been used in the current work. The RCM is driven from a reservoir of compressed air (supplied from shop air) which is pressure regulated to 80*bar*. The pneumatic piston in the driver section moves a horizontal rack & pinion, the pinion of which is connected to a vertical crank. This crank moves the piston through a traditional con-rod assembly. The opposite end of the rack to the driven end is connected to a hydraulic piston (the braking section) which is part of a closed oil loop. The oil is forced through a restriction in the loop when the rack actuates and this restriction provides the load for the RCM.

A▪3 CYLINDER RE-DESIGN

The requirement that the RCM be able to support combustion required that the PMMA cylinder and cylinder head be redesigned to tolerate the increased temperatures and pressures that are associated with combustion. The following sections detail the design features for each of the major components and their assembly to form the new RCM cylinder.

A▪3▪1 PREVIOUS PMMA CYLINDER ASSEMBLY

To put the changes in some context the previous cylinder of the RCM is shown in *Figure A-2*. The assembly consists of a 10*mm* thick PMMA tube with a ⅛" steel plate holding a 10*mm* thick PMMA top window in place (with appropriate o-ring seals). The plate held the top window and cylinder in place under compression via four tie-rods (not shown).
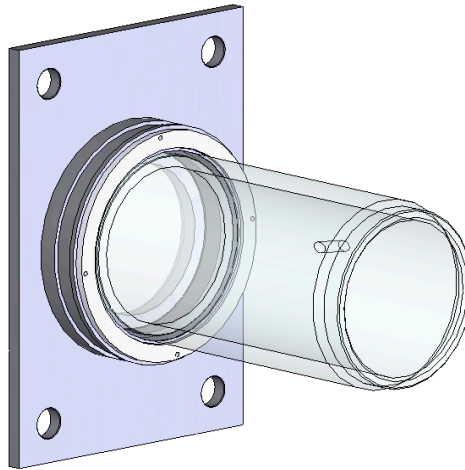
Figure A-2 Old Acrylic RCM Cylinder

A▪3▪2 QUARTZ CYLINDER & CYLINDER HEAD

The existing PMMA cylinder and cylinder head would not be able to withstand the pressures generated from the combustion process, though the flash temperatures would be acceptable. If it were only mechanical properties which were of concern a polymer based solution could be sought, however, the use of UV laser diagnostics necessitated the use of UV transmissible materials. Optical access is desirable on two orthogonal planes and, to maximize the utility of the RCM is, extended to include optical access through the cylinder head. *Corning* KrF Grade HPFS (high purity fused silica), with the properties listed in *Table A-1*, was used to meet the mechanical and optical properties of the cylinder. The quartz components were manufactured by *Gooch & Housego (UK) Ltd*, Ilminster, England. *Figure A-3* shows the quartz portion of the RCM cylinder. Its dimensions allow the top 50% of the stroke to be optically accessible through the bore (which was flame polished) and the four smallest external surfaces. The ⅛" recess ensures repeatable seating against the metallic part of the RCM cylinder (*cf. §A▪3▪4*).

HPFS KrF Grade, Class 7890 0D		
Inclusions		
Total Cross Section per 100cm^3	<0.03	mm^2
Homogeneity	<3	ppm
Impurities		
OH (by weight)	800-1000	ppm
Other than OH	<500ppb	
Mechanical Properties @ 25^{0}C		
Elastic Modulus	72.7	GPa
Shear Modulus	31.4	GPa
Modulus of Rupture, abraded	52.4	MPa
Bulk Modulus	35.4	GPa
Compressive Modulus	1.1	GPa
Poisson's Ratio	0.16	--
Density	2.201	g/cm^2
Thermal Conductivity	1.30	W/mK
Optical Properties		
Transmittance	>99.8	$\%/cm$

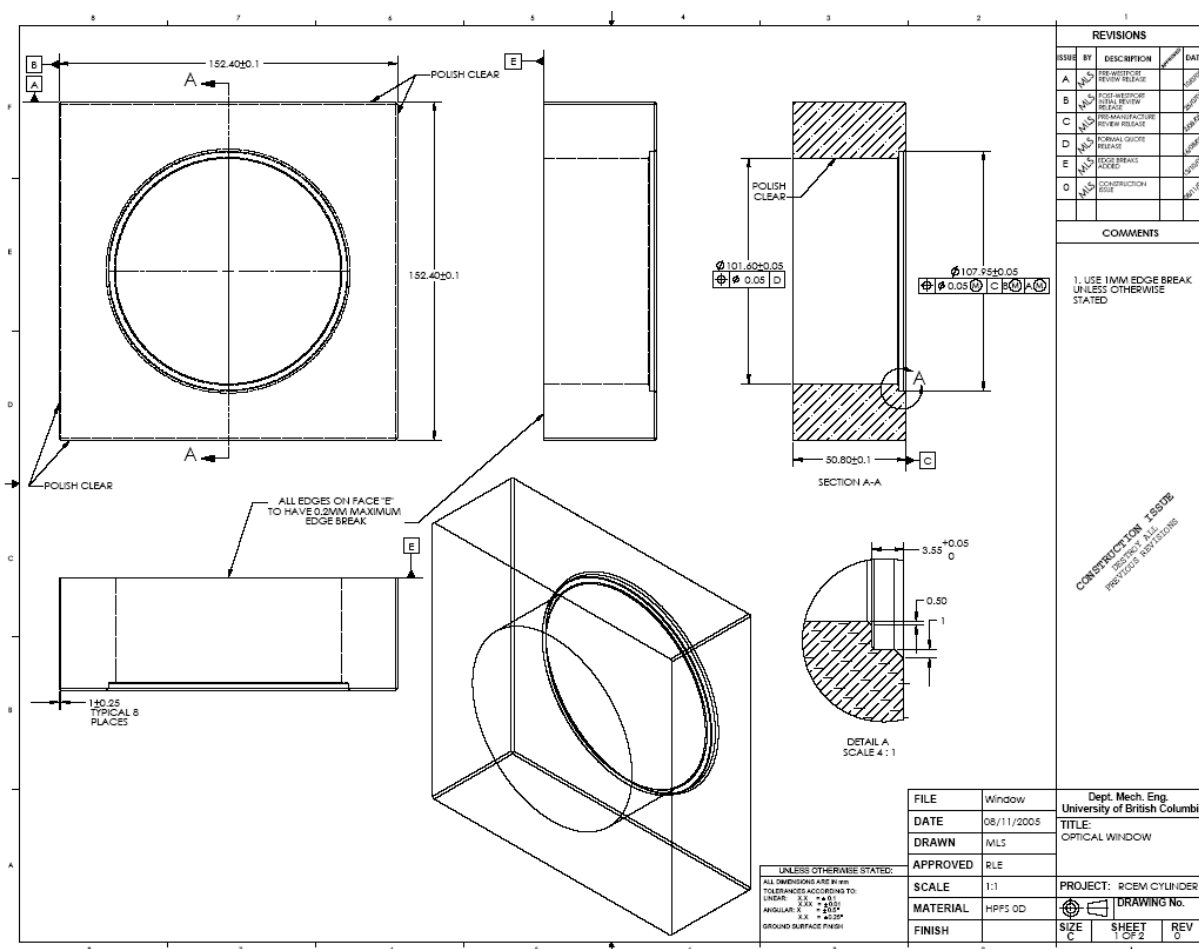**Table A-1 HPFS 7890 (KrF Grade) Properties**

Figure A-3 RCM Quartz Cylinder

218

The quart cylinder head is shown in *Figure A-4*. The window is designed to offer full optical access across the entire bore, except that one edge must be cut by a chord to provide some metallic material to house the direct injector for the fuel system (*cf. §A▪3▪3* for port plate design), hence the final D-shape of the window. The draft provides the seat for the window in the port plate. All quartz components have their edges chamfered to the largest degree possible to minimize the chance of stress concentrations, cracking and scalloping.


Figure A-4 RCM Quartz Cylinder Head (Window)
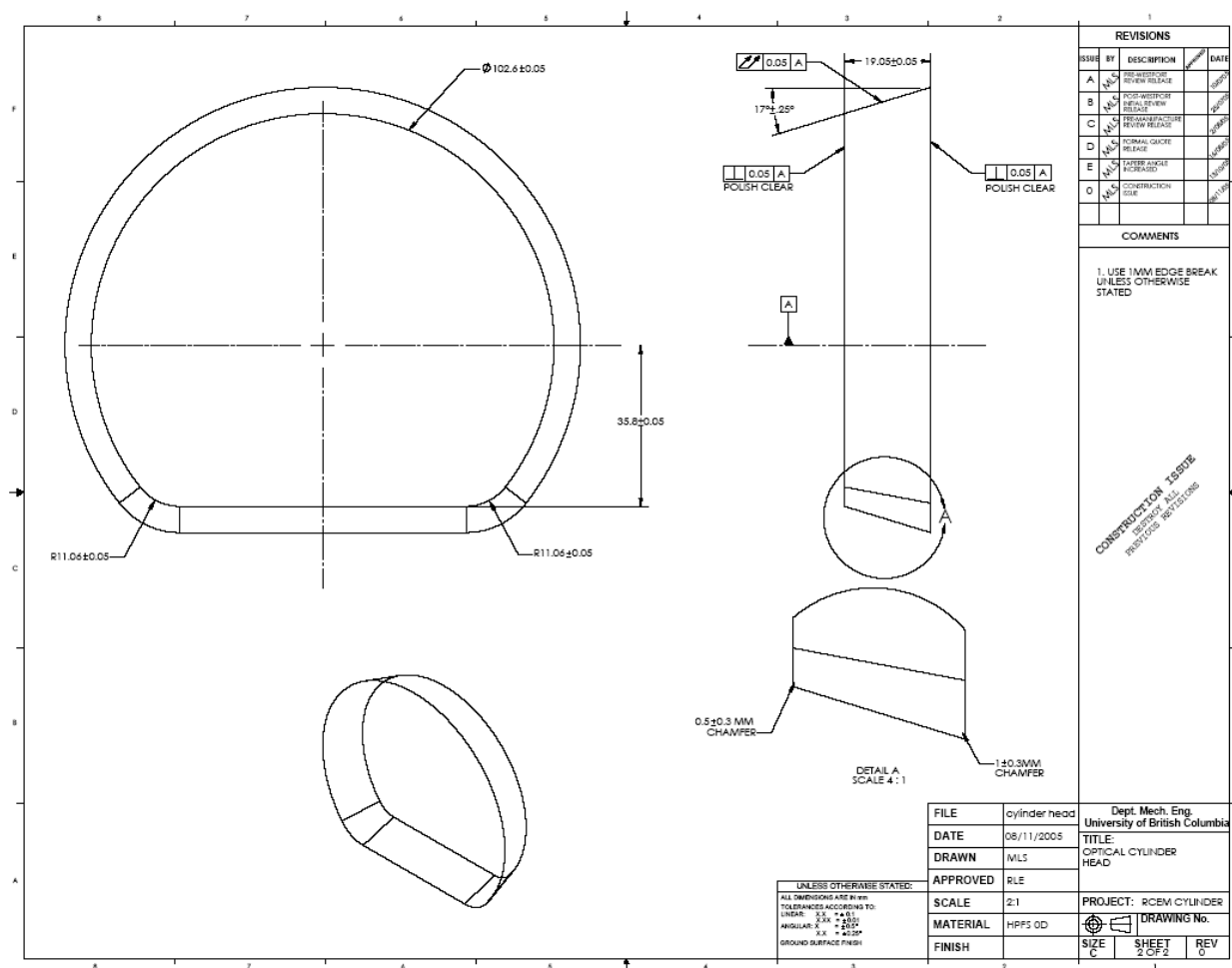
A▪3▪2▪1 FINITE ELEMENT ANALYSIS

A finite element analysis (FEA) was conducted on the quartz cylinder to establish the factor of safety for the design. The pressure loading on the internal surface was determined through minimization of the Gibbs energy for a stoichiometric constant volume combustion at TDC, where the state of the mixture prior to combustion was determined assuming an isentropic compression of the mixture from ambient conditions at BDC. The Gibbs free energy minimization was achieved using the well established freeware *GasEq* (*www.gaseq.co.uk*). Flash thermal loadings were disregarded in this study. The quartz for the cylinder had its properties amended to reflect those of *Table A-1*. Only one quarter of the cylinder was

modelled (reflecting the symmetry of the problem). It was axially constrained on all axial surfaces while no other constraints were imposed. This accurately reflects the physical boundary conditions of the problem.

CosmosWORKS® was used to complete the analysis. *CosmosWORKS*® is a basic FEA software package, the results of which should be used for guidance only. An inability to control meshing and element shape function is severely limiting. The tetrahedral mesh produced had problems in the areas highlighted in *Figure A-5*.
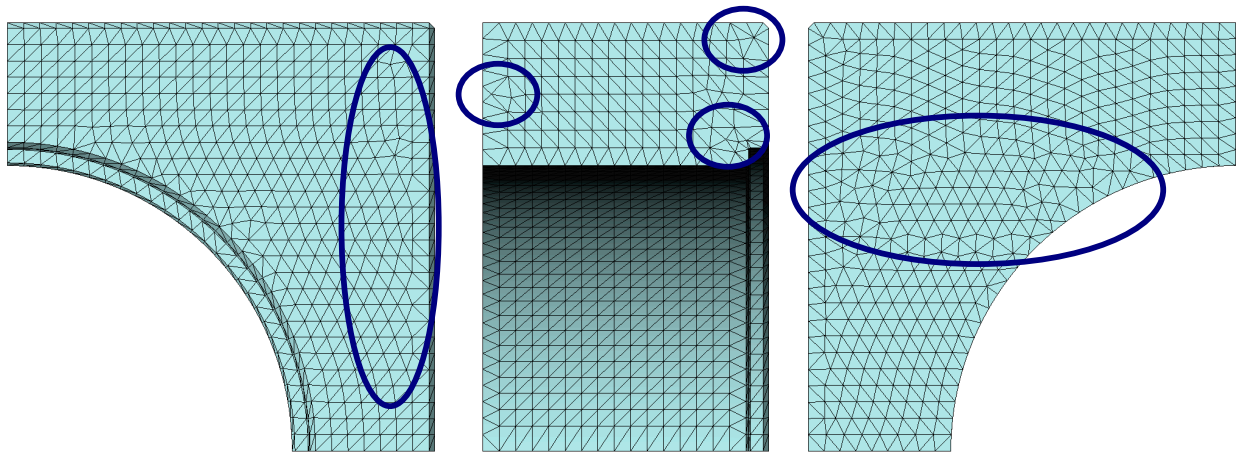

Figure A-5 Problematic Elements in Quartz Cylinder FEA

Of most concern are the elements around the inner recess because of their high aspect ratio. However, inspection of *Figure A-5* shows them all to have a ratio under 10, the critical cut-off for aspect ratio integrity. Further, *CosmosWORKS*® uses adaptive shape functions to minimize the effect of degenerate elements.
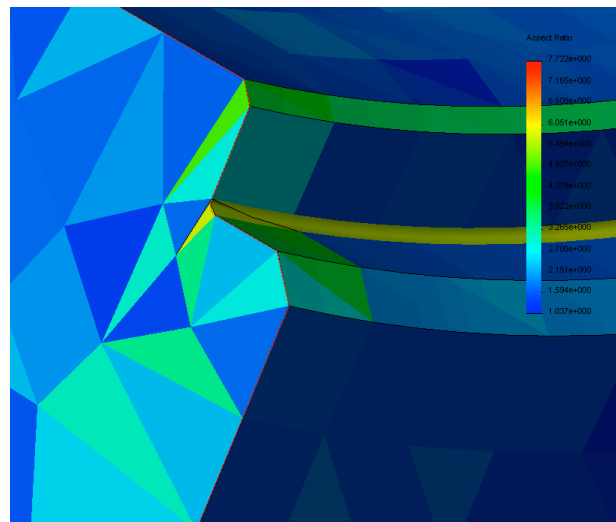
Figure A-6 Element Aspect Ratios in Area of Concern for Quartz Cylinder FEA

Of more concern however is the elemental Jacobian, effectively a measure of the elemental deformation against its parent shape. A high Jacobian suggests excessive deformation for the solution to hold true. Two elements in the model are cause for some concern. They are shown in *Figure A-7*.
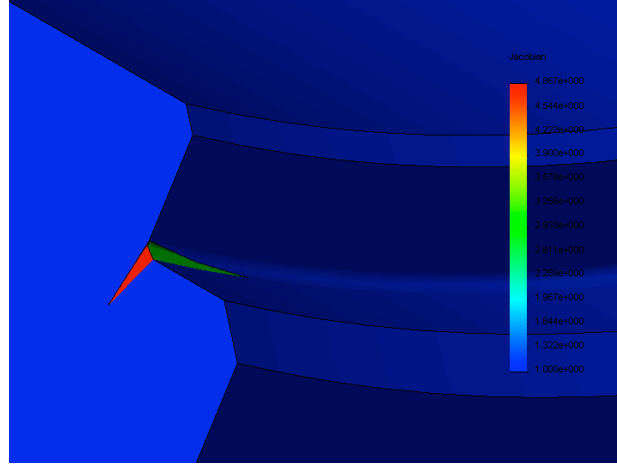
Figure A-7 Elemental Jacobian Values for Quartz Cylinder FEA

Despite these concerns there was still deemed to be merit in continuing with the study. Given the brittle nature of fused silica, a Mohr-Coulomb yield surface is used to asses the failure of the quartz cylinder. The yield criterion for the Mohr-Coloumb surface is defined by *Eqs. B:1 & B:2*.
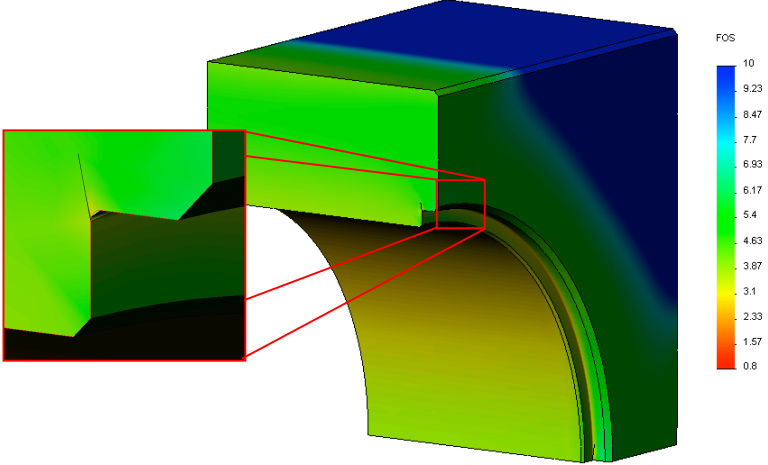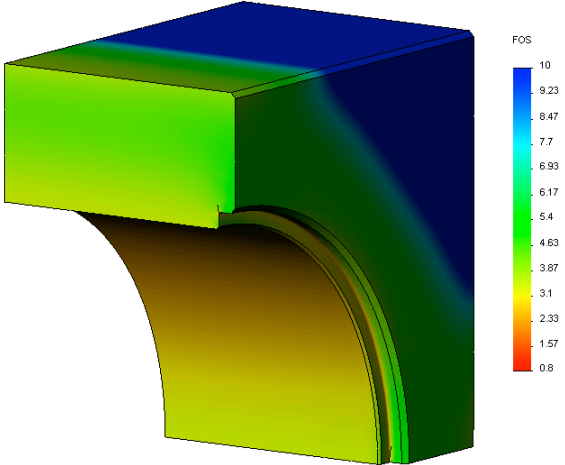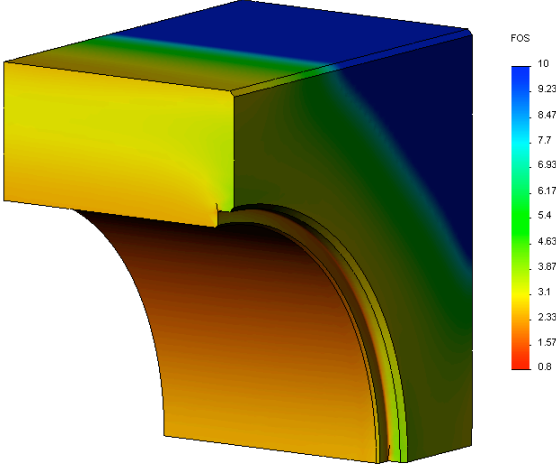
$$\max\left(\frac{|\sigma_1 - \sigma_2|}{2} - c + K\frac{\sigma_1 + \sigma_2}{2}, \frac{|\sigma_2 - \sigma_3|}{2} - c + K\frac{\sigma_2 + \sigma_3}{2}, \frac{|\sigma_3 - \sigma_1|}{2} - c + K\frac{\sigma_3 + \sigma_1}{2}\right) = 0$$
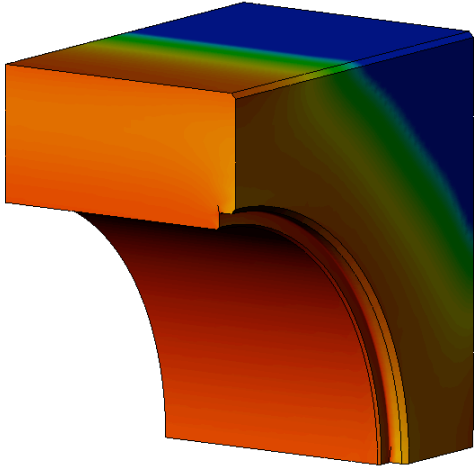
Eq. A2.

where

$$m = \frac{R_c}{R_t}, \quad K = \frac{m-1}{m+1}, \quad \& \quad c = R_c\frac{1}{m+1}$$

Eq. A2

while R_c is the compressive yield strength and R_t the tensile yield of the material. For this analysis, yield is assumed to occur at rupture. As a matter of note, for the case $K=0$ the Von Misses yield surface is retrieved.

For the four compression ratios used in the RCM (5.33, 5.99, 8.18 and 13.78) *Figure A-8* presents the results of the FEA safety analysis. Highlighted in *Figure A-8(a)* is the excessive deformation at the element interface where the elemental Jacobian was too high. This distortion persists in all the analyses.

	r_c	Minimum FOS	Image
(a)	5.33	2.1	
(b)	5.99	1.8	
(c)	8.18	1.3	

r_c	Minimum FOS	Image
(d) 13.78	0.82	

Figure A-8 RCM Quartz Cylinder FOS Values based on a Mohr-Coulomb Yield Criteria for Compression Ratio 5.33(a), 5.19(b), 8.18(c) & 13.78(d)

Given that this analysis is inherently conservative (by virtue of the fact that the combustion is assumed to be at constant volume, while in the RCM the combustion is in an expanding volume) the quartz cylinder is deemed to be amply safe.

A▪3▪3   PORT PLATE

The quartz window must be held securely to form the gas tight seal with the cylinder head. Further, the cylinder head is required to house all the pieces normally found in an ICE head (except the valve system). The component detailed in *Figure A-9* was designed to this. The key features are as follows (going through the views of *Figure A-9* in an anti-clockwise direction from the top right).

The large aperture in the centre of the plate is the mount for the quartz window. The 17^0 draft corresponds to the draft on the window, however, the diameter is over-sized by 1*mm*. The drafted surface then has in it two 1/16" o-ring grooves which provide the mounting surface for the quartz when the Buna-N rings are in place. The o-rings serve to cushion the quartz against metal contact and provide a gas-tight seal against combustion pressure. The hole toward the bottom of the plate is designed to mount the Westport® J43M injector at an angle of 32^0, which keeps the injector out of the image area. The hole in the injector nozzle is spark eroded at an angle which ensures the top edge of the injected fuel plume travels parallel to the fire deck (at a clearance of ~4*mm*). The injector is held in place, against combustion, pressure by four M4 nickel coated mild steel threaded rods which anchor to a plate that braces against the top mounting surface of the injector. Next to the hole for the injector is the tapping for the dynamic pressure transducer (PCB Electronics, 0112A). The set of dowel holes on this face allow the repeatable location of the compression plate which holds the entire cylinder assembly in compression.
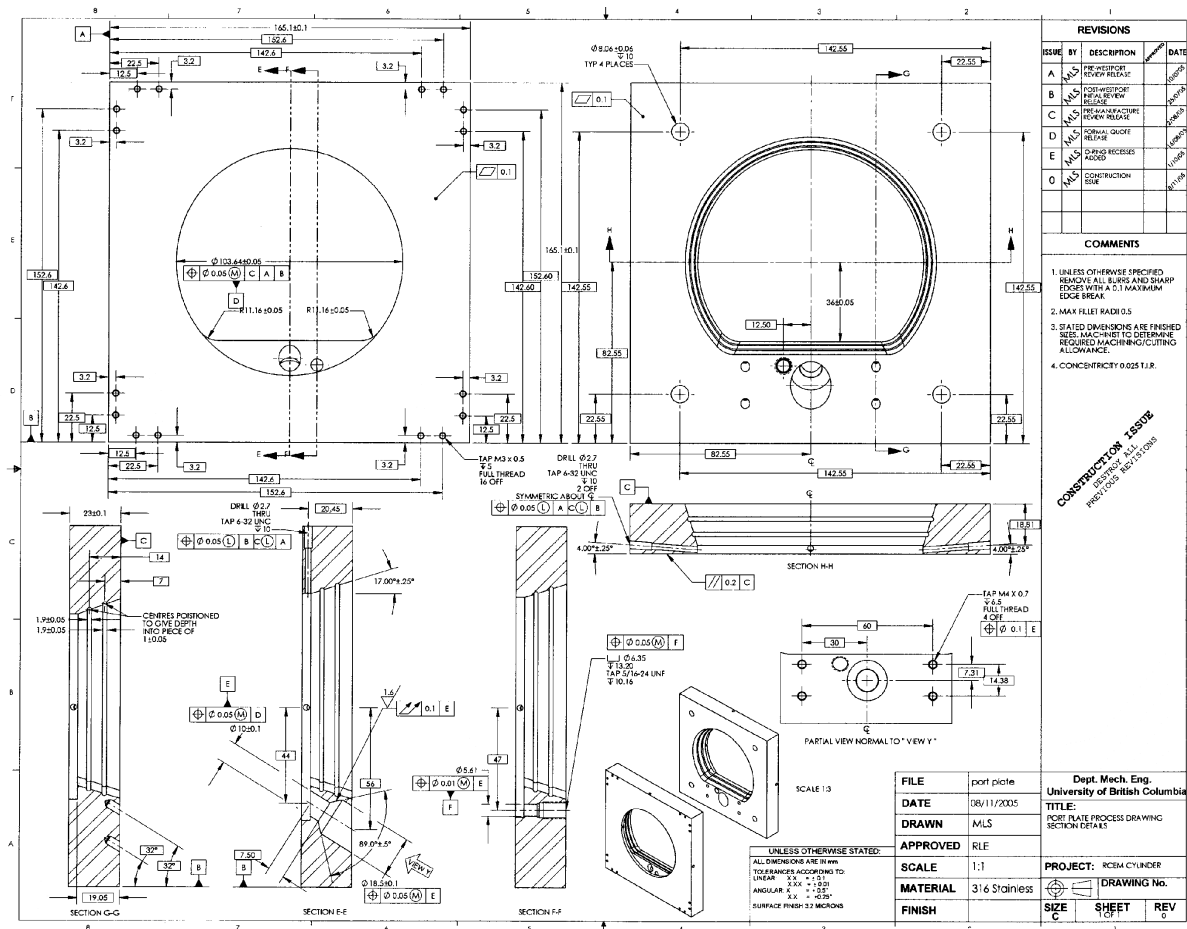
Figure A-9 RCM Port Plate

The series of eight M3 hole pairs take a set of small tangs which allow the quartz cylinder to be held and positioned radially in a repeatable fashion.

A▪3▪3▪1 ELECTRODE & PSC MOUNT

There are three 6-32 UNC holes which extend radially from the circular portion of the central aperture. The hole extending to the top surface of the port plate takes the PSC mount. The other two are for the electrode mounts and have an angle of 4^0 *w.r.t.* the fire deck so that the electrodes intersect the PSC fuel plume. Both mounts have a thread to allow the radial position of the PSC tube/electrode to be altered. The mounts for the PSC capillary and the electrodes are the same (except for their internal bore) and are made of PTFE. The electrode mount is shown in *Figure A-10*.
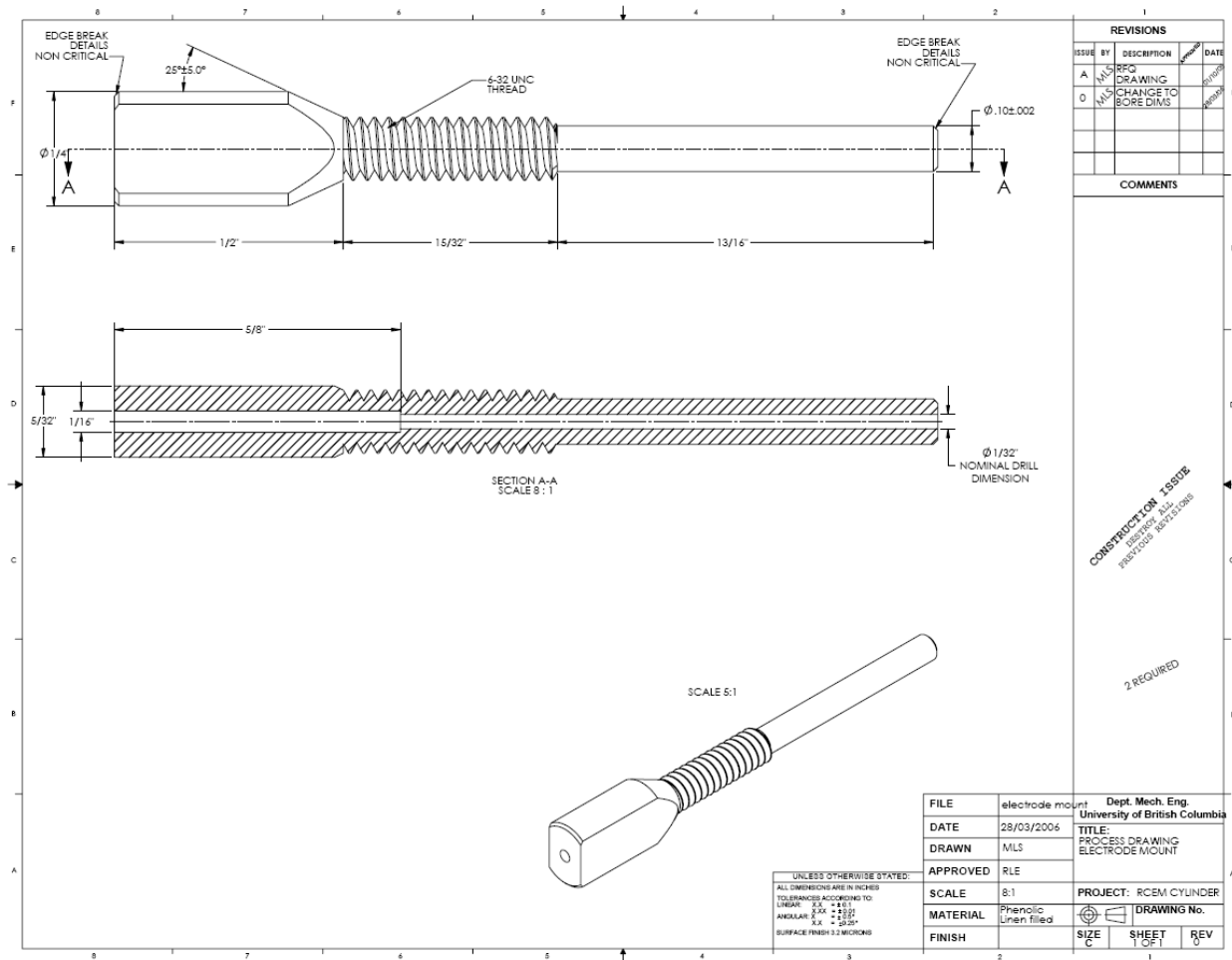
Figure A-10 RCM Electrode Mount

The PSC capillary (OD=1/16") or tungsten electrode (OD=0.030") have an interference fit (of 0.002") on the internal bore of their respective mounts. The mounts locate in the port plate to position the capillary and electrodes accordingly. Assuming a built in cantilever for the capillary and the electrodes their natural frequencies are 5.3*Hz* and 12.7*Hz* respectively. These are both well away form anything that can be expected to be found on the RCM (as are the higher order vibrations) and hence excessive vibration of the tube and electrodes was not deemed to be a concern.

A▪3▪4 CYLINDER

The quartz cylinder does not cover the full stroke of the piston. The majority of the RCM cylinder is made of 316 stainless steel and is responsible for locating the quartz components and cylinder head. The cylinder was machined from a solid billet, with tight tolerances on the internal bore surface finish (1.6 *μm*), circularity (0.1*mm*) and parallelism (0.1*mm*). The running section of the cylinder accounts for the bottom 50% of the stroke, and has the mixture inlet and outlet ports integral to it. The large flange is the sealing surface (sealed with a silicone gasket) for the quartz portion of the cylinder, *cf. Figure A-12*.

225

A▪3▪5   PISTON

The piston used in this study has a flat top-land geometry and modest skirt. The PEEK seals provide the tightest gas-seal possible though are far form gas tight. The final groove on the skirt takes a PEEK runner that is bonded in place and ensures the true running of the piston in the cylinder. The o-ring nearest the top-land is designed to be 3*mm* from the interface between the quartz and the steel at TDC, which avoids it running over the interface and the associated wear and debris concerns. The top-land of the piston is made from polycarbonate and is threaded to allow the fitting of aluminium spacers between it and the piston body. The resultant change in piston length changes the compression ratio of the RCM (given its fixed stroke of 104*mm*). With no spacer and the current 1/8", 3/8" and 5/8" spacers the compression ratios are 5.33, 5.99, 8.18 and 13.78 respectively.

Figure A-11 RCM Piston

A▪3▪6   RCM CYLINDER ASSEMBLY

The components of the preceding sections are held in place by a compression plate (*cf. Figure A-12)* which is secured by a series of tie-rods (not shown) to the crank case of the RCM (as in *Figure A-1*). This

plate ensures that the load-path passes through the components that form the RCM cylinder and in doing so generates a gas-tight seal.
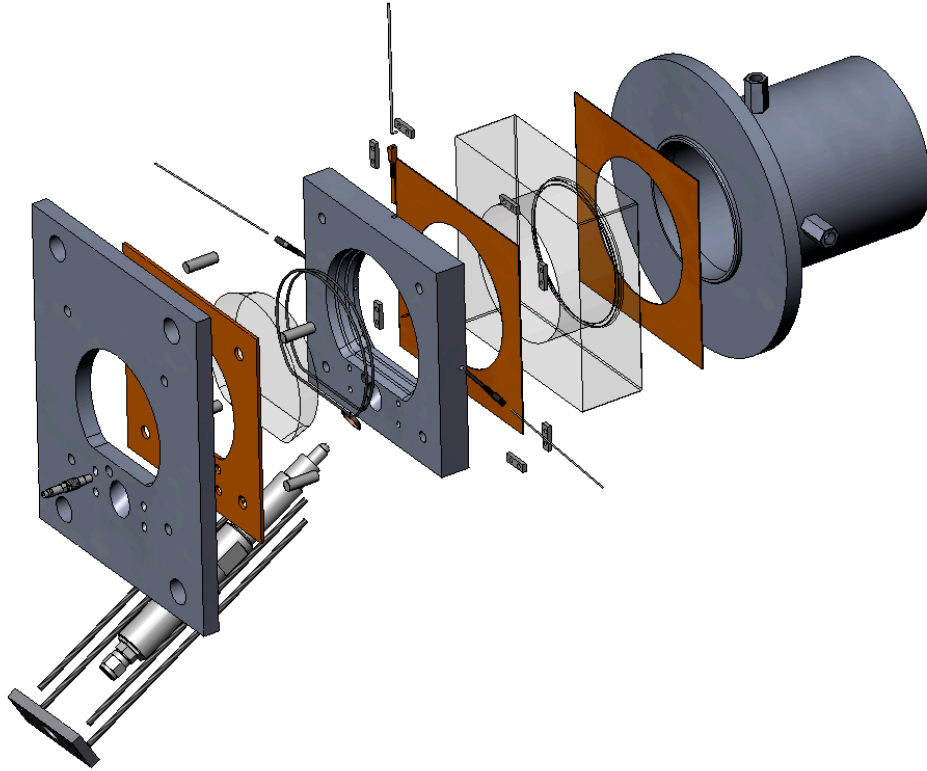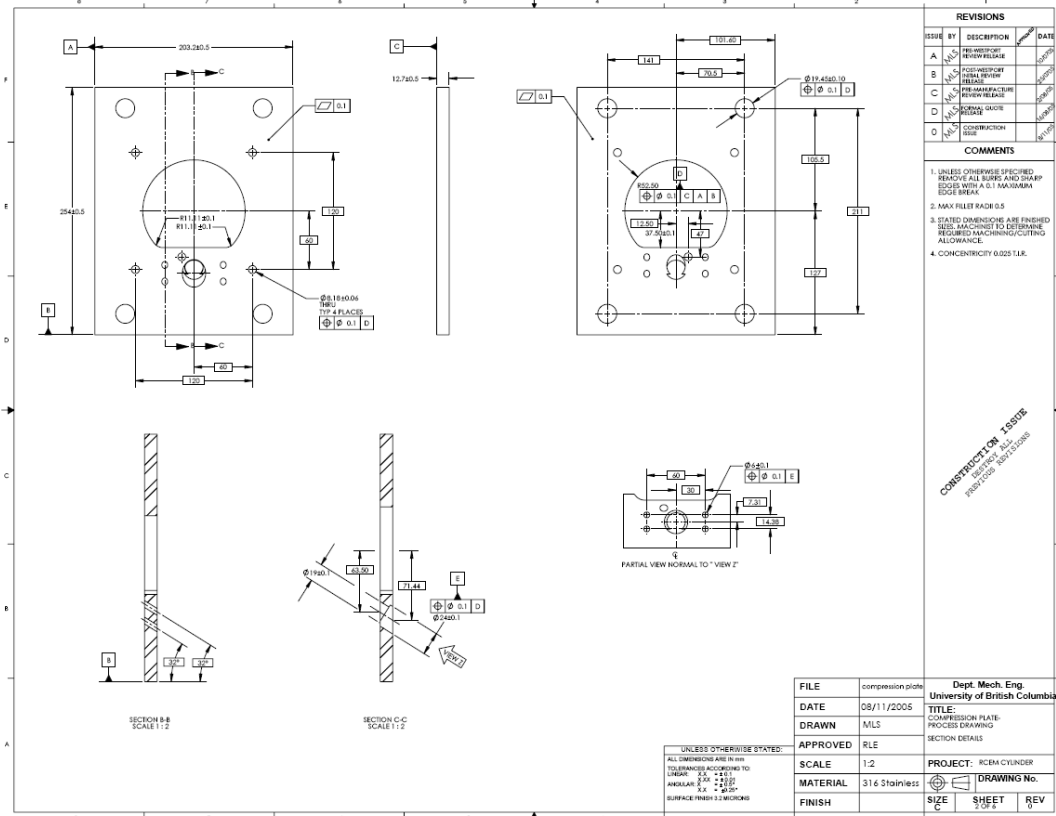

Figure A-12 RCM Cylinder Exploded View

Figure A-13 RCM Compression Plate Drawing

## A▪4 RCM FUELLING SYSTEM

Along with the substantial alterations made to the RCM cylinder there was a need to fuel the RCM with natural gas or methane. The fuelling system was required to deliver fuel as an homogenous premixture; a pure or premixed PSC charge; and pure a DI charge. The final requirement was that any one or all of the fuel sources had the ability to be passed through the acetone seeder so that the fuel could be imaged using LIF. A schematic for the system designed to do this is given in *Figure A-15*, where the valve numbers pertain the settings table given as *Table A-3*.
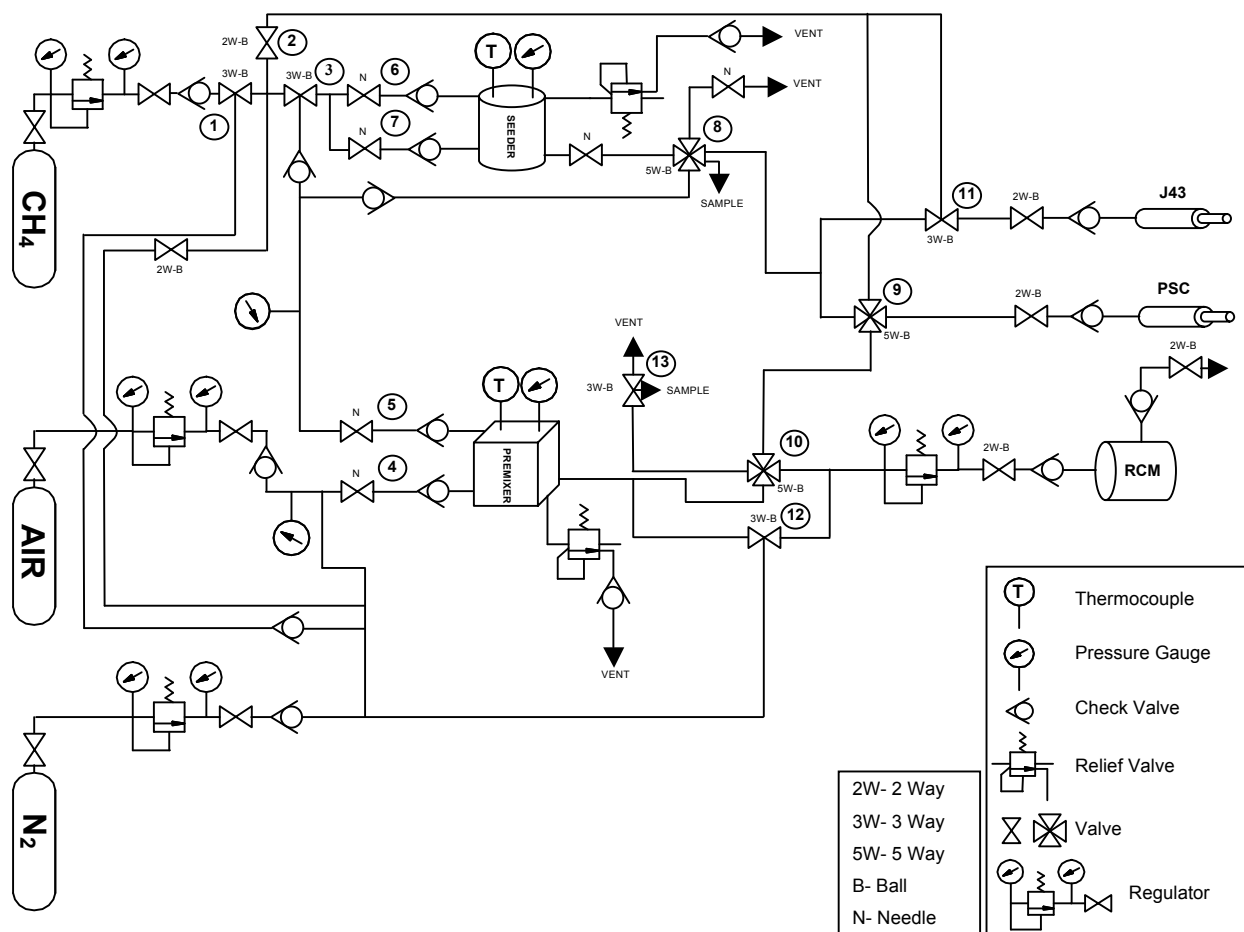
Figure A-14 RCM Fuelling System

All valves are hand operated and mounted on a front facia with the corresponding piping diagram shown in *Figure A-14* (the hard-line pipes are shown as lightweight equivalents). Using partial pressures the operator can prepare a mixture in the premixer. Line pressure for the methane is shown, while the total pressure in the premixer is also listed (which allows the amount of air required for a given composition to be determined).
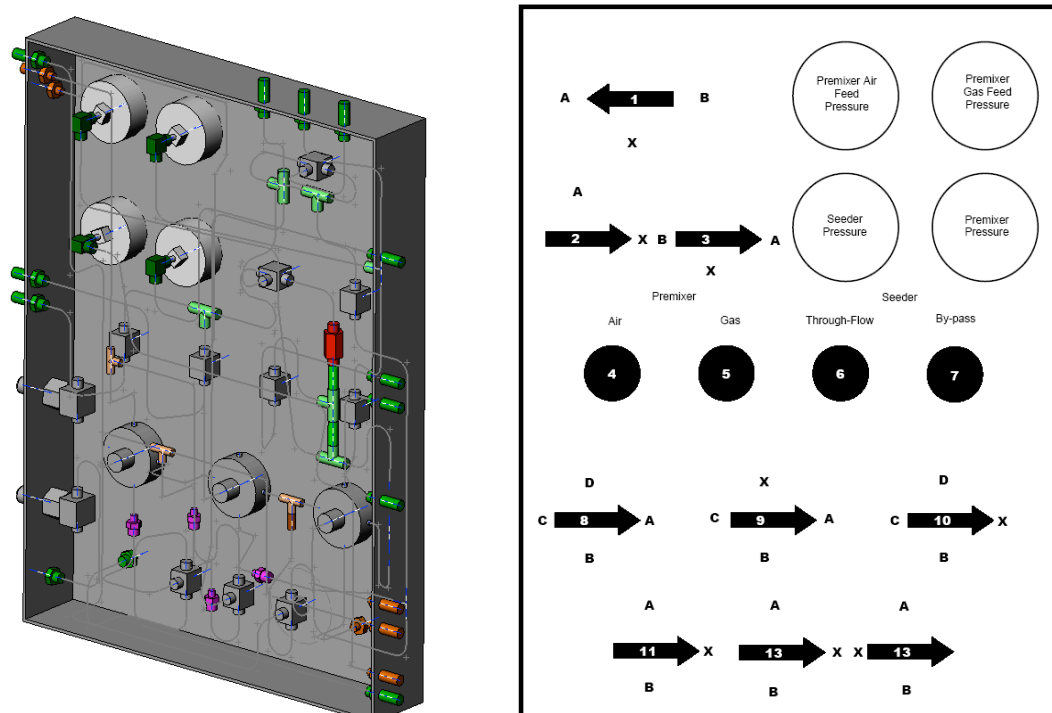
Figure A-15 RCM Fuelling Panel Valving, Piping & Valve Numbering

The fuelling options available are listed in *Table A-2*.

Bulk Charge	PSC	DI
Air	Seeded CH_4	Seeded CH_4
Air	Seeded CH_4	CH_4
Air	CH_4	CH_4
Air	CH_4	Seeded CH_4
Air	Seeded CH_4	Seeded Premix
Air	Seeded CH_4	Seeded Premix
Air	CH_4	Seeded Premix
Air	CH_4	Seeded Premix
Premix	None	None

Table A-2 RCM Fuelling Options

The required valve settings to achieve these states are given in *Table A-3*. Every fuel source has a high pressure two way valve (one outlet to the cylinder and one to vent) as its final stage to allow the fuel system to be fully flushed with nitrogen. Direct venting of the premixer is allowed though the charge may be diluted with air to take it beyond its flammability limit.

Cylinder	PSC	Injection	Valve # 1	2	3	4	5	6	7	8	9	10	11	12	13
Air	-	CH_4	B	A	×	×	×	×	×	B	×	×	A	B	×
	CH_4	-	B	A	×	×	×	×	×	B	B	×	×	B	×
	CH_4	CH_4	B	A	×	×	×	×	×	B	B	×	A	B	×
	Pre (Prep)	-	×	×	×	✓	✓	×	×	B	A	B	×	×	×
	Pre(Run)	-	×	×	×	×	×	×	×	B	A	C	×	B	×
	Pre (Prep)	CH_4	×	×	×	✓	✓	×	×	B	A	B	×	×	×
	Pre(Run)	CH_4	B	A	×	×	♦	×	×	×	A	C	A	B	×
Air	-	CH_4_Seed (Prep)	B	×	A	×	×	✓	✓	D	×	×	×	×	×
	-	CH_4_Seed (Run)	B	×	A	×	×	✓	✓	A	×	×	B	B	×
	CH_4_Seed (Prep)	-	B	×	A	×	×	✓	✓	D	C	×	×	×	×
	CH_4_Seed (Run)	-	B	×	A	×	×	✓	✓	A	C	×	×	B	×
	CH_4_Seed (Prep)	CH_4	B	A	A	×	×	✓	✓	D	C	×	×	×	×
	CH_4_Seed (Run)	CH_4	B	A	A	×	×	✓	✓	A	C	×	A	B	×
	CH_4	CH_4_Seed (Prep)	B	A	A	×	×	✓	✓	D	B	×	B	×	×
	CH_4	CH_4_Seed	B	A	A	×	×	✓	✓	A	B	×	B	B	×
	CH_4_Seed (Prep)	CH_4_Seed (Prep)	B	×	A	×	×	✓	✓	D	×	×	×	×	×
	CH_4_Seed (Run)	CH_4_Seed	×	×	A	×	×	✓	✓	A	C	×	B	B	×
	Pre_Seed (Prep)	-	B	×	A	×	×	✓	✓	D	×	×	×	×	×
	Pre_Seed (Fill)	-	×	×	×	✓	✓	×	×	C	×	×	×	×	×
	Pre_Seed (Run)	-	×	×	×	×	×	×	×	×	A	C	×	B	×
	Pre_Seed (Prep)	CH_4	B	×	A	×	×	✓	✓	D	×	×	×	×	×
	Pre_Seed (Fill)	CH_4	×	×	×	✓	✓	×	×	C	×	×	×	×	×
	Pre_Seed (Run)	CH_4	×	×	×	×	×	×	×	×	A	C	A	B	×
	Pre	CH_4_Seed (Prep)	B	×	A	×	×	✓	✓	D	×	×	×	×	×
	Pre (Fill)	CH_4_Seed	B	×	B	✓	✓	×	×	A	×	×	×	×	×
	Pre (Run)	CH_4_Seed (Run)	×	×	×	×	×	×	×	A	A	C	B	B	×
	Pre_Seed (Prep)	CH_4_Seed	B	×	A	×	×	✓	✓	D	×	×	×	×	×
	Pre_Seed (Fill)	CH_4_Seed	×	×	×	✓	✓	×	×	C	×	×	×	×	×
	Pre_Seed (Run)	CH_4_Seed (Run)	×	×	×	×	×	×	×	A	A	C	B	B	×
Premix	Premix_Conditioning		B	×	B	✓	✓	×	×	×	×	×	×	×	×
	-	CH_4	B	A	×	×	×	×	×	×	×	D	A	×	×
	CH_4	-	B	A	×	×	×	×	×	B	D	×	×	×	×
	CH_4	CH_4	B	A	×	×	×	×	×	B	D	A	×	×	×
	Pre(Cyl_Fill)	-	×	×	×	×	×	×	×	×	×	D	×	×	×
	Pre (Run)	-	×	×	×	×	×	×	×	×	A	C	×	×	×
	Pre(Cyl_Fill)	CH_4	×	×	×	×	×	×	×	×	×	D	×	×	×
	Pre (Run)	CH_4	B	A	×	×	×	×	×	×	×	C	A	×	×
Premix	Premix_Conditioning		B	×	B	✓	✓	×	×	×	×	×	×	×	×
	-	CH_4_Seed (Prep)	B	×	A	×	×	✓	✓	D	×	×	×	×	×
	-	CH_4_Seed (Run)	B	×	A	×	×	✓	✓	A	×	D	B	×	×
	CH_4_Seed (Prep)	-	B	×	A	×	×	✓	✓	D	C	×	×	×	×
	CH_4_Seed (Run)	-	B	×	A	×	×	✓	✓	A	C	D	×	×	×
	CH_4_Seed (Prep)	CH_4	B	A	A	×	×	✓	✓	D	C	×	×	×	×
	CH_4_Seed (Run)	CH_4	B	A	A	×	×	✓	✓	A	C	D	A	×	×
	CH_4	CH_4_Seed (Prep)	B	A	A	×	×	✓	✓	D	B	×	B	×	×
	CH_4	CH_4_Seed	B	A	A	×	×	✓	✓	A	B	D	B	×	×
	CH_4_Seed (Prep)	CH_4_Seed (Prep)	B	×	A	×	×	✓	✓	D	×	×	×	×	×
	CH_4_Seed (Run)	CH_4_Seed	×	×	×	×	×	×	×	A	C	D	B	×	×
	Pre_Seed (Prep)	-	B	×	A	×	×	✓	✓	D	×	×	×	×	×
	Pre_Seed (Fill)	-	×	×	×	✓	✓	×	×	C	×	D	×	×	×
	Pre_Seed (Run)	-	×	×	×	×	×	×	×	A	A	C	×	×	×
	Pre_Seed (Prep)	CH_4	B	×	A	×	×	✓	✓	D	×	×	×	×	×
	Pre_Seed (Fill)	CH_4	×	×	×	✓	✓	×	×	C	×	D	×	×	×
	Pre_Seed (Run)	CH_4	×	×	×	×	×	×	×	A	C	A	×	×	×
	Pre	CH_4_Seed (Prep)	B	×	A	×	×	✓	✓	D	×	×	×	×	×
	Pre (Fill)	CH_4_Seed	B	×	B	✓	✓	×	×	A	×	D	×	×	×
	Pre (Run)	CH_4_Seed (Run)	×	×	×	×	×	×	×	A	A	C	B	×	×
	Pre_Seed (Prep)	CH_4_Seed	B	×	A	×	×	✓	✓	D	×	×	×	×	×
	Pre_Seed (Fill)	CH_4_Seed	×	×	×	✓	✓	×	×	C	×	D	×	×	×
	Pre_Seed (Run)	CH_4_Seed (Run)	×	×	×	×	×	×	×	A	A	C	B	×	×
Premix_Seed	Premix_Conditioning		B	×	A	✓	✓	✓	✓	C	×	×	×	×	×
	-	CH_4	B	A	×	×	×	×	×	×	×	D	A	×	×
	CH_4	-	B	A	×	×	×	×	×	B	D	×	×	×	×
	CH_4	CH_4	B	A	×	×	×	×	×	B	D	A	×	×	×
Premix_Seed	-	CH_4_Seed (Cond)	B	×	A	✓	✓	✓	✓	C	×	×	×	×	×
	-	CH_4_Seed (Run)	×	×	×	×	×	×	×	A	×	D	B	×	×
	CH_4_Seed (Cond)	-	B	×	A	✓	✓	✓	✓	C	×	×	×	×	×
	CH_4_Seed (Run)	-	×	×	×	×	×	×	×	A	C	D	×	×	×
	CH_4_Seed (Cond)	CH_4	B	×	A	✓	✓	✓	✓	C	×	×	×	×	×
	CH_4_Seed (Run)	CH_4	B	A	×	×	×	×	×	A	C	D	A	×	×
	CH_4	CH_4_Seed (Cond)	B	×	A	✓	✓	✓	✓	C	×	×	×	×	×
	CH_4	CH_4_Seed(Run)	B	A	×	×	×	×	×	A	D	B	D	×	×
	CH_4_Seed (Cond)	CH_4_Seed (Cond)	B	×	A	✓	✓	✓	✓	C	×	×	×	×	×
	CH_4_Seed (Run)	CH_4_Seed	×	×	×	×	×	×	×	A	C	D	B	×	×
	Pre_Seed (Cond)	-	B	×	A	✓	✓	✓	✓	C	×	×	×	×	×
	Pre_Seed (Run)	-	×	×	×	×	×	×	×	A	C	×	×	×	×
	Pre_Seed (Cond)	CH_4	B	×	A	✓	✓	✓	✓	C	×	×	×	×	×
	Pre_Seed (Cyl Fill)	CH_4	B	A	×	×	×	×	×	×	A	D	A	×	×
	Pre_Seed (PSC Inj)	CH_4	B	A	×	×	×	×	×	×	A	C	A	×	×
	Pre_Seed (Cond)	CH_4_Seed (Cond)	B	×	A	✓	✓	✓	✓	C	×	×	×	×	×
	Pre_Seed (Cyl Fill)	CH_4_Seed (Cyl Fill)	×	×	×	×	×	×	×	A	×	×	B	×	×
	Pre_Seed (PSC Inj)	CH_4_Seed (PSC Inj)	×	×	×	×	×	×	×	A	A	C	B	×	×

Table A-3 RCM Fuelling Valve Settings

A▪4▪1   FUEL INJECTORS

The natural gas fuel injectors used on the RCM are discussed in detail in the body of this work. The DI injector hole was sized at 0.75*mm* diameter using bespoke *MatLAB*® code and electrostatic discharge machined (EDM'd) 40^0 off the injector centreline. This provides a DI fuel plume with a top edge parallel to the RCM fire-deck. All plume geometry and development calculations were based on the work of Hill *et al.* **[8]**. The tip drawing is shown in *Figure A-16*.
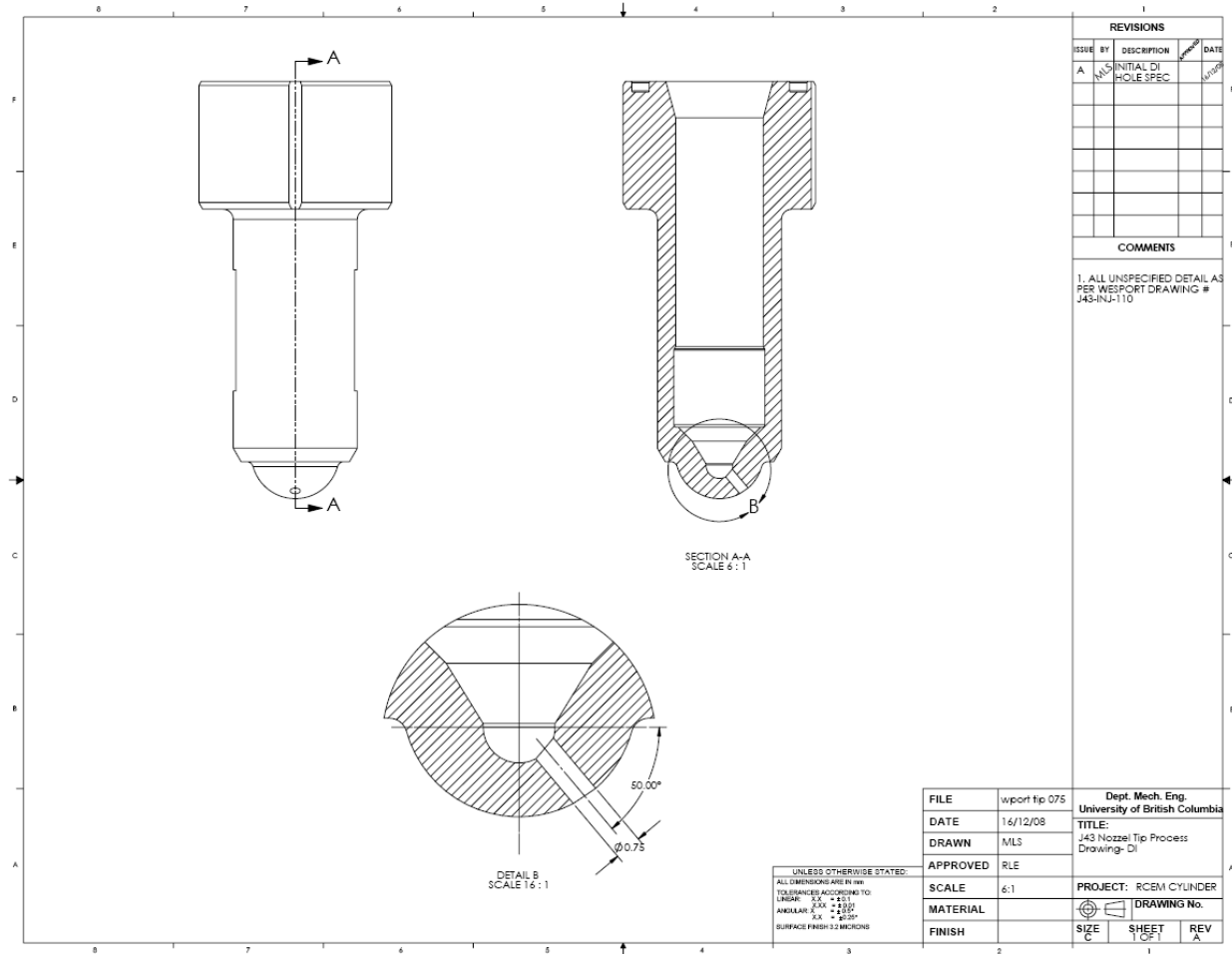

Figure A-16 RCM DI Tip Drawing

Due to poor solenoid response in previous **[7, 367, 415, 416]** and parallel studies the PSC solenoid was replaced with a J43M injector with a 0.26*mm* diameter orifice. This injects at much higher pressure than the old fast acting solenoid, though it does provide much better pulse control. The addition of a significant length of capillary tube to the end of the injector does mitigate these advantages significantly however All injectors are supplied by high pressure flexible thermoplastic hose so as not to excessively load the injectors or their mounts.

A▪4▪2   PSC INJECTOR MOUNT

The J43M used for PSC fuel control was retrofitted to the RCM using the mount shown in *Figure A-17*. The need for the injector to support combustion pressures and temperatures is bypassed in this application, so that the detail of the combustion seal can be omitted. The 0.26*mm* diameter hole in the injector tip was machined (by EDM) to be on the injector centreline, and is the smallest hole that can be produced by EDM. The small hole requirement is a result of needing only a small mass of fuel to form the PSC plume. A brace similar to that used on the DI injector was used to hold the injector in place, with two OEM 'quick release' skewers providing the seating force. These skewers allow easy adjustment of the seating force against the o-ring on the injector tip. It is this o-ring that provides the gas-tight seal.
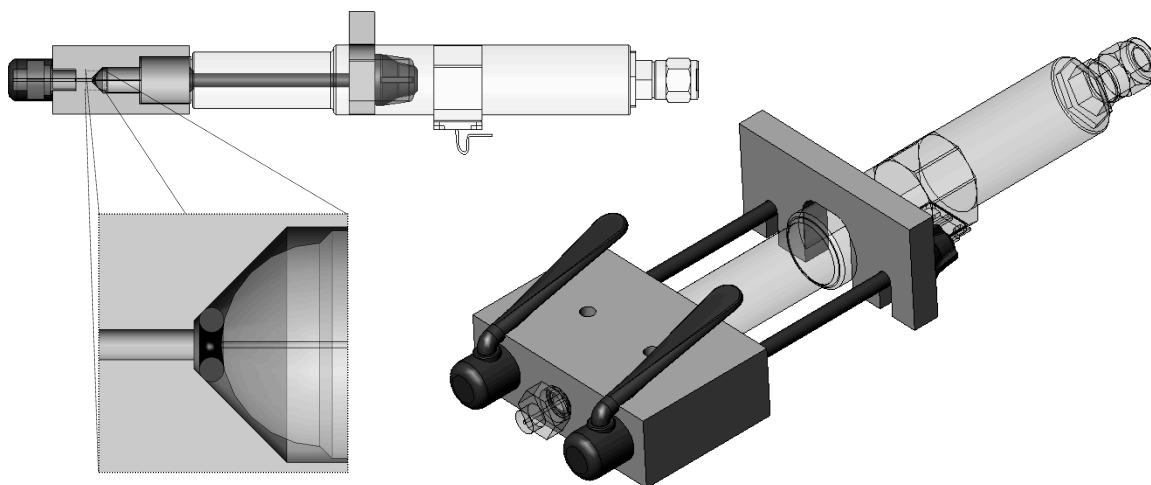
Figure A-17 RCM PSC Injector Mount

A▪5 SEEDER

The acetone seeder is a high pressure bubbler which allows methane/natural gas to be passed through liquid acetone or by-pass it before exiting. The flow path for the methane may be varied between the two routes so that the concentration of acetone in the exit stream may be varied.

The seeder is based upon the design presented by Neij **[259]** in his thesis, though the current design was altered to operate at higher pressures. Since the DI injector requires supply pressures in excess of 1800*psi* (up to a maximum of 3600*psi*) the seeder was designed to operate at up to 2800*psi*.

The pressure vessel was designed to the *1995 American Society of Mechanical Engineers Boiler & Pressure Vessel Code, Section 8: Rules for Construction of Pressure Vessels, Division 1, Part UG*. The flanges are held in place by eight M12 12.9 bolts. The bottom flange is sealed with an ASME 342 ethelyleme-propylene (EPDM) ring for its high resistance to acetone attack, while the top flange is sealed with a similarly specified nitrile (Buna-N) o-ring since nitirle rubbers have a better resistance to methane

corrosion. The o-rings and their recesses on the seeder flanges were specified according to SAE codes *ARP 1231(Rev. A) and 1234A*.
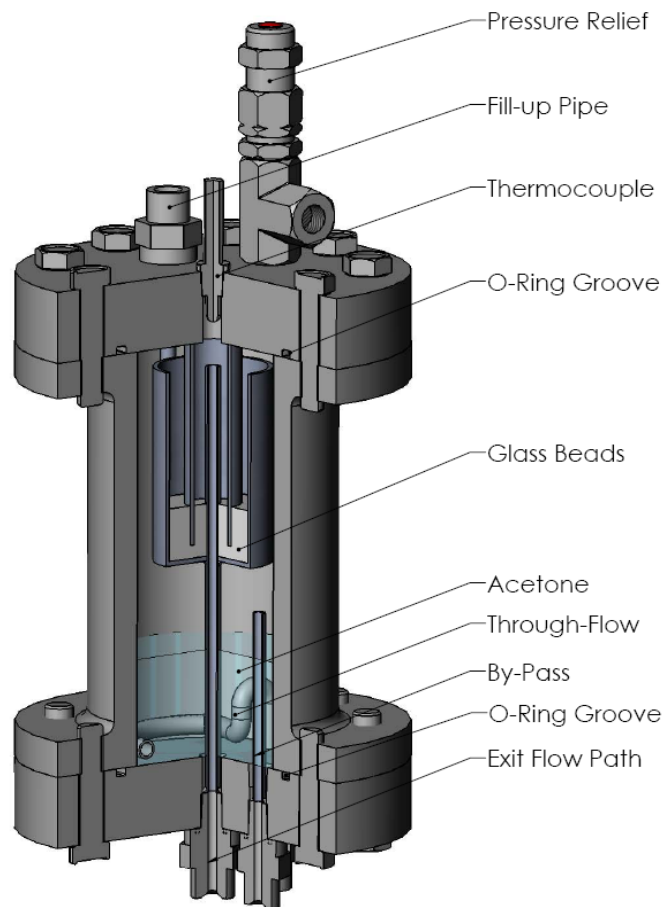
Figure A-18 Acetone Seeder Section View

Tappings are also provided for: emergency pressure relief (set at 4000*psi*); a thermocouple (type-κ); and pressure gauge. Glass beads placed in the exit flow path after the liquid acetone ensure the gas from the two steams is fully mixed.

A complete set of parts, process and assembly drawings for the seeder are presented on the subsequent pages.
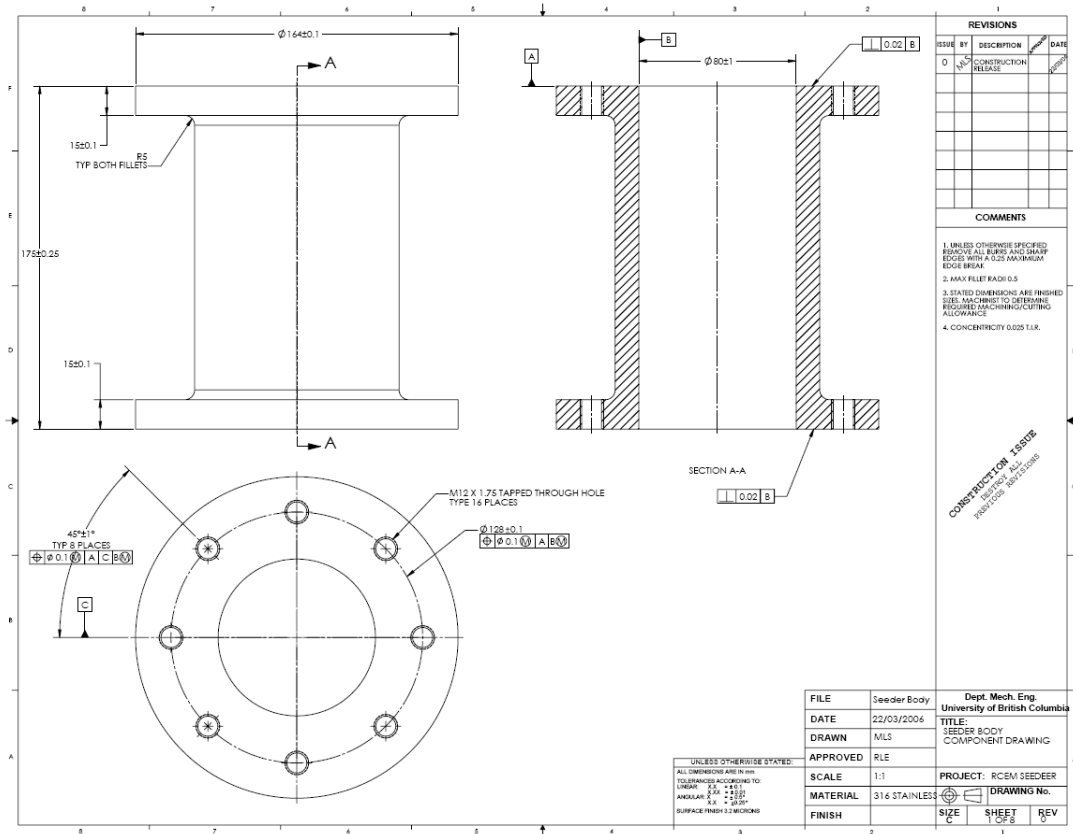
Figure A-19 Acetone Seeder: Body
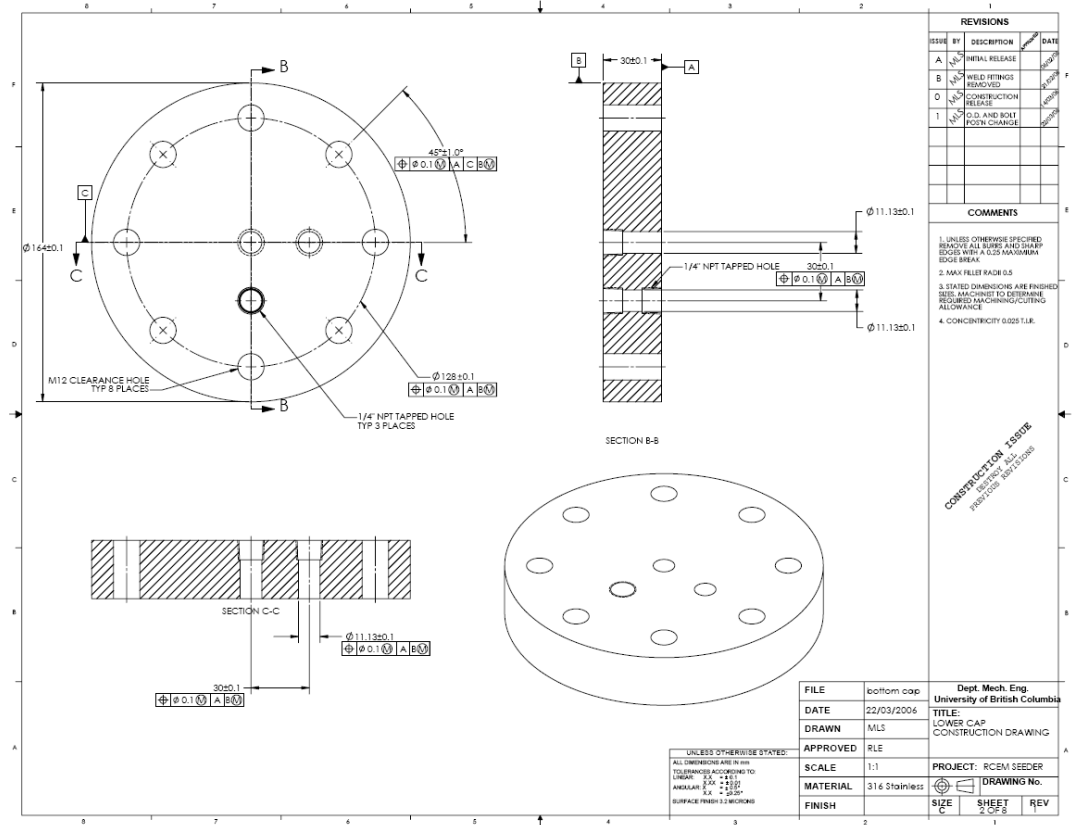
Figure A-20 Acetone Seeder: Bottom Flange

234
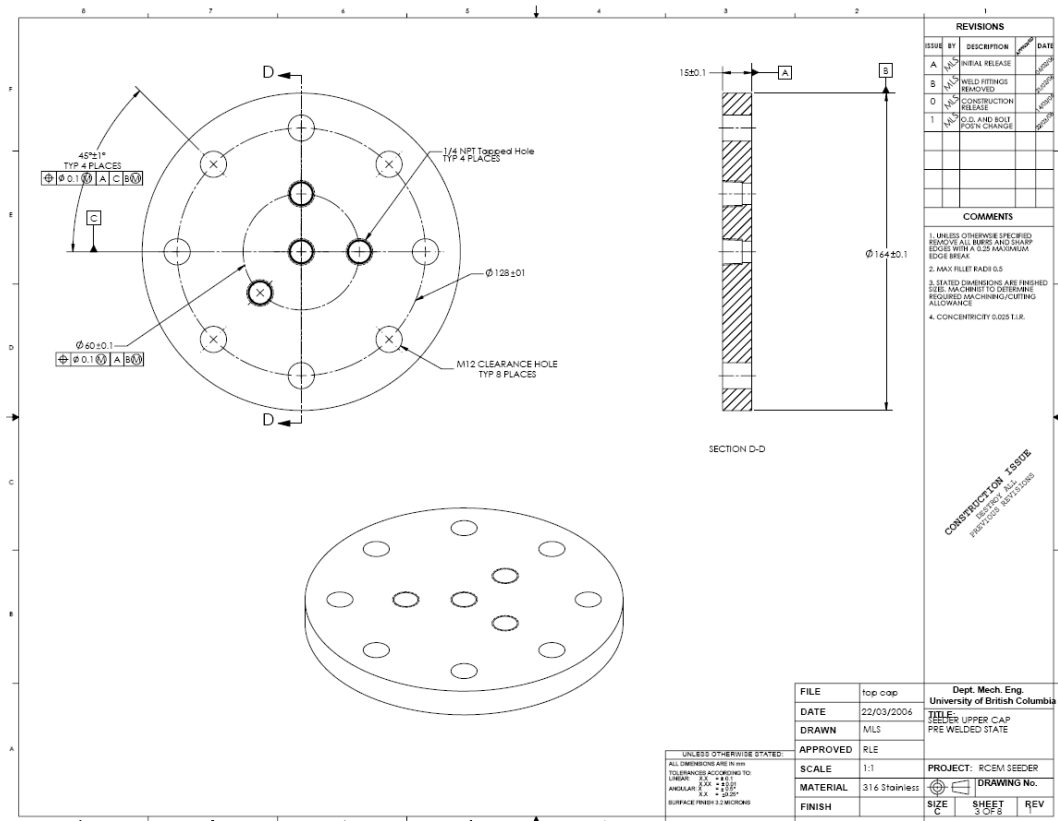
Figure A-21 Acetone Seeder: Top Flange
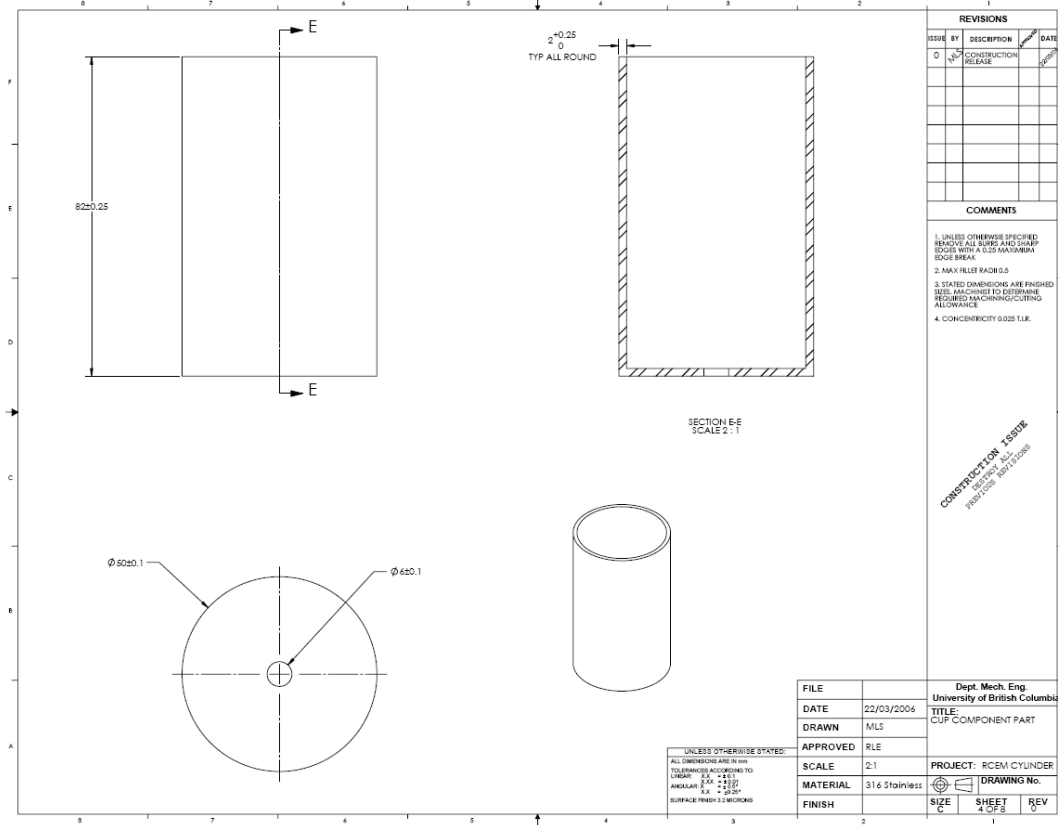
Figure A-22 Acetone Seeder: Cup
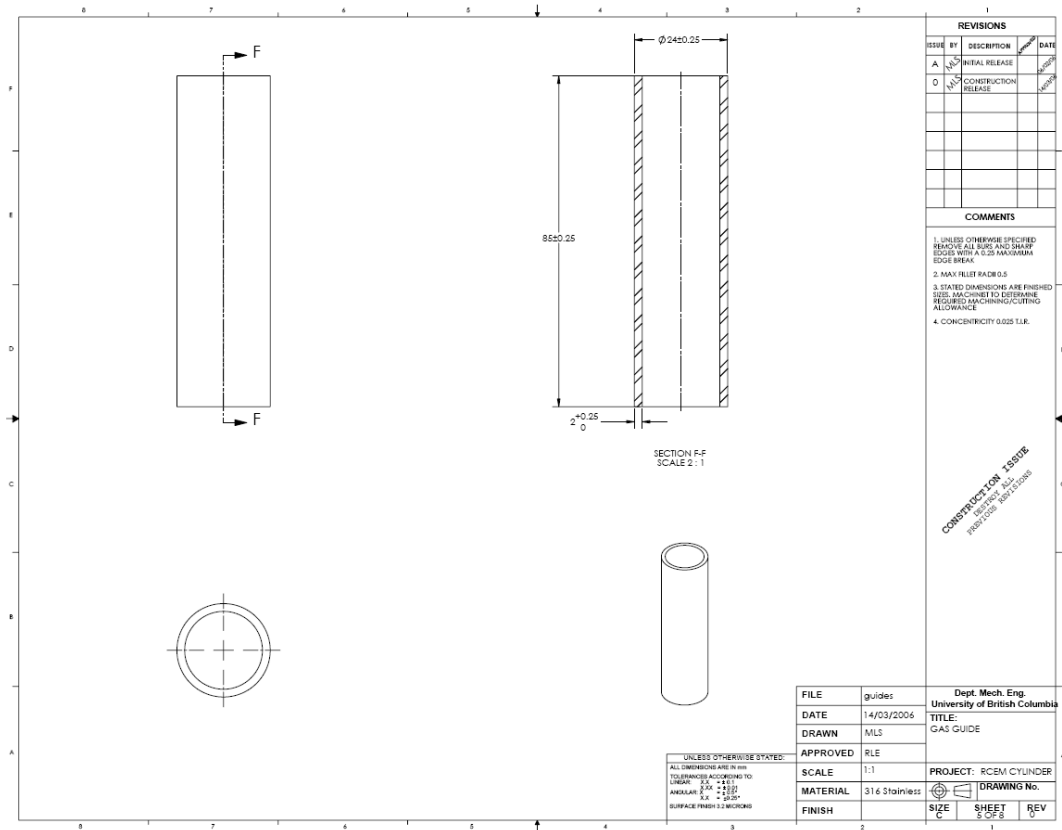
Figure A-23 Acetone Seeder: Guide
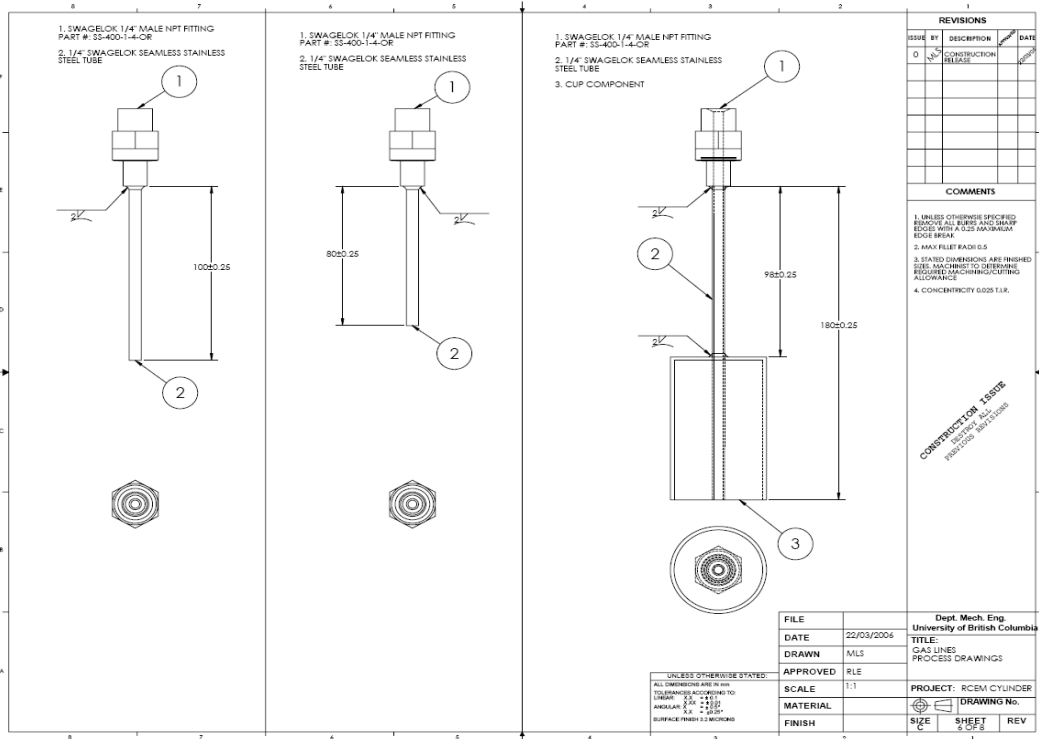
Figure A-24 Acetone Seeder: Pipe Assemblies
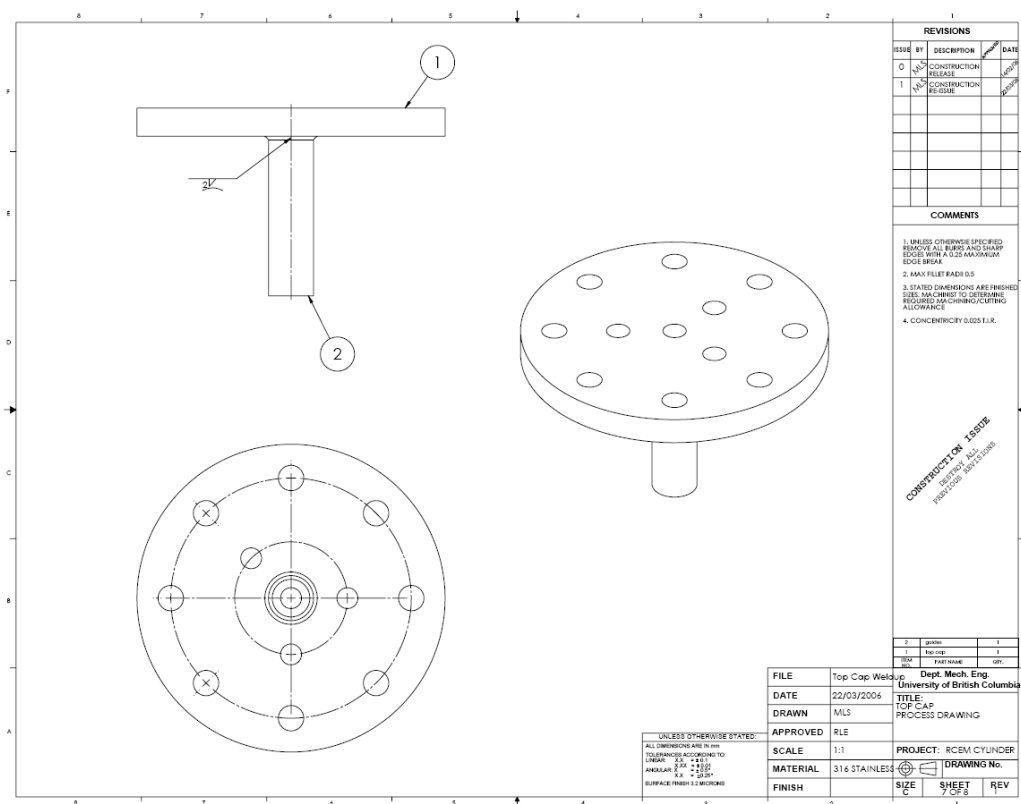
Figure A-25 Acetone Seeder: Top Weld-Up
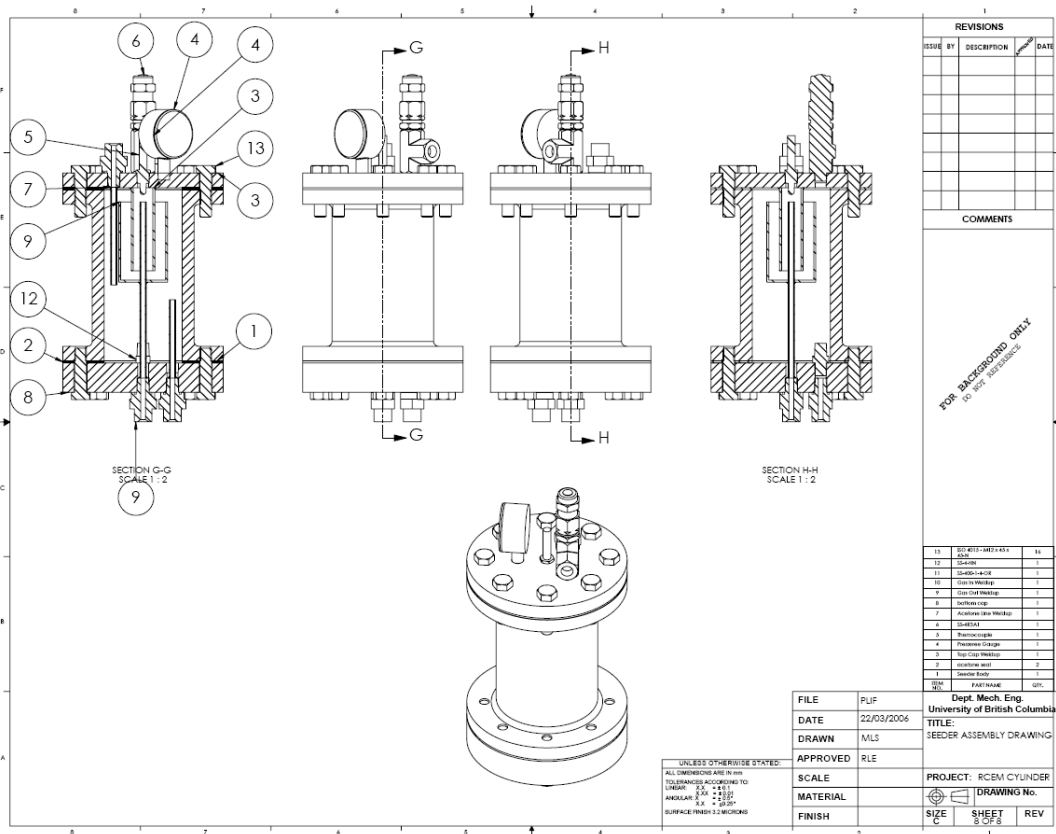
Figure A-26 Acetone Seeder: Assembly Drawing

237

The maximum operating pressure for the seeder is 2800*psi*. To ensure the safe operation of the seeder it was sent for hydrostatic pressure testing at *Enermax Fabricators Inc*., North Vancouver, Canada. Under contract number 11553 the seeder was hydrostatically proof tested with oil to a pressure of 4300*psi*. No failure or leaking was observed.

A▪6 TIMING & CONTROL

The timing and control system for the RCM is detailed extensively in *Appendix B*.

A▪7 SPARK CIRCUIT

An *MSD Blaster 2* (turns ratio 100:1) coil is used to generate the high voltage required for the spark. The primary coil +*ve* is connected to +12*V* through an 0.8*Ω* ballast resistor; the primary –*ve* to the drain of an NPN MOSFET (rated to 200*V*, 15*A*). The MOSFET source is grounded. The MOSFET switches based upon a TTL signal from the BNC connector. The TTL signal, which is received from the RCM triggering circuits (*cf. Appendix B*), is inverted by the 74LS04 and increased to +10*V* using the LTC1693 line driver. The 1*kΩ* resistor protects the MOSFET gate. The signal stability after the LTC1693 is protected from supply voltage fluctuations by the 0.1*μF* ceramic capacitor, for high frequency fluctuations, and against low frequency fluctuations by the 4.7*μF* tantalum capacitor.

In its normal state the circuit flows about 6*A* through the MOSFET (with V_{GS} ~10*V*). Upon triggering the MOSFET gate voltage drops to ~0*V* switching the transistor off. The current is now forced into the RC circuit formed by the 100*kΩ* power resistor and the 0.5*μF* high voltage capacitor. The current through the coil primary decays exponentially as the capacitor charges. As the field lines are cut the voltage produced in the primary is governed by $L\dfrac{di}{dt}$, reaching a value of ~250*V*. The coil secondary now has an induced voltage of about 25*kV*, which generates the spark at the HV terminal. The purpose of the RC circuit is to protect the MOSFET against the high voltages which would otherwise be produced on switching (since *di/dt* would be large). The fast response diode pair prevents the capacitor discharging to the primary coil as the voltage drops on the primary -*ve*. The high voltage capacitors now discharge through the 100*kΩ* resistor.
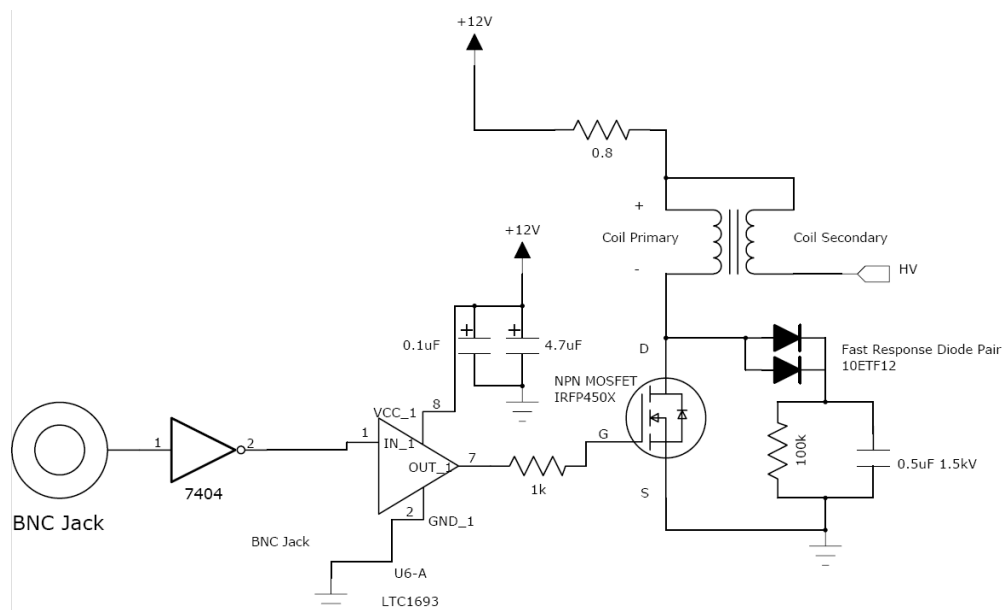
Figure A-27 RCM Spark Circuit, Circuit Diagram

Component	Part #	Value
Inverter	74LS04	---
Line Driver	LTC1693	---
Capacitor (Ceramic)	---	$0.1\mu F$
Capacitor (Tantalum)	---	$4.7\mu F$
Resistor	---	$1k\Omega$
MOSFET (NPN)	IRFP450X	---
Power Resistor	---	$100\ k\Omega$
Capacitor (High Voltage)	---	$0.5\ \mu F,\ 1.5kV$
Fast Response Diode	10ETF12	---
MSD Coil	Blaster 2	100:1
Resistor (Ballast)	MSD Ballast	$0.8k\Omega$

Table A-4 Component Listing for RCM Spark Circuit

A▪8 INSTRUMENTATION & EQUIPMENT LIST

Equipment	Model	Manufacturer	Supporting Software
Laser	CompexPro 102	Lambda Physik	--
Intensified CCD Camera	DiCam Pro	Cooke Corp.	CamWare v2.12
High Speed Camera	Vision Research	Phantom v7.1	Cine Control v605.2
Pressure Transducer (high dynamic response)	0112A	PCB Electronics	--
Charge Amplifier	5010	Kistler Instrument Corp.	--
Oscilloscope	2014B	Tektronix Inc.	OpenChoice Desktop v1.4
Laser Power Meter	FieldMax II	Coherent Inc.	FieldMax II PC v1.2
Thermocouple Reader	HH12A	Omega Inc.	--

Table A-5 Instrument List for RCM

Not listed are the various linear and variable power supplies, the proprietary Westport® injector driver hardware, and the in-house hardware prepared by the author.

Appendix B RCM Timing Control System

B▪1 INTRODUCTION

The design and operation of the rapid compression machine control system is outlined in this appendix. Detailed discussions are presented regarding the design and operation of the electrical circuits and the mechanical details of the chassis on which the circuits are mounted.

B▪2 GENERAL PRINCIPLES OF RCM EVENT CONTROL

The RCM is controlled by a series of TTL circuits which, typically, use LS series DIP chips. All logic is, unless otherwise stated, $+5V$ high with $0V$ low. A rotary encoder provides positional data which is used as the time base for all events. The piston TDC is the reference datum, with all events timed against this. The encoder provides 10000 counts per revolution. The event timings are specified, as appropriate with, a start count and a duration count. The count values, as set on the thumbwheel switches on the front panel of the control box, are set according to the required number counts after the gate (*cf. §B▪3*). Timing w.r.t. TDC is made by knowing that TDC is 5200 counts after the gate.
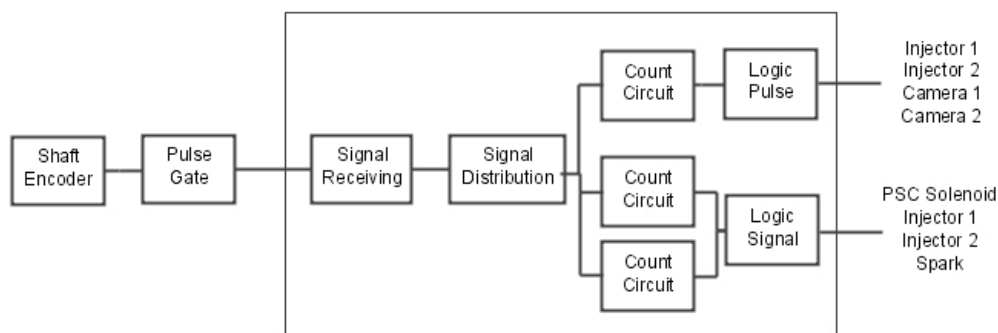
Figure B-1 Information Flow in RCM Control

The RCM control hardware is capable of providing timing for the events listed in *Table B-1*.

Event	Required Input[16] (logic pulse or signal)
Spark	Signal
PSC	Signal
Direct Injection 1	Pulse & Signal
Direct Injection 2	Pulse & Signal
Laser 1	Pulse
Laser 2	Pulse
Camera 1	Pulse
Camera 2	Pulse

Table B-1 RCM Timed Events

Power is stepped down from mains $120V$ A.C. to $12V$ D.C. for distribution to all boards. Each board supply is smoothed with a $25V$ aluminium electrolytic capacitor, and is then stepped down to $+5V$ with a smoothed LM7805 voltage regulator.

B▪3 ENCODER & ENCODER GATE

The rapid compression machine (RCM) has all its timed events synchronised against a common time base-that of the piston crank angle. The RCM crank has a *US Digital H6* incremental rotary encoder attached to

---

[16] A logic pulse is simply a +5V spike, while a logic pulse is a +5V high state for a specified number of encoder counts

it via a 1¼" flexible coupling. The 2500 count encoder uses ×4 quadrature to provide 10000 counts per revolution (*i.e.* 0.036 ^{0}/count). The encoder also provides an index pulse once per revolution.

The operation of the RCM does not guarantee that the driving rack will return to the same point after ever run. To circumvent this, the index from the encoder is used to start the RCM event timings. The encoder is positioned such that the index pulse is received 5200 (~187^0) counts BTDC. The circuit outlined below is designed to gate the encoder pulses so that no pulses are passed to the timing circuits of *§B▪2* prior to the output of encoder index pulse.

The LS7184 decoder takes the pulses of the rotary encoder and provides an output clock pulse train. The floating state on pin 5 provides the ×4 quadrature, while the up or down count (*i.e.* rotary direction indicator) on pin 7 is ascertained from the phase of the pulses on Channel A with respect to Channel B.

The 74HC109 J-K flip flop provides the gating. Pulling pin 1 low through application of the push button switch, J2 (coloured red on the gate box front panel), makes the Q output go low. The flip-flop will stay in this state until J (the encoder index pulse) is asserted. The flip-flop checks the state of its input pins J and K at 10*MHz*, as governed by the crystal oscillator on pin 4 (CP). Gate A of the 5400 series quad-NAND chip allows the encoder pulse chain to pass only when the Q output of the J-K is asserted. When Q is asserted the LED connected to J3 is no longer forward biased so will not illuminate once the index has been received by the J-K and starts to pass the pulse train. The pulse train is now passed through gate D of the 5400 series quad-NAND chip (since pin 12 is asserted and the, inverted, train arrives on pin 13) and inverted by gate D of the 7400 series hex-inverter. The train is now high (+5*V*) with pulses going low (0*V*).

The pulse train is then fed to a line driver, LTC1693, so that the gate can provide enough current and voltage to drive the timing. The output of the LTC1693 provides a high quality square wave independent of supply fluctuation (because of the capacitors on the chip supply pin 8). The 0.1*μF* capacitor smoothes high frequency fluctuations while the 4.7*μF* tantalum capacitor smoothes the lower frequencies. The output pulse train is supplied to a BNC jack, J4.
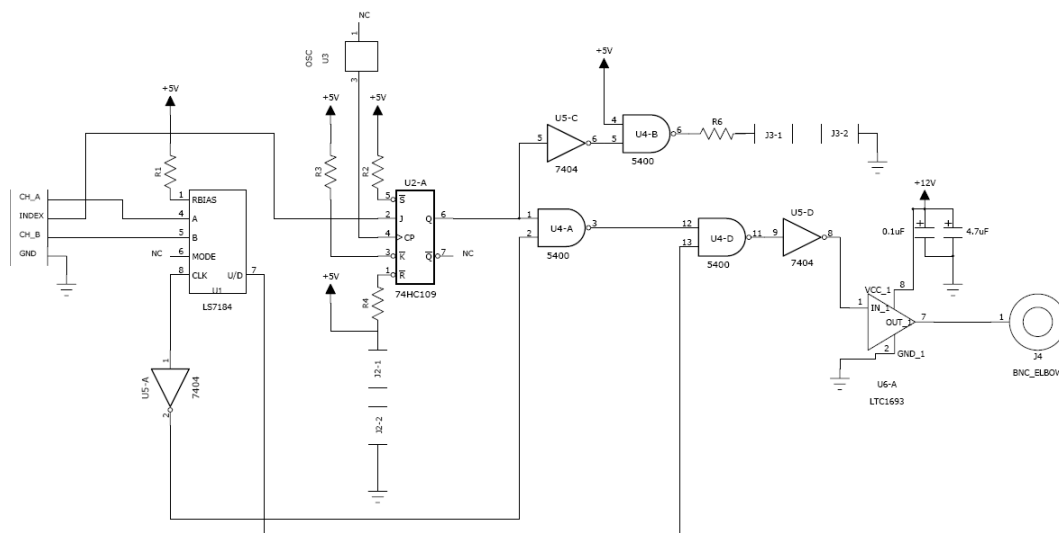
**Figure B-2 Encoder Signal Gate, Circuit Diagram**

The rotary encoder has its output split so that its signals are also provided to and ED3 digital display (not shown in *Figure B-2*), which provides a digital display of the encoder's rotary position. This display resets each time it is powered up, so must be used with caution if trying to find the position of the RCM piston.

Component	Part #	Value
Resistors (unless stated below)	---	4.7kΩ
Resistor R4	---	1kΩ
Resistor R6	---	160Ω
Capacitor (Ceramic)	---	0.1μF
Capacitor (Tantalum)	---	4.7μF
Quad-NAND, 14 pin DIP	74HC54	---
Hex-inverter, 14 pin DIP	74HC04	---
Oscillator	ACH-10.000MHZ-EK	10MHz
J-K flip-flop	74HC109	---
Rotary decoder	LS7184	---

Table B-2 Rotary Encoder Gate, Circuit Components & Values

B▪4 SIGNAL DISTRIBUTION

The signal received from the encoder gate must be distributed to all the timing circuits outlined in *Table B-1*. The pulse train from the encoder gate is received on the BNC jack J1, which has a 50Ω terminating resistor. The signal is inverted by gates A and B of the 74LS04 hex-inverter, before going to the differential line drivers U33 and U35. These AM26LS31 differential drivers split the signal (pins 1, 7, 9 & 15) into two (pins 2, 6, 10 & 14 being *+ve* and pins 3, 5, 11 & 13 being *−ve*) passing half down each line. This allows better high frequency transmission to each of the individual timing circuits. The distribution circuit shown *Figure B:3* in also distributes a 10*MHz* clock signal to the four timing circuits which requires a J-K flip-flop (*cf. §B▪8*).
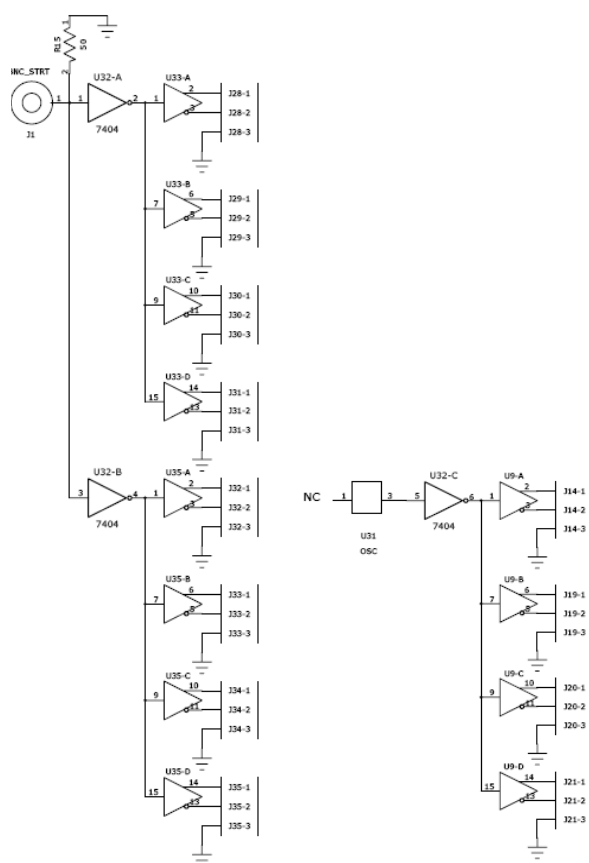
Figure B-3 Pulse Train Distribution, Circuit Diagram

The distribution board also contains circuitry to supply a rest signal to all timing boards and the chips which require it, *Figure B:3*. A SPST pushbutton switch is attached through jumper J3, which upon depression makes pin 1 on the Schmitt-triggered inverters (74LS14) of U23 & 24 go low, while the LED on the other 2 pins of J3 is forward biased and illuminates to show that the rest signal was sent. Switch bounce is minimized through using a 74LS279 R-S latch.
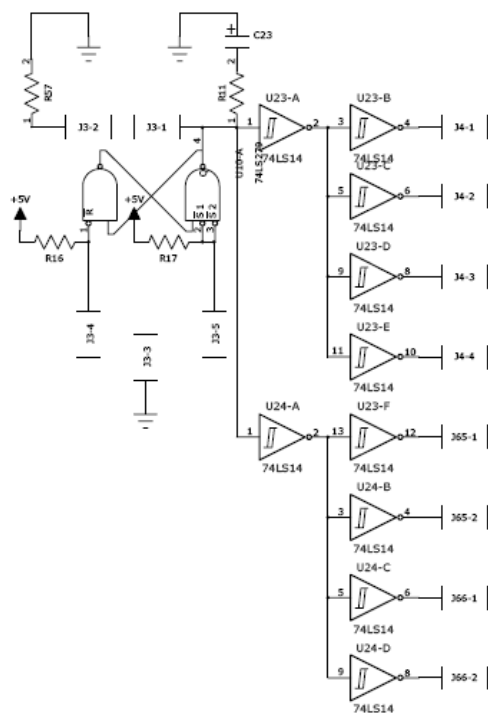
Figure B-4 Reset Signal Distribution, Circuit Diagram

The reset pulse is stretched by the RC time constant of R11 and C23 while the Schmitt-triggered inverters then provide the hard switch required by the reset gates.

B▪5 SIGNAL RECEIVING

The encoder signal from the distribution circuit of *§B▪4*, is received on an AM26LS32 differential line receiver. The 100Ω terminating resistor ensures the difference between the two receiving lines (pins 1 & 2) is maintained, so producing a clear waveform on the receiver output (pin 3). The switch of J57 must also be closed to allow gate A of the AND chip to pass the encoder signal, which is output on pin 3 of the AND chip. When the circuit is active (*i.e.* powered) the LED of J58 is forward biased and illuminated. The 220Ω resistor protects the LED while the 1kΩ pulls down the input on the AND gate.
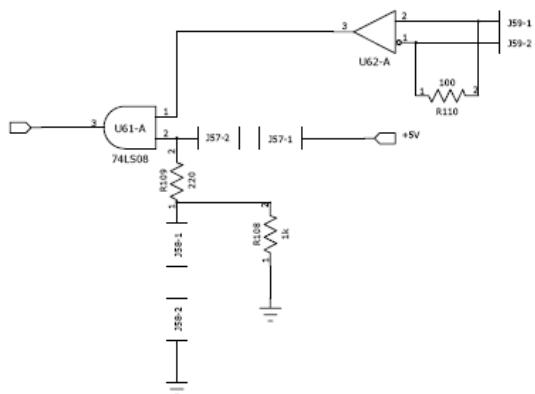
Figure B-5 Encoder Pulse Train Receiving, Circuit Diagram

B▪6 PULSE COUNTER AND COMPARISON CIRCUIT

Integral to the event timing is the ability to count and compare the number of pulses received against a set value. The circuit of performs this task. The gated pulse train is received on ENC_PULSES_1 from the signal receiving circuit of. All counter chips have the present value pins (pins 3-6) held low, and the load (LD) held high so that counting will always start at zero. The first pulse is used to trigger the R-S latch, which then asserts the parallel enable (ENP) on all the 74LS160 synchronous decade counters. All subsequent pulses on the pulse train are then passed to the 74LS160 clock pins (CLK). The unit stage of the counter array (U54, in *Figure B-6*) has its trickle enable asserted at the same time as the ENP. With both enables asserted the counter counts the rising edge of all the pulses received on the CLK, with the output being given on Q0-Q3 (pins 11-14). On count 9 the ripple carry out is asserted so that the next pulse will be counted by the 10's stage (U53), while the unit stage rolls back to zero. U53 thus counts every tenth pulse, on the 99th pulse the RCO of U53 goes high, asserting ENT on U52 allowing U52 to count the 100th pulse. The 100's stage works as the units and 10's stages do. Finally, the 1000's stage (U51) has to have RCO asserted on all previous stages to assert its ENT, which allows the count to take place. When required the chip resets for the 74LS160 and 74LS279 are received from the distribution circuit (*§B▪4*) on START_RST_0_1. Both the 74LS160 and 74LS85 have decoupling capacitors on their power pins (not shown) to provide the power required on the output pins when the states change rapidly upon switching. The capacitor values of $0.1\mu F$ and $0.01\mu F$ are alternated to avoid a resonant response if they are required to discharge simultaneously.

The output of each counter stage is sent to the 74LS85 four bit magnitude comparators on inputs B0-B3. The set values on the comparators (A0-A3) are defined by the user through use of the thumbwheels switches attached to J49-J52. The switches use complimented BCD to set the state, with pull up resistors on each line limiting the low state current draw. The input states A<B and A>B are not used so pins 2 and 4 are tied low, while the required input state A=B necessitates that pin 3 be held high. When this case is satisfied the QA=B pin (6) is asserted. It follows logically that when the count on each stage matches the count specified by the switches for each stage, the A=B output of each comparator will go high, and only in this case will the output of the quad-input AND gate (74LS21) be asserted.
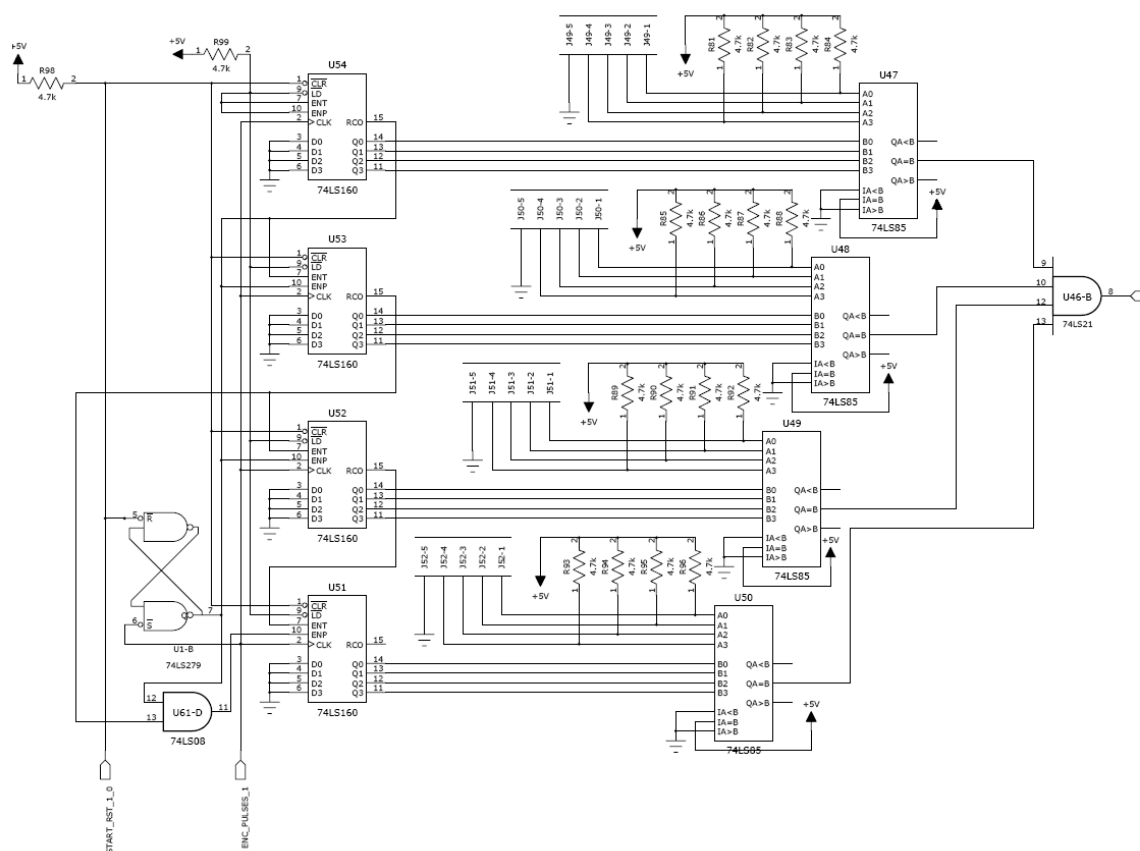
Figure B-6 Pulse Counter and Comparator, Circuit Diagram

B▪7 Logic Pulse Generation

The output of the counter/comparator circuit is the sole input required to trigger a $+5V$ logic pulse from the circuit of *Figure B-7*. A pulse is required to trigger the lasers, the iCCD cameras and injector lift. The assertion of A1 on the 74LS221 monostable multivibrator leads to a logic pulse (pulled up to $+5V$ by the $4.7k\Omega$ resistor) on the output Q. The length of the pulse is governed by the RC time constant of capacitor C47 ($0.1\mu F$, pin 14) and the $10k\Omega$ trim pot on RC (pin 15). The output is made through BNC J53.
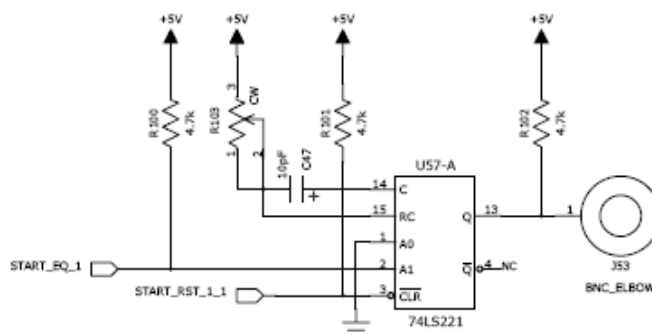
Figure B-7 Logic Pulse Generation, Circuit Diagram

B▪8 LOGIC SIGNAL GENERATION

For the RCM events which require a *+ve* logic signal for a set duration of counts the circuit of *Figure B-7* is used. This circuit is used to provide logic for injector hold signals, spark and PSC solenoid lift. The 74LS109 J-K flip-flop provides switching based upon inputs from two counting circuits. The Q output of the flip-flop is held low until J is asserted (START_EQ). The high signal on J is sent from the counter circuit of *§B▪6* when the specified start count is reached. Q is then active making the BNC connector of J15 also high. Gate A of the 74LS08 AND chip now starts to pass the encoder signal (output on pin 3, WIDTH_COUNT) to a duplicate of the counter circuit of *§B▪6*. The second counter/comparator circuit asserts after the specified number of counts such that K is then asserted (WIDTH_EQ, which is inverted by U11), sending Q low and switching the BNC jack. The flip-flop receives its clock pulse (CP) from the oscillator distribution circuit of *Figure B-4* via an AM26LS32 differential line receiver, U28 (for details about the operation of the line receiver *cf. §B▪4*). The flip-flop is reset by asserting R with a low state, as received from the reset distribution circuit of *Figure B-3*.
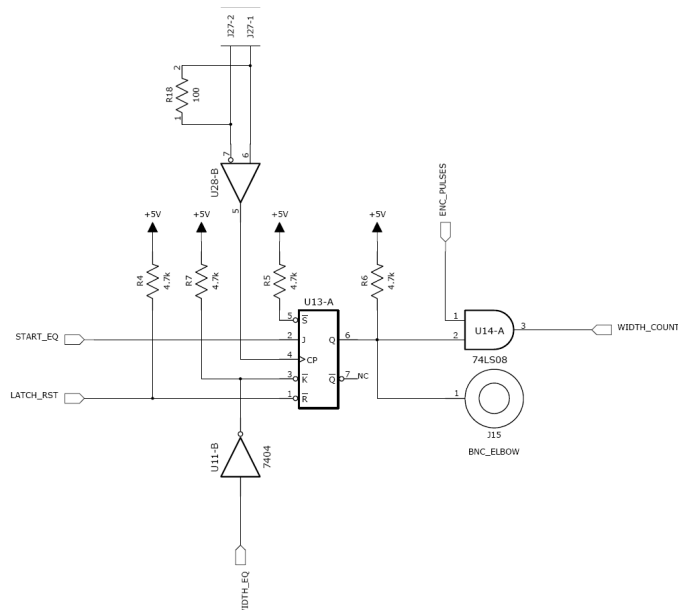
Figure B-8 Logic Signal Generation, Circuit Diagram

B▪9 APPENDIX 1: DESIGN, ELECTRICAL DRAWING SETS, ARTWORK AND COMPONENT LISTS

The following sections discuss how the circuits were designed and implemented.

B▪9▪1 CIRCUIT DESIGN AND TESTING

The RCM control hardware was developed using the *MentorGraphics* design suite *PADS2005*. *PADS Logic* was used to develop the logic and operating principles outlined in *§B▪4-§B▪8*. This logic was transferred on to a board PCB layout with the use of *PADS Layout*, where all component specifications

where defined and finalised. Finally, *PADS Router* was used to specify the traces on the PCB's according to the logic put together in *PADS Logic*. *PADS Router* was also used to generate the Gerber plots required (drill aperture list, drill positions, silk screens, solder masks, artwork and board extents) for PCB production. Upon receipt of the boards, they were populated and tested (an Agilant digital oscilloscope was used to test circuit logic). Manufacturing drawing sets are presented in the following sections. Test results for each board are presented in *Tables B-4, B-5, B-7, B-8, B-10 & B-11*. A full component list for each circuit board is also given (*Tables B-6, B-9 & B-12*).

B▪9▪2   LOGIC PULSE CIRCUITS

This circuit board contains two logic pulse circuits, and is intended to fire one laser and camera pair.
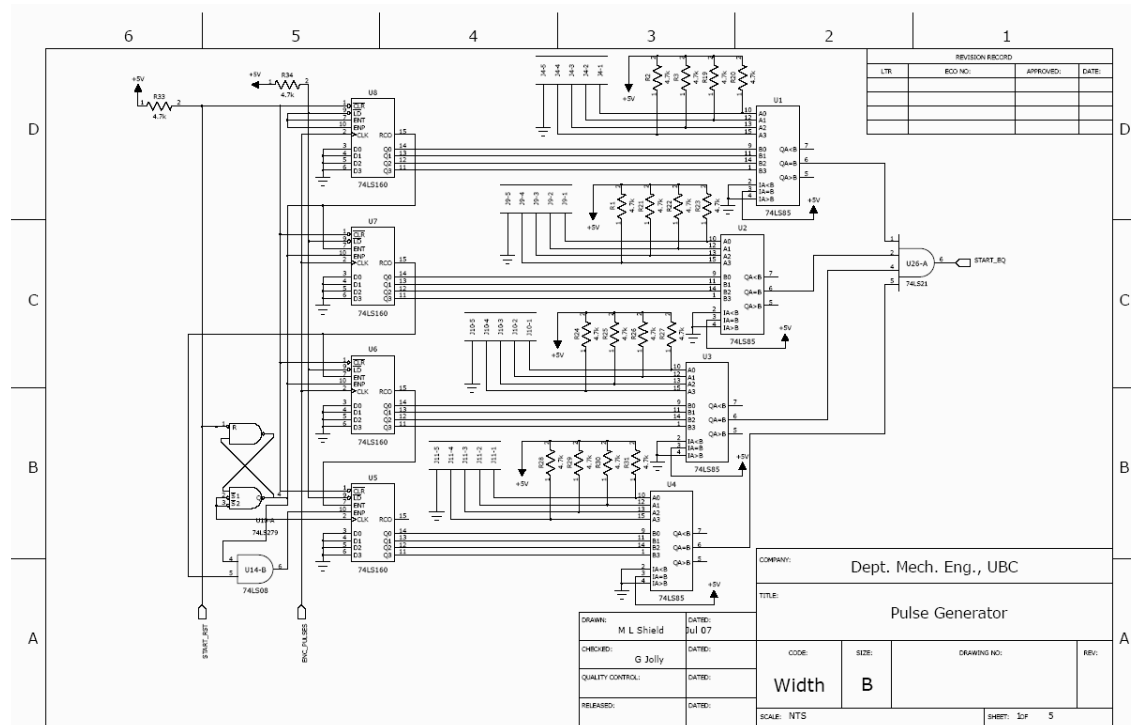

Figure B-9 Start Counter-Gate A, Pulse Circuit
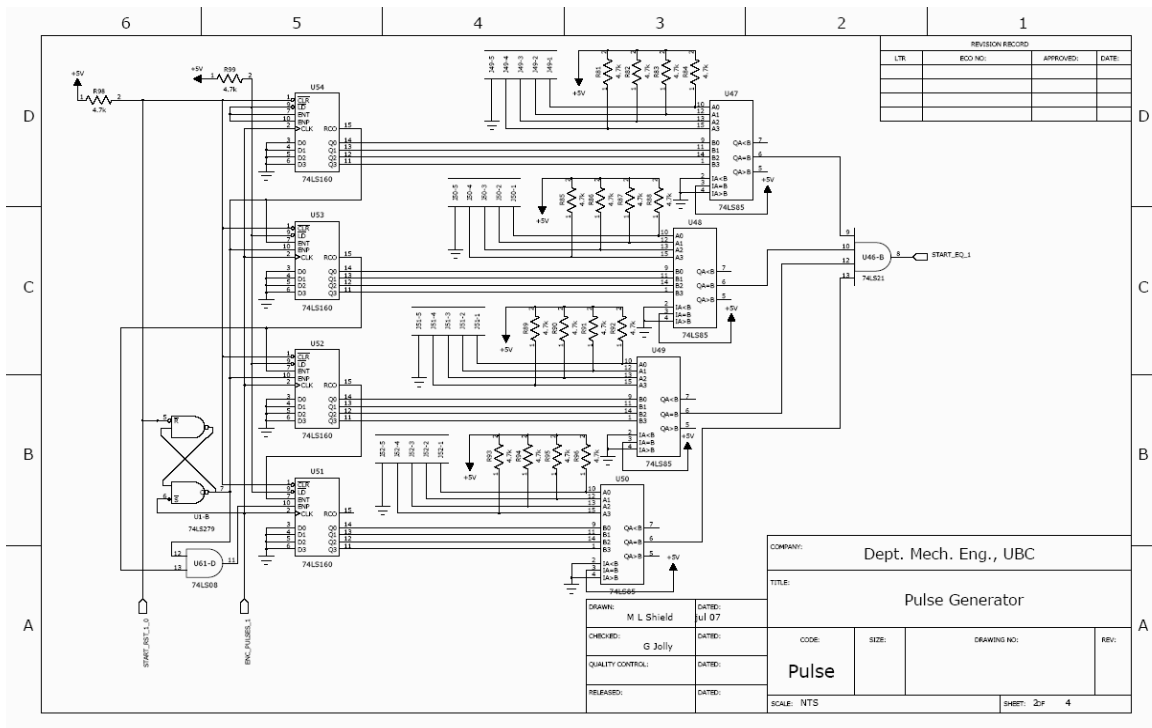
Figure B-10 Start Counter-Gate B, Pulse Circuit
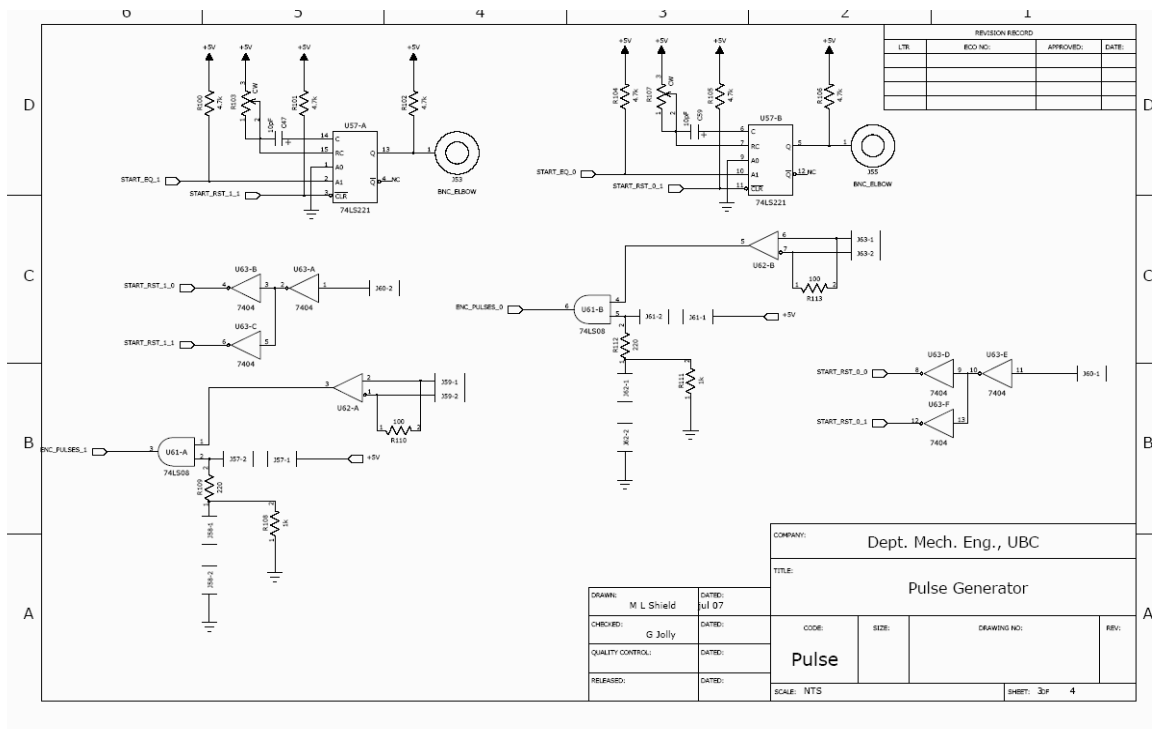
Figure B-11 Latch & Reset Circuits, Pulse Circuit
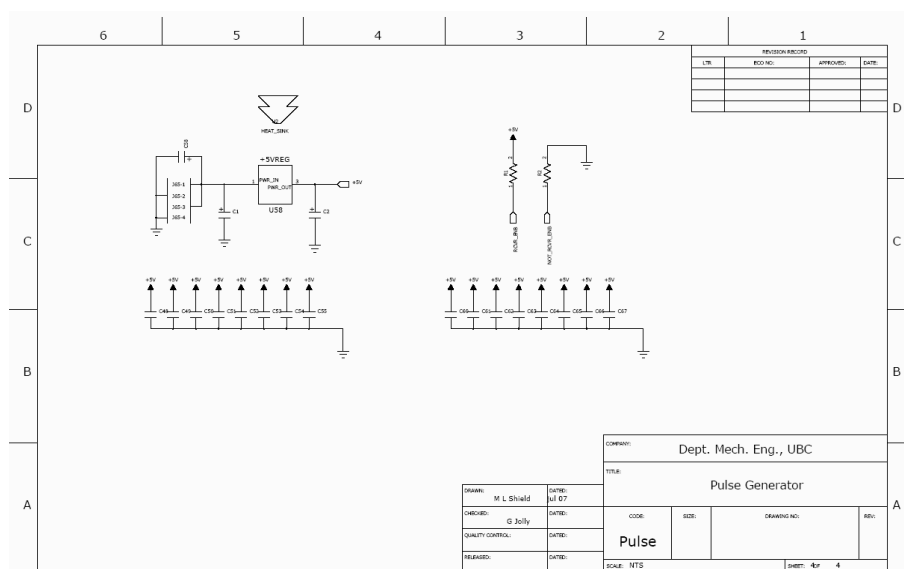
Figure B-12 Smooth Capacitor Circuits, Pulse Circuit

Component	Component #	Part #	Value
Quad-AND, 14 pin DIP	U61	74LS08	---
Dual R-S latch, 14 pin DIP	U1	74LS279	---
Counter, 16 pin DIP	U41-U44, U51-U54	74LS85	---
Comparator, 16 pin DIP	U37-U40, U47-U50	74LS160	---
Resistors (¼*W*)	All R, unless otherwise listed	---	4.7*kΩ*
Dual-4 in AND, 16 pin DIP	U46	74LS21	---
Dual multivibrator, 16 pin DIP	U57	74LS221	---
Hex-inverter, 14 pin DIP	U63	74LS04	---
Liner Receiver, 14 pin DIP	U62	AM26LS32	---
Resistors (¼*W*)	R109, R112	---	220*Ω*
Resistors (¼*W*)	R108, R111	---	1*kΩ*
Resistors (¼*W*)	R110, R113	---	100*Ω*
Trim Pot	R103, R107	---	10*kΩ*
BNC jack	J53, J55	---	---
5 pin sip	J36, J36, J38, J48, J49, J50, J51, J52	---	---
2 pin sip	J57, J58, J62, J61	---	---
4 pin power jack	J65	---	---
Capacitors (Ceramic)	C47, C59	---	*10pF*
Capacitors (Ceramic)	C48-C55	---	*0.01μF*
Capacitors (Ceramic)	C60-C67	---	*0.1μF*
Capacitor (Tantalum)	C1, C2	---	*0.1μF*
Capacitor (Aluminium)	C58	---	*0.1μF*
5V voltage regulator	U58	LM7805	---
Heat Sink	U2	---	---

Table B-3 RCM Logic Pulse Board, Component List

10▪3▪3 LOGIC SIGNAL CIRCUITS

This circuit board contains one logic signal circuit and is intended for use with the PSC solenoid and spark circuit.
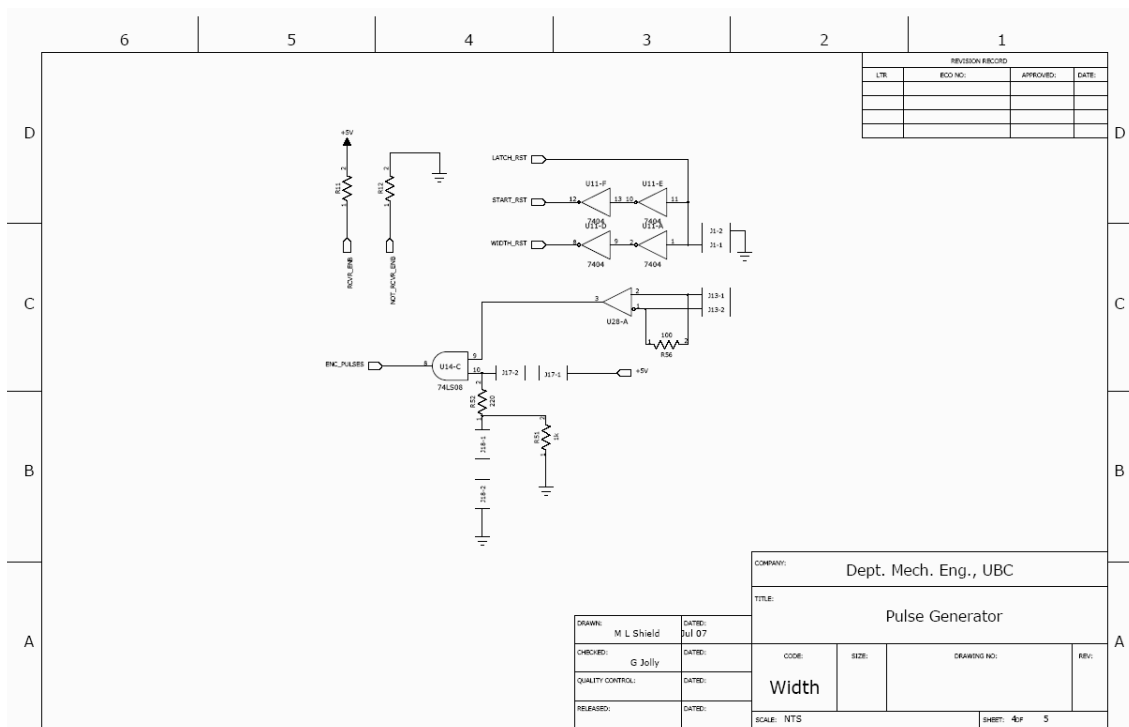

Figure B-13 Start Counter-Gate A, Logic Circuit
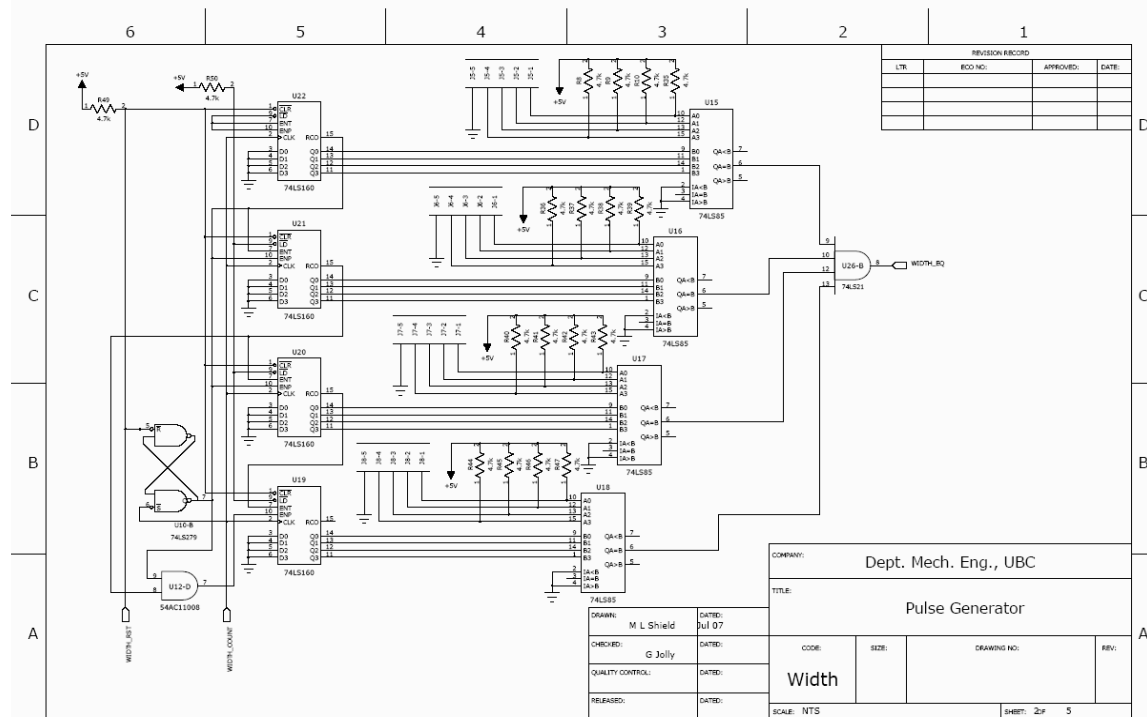
Figure B-14 Start Counter-Gate B, Logic Circuit
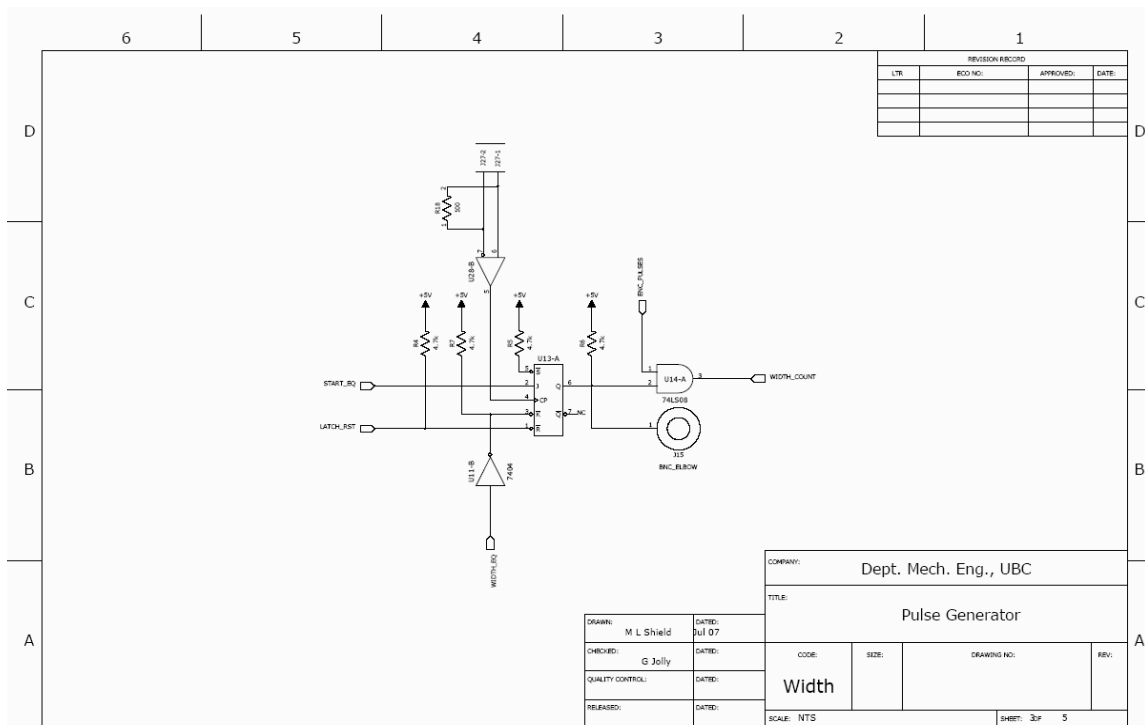
Figure B-15 Latch Circuit

Figure B-16 Signal Receiving, Logic Circuit

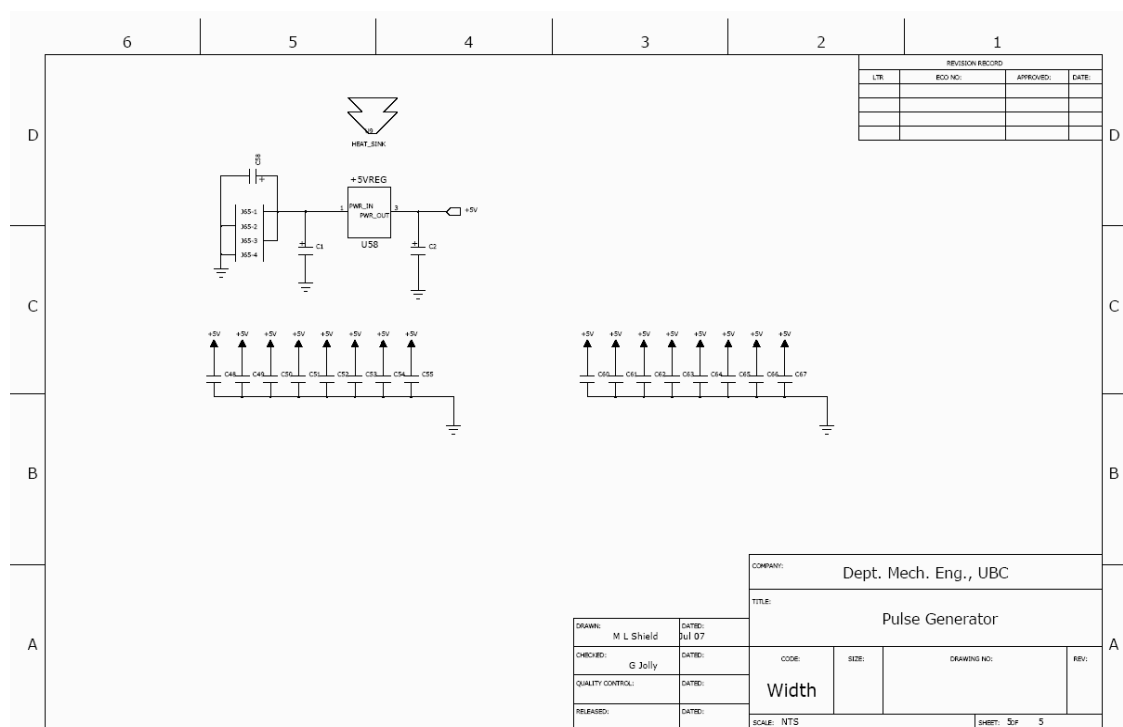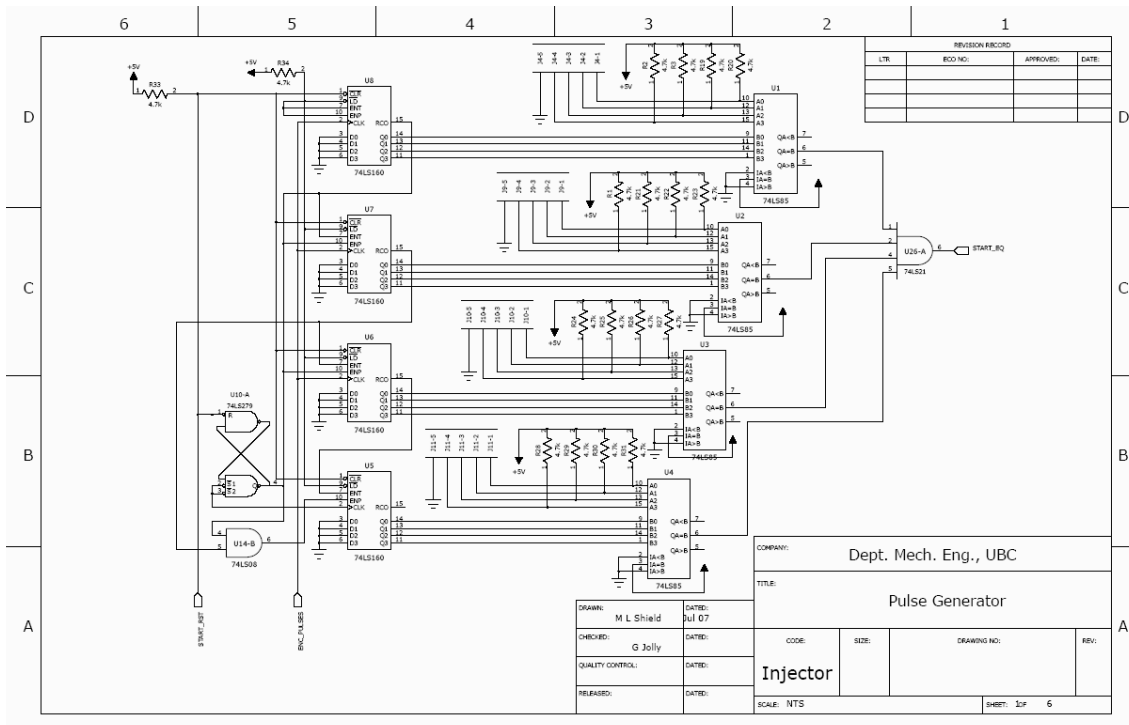**Figure B-17 Smooth Capacitor Circuits, Logic Circuit**

Component	Component #	Part #	Value
Quad-AND, 14 pin DIP	U12, U14	74LS08	---
Dual R-S latch, 14 pin DIP	U10	74LS279	---
Counter, 16 pin DIP	U5-U8, U19-U22	74LS85	---
Comparator, 16 pin DIP	U1-U4, U15-U18	74LS160	---
Resistors ($\frac{1}{4}W$)	All R, unless otherwise listed	---	$4.7k\Omega$
Dual-4 in AND, 16 pin DIP	U26	74LS21	---
Dual J-K flip flop, 16 pin DIP	U13	74LS109	---
Hex-inverter, 14 pin DIP	U11	74LS04	---
Liner Receiver, 14 pin DIP	U28	AM26LS32	---
Resistors ($\frac{1}{4}W$)	R52	---	220Ω
Resistors ($\frac{1}{4}W$)	R51	---	$1k\Omega$
Resistors ($\frac{1}{4}W$)	R56, R18	---	100Ω
BNC jack	J15	---	---
5 pin SIP	J4-J11	---	---
2 pin SIP	J13, J17, J18	---	---
4 pin power jack	J65	---	---
Capacitors (Ceramic)	C48-C55	---	$0.01\mu F$
Capacitors (Ceramic)	C60-C67	---	$0.1\mu F$
Capacitor (Tantalum)	C1, C2	---	$0.1\mu F$
Capacitor (Aluminium)	C58	---	$0.1\mu F$
5V voltage regulator	U58	LM7805	---
Heat Sink	U2	---	---

Table B-4 RCM Logic Signal Board, Component List

10▪3▪4 INJECTOR SIGNAL

This circuit board contains one pulse circuit to specify the injector lift and a width circuit to specify the injector hold duration.

Figure B-18 Counter Circuit, Start, Injector Circuit
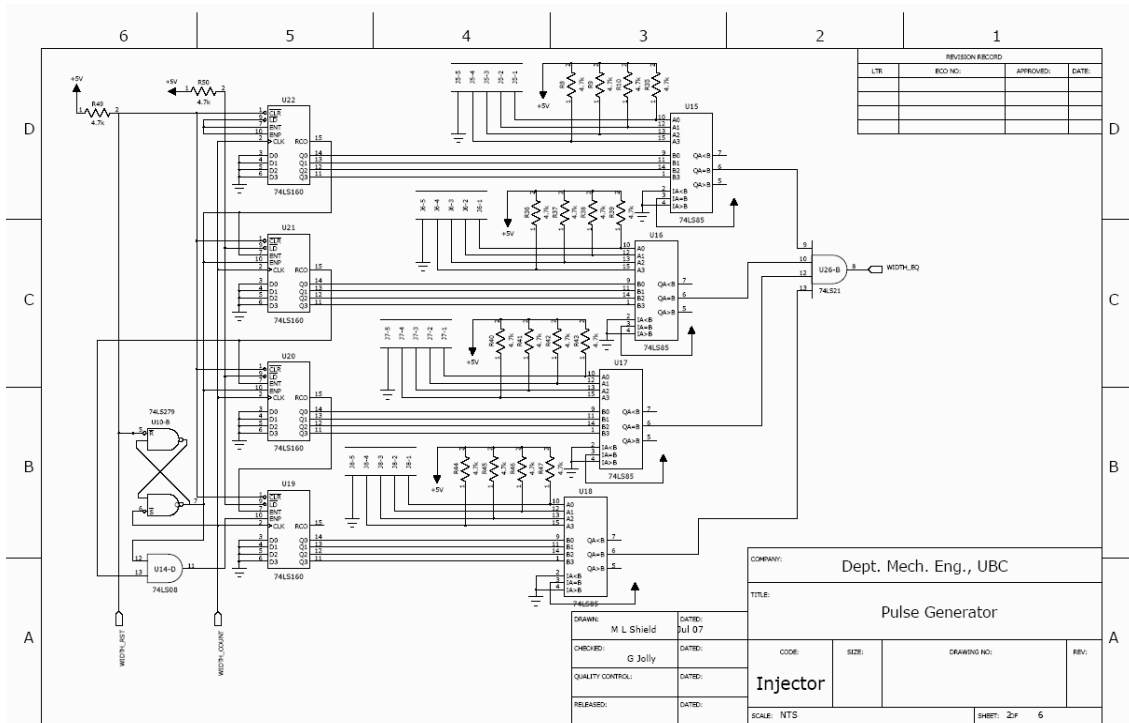
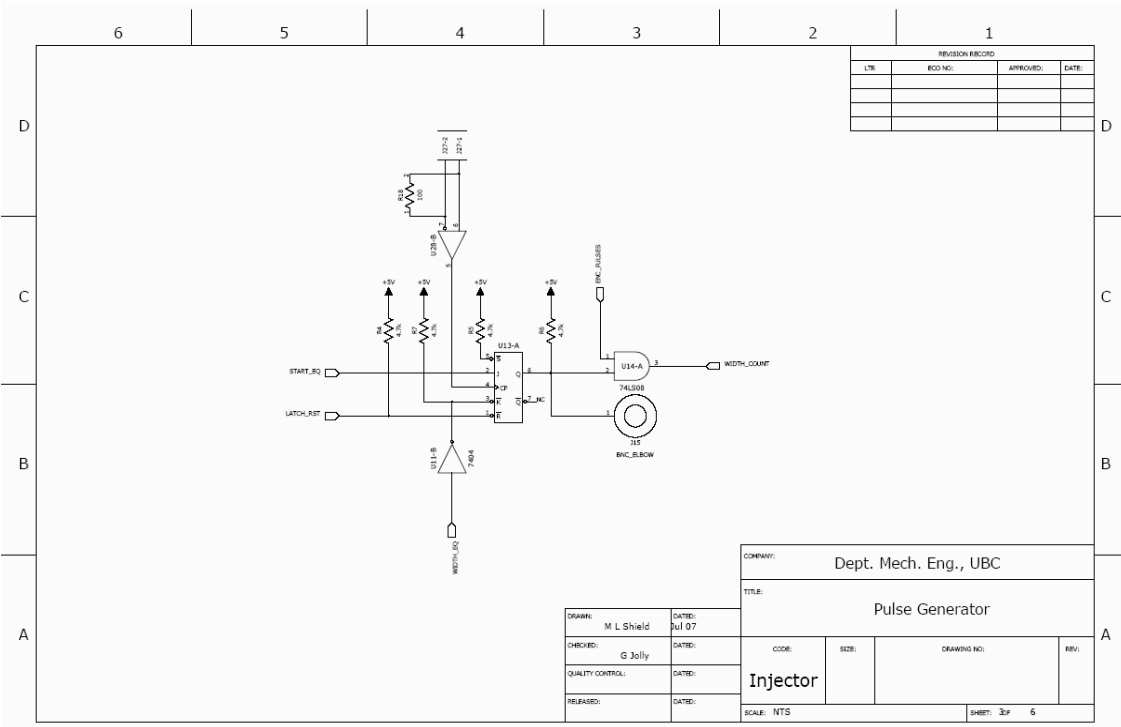**Figure B-19 Counter Circuit, Duration, Injector Circuit**
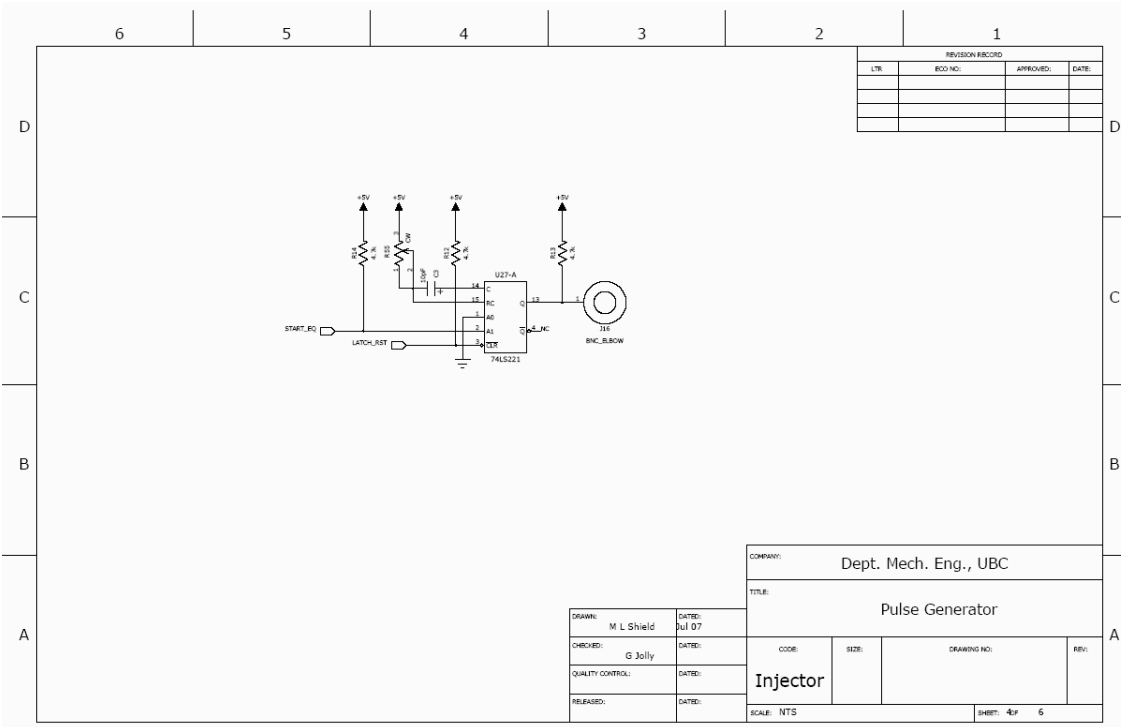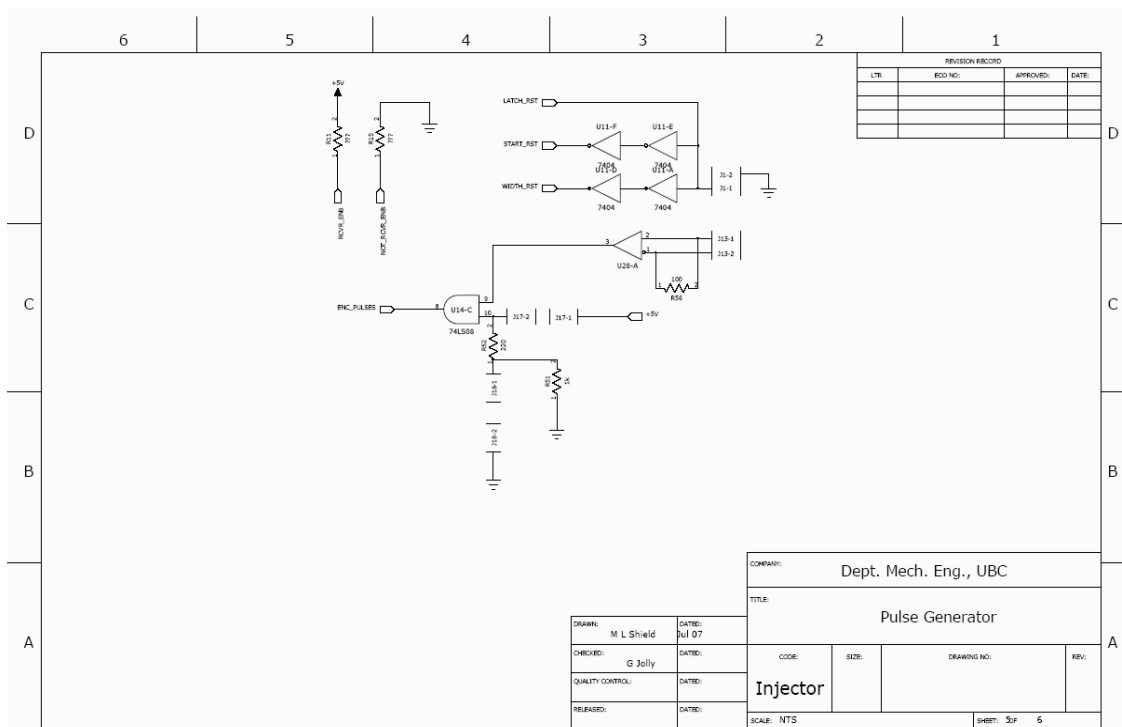
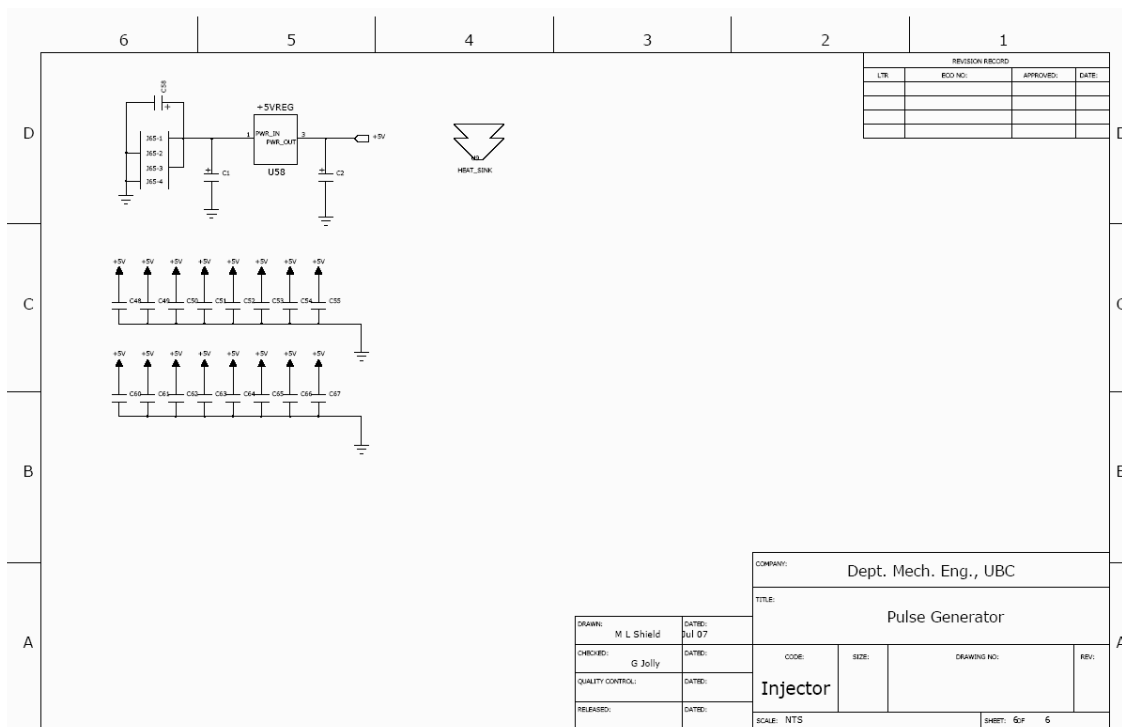**Figure B-20 J-K Flip Flop injector Circuit**

Figure B-21 Reset Circuit, Injector

Figure B-22 Signal Receiving, Injector Circuit

Figure B-23 Smoothing Capacitors, Injector Circuit

Component	Component #	Part #	Value
Quad-AND, 14 pin DIP	U14	74LS08	---
Dual R-S latch, 14 pin DIP	U10	74LS279	---
Counter, 16 pin DIP	U19-U22, U5-U8	74LS85	---
Comparator, 16 pin DIP	U1-U4, U15-U18	74LS160	---
Resistors (¼W)	All R, unless otherwise listed	---	4.7kΩ
Dual-4 in AND, 16 pin DIP	U26	74LS21	---
Dual multivibrator, 16 pin DIP	U27	74LS221	---
Dual J-K flip-flop, 16 pin DIP	U13	74LS109	---
Hex-inverter, 14 pin DIP	U11	74LS04	---
Liner Receiver, 14 pin DIP	U28	AM26LS32	---
Oscillator	U31	ACH-10.000MHZ-EK	10MHz
Resistors (¼W)	R52	---	220Ω
Resistors (¼W)	R51	---	1kΩ
Resistors (¼W)	R18	---	100Ω
Trim Pot	R55	---	10kΩ
BNC jack	J15, J16	---	---
5 pin SIP	J5-J8, J19-J22	---	---
2 pin SIP	J17, J18, J27	---	---
3 pin SIP	J14, J19-J21, J28-J35	---	---
4 pin power jack	J65	---	---
Capacitors (Ceramic)	C47, C59	---	10pF
Capacitors (Ceramic)	C48-C55	---	0.01μF
Capacitors (Ceramic)	C60-C67	---	0.1μF
Capacitor (Tantalum)	C1, C2	---	0.1μF
Capacitor (Aluminium)	C58	---	0.1μF
5V voltage regulator	U58	LM7805	---
Heat Sink	U2	---	---

Table B-5 RCM Injector Board, Component List

B▪9▪3 DISTRIBUTION CIRCUIT

This board receives the signal from the encoder gate and then distributes it.

Component	Component #	Part #	Value
Dual R-S latch, 14 pin DIP	U10	74LS279	---
Resistors (¼*W*)	All R, unless otherwise listed	---	4.7*kΩ*
Hex-inverter, 14 pin DIP	U32, U33	74LS04	---
Liner Receiver, 14 pin DIP	U28	AM26LS32	---
Liner Driver, 14 pin DIP	U9	AM26LS31	---
Resistors (¼*W*)	R15	---	50*Ω*
Trim Pot	R55	---	10*kΩ*
BNC jack	J1	---	---
5 pin SIP	J5-J8, J19-J22	---	---
2 pin SIP	J17, J18, J27	---	---
4 pin power jack	J65	---	---
Capacitors (Ceramic)	C23, C48-C55	---	0.01*μF*
Capacitors (Ceramic)	C60-C67	---	0.1*μF*
Capacitor (Tantalum)	C1, C2	---	0.1*μF*
Capacitor (Aluminium)	C58	---	0.1*μF*
5V voltage regulator	U58	LM7805	---
Heat Sink	U1	---	---

Table B-6 RCM Signal Distribution Board, Component List

Figure B-24 Signal Distribution Circuits

B▪10   APPENDIX 2: MECHANICAL HOUSING

Each circuit board has an aluminium front panel which mounts all LED's and switches. Card guides allow the easy removal and replacement of the circuit-boards, which are held in place with a #8 thumbscrew on the front panel and a locking nut on the BNC jacks at the rear. The control box reset and power supply are mounted on the right of the box with the mains power input and fuse located on the rear of the box. The top cover gives access to all signal and power distribution cables. The mechanical enclosure for the PCB's of the preceding circuits is presented in *Figure B-25*.
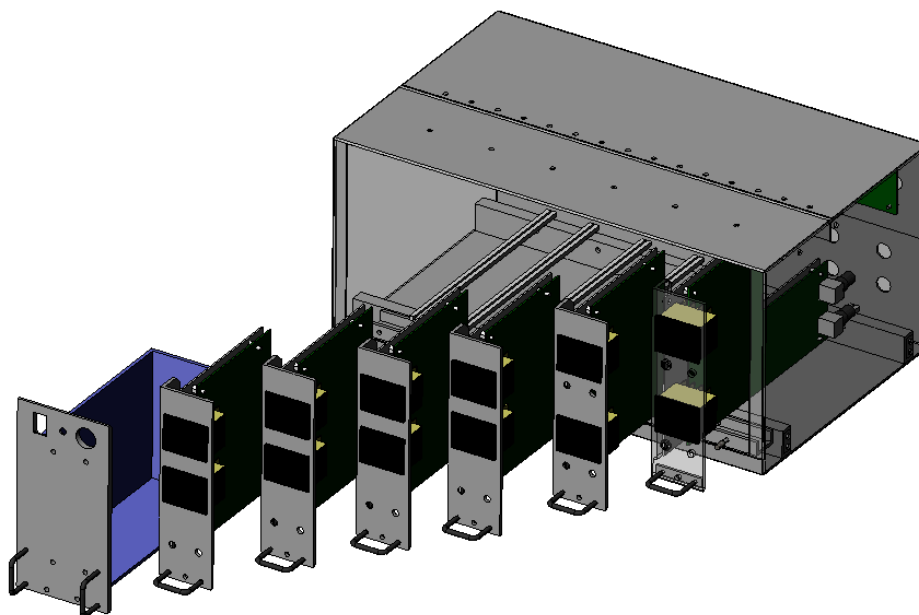
Figure B-25 RCM **Control Circuit Enclosure**

Appendix C
RELATIVE AIR-FUEL-RATIO PDFs

### C▪1 INTRODUCTION

Appendix C presents the relative air-fuel ratio probability density functions for all points in the central composite test matrices at the four stations considered in the capillary injected PSC study and the five stations considered in the insert injected PSC study.
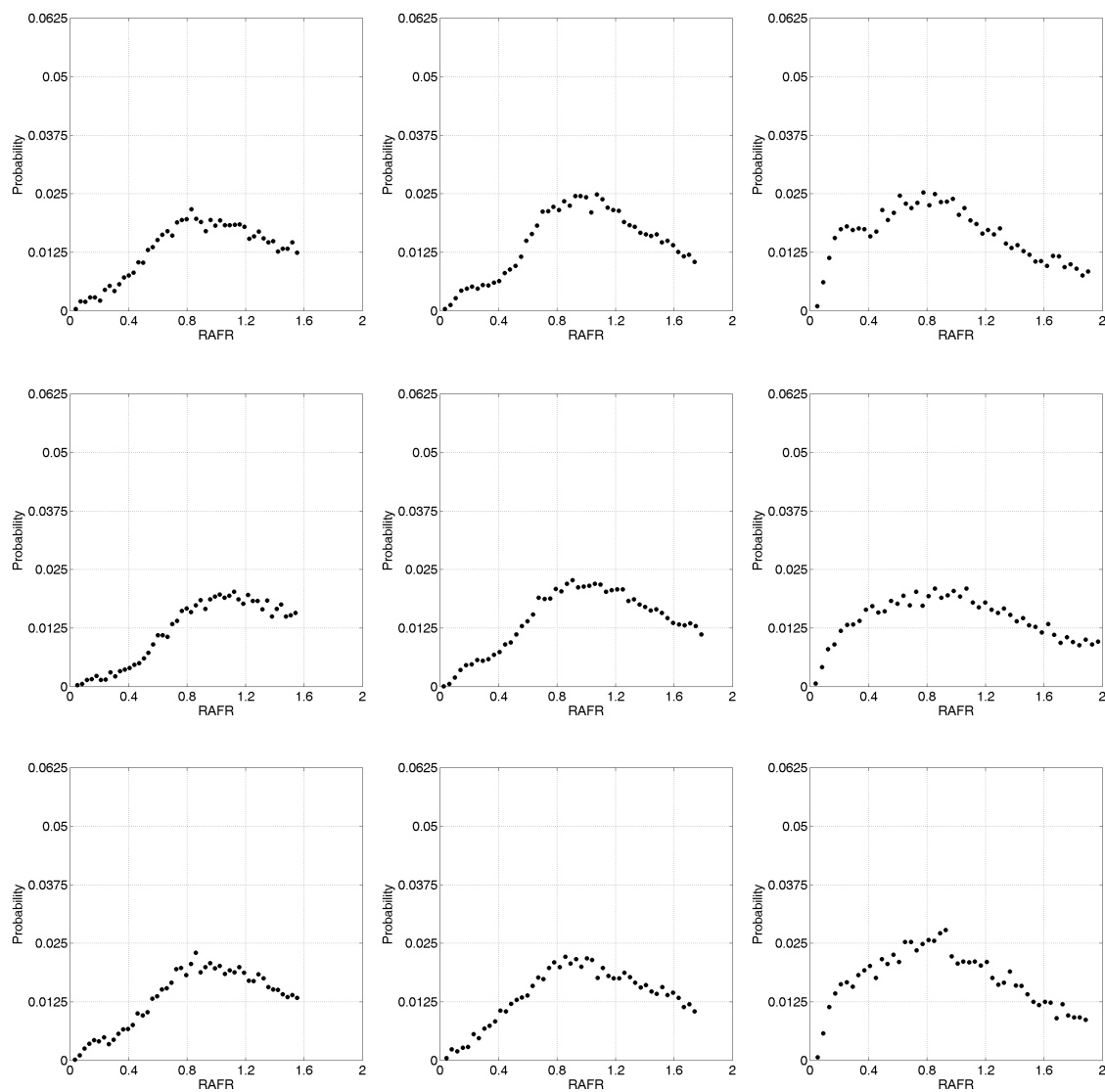
C▪2 RELATIVE AIR-FUEL RATIO PROBABILITY DENSITY FUNCTIONS FOR CAPILLARY INJECTED PSC-DI INTERACTION
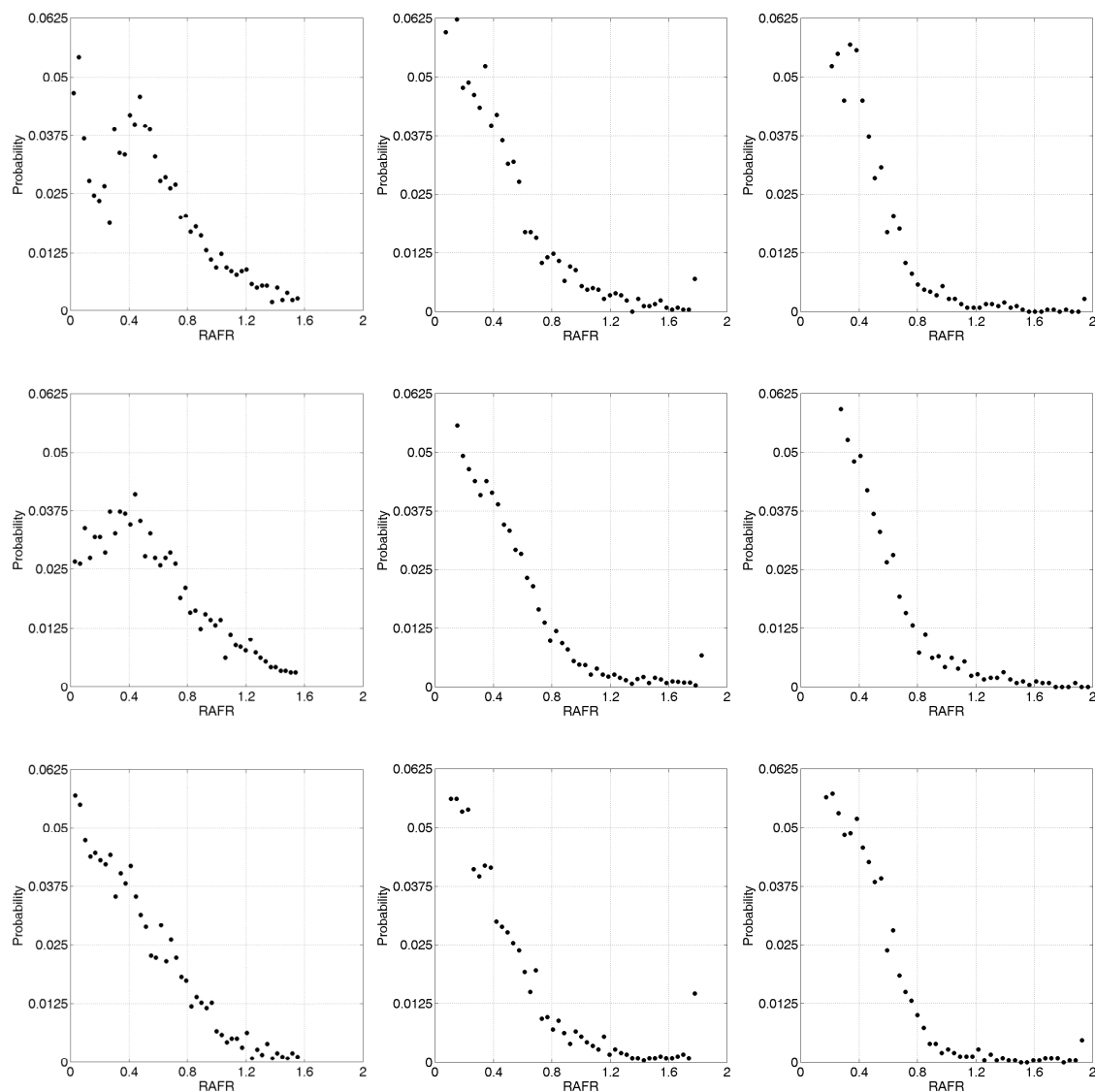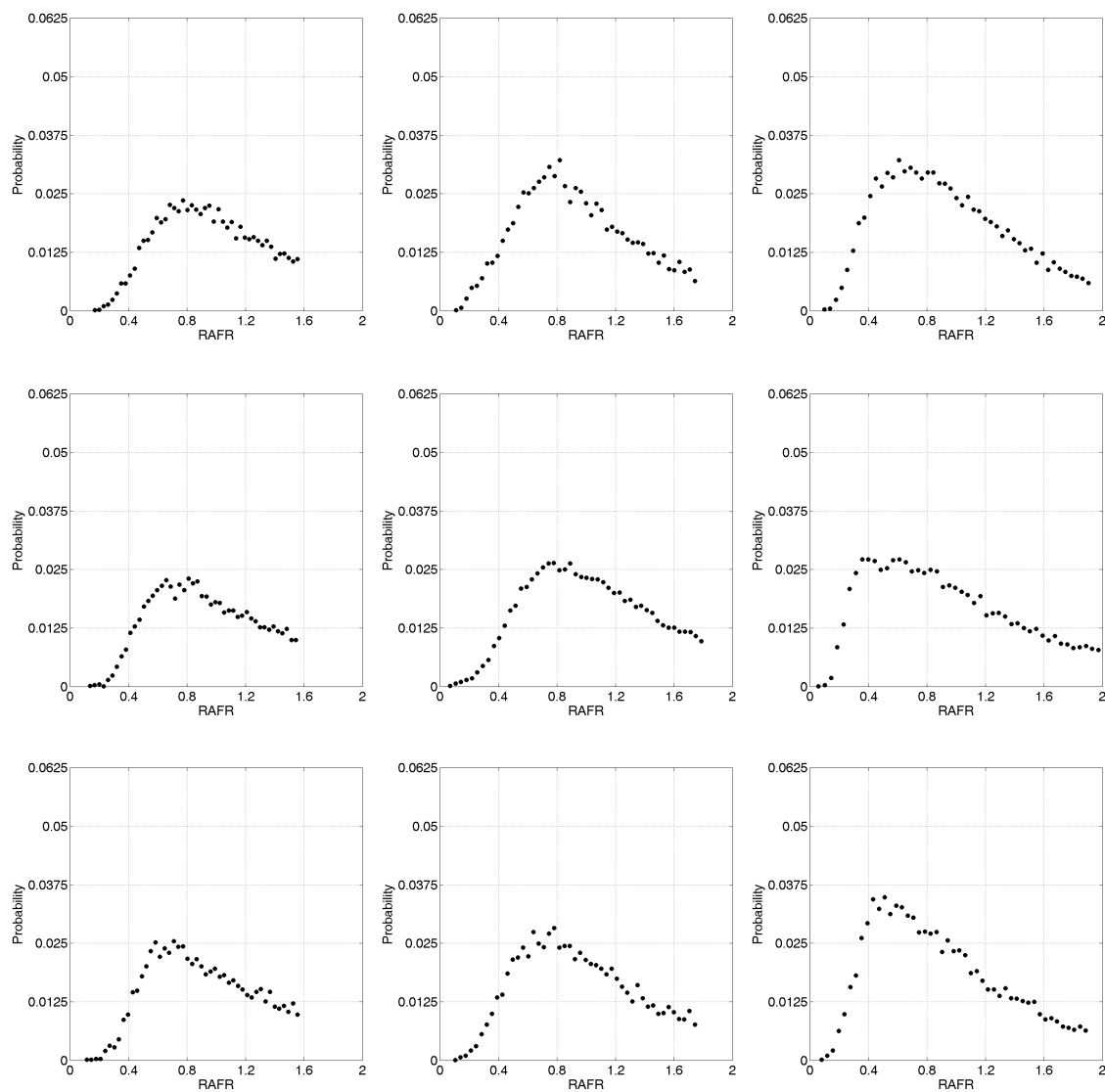

Figure C-1 Relative Air Fuel Ratio Probability Density Functions for Capillary Injected PSC Event with DI at Station One (Following Standard Image Presentation Protocol Used in Main Text, and Station Location as Per *Table 8-1*)

262
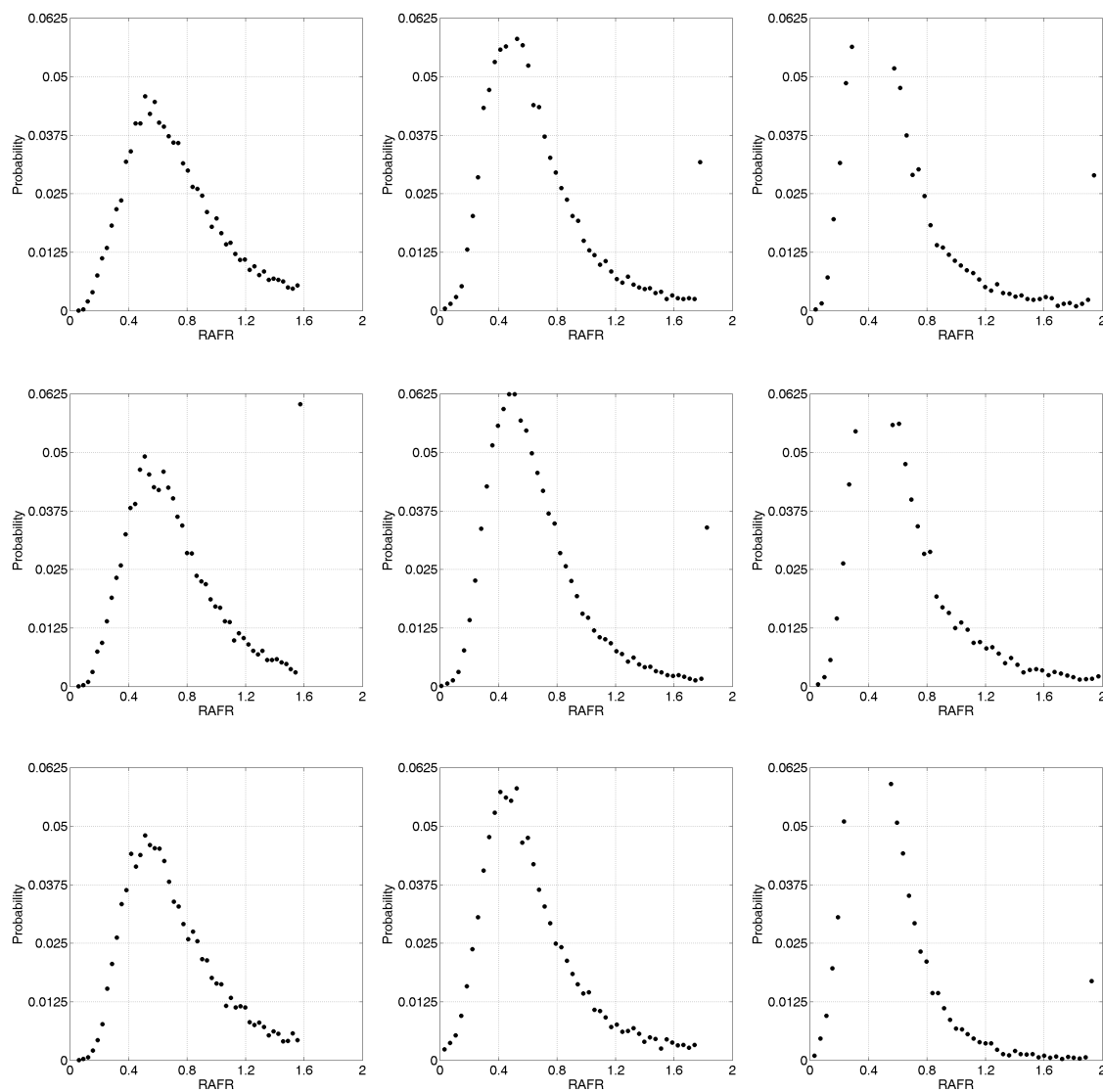
Figure C-2 Relative Air Fuel Ratio Probability Density Functions for Capillary Injected PSC Event with DI at Station Two (Following Standard Image Presentation Protocol Used in Main Text, and Station Location as Per *Table 8-1*)
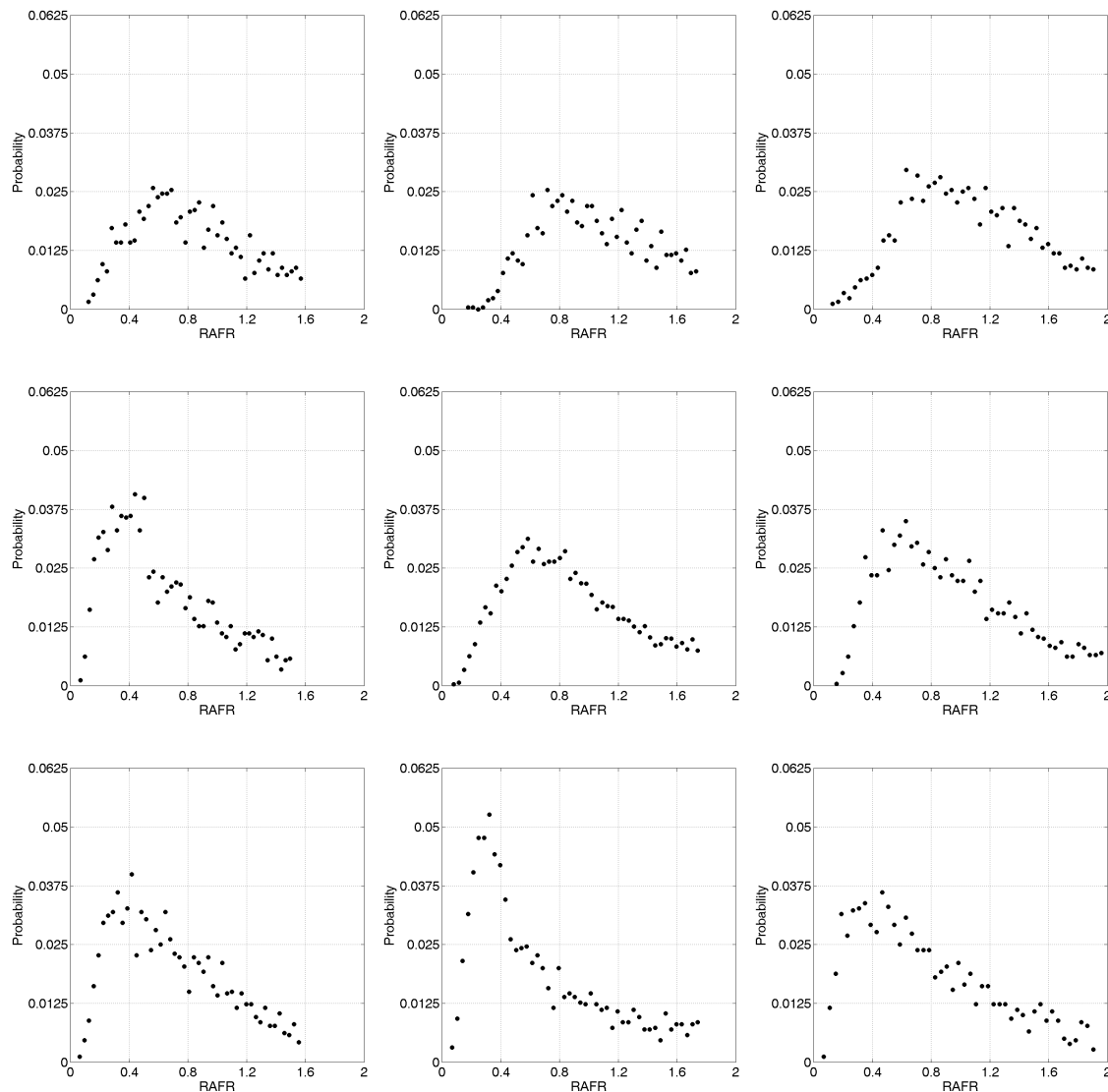
Figure C-3 Relative Air Fuel Ratio Probability Density Functions for Capillary Injected PSC Event with DI at Station Three (Following Standard Image Presentation Protocol Used in Main Text, and Station Location as Per *Table 8-1*)
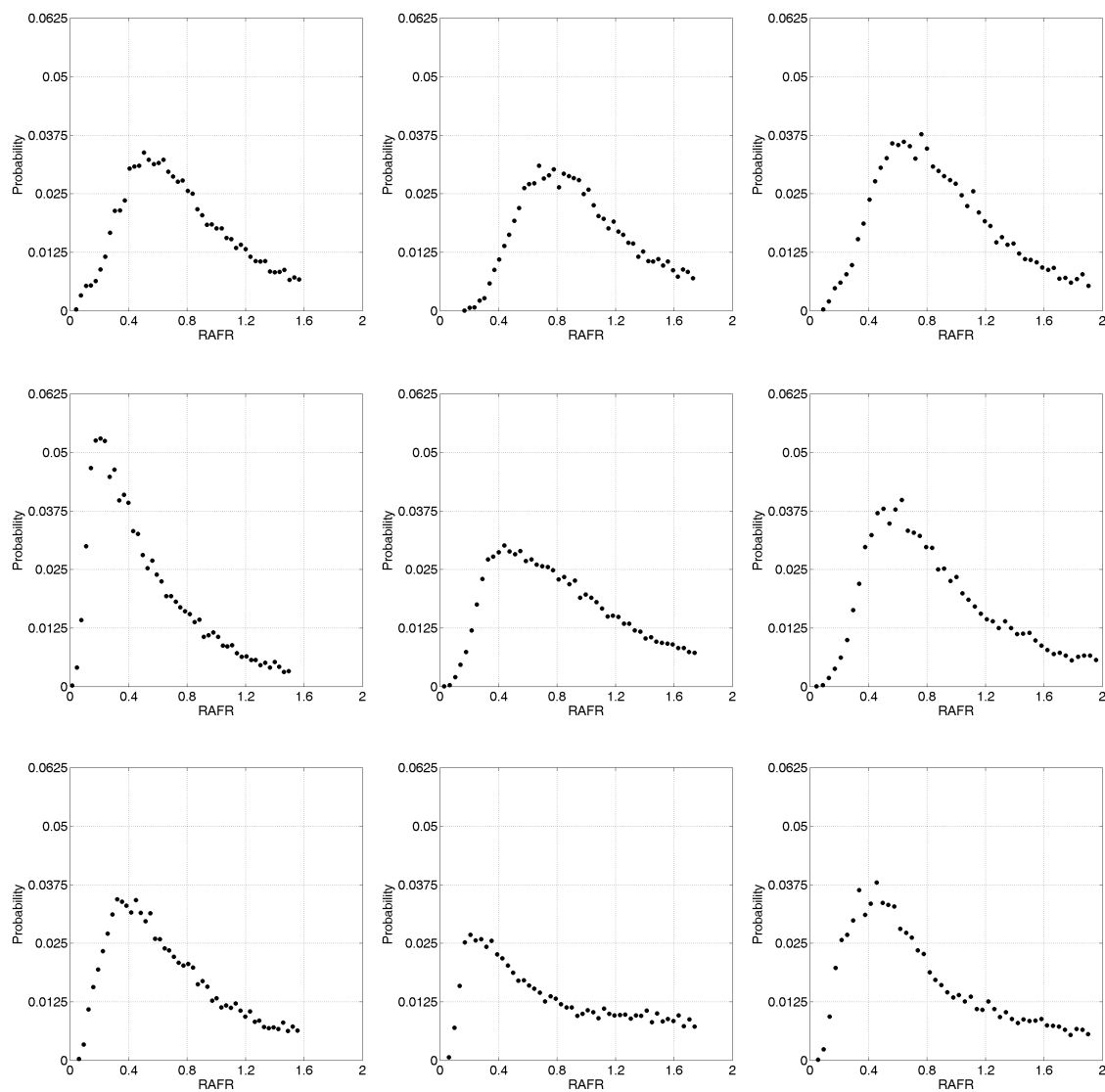
Figure C-4 Relative Air Fuel Ratio Probability Density Functions for Capillary Injected PSC Event with DI at Station Four (Following Standard Image Presentation Protocol Used in Main Text, and Station Location as Per *Table 8-1*)
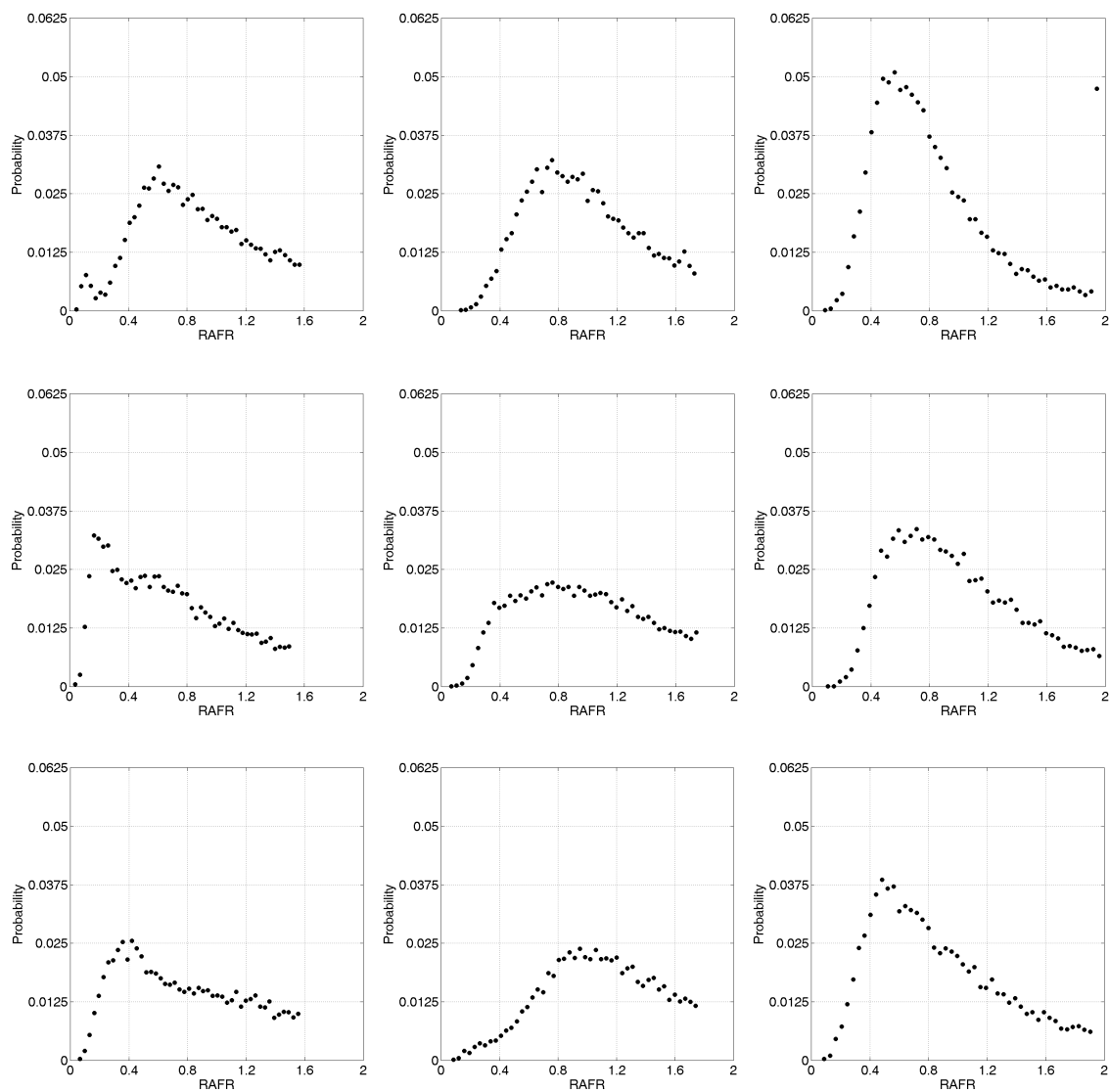
C▪3 RELATIVE AIR-FUEL RATIO PROBABILITY DENSITY FUNCTIONS FOR INSERT INJECTED PSC-DI INTERACTION

Figure C-5 Relative Air Fuel Ratio Probability Density Functions for Insert Injected PSC Event with DI at Station One (Following Standard Image Presentation Protocol Used in Main Text, and Station Location as Per *Table 8-3*)
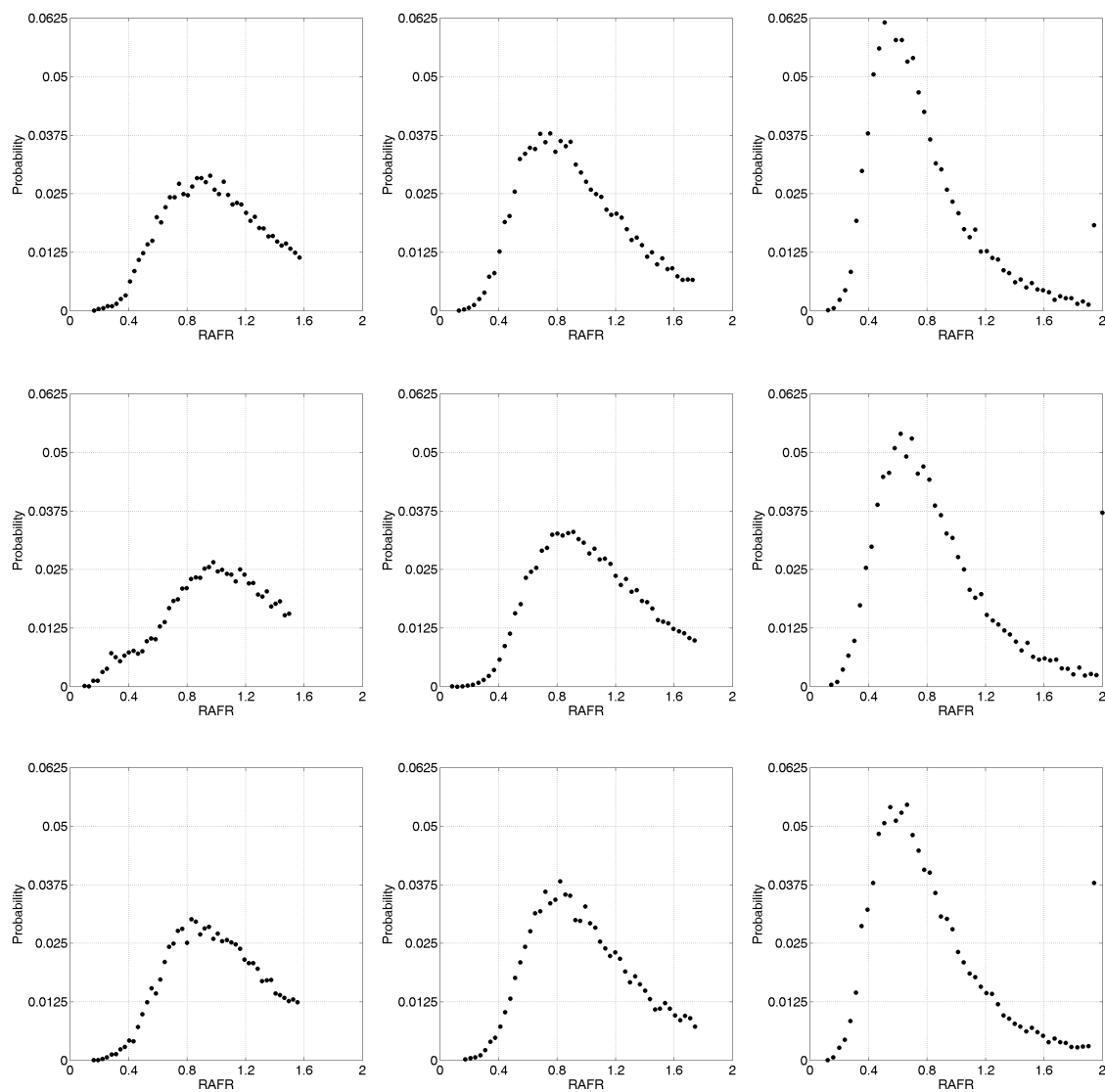
Figure C-6 Relative Air Fuel Ratio Probability Density Functions for Insert Injected PSC Event with DI at Station Two (Following Standard Image Presentation Protocol Used in Main Text, and Station Location as Per *Table 8-3*)
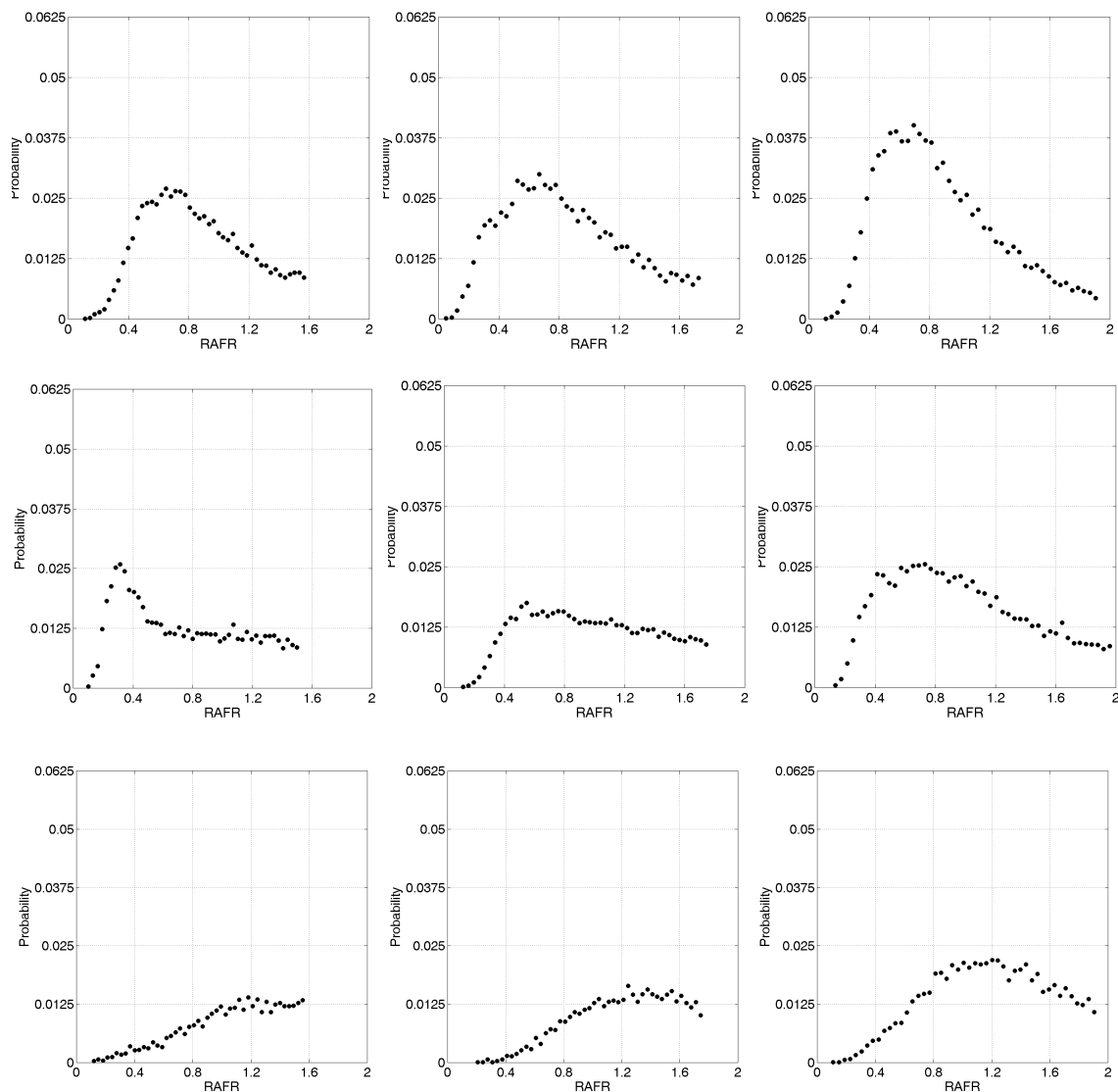
Figure C-7 Relative Air Fuel Ratio Probability Density Functions for Insert Injected PSC Event with DI at Station Three (Following Standard Image Presentation Protocol Used in Main Text, and Station Location as Per *Table 8-3*)

Figure C-8 Relative Air Fuel Ratio Probability Density Functions for Insert Injected PSC Event with DI at Station Four (Following Standard Image Presentation Protocol Used in Main Text, and Station Location as Per *Table 8-3*)

Figure C-9 Relative Air Fuel Ratio Probability Density Functions for Insert Injected PSC Event with DI at Station Five (Following Standard Image Presentation Protocol Used in Main Text, and Station Location as Per *Table 8-3*)

Appendix D
STATISTICAL TREATMENTS

D▪1 INTRODUCTION

Appendix D presents a basic summary of the for four of the most important statistical techniques used in this study, those of central composite test matrix design, the normal and Poisson distributions and the specification of the 95% confidence interval for a data sample.

D▪2 DESIGN OF EXPERIMENTS

The aim of any experimental design is to collect data as parsimoniously as possible, whilst still maintaining the accuracy of the information collected. In general the experimenter is required to fit the experimental response, y, to the variables $x_1, x_2, x_3...x_k$. For a second order response in 2D space the model is fit according to *Eq.D.1*

$$y = \beta_0 + \sum_{i=1}^{k} \beta_i x_i + \sum_{i=1}^{k} \beta_i x_i^2 + \sum \sum_{i<j=2}^{k} \beta_{ij} x_i x_j + \varepsilon \qquad \text{Eq. D.1}$$

where k is the number of experimental factors (or variables). *Eq.D1* exhibits, in order, *main* (or linear) effects, *quadratic* effects, *interaction* effects and an associated error (of which more later). In designing an experiment to provide enough data to accurately evaluate *Eq.D1* it is common practice to use a *central composite design* (CCD) for responses which may have moments up to, and including, the second order. The quadratic response, which will posses only a single maximum or minimum, can be found from the set of points defined by the CCD without extra assumptions. To apply the CCD the experimental variables ξ_1, ξ_2, ξ_3... ξ_k are transformed into the variables $x_1, x_2, x_3...x_k$ of *Eq.D.1*. The coded variables are generally transformed to fit the interval $-\sqrt{k} \leq x_i \leq \sqrt{k}$ (where k is the number of factors).

In general the experimental design will have F factorial points, *2k* axial points and n_c centre-runs (*cf.* Figure xx). The F points provide the linear response and the two-factor interactions, the axial points estimate the pure quadratic terms and the centre-runs estimate the internal pure-error and help with the quadratic term estimation. It can be shown that **[417]** the centre-runs reduce the prediction variance at the centre of the design space, weighting the variance towards the extrema of the space. In general three to five centre-runs avoid severe imbalance and level the predication variance across the response hypersurface.

The response y is bounded in the design space by the interval $-1 \leq x_i \leq 1$, however the designer is still faced with three options as to the location of the design points. The options are shown in *Figure D:1* for a two-dimensional design space ($k=2$). The circumscribed design fits data well across the design space, while the inscribed design provides bias to a central subset of the experimental range (at the expense of the extrema). Finally, the face-centred option, is fair across the entire space, but with poor accuracy for the response quadratic terms. Which design is chosen is a matter for careful consideration by the designer, and must reflect his/her ability to judge the importance of extrema in the experimental range and the experimental accessibility of these points.
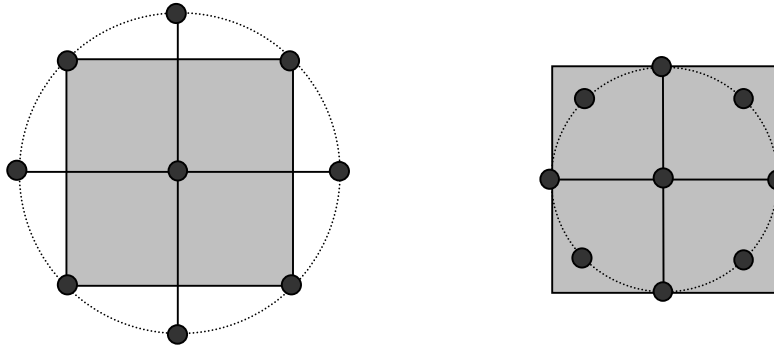
Figure D-1 (a) Circumscribed Central Composite Design (b) Inscribed Central Composite Design, Test Domain Shown in Grey, Data Points as Black Dots

D▪3 RANDOM VARIABLES & THEIR DISTRIBUTIONS

As is standard for most engineering and scientific applications the random variable of concern (which will be addressed in more detail shortly) is considered to be discreet since it is most likely to have a countable or a countably infinite set of values.

The population of concern may be sampled (the purpose of any experiment) to produce the random variable X. X may be comprised of a single event ($X = x_1$), a series of individual events ($X = x_1, x_2, x_3…x_n$) or may be a the results of an arbitrary function applied to individual events ($X = X_1, X_2, X_3…X_n$). The probability of an event taking place is described by the probability density, or simply the density, function $f(z)$.

The first moment of the density distribution (which represents to true population) is the distribution mean, μ, which is the expected value of random variable X and discrete from the sample (arithmetic) mean $\overline{X}$, *viz.*:

$$\overline{X} = \frac{1}{n}\sum_{i=1}^{n} X_i$$

Eq. D.2

If each realisation of X_i is also normally distributed it can be shown that the expected value (*i.e.* the mean) of $\overline{X}$ is equal to the common mean, μ, of the X_i^{th} distribution. Similarly, if the distribution realisations share a common variance, σ^2, the variance of $\overline{X}$ is simply σ^2/n for n realisations. The second moment about the mean for any density function is the variance, σ^2, which corresponds to the expected value of $(X-\mu)^2$, with the corresponding value for a population sample denoted by S^2.

$$S^2 = \frac{1}{n}\sum_{i=1}^{n} (X_i - X)^2$$

Eq. D.3

Variance is often used interchangeably with standard deviation which is, arithmetically, the square root of the variance.

D▪3▪1   THE NORMAL DISTRIBUTION

As with most random variables that are evaluated to high degree of accuracy the transformation of discreet values to continuous ones is made to allow the application of continuous density functions, such as the normal density distribution *Eq.D.4*

$$f_X(z) = \frac{1}{\sqrt{2\pi}\sigma} e^{-(z-\mu)^2/2\sigma^2} \qquad\qquad -\infty < z < \infty \qquad \textbf{Eq. D.4}$$

The non-trivial integration of *Eq.D4* to yield event probabilities is circumvented through the use of normal integral tables. This, and other applications, requires the transformation of the recorded distribution into one which has zero mean and unity variance. This is done through use of the expressions in *Eq.D.5*

$$v = \frac{z - \mu}{\sigma} \qquad\qquad dz = \sigma dv \qquad\qquad \textbf{Eq. D.5}$$

such that *Eq.D4* is now simplified to the normalized distribution of *Eq.D.6*.

$$f_N(v) = \frac{1}{\sqrt{2\pi}} e^{-v^2/2} \qquad\qquad \textbf{Eq. D.6}$$

Integration of the normalized density function from a specified upper percentage point, K_α (defined as $(b-\mu)/\sigma$, where b is the upper percentage point in the original distribution), to infinity evaluates the probability $P\{X>b\}$. Values of this integral for many K_α limits are widely presented. The symmetry of the normal distribution is used to evaluate negative values of K_α through noting that $P\{N<-K_\alpha\} = P\{N>K_\alpha\}$, and similarly $P\{N \geq -K_\alpha\} = 1-P\{N>K_\alpha\}$.

D▪3▪2   THE T DISTRIBUTION

The random variable, t, for the distribution is defined by the quotient of *Eq.D.7* which involves the two independent random variables of the normal, X (with zero mean and unity variance), and chi-squared, χ^2, distributions discussed previously.

$$t = \frac{X\sqrt{v}}{\sqrt{\chi^2}} \qquad\qquad \textbf{Eq. D.7}$$

The resulting density expression is non-trivial in its derivation and inconsequential for the current work. As with the normal and chi-squared distributions, tabulated values of $P\{t \geq t_{\alpha;v}\}$ are widely available, and applicable as described in *§D▪3▪1*.

D▪3▪3   THE POISSON DISTRIBUTION

One of the most simple, yet useful, distributions is that of the Poisson distribution, which has a density function given by *Eq.D.8*

$$f_x(z) = \frac{\lambda^z e^{-\lambda}}{z!} \qquad\qquad \textbf{Eq. D.8}$$

This discreet distribution describes well particulates, electron interaction, radioactive particle behaviour or any event which has a large possible number of outcomes each with a low probability. The application of this distribution is simplified by virtue of one interesting property: the mean and variance are the same and equal to the distribution parameter λ.

D▪4 CONFIDENCE INTERVALS

When a sample mean is calculated, it is important to specify the limits over which the mean is valid. This is most commonly expressed through the used of confidence intervals. In almost all cases the mean and standard deviation of the normally distributed random variable are not know. Under these circumstances the sample standard deviation, *S*, is taken as a proxy for the population standard deviation, with a correction factor included. This correction factor, it can be shown **[368]**, is related to the *t*-distribution such that the confidence interval, about the (known) sample mean is:

$$\pm t_{\alpha/2;n-1} \frac{S}{\sqrt{n}} \qquad \text{Eq. D.9}$$

where $t_{\alpha/2;n-1}$ is the tabulated $100\alpha/2$ percentage point of the *t*-distribution with *n-1* degrees of freedom (*i.e.* 2.5% point for a 95% confidence interval). If the population mean and standard deviation are both unknown *Eq.D.10* must be revised such that the (non-uniform) confidence interval is given by:

$$\left[S\sqrt{\frac{n-1}{\chi^2_{\alpha/2;n-1}}} \quad , \quad S\sqrt{\frac{n-1}{\chi^2_{1-\alpha/2;n-1}}} \right] \qquad \text{Eq. D.10}$$